SURFEX SCIENTIFIC DOCUMENTATION

P. Le Moigne

February 23, 2018

EDITOR : Patrick Le Moigne

Contributing authors :

2018
C. Albergel [(1)], A. Boone [(1)], S. Belamari [(1)], B. Decharme [(1)], M. Dumont [(4)],
P. Le Moigne [(1)], V. Masson [(1)]

2012
A. Boone [(1)], S. Belamari [(1)], E. Brun [(1)], J.-C. Calvet [(1)], B. Decharme [(1)], H. Giordani [(1)],
S. Lafont [(1)], P. Le Moigne [(1)], S. Morin [(4)], V. Vionnet [(1)]

2009
A. Boone [(1)], J.-C. Calvet [(1)], B. Decharme [(1)], S. Faroux [(1)], A.-L. Gibelin [(1)], C. Lebeaupin [(2)],
P. Le Moigne [(1)], J.-F. Mahfouf [(1)], E. Martin [(1)], V. Masson [(1)], D. Mironov [(3)], J. Noilhan [(1)],
P. Tulet [(1)], B. Van Den Hurk [(4)]

[(1)] : CNRM-UMR3589, Météo-France/CNRS, Toulouse, France
[(2)] : Laboratoire de Météorologique Dynamique, Ecole Polytechnique, Palaiseau, France
[(3)] : German Weather Service, Offenbach am Main, Germany
[(4)] : CNRM-UMR3589, Météo-France/CNRS, Grenoble, France
[(5)] : KNMI, The Netherlands

Dissemination Level : public

ISSUE No		DATE	PAGES	DESCRIPTION OF CHANGE
1	V5.0	May 2009	1 - 211	Original
2	V7.2	March 2012	1 - 235	Description of Crocus, Isba-CC, Teb-Veg Bibliography references by chapter
3	V8.0 and V8.1	February 2018	1 - 304	Description of MEB, TARTES, Revision of ISBA-ES, ISBA-DF Revision of TEB+VEG Revision of water surfaces

SURFEX

Part I

SURFACE PROCESSES SCHEME

Chapter 1

Introduction: a brief description of the SURFEX system

Surface modelling in numerical weather prediction has always held an important place in the activities of the Centre National de Recherches Météorologiques (CNRM hereafter). In the late 80's, Isba (Noilhan and Planton (1989); Mahfouf and Noilhan (1996)), a soil vegetation atmosphere transfer scheme (Interaction between Soil Biosphere and Atmosphere) has been developed and it aimed to better simulate the exchanges of energy and water between the land surface and the atmosphere just above. Isba model has been designed to be simple and efficient in order to be put into operations at Météo-France. Isba scheme computes the exchanges of energy and water between the continuum soil-vegetation-snow and the atmosphere above. In its genuine version, the evapotranspiration of the vegetation is controlled by a resistance like proposed by Jarvis (1976) . A more recent version of the model named Isba-A-gs (Calvet *et al.* (1998)) accounts for a simplified photosynthesis model where the evaporation is controlled by the aperture of the stomates, the component of the leaves that regulates the balance between the transpiration and the assimilation of CO2. Nowadays, Isba land surface scheme is used in the French operational and research forecast models. Thanks to the efforts made by the research community at CNRM, French numerical weather prediction models have always been at the forefront of research in terms of surface modelling. More recently, the modelling of urban areas has began to be of great interest in the research community. In 2000, TEB (Town Energy Balance) model, specially designed to represent the exchanges between a town and the atmosphere has enabled advanced studies in this direction (Masson (2000)). The TEB model is based on the canyon concept, where a town is represented with a roof, a road and two facing walls with characteristics playing a key role in the town energy budget. More especially, the ability, of the canyon to trap a fraction of the incoming solar and infrared radiation is taken into account in the model. A special effort has been made this last years to externalize the surface scheme from the embedded surface-atmosphere Meso-NH model. The main idea was to gather all the developments and improvements made in surface schemes in order to make them available for as many people as possible. Not only physical parameterizations have been externalized, but also the preparation of specific surface parameters needed by physical schemes and the initialization of all state variables of the different models: SURFEX (stands for surface externalisée) system was born. Moreover, the surface representation has been improved and thus Surfex system has been enhanced with the specific treatment for water surfaces. Indeed, up to now, the exchanges of energy between water surfaces and the atmosphere were treated in a very simple way, while now a physically based model have been introduced to build a more complex but accurate surface model, available for all atmospheric models. There are two possibilities to compute fluxes over marine surfaces. The simplest one consists in using Charnock's approach to compute the roughness length and fluxes with a constant water surface temperature. Secondly,

a one-dimensional ocean mixing layer model has been introduced (Lebeaupin (2007)) in order to simulate more accurately the sea surface temperature (SST hereafter) and the fluxes at the sea/air interface. This model based on Gaspar (1990) , will be very helpful especially at meso-scale to better represent diurnal cycle of SST. At meso-scale, a good representation of lakes is of great interest especially for Northern countries. In order to improve the treatment of lake areas, the simple but robust Flake model (Mironov (2010)) has been implemented within Surfex system. It allows to have an evolving lake surface temperature and a good description of the energy exchanges within water.

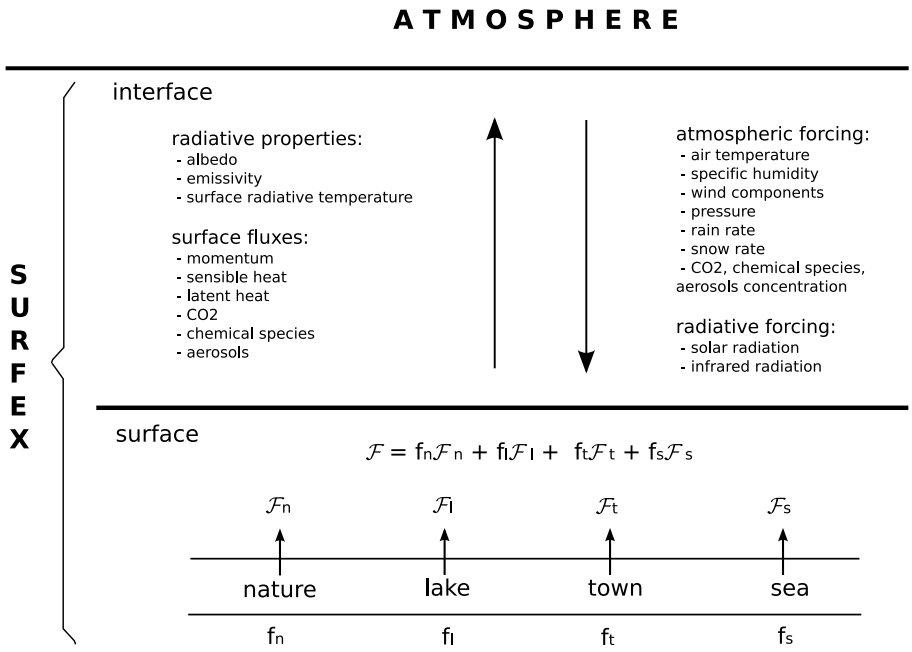

Figure 1.1: Description of the exchanges between an atmospheric model sending meteorological and radiative fields to the surface and Surfex composed of a set of physical models that compute tiled variables $\mathcal{F}_*$ covering a fraction f_* of a unitary grid box and an interface where the averaged variables $\mathcal{F}$ are sent back to the atmosphere

In Surfex, the exchanges between the surface and the atmosphere are realized by mean of a standardized interface (Polcher *et al.* (1998); Best *et al.* (2004)) that proposes a generalized coupling between the atmosphere and surface. During a model time step, each surface grid box receives the upper air temperature, specific humidity, horizontal wind components, pressure, total precipitation, long-wave radiation, short-wave direct and diffuse radiations and possibly concentrations of chemical species and dust. In return, Surfex computes averaged fluxes for momentum, sensible and latent heat and possibly chemical species and dust fluxes and then sends these quantities back to the atmosphere with the addition of radiative terms like surface temperature, surface direct and diffuse albedo and also surface emissivity.

All this information is then used as lower boundary conditions for the atmospheric radiation and turbulent schemes. In Surfex, each grid box is made of four adjacent surfaces: one for nature, one for urban areas, one for sea or ocean and one for lake. The coverage of each of these surfaces is known through the global ECOCLIMAP database (Masson *et al.* (2003)) , which combines land cover maps and satellite information. The Surfex fluxes are the average of the fluxes computed over nature, town, sea/ocean or lake, weighted by their respective fraction.

Bibliography

[1] M. J. Best, A. Beljaars, J. Polcher, and P. Viterbo. A proposed structure for coupling tiled surfaces with the planetary boundary layer. *J. Hydrometeorol.*, 5(6):1271–1278, December 2004.

[2] J. C. Calvet, J. Noilhan, J. L. Roujean, P. Bessemoulin, M. Cabelguenne, A. Olioso, and J. P. Wigneron. An interactive vegetation svat model tested against data from six contrasting sites. *Agric. and For. Meteorol.*, 92(2):73–95, July 1998.

[3] P. Gaspar, Y. Grégoris, and J.-M. Lefevre. A simple eddy kinetic energy model for simulations of the oceanic vertical mixing: Tests at station papa and long-term upper ocean study site. *J. Geophys. Res.*, 95(C9):16179–16193, 1990.

[4] P. G. Jarvis. The interpretation in the variations of leaf water potential and stomatal conductance found in canopies in the field. *Philos. Trans. R. Soc. London*, B. 273:593–610, 1976.

[5] C. Lebeaupin. *Etude du couplage océan-atmosphère associé aux épisodes de pluies intenses en région méditerranéenne*. PhD thesis, University Paul Sabatier, Toulouse, France, 2007.

[6] J. F. Mahfouf and J. Noilhan. Inclusion of gravitational drainage in a land surface scheme based on the force-restore method. *J. Appl. Meteorol.*, 35(6):987–992, June 1996.

[7] V. Masson. A physically-based scheme for the urban energy budget in atmospheric models. *Bound.-Layer Meteorol.*, 94(3):357–397, March 2000.

[8] V. Masson, J.-L. Champeaux, F. Chauvin, C. Meriguet, and R. Lacaze. A global database of land surface parameters at 1-km resolution in meteorological and climate models. *J. Clim.*, 16(9):1261–1282, 2003.

[9] D. Mironov, E. Heise, E. Kourzeneva, B. Ritter, N. Schneider, and A. Terzhevik. Implementation of the lake parameterisation scheme flake into the numerical weather prediction model cosmo. *Boreal Env. Res.*, 15:218–230, 2010.

[10] J. Noilhan and S. Planton. A simple parameterization of land surface processes for meteorological models. *Mon. Weather Rev.*, 117(3):536–549, 1989.

[11] J. Polcher, B. McAvaney, P. Viterbo, M. A. Gaertner, A. Hahmann, J. F. Mahfouf, J. Noilhan, T. Phillips, A. Pitman, C. A. Schlosser, J. P. Schulz, B. Timbal, D. Verseghy, and Y. Xue. A proposal for a general interface between land surface schemes and general circulation models. *Glob. and Planet. Change*, 19(1-4):261–276, December 1998.

Chapter 2

Water surfaces

Contents

2.1 Simple parameterization

2.1.1 Free water surfaces

For ocean surfaces and over inland waters, all the prognostic variables are kept constant.
The surface fluxes are calculated using Eqs. 4.182, 4.183, 4.185 and Eqs. 4.205, 4.206, 4.207 of Isba, taking the relative humidity of the ocean $hu = 1$, and $veg = p_{sn} = 0$. The roughness length is given by Charnock's relation:

$$z_{0sea} = 0.015\frac{u_*^2}{g} \tag{2.1}$$

2.1.2 Sea ice

Sea ice is detected in the model when sea surface temperature (SST) is two degrees below 0°C (i.e. 271.15 K). In this case, in order to avoid an overestimation of the evaporation flux, the calculations are performed with the roughness length of flat snow surfaces:

$$z_{0ice} = 10^{-3}m \tag{2.2}$$

In the same manner, the sea ice albedo is set equal to the fresh snow albedo instead of the free water albedo. This leads to a much brighter surface. This has no effect on the sea ice cover (since there is no evolution of the sea surface parameters), but modifies the lower boundary shortwave flux input for the atmospheric radiative scheme.

2.2 Sea surface turbulent fluxes

In this section, we introduce the various sea surface fluxes parameterizations available in the SURFEX surface scheme, namely the direct parameterization of Louis (1979) and four iterative parameterizations: the MR98 (Mondon and Redelsperger, 1998), the COARE3.0 (Fairall *et al.*, 2003) and the two versions of the ECUME (Belamari, 2005) parameterizations.

2.2.1 Bulk equations

Air-sea turbulent fluxes, *i.e.* the stress or momentum flux τ_{sea}, the sensible heat flux H_{sea} and the latent heat flux LE_{sea} are given by:

$$\left\{ \begin{array}{ll} |\vec{\tau}|_{sea} & = \rho_a(\overline{w'u'})_s \\ H_{sea} & = \rho_a c_{p_a}(\overline{w'\theta'})_s \\ LE_{sea} & = \rho_a \mathcal{L}_v(\overline{w'q'})_s \end{array} \right. \tag{2.3}$$

where w', u', θ' and q' stand for the fluctuations of the vertical speed, horizontal wind, potential temperature and specific humidity. s index stands for sea surface variables whereas a index stands for atmospheric variables at the "measurement's height" (actually at the lowest level of the model). $\mathcal{L}_v$ is the latent heat of seawater vaporization at sea surface, and c_{p_a} is the specific heat of moist air.
For this surface layer, four characteristic length scales can be derived from these surface fluxes, following the Monin and Obukhov (1954) theory, namely:

- the friction velocity u_* such as:

$$u_*{}^2 = -(\overline{w'u'})_s \tag{2.4}$$

- the temperature characteristic length scale θ_*:

$$\theta_* = -\frac{(\overline{w'\theta'})_s}{u_*} \tag{2.5}$$

- the humidity characteristic length scale q_*:

$$q_* = -\frac{(\overline{w'q'})_s}{u_*} \tag{2.6}$$

- and last, the Monin-Obukhov length L:

$$L = \frac{-u_*^3}{\kappa \frac{g}{\theta_v} \left(\overline{w'\theta_v{}'}\right)_s} \tag{2.7}$$

κ denotes the dimensionless von Kármán constant. θ_v is the virtual potential temperature:

$$\theta_v = \theta_a(1.0 + 0.61\ q_a) \tag{2.8}$$

Using the corresponding characteristic length scale θ_{v*} defined as:

$$\theta_{v*} = -\frac{(\overline{w'\theta_v{}'})_s}{u_*} \tag{2.9}$$

leads to another formulation of the Monin-Obukhov length L:

$$L = \left(\frac{u_*^2}{\kappa.g}\right)\left(\frac{\theta_v}{\theta_{v*}}\right) \tag{2.10}$$

where θ_{v*} may be computed as:

$$\theta_{v*} = \theta_*(1.0 + 0.61\ q_a) + 0.61(\theta_a q_*) \tag{2.11}$$

New formulations of the air-sea turbulent fluxes can then be derived using these characteristic length scales:

$$\left\{ \begin{array}{ll} |\vec{\tau}|_{sea} & = -\rho_a u_*^2 \\ H_{sea} & = -\rho_a c_{p_a} u_* \theta_* \\ LE_{sea} & = -\rho_a \mathcal{L}_v u_* q_* \end{array} \right. \tag{2.12}$$

In bulk parameterizations, transfer coefficients for the wind, potential temperature and specific humidity (hereafter referred to as C_D, C_H, and C_E for drag, heat and evaporation) are introduced in order to be able to compute the air-sea turbulent fluxes from mean meteorological gradients in the atmospheric boundary layer:

$$\left\{ \begin{array}{ll} |\vec{\tau}|_{sea} & = -\rho_a C_D . U^2 \\ H_{sea} & = -\rho_a c_{p_a} C_H . U . (\theta_a - \theta_s) \\ LE_{sea} & = -\rho_a \mathcal{L}_v C_E . U . (q_a - q_s) \end{array} \right. \tag{2.13}$$

if the atmospheric convention is chosen, *i.e.* when fluxes are defined positive in case of energy benefit for the atmosphere. Such transfer coefficients can be written as:

$$C_X = \frac{-\overline{w'x'}}{U \Delta x} \tag{2.14}$$

where Δx is the vertical gradient of the meteorological variable x ($= u$, θ or q) between the ocean surface and the atmospheric lowest level, and U denotes the mean value of the relative wind. Using equations 2.12 and 2.13 leads to other formulations of these transfer coefficients as functions of the scaling parameters u_*, θ_* and q_*:

$$\left\{ \begin{array}{l} C_D = \left(\frac{u_*}{U}\right)^2 \\ C_H = \frac{u_* \theta_*}{U(\theta_a - \theta_s)} \\ C_E = \frac{u_* q_*}{U(q_a - q_s)} \end{array} \right. \tag{2.15}$$

Transfer coefficients can also be expressed as functions of the atmospheric stratification and first atmospheric level height z. By applying the Buckingham theorem to the air flow in the surface layer, one may indeed obtain, in neutral conditions, a relationship between the vertical gradient of the mean flow U and the corresponding characteristic length scale u_*:

$$\frac{\partial U}{\partial z} = \frac{u_*}{\kappa z} \tag{2.16}$$

This vertical logarithmic profile obtained for neutral conditions can then be extended to any atmospheric conditions by introducing a function φ_m in order to take into account the stratification of the atmosphere:

$$\frac{\partial U}{\partial z} = \frac{u_*}{\kappa z} \times \varphi_m \left(\frac{z}{L}\right) \tag{2.17}$$

Integrating equation 2.17 allows then to express the vertical gradient of U, and in a similar way the vertical gradients of the potential temperature θ and specific humidity q as functions of the corresponding characteristic length scales u_*, θ_* and q_*:

$$\left\{ \begin{array}{ll} U & = \frac{u_*}{\kappa} \left[\ln\left(\frac{z}{z_0}\right) - \psi_m \left(\frac{z}{L}\right) \right] \\ \theta_a - \theta_s & = \frac{\theta_*}{\kappa} \left[\ln\left(\frac{z}{z_{0_t}}\right) - \psi_h \left(\frac{z}{L}\right) \right] \\ q_a - q_s & = \frac{q_*}{\kappa} \left[\ln\left(\frac{z}{z_{0_q}}\right) - \psi_q \left(\frac{z}{L}\right) \right] \end{array} \right. \tag{2.18}$$

or conversely the characteristic length scales u_*, θ_* and q_* as functions of the vertical gradients in the real atmosphere Δu, $\Delta\theta$ and Δq:

$$\begin{cases} u_* = \frac{\kappa.\Delta u}{\ln\left(\frac{z}{z_0}\right)-\psi_m(\zeta)} \\ \theta_* = \frac{\kappa.\Delta\theta}{\ln\left(\frac{z}{z_{0_t}}\right)-\psi_h(\zeta)} \\ q_* = \frac{\kappa.\Delta q}{\ln\left(\frac{z}{z_{0_q}}\right)-\psi_q(\zeta)} \end{cases} \tag{2.19}$$

ψ_m, ψ_h and ψ_q are stability functions depending on the Monin-Obukhov stability parameter ζ=z/L.
z_0, z_{0_t} and z_{0_q} stand for the roughness lengths for the wind, potential temperature and specific humidity, respectively. The dynamical roughness length z_0 is generally computed thanks to the relationship of Smith (1988):

$$z_0 = \alpha\left(\frac{{u_*}^2}{g}\right) + \beta\left(\frac{\nu}{u_*}\right) \tag{2.20}$$

where α is the Charnock parameter (as detailed hereafter, α may be a constant coefficient or may includes a wind dependency), β is a constant coefficient, and ν is the air kinematic viscosity.

Combining equations 2.15 and 2.18 then leads to new formulations for the exchange coefficients:

$$\begin{cases} C_D = \mathcal{F}_M(z, z_0, \zeta) \times C_{D_n} \\ C_H = \mathcal{F}_H(z, z_0, z_{0_t}, \zeta) \times C_{H_n} \\ C_E = \mathcal{F}_Q(z, z_0, z_{0_q}, \zeta) \times C_{E_n} \end{cases} \tag{2.21}$$

where $\mathcal{F}_M$, $\mathcal{F}_H$ and $\mathcal{F}_Q$ are stability functions:

$$\begin{cases} \mathcal{F}_M(z, z_0, \zeta) = \left[1 - \frac{\psi_m(\zeta)}{\ln\left(\frac{z}{z_0}\right)}\right]^{-2} \\ \mathcal{F}_H(z, z_0, z_{0_t}, \zeta) = \left[1 - \frac{\psi_m(\zeta)}{\ln\left(\frac{z}{z_0}\right)}\right]^{-1} \times \left[1 - \frac{\psi_h(\zeta)}{\ln\left(\frac{z}{z_{0_t}}\right)}\right]^{-1} \\ \mathcal{F}_Q(z, z_0, z_{0_q}, \zeta) = \left[1 - \frac{\psi_m(\zeta)}{\ln\left(\frac{z}{z_0}\right)}\right]^{-1} \times \left[1 - \frac{\psi_q(\zeta)}{\ln\left(\frac{z}{z_{0_q}}\right)}\right]^{-1} \end{cases} \tag{2.22}$$

and where C_{D_n}, C_{H_n} and C_{E_n} stand for the neutral exchange coefficients (*i.e.* for ζ=0):

$$\begin{cases} C_{D_n} = \frac{\kappa^2}{\left[\ln\left(\frac{z}{z_0}\right)\right]^2} \\ C_{H_n} = \frac{\kappa^2}{\ln\left(\frac{z}{z_0}\right)\ln\left(\frac{z}{z_{0_t}}\right)} \\ C_{E_n} = \frac{\kappa^2}{\ln\left(\frac{z}{z_0}\right)\ln\left(\frac{z}{z_{0_q}}\right)} \end{cases} \tag{2.23}$$

In the following sections, we will see that each parameterization uses its own closure hypothesis derived either from a theoretical method or from experimentation to determine the exchange coefficients. These parameterizations also differ in the calculation of the roughness lengths and/or of the neutral transfer coefficients, in the stability functions used to take into account the atmospheric stratification, as well as in the representation of various processes including seawater salinity effect on evaporation, wind gusts, waves effects, and sea spray (Brunke *et al.*, 2003).

2.2.2 Direct parameterization: Louis (1979)

In the SURFEX surface scheme, the parameterization of Louis (1979) may be used through the choice of *CSEA_FLUX='DIRECT'* in the *NAM_SEAFLUXn* namelist. In this parameterization (for which two versions are available as detailed hereafter), the exchange coefficients at the air-sea interface are computed from their values in neutral conditions using stability functions depending on the Richardson number Ri that is defined as the ratio between the potential and kinetic energy of the surface layer:

$$Ri = \frac{g.z}{U^2}\left(\frac{\theta_{v_a} - \theta_{v_s}}{\overline{\theta_v}}\right) \tag{2.24}$$

where g is the gravity and $\overline{\theta_v}$ is the mean virtual potential temperature of the atmospheric layer.
No specific computation is made for the humidity, as the corresponding exchange coefficient and roughness length are set to be equal to those of the potential temperature, *i.e.*:

$$\begin{cases} C_E = C_H \\ z_{0_q} = z_{0_t} \quad (\text{hereafter referred to as } z_{0_H}) \end{cases} \tag{2.25}$$

2.2.2.1 Roughness lengths

The dynamical and heat roughness lengths z_0 and z_{0_H} are estimated with a distinction between the free sea water and the sea ice by a temperature criterion with a threshold at -2°C (Tab. 2.1):
$\rightarrow$ in sea ice case, roughness lengths are the same than for the snow,
$\rightarrow$ over free seawater, roughness lengths are reduced to the relationship of Charnock (1955), *i.e.* $\alpha = 0.015$ and $\beta = 0$ in equation 2.20.

	For $T \leq -2°\text{C}$	For $T > -2°\text{C}$
Wind	$z_{0_{seaice}} = z_{0_{snow}} = 10^{-3}$	$z_0 = 0.015\left(\frac{u_*^2}{g}\right)$
Heat	$z_{0_{H_{seaice}}} = z_{0_{Hsnow}} = 10^{-4}$	$z_{0_H} = 0.015\left(\frac{u_*^2}{g}\right)$

Table 2.1: Roughness lengths (in meters) in the parameterization of Louis (1979).

2.2.2.2 Parameters and derived Richardson's numbers

In the formulations of the exchange coefficients for the wind (C_D, Table 2.2) and temperature / humidity (C_H=C_E, Table 2.3), b, d and k are constant parameters:

$$\begin{cases} b = 5 \\ d = 5 \\ k = 1 \end{cases} \tag{2.26}$$

Ri_{SD} and Ri_{SH} are modified Richardson's numbers:

$$Ri_{SD} = \frac{Ri}{1+\gamma.Ri} \qquad \text{and} \qquad Ri_{SH} = \frac{Ri}{(1+\gamma.\delta Ri)^{\frac{1}{\delta}}} \tag{2.27}$$

with γ=(*XUSURIC*$\times$*XUSURICL*). *XUSURIC* and *XUSURICL* are critical Richardson's numbers:

$$\begin{cases} XUSURIC = 1 \\ XUSURICL = 4 \end{cases} \tag{2.28}$$

δ is a constant depending on the value of a third critical Richardson's number *XUSURID*: δ=1 if *XUSURID*=0, else δ=3. Note that usually δ=3 as default value for *XUSURID* is 0.035.

2.2.2.3 Exchange coefficient for the wind (C_D)

	Primitive formulation *LDRAG_COEF_ARP='.FALSE.'*	*New* formulation *LDRAG_COEF_ARP='.TRUE.'*
Neutral (Ri=0)	$C_{D_n} = \frac{\kappa^2}{\left[\ln\left(\frac{z}{z_0}\right)\right]^2}$	$C_{D_n} = \frac{\kappa^2}{\left[\ln\left(1+\frac{z}{z_0}\right)\right]^2}$
Stable ($Ri > 0$)	$C_D = \left(\frac{1}{1+2b\left(\frac{Ri}{\sqrt{1+d.Ri}}\right)}\right) C_{D_n}$	$C_D = \left(\frac{1}{1+2b\left(\frac{Ri_{SD}}{\sqrt{1+\left(\frac{d}{k}\right)Ri_{SD}}}\right)}\right) C_{D_n}$
Unstable ($Ri < 0$)	$C_D = \left(1 - \frac{2b.Ri}{1+2b.CM_*.\mathcal{X}^{PM_*}.C_{D_n}\sqrt{\mathcal{R}}}\right) C_{D_n}$	
	$\mathcal{X} = \left(\frac{z}{z_0}\right)$ $\mathcal{R} = -Ri$	$\mathcal{X} = \left(1+\frac{z}{z_0}\right)$ $\mathcal{R} = \left(1+\frac{z}{z_0}\right)(-Ri)$
	CM_* and PM_* are 3rd order polynomials in $\ln(z_0/z_{0_H})$:	
	$CM_* = c_{m_0} + c_{m_1}\left[\ln\left(\frac{z_0}{z_{0_H}}\right)\right] + c_{m_2}\left[\ln\left(\frac{z_0}{z_{0_H}}\right)\right]^2 + c_{m_3}\left[\ln\left(\frac{z_0}{z_{0_H}}\right)\right]^3$	
	c_{m_0}= +6.8741, c_{m_1}= +2.6933 c_{m_2}= -0.3601, c_{m_3}= +0.0154	c_{m_0}= +7.5, c_{m_1}= +2.39037 c_{m_2}= -0.28583, c_{m_3}= +0.01074
	$PM_* = p_{m_0} + p_{m_1}\left[\ln\left(\frac{z_0}{z_{0_H}}\right)\right] + p_{m_2}\left[\ln\left(\frac{z_0}{z_{0_H}}\right)\right]^2 + p_{m_3}\left[\ln\left(\frac{z_0}{z_{0_H}}\right)\right]^3$	
	p_{m_0}= +0.5233, p_{m_1}= -0.0815 p_{m_2}= +0.0135, p_{m_3}= -0.0010	p_{m_0}= +0.0, p_{m_1}= -0.07028 p_{m_2}= +0.01023, p_{m_3}= -0.00067

Table 2.2: Exchange coefficient for the wind in the parameterization of Louis (1979).

Note that, in the new formulation, if the same roughness length is used for both the potential temperature/specific humidity and the wind ($z_0 = z_{0_H}$, corresponding to *LDZ0H='.FALSE.'*), then:

$$\begin{cases} CM_* = 7.5 \\ PM_* = 0.0 \end{cases} \tag{2.29}$$

and the formulation of the exchange coefficient for the wind then reduces in unstable conditions to:

$$C_D = \left(1 - \frac{2b.Ri}{1 + 15b.C_{D_n}\sqrt{\left(1+\frac{z}{z_0}\right)(-Ri)}}\right) C_{D_n} \tag{2.30}$$

2.2.2.4 Exchange coefficient for the temperature / humidity (C_H=C_E)

	Primitive formulation *LDRAG_COEF_ARP='.FALSE.'*	*New* formulation *LDRAG_COEF_ARP='.TRUE.'*
Neutral (Ri=0)	$C_{H_n} = \frac{\kappa^2}{\ln\left(\frac{z}{z_0}\right)\ln\left(\frac{z}{z_{0_H}}\right)}$	$C_{H_n} = \frac{\kappa^2}{\ln\left(1+\frac{z}{z_0}\right)\ln\left(1+\frac{z}{z_{0_H}}\right)}$
Stable ($Ri > 0$)	$C_H = \left(\frac{1}{1+3b.Ri\sqrt{1+d.Ri}}\right) C_{H_n}$	$C_H = \left(\frac{1}{1+3b.Ri_{SH}\sqrt{1+dk.Ri_{SH}}}\right) C_{H_n}$
Unstable ($Ri < 0$)	$C_H = \left(1 - \frac{3b.Ri}{1+3b.CH_*.{\mathcal{X}_H}^{PH_*}.C_{H_n}\sqrt{\mathcal{R}_H}}\right) C_{H_n}$	
	$\mathcal{X}_H = \left(\frac{z}{z_{0_H}}\right)$ $\mathcal{R}_H = -Ri$	$\mathcal{X}_H = \left(1+\frac{z}{z_{0_H}}\right)$ $\mathcal{R}_H = \left(1+\frac{z}{z_{0_H}}\right)(-Ri)$
	CH_* and PH_* are 3rd order polynomials in $\ln(z_0/z_{0_H})$:	
	$CH_* = c_{h_0} + c_{h_1}\left[\ln\left(\frac{z_0}{z_{0_H}}\right)\right] + c_{h_2}\left[\ln\left(\frac{z_0}{z_{0_H}}\right)\right]^2 + c_{h_3}\left[\ln\left(\frac{z_0}{z_{0_H}}\right)\right]^3$	
	c_{h_0}= +3.2165, c_{h_1}= +4.3431 c_{h_2}= +0.5360, c_{h_3}= -0.0781	c_{h_0}= +5.0, c_{h_1}= +4.51268 c_{h_2}= +0.34012, c_{h_3}= -0.05330
	$PH_* = p_{h_0} + p_{h_1}\left[\ln\left(\frac{z_0}{z_{0_H}}\right)\right] + p_{h_2}\left[\ln\left(\frac{z_0}{z_{0_H}}\right)\right]^2 + p_{h_3}\left[\ln\left(\frac{z_0}{z_{0_H}}\right)\right]^3$	
	p_{h_0}= +0.5802, p_{h_1}= -0.1571 p_{h_2}= +0.0327, p_{h_3}= -0.0026	p_{h_0}= +0.0, p_{h_1}= -0.09421 p_{h_2}= +0.01463, p_{h_3}= -0.00099

Table 2.3: Exchange coefficient for the temperature / humidity in the parameterization of Louis (1979).

Note that, in the new formulation, if the same roughness length is used for both the potential temperature/specific humidity and the wind ($z_0 = z_{0_H}$, corresponding to *LDZ0H='.FALSE.'*), then:

$$\begin{cases} CH_* = 5.0 \\ PH_* = 0.0 \end{cases} \tag{2.31}$$

and the formulation of the exchange coefficient for the potential temperature / specific humidity then reduces in unstable conditions to:

$$C_H = \left(1 - \frac{3b.Ri}{1+15b.C_{H_n}\sqrt{\left(1+\frac{z}{z_{0_H}}\right)(-Ri)}}\right) C_{H_n} \tag{2.32}$$

2.2.3 Iterative parameterizations

Bulk equations can also be solved with iterative methods to compute the Monin-Obukhov characteristic length scales from which the turbulent air-sea fluxes are derived. Among these iterative methods, the algorithm of Liu *et al.* (1979) known as the LKB algorithm is the most used and was in particular a base for several parameterizations developments such as the COARE (Fairall *et al.*, 1996b, 2003), MR98 (Mondon and Redelsperger, 1998) and ECUME (Belamari 2005) parameterizations. Such iterative algorithms either use a number of iterations fixed *a priori* (*e.g.* MR98, COARE3.0 and ECUME), or rely on a convergence criterion depending on the parameterization (*e.g.* ECUME6).
Note that the iterative parameterizations available in the SURFEX surface scheme use similar stability functions (the Businger functions with different numerical values, Table 2.6). All of them also may include additional refinements such as a salinity correction for the saturated vapor pressure, the computation of a wind subgrid correction, sensible heat flux and wind stress corrections due to the rainfall, or Webb effect as detailed in section 2.2.3.5.

2.2.3.1 The MR98 parameterization

In SURFEX, the MR98 parameterization (Mondon and Redelsperger, 1998) may be used through the choice of *CSEA_FLUX='ITERAT'* in the *NAM_SEAFLUXn* namelist.
This parameterization is in fact a declination of the COARE algorithm with different numerical values for the Businger stability functions and in the gustiness correction computation.

A first **preliminary step** insures the **initialization** of all the required variables, with namely:

1. the computation of the vertical gradients of the wind, potential temperature and specific humidity:

$$\begin{cases} \Delta u = U \\ \Delta\theta = \theta_a - \theta_s \\ \Delta q = q_a - q_s \end{cases} \tag{2.33}$$

2. the estimation of the Monin-Obukhov characteristic length scales:

$$\begin{cases} u_* &= 0.04 \times \Delta u \\ \theta_* &= 0.04 \times \Delta\theta \\ q_* &= 0.04 \times \Delta q \\ \theta_{v*} &= \theta_*(1.0 + 0.61\ q_a) + 0.61(q_*\theta_a) \end{cases} \tag{2.34}$$

The **second step** then consists in an **iterative loop** with a fixed number of iterations (IITERMAX=10) in order to update:

1. the Monin-Obukhov length L (following equation 2.10) and stability parameter ζ:

$$\zeta = MAX(\tfrac{z}{L}; -20\,000) \text{ if } \theta_{v*} \geq 10^{-6}, \text{ else } \zeta = 0.$$

2. the stability functions ψ_m and ψ_h as ψ_q is supposed to be equal to ψ_h (section 2.2.3.4)

3. the dynamical roughness length z_0 following the formulation of Smith (1988) with α=0.011 and β=0.11 in equation 2.20, and with the air kinematic viscosity ν computed as a function of the air temperature T_a at the first atmospheric level: $\nu = 1.318\ 10^{-5} + 9.282\ 10^{-8} T_a$ (with T_a in Kelvin)

4. the roughness lengths for the potential temperature and specific humidity z_{0_t} and z_{0_q} using formulations depending on the value of u_* (Table 2.4)

5. and last, the characteristic length scales u_*, θ_* and q_* derived from equations 2.19.

At the end of the iterative loop, air-sea turbulent fluxes are then computed following equations 2.12.

	For $u_* \leq 0.23$ m.s^{-1}	For $u_* > 0.23$ m.s^{-1}
Potential temperature	$z_{0_t} = 0.015\left(\frac{{u_*}^2}{g}\right) + 0.18\left(\frac{\nu}{u_*}\right)$	$z_{0_t} = 0.14\left(\frac{\nu}{u_*-0.2}\right) + 7.10^{-6}$
Specific humidity	$z_{0_q} = 0.0205\left(\frac{{u_*}^2}{g}\right) + 0.294\left(\frac{\nu}{u_*}\right)$	$z_{0_q} = 0.20\left(\frac{\nu}{u_*-0.2}\right) + 9.10^{-6}$

Table 2.4: Roughness lengths for the temperature (z_{0_t}) and humidity (z_{0_q}) in the MR98 parameterization.

2.2.3.2 The COARE 3.0 parameterization

The COARE (Coupled Ocean-Atmosphere Response Experiment) algorithm was initially developed during the TOGA (Tropical Ocean and Global Atmosphere) experiment. Several versions were then produced, among them the 2.5b version (Fairall *et al.*, 1996b) which was successfully used during several measurement campaigns in several locations overall the globe. Taking into account air-sea interaction data from the NOAA/ETL dataset and from the HEXMAX data reanalysis, the validation of this algorithm had been extended leading to the last version 3.0 of the COARE algorithm (Fairall *et al.*, 2003) that is available in the SURFEX surface scheme (Lebeaupin Brossier *et al.*, 2009) through the choice of *CSEA_FLUX='COARE3'* in the *NAM_SEAFLUXn* namelist.

As in MR98, the COARE 3.0 algorithm begins with a first **preliminary step** that insures the **initialization** of all the required variables, namely:

1. the vertical gradients of the wind, potential temperature and specific humidity (Δu, $\Delta\theta$ and Δq)

2. the dynamical roughness length z_0 computed following the relationship of Smith (1988) using in equation 2.20 a constant value for the Charnock parameter (α=0.011), with β=0.11, with the air kinematic viscosity ν computed following Andrea (1989):

$$\nu = 1.326\ 10^{-5}\left[1 + 6.542\ 10^{-3}\ t_a + 8.301\ 10^{-6}\ {t_a}^2 - 4.84\ 10^{-9}\ {t_a}^3\right] \tag{2.35}$$

   where t_a stands for the air temperature (in °C), and with the initial value of the friction velocity u_* estimated as a function of the wind vertical gradient between the sea surface and 10 meters height in neutral conditions ($u_* = 0.035 \times \Delta u_{10n}$)

3. the roughness lengths for temperature and humidity z_{0_t} and z_{0_q} (derived from the dynamical one)

4. the characteristic length scales u_*, θ_* and q_* using equations 2.19 in which the Monin-Obukhov stability parameter ζ is computed as a function of a bulk Richardson number Ri_b (Grachev and Fairall, 1997):

$$\begin{cases} \zeta = C.Ri_b\left[1 + \left(\frac{Ri_b}{Ri_{bc}}\right)\right]^{-1} & \text{if } Ri_b < 0 \quad \text{(unstable conditions)} \\ \zeta = C.Ri_b\left[1 + 3\left(\frac{Ri_b}{C}\right)\right]^{-1} & \text{if } Ri_b \geq 0 \quad \text{(stable conditions)} \end{cases} \tag{2.36}$$

with:

$$\begin{cases} Ri_b = -\frac{g.z}{T_a}\left[\frac{\Delta\theta+0.61\ T_a\ \Delta q}{\Delta u^2}\right] \\ Ri_{bc} = -z\left[0.004 \times z_{BL} \times {\beta_{gust}}^3\right]^{-1} \\ C = \kappa\frac{C_H}{C_D} \end{cases} \tag{2.37}$$

Ri_{bc} stands for the saturation value of Ri_b. z_{BL} and β_{gust} are the same parameters as those used in the computation of the wind subgrid correction w_g (section 2.2.3.5): z_{BL} is the atmospheric boundary layer depth (fixed to 600 meters), β_{gust} is a gustiness factor (β_{gust}=1.2 following results from the TOGA-COARE experiment). C_H and C_D are the temperature and wind exchange coefficients, respectively. This computation of ζ from Ri_b leads to a better background of the stability parameter, and allows to reduce the iterations number of the iterative loop (*NITERMAX*=1 if $\zeta > 50$, else *NITERMAX*=3).

As a **second step**, the **iterative loop** then insures the computation of:

1. the dynamical roughness length z_0 using:

   - either the relationship of Smith (1988) with β=0.11 in equation 2.20 and with a wind dependency introduced for the Charnock parameter (Hare *et al.*, 1999):

$$\begin{cases} \alpha = 0.011 & \text{if} \quad 0\ \text{m.s}^{-1} \leq U \leq 10\ \text{m.s}^{-1} \\ \alpha = 0.011 + (0.018 - 0.011)\left(\frac{U-10}{18-10}\right) & \text{if} \ \ 10\ \text{m.s}^{-1} < U \leq 18\ \text{m.s}^{-1} \\ \alpha = 0.018 & \text{if} \ \ 18\ \text{m.s}^{-1} < U \end{cases} \tag{2.38}$$

   - or more elaborated formulations that take into account the gravity waves' effects on roughness:

Oost *et al.*, 2002	$z_0 = \left(\frac{50}{2\pi}\right) L_{wv} \left(\frac{u_*}{C_{wv}}\right)^{4.5} + 0.11\left(\frac{\nu}{u_*}\right)$
Taylor and Yelland, 2001	$z_0 = 1200\ H_{wv} \left(\frac{H_{wv}}{L_{wv}}\right)^{4.5} + 0.11\left(\frac{\nu}{u_*}\right)$

(2.39)

   with:

$$\begin{cases} C_{wv} = \frac{g}{2\pi}(0.729\ U) \\ L_{wv} = \frac{g}{2\pi}(0.729\ U)^2 \\ H_{wv} = 0.018\ U^2 \times (1 + 0.015\ U) \end{cases} \tag{2.40}$$

2. the roughness lengths for temperature and humidity z_{0_t} and z_{0_q} that are directly derived from z_0:

$$z_{0_t} = z_{0_q} = MIN\left(1.15\ 10^{-4}, 5.5\ 10^{-5}\left(\frac{\nu}{z_0 u_*}\right)^{0.6}\right) \tag{2.41}$$

3. the Monin-Obukhov stability parameter ζ=z/L with L computed as:

$$L = \left(\frac{u_*^2}{\kappa.g}\right)\left[\frac{T_a(1.0 + 0.61\ q_a)}{\theta_*(1.0 + 0.61\ q_a) + 0.61(T_a q_*)}\right] \tag{2.42}$$

   (you may note the difference with respect to the exact formulation of L given by equation 2.10)

4. the stability functions ψ_m and ψ_h as ψ_q is supposed to be equal to ψ_h (section 2.2.3.4)

5. and last, the characteristic length scales u_*, θ_* and q_* using equations 2.19.

At the end of the iterative loop, the final values of the characteristic length scales are then used to derive:

- the exchange coefficients C_D, C_H and C_E (from equations 2.15),
- the air-sea turbulent fluxes τ_{sea}, H_{sea} and LE_{sea} (from equations 2.12),
- and last, the dynamical roughness length z_0 computed using a *subgrid* formulation derived from that of Smith (1988) but aiming to take into account the subgrid effects through a modified second term:

$$z_0 = \alpha \left(\frac{{u_*}^2}{g} \right) + \beta \left(\frac{C_D}{C_{D_n}} \right) \tag{2.43}$$

where α is the wind dependent Charnock parameter defined as in equations 2.38, β=10^{-5}, and C_{D_n} is the wind neutral exchange coefficient computed following equation 2.23. The roughness lengths for temperature and humidity are then directly obtained as $z_{0_t} = z_{0_q} = z_0$.

2.2.3.3 The ECUME parameterization

The ECUME (Exchange Coefficients from Unified Multi-campaigns Estimates) parameterization is a bulk iterative parameterization developed at CNRM in order to obtain an optimized parameterization covering a wide range of atmospheric and oceanic conditions. Two versions of this last iterative parameterization are in fact available in the SURFEX surface scheme and may be used through the choice of *CSEA_FLUX='ECUME'* or *CSEA_FLUX='ECUME6'* in the *NAM_SEAFLUXn* namelist. Both of them rely on in-situ air-sea fluxes measurements performed during several cruises (Table 2.5). As these cruises cover only low to moderate wind conditions (Weill *et al.*, 2003), additional specific results obtained for very strong winds (Powell *et al.*, 2003 ; Donelan *et al.*, 2004 ; French *et al.*, 2007 ; Drennan *et al.*, 2007) were also used in order to take into account the saturation and even decrease of the exchange coefficients for wind speeds higher than 33 ms^{-1}.

Experiment	used in ECUME	used in ECUME6
SEMAPHORE (Eymard *et al.*, 1996)	⋆	
CATCH (Eymard *et al.*, 1999)	⋆	
FETCH (Hauser *et al.*, 2003)	⋆	⋆
EQUALANT (Gouriou *et al.*, 2001)	⋆	⋆
POMME (Mémery *et al.*, 2005)	⋆	⋆
EGEE/AMMA (Bourras *et al.*, 2009)		⋆

Table 2.5: Air-sea fluxes measurements campaigns used in ECUME / ECUME6 parameterizations.

The key difference between the two parameterizations is that the original one (*ECUME*, see Belamari, 2005 for more details) provides formulations of the neutral exchange coefficients at 10m (drag coefficient $C_{D_{10n}}$, heat coefficient $C_{H_{10n}}$ and evaporation coefficient $C_{E_{10n}}$) as functions of the neutral vertical wind gradient between the sea surface and 10m-height Δu_{10n} (Figure 2.1, left part) while the new one (*ECUME6*) provides formulations of derived parameters for the wind $\mathcal{P}_{u_{10n}}$, potential temperature $\mathcal{P}_{\theta_{10n}}$ and specific humidity $\mathcal{P}_{q_{10n}}$ (Figure 2.1, right part), defined as:

$$\begin{cases} \mathcal{P}_{u_{10n}} = \left(\frac{C_{D_{10n}}}{\sqrt{C_{D_{10n}}}} \right) \times \Delta u_{10n} \\ \mathcal{P}_{\theta_{10n}} = \left(\frac{C_{H_{10n}}}{\sqrt{C_{D_{10n}}}} \right) \times \Delta u_{10n} \\ \mathcal{P}_{q_{10n}} = \left(\frac{C_{E_{10n}}}{\sqrt{C_{D_{10n}}}} \right) \times \Delta u_{10n} \end{cases} \tag{2.44}$$

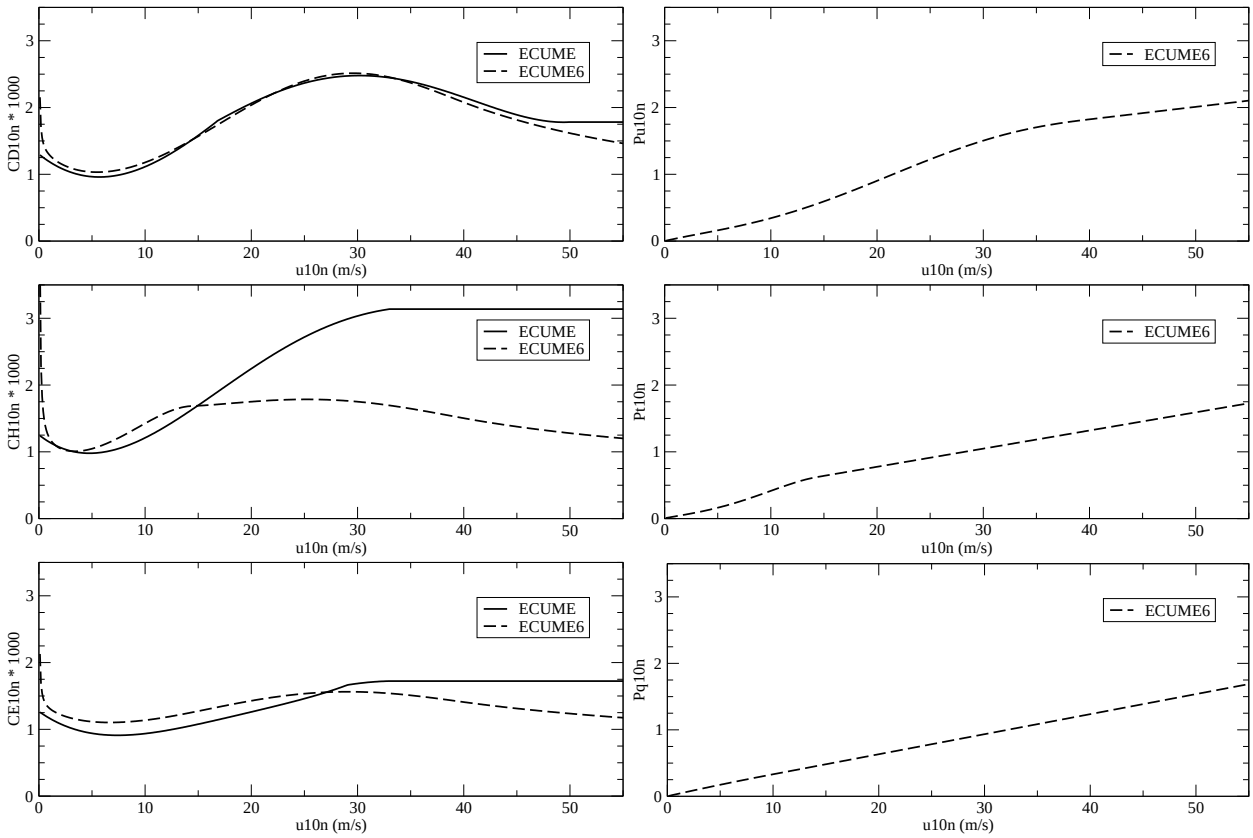

Figure 2.1: Left: Neutral coefficients at 10 meters $C_{D_{10n}}$, $C_{H_{10n}}$ and $C_{E_{10n}}$ in the ECUME (solid line) and derived from the ECUME6 (dashed line) formulations. Right: Neutral parameters at 10 meters $\mathcal{P}_{u_{10n}}$, $\mathcal{P}_{\theta_{10n}}$ and $\mathcal{P}_{q_{10n}}$ in the ECUME6 formulation.

The definition of these new parameters was motivated by the wide dispersion of the scatterplots providing the observed neutral exchange coefficients as a function of the neutral wind at 10 meters, in contrast to those of these new parameters.

As in the two other iterative parameterizations, the ECUME and ECUME6 algorithms begin with a first **preliminary step** that insures the **initialization** of all the required variables, namely:

1. the vertical gradients of the wind, potential temperature and specific humidity at the air-sea interface (Δu, $\Delta\theta$ and Δq)

2. the corresponding neutral vertical gradients:

$$\begin{cases} \Delta u_{10n} = \Delta u \\ \Delta\theta_{10n} = \Delta\theta \times d_0 \\ \Delta q_{10n} = \Delta q \end{cases}$$

with:

$$\begin{cases} d_0 = 1.2 + 6.3\ 10^{-3} MAX(\Delta u - 10\ ,\ 0) & \text{in ECUME} \\ d_0 = 1.0 & \text{in ECUME6} \end{cases}$$

In ECUME6, an initial guess is also made for the characteristic length scales as initial values of u_*, θ_* and q_* are required by the convergence criterion:

$$\begin{cases} u_* = 0.04\ \Delta u \\ \theta_* = 0.04\ \Delta\theta \\ q_* = 0.04\ \Delta q \end{cases}$$

As a **second step**, the **iterative loop** then insures the computation of:

1. the neutral exchange coefficients/parameters as functions of the neutral vertical wind gradient between the sea surface and 10m-height Δu_{10n}:

	ECUME	ECUME6
	Neutral coefficient	Neutral parameter
Momentum	$C_{D_{10n}} = f_u(\Delta u_{10n})$	$\mathcal{P}_{u_{10n}} = g_u(\Delta u_{10n})$
Heat	$C_{H_{10n}} = f_\theta(\Delta u_{10n})$	$\mathcal{P}_{\theta_{10n}} = g_\theta(\Delta u_{10n})$
Moisture	$C_{E_{10n}} = f_q(\Delta u_{10n})$	$\mathcal{P}_{q_{10n}} = g_q(\Delta u_{10n})$

2. the characteristic length scales u_*, θ_* and q_* derived from the previous coefficients/parameters:

	ECUME	ECUME6
	Scaling parameters	
Momentum	$u_* = \sqrt{C_{D_{10n}}}.\Delta u_{10n}$	$u_* = \mathcal{P}_{u_{10n}}$
Heat	$\theta_* = \left(\frac{C_{H_{10n}}}{\sqrt{C_{D_{10n}}}}\right).\Delta\theta_{10n}$	$\theta_* = \mathcal{P}_{\theta_{10n}}\left(\frac{\Delta\theta_{10n}}{\Delta u_{10n}}\right)$
Moisture	$q_* = \left(\frac{C_{E_{10n}}}{\sqrt{C_{D_{10n}}}}\right).\Delta q_{10n}$	$q_* = \mathcal{P}_{q_{10n}}\left(\frac{\Delta q_{10n}}{\Delta u_{10n}}\right)$

3. the stability parameter ζ=z/L constrained to be in the range [-200.0;0.25], using for the Monin-Obukhov length L the same approximate formulation as in COARE3.0 (equation 2.42)

4. the stability functions ψ_m and ψ_h as ψ_q is supposed to be equal to ψ_h (section 2.2.3.4)

5. and last, the neutral vertical gradients:

$$\begin{cases} \Delta u_{10n} = \Delta u - \frac{u_*}{\kappa}\left[\ln\left(\frac{z}{10}\right) - \psi_m(\zeta)\right] \\ \Delta\theta_{10n} = \Delta\theta - \frac{\theta_*}{\kappa}\left[\ln\left(\frac{z}{10}\right) - \psi_h(\zeta)\right] \\ \Delta q_{10n} = \Delta q - \frac{q_*}{\kappa}\left[\ln\left(\frac{z}{10}\right) - \psi_q(\zeta)\right] \end{cases}$$

At the end of the iterative loop, the final values of the characteristic length scales are then used to derive:

- the exchange coefficients C_D, C_H and C_E (from equations 2.15),
- the air-sea turbulent fluxes τ_{sea}, H_{sea} and LE_{sea} (from equations 2.13 in ECUME and 2.12 in ECUME6),
- and last, the roughness lengths:
  - in ECUME, the dynamical roughness length z_0 is computed in a single way using the *subgrid* formulation (equation 2.43) with β=10^{-5}
  - in ECUME6, the dynamical roughness length z_0 may be computed in three different ways depending on the choice of a dedicated parameter (*KZ0*):
    * using the *subgrid* formulation with β=10^{-5} in equation 2.43 if *KZ0*=0
    * using the relationship of Smith (1988) with β=0.11 in equation 2.20 if *KZ0*=1
    * from the characteristic length scale u_*, using a formulation derived from equation 2.19 if *KZ0*=2:

$$z_0 = z\left(\exp\left[\kappa\frac{\Delta u}{u_*} + \psi_m(\zeta)\right]\right)^{-1} \tag{2.45}$$

  Note that if the dynamical roughness length z_0 is computed using the *subgrid* formulation or the relationship of Smith (1988), the Charnock parameter α may be either constant if *CCHARNOCK='OLD'* (then α=0.021) or wind dependent as in COARE3.0 (equation 2.38) if *CCHARNOCK='NEW'*.

The ECUME and ECUME6 parameterizations include other specific points:

1. No waves effects are taken into account in these parameterizations.

2. A stochastic perturbation may be applied to the air-sea turbulent fluxes (logical *OPERTFLUX*) in both parameterizations.

3. In ECUME, the number of iterations is prescribed (fixed to 10), while in ECUME6 a convergence criterion is used: the iterative loop is stopped when the difference between the scale parameters of two successive iterations is inferior to a prescribed threshold (10^{-6} ms^{-1} for u_*, 10^{-6} K for θ_* and 10^{-9} kg/kg for q_*). Note that an important effort was done for the ECUME6 algorithm in order to ensure the convergence in maximum 10 iterations whatever the meteo-oceanic conditions (Belamari, 2005).

4. In ECUME, a correction may be applied to the neutral coefficient for humidity (default is *XICHCE*=0):

$$C_{E_{10n}} = C_{E_{10n}}(1 - XICHCE) + C_{H_{10n}}(XICHCE) \quad \text{with} \quad 0.0 \leq XICHCE \leq 1.0$$

2.2.3.4 Stability functions used in the iterative parameterizations

The stability functions ψ_m and ψ_h used in the four iterative parameterizations to correct the wind, potential temperature and specific humidity logarithmic profiles in the boundary layer according to the atmospheric stratification are all modified Businger's functions as detailed hereafter. ECUME* stands for both ECUME and ECUME6, and ψ_* represents either ψ_m or ψ_h depending on the considered parameter.
You may note that in unstable conditions the stability functions result from two contributions: a *Kansas* part to represent the classical unstability, and a *Convective* part to take into account the free convection, with a weight f depending on the Monin-Obukhov stability parameter ζ. In the MR98 parameterization, a different formulation is used for the weight f but we do not mention it here as the resulting formulation of the stability functions including the two contributions is rigorously equivalent.

	Wind	Potential temperature
Stable ($\zeta \geq 0$)	**MR98** $\psi_*(\zeta) = -4.7\,\zeta$	
	ECUME* $\psi_*(\zeta) = -7.0\,\zeta$	
	COARE3.0 $\psi_*(\zeta) = -\left[1 + \zeta + \frac{2}{3}\left(\frac{\zeta - 14.28}{\exp(\Gamma)}\right) + 8.525\right]$ with $\Gamma = MIN(50,\ 0.35\zeta)$	
Unstable ($\zeta < 0$)	$\psi_*(\zeta) = (1-f)\psi_{*K} + f\psi_{*C}$ with $f = \frac{\zeta^2}{1+\zeta^2}$	
Kansas	$\psi_{mK} = 2.\ln\left(\frac{1+x}{2}\right) + \ln\left(\frac{1+x^2}{2}\right) - 2.\arctan(x) + \frac{\pi}{2}$	$\psi_{hK} = 2.\ln(\frac{1+x^2}{2})$
	with:	
	MR98 $x = (1 - 16\,\zeta)^{\frac{1}{4}}$	
	ECUME* $x = (1 - 16\,\zeta)^{\frac{1}{4}}$	
	COARE3.0 $x = (1 - 15\,\zeta)^{\frac{1}{4}}$	
Convective	$\psi_{*C} = \frac{3}{2}\,\ln\left(\frac{1+y+y^2}{3}\right) - \sqrt{3}.\arctan\left(\frac{1+2y}{\sqrt{3}}\right) + \frac{\pi}{\sqrt{3}}$	
	with:	
	MR98 $y = (1 - 12.87\,\zeta)^{\frac{1}{3}}$	
	ECUME* $y = (1 - 12.87\,\zeta)^{\frac{1}{3}}$	
	COARE3.0 $y = (1 - 10.15\,\zeta)^{\frac{1}{3}}$	$y = (1 - 34.15\,\zeta)^{\frac{1}{3}}$

Table 2.6: Stability functions used in the iterative parameterizations.

2.2.3.5 Additional refinements included in the iterative parameterizations

Each of the four iterative parameterizations may include some refinements as detailed in Table 2.7.

1. **Salinity correction:** A reduction of 2% may be applied to the saturated vapor pressure P_{sat} used in the computation of the specific humidity at the sea surface q_s in order to take into account the

decreasing of P_{sat} due to seawater salinity (Kraus, 1972):

$$q_s = q_s(P_{sat}) \quad \text{with} \quad P_{sat} = 0.98 \times P_{sat}(T_s) \tag{2.46}$$

2. **Explicit dependency to sea surface salinity:** In ECUME6, if the sea surface salinity (SSS) field is available in the SURFEX surface scheme, an explicit dependency to the SSS may be used in the computation of both the saturated vapor pressure P_{sat} from which the specific humidity at the sea surface q_s is derived (Sharqawy *et al.*, 2010), and the latent heat of seawater vaporization $\mathcal{L}_v$:

$$\begin{cases} q_s = q_s(P_{sat}) \quad \text{with} \quad P_{sat} = P_{sat}(T_s, SSS) \\ \mathcal{L}_v = \mathcal{L}_v(SSS) \end{cases}$$

3. **Wind subgrid correction:** The relative wind - and therefore the wind gradient - may be increased by a subgrid correction (w_g) introduced in order to take into account the gustiness impact:

$$\Delta u = \sqrt{U^2 + {w_g}^2} \qquad \text{with} \qquad w_g = \beta_{gust}(B_F.z_{BL})^{\frac{1}{3}} \tag{2.47}$$

z_{BL} is the atmospheric boundary layer depth (in meters), β_{gust} is a constant coefficient, and B_F is the surface buoyancy flux:

$$B_F = -g.u_*.\mathcal{F}$$

If $B_F \leq 0$, the wind correction w_g is set to a minimal value $w_{g_{min}}$.

4. **Wind stress correction** and **Heat flux correction** due to rainfall: As rainfall tends to increase the surface drag and to cool the ocean, two additional contributions τ_r (Fairall *et al.*, 1996b) and H_r (Gosnell *et al.*, 1995) may be computed in order to correct the surface wind stress and sensible heat flux, respectively:

$$\begin{cases} \tau_r = -\gamma\, \mathcal{R} \times U \\ H_r = \mathcal{R}\, c_{p_{lw}} \alpha_c (T_s - T_a) \left(1 + \frac{1}{B}\right) \end{cases} \tag{2.48}$$

$\mathcal{R}$ denotes the precipitation rate (in kg.s^{-1}.m^{-2}). $c_{p_{lw}}$ is the rain specific heat including a dependency to the rain temperature (supposed to be equal to that of the air). α_c is a dimensionless parameter called the wet-bulb factor:

$$\alpha_c = \left[1 + \frac{L_r\, d_v}{c_{p_d}\, d_h} \left(\frac{dq_{sat}}{dT}\right)\right]^{-1} \tag{2.49}$$

where L_r is the latent heat of rain vaporization (in J.kg^{-1}), c_{p_d} is the specific heat of dry air (in J.K^{-1}.kg^{-1}), d_v and d_h are the diffusivities for water vapor (Pruppacher and Klett, 1978) and heat, respectively. The slope of the saturated specific humidity at atmospheric level $q_{sat}(\theta_a)$ as a function of the temperature is derived from the Clausius-Clapeyron relation:

$$\frac{dq_{sat}}{dT} = \lambda \left[\frac{L_r\, q_{sat}(\theta_a)}{R_v\, {T_a}^2}\right]$$

B is the Bowen ratio:

$$B = \mu \left(\frac{c_{p_d}}{L_r}\right) \left(\frac{T_s - T_a}{q_s - q_a}\right)$$

5. **Webb correction:** This small correction may be applied to the latent heat flux in order to take into account the air density variations when the humidity varies under the evaporation action:

$$LE_{Webb} = \rho_a\, \mathcal{L}_v\, \overline{w}\, q_a$$

where $\mathcal{L}_v$ is the latent heat of seawater vaporization at sea surface, and $\overline{w}$ is the mean value of the vertical speed perturbations:

$$\overline{w} = 1.61\ \overline{w'q'} + (1 + 1.61\ q_a)\frac{\overline{w'\theta'}}{T_a} = -\left[1.61\ u_* q_* + (1 + 1.61\ q_a)\frac{u_*\theta_*}{T_a}\right]$$

	MR98	COARE3.0	ECUME	ECUME6
Salinity correction	Yes	Yes	Yes	Yes
Explicit dependency to sea surface salinity	No	No	No	Yes [1]
Wind subgrid correction	Yes with: $w_{g_{min}}$=0.0 ms^{-1} β_{gust}=0.6 z_{BL}=650 m $\mathcal{F} = \frac{\theta_{v*}}{\theta_v}$	Yes [2] with: $w_{g_{min}}$=0.2 ms^{-1} β_{gust}=1.2 z_{BL}=600 m $\mathcal{F} = \frac{\theta_* + 0.61(T_a q_*)}{T_a}$	Yes [2] with: $w_{g_{min}}$=0.0 ms^{-1} β_{gust}=1.2 z_{BL}=600 m $\mathcal{F} = \frac{\theta_{v*} - 0.61(\theta_a - T_a)q_*}{T_a}$	No
Wind stress correction due to rainfall	No	Yes [3] with γ=0.85	Yes [3] with γ=1.0	Yes [3] with γ=0.85
Heat flux correction due to rainfall	No	Yes with: λ=1 μ=1	Yes with: $\lambda = \frac{R_v}{R_d}$ $\mu = \frac{d_h}{d_v}$	Yes with: λ=1 $\mu = \frac{d_h}{d_v}$
[1] If the sea surface salinity field is available in the SURFEX surface scheme. Else, only the standard "Salinity correction" is applied.				
[2] Logical *LPWG* in the *NAM_SEAFLUXn* namelist.				
[3] Logical *LPRECIP* in the *NAM_SEAFLUXn* namelist.				

Table 2.7: Additional refinements available (or not) in the iterative parameterizations.

Note that:

1. In the various formulations of the surface buoyancy flux B_F, θ_v is the air virtual potential temperature (equation 2.8), θ_{v*} is the associated characteristic length scale given by equation 2.11, θ_a and T_a are the air potential temperature and air temperature, respectively. This leads to different formulations in COARE3.0 and ECUME when compared to the (exact) one used in MR98.

2. In the heat flux correction due to rainfall, λ and μ should be equal to 1 to be fully consistent with Gosnell *et al.* (1995).

2.3 Coupling with a 1D TKE oceanic model

2.3.1 Coupling objectifs and principles

The main objective of the coupling is to improve the fine scale air-sea exchanges modelling in the SURFEX surface scheme. To better represent the fine scale air-sea interactions, it is necessary to take into account the oceanic dynamics and the thermal content evolution (Lebeaupin *et al.* (2007, 2009)) .

The coupled system's principle consists in modelling a seawater column under each grid point containing a fraction of sea and limited by the bottom (Figure 2.2). The ocean model used is the uni-dimensional model described by Gaspar *et al.* (1990) [see section 2.3.2] which allows to represent the oceanic vertical mixing according to a parameterization of turbulence from Bougeault and Lacarrère (1989) adapted to ocean. By the turbulent vertical mixing modelling, the 1D ocean model allows to represent the heat, water and momentum exchanges from the superficial oceanic layers in direct interaction with the atmosphere and subjected to radiative effects, to the deepest layers. The turbulent vertical mixing is based on a parameterization of the second-order turbulent moments expressed as a function of the turbulent kinetic energy (Gaspar *et al.* , 1990). In this formulation, the vertical mixing coefficients are based on the calculation of two turbulent length scales representing upward and downward conversions of turbulent kinetic energy (TKE) into potential energy (Gaspar *et al.* , 1990). By allowing a response to high frequencies in the surface forcing, the scheme improved the representation of the vertical mixed layer structure, sea surface temperature and upper-layer current (Blanke and Delecluse, 1993). However, this parameterization fails to properly simu-

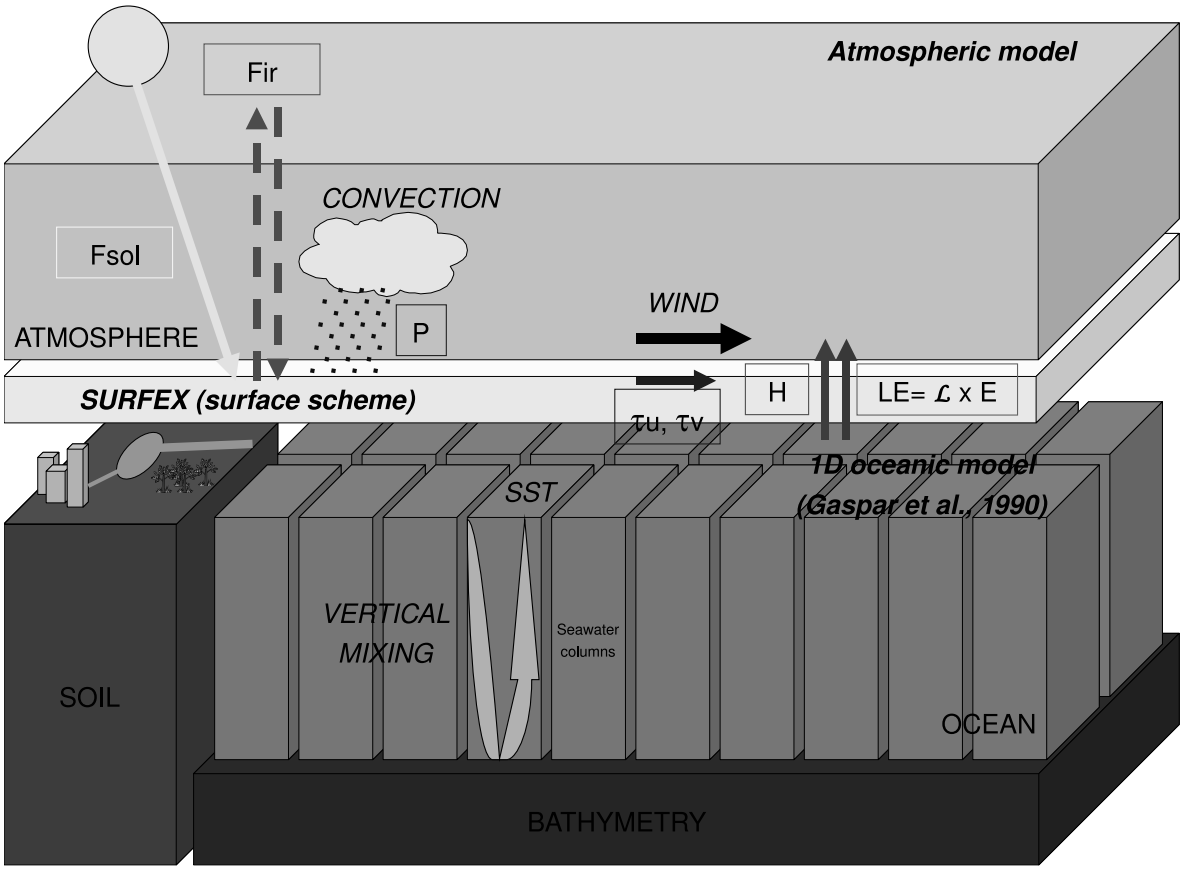

Figure 2.2: The high-resolution ocean-atmosphere coupled system between (MESO-NH) SURFEX and the 1D oceanic model.

late the mixing in strongly stable layers in the upper thermocline (Large*et al.* , 1994 ; Kantha and Clayson, 1994). Consequently, a parameterization of the diapycnal mixing (Large *et al.* , 1994) was introduced into Gaspar's turbulence parameterization model in order to take into account the effects of the vertical mixing occurring in the thermocline (Josse, 1999). This non local source of mixing, mainly due to internal wave breaking and current shear between the mixed layer and upper thermocline, impacts the temperature, salinity, momentum and turbulent kinetic energy inside the mixed layer particularly during restratification periods. This parameterization was widely used, for instance to study successfully the diurnal cycle in the Equatorial Atlantic (Wade *et al.* , 2011), the Equatorial Atlantic cold tongue (Giordani *et al.* , 2011), the production of modal waters in the North-East Atlantic (Giordani *et al.* , 2005b) or to derive surface heat flux corrections (Caniaux *et al.* , 2005b). Note that horizontal and vertical advections can be easily prescribed in the 1D-mixing model to perform realistic simulations in heterogeneous situations.

2.3.2 Description of the 1D oceanic model in TKE equation

The 1D model includes a prognostic equation for the turbulent kinetic energy (e) with a 1.5 order closure. The other prognostic variables are the temperature (T), the salinity (S), and the current [$\vec{u} = (u, v)$].

Prognostic equations for T, S, u and v

Each of the prognostic variables (α) is decomposed in a mean value ($\overline{\alpha}$) and a perturbation around this mean value (α'), so $\alpha = \overline{\alpha} + \alpha'$. For each seawater column, T, S, u and v evolve under the turbulent vertical mixing effect. This mixing depends of air-sea interface fluxes.
The conservative equations are:

$$\begin{cases} \frac{\partial T}{\partial t} = \frac{F_{sol}}{\rho_0 c_p}\frac{\partial I(z)}{\partial z} - \frac{\partial \overline{T'w'}}{\partial z} \\ \\ \frac{\partial S}{\partial t} = -\frac{\partial \overline{S'w'}}{\partial z} \\ \\ \frac{\partial \vec{u}}{\partial t} = -f\vec{k} \times \vec{u} - \frac{\partial \overline{\vec{u}'w'}}{\partial z} \end{cases} \tag{2.50}$$

where w is the vertical velocity, ρ_0 is a reference density, c_p is the specific heat, f is the Coriolis parameter. $\vec{k}$ is the unit vertical along the vertical, F_{sol} is the solar radiation received by the surface, and $I(z)$ is the solar radiation fraction reaching the depth z ($I(z)$ function decreases exponentially with depth).
The conditions at the top of the model (z=0) are:

$$\begin{cases} -\overline{T'w'}(0) = \frac{F_{nsol}}{\rho_0 c_p} = \frac{H+LE+F_{ir}}{\rho_0 c_p} \\ \\ -\overline{S'w'}(0) = \frac{E-P}{\rho_0 c_p} \\ \\ -\overline{\vec{u}'w'}(0) = \frac{\vec{\tau}}{\rho_0 c_p} \end{cases} \tag{2.51}$$

Fluxes are positive here downwards.

Finally, the forcing variables to give to the oceanic model are:

- the solar radiation F_{sol}
- the infra-red radiation F_{ir}
- the evaporation rate E proportional to the latent heat flux $E = \frac{LE}{\mathcal{L}}$

- the sensible heat flux H
- the zonal and meridional stress components $\vec{\tau} = (\tau_u, \tau_v)$
- the precipitation rate P

F_{nsol} is defined as the sum of the sensible H, the latent heat flux LE and the infra-red radiation F_{ir} and is named non-solar flux.
The closure relationships are given by:

$$\begin{cases} -\overline{T'w'} = K_h \frac{\partial \overline{T}}{\partial z} \\ -\overline{S'w'} = K_s \frac{\partial \overline{S}}{\partial z} \\ -\overline{\vec{u}'w'} = K_m \frac{\partial \overline{\vec{u}}}{\partial z} \end{cases} \tag{2.52}$$

The K_* are diffusivity coefficients linked to the turbulent kinetic energy by:

$$K = c_k l_k \overline{e}^{\frac{1}{2}} = K_h = K_s = \frac{K_m}{Prt} \simeq K_m \tag{2.53}$$

where c_k is a constant to determine; l_k is a mixing length and Prt is the Prandlt's number.

Prognostic equation for turbulent kinetic energy

The equation for TKE $e = \frac{1}{2}(u'^2 + v'^2 + w'^2)$ is given by:

$$\frac{\partial \overline{e}}{\partial t} = -\frac{\partial}{\partial z}\left(\overline{e'w'} + \frac{\overline{p'w'}}{\rho_0}\right) - \overline{\vec{u}'w'} \times \frac{\partial \overline{\vec{u}}}{\partial z} + \overline{b'w'} - \epsilon \tag{2.54}$$

where p is pressure; $\epsilon = c_\epsilon l_\epsilon \overline{e}^{\frac{3}{2}}$ is dissipation; $b = g\frac{\rho - \rho_0}{\rho_0}$ is the buoyancy. The seawater density is diagnosed from temperature and salinity:

$$\rho = \rho_0 + (T - T_{ref}) \times [-0.19494 - 0.49038(T - T_{ref})] + 0.77475(S - S_{ref})$$

where $T_{ref} = 13.5$ C, $S_{ref} = 32.6$ psu and $\rho_0 = 1024.458$ kg/m^3.
The vertical TKE flux is parameterized:

$$-\left(\overline{e'w'} + \frac{\overline{p'w'}}{\rho_0}\right) = K_e \frac{\partial \overline{e}}{\partial z} \tag{2.55}$$

with

$$K_e = c_\epsilon l_\epsilon \overline{e}^{\frac{1}{2}} \tag{2.56}$$

The Bougeault and Lacarrère mixing length are:

$$l_\epsilon = (l_u l_d)^{\frac{1}{2}} \tag{2.57}$$

$$l_k = min(l_u, l_d)\ pour\ k = h, s\ and\ m \tag{2.58}$$

l_u and l_d (for "up" and "down") are estimated as the upwards and downwards distances for which the kinetic energy is transformed in potential energy:

$$\overline{e}(z) = \frac{g}{\rho_0} \int_z^{z+l_u} [\overline{\rho}(z) - \rho(z')] dz' \tag{2.59}$$

$$\overline{e}(z) = \frac{g}{\rho_0} \int_z^{z-l_d} [\overline{\rho}(z) - \rho(z')] dz' \tag{2.60}$$

Discretization

The temporal integration scheme is a semi-implicit scheme for T and S. For the horizontal current $\vec{u} = (u, v)$, the integration scheme is implicit/semi-implicit.
The discretization is here described in detail for the temperature. The same could be done for the salinity, the TKE and the current in complex notation ($\vec{u} \rightarrow u + iv$, $i^2 = -1$).
The equation

$$\frac{\partial T}{\partial t} = \frac{F_{sol}}{\rho_0 c_p}\frac{\partial I(z)}{\partial z} - \frac{\partial}{\partial z}\left(-K\frac{\partial \overline{T}}{\partial z}\right)$$

is decomposed as:

$$\frac{T_k^{t+1} - T_k^t}{\Delta t} = \frac{F_{sol}}{\rho_0 c_p}\frac{\partial I(z)}{\partial z} + \frac{1}{\Delta z_2(k)}[K(k+1)\frac{T_{k+1}^{t+1} - T_k^{t+1}}{\Delta z_1(k)} - K(k)\frac{T_k^{t+1} - T_{k-1}^{t+1}}{\Delta z_1(k)}] \tag{2.61}$$

$$T_{k-1}^{t+1}\left(-\frac{K(k)}{\Delta z_1 \Delta z_2}\right) + T_k^{t+1}\left(\frac{1}{\Delta t} + \frac{K(k+1) - K(k)}{\Delta z_1 \Delta z_2}\right) + T_{k+1}^{t+1}\left(-\frac{K(k+1)}{\Delta z_1 \Delta z_2}\right) = \frac{1}{\Delta t}T_k^t + \frac{F_{sol}}{\rho_0 c_p}\frac{\partial I}{\partial z}$$

In a matricial writing following the vertical levels (k):

$$[\mathcal{M}]\left(T^{t+1}\right) = \frac{1}{\Delta t}\left(T^t\right) + [\frac{F_{sol}}{\rho_0 c_p}\frac{\partial I(z)}{\partial z}] \tag{2.62}$$

$$[\mathcal{M}] = \begin{pmatrix} . & . & 0 & & & & \\ . & . & . & 0 & & & \\ 0 & \beta_k & \alpha_k & \gamma_k & 0 & & \\ - & - & - & - & - & - & - \\ & & & 0 & . & . & . \\ & & & & 0 & . & . \end{pmatrix} \tag{2.63}$$

$$\alpha_k = \frac{1}{\Delta t} + \frac{K(k+1) - K(k)}{\Delta z_1 \Delta z_2}$$

$$\beta_k = -\frac{K(k)}{\Delta z_1 \Delta z_2}$$

$$\gamma_k = -\frac{K(k+1)}{\Delta z_1 \Delta z_2}$$

$[\mathcal{M}]$ is a tri-diagonal matrix to invers.

The vertical grid must be a z-coordinates grid as described by Fig. 2.3.
To take into account the bathymetry effects on the oceanic vertical mixing, we introduced a bathymetry index (as the sea-land mask) which is worth 0 for free sea and 1 for levels under the sea-bed. For the vertical levels which have a bathymetry index equal to 1, we impose the prognostic variables values equal to the last free-sea level values. The 1D model thus does not carry out any energy transfer towards or coming from the bottom. Only the energy contained in the higher free levels is taken into account.
We also introduced a diagnosis of mixed layer depth. The mixed layer base is diagnosed with an arbitrary criterion on the density profile: we assume that the thermocline corresponds to the vertical level for which the seawater density is superior to a 0.02 kg m^{-3} variations compared to the density for a reference level (taken at 5m depth).
Finally, the oceanic model must be initialized in temperature, salinity and current either from an oceanic analysis or from climatologies.

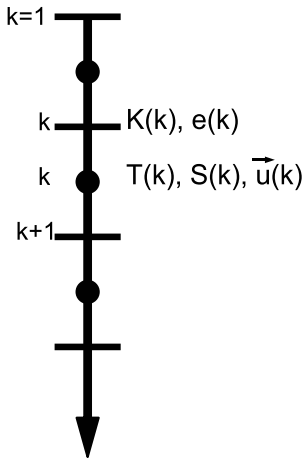

Figure 2.3: Vertical grid description of the 1D oceanic model from Gaspar et al. (1990) .

2.4 Inland Water: Lake Model FLake

In this section, a lake model (parameterisation scheme) capable of predicting the temperature structure of lakes of various depth on time scales from a few hours to many years is presented. A detailed description of the model, termed FLake, is given in Mironov (2010). FLake is an integral (bulk) model. It is based on a two-layer parametric representation of the evolving temperature profile within the water column and on the integral energy budget for these layers. The structure of the stratified layer between the upper mixed layer and the basin bottom, the lake thermocline, is described using the concept of self-similarity (assumed shape) of the temperature-depth curve. The same concept is used to describe the temperature structure of the thermally-active upper layer of bottom sediments and of the ice and snow cover. An entrainment equation for the depth of a convectively-mixed layer and a relaxation-type equation for the depth of a wind-mixed layer in stable and neutral stratification are developed on the basis of the turbulence kinetic energy (TKE) equation integrated over the mixed layer. Both mixing regimes are treated with due regard for the volumetric character of solar radiation heating. Simple thermodynamic arguments are invoked to develop the evolution equations for the ice and snow depths. The system of ordinary differential equations for the time-dependent prognostic quantities that characterise the evolving temperature profile, see Figs. 2.4 and 2.5, is closed with algebraic (or transcendental) equations for diagnostic quantities, such as the heat flux through the lake bottom and the equilibrium mixed-layer depth in stable or neutral stratification.

The resulting lake model is computationally very efficient but still incorporates much of the essential physics.

Within FLake, the lake water is treated as a Boussinesq fluid, i.e. the water density is taken to be constant equal to the reference density except when it enters the buoyancy term in the TKE equation and the expression for the buoyancy frequency.

The other thermodynamic parameters are considered constant except for the snow density and the snow heat conductivity.

2.4.1 Equation of State

We utilise the quadratic equation of state of the fresh water,

$$\rho_w = \rho_r \left[1 - \frac{1}{2} a_T \left(\theta - \theta_r \right)^2 \right], \tag{2.64}$$

where ρ_w is the water density, $\rho_r = 999.98 \approx 1.0 \cdot 10^3$ kg·m^{-3} is the maximum density of the fresh water at the temperature $\theta_r = 277.13$ K, and $a_T = 1.6509 \cdot 10^{-5}$ K^{-2} is an empirical coefficient (Farmer and Carmack (1981)). Equation (2.64) is the simplest equation of state that accounts for the fact that the temperature of maximum density of the fresh water exceeds its freezing point $\theta_f = 273.15$ K. According to Eq. (2.64), the thermal expansion coefficient α_T and the buoyancy parameter β depend on the water temperature,

$$\beta(\theta) = g\alpha_T(\theta) = g a_T(\theta - \theta_r), \tag{2.65}$$

where $g = 9.81$ m·s^{-2} is the acceleration due to gravity.

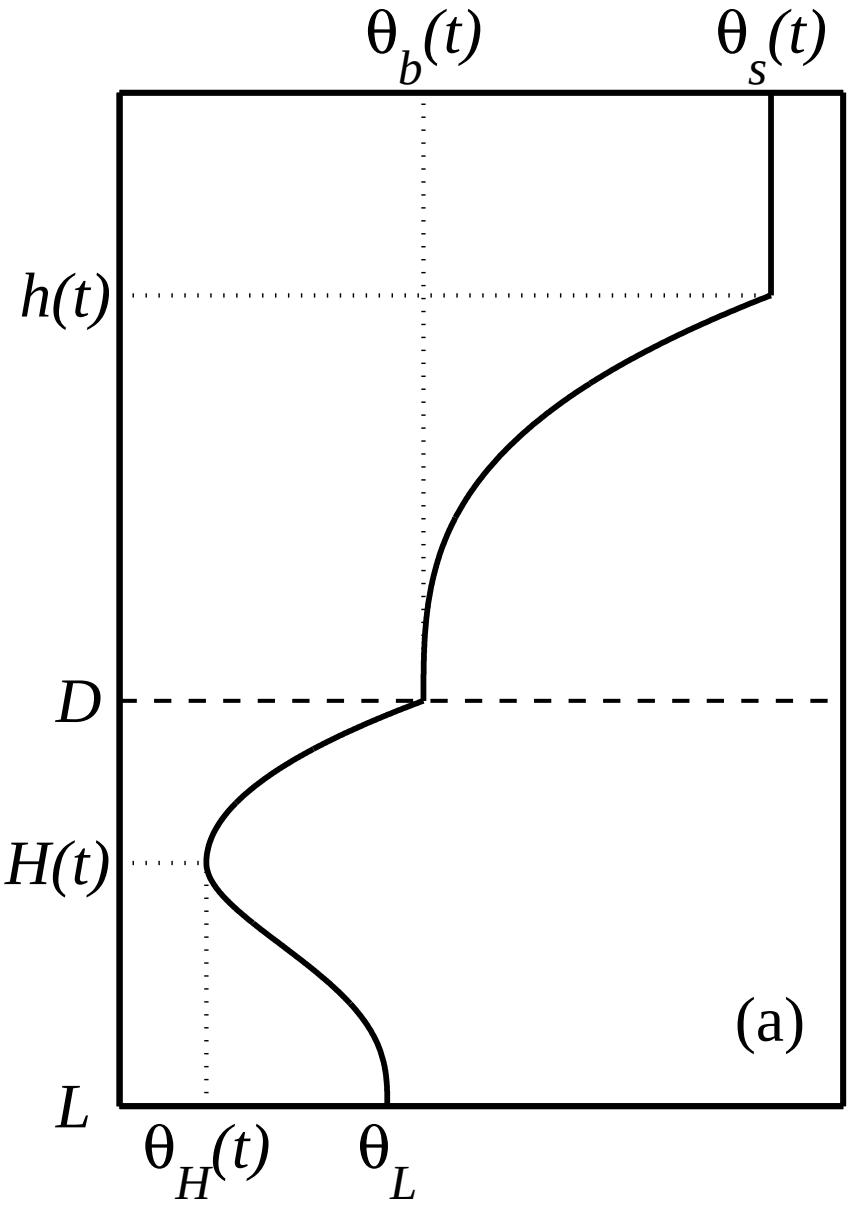

Figure 2.4: Schematic representation of the temperature profile in the mixed layer, in the thermocline, and in the thermally active layer of bottom sediments. The evolving temperature profile is specified by several time-dependent quantities. These are the mixed-layer temperature $\theta_s(t)$ and its depth $h(t)$, the temperature $\theta_b(t)$ at the water-bottom sediment interface, the shape factor $C_\theta(t)$ with respect to the temperature profile in the thermocline, the temperature $\theta_H(t)$ at the lower boundary of the upper layer of bottom sediments penetrated by the thermal wave, and the depth $H(t)$ of that layer. The temperature θ_L at the outer edge $z = L$ of the thermally active layer of bottom sediments is constant.

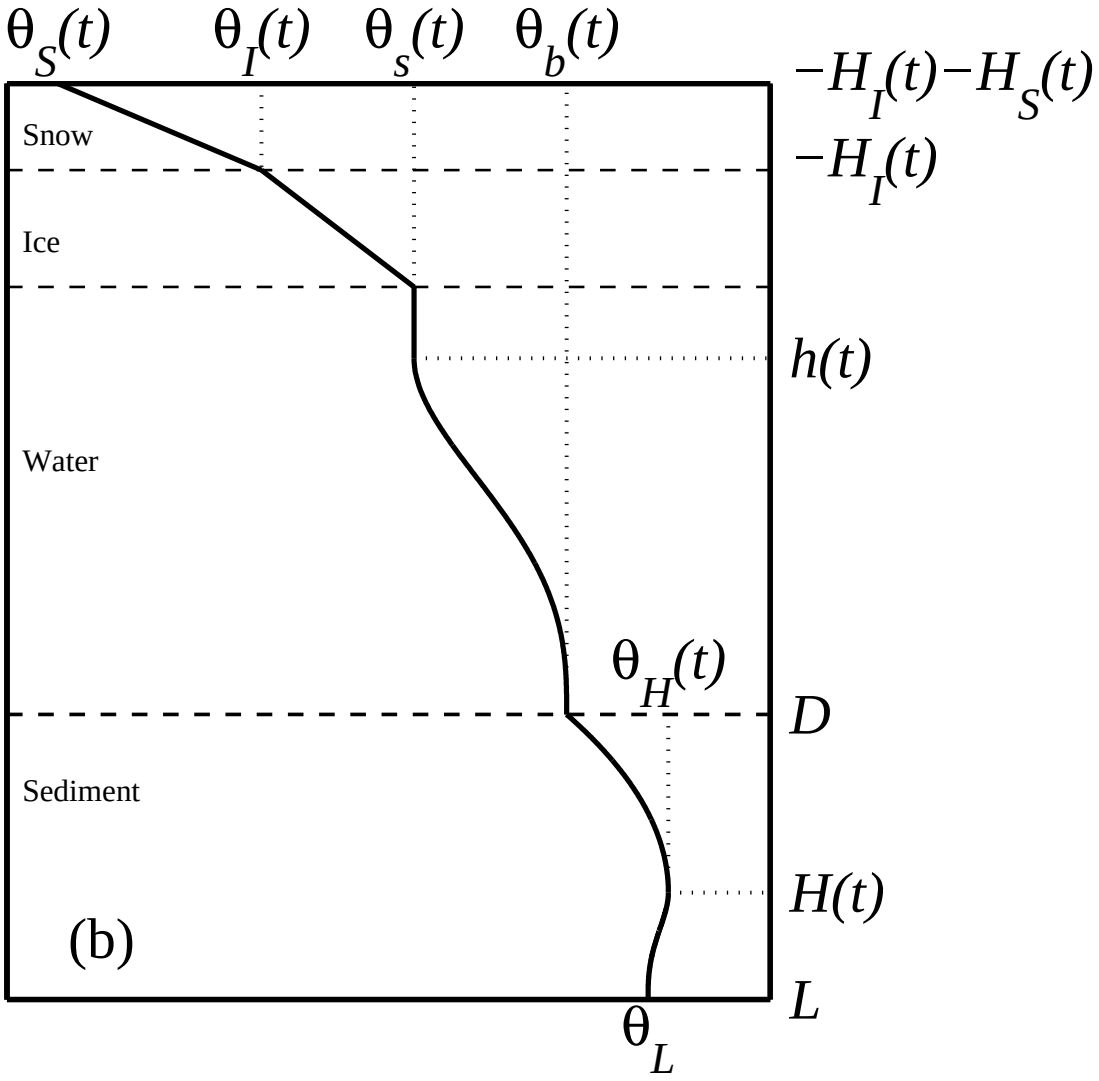

Figure 2.5: Apart from $\theta_s(t)$, $h(t)$, $\theta_b(t)$, $C_\theta(t)$, $\theta_H(t)$, and $H(t)$ (see Fig. 2.4), four additional quantities are computed in case the lake is covered by ice and snow. These are the temperature $\theta_S(t)$ at the air-snow interface, the temperature $\theta_I(t)$ at the snow-ice interface, the snow depth $H_S(t)$, and the ice depth $H_I(t)$.

2.4.2 The Water Temperature

Parameterization of the Temperature Profile and the Heat Budget

We adopt the following two-layer parameterization of the vertical temperature profile:

$$\theta = \begin{cases} \theta_s & \text{at} \quad 0 \le z \le h \\ \theta_s - (\theta_s - \theta_b)\Phi_\theta(\zeta) & \text{at} \quad h \le z \le D, \end{cases} \tag{2.66}$$

where $\Phi_\theta \equiv (\theta_s - \theta) / (\theta_s - \theta_b)$ is a dimensionless function of dimensionless depth $\zeta \equiv (z - h) / (D - h)$. The thermocline extends from the mixed-layer outer edge $z = h$ to the basin bottom $z = D$. Hereinafter the arguments of functions dependent on time and depth are not indicated (cf. Figs. 2.4 and 2.5).

According to Eq. (2.66), h, D, θ_s, θ_b, and the mean temperature of the water column, $\overline{\theta} \equiv D^{-1} \int_0^D \theta dz$, are related through

$$\overline{\theta} = \theta_s - C_\theta(1 - h/D)(\theta_s - \theta_b), \tag{2.67}$$

where

$$C_\theta = \int_0^1 \Phi_\theta(\zeta) d\zeta \tag{2.68}$$

is the shape factor.

The parameterization of the temperature profile (2.66) should satisfy the heat transfer equation

$$\frac{\partial}{\partial t}(\rho c \theta) = -\frac{\partial}{\partial z}(Q + I), \tag{2.69}$$

where Q is the vertical turbulent heat flux, and I is the heat flux due to solar radiation.

Integrating Eq. (2.69) over z from 0 to D yields the equation of the total heat budget,

$$D\frac{d\overline{\theta}}{dt} = \frac{1}{\rho_w c_w}\left[Q_s + I_s - Q_b - I(D)\right], \tag{2.70}$$

where c_w is the specific heat of water, Q_s and I_s are the values of Q and I, respectively, at the lake surface, and Q_b is the heat flux through the lake bottom. The radiation heat flux I_s that penetrates into the water is the surface value of the incident solar radiation flux from the atmosphere multiplied by $1 - \alpha_w$, α_w being the albedo of the water surface with respect to solar radiation. The surface flux Q_s is a sum of the sensible and latent heat fluxes and the net heat flux due to long-wave radiation at the air-water interface.

Integrating Eq. (2.69) over z from 0 to h yields the equation of the heat budget in the mixed layer,

$$h\frac{d\theta_s}{dt} = \frac{1}{\rho_w c_w}\left[Q_s + I_s - Q_h - I(h)\right], \tag{2.71}$$

where Q_h is the heat flux at the bottom of the mixed layer.

Given the surface fluxes Q_s and I_s (these are delivered by the driving atmospheric model or are known from observations), and the decay law for the flux of solar radiation , Eqs. (2.67), (2.70) and (2.71) contain seven unknowns, namely, h, $\overline{\theta}$, θ_s, θ_b, Q_h, Q_b and C_θ. The mixed layer depth, the bottom heat flux and the shape factor are considered in what follows. One more relation is required. Following Filyushkin and Miropolsky (1981), Tamsalu *et al.* (1997) and Tamsalu and Myrberg (1998), we assume that in case of the mixed layer deepening, $dh/dt > 0$, the profile of the vertical turbulent heat flux in the thermocline can be represented in a self-similar form. That is

$$Q = Q_h - (Q_h - Q_b)\Phi_Q(\zeta) \qquad \text{at} \;\; h \le z \le D, \tag{2.72}$$

where the shape function Φ_Q satisfies the boundary conditions $\Phi_Q(0) = 0$ and $\Phi_Q(1) = 1$. Equation (2.72) is suggested by the travelling wave-type solution to the heat transfer equation. If the mixed layer and the thermocline develop on the background of a deep stably or neutrally stratified quiescent layer (this situation is encountered in the ocean and in the atmosphere), the travelling wave-type solution shows that both the temperature profile and the profile of the turbulent heat flux are described by the same shape function, i.e. $\Phi_\theta(\zeta) = \Phi_Q(\zeta)$. In lakes, the thermocline usually extends from the bottom of the mixed layer down to the basin bottom (except for very deep lakes). In this case, the travelling wave-type solution to the heat transfer equation also suggests self-similar profiles of the temperature and of the heat flux, however the relation between the shape functions $\Phi_\theta(\zeta)$ and $\Phi_Q(\zeta)$ is different. The issue is considered in Mironov (2008).
Integrating Eq. (2.69) with due regard for Eqs. (2.66) and (2.72) over z' from h to $z > h$, then integrating the resulting expression over z from h to D, we obtain

$$\frac{1}{2}(D-h)^2\frac{d\theta_s}{dt} - \frac{d}{dt}\left[C_{\theta\theta}(D-h)^2(\theta_s-\theta_b)\right] =$$

$$\frac{1}{\rho_w c_w}\left[C_Q(D-h)(Q_h-Q_b) + (D-h)I(h) - \int_h^D I(z)dz\right], \tag{2.73}$$

where

$$C_Q = \int_0^1 \Phi_Q(\zeta)d\zeta \tag{2.74}$$

is the shape factor with respect to the heat flux, and

$$C_{\theta\theta} = \int_0^1 d\zeta \int_0^{\zeta'} \Phi_\theta(\zeta')d\zeta' \tag{2.75}$$

is the dimensionless parameter. The analysis in Mironov (2008) suggests that $C_Q = 2C_{\theta\theta}/C_\theta$.
In case of the mixed-layer stationary state or retreat, $dh/dt \leq 0$, Eq. (2.72) is not justified. Then, the bottom temperature is assumed to be "frozen",

$$\frac{d\theta_b}{dt} = 0. \tag{2.76}$$

If $h = D$, then $\theta_b = \theta_s = \overline{\theta}$ and the mean temperature is computed from Eq. (2.70).

The skin temperature module

The objective of introducing a skin temperature was to simulate a surface temperature representative of the energy budget at the lake surface, where the total derivative of temperature is in balance with the diffusion of the temperature plus a heat source, due to the divergence of the net radiation flux at the surface. In this optional module, the thickness of the skin layer is assumed to be constant and equal to 1 mm. During a model time step, this new surface temperature is then used to compute the new surface heat fluxes in the atmosphere, the new thickness of the mixed layer and the new thermocline profile.
The 1D heat transfer of heat in the lake writes:

$$\rho_w c_w \frac{d\theta}{dt} = \kappa_w \nabla\theta + F \tag{2.77}$$

Where θ is the water temperature, ρ_w and c_w the water density and heat capacity respectively, κ_w is the water heat transfer conductivity and F a source term.

For a lake, F can be simplified into the divergence of the solar radiation I neglecting the divergence of the longwave radiation, which is a common assumption. At the continuum scale, decomposing an instantaneous

field into an average plus a fluctuation and applying the Reynolds averaging operator to eq. 2.77 allows expressing the tendency of temperature. In the vicinity of the viscous layer, the turbulent term is negligible when compared to the diffusion term. If, on top of that, an assumption of horizontal homogeneity is applied to a steady state, eq. 2.77 can be transformed into leads to:

$$\kappa_w \frac{\partial^2 \theta}{\partial z^2} + \frac{\partial I}{\partial z} = 0 \tag{2.78}$$

where I, the solar radiation that penetrates the water up to depth z follows a Beer-Lambert decay law depending depth z and the extinction coefficient of radiation in the water ϵ.
Equation 2.78 can be integrated between the surface and the depth h to give the expression of the skin temperature θ_{skin} as a function of Q_s, I_s, θ_s and depth h:

$$\theta_{skin} = \theta_s + \frac{h}{\kappa_w}\left[Q_s + I_s\left(1 - \frac{1 - e^{-\epsilon h}}{\epsilon h}\right)\right] \tag{2.79}$$

Details of the computation can be found in Le Moigne *et al.* (2016).

The Mixed-Layer Depth

Convective deepening of the mixed layer is described by the entrainment equation. This equation is conveniently formulated in terms of the dependence of the so-called entrainment ratio A on one or the other stratification parameter. The entrainment ratio is a measure of the entrainment efficiency. It is commonly defined as a negative of the ratio of the heat flux due to entrainment at the bottom of the mixed layer, Q_h, to an appropriate heat flux scale, Q_*. In case of convection driven by the surface flux, where the forcing is confined to the boundary, the surface heat flux Q_s serves as an appropriate flux scale. This leads to the now classical Deardorff (1970a, 1970b) convective scaling, where h and $|h\beta Q_s/(\rho_w c_w)|^{1/3}$ serve as the scales of length and velocity, respectively.
The Deardorff scaling is unsuitable for convective flows affected by the solar radiation heating that is not confined to the boundary but is distributed over the water column. If the mixed-layer temperature exceeds the temperature of maximum density, convective motions are driven by surface cooling, whereas radiation heating tends to stabilise the water column, arresting the mixed layer deepening (Soloviev (1979); Mironov and Karlin (1989)). Such regime of convection is encountered in the oceanic upper layer (e.g. Kraus and Rooth (1961), Soloviev and Vershinskii (1982), Price *et al.* (1986) and in fresh-water lakes (e.g. Imberger (1985)). If the mixed-layer temperature is below that of maximum density, volumetric radiation heating leads to de-stabilisation of the water column and thereby drives convective motions. Such regime of convection is encountered in fresh-water lakes in spring. Convective mixing often occurs under the ice, when the snow cover overlying the ice vanishes and solar radiation penetrates down through the ice (e.g. Farmer (1975), Mironov and Terzhevik (2000), Mironov *et al.* (2002), Jonas *et al.* (2003)).
In order to account for the vertically distributed character of the radiation heating, we make use of a generalised convective heat flux scale

$$Q_* = Q_s + I_s + I(h) - 2h^{-1}\int_0^h I(z)dz, \tag{2.80}$$

and define the convective velocity scale and the entrainment ratio as

$$w_* = \left[-h\beta(\theta_s)Q_*/(\rho_w c_w)\right]^{1/3}, \qquad A = -Q_h/Q_*, \tag{2.81}$$

respectively. In order to specify A, we employ the entrainment equation in the form

$$A + \frac{C_{c2}}{w_*}\frac{dh}{dt} = C_{c1}, \tag{2.82}$$

where C_{c1} and C_{c2} are dimensionless constants (the estimates of these and other empirical constants of the model are discussed in Section 2.4.5 and summarised in the Appendix). The second term on the l.h.s. of Eq. (2.82) is the spin-up correction term introduced by Zilitinkevich (1975). This term prevents an unduly fast growth of h when the mixed layer is shallow. If the spin-up term is small, Eq. (2.82) reduces to a simple relation $A = C_{c1}$ that proved to be a sufficiently accurate approximation for a large variety of geophysical and laboratory convective flows Zilitinkevich (1991).

Equations (2.80), (2.81) and (2.82) should be used to compute the mixed-layer depth when the buoyancy flux $B_* = \beta(\theta_s)Q_*/(\rho_w c_w)$ is negative. The quantity $-hB_* \equiv w_*^3$ is a measure of the generation rate of the turbulence kinetic energy in a layer of depth h by the buoyancy forces (see a discussion in Mironov *et al.* (2002)). A negative B_* indicates that the TKE is generated through convective instability. Otherwise, the TKE is lost to work against the gravity. This occurs when the density stratification is stable. A different formulation for the mixed-layer depth is then required.

Mironov *et al.* (1991) used a diagnostic equation to determine the wind-mixed layer depth in stable and neutral stratification. That is, h was assumed to adjust to external forcing on a time scale that does not exceed the model time step. This assumption is fair if seasonal changes of temperature and mixing conditions are considered and the model time step is typically one day. The assumption is likely to be too crude to consider diurnal variations. To this end, We utilise a relaxation-type rate equation for the depth of a stably or neutrally stratified wind-mixed layer. It reads

$$\frac{dh}{dt} = \frac{h_e - h}{t_{rh}}. \tag{2.83}$$

Here, h_e is the equilibrium mixed-layer depth, and t_{rh} is the relaxation time scale given by

$$t_{rh} = \frac{h_e}{C_{rh}u_*}, \tag{2.84}$$

where $u_* = |\tau_s/\rho_w c_w|^{1/2}$ is the surface friction velocity, τ_s being the surface stress, and C_{rh} is a dimensionless constant. A rate equation (2.83) with the relaxation time scale proportional to the reciprocal of the Coriolis parameter [that is a particular case of Eq. (2.84) with h_e specified through Eq. (2.85)] was favourably tested by Zilitinkevich *et al.* (2002) and Zilitinkevich and Baklanov (2002) against data from atmospheric measurements and was recommended for practical use.

In order to specify h_e, we make use of a multi-limit formulation for the equilibrium depth of a stably or neutrally stratified boundary layer proposed by Zilitinkevich and Mironov (1996). Based on the analysis of the TKE budget, these authors proposed a generalised equation for the equilibrium boundary-layer depth that accounts for the combined effects of rotation, surface buoyancy flux and static stability at the boundary-layer outer edge [Eq. (30) in op. cit.]. That equation reduces to the equations proposed earlier by Rossby and Montgomery (1935), Kitaigorodskii (1960) and Kitaigorodskii and Joffre (1988) in the limiting cases of a truly neutral rotating boundary layer, the surface-flux-dominated boundary layer, and the imposed-stability-dominated boundary layer, respectively. It also incorporates the Zilitinkevich (1972) and the Pollard *et al.* (1973) equations that describe the intermediate regimes, where the effects of rotations and stratification essentially interfere and are roughly equally important. We adopt a simplified version of the Zilitinkevich and Mironov (1996) equation [Eq. (26) in op. cit.] that does not incorporate the Zilitinkevich (1972) and the

Pollard *et al.* (1973) scales. It reads

$$\left(\frac{fh_e}{C_n u_*}\right)^2 + \frac{h_e}{C_s L} + \frac{Nh_e}{C_i u_*} = 1, \tag{2.85}$$

where $f = 2\Omega \sin\phi$ is the Coriolis parameter, $\Omega = 7.29 \cdot 10^{-5}$ s^{-1} is the angular velocity of the earth's rotation, ϕ is the geographical latitude, L is the Obukhov length, N is the buoyancy frequency below the mixed layer, and C_n, C_s and C_i are dimensionless constants. A generalised formulation for the Obukhov length is used, $L = u_*^3/(\beta Q_*/\rho_w c_w)$, that accounts for the vertically distributed character of the solar radiation heating (note that the von Kármán constant is not included into the definition of L). A mean-square buoyancy frequency in the thermocline, $\overline{N} = \left[(D-h)^{-1}\int_h^D N^2 dz\right]^{1/2}$, is used as an estimate of N in Eq. (2.85).

One further comment is in order. Zilitinkevich *et al.* (2002) reconsidered the problem of the equilibrium stable boundary-layer depth. They concluded that the Zilitinkevich (1972) scale, $|u_* L/f|^{1/2}$, and the Pollard *et al.* (1973) scale, $u_*/|Nf|^{1/2}$, are the appropriate depth scales for the boundary layers dominated by the surface buoyancy flux and by the static stability at the boundary-layer outer edge, respectively. In other words, h_e depends on the Coriolis parameter no matter how strong the static stability. This is different from Eq. (2.85) where the limiting scales are L and u_*/N, respectively. The problem was further examined by Mironov and Fedorovich (2010). They showed that the above scales are particular cases of more general power-law formulations, namely, $h/L \propto (|f|L/u_*)^{-p}$ and $hN/u_* \propto (|f|/N)^{-q}$ for the boundary layers dominated by the surface buoyancy flux and by the static stability at the boundary-layer outer edge, respectively. The Zilitinkevich (1972) and Pollard *et al.* (1973) scales are recovered with $p = 1/2$ and $q = 1/2$, whereas the Kitaigorodskii (1960) and Kitaigorodskii and Joffre (1988) are recovered with $p = 0$ and $q = 0$. Scaling arguments are not sufficient to fix the exponents p and q. They should be evaluated on the basis of experimental data. Available data from observations and from large-eddy simulations are uncertain. They do not make it possible to evaluate p and q to sufficient accuracy and to conclusively decide between the alternative formulations for the boundary-layer depth. Leaving the evaluation of p and q for future studies, we utilise Eq. (2.85). This simple interpolation formula is consistent with the complexity of the present lake model and is expected to be a sufficiently accurate approximation for most practical purposes.

One more limitation on the equilibrium mixed-layer depth should be taken into account. Consider the situation where the mixed-layer temperature exceeds the temperature of maximum density, the surface flux Q_s is negative, whereas the heat flux scale Q_* given by Eq. (2.80) is positive (this can take place if $-Q_s/I_s < 1$). A positive Q_* indicates the the mixed layer of depth h is statically stable. A negative Q_s, however, indicates that convective instability should take place, leading to the development of a convectively mixed layer whose deepening is arrested by the solar radiation heating. The equilibrium depth h_c of such mixed layer is given by (see e.g. Mironov and Karlin (1989))

$$Q_*(h_c) = Q_s + I_s + I(h_c) - 2h_c^{-1}\int_0^{h_c} I(z)dz = 0. \tag{2.86}$$

This regime of convection is encountered on calm sunny days. If the wind suddenly ceases, Eq. (2.85) predicts a very shallow stably-stratified equilibrium mixed layer to which the mixed layer of depth $h > h_e$ should relax. In fact, however, the mixed layer would relax towards a convectively mixed layer whose equilibrium depth is given by Eq. (2.86). In order to account for this constraint, we require that $h_e \geq h_c$ if $Q_*(h) > 0$ and $\theta_s > \theta_r$.

2.4.3 The Water–Bottom Sediment Interaction

Parameterization of the Temperature Profile and the Heat Budget We adopt the following two-layer parametric representation, of the evolving temperature profile in the thermally active layer of bottom sediments proposed by Golosov *et al.* (1998):

$$\theta = \begin{cases} \theta_b - [\theta_b - \theta_H]\,\Phi_{B1}(\zeta_{B1}) & \text{at} \quad D \le z \le H \\ \theta_H - [\theta_H - \theta_L]\,\Phi_{B2}(\zeta_{B2}) & \text{at} \quad H \le z \le L, \end{cases} \tag{2.87}$$

Where, θ_L is the (constant) temperature at the outer edge $z = L$ of the thermally active layer of the sediments, θ_H is the temperature at the depth H where the vertical temperature gradient is zero, and $\Phi_{B1} \equiv (\theta_b - \theta)/(\theta_b - \theta_H)$ and $\Phi_{B2} \equiv (\theta_H - \theta)/(\theta_H - \theta_L)$ are dimensionless functions of dimensionless depths $\zeta_{B1} \equiv (z - D)/(H - D)$ and $\zeta_{B2} \equiv (z - H)/(L - H)$, respectively.
The parameterization (2.87) should satisfy the heat transfer equation (2.69), where the heat flux Q is due to molecular heat conduction and the bottom sediments are opaque to radiation. Integrating Eq. (2.69) over z from $z = D$ to $z = H$ with due regard for Eq. (2.87), we obtain

$$\frac{d}{dt}\left[(H - D)\theta_b - C_{B1}(H - D)(\theta_b - \theta_H)\right] - \theta_H \frac{dH}{dt} = \frac{1}{\rho_w c_w}\left[Q_b + I(D)\right], \tag{2.88}$$

where the heat flux at $z = H$ is zero by virtue of the zero temperature gradient there.
Integrating Eq. (2.69) over z from $z = H$ to $z = L$, we obtain

$$\frac{d}{dt}\left[(L - H)\theta_H - C_{B2}(L - H)(\theta_H - \theta_L)\right] + \theta_H \frac{dH}{dt} = 0, \tag{2.89}$$

where the heat flux at $z = L$ (the geothermal heat flux) is neglected.
The shape factors C_{B1} and C_{B2} are given by

$$C_{B1} = \int_0^1 \Phi_{B1}(\zeta_{B1}) d\zeta_{B1}, \qquad C_{B2} = \int_0^1 \Phi_{B2}(\zeta_{B2}) d\zeta_{B2}. \tag{2.90}$$

Heat Flux through the Bottom The bottom heat flux Q_b is due to molecular heat conduction through the uppermost layer of bottom sediments. It can be estimated as the product of the negative of the temperature gradient at $z = D + 0$ and the molecular heat conductivity. The uppermost layer of bottom sediments is saturated with water. Its water content typically exceeds 90% and its physical properties, including the heat conductivity, are very close to the properties of the lake water. Then, the heat flux through the lake bottom is given by

$$Q_b = -\kappa_w \frac{\theta_H - \theta_b}{H - D} \Phi'_{B1}(0), \tag{2.91}$$

where κ_w is the molecular heat conductivity of water. This relation closes the problem.
It should be stressed that Eqs. (2.88), (2.89) and (2.91) do not contain the molecular heat conductivity of bottom sediments, a quantity that is rarely known to a satisfactory degree of precision. It is through the use of the integral (bulk) approach, based on the parameterization (2.87) of the temperature profile, that the molecular heat conductivity of bottom sediments is no longer needed.

2.4.4 Ice and Snow Cover

In this section, a two-layer thermodynamic (no rheology) model of the ice and snow cover is described. It is based on a self-similar parametric representation of the temperature profile within ice and snow and on the integral heat budgets of the ice and snow layers. The approach is, therefore, conceptually similar to

the approach used above to describe the temperature structure of the mixed layer, of the lake thermocline, and of the thermally active layer of bottom sediments. Notice that the assumption about the shape of the temperature profile within the ice, the simplest of which is the linear profile, is either explicit or implicit in a number of ice models developed to date. A model of ice growth based on a linear temperature distribution was proposed by Stefan as early as 1891.

Parameterization of the Temperature Profile and the Heat Budget We adopt the following parametric representation of the evolving temperature profile within ice and snow:

$$\theta = \begin{cases} \theta_f - [\theta_f - \theta_I]\Phi_I(\zeta_I) & \text{at} \quad -H_I \le z \le 0 \\ \theta_I - [\theta_I - \theta_S]\Phi_S(\zeta_S) & \text{at} \quad -[H_I + H_S] \le z \le -H_I. \end{cases} \tag{2.92}$$

Here, z is the vertical co-ordinate (positive downward) with the origin at the ice-water interface, H_I is the ice thickness, H_S is the thickness of snow overlaying the ice, θ_f is the fresh-water freezing point, θ_I is the temperature at the snow-ice interface, and θ_S is the temperature at the air-snow interface. Notice that the freezing point of salt water is a decreasing function of salinity. A model that accounts for this dependence and is applicable to the ice over salt lakes or seas is presented by Mironov and Ritter (2004). Dimensionless universal functions $\Phi_I \equiv (\theta_f - \theta)/(\theta_f - \theta_I)$ and $\Phi_S \equiv (\theta_I - \theta)/(\theta_I - \theta_S)$ of dimensionless depths $\zeta_I \equiv -z/H_I$ and $\zeta_S \equiv -(z + H_I)/H_S$, respectively, satisfy the boundary conditions $\Phi_I(0) = 0$, $\Phi_I(1) = 1$, $\Phi_S(0) = 0$, and $\Phi_S(1) = 1$.

According to Eq. (2.92), the heat fluxes through the ice, Q_I, and through the snow, Q_S, due to molecular heat conduction are given by

$$Q_I = -\kappa_i \frac{\theta_f - \theta_I}{H_I} \frac{d\Phi_I}{d\zeta_I}, \qquad Q_S = -\kappa_s \frac{\theta_I - \theta_S}{H_S} \frac{d\Phi_S}{d\zeta_S}, \tag{2.93}$$

where κ_i and κ_s are the heat conductivities of ice and snow, respectively.

The parameterization of the temperature profile (2.92) should satisfy the heat transfer equation (2.69). Integrating Eq. (2.69) over z from the air-snow interface $z = -(H_I + H_S)$ to just above the ice-water interface $z = -0$ with due regard for the parameterization (2.92), we obtain the equation of the heat budget of the snow-ice cover,

$$\frac{d}{dt}\{\rho_i c_i H_I [\theta_f - C_I(\theta_f - \theta_I)] + \rho_s c_s H_S [\theta_I - C_S(\theta_I - \theta_S)]\} - \rho_s c_s \theta_S \frac{d}{dt}(H_I + H_S) =$$

$$Q_s + I_s - I(0) + \kappa_i \frac{\theta_f - \theta_I}{H_I} \Phi_I'(0). \tag{2.94}$$

Here, ρ_i and ρ_s are the densities of ice and of snow, respectively, c_i and c_s are specific heats of these media, and Q_s and I_s are the values of Q and I, respectively, at the air-snow or, if snow is absent, at the air-ice interface. The radiation heat flux I_s that penetrates into the interior of snow-ice cover is the surface value of the incident solar radiation flux from the atmosphere multiplied by $1 - \alpha_i$, α_i being the albedo of the ice or snow surface with respect to solar radiation. The dimensionless parameters C_I and C_S, the shape factors, are given by

$$C_I = \int_0^1 \Phi_I(\zeta_I) d\zeta_I, \qquad C_S = \int_0^1 \Phi_S(\zeta_S) d\zeta_S. \tag{2.95}$$

The heat flux at the snow-ice interface is assumed to be continuous, that is

$$-\kappa_i \frac{\theta_f - \theta_I}{H_I} \Phi_I'(1) = -\kappa_s \frac{\theta_I - \theta_S}{H_S} \Phi_S'(0). \tag{2.96}$$

Equations (2.94) and (2.96) serve to determine temperatures at the air-snow and at the snow-ice interfaces, when these temperatures are below the freezing point, i.e. when no melting at the snow surface (ice surface, when snow is absent) takes place. During the snow (ice) melting from above, the temperatures θ_S and θ_I remain equal to the freezing point θ_f, and the heat fluxes Q_S and Q_I are zero.

Snow and Ice Thickness The equations governing the evolution of the snow thickness and of the ice thickness are derived from the heat transfer equation (2.69) that incorporates an additional term on its right-hand side, namely, the term $f_M(z)L_f dM/dt$ that describes the rate of heat release/consumption due to accretion/melting of snow and ice. Here, M is the mass of snow or ice per unit area, L_f is the latent heat of fusion, and $f_M(z)$ is a function that satisfies the normalization conditions $\int_{H_I}^{H_I+H_S} f_M(z)dz = 1$ and $\int_0^{H_I} f_M(z)dz = 1$ for snow and ice, respectively.
The accumulation of snow is not computed within the ice-snow model. The rate of snow accumulation is assumed to be a known time-dependent quantity that is provided by the atmospheric model or is known from observations. Then, the evolution of the snow thickness during the snow accumulation and no melting is computed from

$$\frac{d\rho_s H_S}{dt} = \left(\frac{dM_S}{dt}\right)_a, \tag{2.97}$$

where $M_S = \rho_s H_S$ is the snow mass per unit area, and $(dM_S/dt)_a$ is the (given) rate of snow accumulation. When the temperature θ_I at the upper surface of the ice is below the freezing point θ_f, the heat conduction through the ice causes the ice growth. This growth is accompanied by a release of heat at the lower surface of the ice that occurs at a rate $L_f dM_I/dt$, where $M_I = \rho_i H_I$ is the ice mass per unit area. The normalization function f_M is equal to zero throughout the snow-ice cover except at the ice-water interface where $f_M = \delta(0)$, $\delta(z)$ being the Dirac delta function. Integrating Eq. (2.69) from $z = -0$ to $z = +0$ with due regard for this heat release yields the equation for the ice thickness. It reads

$$L_f \frac{d\rho_i H_I}{dt} = Q_w + \kappa_i \frac{\theta_f - \theta_I}{H_I}\Phi'_I(0), \tag{2.98}$$

where Q_w is the heat flux in the near-surface water layer just beneath the ice. If the r.h.s. of Eq. (2.98) is negative, i.e. the negative of the heat flux in the water, Q_w, exceeds the negative of the heat flux in the ice, $Q_I|_{z=0}$, ice ablation takes place.
As the atmosphere heats the snow surface, the surface temperature eventually reaches the freezing point and the snow and ice melting sets in. This process is accompanied by a consumption of heat at rates $L_f d\rho_s H_S/dt$ and $L_f d\rho_i H_I/dt$ for snow and ice, respectively. Notice that the exact form of the normalization function f_M is not required by virtue of the normalization conditions considered above. Integrating Eq. (2.69) from $z = -(H_I + H_S) - 0$ to $z = -H_I$ with due regard for the heat loss due to snow melting and adding the (given) rate of snow accumulation yields the equation for the snow thickness,

$$L_f \frac{d\rho_s H_S}{dt} = -(Q_s + I_s) + I(-H_I) + L_f \left(\frac{dM_S}{dt}\right)_a + c_s \theta_f H_S \frac{d\rho_s}{dt}. \tag{2.99}$$

Integrating Eq. (2.69) from $z = -H_I$ to $z = +0$ with due regard for the heat loss due to ice melting yields the equation for the ice thickness,

$$L_f \frac{d\rho_i H_I}{dt} = Q_w + I(0) - I(-H_I). \tag{2.100}$$

If the ice melts out earlier than snow, the snow depth is instantaneously set to zero.

The Temperature Profile beneath the Ice The simplest assumption is to keep the temperature profile unchanged over the entire period of ice cover. This assumption is fair for deep lakes, where the heat flux through the bottom is negligibly small. In shallow lakes, this assumption may lead to an underestimation of the mean temperature. The heat accumulated in the thermally active upper layer of bottom sediments during spring and summer is returned back to the water column during winter, leading to an increase of the water temperature under the ice. The water temperature under the ice can also increase due to heating by solar radiation penetrating down through the ice. The thermodynamic regimes encountered in ice-covered lakes are many and varied. Their detailed description requires a set of sophisticated parameterizations. The use of such parameterizations in the framework of the present lake model is, however, hardly justified. The point is that it is the snow (ice) surface temperature that communicates information to the atmosphere, the water temperature is not directly felt by the atmospheric surface layer. It is, therefore, not vital that the temperature regimes in ice-covered lakes be described in great detail. Only their most salient features should be accounted for, first of all, the heat budget of the water column.

When the lake is ice-covered, the temperature at the ice-water interface is fixed at the freezing point $\theta_s = \theta_f$. In case the bottom temperature is less than the temperature of maximum density, $\theta_b < \theta_r$, the mixed-layer depth and the shape factor are kept unchanged, $dh/dt = 0$ and $dC_\theta/dt = 0$, the mean temperature $\overline{\theta}$ is computed from Eq. (2.70) and the bottom temperature θ_b is computed from Eq. (2.67). If the entire water column appears to be mixed at the moment of freezing, i.e. $h = D$ and $\theta_s = \overline{\theta} = \theta_b$, the mixed layer depth is reset to zero, $h = 0$, and the shape factor is set to its minimum value, $C_\theta = 0.5$ (see Section 2.4.5).

The heat flux from water to ice is estimated from

$$Q_w = -\kappa_w \frac{\theta_b - \theta_s}{D}, \tag{2.101}$$

if $h = 0$, and $Q_w = 0$ otherwise. Notice that the estimate of Q_w given by Eq. (2.101) and the shape factor $C_\theta = 0.5$ correspond to a linear temperature profile over the entire water column. A linear profile is encountered in ice-covered shallow lakes when $\theta_b < \theta_r$ and the heat flux is from the bottom sediments to the lake water.

As the bottom temperature reaches the temperature of maximum density, convection due to bottom heating sets in. To describe this regime of convection in detail, a convectively mixed layer whose temperature is close to θ_r, and a thin layer adjacent to the bottom, where the temperature decreases sharply from $\theta_b > \theta_r$ to θ_r, should be thoroughly considered. We neglect these peculiarities of convection due to bottom heating and adopt a simpler model where the bottom temperature is fixed at the temperature of maximum density, $\theta_b = \theta_r$. The mean temperature $\overline{\theta}$ is computed from Eq. (2.70). If $h > 0$, the shape factor C_θ is kept unchanged, and the mixed-layer depth is computed from Eq. (2.67). As the mixed-layer depth approaches zero, Eq. (2.67) is used to compute the shape factor C_θ that in this regime would increase towards its maximum value C_θ^{max}. The heat flux from water to ice is estimated from

$$Q_w = -\kappa_w \frac{\theta_b - \theta_s}{D} \max\left[1, \Phi'_\theta(0)\right], \tag{2.102}$$

if $h = 0$, and $Q_w = 0$ otherwise.

One more regime of convection is often encountered in ice-covered lakes. In late spring, the snow overlying the ice vanishes and solar radiation penetrates down through the ice. As the mixed-layer temperature is below that of maximum density, the volumetric radiation heating leads to de-stabilisation of the water column and thereby drives convective motions. Such regime of convection was analysed by Farmer (1975), Mironov and Terzhevik (2000), Mironov *et al.* (2002), and Jonas *et al.* (2003), among others. A parameterization of convection due to solar heating (e.g. a parameterization based on a bulk model developed by Mironov *et al.* (2002)) can, in principle, be incorporated into the present model. We do not do so, however, considering

that the major effect of convection beneath the ice is to redistribute heat in the vertical and that it takes place over a limited period of time.

2.4.5 Empirical Relations and Model Constants

The Shape Functions

We adopt the following polynomial approximation of the shape function $\Phi_\theta(\zeta)$ with respect to the temperature profile in the thermocline:

$$\Phi_\theta = \left(\frac{40}{3}C_\theta - \frac{20}{3}\right)\zeta + (18 - 30C_\theta)\,\zeta^2 + (20C_\theta - 12)\,\zeta^3 + \left(\frac{5}{3} - \frac{10}{3}C_\theta\right)\zeta^4. \tag{2.103}$$

The shape factor C_θ is computed from

$$\frac{dC_\theta}{dt} = \text{sign}(dh/dt)\frac{C_\theta^{max} - C_\theta^{min}}{t_{rc}}, \qquad C_\theta^{min} \le C_\theta \le C_\theta^{max}, \tag{2.104}$$

where t_{rc} is the relaxation time scale, and sign is the signum function, sign(x)=-1 if $x \le 0$ and sign(x)=1 if $x > 0$. The minimum and maximum values of the shape factor are set to $C_\theta^{min} = 0.5$ and $C_\theta^{max} = 0.8$. During the mixed-layer deepening, $dh/dt > 0$, the temperature profile evolves towards the limiting curve, characterised by a maximum value of the shape factor, $C_\theta^{max} = 0.8$, and the maximum value of the dimensionless temperature gradient at the upper boundary of the thermocline, $\Phi'_\theta(0) = 4$. During the mixed-layer stationary state or retreat, $dh/dt \le 0$, the temperature profile evolves towards the other limiting curve, characterised by a minimum value of the shape factor, $C_\theta^{min} = 0.5$, and the zero temperature gradient at the upper boundary of the thermocline, $\Phi'_\theta(0) = 0$. Notice that $C_\theta^{min} = 0.5$ is consistent with a linear temperature profile that is assumed to occur under the ice when the bottom temperature is less than the temperature of maximum density (see Section 2.4.4).

According to Eq. (2.103), the dimensionless parameter $C_{\theta\theta}$ defined through Eq. (2.75) is given by

$$C_{\theta\theta} = \frac{11}{18}C_\theta - \frac{7}{45}. \tag{2.105}$$

The relaxation time t_{rc} is estimated from the following arguments. The time t_{rc} is basically the time of the evolution of the temperature profile in the thermocline from one limiting curve to the other, following the change of sign in dh/dt. Then, a reasonable scale for t_{rc} is the thermal diffusion time through the thermocline, that is a square of the thermocline thickness, $(D-h)^2$, over a characteristic eddy temperature conductivity, K_{H*}. Using a mean-square buoyancy frequency in the thermocline, $\overline{N} = \left[(D-h)^{-1}\int_h^D N^2 dz\right]^{1/2}$, as an estimate of N and assuming that the TKE in the thermocline scales either on the convective velocity w_*, Eq. (2.81), or on the surface friction velocity u_*, we propose (see Mironov (2008) for details)

$$t_{rc} = \frac{(D-h)^2\overline{N}}{C_{rc}u_T^2}, \qquad u_T = \max(w_*, u_*), \tag{2.106}$$

where C_{rc} is a dimensionless constant estimated at 0.003 (this value may be altered as new information becomes available).

We adopt the following polynomial approximations of the shape functions $\Phi_{B1}(\zeta_{B1})$ and $\Phi_{B2}(\zeta_{B2})$ with respect to the temperature profile in bottom sediments (cf. Golosov *et al.* (1998)):

$$\Phi_{B1} = 2\zeta_{B1} - \zeta_{B1}^2, \qquad \Phi_{B2} = 6\zeta_{B2}^2 - 8\zeta_{B2}^3 + 3\zeta_{B2}^4. \tag{2.107}$$

which are the simplest polynomials that satisfy a minimum set of constraints. The conditions $\Phi_{B1}(0) = \Phi_{B2}(0) = 0$ and $\Phi_{B1}(1) = \Phi_{B2}(1) = 1$ follow from the definition of ζ_{B1}, ζ_{B2}, Φ_{B1}, and Φ_{B2}. The

conditions $\Phi'_{B1}(1) = \Phi'_{B2}(0) = \Phi'_{B2}(1) = 0$ provide a zero temperature gradient at the depths $z = H$ and $z = L$, and the condition $\Phi''_{B2}(1) = 0$ follows from the requirement that the temperature θ_L at the outer edge $z = L$ of the thermally active layer of the sediments is constant in time. The shape factors that correspond to Eq. (2.107) are $C_{B1} = 2/3$ and $C_{B2} = 3/5$.

As a zero-order approximation, the simplest linear temperature profile within snow and ice can be assumed, $\Phi_S(\zeta_S) = \zeta_S$ and $\Phi_I(\zeta_I) = \zeta_I$. This gives $C_S = C_I = 1/2$. Although a linear profile is a good approximation for thin ice, it is likely to result in a too thick ice in cold regions, where the ice growth takes place over a long period, and in a too high thermal inertia of thick ice. A slightly more sophisticated approximation was developed by Mironov and Ritter (2004) who assumed that the ice thickness is limited by a certain maximum value H_I^{max} and that the rate of ice growth approaches zero as H_I approaches H_I^{max} (the snow layer over the ice was not considered). They proposed

$$\Phi_I = \left[1 - \frac{H_I}{H_I^{max}}\right]\zeta_I + \left[(2 - \Phi_{*I})\frac{H_I}{H_I^{max}}\right]\zeta_I^2 + \left[(\Phi_{*I} - 1)\frac{H_I}{H_I^{max}}\right]\zeta_I^3, \tag{2.108}$$

where Φ_{*I} is a dimensionless constant. The shape factor that corresponds to Eq. (2.108) is

$$C_I = \frac{1}{2} - \frac{1}{12}(1 + \Phi_{*I})\frac{H_I}{H_I^{max}}. \tag{2.109}$$

The physical meaning of the above expressions can be elucidated as follows. The relation $\Phi'_I(0) = 1 - H_I/H_I^{max}$ that follows from Eq. (2.108) ensures that the ice growth is quenched as the ice thickness approaches its maximum value. Equation (2.109) suggests that the shape factor C_I decreases with increasing ice thickness. A smaller C_I means a smaller relative thermal inertia of the ice layer of thickness H_I [the absolute thermal inertia is measured by the term $C_I H_I$ that enters the l.h.s. of Eq. (2.94)]. This is plausible as it is mostly the upper part of thick ice, not the entire ice layer, that effectively responds to external forcing. For use in the global numerical weather prediction model GME of the German Weather Service, Mironov and Ritter (2004) proposed an estimate of $H_I^{max} = 3$ m. This value is typical of the central Arctic in winter. The allowable values of Φ_{*I} lie in the range between -1 and 5. $\Phi_{*I} > 5$ yields an unphysical negative value of C_I as the ice thickness approaches H_I^{max}. $\Phi_{*I} < -1$ gives C_I that increases with increasing H_I. There is no formal proof that this may not occur, but it is very unlikely. A reasonable estimate is $\Phi_{*I} = 2$. With this estimate C_I is halved as H_I increases from 0 to H_I^{max}. Notice that the linear temperature profile is recovered as $H_I/H_I^{max} \ll 1$, i.e. when the ice is thin.

It should be stressed that, although the shape functions are useful in that they provide a continuous temperature profile trough the snow, ice, water and bottom sediments, their exact shapes are not required in the present model. It is not $\Phi_\theta(\zeta)$, $\Phi_{B1}(\zeta_{B1})$, $\Phi_{B2}(\zeta_{B2})$, $\Phi_S(\zeta_S)$ and $\Phi_I(\zeta_I)$ per se, but the shape factors C_θ, C_{B1}, C_{B2}, C_S and C_I, and the dimensionless gradients $\Phi'_\theta(0)$, $\Phi'_{B1}(0)$, $\Phi'_S(0)$, $\Phi'_I(0)$ and $\Phi'_I(1)$, that enter the model equations. The estimates of these parameters are summarised in Table 2.8.

Constants in the Equations for the Mixed-Layer Depth The estimates of $C_{c1} = 0.2$ and $C_{c2} = 0.8$ in Eq. (2.82) were recommended by Zilitinkevich (1991). They were obtained using laboratory, atmospheric and oceanic data. Apart from being commonly used in mixed-layer models of penetrative convection driven by the surface buoyancy flux, these values were successfully used by Mironov and Karlin (1989) to simulate day-time convection in the upper ocean that is driven by surface cooling but inhibited by radiation heating, and by Mironov and Terzhevik (2000) and Mironov *et al.* (2002) to simulate spring convection in ice-covered lakes where convective motions are driven by volumetric radiation heating of the water at temperature below the temperature of maximum density (Mironov *et al.* (2002) used $C_{c2} = 1.0$). A slightly modified estimate

of $C_{c1} = 0.17$ was obtained by Fedorovich *et al.* (2004) from large-eddy simulation data. We adopt the estimates of $C_{c1} = 0.17$ and $C_{c2} = 1.0$ for use in the equation of convective entrainment.
For use in Eq. (2.85) for the equilibrium mixed-layer depth in stable or neutral stratification, we adopt the estimates of $C_n = 0.5$, $C_s = 10$ and $C_i = 20$ obtained by Zilitinkevich and Mironov (1996). The estimates of C_s and C_i are based on a limited amount of data and may need to be slightly altered as new (and better) data become available. The estimate of C_n was corroborated by the results from further studies (Zilitinkevich and Esau, 2002) and is reliable.
The estimates of the dimensionless constant C_{rh} in the relaxation-type rate equation for the depth of a stably or neutrally stratified wind-mixed layer, Eqs. (2.83) and (2.84), are not abundant. Kim (1976) and Deardorff (1983) recommended that the value of $C_{rh} = 0.28$ be used to describe entrainment into a homogeneous fluid. The same value was used by Zeman (1979), and a slightly lower value of $C_{rh} = 0.26$ by Zilitinkevich *et al.* (1979). The rate equations given by Khakimov (1976) and Zilitinkevich *et al.* (2002) use the reciprocal of the Coriolis parameter as the relaxation time scale. Their rate equations suggest the values of $C_{rh} = 0.45$ and $C_{rh} = 0.5$, respectively. A similar form of the rate equation was proposed earlier by Deardorff (1971) who used a much lower value of $C_{rh} = 0.025$. We adopt an estimate of $C_{rh} = 0.03$ suggested by the sensitivity experiments with the present lake model (keeping in mind that this value may need to be altered).
The estimates of dimensionless constants in the equations for the mixed-layer depth are summarised in Table 2.8.

Thermodynamic Parameters The exponential approximation of the decay law for the flux of solar radiation is commonly used in applications. It reads

$$I(t,z) = I_s(t) \sum_{k=1}^{n} a_k \exp[-\gamma_k(z + H_S + H_I)], \tag{2.110}$$

where I_s is the surface value of the solar radiation heat flux multiplied by $1 - \alpha$, α being the albedo of the water, ice or snow surface with respect to solar radiation, n is the number of wavelength bands, a_k are fractions of the total radiation flux for different wavelength bands, and $\gamma_k(z)$ are attenuation coefficients for different bands. The attenuation coefficients are piece-wise constant functions of height, i.e. they have different values for water, ice and snow but remain depth-constant within these media. The optical characteristics of water are lake-specific and should be estimated in every particular case. Rough estimates of a_k and γ_k for ice and snow are given by Launiainen and Cheng (1998).
The lake model includes a number of thermodynamic parameters. They are summarised in Table 2.9. These thermodynamic parameters can be considered constant except for the snow density and the snow heat conductivity that depend, among other things, on the snow thickness and the snow age. As a first approximation, the following empirical formulations (Heise *et al.* (2003)) can be used that relate ρ_s and κ_s to the snow thickness:

$$\rho_s = \min\left\{\rho_s^{max}, |1 - H_S\Gamma_{\rho_s}/\rho_w|^{-1}\,\rho_s^{min}\right\}, \tag{2.111}$$

where $\rho_s^{min} = 100$ kg·m^{-3} and $\rho_s^{max} = 400$ kg·m^{-3} are minimum and maximum values, respectively, of the snow density, and $\Gamma_{\rho_s} = 200$ kg·m^{-4} is an empirical parameter, and

$$\kappa_s = \min\left\{\kappa_s^{max}, \kappa_s^{min} + H_S\Gamma_{\kappa_s}\rho_s/\rho_w\right\}, \tag{2.112}$$

where $\kappa_s^{min} = 0.2$ J·m^{-1}·s^{-1}·K^{-1} and $\kappa_s^{max} = 1.5$ J·m^{-1}·s^{-1}·K^{-1} are minimum and maximum values, respectively, of the snow heat conductivity, and $\Gamma_{\kappa_s} = 1.3$ J·m^{-2}·s^{-1}·K^{-1} is an empirical parameter.

2.4.6 Conclusions

A lake model suitable to predict the vertical temperature structure in lakes of various depths on time scales from a few hours to many years is developed. The model, termed FLake, is based on a two-layer parametric representation of the evolving temperature profile and on the integral budget of energy for the layers in question. The structure of the stratified layer between the upper mixed layer and the basin bottom, the lake thermocline, is described using the concept of self-similarity (assumed shape) of the temperature-depth curve. The same concept is used to describe the temperature structure of the thermally active upper layer of bottom sediments and of the ice and snow cover. An entrainment equation is used to compute the depth of a convectively-mixed layer. A relaxation-type equation is used to compute the wind-mixed layer depth in stable and neutral stratification, where a multi-limit formulation for the equilibrium mixed-layer depth accounts for the effects of the earth's rotation, of the surface buoyancy flux, and of the static stability in the thermocline. Both mixing regimes are treated with due regard for the volumetric character of solar radiation heating. Simple thermodynamic arguments are invoked to develop the evolution equations for the ice and snow depths. Using the integral (bulk) approach, the problem of solving partial differential equations (in depth and time) for the temperature and turbulence quantities is reduced to solving ordinary differential equations for the time-dependent parameters that specify the evolving temperature profile. The result is a computationally efficient lake model that incorporates much of the essential physics.

It must be emphasised that the empirical constants and parameters of FLake are not application-specific. That is, once they have been estimated using independent empirical and numerical data, they should not be re-evaluated when the model is applied to a particular lake. There are, of course, lake-specific external parameters, such as depth to the bottom and optical characteristics of water, but these are not part of the model physics. In this way FLake does not require "re-tuning", a procedure that may improve an agreement with a limited amount of data and is sometimes justified. This procedure should, however, be considered as a bad practice and must be avoided whenever possible as it greatly reduces the predictive capacity of a physical model (Randall and Wielicki, 1997).

Apart from the depth to the bottom and the optical characteristics of lake water, the only lake-specific parameters are the depth L of the thermally active layer of bottom sediments and the temperature θ_L at that depth. These parameters should be estimated only once for each lake, using observational data or empirical recipes (e.g. Fang and Stefan (1998)). In a similar way, the temperature at the bottom of the thermally active soil layer and the depth of that layer are estimated once and then used in an NWP model as two-dimensional external-parameter arrays.

The proposed lake model is intended for use, first of all, in NWP and climate models as a module (parameterization scheme) to predict the lake surface temperature. Apart from NWP and climate modelling, practical applications where simple bulk models are favoured over more accurate but more sophisticated models (e.g. second-order turbulence closures) include modelling aquatic ecosystems. For ecosystem modelling, a sophisticated physical module is most often not required because of insufficient knowledge of chemistry and biology.

Appendix. A Summary of Model Parameters

Table 2.8: Empirical Constants and Parameters

Constant/ Parameter	Recommended Value/ Computed from	Comments
C_{c1}	0.17	
C_{c2}	1.0	
C_n	0.5	
C_s	10	
C_i	20	
C_{rh}	0.03	
C_{rc}	0.003	
C_θ	Eq. (2.104)	
C_θ^{min}	0.5	
C_θ^{max}	0.8	
$C_{\theta\theta}$	Eq. (2.105)	
C_Q	$2C_{\theta\theta}/C_\theta$	
C_{B1}	2/3	
C_{B2}	3/5	
C_I	1/2	Optionally Eq. (2.109)
C_S	1/2	
$\Phi'_\theta(0)$	Eqs. (2.103) and (2.104)	
$\Phi'_{B1}(0)$	2	
$\Phi'_I(0)$	1	Optionally Eq. (2.108)
$\Phi'_I(1)$	1	Optionally Eq. (2.108)
$\Phi'_S(0)$	1	
Φ_{*I}	2	
H_I^{max}	3 m	

Table 2.9: Thermodynamic Parameters

Notation	Parameter	Dimensions	Estimate/ Computed from
g	Acceleration due to gravity	$\mathrm{m{\cdot}s^{-2}}$	9.81
θ_r	Temperature of maximum density of fresh water	K	277.13
θ_f	Fresh water freezing point	K	273.15
a_T	Coefficient in the fresh-water equation of state	$\mathrm{K^{-2}}$	$1.6509 \cdot 10^{-5}$
ρ_w	Density of fresh water	$\mathrm{kg{\cdot}m^{-3}}$	Eq. (2.64)
ρ_r	Maximum density of fresh water	$\mathrm{kg{\cdot}m^{-3}}$	$1.0 \cdot 10^3$
ρ_i	Density of ice	$\mathrm{kg{\cdot}m^{-3}}$	$9.1 \cdot 10^2$
ρ_s	Density of snow	$\mathrm{kg{\cdot}m^{-3}}$	Eq. (2.111)
L_f	Latent heat of fusion	$\mathrm{J{\cdot}kg^{-1}}$	$3.3 \cdot 10^5$
c_w	Specific heat of water	$\mathrm{J{\cdot}kg^{-1}{\cdot}K^{-1}}$	$4.2 \cdot 10^3$
c_i	Specific heat of ice	$\mathrm{J{\cdot}kg^{-1}{\cdot}K^{-1}}$	$2.1 \cdot 10^3$
c_s	Specific heat of snow	$\mathrm{J{\cdot}kg^{-1}{\cdot}K^{-1}}$	$2.1 \cdot 10^3$
κ_w	Molecular heat conductivity of water	$\mathrm{J{\cdot}m^{-1}{\cdot}s^{-1}{\cdot}K^{-1}}$	$5.46 \cdot 10^{-1}$
κ_i	Molecular heat conductivity of ice	$\mathrm{J{\cdot}m^{-1}{\cdot}s^{-1}{\cdot}K^{-1}}$	2.29
κ_s	Molecular heat conductivity of snow	$\mathrm{J{\cdot}m^{-1}{\cdot}s^{-1}{\cdot}K^{-1}}$	Eq. (2.112)

Bibliography

[1] S. Belamari. Report on uncertainty estimates of an optimal bulk formulation for surface turbulent fluxes. Technical report, Marine EnviRonment and Security for the European Area - Integrated Project (MERSEA IP), Deliverable D4.1.2, 29p, 2005.

[2] B. Blanke and P. Delecluse. Variability of the tropical atlantic ocean simulated by a general circulation model with two different mixed-layer physics. *Journal of Physical Oceanography*, 23:1363–1388, 1993.

[3] P. Bougeault and P. Lacarrère. Parameterization of orography-induced turbulence in a mesobeta scale model. *Mon. Wea. Rev.*, 117:1872–1890, 1989.

[4] M. A. Brunke, C. W. Fairall, X. Zeng, L. Eymard, and J. A. Curry. Which bulk aerodynamic algorithms are least problematic in computing ocean surface turbulent fluxes? *J. Clim.*, 16:619–636, 2003.

[5] G. Caniaux, S. Belamari, H. Giordani, and A. Paci. A one Year Sea Surface Heat Budget in the North Eastern Atlantic Basin during the POMME Experiment : Part II : Flux Correction. *Journal of Geophysical Research*, 110:15pp, 2005.

[6] H. Charnock. Wind stress on a water surface. *Q. J. R. Meteorol. Soc.*, 81(350):639–640, 1955.

[7] J. W. Deardorff. Convective velocity and temperature scales for unstable planetary bound-ary layer and for rayleigh convection. *J. Atmos. Sci.*, 29:1211–1212, 1970.

[8] J. W. Deardorff. Preliminary results from numerical integration of the unstable planetary boundary layers. *J. Atmos. Sci.*, 27:1209–1211, 1970.

[9] J. W. Deardorff. Rate of growth of the nocturnal boundary layer. In *Symposium on Air Pollution, Turbulence and Diffusion, Las Cruces, N. M., NCAR ms. No. 71-246*, 1971.

[10] J. W. Deardorff. A multi-limit mixed-layer entrainment formulation. *J. Phys. Oceanogr.*, 13:988–1002, 1983.

[11] C. W. Fairall, E. F. Bradley, J. E. Hare, A. A. Grachev, and Edson J. B. Bulk parameterization of airsea fluxes: Updates and verification for the coare algorithm. *J. Clim.*, 16:571–591, 2003.

[12] C.W. Fairall, E. F. Bradley, D. P. Rogers, J. B. Edson, and G. S. Young. Bulk parameterization of air-sea fluxes for tropical ocean-global atmosphere coupled-ocean atmosphere response experiment. *J. Geophys. Res.*, 101:3747–3764, 1996.

[13] X. Fang and H. G. Stefan. Temperature variability in lake sediments. *Water Resour. Res.*, 34:717–729, 1998.

[14] D. M. Farmer. Penetrative convection in the absence of mean shear. *Q. J. R. Meteorol. Soc.*, 101:869–891, 1975.

[15] D. M. Farmer and E. C. Carmack. Wind mixing and restratification in a lake near the temperature of maximum density. *J. Phys. Oceanogr.*, 11:1516–1533, 1981.

[16] E. Fedorovich, R. Conzemius, and D. Mironov. Convective entrainment into a shear-free, lineraly stratified atmosphere: bulk models reevaluated through large eddy simulations. *J. Atmos. Sci.*, 61:281–295, 2004.

[17] B. N. Filyushkin and Y. Z. Miropolskij. Seasonal variability of the upper thermocline and self-similarity of temperature profiles. *Okeanol.*, 21:416–424, 1981.

[18] P. Gaspar, Y. Grégoris, and J.-M. Lefevre. A simple eddy kinetic energy model for simulations of the oceanic vertical mixing: Tests at station papa and long-term upper ocean study site. *J. Geophys. Res.*, 95(C9):16179–16193, 1990.

[19] H. Giordani and G. Caniaux. Diagnosing Vertical Motion in the Equatorial Atlantic. *Ocean Dynamics*, 61(12):1995–2018, 2011.

[20] H. Giordani, G. Caniaux, L. Prieur, A. Paci, and S. Giraud. A One Year Mesoscale Simulation of the Northeast Atlantic : Mixed Layer Heat and Mass Budgets during the POMME Experiment. *Journal of Geophysical Research*, 110(C07S08):19pp, 2005.

[21] I. Zverev Golosov, S. and A. Terzhevik. Modelling thermal structure and heat interaction between a water column and bottom sediments. Technical report, Report No. 3220 [LUTVDG/(TVVR-3220) 1-41(1998)], Dept. of Water Resources Engineering, Inst. of Technology, Univ. of Lund, Lund, Sweden, 41 p, 1998.

[22] A. A. Grachev and C. W. Fairall. Dependence of the monin-obukhov stability parameter on the bulk richardson number over the ocean. *J. Appl. Meteorol.*, 36:406–414, 1997.

[23] J. E. Hare, P. O. G. Persson, C. W. Fairall, and J. B. Edson. Behavior of charnocks relationship for high wind conditions. In *13th Symp. on Boundary Layers and Turbulence, Amer. Meteor. Soc., Dallas, TX, 252-255*, 1999.

[24] E. Heise, M. Lange, B. Ritter, and R. Schrodin. Improvement and validation of the multilayer soil model. Technical report, COSMO Newsletter, No. 3, Consortium for Small-Scale Modelling, Deutscher Wetterdienst, Offenbach am Main, Germany, 198-203, 2003.

[25] J. Imberger. The diurnal mixed layer. *Limnol. Oceanogr.*, 30:737–770, 1985.

[26] T. Jonas, A. Y. Terzhevik, D. V. Mironov, and A. Wuest. Investigation of radiatively-driven convection in an ice covered lake using temperature microstructure technique. *J. Geophys. Res.*, 108(14):1–18, 2003.

[27] P. Josse, G. Caniaux, H. Giordani, and S. Planton. Intercomparaison of oceanic and atmospheric forced and coupled mesoscale simulations. Part I: Surface fluxes. *Annales Geophysicae*, 17:566–576, 1999.

[28] L.H. Kantha and C.A. Clayson. An improved mixed layer model for geosphysical applications. *Journal of Geophysical Research*, 99(C12):25235–25266, 1994.

[29] I. R. Khakimov. The wind profile in the neutrally stratified atmospheric boundary layer. *Izv. Akad. Nauk SSSR. Fizika Atmosfery i Okeana*, 12:628–630, 1976.

[30] J.-W. Kim. A generalized bulk model of the oceanic mixed layer. *J. Phys. Oceanogr.*, 6:686–695, 1976.

[31] S. A. Kitaigorodskii. On the computation of the thickness of the wind-mixing layer in the ocean. *Izv. AN SSSR. Ser. geofiz.*, 3:425–431, 1960.

[32] S. A. Kitaigorodskii and S. M. Joffre. In search of simple scaling for the heights of the stratified atmospheric boundary layer. *Tellus*, 40A:419–433, 1988.

[33] and Rooth C. Kraus, E. B. Temperature and steady state vertical heat flux in the ocean surface layers. *Tellus*, 19:231–238, 1961.

[34] E. B. Kraus. *Atmosphere-ocean interactions*. Oxford University press, London, 1972.

[35] W.G. Large, J.C. McWilliams, and S. Doney. Ocean vertical mixing : a review and a model with nonlocal boundary layer parameterization. *Reviews of Geophysics*, 32(4):363–403, 1994.

[36] J. Launiainen and B. Cheng. Modelling of ice thermodynamics in natural water bodies. *Cold. Reg. Sci. Technol.*, 27:153–178, 1998.

[37] P. Le Moigne, J. Colin, and B. Decharme. Impact of lake surface temperatures simulated by the flake scheme in the cnrm-cm5 climate model. *Tellus A*, 68, 2016.

[38] C. Lebaupin-Brossier, V. Ducrocq, and H. Giordani. Two-way one-dimensional high-resolution airsea coupled modelling applied to mediterranean heavy rain events. *Q. J. R. Meteorol. Soc.*, 135:187–204, 2009.

[39] D. Mironov and E. Fedorovich. On the limiting effect of the earth's rotation on the depth of a stably stratified boundary layer. *Q. J. R. Meteorol. Soc.*, 136:1473–1480, 2010.

[40] D. Mironov and B. Ritter. A new sea ice model for gme. Technical report, Technical Note, Deutscher Wetterdienst, Offenbach am Main, Germany, 12 p, 2004.

[41] D. Mironov, A. Terzhevik, G. Kirillin, T. Jonas, J. Malm, and D. Farmer. Radiatively driven convection in ice-covered lakes: Observations, scaling, and a mixed layer model. *J. Geophys. Res.*, 107(7):1–16, 2002.

[42] D. V. Mironov. Parameterization of lakes in numerical weather prediction. description of a lake model. Technical report, COSMO Technical Report, No. 11, Deutscher Wetterdienst, Offenbach am Main, Germany, 41 pp, 2008.

[43] D. V. Mironov, S. D. Golosov, S. S. Zilitinkevich, K. D. Kreiman, and A. Yu. Terzhevik. *Modelling Air-Lake Interaction. Physical Background*, chapter Seasonal changes of temperature and mixing conditions in a lake, pages 74–90. Springer-Verlag, Berlin, etc., 1991.

[44] D. V. Mironov and L. N. Karlin. Penetrative convection due to surface cooling with vertically distributed heating. *Dokl. Akad. Nauk SSSR.*, 309:1336–1340, 1989.

[45] D. V. Mironov and A. Yu. Terzhevik. Spring convection in ice-covered fresh-water lakes. *Izv. Akad. Nauk SSSR. Fizika Atmosfery i Okeana*, 36:627–634, 2000.

[46] S. Mondon and J.-L. Redelsperger. Study of a fair weather boundary layer in toga-coare: Parameterization of surface fluxes in large-scale and regional models for light wind conditions. *Bound.-Layer Meteorol.*, 88:4776, 1998.

[47] R. T. Pollard, P. B. Rhines, and R. O. R. Y. Thompson. The deepening of the wind-mixed layer. *Geophys. Fluid Dyn.*, 3:381–404, 1973.

[48] J. F. Price, R. A. Weller, and R. Pinkel. Diurnal cycling: observations and models of the upper ocean response to diurnal heating. *J. Geophys. Res.*, 91:8411–8427, 1986.

[49] D. A. Randall and B. A. Wielicki. Measurements, models, and hypotheses in the atmospheric sciences. *Bull. Amer. Met. Soc*, 78:399–406, 1997.

[50] C. G. Rossby and R. B. Montgomery. The layer of frictional influence in wind and ocean currents. *Pap. Phys. Oceanogr. Meteorol.*, 3:1–101, 1935.

[51] S. D. Smith. Coefficients for sea surface wind stress, heat flux, and wind profiles as a function of wind speed and temperature. *J. Geophys. Res.*, 93:15467–15472, 1988.

[52] A. V. Soloviev. lsquothin thermal structure of the ocean surface layer in the polymode-77 region, izvestiya. *Atmos. Oceanic Phys.*, 15:750–754, 1979.

[53] A. V. Soloviev and N. V. Vershinskii. The vertical structure of the thin surface layer of the ocean under conditions of low wind speed. *Deep-Sea Res.*, 29:1437–1449, 1982.

[54] P. Mlkki Tamsalu, R. and K. Myrberg. Self-similarity concept in marine system modelling. *Geophysica*, 2:51–68, 1997.

[55] R. Tamsalu and K. Myrberg. A theoretical and experimental study of the self-similarity concept. Technical report, Report series of the Finnish Institute of Marine Research, 1998.

[56] M. Wade, G. Caniaux, Y. DuPenhoat, M. Dengler, H. Giordani, and R. Hummels. A one-dimensional modeling study of the diurnal cycle in the equatorial atlantic at the PIRATA buoys during the EGEE-3 campaign. *Ocean Dynamics*, 61(1):1–20, 2011.

[57] O. Zeman. Parameterization of the dynamics of stable boundary layers and nocturnal jets. *J. Atmos. Sci.*, 36:792–804, 1979.

[58] S. Zilitinkevich and A. Baklanov. Calculation of the height of the stable boundary layer in practical applications. *Bound.-Layer Meteorol.*, 105:389–409, 2002.

[59] S. Zilitinkevich, A. Baklanov, J. Rost, A.-S. Smedman, V. Lykosov, and P. Calanca. Diagnostic and prognostic equations for the depth of the stably stratified ekman boundary layer. *Q. J. R. Meteorol. Soc.*, 128:25–46, 2002.

[60] S. S. Zilitinkevich. On the determination of the height of the ekman boundary layer. *Bound.-Layer Meteorol.*, 3:141–145, 1972.

[61] S. S. Zilitinkevich. Comments on a model for the dynamics of the inversion above a convective boundary layer. *J. Atmos. Sci.*, 32:991–992, 1975.

[62] S. S. Zilitinkevich, D. V. Chalikov, and Yu. D. Resnyansky. Modelling the oceanic upper layer. *Oceanologica Acta*, 2:219–240, 1979.

[63] S. S. Zilitinkevich and D. V. Mironov. A multi-limit formulation for the equilibrium depth of a stably stratified boundary layer. *Bound.-Layer Meteorol.*, 81:325–351, 1996.

[64] S.S. Zilitinkevich. *Turbulent Penetrative Convection*. Avebury Technical, Aldershot, 1991.

Chapter 3

Urban and artificial areas

Contents

3.1 Introduction

3.1.1 Modelling cities in atmospheric models

Due to the complexity and diversity of towns around the world, conclusions drawn from experimental studies on the interaction between the atmosphere and urbanized areas most of the time are limited either to a particular site or physical processes. To overcome this problem, numerical studies are aimed to simulate the urban climatology or energy budget. However, they still follow some simplified approaches. Building-resolving models - i.e. models in which individual building shapes are described - allow, from a long time ago, the detailed examination of some processes (radiative effects see for e.g. Terjung *et al.* (1980), or wind channeling), but because of computational cost, applications are limited to local urbanization and comfort studies. Even now, the use of such models is limited to the neighbourhood scale (typically 1km^2 or less).
Performing a coupling between the urban surface and the atmosphere in atmospheric models requires a different approach, that allows to simulate the effects of cities at a larger scale. Before year 2000, and still in most climate models and numerous numerical weather prediction models, the most common way to do this was (ans is) to use a vegetation-atmosphere transfer model whose parameters have been modified (Seaman *et al.* (1989), Menut (1997)), as opposed to an urban model. Cities are then modeled as bare soil or a concrete

plate. The roughness length is often large (one to a few meters, see Wieringa (1993) or Petersen (1997)). The soil moisture availability (or the soil depth) is reduced, so that the Bowen ratio is shifted towards high values (large sensible heat flux).
However, these approaches do not allow to represent accurately most of the physical processes in cities, and their consequences, such as the urban heat island at night. This is why several models were developed since year 2000, based on a simplified geometrical representation of the buiildings: the 'urban canyon'. The 'canyon' model, from Oke and colleagues was developed during the seventies, and is dedicated to urban streets: a road is bordered by two facing building walls. such an approach allows to capture the most pertinent processes: radiative trapping inside the canyon, impact on flow, higher surface in contact with the atmosphere available for heat storage., imperviousness of the buildings and roads, etc...

The first two models of this type are TEB (Masson 2000) and BEP (Martilli *et al.* 2002). Several other models following this philosophy were developed in the ten next years (see reviews in Masson 2006 and Martilli 2007). Up to 25 urban models participated to a recent intercomparison exercice (Grimmond *et al.* 2010, 2011). The conclusions of this study was that either simple models (as LUMPS, using statistical relationships based on urban fluxes observations) or the most 'complex' ones, with the most physics in it, performed the better to reproduce the energy balance. However, simpler models are not able to simulate diagnostic quantities, such as air temperatre, energy consumption of buildings, etc, that more complex models, such as TEB (included in SURFEX), can do. This limits their range of use. Furthermore, another conclusion was that it was necessary to improve the representation of vegetation.

3.1.2 Objectives of the Town Energy Balance scheme

The TEB model is aimed to simulate the turbulent fluxes into the atmosphere at the surface of a mesoscale atmospheric model which is covered by buildings, roads, or any artificial material. It should parameterize both the urban surface and the roughness sublayer, so that the atmospheric model only 'sees' a constant flux layer as its lower boundary.
It must be considered as a part of the surface parameterization of the atmospheric model. The fluxes should be computed for each land occupation type by the appropriate scheme, and then averaged in the atmospheric model grid mesh, with respect to the proportion occupied by each type. For example, a partition should be: (1) sea; (2) inland water; (3) natural and cultivated terrestrial surface; (4) towns. The following fluxes are calculated: latent and sensible heat fluxes (W m^{-2}), upward radiative fluxes (W m^{-2}) and momentum fluxes (m^2 s^{-2}). Many other indicators can be computed, especially to estimate local urban climate, energy consumption, water runoff, thermal comfort, ...

3.1.3 Overview of the Town Energy Balance scheme

The physics treated by the TEB (Town Energy Balance, Masson 2000) scheme is relatively complete. Due to the complex shape of the city surface, the urban energy budget is split into different parts: a minimum of **three** surface energy budgets are considered: one for the roofs, roads, and walls. One second wall energy budget is added if walls are treated separately to take into account orientation effetcs. Up to two energy budgets are added for snow when it is present on roofs or roads. Some of the physics were derived from the literature (long wave radiation or thermal conduction through the surfaces), since they are classically assumed to estimate temperatures in conditions without feedback towards the atmosphere (during nights with calm wind). However, most parts of the physics need an original approach (short wave radiation,

thermodynamical and anthropogenic flux treatment, rain and snow), since they occur when interaction with the atmosphere is strong.

The representation of urban vegetation has been improved in the recent years, with **gardens** and **greenroofs**. A **Building Energy Module** (BEM) is also implemented in order to represents the energetics inside the buildings. This allows to simulate indicators such as energy consumption of domestic ehating and air conditioning.

3.1.4 TEB patches

Cities are very heterogeneous. Therefore, averaged urban characteristics in a grid mesh may be considered as a broad approximation in regards of certain scientific objectives. From the point of view of the coupling of the urban surface to the atmosphere, an averaged description of the urban fabric in each grid mesh can be considered sufficient, since only the energy fluxes towards the atmosphere are needed (and they are mostly governed by the atmospheric forcing and the overall view of the urban fabric, such as building density, wall density, mean building height, etc...).

However, in order to simulate the details in some applications, such as for example to estimate the human comfort in perpendicular roads, or to represent the energetics of different buildings in the grid mesh, one may need to have several computations of TEB in the same grid mesh. For example, one could perform a simulation for 2 canyons with perpendicular roads. This is possible, by using **patches** for TEB. While such patches are often used for the natural part of the grid, especially for climate simulation, this is not the case for TEB. However, if needed, the possibility to activate patches for TEB is implemented in SURFEX. Per default, only road directions change when using several patches (4 roads at 45 from each other when using 4 patches for example). When using several patches, the user needs to define what are the differences between the patches (e.g. patches with different building heights, with different building materials, etc...).

The description of the physics of the model in the subsequent sections are all done for only one patch, but are valid if you use several patches as well.

3.1.5 Town geometry description

Numerous fine-scale studies on building climatology exist. In those, several individual buildings are usually present in order to study their radiative interaction, the wind channeling effects, or the building insulation. The **canyon** concept, developed by city climatologists (e.g. Oke (1987)), uses such a framework: it considers a single road, bordered by facing buildings. In these studies, models are, at best, forced by atmospheric data (radiation, wind above the roofs) but are not in interaction with it.

The TEB model is aimed to parameterize town-atmosphere dynamic and thermodynamic interactions. It is applicable for mesoscale atmospheric models (a grid mesh larger than a hundred meters typically). Then, spatial averaging of the town characteristics as well as its effect on the atmosphere, are necessary. The individual shapes of each building are no longer taken into account. The TEB geometry is based on the canyon hypothesis. However, a single canyon would be too restrictive at the considered horizontal scale.

We therefore use the following original city representation:

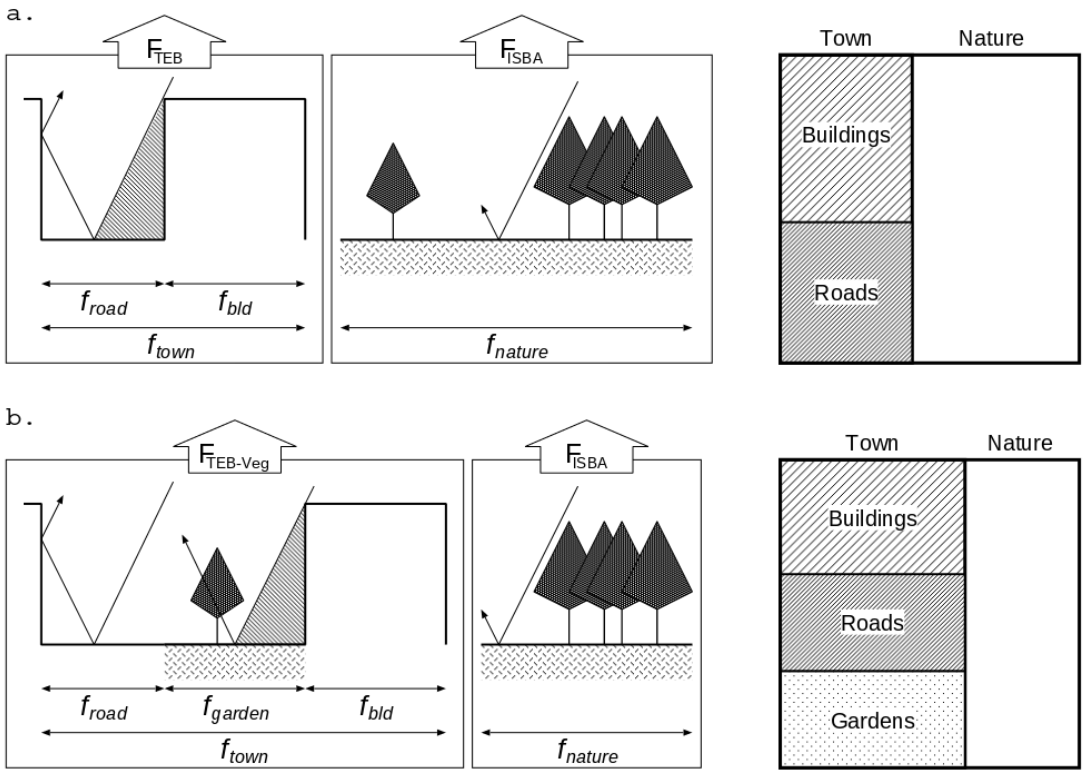

Figure 3.1: Overall implementation of gardens in TEB a) original version without garden; b) with gardens

1. the buildings have the same height and width (in the model mesh). The roof level is at the surface level of the atmospheric model.
2. buildings are located along identical roads, the length of which is considered far greater than their width. The space contained between two facing buildings is defined as a canyon.
3. any road orientation is possible. At that point, two options are possible:
   (a) only the information on the main road orientation is kept in each grid mesh. This option induces to simulate two wall energy balances instead of one, because of shading effects. However, it can be pertinent to estimate canyon micro-climate and human comfort for a specific road direction.
   (b) all directions exist with the same probability. This hypothesis allows the computation of averaged forcing for road and wall surfaces. In other words, when the canyon orientation appears in a formula (with respect to the sun or the wind direction), it is averaged over 360°. In this way, no discretization is performed on the orientation.

The parameters for the morphological description of the city, and the surface temperatures, are given below. The urban vegetation on ground (gardens, small parks, etc...) can be either simulated outside the city, as is done by the large majority of the Urban Canopy Models, or, for more realism, inside the canyon. This has been implemented by Lemonsu *et al.* (2012), and allows the physical interactions between the buildings and the vegetation(e.g. shadows). More details will be provided in section 3.5.

- f_{bld} the fraction of buildings (as seen from bird's view) relative to the urban surface, T_{roof} (ot T_R) the surface temperature of roofs. The roof surfaces can be composed of several subsurfaces:

  - structural roof
  - green roof
  - solar panel (that can shelter both structural and green roofs)

- f_{road} (or f_r) the fraction of impervious surfaces relative to the urban surface, T_{road} 'or T_r) the surface temperature of these impervious surfaces.
- f_{garden} the fraction of gardens relative to the urban surface (is equal to zero when the urban vegetation is not treated within TEB in the SURFEX grid mesh), and T_{garden} the surface temperature of gardens (including all effects influencing it, as the presence of snow mantel on vegetation).
- h/w the ratio between building's height h and (idealized) modelled canyon width w (that can take into account vegetation if gardens are simulated), T_{facade_A} and T_{facade_B} the temperature of both facades A and B. The facades include structural walls and windows (the latter are present only if the Building energy Module is used):
  - T_{win} the surface temperature of windows (supposed identical whatever the wall, A or B), f_{win} is the fraction of windows relative to the surface of facade.
  - T_{wall_A} and T_{wall_B} the surface temperature of each wall, $(1 - f_{win})$ is the surface of structural wall relative to the surface of the facade.

Note that a parameter is not easy to estimate: the h/w canyon aspect ratio. It can be computed following many different hypotheses, for example from 3D buildings databases. Because the more important physical processes leading to the Urban Heat Island phenomena are directly linked to the surface of walls (storage term and convection term), and because the surface of wall is an indicator that is relatively straightforward to compute, the h/w aspect ratio is computed following:

$$h/w = \frac{1}{2}\frac{R_{wall-hor}}{1 - f_{bld}}$$

where $R_{wall-hor}$ is the ratio of wall to horizontal (town) surface.

3.1.6 Summary of the chapter

The following sections successively present:

- the basics of TEB, for impervious surfaces only
- the representation of urban vegetation: gardens and greenroofs
- the Building Energy Module
- the Surface Boundary Layer module (cf chapter 5), when applied in TEB
- miscellaneous indicators
- the description of the architectural characteristics of the building

A list of the most important input parameters and of the prognostic variables of the scheme are given in Appendix fot heis chapter in Tables 3.2 and 3.3. Only the most importants features are described. For further details, the reader is invited to read the referenced papers.

3.2 Basics of the Town Energy Budget scheme

In this section, the focus will be done to describe the processes of the simplest version of the model (without gardens, building energy module). However, some of the processes, especially those exchanging with the different type of surfaces (as the radiative exchanges), need to take into account the more detailed parameterizations when they are used. In order to avoid redundancy in the description of these processes, the equations with all the terms will be presented.

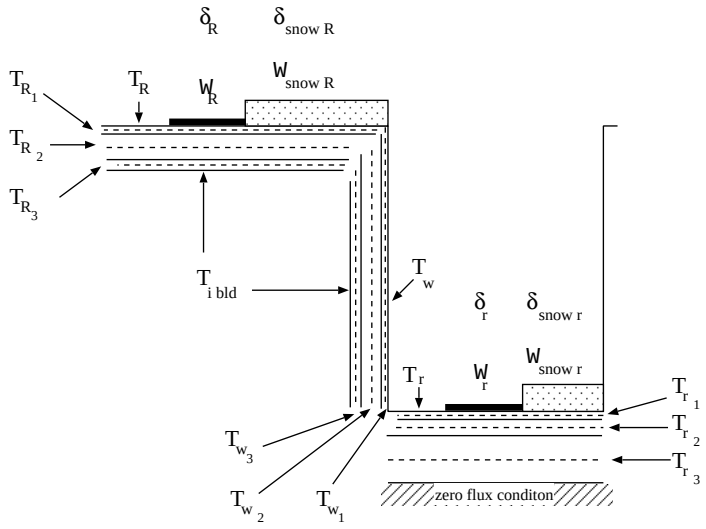

Figure 3.2: Canyon geometry in the TEB scheme (without gardens, building's energy module, greenroofs), and its prognostic variables.

The TEB model does not use one urban surface temperature (representative of the entire urban cover), but **three** (or **four**) surface temperatures, representative of roofs, roads and walls (1 generic wall, or 2 separate facing walls in case of oriented road). There are two reasons for that:

- urban climatologists generally consider complex (non-flat) geometry cases, in particular the 'canyon' geometry. In order to be consistent with their findings, the TEB model uses a complex surface consisting of multiple explicit energy budgets.
- one spatially-averaged surface temperature is often used in soil-vegetation schemes, in order to compute the turbulent fluxes towards the atmosphere following the Monin-Obukhov similarity theory. However, over towns, the use of only one surface temperature is debatable, because it has been observed that the Monin-Obukhov similarity theory does not apply for temperature in the urban roughness sublayer.

The second point will be adressed in more detail in section 3.2.6. The parameters of the scheme depend directly on building shapes and construction materials. This makes the TEB scheme easy to initialize, without the need for any atmospheric data for parameter tuning. Construction material characteristics can be found in the literature (e.g. see Oke (1988)), or defined locally depending on the building's type, use and date of construction (see section **??**).

Because the two walls of the canyon behave identically (in term of representation of the processes), except for direct solar radiation (one wall is under sunlight, the other in shadows), longwave radiation, and wind

exposition (leeward and windward), all the presentation of the processes hereafter are done for only one wall, with the index w. Specific effects of road direction on the processes will be specifically mentioned: the quantities related to the walls (A and B indicating the two facing walls) will there be noted w_A and w_B, instead of simply w.

These hypotheses, as well as the formulations chosen for the physics (see hereafter), allow the development of a relatively simple scheme from the geometric point of view, but taking into account most of the physical processes.

3.2.1 Temperature evolution equations

As discussed above, the urban surface is very inhomogeneous with respect to shape and building materials. Urban climatologists need at least four surfaces to describe it: the roof, the road, and two facing walls. The problem considered here (the evaluation of the turbulent and radiative fluxes from the urban cover to the atmosphere) allows the treatment of only three types of surfaces (roof, road, wall), while keeping enough accuracy to correctly represent the different terms of the surface energy budget. This is why the TEB model uses several surface temperatures, T_R, T_r and T_{w_A} (and T_{w_B} eventually) representative of roofs, roads and walls, respectively.
Furthermore, in order to treat the conduction fluxes to or from the building interiors (roof, wall) or the ground (road), each surface type is discretized into several layers (Figure 3.2). Per convention, the layer with subscript 1 is the one in contact with the air (hereafter 'surface layer').
The equations describing the evolution of the temperatures of the layers (representative of the middle of the layer) are based on energy budget considerations.

The prognostic equations for the surface layers of the roof, wall (either A or B) and road respectively, read:

$$\begin{aligned}
C_{R_1}\frac{\partial T_{R_1}}{\partial t} = &\ (1-\delta_{snowR}) & \frac{1}{d_{R_1}}\left(S^*_R + L^*_R - H_R - LE_R - G_{R_{1,2}}\right)\\
&+\delta_{snowR} & \frac{1}{d_{R_1}}\left(G_{R_{snow,1}} - G_{R_{1,2}}\right)\\
C_{w_1}\frac{\partial T_{w_1}}{\partial t} = & & \frac{1}{d_{w_1}}\left(S^*_w + L^*_w - H_w - G_{w_{1,2}}\right)\\
C_{r_1}\frac{\partial T_{r_1}}{\partial t} = &\ (1-\delta_{snowr}) & \frac{1}{d_{r_1}}\left(S^*_r + L^*_r - H_r - LE_r - G_{r_{1,2}}\right)\\
&+\delta_{snowr} & \frac{1}{d_{r_1}}\left(G_{r_{snow,1}} - G_{r_{1,2}}\right)
\end{aligned}$$

These equations can be written in a generic way:

$$C_{\star_1}\frac{\partial T_{\star_1}}{\partial t} = (1-\delta_{snow\star})\frac{1}{d_{\star_1}}\left(S^*_\star + L^*_\star - H_\star - LE_\star - G_{\star_{1,2}}\right) + \delta_{snow\star}\frac{1}{d_{\star_1}}\left(G_{\star_{snow,1}} - G_{\star_{1,2}}\right) \quad (3.1)$$

Where, the subscript $_\star$ stands either for $_R$, $_r$ or $_w$, describing roof, road and wall variables (only roof and road for water variables) respectively. This convention is used in the rest of this paper.
$T_{\star_k}$ is the temperature of the k^{ith} layer of the considered surface (in the above equations, $k = 1$). $C_{\star_k}$ represents the heat capacity, λ_k the thermal conductivity and $d_{\star_k}$ the layer thickness.

The fluxes $S^*_\star$, $L^*_\star$, $H_\star$, $LE_\star$, $G_{\star_{1,2}}$ and $G_{\star_{snow,1}}$ stand for net solar radiation, net infra-red radiation, sensible heat flux, latent heat flux, and conduction heat flux between surface layer and the underlying layer, conduction heat fluxes between the base of the snow mantel and the surface, respectively. $\delta_{snow\star}$ is the snow fraction on the surface (which is zero on the walls).
It is assumed that the surface layer of each surface is sufficiently thin such that the layer averaged temperature can be used to evaluate the radiative and turbulent surface fluxes. This means that the surface temperatures $T_\star$ are computed as:

$$T_\star = T_{\star_1}$$

For the sake of clarity, the $_1$ subscript will be removed in the next sections.

The other layer temperatures evolve according to a simple heat conduction equation. For the k^{ith} layer:

$$C_{\star_k}\frac{\partial T_{\star_k}}{\partial t} = \frac{1}{d_{\star_k}}\left(G_{\star_{k-1,k}} - G_{\star_{k,k+1}}\right) \tag{3.2}$$

In these equations, the conduction flux between layers k and $k+1$ reads (for $k < n$ where n is the number of layers):

$$G_{\star_{k,k+1}} = \overline{\lambda}_{k,k+1}\frac{T_{\star_k} - T_{\star_{k+1}}}{\frac{1}{2}(d_{\star_k} + d_{\star_{k+1}})} \tag{3.3}$$

with

$$\overline{\lambda}_{k,k+1} = \frac{d_{\star_k} + d_{\star_{k+1}}}{(d_{\star_k}/\lambda_k) + (d_{\star_{k+1}}/\lambda_{k+1})} \tag{3.4}$$

The lower boundary conditions for the roofs and walls are given by the building internal temperature, the road one being represented as a zero flux lower boundary. The fluxes between the n^{th} layer (the inner layer) and the underlying material are then:

$$G_{R_{n,n+1}} = \lambda_n\frac{T_{R_n} - T_{i_{bld}}}{\frac{1}{2}(d_{R_n})} \tag{3.5}$$

$$G_{w_{n,n+1}} = \lambda_n\frac{T_{w_n} - T_{i_{bld}}}{\frac{1}{2}(d_{w_n})} \tag{3.6}$$

$$G_{r_{n,n+1}} = 0 \tag{3.7}$$

Due to large temperature gradients which can exist, and because of the multi-layer structure of the walls or the roofs, it is recommended that at least 5 layers are used to represent each surface. This is done automatically by the model per default, that computes layers for the conduction equation within the roofs and walls with fine layers outside and inside, and, for the road, finer layers in contact to the atmosphere. Note that these computation layers are different from the information given to describe the materials that compose the building. There any number of layer and any thickness can be given (for example one layer of concrete of 30cm and one insulation layer of 5cm).

3.2.2 Longwave budget

Initially, in the historic version of the model (Masson 2000), the trapping of long-wave radiation by the canyon surfaces was computed with one re-emission taken into account (from the Johnson *et al.* (1991) formulation). However, with the separation of walls (with road orientation) and the addition of additional components to the urban system with the gardens and the windows (for the Building Energy Module), the

number of surfaces exchanging with other surfaces increased a lot. An approximate linear version of the longwave exchanges between any two surfaces is now used. Such an approximation is classicaly used in buildings energetics codes. The approximation is good when emissivities are high (typically larger than 0.9), which is the case for most surfaces, except for metal ones.

The net Longwave budget for surface S1 due to the exchange of energy between surfaces S1 and S2 is now simulated as :

$$L_{S_1 \text{ from } S_2} = 4\sigma\epsilon_{S_1}\epsilon_{S_2}\Psi_{S_1S_2}\left(\frac{1}{2}(T_{S_1}+T_{S_2})\right)^3(T_{S_2}-T_{S_1}) \tag{3.8}$$

Where ϵ_{S_*} are the emissivities of each surface, σ is the Stefan constant, T_{S_*} the temperature of each surface, and $\Psi_{S_1S_2}$ the view factor under which surface S_1 sees surface S_2. For the exchanges with the sky, a sky temperature is defined from the incoming downwards longwave radiation, $L^{\downarrow}$, assuming (formally) an emissivity of 1, $T_{sky} = \left(L^{\downarrow}/\sigma\right)^{\frac{1}{4}}$.

The view factors are needed. They are computed for the TEB geometry (an infinite canyon) according to Noilhan (1981):

$$\Psi_r = [(h/w)^2+1]^{1/2} - h/w \tag{3.9}$$

$$\Psi_w = \frac{1}{2}\{h/w + 1 - [(h/w)^2+1]^{1/2}\}/(h/w) \tag{3.10}$$

These factors represent the fraction of sky seen from the road and one wall respectively, compared to the sky fraction that a flat horizontal surface would see without obstruction. The sky-factor for the roof is then equal to 1. If the buildings are very low, Ψ_r tends to 1 and Ψ_w to 0.5 (one wall then sees one half of the sky). In this case, longwave radiative fluxes from the roads will be undisturbed by the walls. On the contrary, if the buildings are very tall, both sky factors tend to zero, and radiative exchanges will mostly occur between the walls, and less energy will escape towards the sky.

The net longwave radiation absorbed by the snow-free road and wall surfaces is given by the following equations.

$$\begin{array}{lcllll}
L_r^* = & & 4\sigma\epsilon_r & \Psi_r & \left(\frac{1}{2}(T_{sky}+T_r)\right)^3 & (T_{sky}-T_r) \\
& + & 4\sigma\epsilon_r\epsilon_w & \frac{1}{2}(1-\Psi_r)(1-f_{win}) & \left(\frac{1}{2}(T_{w_A}+T_r)\right)^3 & (T_{w_A}-T_r) \\
& + & 4\sigma\epsilon_r\epsilon_w & \frac{1}{2}(1-\Psi_r)(1-f_{win}) & \left(\frac{1}{2}(T_{w_B}+T_r)\right)^3 & (T_{w_B}-T_r) \\
& + & 4\sigma\epsilon_r\epsilon_w & (1-\Psi_r)f_{win} & \left(\frac{1}{2}(T_{win}+T_r)\right)^3 & (T_{win}-T_r) \\
L_{w_A}^* = & & 4\sigma\epsilon_w & \Psi_w & \left(\frac{1}{2}(T_{sky}+T_{w_A})\right)^3 & (T_{sky}-T_{w_A}) \\
& + & 4\sigma\epsilon_r\epsilon_w & \Psi_w\delta_{road}(1-\delta_{snow_r}) & \left(\frac{1}{2}(T_r+T_{w_A})\right)^3 & (T_r-T_{w_A}) \\
& + & 4\sigma\epsilon_{r_{snow}}\epsilon_w & \Psi_w\delta_{road}\delta_{snow_r} & \left(\frac{1}{2}(T_{r_{snow}}+T_{w_A})\right)^3 & (T_{r_{snow}}-T_{w_A}) \\
& + & 4\sigma\epsilon_r\epsilon_w & \Psi_w\delta_{garden} & \left(\frac{1}{2}(T_{garden}+T_{w_A})\right)^3 & (T_{garden}-T_{w_A}) \\
& + & 4\sigma\epsilon_w^2 & (1-2\Psi_w)(1-f_{win}) & \left(\frac{1}{2}(T_{w_B}+T_{w_A})\right)^3 & (T_{w_B}-T_{w_A}) \\
& + & 4\sigma\epsilon_w^2 & (1-2\Psi_w)f_{win} & \left(\frac{1}{2}(T_{win}+T_{w_A})\right)^3 & (T_{win}-T_{w_A})
\end{array}$$

By inverting the snow-covered and snow-free road characteristics in Eq. 3.11, the longwave radiative budget on top of snow mantel can be defined. To find the longwave balance of wall B, one inverts A and B indices. $\delta_{road} = f_{road}/(f_{road}+f_{garden})$ and $\delta_{garden} = f_{garden}/(f_{road}+f_{garden})$ are the fractions of road

and garden relative to the canyon surface, respectively.

To deduce Eqs 3.11, we used the fact that if Ψ_r represents the contribution of the sky to the road viewing, then $(1 - \Psi_r)$ is the contribution of the two walls. For the budget of one wall, the sky-view factor is Ψ_w, the road view factor is Ψ_w (per symmetry), and the facing wall view factor is $(1 - 2\Psi_w)$.

3.2.3 Solar radiation

Diffuse solar radiation

Diffuse solar radiation $S^{\downarrow}_{\star}$ is supposed to reach each surface according to the sky view factors of each surface $S^{\downarrow}_{\star} = \Psi_{\star} S^{\downarrow}$. A part of this energy is reflected, depending on the albedo of each surface $\alpha_{\star}$. The reflected energy can then be again absorbed by the other surfaces, and so on. This is described in section 3.2.3.

Direct solar radiation for averaged directions

Because of shadow effects, special computations are required to estimate the solar flux received either by the walls or the roads.
Let $S^{\Downarrow}$ be the direct solar radiation received by an **horizontal** surface at the first atmospheric model level. The roof surface receives this amount of radiation.
Let θ be the angle between the sun direction and the canyon axis, and λ be the solar zenith angle (from zenith). Let us first consider a road perpendicular to the sun direction ($\theta = \frac{\pi}{2}$, Figure 3.3). $\lambda_0 = \arctan(w/h)$ is defined as the zenith angle for which the sun begins to illuminate the road. It can be noted that whatever the sun position, one of the two walls is in shadow, the other one is (partially) in light.
The mean direct solar fluxes received by both walls and by the road, for a street direction perpendicular to the sun, are:

$$
\begin{aligned}
S^{\Downarrow}_{w}(\theta = \frac{\pi}{2}) &= \begin{cases} \frac{1}{2}\frac{w}{h} S^{\Downarrow} & if\ \lambda > \lambda_0 \\ \frac{1}{2}\tan(\lambda) S^{\Downarrow} & if\ \lambda < \lambda_0 \end{cases} \\
S^{\Downarrow}_{r}(\theta = \frac{\pi}{2}) &= \begin{cases} 0 & if\ \lambda > \lambda_0 \\ \left(1 - \frac{h}{w}\tan(\lambda)\right) S^{\Downarrow} & if\ \lambda < \lambda_0 \end{cases}
\end{aligned}
$$

In order to take into account the other canyon orientations, one should replace w by $w/\sin(\theta)$ in the above expressions, and then multiply the wall fluxes by $\sin(\theta)$. Then let θ_0 be the critical canyon orientation for which the road is no longer in the light (or for which the radiation is minimum if the sun is high enough), i.e.:

$$
\theta_0 = \arcsin\left(\min\left[\frac{w}{h}\frac{1}{\tan(\lambda)}; 1\right]\right)
$$

Averaging a flux with respect to the canyon orientation is performed with two integrations, one between $\theta = 0$ and $\theta = \theta_0$, and the other one between $\theta = \theta_0$ and $\theta = \frac{\pi}{2}$. The direct solar fluxes for walls, roads and roofs then read:

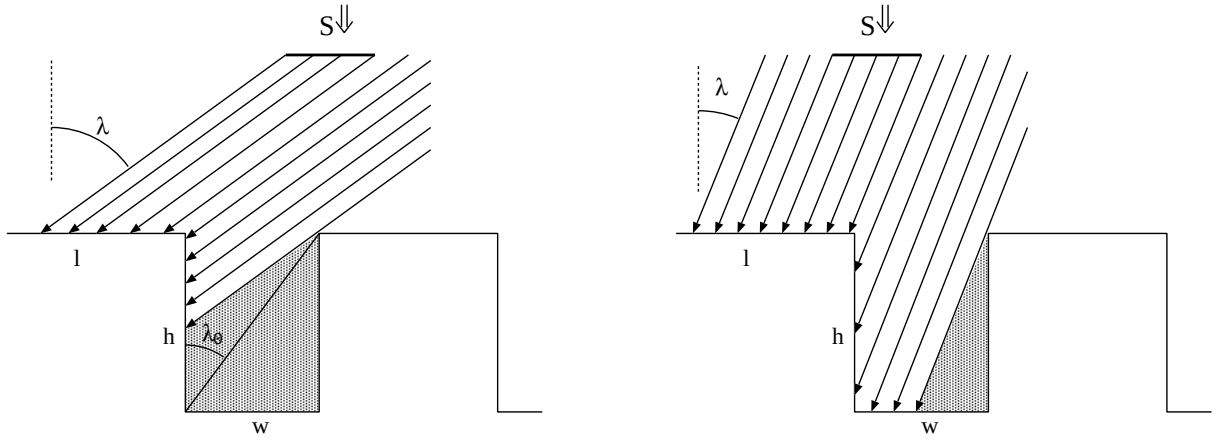

road perpendicular to sun direction

Sun low over the horizon $\lambda > \lambda_0$

road perpendicular to sun direction

Sun high over the horizon $\lambda < \lambda_0$

Figure 3.3: Solar radiation input for a road perpendicular to the sun azimuth. In the TEB scheme, the contribution of all the other road directions are averaged with this one.

$$S_r^{\Downarrow} = S^{\Downarrow} \left[\frac{2\theta_0}{\pi} - \frac{2}{\pi}\frac{h}{w} tan(\lambda)\left(1 - \cos(\theta_0)\right)\right] \tag{3.11}$$

$$S_{garden}^{\Downarrow} = S_r^{\Downarrow} \tag{3.12}$$

$$S_w^{\Downarrow} = S^{\Downarrow} \left[\frac{w}{h}\left(\frac{1}{2} - \frac{\theta_0}{\pi}\right) + \frac{1}{\pi} tan(\lambda)\left(1 - \cos(\theta_0)\right)\right] \tag{3.13}$$

$$S_{win}^{\Downarrow} = S_w^{\Downarrow} \tag{3.14}$$

$$S_R^{\Downarrow} = S^{\Downarrow} \tag{3.15}$$

Note that from the previous equations, one can check the conservation relation $S_r^{\Downarrow} + 2\frac{h}{w} S_w^{\Downarrow} = S^{\Downarrow}$.

Direct solar radiation for a given canyon direction

When the road direction is taken into account, the amount of energy received is not the same for both walls. One is shaded (per convention here it will be wall B, but it depends in the model of the azimuthal position of the sun relative to the axis of the road), and the other one is under sunlight (at least partially). The formulae for the direct solar energy received are then (see Lemonsu *et al.* 2012 for details) :

$$S_r^{\Downarrow} = S^{\Downarrow} \max\left[0\ , 1 - \frac{\frac{h}{w} tan(\lambda)}{sin|\theta_{sun} - \theta_{can}|}\right] \tag{3.16}$$

$$S_{garden}^{\Downarrow} = S_r^{\Downarrow} \tag{3.17}$$

$$S_{w_A}^{\Downarrow} = S^{\Downarrow} - S_r^{\Downarrow}\frac{w}{h} \tag{3.18}$$

$$S_{w_B}^{\Downarrow} = 0 \tag{3.19}$$

$$S_{win}^{\Downarrow} = \tfrac{1}{2}(S_{w_A}^{\Downarrow} + S_{w_B}^{\Downarrow}) \tag{3.20}$$

Solar radiation reflectionsi

The scattered solar radiation received by the surfaces ($S_\star^\downarrow$) is directly deduced from the sky-view factors. Because of the canyon shape and the possible high albedo of the surfaces (white paint, snow), the shortwave radiative budget is computed by resolving a geometric system for an infinite number of reflections. The reflections are assumed to be isotropic: there is no specular reflection in this model. Details of the following calculations are given in Appendix A for the simpler case with averaged canyon direction (no difference between wall A and B). The complete demonstration is given in Lemonsu *et al.* 2012.

The total solar radiation absorbed by each of the surface types is given by :

$$
\begin{aligned}
\mathcal{A}_r(\infty) &= (1-\alpha_r)\left[S_r^\Downarrow + S_r^\downarrow + (1-\Psi_r)W_\infty\right] \\
\mathcal{A}_{snow_r}(\infty) &= (1-\alpha_{snow_r})\left[S_r^\Downarrow + S_r^\downarrow + (1-\Psi_r)W_\infty\right] \\
\mathcal{A}_g(\infty) &= (1-\alpha_g)\left[S_r^\Downarrow + S_r^\downarrow + (1-\Psi_r)W_\infty\right] \\
\mathcal{A}_{w_A}(\infty) &= (1-\alpha_w)\left[\frac{1}{2}(S_{w_A}^\Downarrow + S_{w_A}^\downarrow + S_{w_B}^\Downarrow + S_{w_B}^\downarrow) + \tilde{\alpha}_{ground}\Psi_w(S_r^\Downarrow + S_r^\downarrow)\right. \\
&\quad \left. +\tilde{\alpha}_{ground}\Psi_w(1-\Psi_r)W_\infty + (1-2\Psi_w)W_\infty\right] \\
&\quad + \left[(1-\alpha_w)\left(1 + \frac{\tilde{\alpha}_{fac}(1-2\Psi_w)}{1+\tilde{\alpha}_{fac}(1-2\Psi_w)}\right)\frac{S_{w_A}^\Downarrow + S_{w_A}^\downarrow - S_{w_B}^\Downarrow - S_{w_B}^\downarrow}{2}\right] \\
\mathcal{A}_{w_B}(\infty) &= (1-\alpha_w)\left[\frac{1}{2}(S_{w_A}^\Downarrow + S_{w_A}^\downarrow + S_{w_B}^\Downarrow + S_{w_B}^\downarrow) + \tilde{\alpha}_{ground}\Psi_w(S_r^\Downarrow + S_r^\downarrow)\right. \\
&\quad \left. +\tilde{\alpha}_{ground}\Psi_w(1-\Psi_r)W_\infty + (1-2\Psi_w)W_\infty\right] \\
&\quad - \left[(1-\alpha_w)\left(1 + \frac{\tilde{\alpha}_{fac}(1-2\Psi_w)}{1+\tilde{\alpha}_{fac}(1-2\Psi_w)}\right)\frac{S_{w_A}^\Downarrow + S_{w_A}^\downarrow - S_{w_B}^\Downarrow - S_{w_B}^\downarrow}{2}\right]
\end{aligned}
$$

with

$$
W_\infty = \frac{\tilde{\alpha}_{fac}(S_{w_A}^\Downarrow + S_{w_A}^\downarrow + S_{w_B}^\Downarrow + S_{w_B}^\downarrow)/2 + \tilde{\alpha}_{fac}\Psi_w\tilde{\alpha}_{ground}(S_r^\Downarrow + S_r^\downarrow)}{1-\tilde{\alpha}_{ground}\tilde{\alpha}_{fac}\Psi_w(1-\Psi_r) - \tilde{\alpha}_{fac}(1-2\Psi_w)}
$$

Where $\tilde{\alpha}_{fac} = f_{win}\alpha_{win} + (1-f_{win})\alpha_w$ and $\tilde{\alpha}_{ground} = \delta_{road}\left((1-\delta_{snow_r})\alpha_{road} + \delta_{snow_r}\alpha_{snow_r}\right) + \delta_{garden}\alpha_{garden}$ are the **agregated albedo** of the facade (wall+window) and canyon ground (road+garden), respectively.

Solar energy reaching the windows $\mathcal{A}_{win}$ is then given by the averaged value of energy received by walls A and B (by formally replacing $(A-\alpha_w)$ by $(1-\alpha_{win})$ in the formula). Note that all this energy will not be absorbed by the window, since part of it will reach the interior of the building (see the BEM section for details). Similarly, the solar energy *reaching* the garden is deduced from the one absorbed by the road $\left[S_{garden}^\Downarrow + S_{garden}^\downarrow + (1-\Psi_r)W_\infty\right]$.

3.2.4 Anthropogenic fluxes

Due to human activity, heat and moisture are released towards the atmosphere. The two main sources come from domestic heating and from combustion.

Domestic heating is explicitly resolved by assuming a constant minimal internal temperature, whatever the external temperature. The default value is 290.15 K. The heat is then released towards the wall/roof

surfaces and then towards the atmosphere through the conduction flux formulation.

The combustion source is split into two contributions in the TEB model: traffic and industry. For each, the heat and moisture fluxes, averaged on the town surface ($H_{traffic}$ and $LE_{traffic}$, $H_{industry}$ and $LE_{industry}$), are specified by the user (from available information on the town activity).
However, these fluxes do **not** directly modify the surface energy budgets since they are released into the air. The traffic related fluxes will modify the canyon air budget (they are incorporated in Equation 3.25, see next section). The industry fluxes are assumed to influence the atmosphere directly.

3.2.5 Turbulent fluxes for momentum

Treatment of the urban roughness sublayer

In this section, the method to compute the turbulent fluxes between the surfaces and the atmospheric model will be presented. The resolution of the atmospheric model is far too low to be able to represent the urban roughness sublayer motions, as it applies to the mesoscale. The atmospheric models do not usually parameterize the exchange processes in this layer: it is done by the surface scheme. If the first atmospheric level is outside the roughness sublayer, the traditional surface layer formulations can be used to compute the turbulent fluxes. The problem is that the roughness sublayer can have a substantial extension over an urban surface (several tens of meters), and the first level of the atmospheric model (often a couple of tens of meters) is often within it.

It is therefore necessary to have a closer look to the parameterization of the fluxes. Feigenwinter *et al.* (1999) conducted measurements on a 50m height mast in the city of Basel (Switzerland). The authors found that the mechanical properties in the roughness sublayer (such as profiles of velocity variances, non-dimensionalized velocity variances and spectra of wind components) behave similarly to rural surface layers. Furthermore, they concluded that these quantities are quite well parameterized within the Monin-Obukhov similarity theory, if local Monin-Obukhov length is applied.
Following their results, the TEB scheme computes the **momentum fluxes for the entire urban (or suburban) cover**.
The momentum fluxes can be computed using two main approaches:

The drag approach with the Surface Boundary Layer scheme

In this case, the wind, temperature, moisture and turbulent kinetic energy profiles are defined within and above the canyon. The friction is not explicitly calculated by a single formulation, but simulated but the effect of the drag force of the buildings (see section 3.5) for more details.

The roughness length approach

More classicaly, when the SBL scheme is not used, a roughness length formulation taking into account stability coefficients is used. The stability coefficients that are available in TEB are:

- Brutsaert (1982)
- Mascart *et al.* (1995)
- Kondo *et al.* (2007)

We recommend to use the Kondo *et al.* (2007) formulation, that was derived specifically for urban areas.

The momentum fluxes are computed for the entire urban surface. However, one difficulty lies in the determination of the roughness length to use in urban areas. Wieringa (1993) reviewed some experimental roughness length estimations for rather homogeneously built-up areas. Dense low building roughness lengths were found between 0.4 and 0.7m, and those for regularly-built towns ranged from 0.7 to 1.5m. In these experiments, they are approximately equal to 1/10 of the houses or building heights. Bottema (1997) presents a model computing roughness lengths from building shapes and relative positions (normal or staggered). He found the modeled $z_{0_{town}}$ to be in agreement with the available measurements. Sensitivity experiments of his model show that the ratio $z_{0_{town}}/h$ ranges from 0.05 to 0.1 (except for very sparsely built areas). Therefore, as a first approximation, the roughness length in the TEB model is set equal to:

$$z_{0_{town}} = h/10$$

(with an arbitrary limit of 5m), but it can be specified independently, either from in-situ measurements or more complicated formulations (see for example the review of Grimmond (1999)).

3.2.6 Turbulent fluxes for heat and moisture

Considerations on the turbulent transfer of heat and moisture

In contrast, Feigenwinter *et al.* (1999) found that the temperature characteristics, and in particular the turbulent heat flux, cannot be satisfactorily reproduced by the Monin-Obukhov similitude framework. They attribute this discrepancy to 'thermal inhomogeneity and/or different source areas'. The use of one unique surface exchanging heat with the atmosphere (the classical surface layer approach) becomes debatable.
The approach of the TEB scheme is to suppose that there are **two** major sources of heat from the artificial cover towards the atmosphere, leading to **two** turbulent heat fluxes. These two different surfaces are the **roofs** on the one hand, and the **canyon systems** on the other hand (see Figure 3.4). The two flux contributions are averaged relative to their horizontal areas: this is a way to represent the mixing in the urban roughness sublayer.

Both for roof and roads, one will also explicitly suppose that the transfer coefficient for turbulent heat and moisture fluxes are identical (but different than for momentum). Very few direct measurements of turbulent moisture fluxes exist in the literature to validate or invalidate this hypothesis.

Exchange coefficients between surfaces and atmosphere

All heat and moisture fluxes are computed using exchange coefficient, based on aerodynamical resistances (or conductances), and the difference between the surface temperature of the considered surface (roof, road, wall) and the air temperature (either above roof or in the canyon).

The horizontal surfaces use formulations that take into account vertical atmospheric stability effects. While this is is questionable for roofs (where air turbulence even at proximity of the surface is strongly influenced by the buildings shape, this is probably pertinent for roads. The three possible formulations to compute the aerodynamical resistances RES_R and RES_r are:

- Brutsaert (1982)

- Mascart *et al.* (1995)
- Kondo *et al.* (2007)

Between these three, we recommend Kondo *et al.* (2007), that was specifically developed for cities. Please note that there is also another possible option for roofs (see below).

These formulations are used either for roads (with roughness length of 5cm) or roofs (with roughness length of 15cm, as observed by Sturrock *et al.* (1977)). However, the flow inside the canyon being often highly turbulent even for low wind speeds. One takes into account in the wind estimation inside the canyon for the exchange coefficients formulation. Both the mean wind (U_{can}, see below for its estimation) and a turbulent scale due to local canyon convection ($w_* = \left(\frac{g}{T_{can}} Q_0 h\right)^{1/3}$) are then used, combined as an 'effective' canyon wind equal to : $\sqrt{U_{can}^2 + (u_* + w_*)^2}$, Where $u_* + w_*$ is the turbulent wind and Q_0 encompasses both road and wall turbulent heat fluxes.

When the SBL scheme is not used, one also need to compute the heat and moisture fluxes between the canyon air and the atmosphere above. This is done using the same formulations as above (leading to the estimation of canyon resistance, noted RES_{top}), but using the roughness lentgh for the whole urban fabric (the same as for the momentum formulation), instead of the surface roughness lengths.

For walls, two formulations are available. The first one is the Rowley *et al.* (1930) and Rowley *et al.* (1932) aerodynamic formulations. They were obtained from in-situ measurements. These formulae are also used in the canyon circulation model of Mills (1993). It writes:

$$RES_w = \quad C_{p_d} \rho_a \quad (11.8 + 4.2 U_{can})^{-1} \tag{3.21}$$

For buildings, a recent development in the model was to introduce a formulation of the exchanges coefficients directly dereived from state-of-the-art codes in Building energetics (energy+), by Pigeon *et al.* (2014). This is the DOE-2 option (description in http://apps1.eere.energy.gov/buildings/energyplus/pdfs/engineeringreference.pdf). It takes into account the windward and leeward effects on exchange coefficients. Those coefficient lead to coefficient generally 2.5 times smaller than the other formulations.
The DOE-2 option can then be chosen for roof RES_R and wall RES_w exchange coefficients, in place of the stability fgunction and Rowley formulations, respectively.

All possible options are summarized in Table 3.1.

Heat fluxes

The effect on temperature and specific humidity of the difference in height between the atmospheric level and the roof level is corrected using the Exner function $\Pi = (p/p0)^{R_d/C_{p_d}}$, where p is the pressure (p_s and p_a are the surface pressure and the first level pressure in the atmospheric model respectively), p_0 is a reference pressure (equal to 100000 Pa), and R_d the gas constant for dry air. One defines:

$$\begin{aligned} \hat{T_a} = & \quad T_a \Pi_s / \Pi_a \\ \hat{q_a} = & \quad q_a \; q_{sat}(\hat{T_a}, p_s) / q_{sat}(T_a, p_a) \end{aligned}$$

	roofs	roads	walls	windows (if BEM)	canyon air and above (if not SBL scheme)
Brutsaert (1982)	X (z_0 =15cm)	X (z_0 =5cm)			X ($z_{0_{town}}$)
Mascart (1995)	X (z_0 =15cm)	X (z_0 =5cm)			X ($z_{0_{town}}$)
Kondo *et al.* (2007)	X (z_0 =15cm)	X (z_0 =5cm)			X ($z_{0_{town}}$)
Rowley (1930)			X		
DOE-2	X		X	X	

Table 3.1: Possible options for exchanges coefficients

The heat and moisture turbulent fluxes between roof and atmosphere read:

$$\begin{aligned} H_R = &\quad C_{p_d}\rho_a \quad (\hat{T_a} - T_{can})/RES_R \\ LE_R = &\quad L_v\rho_a \quad (\hat{q_a} - q_{can})/RES_R \end{aligned}$$

where ρ_a is the air density at first atmospheric level, and C_{p_d} the heat capacity of dry air.
The heat fluxes between the canyon surfaces and the canyon air read:

$$\begin{aligned} H_r = &\quad C_{p_d}\rho_a \quad (T_r - T_{can})/RES_r \\ H_w = &\quad C_{p_d}\rho_a \quad (T_w - T_{can})/RES_w \\ LE_r = &\quad L_v\rho_a \quad \delta_r(q_{_{sat}}(T_r, p_s) - q_{can})/RES_r \\ LE_w = &\quad 0 \end{aligned}$$

The turbulent heat fluxes between the canyon air and the atmosphere are computed from the temperature and humidity inside the canyon. The fluxes between surfaces and canyon air follow an empirical formulation. The air characteristics inside the canyon are deduced from the continuity between the fluxes coming from the surfaces and the flux with the atmosphere (inspired by the vegetation canopy scheme of Deardorff (1978)). The heat fluxes are used in the energy budget conservation equations involving the surface temperatures. This is why a precise approach has been chosen, specific to each surface. Figure 3.4 displays a summary of the TEB options.

Above the canyon, the fluxes are estimated from classical surface boundary layer laws. However in these formulae, the air characteristics in the canyon (T_{can} and q_{can}) are used instead of the surface characteristics.

$$\begin{aligned} H_{top} = &\quad C_{p_d}\rho_a \quad (\hat{T_a} - T_{can})/RES_{top} \\ LE_{top} = &\quad L_v\rho_a \quad (\hat{q_a} - q_{can})/RES_{top} \end{aligned}$$

3.2.7 Water reservoirs evolution

Liquid or solid precipitation intercepted by urban surfaces is rarely addressed in the literature, except for sewer system and hydrological considerations. An exception is Grimmond *et al.* (1991b), however, in which the model used was initially dedicated to forest studies, and is limited to the water budget, computed from the Penman Monteith equation. They added anthropogenic water sources and used the Grimmond *et al.* (1991a) heat storage flux formulation.

Thanks to the presence of the surface temperatures in the TEB scheme, the saturation specific humidity, and then the turbulent latent heat flux can be computed more easily (see section 3.2.6).
The liquid precipitation is intercepted by both roofs and roads. There is runoff from roofs and roads to the sewer system. Roads and roofs can be covered by a certain amount of water, parameterized by the variables W_r and W_R, respectively. These surfaces are impervious. Then, instead of defining a relative humidity, it is more judicious to treat the fraction of surface covered by the water, δ_{water_r} and δ_{water_R}. This part is saturated (fractional water pools), while the other part is assumed to be dry. Water evaporates when the air humidity is not saturated until all water has disappeared from the impervious surface.
The snow-free fraction of the surface occupied by liquid water is computed as: $\delta_{water_\star} = (W_\star/W_{\star_{max}})^{\frac{2}{3}}$, (Noilhan and Planton (1989)), where $W_{\star_{max}}$ is the maximum water amount on the surface.

Furthermore, urban dew is taken into account (in case of negative latent heat flux), as its occurrence can have significant effects, as pointed out by Richards (1998). It requires a special treatment: when conditions are present for dew to occur (air humidity larger than the surface saturation humidity), the surface is considered wet ($\delta_{water_*} = 1$). This allows then a (negative) latent heat flux, which can fill the interception reservoirs. These treatments are deduced from those for the foliage interception reservoirs in vegetation schemes (Deardorff (1978), Noilhan and Planton (1989)).

Addition of an anthropogenic water source was not retained in TEB, because it does not compute evaporation over gardens or parks. Irrigation water input should be taken into account through the vegetation scheme dedicated to these natural surfaces. However, anthropogenic fluxes of water vapor directly into the air exist in the scheme (see section 3.2.6), in order to represent factory release for example.

Finally, the water-reservoir evolution equation is (for roof or road):

$$\frac{\partial W_\star}{\partial t} = R - LE_\star/L_v \qquad (W_\star < W_{\star_{max}}) \tag{3.22}$$

where R is the rain rate (kg m^{-2} s^{-1}) and L_v is the latent heat of vaporization.
The reservoirs are of small capacity (the water in excess is lost as runoff). They are set equal to $W_{R_{max}}$=$W_{r_{max}}$=1 kg m^{-2}, which is well in the range of values explored by Grimmond and Oke (1991). The total depletion of the reservoirs by evaporation requires, in general, a few hours for daytime conditions.

Additionnaly, the water during rainfall is supposed to fall at the temperature of the air. Therefore, because there is no specific energy budget for the water reservoirs, the rainfall water is supposed to instantaneously take the temperature of the surface (roof or road). This induces an immediate sensible heat flux (contrary to the future latent heat flux that will be caused by evaporation). This heat flux, that is immediatly incorporated into the corresponding surface layer (roof or road) heat budget, is equal to :

$$H_{rain_\star} = C_{water} R (T_a - T_\star) \tag{3.23}$$

where C_{water} is the heat capacity of water, supposed equal to 4218 $J\,kg^{-1}\,K^{-1}$.

3.2.8 Snow effects

Snow is intercepted by roofs and roads. A snow scheme is implemented on each surface type. Snow density, albedo, temperature and thickness of water equivalent depth are parameterized. Radiation, sensible heat flux, sublimation, conduction and melting are taken into account.

The evolution rate of snow albedo is enhanced (and its minimum value lowered) in order to represent car pollution (dirty snow). A time-dependent drainage term is included to take into account snow-plow work (if any).
The snow fraction on roof or road surfaces is set equal to a function of the snow interception reservoir (W_{snow*}): $\delta_{snow*} = (W_{snow*})/(W_{snow*} + W_{snow*max})$. The parameter $W_{snow*max}$ is set equal to 1 kg m^{-2}. The snow has an effect on:

- the energy budget of the surfaces (as part of the downward flux comes from the base of the snow),
- the heat fluxes from the road towards the canyon or from the roof towards the atmosphere,
- the radiative calculations for the canyon surfaces, because of the snow albedo, emissivity and temperature.

3.2.9 Atmospheric quantities inside the canyon

In order to compute the momentum and energy fluxes of the different surfaces, one needs to know the air temperature, humidity and wind speed in the canyon and above the surfaces. Depending if the Surface Boundary Layer scheme is active or not, there are two ways to estimate these.

In the case of the Surface Boundary Layer scheme

In this case, the wind, temperature and humidity profiles are known. For the roof fluxes computations, one uses the atmospheric quantities at the first SBL layer above the roof. For the road fluxes computations, one uses the atmospheric quantities at the first SBL layer, typically 50cm above ground. For the wall fluxes computations, one uses the atmospheric quantities at middle height of the canyon, interpolated from the SBL levels.

Wind inside the Canyon

In the absence of the SBL scheme (and associated profiles), one needs to estimate the wind, air temperature and humidity at mid height of the canyon, in order to compute the road and wall fluxes. Roof fluxes are directly computed using the information at forcing level.

The horizontal wind speed, U_{can}, is estimated at half the height of the canyon. First, the horizontal wind speed at the top of the canyon is deduced from the logarithmic law above it (Figure 3.4, right side), and the displacement height is equal to two thirds of the building height from road surface (i.e. at $h/3$ under the roof level - which is the zero height of the atmospheric model -, a classical assumption for plant canopies). Furthermore, in order to consider all canyon orientations, and since only the along canyon wind is considered, an integration over 360° is performed. At canyon top, this gives:

$$U_{top} = \frac{2}{\pi} \frac{\ln\left(\frac{h/3}{z_{0_{town}}}\right)}{\ln\left(\frac{\Delta z + h/3}{z_{0_{town}}}\right)} ||\vec{U_a}||$$

where Δz is the height of the first atmospheric model level above the roofs.

To calculate U_{can}, a vertical profile of the wind inside the canyon is assumed. An exponential form is chosen (as is done in vegetation canopies, cf e.g. Arya (1988)). Such a profile applied at half-height gives:

$$U_{can} = U_{top}\exp(-N/2)$$

N must be determined. Rotach (1995) finds from his case study ($h/w = 1$), that $U_{can} \sim 0.75U_{top}$. Studies in corn fields ($h/w \sim 4$), which could be assimilated to narrow streets, give $U_{can} \sim 0.4U_{top}$ (Arya 1988). Therefore, the parameter $N = 0.5h/w$ should be pertinent.
Then:

$$U_{can} = \frac{2}{\pi}\exp\left(-\frac{1}{4}\frac{h}{w}\right)\frac{\ln\left(\frac{h/3}{z_{0_{town}}}\right)}{\ln\left(\frac{\Delta z+h/3}{z_{0_{town}}}\right)}||\vec{U_a}|| \tag{3.24}$$

Canyon temperature and humidity

These quantities can be considered as output of a meteorological forecast. They are computed diagnostically: the equilibrium between thermodynamic fluxes for the canyon air is assumed to be valid at each time step. **The anthropogenic flux due to traffic is also taken into account**. Note that in this formula, $H_{traffic}$, representative of the whole urban surface, has been scaled to the road surface.

$$H_{top} = \delta_r(1-\delta_{snowr})H_r + \delta_r\delta_{snowr}H_{snowr} + \delta_{garden}H_{garden} \quad + H_{traffic}\frac{1}{1-f_{bld}} \quad + \frac{2h}{w}\left[(1-f_{win})H_w + f_w\right.$$

$$LE_{top} = \delta_r(1-\delta_{snowr})LE_r + \delta_r\delta_{snowr}LE_{snowr} + \delta_{garden}LE_{garden} \quad + LE_{traffic}\frac{1}{1-f_{bld}}$$

Then

$$T_{can} = \frac{\delta_r(1-\delta_{snowr})\frac{T_r}{RES_r} + \frac{2h}{w}\left((1-f_{win})\frac{T_w}{RES_w} + f_{win}\frac{H_{win}}{C_{p_d}\rho_a}\right) + \frac{\hat{T_a}}{RES_{top}} + \frac{H_{traffic}}{C_{p_d}\rho_a(1-f_{bld})} + \delta_{garden}\frac{H_{garden}}{C_{p_d}\rho_a} + \delta_r\delta_{s}}{\delta_r(1-\delta_{snowr})\frac{1}{RES_r} + \frac{2h}{w}(1-f_{win})\frac{1}{RES_w} + \frac{1}{RES_{top}}} \tag{3.27}$$

and

$$q_{can} = \frac{\delta_r(1-\delta_{snowr})\frac{\delta_{water_r}q_{sat}(T_r,p_s)}{RES_r} + \frac{\hat{q_a}}{RES_{top}} + \frac{LE_{traffic}}{L_v\rho_a(1-f_{bld})} + \delta_{garden}\frac{LE_{garden}}{L_v\rho_a} + \delta_r\delta_{snowr}\frac{LE_{r_{snow}}}{L_v\rho_a}}{\delta_r(1-\delta_{snowr})\frac{\delta_{water_r}}{RES_r} + \frac{1}{RES_{top}}} \tag{3.28}$$

3.2.10 Averaged fluxes at town scale

As mentioned above, the averaging operation performed to obtain the turbulent fluxes at town scale is in itself a way to solve the problem of the roughness sublayer: it mimics the mixing of the different sources of turbulent heat fluxes, and then produces **fluxes which are representative of the upper part of the surface layer**, above the roughness sublayer. The energy fluxes released by the industrial activities is also added at this stage.
The total heat fluxes from the artificial material areas towards the atmosphere are then:

$$H_{town} = f_{bld}H_R + (1-f_{bld})H_{top} + H_{industry} \tag{3.29}$$

$$LE_{town} = f_{bld}LE_R + (1-f_{bld})LE_{top} + LE_{industry} \tag{3.30}$$

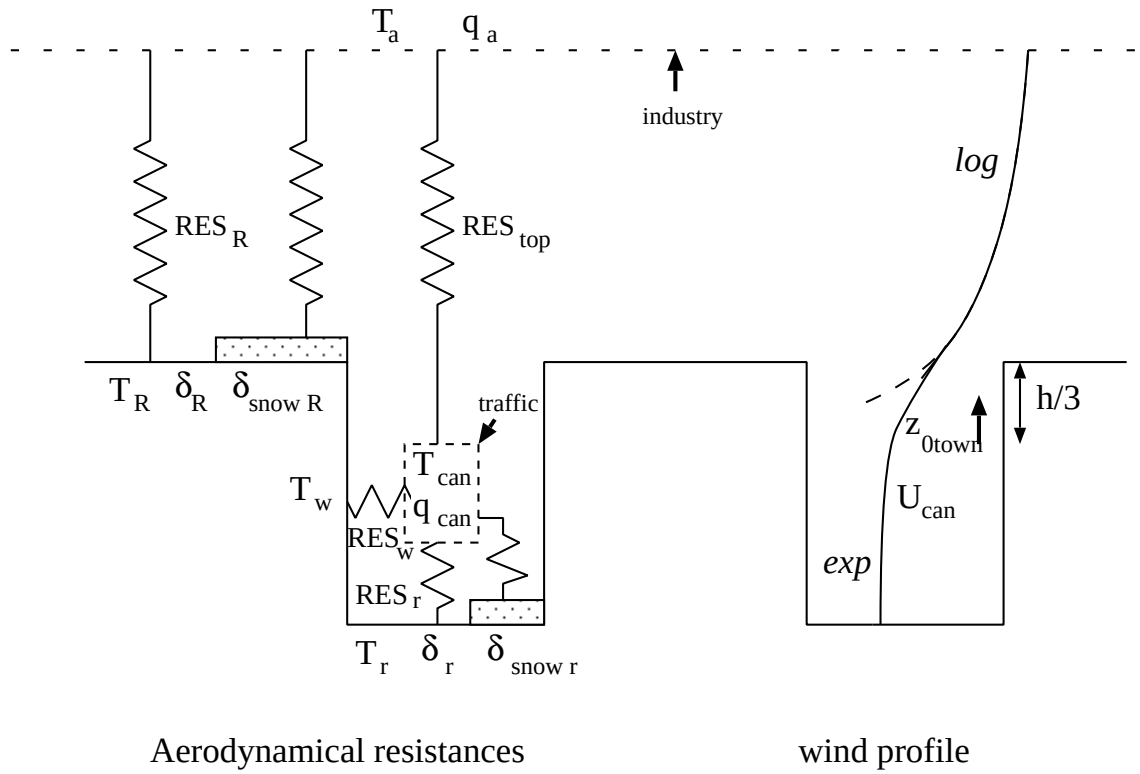

Figure 3.4: Scheme options for: (a) aerodynamic resistances; (b) wind profile within and above the canyon.

In order to have the total turbulent fluxes H, LE from the surface towards the atmospheric model, these fluxes should be averaged with those computed by the vegetation scheme for the other land surfaces (city parks, gardens, fields, forest, bare soil...) and those from water covered surfaces (rivers, lakes, sea...).

3.3 Urban vegetation: gardens and greenroofs

3.3.1 Philosophy of vegetation in TEB

Cities are not only composed of impervious surfaces. Urban vegetation plays an important role, of course in suburban areas, where gardens are often mixed within buildings and houses, but also in dense urban centers, with parks, street trees, and vegetated courtyard or small gardens. Vegetation in cities give to a lot of ecosystemic services, such as:

- climatic effects: reduction of urban heat, runoff management
- absorption of CO_2
- biodiversity enhancement (both vegetal and animal)
- recreative locations
- prefered location for soft travel modes
- improvement of wellbeing and health, reduction of stress
- real estate improvement
- etc...

While of course it is not the aim of TEB to simulate all these effetcs, the importance of urban vegetation on micro-climate lead to simulate its role more precisely. However, the overall ecosystemic services of urban vegetation show why in most urban planning strategies, and especially in relation with adaptation to climate change, the question of vegetation is of prime importance.

This is why in TEB we have developed the representation of urban vegetation, for garden (and ground vegetation in general) and greenroofs. The strategy was not to develop from scratch an urban vegetation model, but to couple TEB with ISBA, that is used in SURFEX for natural continental covers. This enable to capitalize on all the developments done in ISBA on the physics and biologics of plants. For example, this allows to simulate the CO_2 flux due to soil and plant respiration and photosynthesis.

This means that ISBA can, for each grid point, be called several times independently: for the natural part of the grid mesh, for the garden, and for the greenroofs. Each occurrence of ISBA will have its own descriptive variables and prognostic variables (e.g. the soil moisture will be different in natural cover, on the greenroofs and in the garden).

3.3.2 Gardens

The main change is first the definition of the town fraction. This now includes the urban vegetation that interacts with the nearby buildings. This encompasses street trees, gardens, small parcks and green corridors. However, large parks, where most of the vegetation is far from the buildings and do not *directly* interact with them (no shadows for example), should still be included in the nature part of the grid mesh. The town part now contains the building fraction, the urban vegetation fraction, and the impervious surfaces (as roads, parkings) fraction (the sum of all three being equal to 1). The first impact to incorporate the vegetation within the town part of the grid mesh is that allows to **more accurately described the urban**

morphology. Indeed, the vegetation being included within the canyon, the space being the buildings is larger, and more coherent with the reality. This, in itself, modifies the simulation of all the processes already presented for the version of TEB without gardens (that most often depend on geometry).

The other impacts are physical: the buildings send shadows on the gardens. This changes the solar radiation received by the vegetation. The infra-red radiation is also increased, due to the interactions with the walls. The vegetation also is sensitive to the canyon microclimate and influence it in return. All these effects are taken into account. All details are given in Lemonsu *et al.* (2012).

1. First, radiative exchanges are computed between all the canyon surfaces, including now the vegetation, both for solar (still with an infinite number of reflections)(see section 3.7), and infra-red (with the approximation of net exchanges between one surface and all of those that are seen by it, see section 3.2.2). These radiative information is using the albedo, surface temperature and emissivity of the garden. Those quantities are estimated from previous time-step of the garden ISBA model.
2. Then the solar and infrared radiation received by the garden (taking into account shadowing and radiative trapping by the canyon) are sent to ISBA, with all the other meteorological information (air temperature, humidity, wind, pressure, rainfall, snowfall) representative of the canyon. Please note here that the atmospheric data is estimated, not from the forcing level that is above the buildings, but from the middle of the canyon if no SBL scheme is used, or at first SBL level (typically 0.5m) if hte SBL scheme is used.
3. ISBA computes the energy fluxes. Note here that all the physics of ISBA are available. For example, snow mantel in garden is simulated by the snow scheme chosen in ISBA. The reader should refer to the chapter describing the ISBA model for a description of all the processes in the model.
4. Finally the turbulent and fluxes are sent back to the canyon, at the bottom of the canyon. These fluxes are averaged with the fluxes coming from the road, and then influence the rest of the canyon as the road fluxes do in the version of the model without gardens do.

3.3.3 Greenroofs

The need to prepare cities for climate change adaptation requests the urban modeller community to implement sustainable adaptation strategies within their models to be tested against specific city morphologies and scenarios. Greening city roofs is part of these strategies. In this context, the greenroof module for TEB (town energy balance) has been developed to model the interactions between buildings and greenroof system at the scale of the city. This module, which combines the ISBA model (Interaction between Soil Biosphere and Atmosphere) and TEB, allows for one to describe an extensive greenroof composed of four functional layers (vegetation grasses or sedums; substrate; retention/drainage layers; and artificial roof layers) and to model vegetation-atmosphere fluxes of heat, water and momentum, as well as the hydrological fluxes throughout the substrate and the drainage layers, and the thermal fluxes throughout the natural and artificial layers of the greenroof. TEB-greenroof is therefore be able to represent the impact of climate forcings on the functioning of greenroof vegetation and, conversely, the influence of the greenroof on the local climate.

The greenroof also modifies strongly the roof energy balance, since the surface energy budget is replaced by the conduction flux at the base of the greenroof retention/drainage layer. This impacts the buildings energetics a lot when the BEM module is active. The greenroof acts as a supplementary insulation layer in

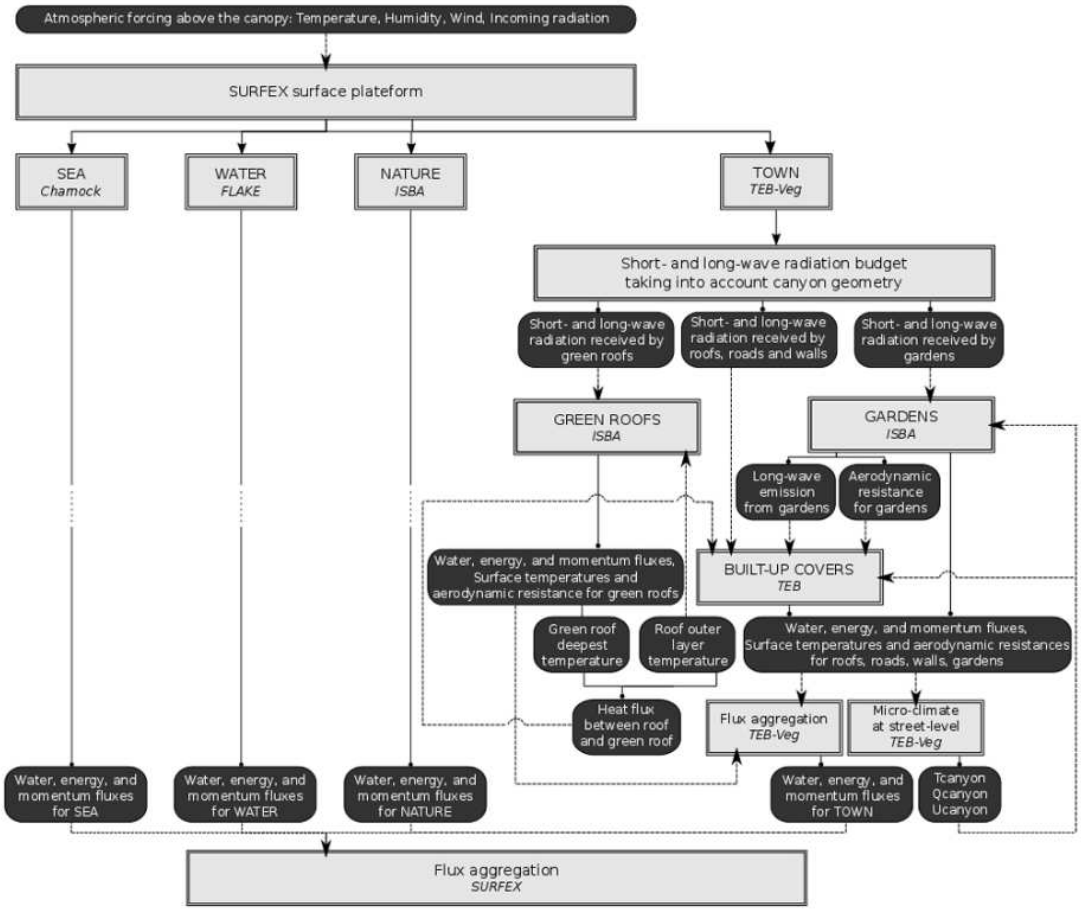

Figure 3.5: Overall algorithm of greenroof and gardens in TEB

addition to the effect of cooling due to the increased evaporation.

As established previously, the heat and water transfers involved in the natural layers of greenroofs (atmosphere, vegetation, and substrate and hydrological control layers) are similar to those of perfectly natural surfaces. They can therefore be simulated, as is the case in the models previously examined, by a standard soil and vegetation model, provided that it is calibrated to reflect the peculiar characteristics of the soil-forming materials used for the construction of greenroofs. Therefore, the strategy proposed and ultimately retained for the inclusion of greenroofs within TEB is to use a soil and vegetation model that can not only be calibrated for a specific soil but would also have the ability to overcome the limitations of existing models. The ideal model should allow for a coupled modelling of greenroof hydrological and energetic performances, employ sufficiently detailed parameterizations to describe the physical processes involved (including evapotranspiration and soil water flows), and at the same time have spatial resolutions (i.e. time calculations) suitable for modelling applications at city scale.

From a physical point of view, the main change in TEB induced by the implementation of greenroofs is the modification of the surface flux condition at the top of the roof. Instead of being computed from the surface energy balance (with the interaction of radiation, sensible and latent turbulent heat fluxes and conduction), the energy tranfer boundary condition of the top layer of the roof is replaced by a heat conduction flux (de Munck *et al.* 2013):

$$G_{N-R} = \overline{\lambda_{N-R}}(T_{N_n} - T_{R_1}) \tag{3.31}$$

T_{N_n} and $-T_{R_1}$ re, respectively, the temperatures of the deepest sub-layer of the natural roof and the top layer of the artificial roof. $\overline{\lambda_{N-R}}$ is the interfacial thermal conductivity between the two layers, approximated using the characteristics of the bottom layer of the greenroof.
The equation evolution of the top layer roof temperature (presented previously in section 3.2.1) is then modified as :

$$\begin{aligned} C_{R_1}\frac{\partial T_{R_1}}{\partial t} = \quad & (1 - f_{greenroof}) \quad \left[(1 - \delta_{snowR})\left(S_R^* + L_R^* - H_R - LE_R - G_{R_{1,2}}\right) + \delta_{snowR}\left(G_{R_{snow,1}} - G_{R_{1,2}}\right)\right]\frac{1}{d_R} \\ & + f_{greenroof} \qquad (G_{N-R} - G_{R_{1,2}})\frac{1}{d_{R_1}} \end{aligned}$$

Due to the presence of waterproofing membranes, no hydrological coupling is required between the soilvegetation model and the building model, and the excess water and the water that percolates leaves the system and are collated as the green roof outlet drainage. This will allow for connection to urban drainage systems when these are developed within a future version of TEB.

The multi-soil-layer diffusion version of ISBA is used to simulate the greenroofs substrate. For standard applications of ISBA to natural soils, the thermal characteristics for dry soil and the hydrological characteristics are deduced from empirical formulations, called pedotransfer functions, which connect these characteristics to the user-input soil texture properties (sand and clay fractions, Decharme et al., 2011). But the pedotransfer functions derived for natural soils are not really adapted to the soil-forming materials constituting the substrate or the drainage layers of a greenroof. Consequently, whenever possible, it is better to directly define greenroof-specific thermal and hydrological characteristics. However, when thermal characteristics for greenroof materials are available, hydrological characteristics are not only hard to find but also consist in lab measurements which do not reflect in situ conditions such as soil compaction or root presence/growth. Indeed, root growth results in the formation of soil microstructures, which modifies the intrinsic soil hydrological behaviour. De Munck *et al.* (2013) proposes to use pedotransfer parameters based on organic matter. The best calibration ensemble obtained in this study for the drainage layer whose texture, porosity and hydrological behaviour are complex displays hydrological characteristics which are all typical of the behaviour of organic matter (peat): high porosity and saturated hydraulic conductivity. Such characteristics are therefore recommended for extensive greenroofs. Intensive greenroofs, that are composed of trees with a deeper soil structure (typically 1m), can be represented by the classical values of ISBA soils.

3.3.4 Irrigation and watering

Irrigation of gardens is somehow a common practice. Under most of climates during the hot season, it is also necessary to irrigate the vegetation on greenroofs in order to avoid the drying of the plants. Furthermore, road watering is also considered as a possibility to avoid extreme heat during heat waves. Such a practice is indeed several centuries old in Japan, known as Uchimizu.

In TEB watering of gardens, greenroofs and roads is possible. This allows to take into accounts some aspects linked to water management and adaptation of cities to climate. This is done with the following approach, for each three types of surfaces (separately). The user provides maps or data for:

- the first and last month when watering occurs (both are included in the watering period). First month can be later in the calendar than the end day (for summer in the southern hemisphere for example).
- the begining (included) and end (excluded) hour of the watering period each day. The begining hour can be later than the end one from a clock point of view (for nighttime watering for example).
- the total amount of water per 24h per square meter that will be used during the watering.

The amount of water ($kg/m^2/24h$) will be equaly distributed during the defined period within the day, if the present month is a month of watering. Note that, for the same total amount of water during the day, this will induce larger instantaneaous flows if the period of watering is short and smaller flows if the period is long. For roads, the water is added to the road water reservoir W_r. For greenroofs and gardens, the water is directly added in the first layer of the soil in ISBA (not added to the rainfall). This simulated ground based irrigation systems, and avoid the interception of water by the trees and low plant leaves.

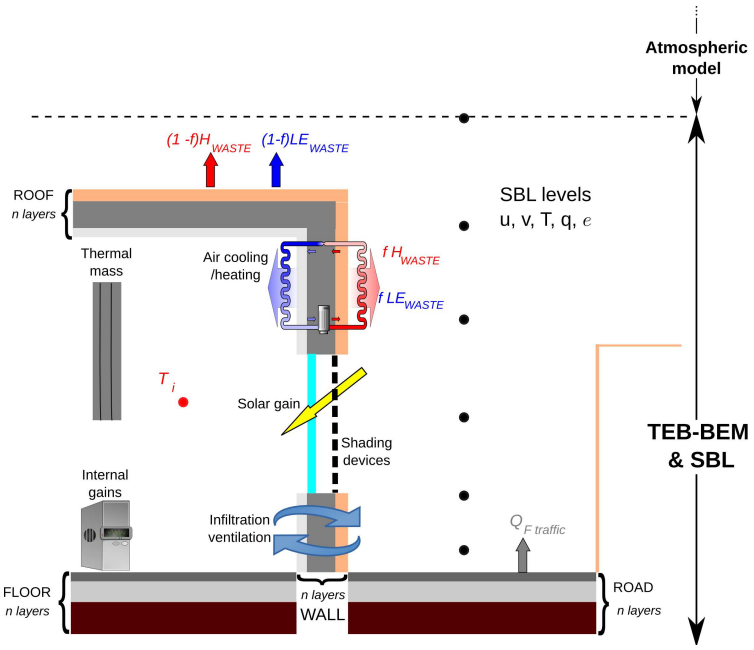

Figure 3.6: Diagram of a building and an urban canyon. The main physical processes included in BEM-TEB are represented: heat storage in building and urban construction materials, internal heat gains, solar heat fluxes, waste heat from HVAC systems, etc. The diagram also represents the multi-layer version of the TEB scheme and the possibility of coupling it with an atmospheric mesoscale model.

3.4 The Building Energy Module

The energy consumption of heating, ventilation and air-conditioning (HVAC) systems in buildings has become an important factor in the design and analysis of urban areas. HVAC systems are responsible for waste heat emissions that can contribute (among other causes) to the increase in air temperature observed in urban areas with respect to their undeveloped rural surroundings. This increase in air temperature in cities, a phenomenon known as the urban heat island (UHI) effect, can affect the energy consumption of HVAC systems and the waste heat emissions associated with them. The use of HVAC systems is expected to increase in the following years as a consequence of global-scale and urban-scale climate warming; therefore, urban climate models, such as the Town Energy Balance (TEB) scheme (Masson, 2000), has been improved in order to represent future scenarios of climate conditions and energy consumption in urban areas.

Bueno *et al.* (2012) and Pigeon *et al.* (2014) implemented a Buidling Energy Module (BEM) in TEB. The reader is invited to refer to these articles for more details.

3.4.1 Buildings description

The BEM implemented in TEB considers a single thermal zone, a generic thermal mass to represent the thermal inertia of the indoor materials, the heat gains resulting from transmitted solar radiation and the internal sources of heat, infiltration and ventilation. The heat conduction through the envelope of the building is calculated using a finite difference method individually for each surface (roof, wall and floor). An overview of all the processes simulated with the BEM implemented in TEB are displayed in figure 3.6.

3.4.2 Buildings energy budgets

BEM uses a heat balance method to calculate indoor thermal conditions and building energy demand. An energy balance is applied to each indoor surface (si: wall, window, floor, roof, and internal mass), accounting for conduction, convection, and radiation heat component. The convection and radiation terms are calculated from a standard heat transfer coefficient formulation, $Q = h\Delta T$.

The longwave radiative exchanges between all the surfaces in the interior of the building are computed using the same type of approximation as for outdoor exchanges:

$$L_{S_1 \text{ from } S_2} = 4\sigma\epsilon^2 F_{S_1 S_2} \left(\frac{1}{2}(T_{S_1} + T_{S_2})\right)^3 (T_{S_2} - T_{S_1}) \tag{3.32}$$

where $F_{S_1 S_2}$ is the configuration factor between surfaces 1 and 2, and where the emissivity ϵ of internal surfaces has been supposed to be equal for all surfaces (and set by default to 0.9). All the expressions of the configuration factors are given in Bueno *et al.* (2012).

The convection terms between each internal surface si and the indoor air are computed as:

$$Q_{cv} = h_{cv}(T_{si} - T_i) \tag{3.33}$$

where T_{si} and T_i are the surface and indoor air temperatures respectively. The convective heat transfer coefficient has the following values: $h_{cv} = 3.076 W m^{-2} K^{-1}$ for a vertical surface (walls, internal mass); $h_{cv} = 0.948 W m^{-2} K^{-1}$ for a horizontal surface with reduced convection (floor surface with $T_{si} = T_{floor_1} < T_i$ and ceiling surface with $T_{si} = T_{roof_k} > T_i$) ; and $h_{cv} = 4.040 W m^{-2} K^{-1}$ for a horizontal surface with enhanced convection.

The energy budget of internal air is also simulated (see below).

3.4.3 Inside solar irradiation, sheltering

Window effects have been introduced in the outdoor energy balance of the TEB model. The external surfaces of windows participate in the outdoor energy balance in the same manner as other urban surfaces (walls, road, garden, etc.). Window surfaces are semi-transparent and therefore have three optical properties (albedo, absorptivity, and transmittance). Two coupled surface energy balances are solved to calculate the internal and external surface temperatures of windows. Each surface energy balance accounts for the convective and radiative heat fluxes reaching the surface and the steady-state heat conduction through the window. Building energy models usually consider the dependence of the solar heat transmitted through windows on the angle of incidence of the sun. However, simulations with EnergyPlus for different window orientations show that for an average-oriented canyon, the solar transmittance of windows (τ_{win}) can be approximated by a uniform value of 0.75 times the solar heat gain coefficient (SHGC). The SHGC can be found in window catalogues and represents the fraction of incoming solar radiation that participates in the indoor energy balance. Using the solar energy reaching the window (cf section 3.2.3), the solar heat transmitted through windows is then calculated as:

$$S_{indoor} = \mathcal{A}_{win} \tau_{win} f_{win} \tag{3.34}$$

The solar absorptivity of windows is calculated as a function of the U-factor and the SHGC (Pigeon *et al.* 2014), by using the equations proposed in EnergyPlus documentation (description in http://apps1.eere.energy.gov/buildings/energyplus/pdfs/engineeringreference.pdf). The U-factor can also be found in window catalogues and measures the window conductance, including the convective and longwave heat transfer coefficients at both sides of the window. The window albedo is calculated so that the three optical properties (albedo, absorptivity, and transmittance) sum to unity. As seen above, the model uses an area-averaged facade albedo to calculate solar reflections by weighting the albedo of walls and windows with the glazing ratio of buildings.

It is also possible to simulate shelters on the window, and the periods during which shelters are on. BEM also includes a simplified model to account for window shadowing devices. If the solar radiation reaching the window is above a predefined threshold, the model considers that shades are placed outside and in front of the windows. These shades are characterized by a predefined transmittance. The model reduces the solar radiation reaching the windows by changing its optical properties. The solar radiation that is not reflected, absorbed, or transmitted by the windows is assumed to be converted into a sensible heat flux towards the urban canyon.

3.4.4 Domestic Heating and Air conditioning

To calculate the dynamic evolution of indoor air temperature between a cooling and a heating thermal set point, BEM solves a sensible heat balance at the indoor air. The sensible heat balance is composed of the convective heat fluxes from indoor surfaces, the convective fraction of internal heat gains, the infiltration sensible heat flux, and the sensible heat flux supplied by the HVAC system.

$$V_{bld}\rho C_p\frac{dT_i}{dt} = \sum_{si} A_{si}h_{cv,si}(T_{si}-Ti)+Q_{ig}(1-f_{rd})(1-f_{lat})+\dot{V}_{inf}\rho C_p(T_{can}-T_i)+\dot{m}_{sys}C_p(T_{sys}-T_i) \tag{3.35}$$

where T_i is the indoor air temperature; V_{bld} ,ρ and c_p are the volume, density and specific heat of the indoor air, respectively; A_{si} is the area of the indoor surface of each type (wall, window, floor, roof, and internal mass); Q_{ig} represents the internal heat gains; f_{lat} is the latent fraction of internal heat gains; f_{rd} is the radiant fraction of sensible internal heat gains; $\dot{V}_{inf}$ is the infiltration air flowrate; T_{can} is the outdoor air temperature; and $\dot{m}_{sys}$ and T_{sys} are the mass flowrate and temperature of the air supplied by the HVAC system.

3.4.5 Waste heat emissions

The waste heat released into the environment by a cooling system is given by :

$$Q_{waste,cool} = Q_{exch,cool} + Q_{HVAC,cool}$$

where $Q_{exch,cool} = \dot{m}_{sys}C_p(T_{sys} - T_i)$ is the thermal energy exchanged between the cooling system and the indoor air, and $Q_{HVAC,cool}$ is the energy consumption of the cooling system (e.g. electricity). The user can specify the sensible-latent split of the waste heat produced by the cooling system, depending on whether the system is air-condensed, water-condensed, or both. The user can also define which fraction of

this waste heat/humidity is released into the canyon (e.g. for individual air-conditionning systems located on each balcony) or above roofs (for centralized systems).

For the heating system, the waste heat flux is related to the energy contained in the combustion gases and is given by:

$$Q_{waste,heat} = Q_{HVAC,heat} - Q_{exch,heat}$$

where $Q_{HVAC,heat}$ is the energy consumption of the heating system (e.g. gas).

3.4.6 Ventilation and infiltration

The flow rate $\dot{V}_{inf}$ in equation 3.35 describes the amount of air exchanged between indoor and outdoor. This exchange of air lead to modification of heat and moisture inside but also outside. For example, heated buildings will heat the outside air through conduction trhough the walls and roofs but also directly by air transfers. Those air transferts have three potential sources: inflitration, ventilation, natural ventilation. All these three processes can be simulated in TEB. Note that all are optional, but infiltration is per defaut activated, while the two others are not.

Infiltration

Infiltration refers to the flow of air induced voluntary, e.g. by slits in walls and windows, or involuntary, due to cracks and defaults of the structure of the building. The infiltration flow rate $\dot{V}_{inf}$ is typically of the order of 0.5 vol/h (where vol refers to the volume of air in the building).

Mechanical Ventilation

Mechanical ventilation is related to systems that force the exchange of air between indoor and outdoor. This allows for example to evacuate humidity from bathrooms or kitchens. This type of equipment is common in recent buildings and houses. The formulation is the same as for infiltration, but with an exchange rate that can be larger. Double-flow mechanical ventilation can also reduce the heat loss during the exchange of air between indoor and outdoor (this is parameterized using a smaller ventilation coefficient).

Natural Ventilation

People can open windows and doors. This leads to natural ventilation. This can be done for example for aeration, to go inside or outside, or for ventilation of the building, e.g. to reduce the indoor temperature if it is cooler outside. The latter process is parameterized in TEB. Contrary to inflitration and mechnaical ventilation, the flowrate in the case of natural ventilation is dependent of the external meteorological conditions. This flow will be larger if the wind is stronger, or if the temperature difference between indoor and outdoor air is larger. The formulations for the natural ventilation coefficient is given in Bueno *et al.* 2012, as well as the hypotheses done on the behaviour of people on the condition of opening and closing of windows.

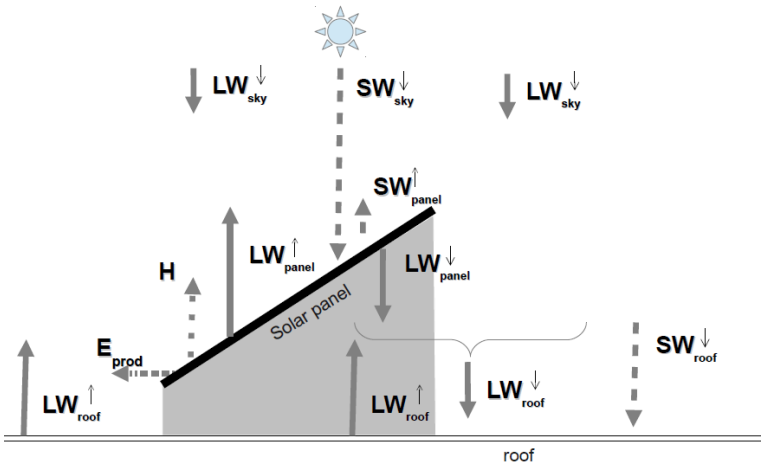

Figure 3.7: Schematic diagram of the energy balance of the solar panel and its impact on radiation received by the roof (dashed arrows: solar fluxes; plain arrows: long-waves fluxes; dotted arrow: sensible heat

3.4.7 Solar panels

Solar panels can be simulated on the roofs (Masson *et al.* 2014). An additional energy balance is then computed for the solar panel, taking into account solar radiation (from above and reflected upwards), long-wave radiation (received both from above and below, and emitted/reflected both upwards and downwards), convection and energy production. No heat storage is taken into account, the solar panel being supposed thin enough. The presence of solar panels also impacts the underlying surfaces: **structural roof and grennroof**. solar panels modifiy their energy balance, by sheltering the solar radiation (in an amount equal to their surface coverage f_{panel}), and modify the longwave balance.

For downwards longwave emission, solar panel is supposed of emissivity 1 and at air temperature. For the upwards longwave emitted terms, the solar panel temperature takes into account air temperature and solar irradiance (that itself uses an empirical coefficient $FT = 1.1$ to take simulates the geometrical effect of the tilting of the solar panel towards the sun). Default value for emissivity of solar panels is 0.9.

$$T_{panel} = T_a + k_T \times FT(SW_{\Downarrow} + SW_{\downarrow}) \tag{3.36}$$

Two types of solar panels can be simulated:

- thermal panels, for hot water production
- photovoltaic panels, for electricity production

Thermal panels are more efficient than photovoltaic panels (efficientcy coefficient of 0.6 instead of 0.14, per default). However, thermal panels are more complicated to install, and only a limited amount of solar panels is necessary for warming water, depending on the need in hot water. In TEB, thermal panels are supposed to be installed on residential buildings only (note that this requires to have an information on the fraction of residential buildings in the grid mesh). It is then necessary to define what proportion of the roof area is required for thermal panels, and how much area remains available for PV panels. In residential buildings, one supposes that the density is typically 1 occupant per $30m^2$ of floor area. Furthermore, $1m^2$

of thermal panel is needed per capita. This means $1m^2$ of panel per $30m^2$ of floor area. For single story accommodation, $1/30$ of the roof is then equipped with thermal panels, and ($f_{panel}1/30$) by PV panels. If the building has two stories, thermal panels will occupy $2/30$ of the roof area, and so on. So if N_{floor} is the number of floors of the building (variable calculated in TEB), the proportions of thermal panels ($f_{ther\ panel}$) and and photovoltaic panels ($f_{phot\ panel}$) are calculated as :

$$\begin{aligned} f_{ther\ panel} &= \min(N_{floor}/30; f_{panel}) \\ f_{phot\ panel} &= f_{panel} - f_{ther\ panel} \end{aligned}$$

All details on the production of energy by both types of panels is given in Masson *et al.* (2014). The energy produced by the solar panels, that influences its energy balance, is computed as:

$$E_{prod} = (f_{ther\,panel} E_{ther\,prod} + f_{phot\,panel} E_{phot\,prod})/f_{panel} \qquad (W/m^2 \text{ of solar panel})$$

And finally, the sensible heat flux H_{panel} that is not easy to parameterize, is found as the residual of the solar panel energy balance.

3.5 The Surface Boundary Layer module, when applied in TEB

The TEB-SBL (for Surface Boundary Layer) version of TEB has been recently developed in order to improve prediction of the meteorological fields inside the street canyon (Hamdi *et al.* (2008), Masson *et al.* (2009)). It resolves the surface boundary layer inside and above urban canopy by introducing a drag force approach - based on Yamada (1982) for vegetation canopies - in order to take into account the influence of buildings on the local atmospheric characteristics.

3.5.1 Drag by buildings

The equations for momentum, turbulent kinetic energy, air temperature, and specific humidity follow the same general expression (here for momentum):

$$\frac{\partial U}{\partial t} = F_U + \left.\frac{\partial U}{\partial t}\right|_{TEB} \tag{3.37}$$

According to Martilli (2002) , the momentum equation includes, besides the general forcing term F_U, a contribution from the area-average effect of the subgrid urban elements that is partitionned into a contribution from vertical surfaces (buildings and walls) and a contribution from horizontal surfaces (roofs and roads). For the present version of TEB-Veg that only takes into account low vegetation, the garden contribution is included in the horizontal term:

$$\left.\frac{\partial U}{\partial t}\right|_{TEB}^{H} = -C_d U^2 \frac{S_H}{V_{air}} \tag{3.38}$$

where C_d is the drag coefficient, S_H the horizontal surface area of roofs, roads, and gardens, and V_{air} the volume of air in the urban grid cell. The drag coefficient is equal to (the π term coming from averaging of the drag coefficient along all wind directions) :

$$C_d = 0.4/\pi \tag{3.39}$$

For temperature (T) and humidity (q), the contributions from gardens are taken into account through the sensible and latent heat fluxes:

$$\left.\frac{\partial T}{\partial t}\right|_{TEB} = \left(\frac{Q_{H_R} + Q_{H_r} + Q_{H_g}}{\rho C_p}\right)\frac{S_H}{V_{air}} + \frac{Q_{H_w}}{\rho C_p}\frac{S_V}{V_{air}} \tag{3.40}$$

$$\left.\frac{\partial q}{\partial t}\right|_{TEB} = \left(\frac{Q_{E_R} + Q_{E_r} + Q_{E_g}}{\rho}\right)\frac{S_H}{V_{air}} \tag{3.41}$$

with Q_{H_R}, Q_{H_r}, and Q_{H_g} the sensible heat fluxes for roofs, roads, and gardens (same for the latent heat flux), Q_{H_w} the sensible heat fluxes for walls, and S_V the vertical surface area of walls.

3.5.2 Mixing length

Vertical turbulent exchanges within the canyon (and also above the canyon) are parameterized with the turbulent scheme of Cuxart *et al.* (2000). This scheme uses an equation for the turbulent kinetic energy, and is closed with a mixing length. Hamdi *et al.* (2008) use a constant mixing length within the canyon, equal to the building height. Here, we improve this representation following the works of Santiago and Martilli (2010) , that used fluid dynamics models to explicitly simulate the motions within the canyon to derive a vertical profile of the mixing length.

The mixing length (L) is parameterized as :

$$\frac{L}{C} = \min\left[\, 2.24(h-d)\ ,\ z\,\right] \qquad \text{for} \qquad \frac{z}{h} < 1. \tag{3.42}$$

$$\frac{L}{C} = \max\left[\, 2.24(h-d)\ ,\ z-d\,\right] \qquad \text{for} \qquad \frac{z}{h} > 1.5 \tag{3.43}$$

with a continuous linear transition between the top of the canopy layer and the base of the inertial sublayer, and where the displacement height d is also parameterized following Santiago and Martilli (2010):

$$d = \max\left[\, \frac{3}{4}\, h\ ,\ \lambda_f^{0.13}\, h\,\right] \tag{3.44}$$

Here z is the height above ground, h is the building height, λ_f is the frontal area density, that is derived from other TEB geometric parameters assuming no prefered direction of buildings with respect to the wind direction ($\lambda_f = [\frac{h}{w} f_{bld}]/\frac{\pi}{2}$, with w being the road width and f_{bld} the building fraction). C is dependant on the turbulence scheme constants and of the atmospheric stability, using Monin-Obukhov stability functions (Redelsperger (2001)). Note that near the surface, one limits the mixing length to reproduce the effect of the surface on the turbulent eddies.

3.6 Miscellaneous indicators

3.6.1 Thermal comfort

A lot of indices (more than 50!) exist to evaluate the thermal comfort of human beings. This is the science of bioclimatology. The COST action 730 recently proposed a new index: the Universal Thermal Climate Index (UTCI) (http://www.utci.org/). This is the index that is estimated in TEB to represent the thermal comfort of people. This index takes into account effects of wind, temperature, humidity and radiation. It makes implicit hypotheses on the activity and clothing of the person for which the UTCI is estimated. Therefore, this index should be understood as an index relative to a typical person, but the actual sensation of people may of course be different. The UTCI provide a temperature value, that can be compared to a temperature scale to infer the amount of comfort or cool or heat discomfort.

In TEB, we calculate the UTCI for :

- outdoor condition, in sunlight
- outdoor condition, in shade
- indoor condition (pertinent only without AC system in summer)

Mean radiant temperature

To calculate the UTCI, one must first estimate radiant temperature. This is done using the radiative terms computed by TEB. For outdoor computations, one first estimate the view factors of ground, facades and sky for a human body (of mean height $h_{human} = 1.7m$):

$$\begin{aligned} F_{human-fac} &= \left(\sqrt{h_{human}^2 + \tfrac{w^2}{4}} + \sqrt{h^2 + \tfrac{w^2}{4}} - w/2 - \sqrt{(h - h_{human})^2 + \tfrac{w^2}{4}}\right) /(2h_{human}) \\ F_{human-ground} &= \tfrac{1}{2}\left[\tfrac{w}{2h_{human}} + 1 - \sqrt{\left(\tfrac{w}{2h_{human}}\right)^2 + 1}\right] \\ F_{human-sky} &= 1 - F_{human-fac} - F_{human-ground} \end{aligned}$$

where w is the canyon width, computed from input TEB parameters as:

$$w = 2h(1 - f_{bld})/R_{wall-hor}$$

The radiation received by the human body, from solar diffuse and infra-red radiation (so for a person in shade), is estimated as:

$$\begin{aligned} RAD_{body,shade} = (1 - \alpha_{body})/\epsilon_{body} & \left[F_{human-sky}S^{\downarrow} + F_{human-fac}S_{fac} + F_{human-fac}S_{ground}\right] \\ + & \left[F_{human-sky}L^{\downarrow} + F_{human-fac}L_{fac} + F_{human-fac}L_{ground}\right] \end{aligned} \quad (3.45)$$

where $\alpha_{body} = 0.3$ is the albedo of human body, $\epsilon_{body} = 0.97$ the emissivity of human body, and S_{fac}, S_{ground} the solar radiation reflected by facades and ground (garden and road together) respectively, and L_{fac}, L_{ground} the longwave radiation emitted/reflected by facades and ground, respectively.

For the evaluation of the UTCI in sunlight, the amount of solar radiation received by the human body is added. This is done taking into account the solar elevation angle (deduced from the zenithal angle as $\gamma = \frac{\pi}{2} - \lambda$), because the human being is supposed standing in upright position.

$$S^{\Downarrow}_{body} = S^{\Downarrow} \times 0.308 \cos\left[\gamma(1 - \gamma^2/14.744)\right]$$
$$RAD_{body,sun} = RAD_{body,shade} + S^{\Downarrow}_{body}(1 - \alpha_{body})/\epsilon_{body}$$

And finally the mean radiant temperature, either in shade or sun, is equal to :

$$T_{mrt} = (RAD_{body,\star}/\sigma)^{\frac{1}{4}} \tag{3.46}$$

Universal Thermal Climate Index

Then, the UTCI indices are computed using an approximated form of a complete human body energy balance model. This approximated form is a polynomial formulae, taking into account air temperature at 2 meters (°C), vapor pressure at 2 meters (hpa), wind at 10m (ms^{-1}), and mean radiant temperature (°C).

For indoor index computations, the radiative temperature is computed using the radiation emitted by each interior surface, the wind is supposed equal to $0.5 ms^{-1}$.

For outdoor index computations, the mean radiant temperature is computed according to the above shade or sunlight formulae. If the SBL scheme is not used, the wind is taken at 10m above roofs level or at forcing level, and the temperature and humidity are equal to the canyon air temperature and humidity. If the SBL scheme is used, the wind is equal interpolated 10m above the ground (road and garden) from the SBL layers, and the temperature and humidity are equal to the air temperature and humidity 2m above ground level.

symbol	designation of symbol	unit
geometric parameters		
a_{town}	fractional area occupied by artificial material	-
f_{bld}	fractional artificial area occupied by buildings	-
f_{garden}	fractional artificial area occupied by urban vegetation	-
$1 - f_{bld}$ - f_{garden}	fractional artificial area occupied by roads	-
f_{win}	fractional area occupied by windows relative to the whole facade surface	-
$1 - f_{win}$	fractional area occupied by structural walls relative to the whole facade surface	-
$f_{greenroof}$	fractional area occupied by greenroofs relative to the roof surface	-
h	building height	m
h/w	canyon aspect ratio	-
$z_{0_{town}}$	dynamic roughness length for the building/canyon system	m
radiative parameters		
α_R, α_r, α_w	roof, road and wall albedos	-
ϵ_R, ϵ_r, ϵ_w	roof, road and wall emissivities	-
α_{garden}, α_{win}	garden and window albedos	-
ϵ_{garden}, ϵ_{win}	garden and window emissivities	-
thermal parameters		
d_{R_k}, d_{r_k}, d_{w_k}	thickness of the k^{th} roof, road or wall layer	m
λ_{R_k}, λ_{r_k}, λ_{w_k}	thermal conductivity of the k^{th} roof, road or wall layer	W m^{-1} K^{-1}
C_{R_k}, C_{r_k}, C_{w_k}	heat capacity of the k^{th} roof, road or wall layer	J m^{-1} K^{-1}
U_{win}	U-factor of windows	-

Table 3.2: Parameters of the TEB scheme. *Note that a_{town} is not strictly a parameter of the TEB scheme, but is used to average the output TEB fluxes with those computed for the vegetation and water portions of the grid mesh. Note also that some surfaces between the buildings, such as gardens or parks for example, are* **not** *treated by the TEB model, but modify the canyon width, w.*

symbol	designation of symbol
prognostic variables	
$T_{R_k}, T_{r_k}, T_{w_k}$	temperature of the k^{th} roof, road or wall layer
W_R, W_r	roof and road water interception reservoir
T_{win_k}	window temperatures
T_{mass_k}, T_{floor_k}	temperature of the k^{th} internal mass or floor layer
$T_{i_{bld}}$	building interior air temperature
$W_{snow\,R}, W_{snow\,r}$	roof and road snow interception reservoir
$T_{snow\,R}, T_{snow\,r}$	roof and road snow temperature
$\rho_{snow\,R}, \rho_{snow\,r}$	roof and road snow density
$\alpha_{snow\,R}, \alpha_{snow\,r}$	roof and road snow albedo
diagnostic variables	
T_{can}	canyon air temperature
q_{can}	canyon air specific humidity
U_{can}	along canyon horizontal wind
α_{town}	town effective albedo
$T_{s_{town}}$	town area averaged radiative surface temperature
input energy fluxes	
$L^{\downarrow}$	downward infra-red radiation on an horizontal surface
$S^{\downarrow}$	downward **diffuse** solar radiation on an horizontal surface
$S^{\Downarrow}$	downward **direct** solar radiation on an horizontal surface
! $H_{traffic}$	anthropogenic sensible heat flux released in the canyon
$LE_{traffic}$	anthropogenic latent heat flux released in the canyon
$H_{industry}$	anthropogenic sensible heat flux released by industries
$LE_{industry}$	anthropogenic latent heat flux released by industries
other energy input	
$T_{heat\ target_{bld}}$	domestic heating target for interior air temperature
$T_{cool\ target_{bld}}$	air-conditioning target for interior air temperature
output energy fluxes	
S_R^*, S_r^*, S_w^*	net solar radiation budget for roofs, roads and walls
L_R^*, L_r^*, L_w^*	net infra-red radiation budget for roofs, roads and walls
H_R, H_r, H_w	turbulent sensible heat flux for roofs, roads and walls
LE_R, LE_r, LE_w	turbulent latent heat flux for roofs, roads and walls
$G_{R_{k,k+1}}, G_{r_{k,k+1}}, G_{w_{k,k+1}}$	conduction heat flux between k^{th} and $k+1^{th}$ roof, road or wall
H_{town}	town averaged turbulent sensible heat flux
LE_{town}	town averaged turbulent latent heat flux

Table 3.3: Energy fluxes and variables in the TEB scheme

Bibliography

[1] S.P. Arya. *Introduction to Micrometeorology*. Academic Press, Inc., 1988.

[2] M. Bottema. Roughness modelling in relation to pollutant dispersion. *Atmos. Environ.*, 31(18):3059–3075, 1997.

[3] B. Bueno, G. Pigeon, L. K. Norford, K. Zibouche, and C. Marchadier. Development and evaluation of a building energy model integrated in the teb scheme. *Geoscientific Model Development*, 5(2):433–448, 2012.

[4] P. Bougeault Cuxart, J. and J.-L. Redelsperger. A turbulence scheme allowing for mesoscale and large-eddy simulations. *Q. J. R. Meteorol. Soc.*, 116:1–30, 2000.

[5] C. De Munck, Lemonsu A., Bouzouidja R., Masson V., and Claverie R. The greenroof module (v7.3) for modelling green roof hydrological and energetic performances within teb. *Geoscientific Model Development*, 6:1941–1960, 2013.

[6] J. Deardorff. Efficient prediction of ground temperature and moisture with inclusion of a layer of vegetation. *J. Geophys. Res.*, 83:1889–1903, 1978.

[7] B. Decharme, A. Boone, C. Delire, and J. Noilhan. Local evaluation of the interaction between soil biosphere atmosphere soil multilayer diffusion scheme using four pedotransfer functions. *J. Geophys. Res.*, 116(D20), October 2011.

[8] C. Feigenwinter, R. Vogt, and E. Parlow. Vertical structure of selected turbulence characteristics above an urban canopy. *Theor. Appl. Climatol.*, 62:5163, 1999.

[9] C. S. B. Grimmond, M. Blackett, M. J. Best, J.-J. Baik, S. E. Belcher, J. Beringer, S. I. Bohnenstengel, I. Calmet, F. Chen, A. Coutts, A. Dandou, K. Fortuniak, M. L. Gouvea, R. Hamdi, M. Hendry, M. Kanda, T. Kawai, Y. Kawamoto, H. Kondo, E. S. Krayenhoff, S.-H. Lee, T. Loridan, A. Martilli, V. Masson, S. Miao, K. Oleson, R. Ooka, G. Pigeon, A. Porson, Y.-H. Ryu, F. Salamanca, G.J. Steeneveld, M. Tombrou, J. A. Voogt, D. T. Young, and N. Zhang. Initial results from phase 2 of the international urban energy balance model comparison. *Int. J. Clim.*, 31(2):244–272, 2011.

[10] C. S. B. Grimmond, M. Blackett, M. J. Best, J. Barlow, J-J. Baik, S. E. Belcher, S. I. Bohnenstengel, I. Calmet, F. Chen, A. Dandou, K. Fortuniak, M. L. Gouvea, R. Hamdi, M. Hendry, T. Kawai, Y. Kawamoto, H. Kondo, E. S. Krayenhoff, S-H. Lee, T. Loridan, A. Martilli, V. Masson, S. Miao, K. Oleson, G. Pigeon, A. Porson, Y-H. Ryu, F. Salamanca, L. Shashua-Bar, G-J. Steeneveld, M. Tombrou, J. Voogt, D. Young, and N. Zhang. The international urban energy balance models comparison project: First results from phase 1. *J. Appl. Meteorol. Climatol.*, 49(6):1268–1292, February 2010.

[11] C.S.B. Grimmond and 38:12621292 1999b Oke, T.R. Aerodynamic Properties of urban areas derived from Analysis of Surface form. J. Appl. Meteorol. Aerodynamic properties of urban areas derived from analysis of surface form. *J. Appl. Meteorol.*, 38:1262–1292, 1999.

[12] C.S.B. Grimmond and T.R. Oke. An evapotranspiration-interception model for urban areas. *Water Resour. Res.*, 27:1739–1755, 1991.

[13] R. Hamdi and V. Masson. Inclusion of a drag approach in the town energy balance (teb) scheme: Offline 1d evaluation in a street canyon. *J. Appl. Meteorol. Climatol.*, 47(10):2627–2644, October 2008.

[14] G.T. Johnson, T.R. Oke, T.J. Lyons, D.G. Steyn, I.D. Watson, and J.A. Voogt. Simulation of surface urban heat islands under ideal conditions at night. part i: theory and tests against field data. *Bound.-Layer Meteorol.*, 56:275–294, 1991.

[15] A. Lemonsu, V. Masson, L. Shashua-Bar, E. Erell, and D. Pearlmutter. Inclusion of vegetation in the town energy balance model for modeling urban green areas. *Geoscientific Model Development Discussions*, 5(2):1295–1340, 2012.

[16] Alberto Martilli. Numerical study of urban impact on boundary layer structure: Sensitivity to wind speed, urban morphology, and rural soil moisture. *J. Appl. Meteorol.*, 41(12):1247–1266, December 2002.

[17] Alberto Martilli. Current research and future challenges in urban mesoscale modelling. *International Journal of Climatology*, 27(14):1909–1918, 2007.

[18] P. Mascart, J. Noilhan, and H. Giordani. A modified parameterization of flux-profile relationships in the surface layer using different roughness length values for heat and momentum. *Bound.-Layer Meteorol.*, 72:331–344, 1995.

[19] V. Masson. A physically-based scheme for the urban energy budget in atmospheric models. *Bound.-Layer Meteorol.*, 94(3):357–397, March 2000.

[20] V. Masson. Urban surface modeling and the meso-scale impact of cities. *Theor. and Appl. Clim.*, 84:35–45, 2006. 10.1007/s00704-005-0142-3.

[21] V. Masson, Bonhomme M., Salagnac J.-L., Briottet X., and Lemonsu A. Solar panels reduce both global warming and urban heat island. *Front. Environ. Sci*, 2(14):1–10, 2014.

[22] Valéry Masson and Yann Seity. Including atmospheric layers in vegetation and urban offline surface schemes. *J. Appl. Meteor. Climatol.*, 48(7):1377–1397, July 2009.

[23] L. Menut. *Etude expérimentale et théorique de la couche limite Atmosphérique en agglomération parisienne (experimental and theoretical study of the ABL in Paris area)*. PhD thesis, University Pierre et Marie Curie, Paris, France, 1997.

[24] J. Noilhan. A model for the net total radiation flux at the surfaces of a building. *Build. and Environ.*, 16(4):259–266, 1981.

[25] J. Noilhan and S. Planton. A simple parameterization of land surface processes for meteorological models. *Mon. Weather Rev.*, 117(3):536–549, 1989.

[26] T. R. Oke. *Boundary Layer Climates*. Methuen, London and New York, 1987. 435 pp.

[27] T. R. Oke. The urban energy balance. *Prog. Phys. Geogr.*, 12:471–508, 1988.

[28] R.L. Petersen. A wind tunnel evaluation of methods for estimating surface roughness length at industrial facilities. *Atmos. Environ.*, 31(1):45–57, 1997.

[29] G. Pigeon, Zibouche K., Bueno B., Le Bras J., and Masson V. Evaluation of building energy simulations with the teb model against energyplus for a set of representative buildings in paris. *Energy and Buildings*, 76:1–14, 2014.

[30] J.-L. Redelsperger, F. Mahe, and P. Carlotti. A simple and general subgrid model suitable both for surface layer and free-stream turbulence. *Bound.-Layer Meteorol.*, 101:375–408, 2001.

[31] K. Richards and T.R. Oke. Dew in urban environments. In *IInd AMS Urban Environment Symposium*, 1998.

[32] Algren A.B. Rowley, F.B. and Blackshaw. Surface conductances as affected by air velocity, temperature and character of surface. *ASHRAE Trans.*, 36:429–446, 1930.

[33] F.B. Rowley and W.A. Eckley. Surface coefficients as affected by wind direction. *ASHRAE Trans.*, 38:33–46, 1932.

[34] J. Santiago and A. Martilli. A dynamic urban canopy parameterization for mesoscale models based on computational fluid dynamics reynolds-averaged navierstokes microscale simulations. *Bound.-Layer Meteorol.*, 137:417–439, 2010. 10.1007/s10546-010-9538-4.

[35] N.L. Seaman, F. Ludwig, E.G. Donall, T.T. Warner, and C.M. Bhumralkar. Numerical studies of urban planetary boundary-layer structure under realistic synoptic conditions. *J. Appl. Meteorol.*, 28:760781, 1989.

[36] N.S. Sturrock and R.J. Cole. The convective heat exchange at the external surface of buildings. *Build. and Environ.*, 12:207–214, 1977.

[37] W.H. Terjung and P.A. ORourke. Influences of physical structures on urban energy budgets. *Bound.-Layer Meteorol.*, 19:421–439, 1980.

[38] Brutsaert W. *Evaporation into the atmosphere: Theory, History and Applications*. D. Reidel, Hingham Mass., 1982.

[39] J. Wieringa. Representative roughness parameters for homogeneous terrain. *Bound.-Layer Meteorol.*, 63:323–363, 1993.

[40] Tetsuji Yamada. *Journal of the Meteorological Society of Japan*, 60:439–454, 1982.

Chapter 4

Soil and vegetation

Contents

4.1 ISBA surface scheme

4.1.1 Surface snow fractions

Snow is known to have a significant impact on heat conduction fluxes owing to its relatively high insulating properties. In addition, it can significantly reduce turbulent transfer owing to reduced surface roughness, and it has a relatively large surface albedo thereby impacting the surface net radiation budget. Thus, for spatially distributed (parcel, meso, regional and/or global scales), the parameterization of its areal coverage turns out to be a critical aspect of land surface model (LSM) representation of snowpack-atmosphere interactions and sub-surface soil and hydrological processes. For example, the areal snow cover fraction for each patch of the ISBA land surface model has an impact on the total upwelling radiative and turbulent fluxes, in addition to soil freezing (depth and intensity), and snow melt rates. In ISBA (like many other land surface models), the total snow fraction for a given surface is comprised of several component fractions which are described herein.
First, the snow fraction over vegetation is computed from

$$p_{snv} = \frac{h_s}{h_s + w_{sv}\, z_0} \tag{4.1}$$

where z_0 is the surface roughness length (including the effects of snow cover, soil, vegetation...). h_s (m) is the single-layer total snow depth. It is defined as

$$h_s = W_s/\rho_s \tag{4.2}$$

where ρ_s (kg m^{-3}) is the average single-layer snowpack density and W_s (kg m^{-2}) is the single-layer bulk snow water equivalent (or SWE). The empirical parameter w_{sv} is a coefficient set to 5 (default). The snow cover fraction for the bareground portion of the patch is given by

$$p_{sng} = \frac{W_s}{(W_s + W_{crn})} \tag{4.3}$$

The critical snow water equivalent is defined as $W_{crn} = 10$ kg m^{-2}.
Note that the formulation for p_{sng} is slightly different for the multi-layer snow schemes. In this case, it is defined as

$$p_{sng} = \min\left(1,\, D_n/D_{ng}\right) \tag{4.4}$$

where D_n is the total depth for a multi-layer snow scheme option and D_{ng} (m) a ground snow depth threshold set to 0.01 m. Note that D_n is analogous to h_s, but different symbols are used to distinguish between the single-layer snow-scheme bulk depth, h_s, and the total depth, D_n, as a sum of multiple layer thicknesses for the multi-layer snow scheme options.

The total snow cover fraction, p_{sn} is computed as the sum between the bare ground snow covered fraction, p_{sng}, and the fraction of vegetation covered by snow, p_{snv}, weighted by the vegetation fraction of the patches covered by vegetation, veg as

$$p_{sn} = (1 - veg)p_{sng} + veg\, p_{snv} \tag{4.5}$$

veg is specified for each vegetation patch: it is equal to 0.0 for bare soil, 0.95 for grassland/tundra as well as for temperate and boreal forests, and varies exponentially according to the leaf area index (LAI) for crop types. As a final note, a recent explicit canopy vegetation (bulk-layer) option (called the multi-energy budget or ISBA-MEB option) has been added to ISBA. In this parameterization, neither veg or p_{snv} are used (thus for MEB, $p_{sn} = p_{sng}$): thus MEB has a much lower dependence on the empirical snow fraction parameterization. In addition, vegetation can be buried (for sufficiently deep snowpacks) in the vertical sense for MEB: see Section 4.1.9 for details.

4.1.2 Force restore approach

Treatment of the soil heat content

The prognostic equations for the surface temperature T_s and its mean value T_2 over one day τ, are obtained from the force-restore method proposed by Bhumralkar (1975) and Blackadar (1976):

$$\frac{\partial T_s}{\partial t} = C_T(R_n - H - LE) - \frac{2\pi}{\tau}(T_s - T_2) \tag{4.6}$$

$$\frac{\partial T_2}{\partial t} = \frac{1}{\tau}(T_s - T_2) \tag{4.7}$$

where H and LE are the sensible and latent heat fluxes, and R_n is the net radiation at the surface. The surface temperature T_s evolves due to both the diurnal forcing by the heat flux $G = R_n - H - LE$ and a restoring term towards its mean value T_2. In contrast, the mean temperature T_2 only varies according to a slower relaxation towards T_s.
The coefficient C_T is expressed by

$$C_T = 1/\left[\frac{(1 - veg)(1 - p_{sng})}{C_g} + \frac{veg(1 - p_{snv})}{C_v} + \frac{p_{sn}}{C_s}\right] \tag{4.8}$$

where veg is the fraction of vegetation, C_g is the ground heat capacity, C_s is the snow heat capacity, and C_v is the vegetation heat capacity. The snow cover fraction for the bare-ground portion of the patch is computed from Eq. 4.3. The partitioning of the grid into bare soil, vegetation, and snow areas, is indicated in Fig.(4.1)
.
The heat capacities of the ground and snow canopies are respectively given by

$$C_g = C_{gsat}\,(w_{sat}/w_2)^{b/2\log 10} \qquad \left(C_g \leq 1.5 \times 10^{-5}\right) \tag{4.9}$$

where G_{gsat} (K m^2 J^{-1}) is the heat capacity at saturation, and w_{sat} the volumetric moisture content of the soil at saturation; and

$$C_s = 2\left(\frac{\pi}{\lambda_s c_s \tau}\right)^{1/2} \tag{4.10}$$

where $\lambda_s = \lambda_i \times {\rho_s}^{1.88}$; $c_s = c_i(\rho_s/\rho_i)$: λ_i is the ice conductivity; c_i is the heat capacity of ice; and ρ_i is the relative density of ice (Douville, 1994; Douville *et al.* 1995).

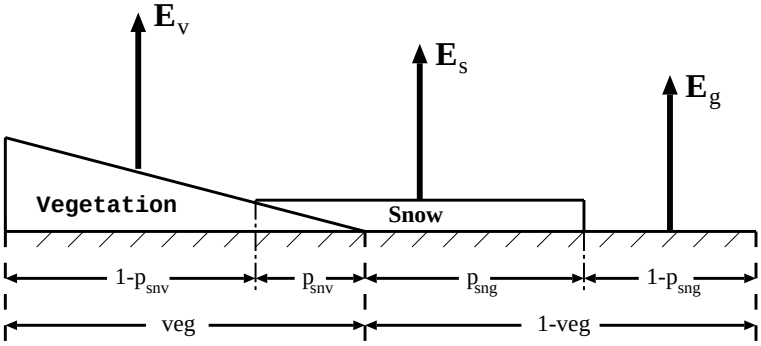

Figure 4.1: Partitioning of the grid

After an intermediate surface temperature $T_s{}^*$ is evaluated from Eq. (4.6), the cooling due to the melting of snow is considered following

$$T_s{}^+ = T_s{}^* - C_T\, L_f\, M_{lt} \Delta t \tag{4.11}$$

where L_f is the latent of fusion, Δt is the timestep, and the melting rate of snow is

$$M_{lt} = p_{sn} \left(\frac{T_n - T_0}{C_s L_f \Delta t} \right) \qquad (M_{lt} \geq 0) \tag{4.12}$$

and

$$T_n \;=\; (1 - veg) T_s{}^* + veg\, T_2 \tag{4.13}$$

Similarly, the intermediate mean temperature $T_2{}^*$ is also modified due to the melting/freezing of water in the soil layer occurring for temperatures (Boone *et al.* 2000). The resulting mean temperature is

$$T_2{}^+ = T_2{}^* + (\Delta w_2)_{frozen}\, L_f\, C_g\, d_f \tag{4.14}$$

with

$$(\Delta w_2)_{frozen} \;=\; \begin{cases} [1 - (T_2{}^* - 268.16)\,/5]\;[w_2(t) - w_2(t - \Delta t)] \\ 0 \qquad\qquad\qquad\qquad\qquad\qquad T_2 \geq 0 \text{ or } T_2 \leq T_f - 5 \end{cases} \tag{4.15}$$

where $d_f = 0.15$ m is an estimated average of the penetration of the diurnal wave into the soil. Only the mean temperature T_2 is modified by this factor. The surface temperature T_s, however, indirectly feels this effect through the relaxation term in Eq. 4.6. Finally, Note that the single-bulk snow layer hydrology is described in Section 4.1.7.

Treatment of the soil water

Equations for w_g and w_2 are derived from the force-restore method applied by Deardorff (1977) to the ground soil moisture:

$$\frac{\partial w_g}{\partial t} \;= \frac{C_1}{\rho_w d_1}(P_g - E_g) - \frac{C_2}{\tau}(w_g - w_{geq}) \qquad (0 \leq w_g \leq w_{sat}) \tag{4.16}$$

$$\frac{\partial w_2}{\partial t} \;= \frac{1}{\rho_w d_2}(P_g - E_g - E_{tr}) - \frac{C_3}{d_2 \tau} \max\left[0,\, (w_2 - w_{fc})\right] \qquad (0 \leq w_2 \leq w_{sat}) \tag{4.17}$$

where P_g is the flux of liquid water reaching the soil surface (including the melting), E_g is the evaporation at the soil surface, E_{tr} is the transpiration rate, ρ_w is the density of liquid water, and d_1 is an arbitrary normalization depth of 1 centimeter. In the present formulation, all the liquid water from the flux P_g goes into the reservoirs w_g and w_2, even when snow covers fractions of the ground and vegetation. The first term on the right hand side of Eq. (12) represents the influence of surface atmospheric fluxes when the contribution of the water extraction by the roots is neglected. The coefficients C_1 and C_2, and the equilibrium surface volumetric moisture w_{geq}, have been calibrated for different soil textures and moistures (Noilhan and Planton (1989)).

The expression for C_1 differs depending on the moisture content of the soil. For wet soils (i.e., $w_g \geq w_{wilt}$), this coefficient is expressed as

$$C_1 = C_{1sat} \left(\frac{w_{sat}}{w_g} \right)^{b/2+1} \tag{4.18}$$

For very dry soils (i.e., $w_g < w_{wilt}$), the vapor phase transfer needs to be considered in order to reproduce the physics of water exchange. These transfers are parameterized as a function of the wilting point w_{wilt}, the soil water content w_g, and the surface temperature T_s, using the Gaussian expression (Braud *et al.* (1993), Giordani (1993)

$$C_1 = C_{1max} \exp \left[-\frac{(w_g - w_{max})^2}{2\sigma^2} \right] \tag{4.19}$$

where w_{max}, C_{1max}, and σ are, respectively, the abscissa of the maximum, the mode, and the standard deviation of the Gaussian functions (see Appendix 4.1.12). The other coefficient, C_2, and the equilibrium water content, w_{geq}, are given by

$$C_2 = C_{2ref} \left(\frac{w_2}{w_{sat} - w_2 + 0.01} \right) \tag{4.20}$$

$$w_{geq} = w_2 - a\, w_{sat} \left(\frac{w_2}{w_{sat}} \right)^p \left[1 - \left(\frac{w_2}{w_{sat}} \right)^{8p} \right] \tag{4.21}$$

For the w_2 evolution, Eq. (13) represents the water budget over the soil layer of depth d_2. The drainage, which is proportional to the water amount exceeding the field capacity (i.e., $w_2 - w_{fc}$), is considered in the second term of the equation (see Mahfouf and Noilhan (1996)). The coefficient C_3 does not depend on w_2 but simply on the soil texture (see Appendix 4.1.11). Similarly, run-off occurs when w_g or w_2 exceeds the saturation value w_{sat} or when a sub-grid runoff scheme is used. Coefficients C_{1sat}, C_{1max}, C_{2ref} and p are made dependent on the soil texture (Noilhan and Mahfouf (1996))

Root zone soil layer option In the standard two-soil layer version of ISBA, it is not possible to distinguish the root zone and the total soil water reservoirs. With the three-layer version, the deepest soil layer may provide water to the root zone through capillary rises only, and the available water content for transpiration is defined as $(w_{sat} - w_{sat}) \times d_2$.

The bulk soil layer (referred to as w_2 in the previous sections) is divided into a root-zone layer (with a depth d_2) and base-flow layer (with a thickness defined as $d_3 - d_2$). The governing equations for the time evolution

of soil moisture for the two sub-surface soil layers are written following Boone *et al.* (1999) as

$$\frac{\partial w_2}{\partial t} = \frac{1}{\rho_w d_2}\left(P_g - E_g - E_{tr}\right) - \frac{C_3}{d_2\tau}\max\left[0,\ (w_2 - w_{fc})\right] - \frac{C_4}{\tau}\left(w_2 - w_3\right) \tag{4.22}$$

$$\begin{aligned}\frac{\partial w_3}{\partial t} &= \frac{d_2}{(d_3 - d_2)}\left\{\frac{C_3}{d_2\tau}\max\left[0,\ (w_2 - w_{fc})\right] + \frac{C_4}{\tau}\left(w_2 - w_3\right)\right\} \\ &\quad - \frac{C_3}{(d_3 - d_2)\,\tau}\max\left[0,\ (w_3 - w_{fc})\right]\end{aligned} \tag{4.23}$$

where both w_2 and w_3 are $\leq w_{sat}$. C_4 represents the vertical diffusion coefficient and it is defined as

$$C_4 = C_{4\,ref}\,\overline{w}_{2,3}{}^{C_{4b}} \tag{4.24}$$

where $\overline{w}_{2,3}$ represents the interpolated volumetric water content representative of the values at the layer interface (d_2). The $C_{4\,ref}$ and C_{4b} coefficients are defined using the soil sand and clay contents, consistent with the other model parameters (see the section on model coefficients). In addition, the $C_{4\,ref}$ coefficient is scaled as a function of grid geometry. The equations are integrated in time using a fully implicit method.

Exponential profile of the saturated hydraulic conductivity In this version, the soil column assumes an exponential profile of the saturated hydraulic conductivity, k_{sat}, with soil depth (Decharme *et al.* 2006). This parameterization depends only on two parameters, which represent the rate of decline of the k_{sat} profile and the depth where k_{sat} reaches its so-called "compacted" value.

$$k_{sat}(z) = k_{sat,c}\exp\left[-f(z - d_c)\right] \tag{4.25}$$

where z (m) is the depth of the soil profile, f (m^{-1}) is the exponential profile decay factor and d_c (m) the compacted depth where k_{sat} reaches its compacted value, $k_{sat,c}$ given by Clapp and Hornberger (1978). In the standard approach, f varies with soil properties (texture and/or rooting depth) but can not exceed 2 m^{-1} and d_c assumes to be equal to rooting depth d_2. Sensitivity tests to these parameters and a detailed discussion about this parameterization can be found in Decharme *et al.* (2006). The main hypothesis is that roots and organic matter favor the development of macropores and enhance the water movement near the soil surface, and that soil compaction is an obstacle for vertical water transfer in the deeper soil. This exponential soil profile increases the saturated hydraulic conductivity at the surface by approximately a factor 10, and its mean value increases in the root zone and decreases in the deep layer in comparison with the values given by Clapp and Horneberger (1978). In ISBA, all hydraulic force-restore coefficients ($C1$, $C2$, $C3$ and $C4$) are re-formulated to take into account this k_{sat} profile.

Treatment of runoff in the ISBA initial version Run-off occurs when w_2 exceeds the saturation value w_{sat}. In its standard version, ISBA simulates surface runoff through the saturation excess mechanism (also known as Dune mechanism), therefore, runoff is only produced when the soil is saturated (i.e. w_2 exceeds the saturation value w_{sat}). Note that if w_3 exceeds the saturation, the excess water is added to the drainage term.

When the scale of variability of runoff production is smaller than the typical scale of the grid scale (which is common in most applications), the soil almost never saturates and the runoff production is very low, even though, in reality, a fraction of the cell is saturated and does produce surface runoff.

In order to account for subgrid scale runoff, three parametrisations are available and are described hereafter.

The variable Infiltration Capacity (VIC) scheme. This subgrid parametrisation was introduced by Habets *et al.* (1999) following the approach of the Variable Infiltration Capacity (VIC) scheme, described in Wood *et al.* (1998) and Dumenil and Todini (1992) and inspired from the Nanjing model Zhao (1992). In this scheme it is considered that the infiltration capacity (the maximum depth of water that can be stored in the soil column) varies non-linearly within the grid cell. The fraction of the grid cell that is saturated is a function of some soil parameters (the soil water content at saturation, the wilting point and the root depth), the soil water content of the root zone (w_2) and a new parameter, called b, which represents the shape of the heterogeneity distribution of effective soil moisture capacity. (Note, b is not to be confused with b, which is used to compute the exponent of the soil pedotransfer functions).
This approach is summarized in Fig. 4.2. A grid cell is assumed to be composed of an infinity of elementary reservoirs, whose infiltration capacity continuously varies from 0 and a maximum value i_m. The mean water content (wg_2) is the sum of the water content of all the reservoirs.
i is the water content of the non saturated elementary reservoirs (all reservoirs with a water content below i are saturated). $A(i)$ is the saturated fraction of the cell. In case of precipitation (P), all reservoirs with an infiltration capacity lower than $i + P$ will be filled, and then produce runoff. The runoff is the sum of the contribution of the elementary reservoirs.
In this scheme, the infiltration capacity is given by :

$$i = i_m \left[1 - (1 - A(i))^{\frac{1}{b}}\right] \Longleftrightarrow A(i) = 1 - \left(1 - \frac{i_0}{i_m}\right)^{b} \tag{4.26}$$

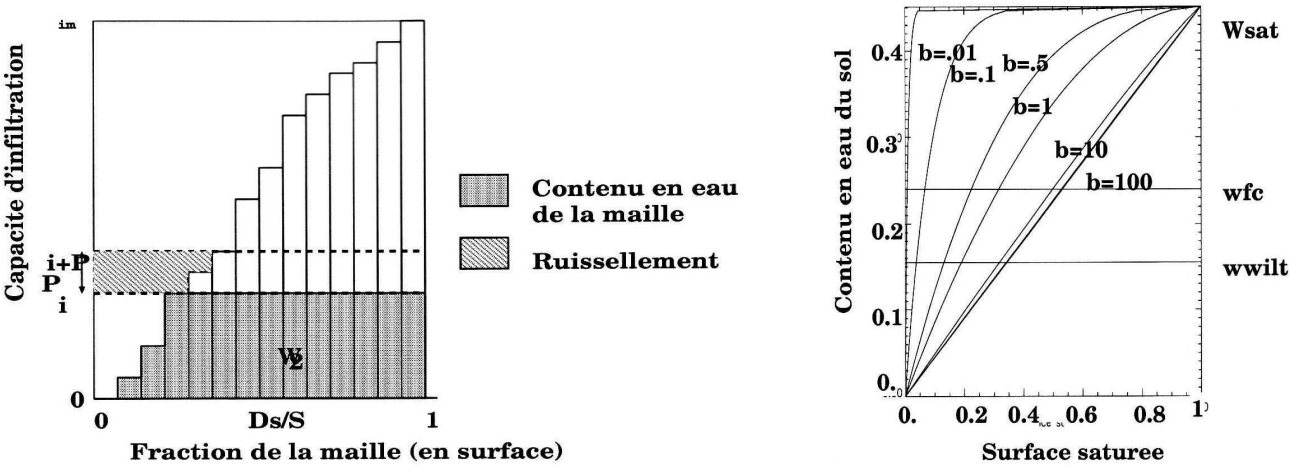

Figure 4.2: Simplified scheme of the VIC subgrid runoff. Left : principles. Right : variation of the saturated proportion of the grid cell for several values of the soil water content and of the parameter b in the VIC model. In Isba, the saturated fraction of the grid is computed between w_{wilt} and w_{sat}.

where $A(i)$ is the fraction of the grid cell whose the infiltration capacity is lower than i ($0 \leq A(i) \leq 1$), i_m is the maximum infiltration capacity of the grid cell, and b is the curvature parameter, which controls the distribution function A : the runoff is high when b is high, and low when b is small.
In the grid cell, the runoff is given by :

$$Q_r = \int_i^{i+P} A(i)di = P + \frac{i_m}{b+1}\left[\left(1 - \frac{i+P}{i_m}\right)^{\mathrm{b}+1} - \left(1 - \frac{i}{i_m}\right)^{\mathrm{b}+1}\right] \tag{4.27}$$

For a water content w_2, the saturated fraction of the grid cell ($A(w_2)$) is given by:

$$A(w_2) = 1 - \left(1 - \frac{w_2}{w_{sat}}\right)^{\frac{\mathrm{b}}{\mathrm{b}+1}} \tag{4.28}$$

After preliminary testing of this parameterization on the Adour watershed, Habets *et al.* (1999) found that the parameterization generated too much runoff in summer for dry soil conditions. To avoid this problem, a threshold was introduced in the soil wetness, $w_{c,min}$, below which runoff was not produced. This threshold was set to be the wilting point ($w_{c,min} = w_{wilt}$). Note that this threshold is somewhat arbitrary in terms of it's relationship to surface runoff. For example, a recent study using ISBA has shown that for a tropical catchment the relationship with wilting point is weak and a larger threshold value of $w_{c,min}$ produces optimal results (Getirana et al., 2014). So, $w_{c,min} = w_{wilt}$ should be used by default, but a different value could be best for a given catchment or climate (Note, currently $= w_{wilt}$ is hard-coded).
The discretized form of Q_r used within the model can be written as

$$Q_{r\,\mathrm{crit}} = \left[1 - \frac{(w_2 - w_{c,min})}{(w_{sat} - w_{c,min})}\right]^{1/(1+\mathrm{b})} - \frac{R_t \Delta t}{\rho_w z_r}\left[\frac{1}{(1+\mathrm{b})\,(w_{sat} - w_{c,min})}\right] \tag{4.29a}$$

$$Q_r = R_t - \frac{\rho_w z_r}{\Delta t}\left\{(w_{sat} - w_2) - (w_{sat} - w_{c,min})\left[\max\left(0,\, Q_{r\,\mathrm{crit}}\right)\right]^{1+\mathrm{b}}\right\} \tag{4.29b}$$

with the constraints:

$$Q_r = 0 \qquad \text{if} \quad (Q_r < 0) \quad \text{or} \quad (w_2 \leq w_{c,min}) \tag{4.30}$$

where R_t (m s^1) is the through-fall rate (sum of canopy drip, precipitation and snow-melt).

TOPMODEL approach TOPMODEL (TOPography based MODEL) attempted to combine the important distributed effects of channel network topology and dynamic contributing areas for runoff generation (Beven and Kirkby (1979), Silvapalan *et al.* (1987)). This formalism takes into account topographic heterogeneities explicitly by using the spatial distribution of the topographic indices, $\lambda_i(m)$, in each grid-cell defined as follows:

$$\lambda_i = \ln\left(a_i / \tan\beta_i\right) \tag{4.31}$$

where $a_i(m)$ is the drainage area per unit of contour of a local pixel, i, and $\tan\beta_i$ approximates the local hydraulic gradient where β_i is the local surface slope. If the pixel has a large drainage area and a low local slope, its topographic index will be large and thus, its ability to be saturated will be high. Then, this topographic index can be related to a local water deficit, and using the spatial distribution of the topographic indices over the grid cell, a saturated fraction, f_{sat}, inversely proportional to the grid cell mean deficit, $D_t(m)$, can be defined. The "coupling" between TOPMODEL and ISBA was proposed by Habets and Saulnier (2001) and generalized by Decharme *et al.* (2006). The active layer used for the ISBA-TOPMODEL coupling is the rooting layer, and not the total soil column. TOPMODEL describes generally

the evolution of a water storage deficit near the soil surface that reacts quasi-instantaneously following rainy events (Beven and Kirkby, 1979). In that case, the root zone appears to be a reasonable compromise in ISBA. So, the relation between the grid cell mean deficit and the soil moisture computed by ISBA is simply expressed as:

$$0 \leq D_t = (w_{sat} - w_2) \times d_2 \leq d_0 \tag{4.32}$$

where $d_2(m)$ is the rooting depth and $d_0(m)$ the maximum deficit computed as the difference between the saturation, w_sat, and the wilting point, w_wilt :

$$d_0 = (w_{sat} - w_{wilt}) \times d_2 \tag{4.33}$$

So for a given rooting soil moisture, w_2, a mean deficit, D_t, is calculated and it is therefore possible to determine the saturated fraction of the grid-cell. The runoff, Q_{top}, is thus simply given by: $Q_{top} = P_g \times f_{sat}$ where P_g is the throughfall rain rate. For w_2 lower than the wilting point, the mean deficit is a maximum, $D_t = d_0$, $f_{sat} = 0$ and no surface runoff occurs. Note that, the spatial distribution of the topographic index in each grid-cell can be computed with the three- parameter gamma distribution introduced by Silvapalan *et al.* (1987). The three parameters are derived from the mean, standard deviation, and skewness of the actual distribution that can be done by the HYDRO1K dataset at a 1 km resolution or another database. This TOPMODEL approach has been intensively validated both at the regional and global scale (Decharme *et al.* (2006), Decharme and Douville (2006 and 2007)).

Horton runoff approach. The Horton runoff occurs for a rainfall intensity that exceeds the effective maximum infiltration capacity. This infiltration excess mechanism tends to dominate the overland flow production in most desert or semiarid regions where short rainfall events can be very intense, but also where the absence of vegetation and other organic matter prevents the development of a porous soil structure through which water can move easily. The development of a thin crust at the soil surface can also inhibit the infiltration (arid or frozen soil). So the Horton runoff, Q_{hort}, is calculated using two infiltration functions following Decharme and Douville (2006):

$$Q_{hort} = (1 - \delta_f) \times \max(0, S_m + P_g - I_{unf}) + \delta_f \max(0, S_m + P_g - I_f) \tag{4.34}$$

where S_m is snowmelt, P_g the throughfall rain rate, I_{unf} and I_f the infiltration functions over unfrozen and frozen soil, and δ_f the fraction of the frozen soil. These functions depend on root zone soil moisture conditions as well as on soil hydraulic properties. When the Horton runoff (being estimated only on the non-saturated fraction of the grid) is activated with the VIC or the TOPMODEL runoff, the surface runoff is given by :

$$Q_s = Q_{top\_or\_vic} + (1 - f_{sat})\, Q_{hort} \tag{4.35}$$

Treatment of drainage The gravitational drainage when $w > w_{fc}$ is given by the following equations (Mahfouf and Noilhan, 1996; Boone *et al.* 1999) :

$$K_2 = \frac{C_3}{\tau}\frac{d_3}{d_2}\max[0, (w_2 - w_{fc})] \tag{4.36}$$

$$K_3 = \frac{C_3}{\tau}\frac{d_3}{d_3 - d_2}\max[0, (w_3 - w_{fc})] \tag{4.37}$$

where τ is a characteristic time (one day). C_3 is the *force-restore* parameter which account for the speed at which the humidity profile is restored to the field capacity. This parameter depends on the hydraulic properties of the soil (Noilhan and Mahfouf, 1996). In ISBA, it can be described by an empirical equation and depends on the proportion of clay in the grid cell.

$$C_3 = 5.327 \cdot X_{clay}^{-1.043} \tag{4.38}$$

Treatment of soil ice

The inclusion of soil freezing necessitates the addition of so-called phase change to the thermal and hydrological transfer equations. In addition, a freezing/drying wetting/thawing analogy is used to model changes in the force-restore coefficients so that they must also be modified accordingly. Terms which have been added to the baseline ISBA scheme are underlined in this section, while terms which are modified are denoted using an $*$ superscript. Additional details related to soil freezing scheme can be found in Boone *et al.* (2000) and Boone (2000).

The basic prognostic equations including soil ice are expressed as

$$\frac{\partial T_s}{\partial t} = {C_T}^* \left[R_n - H - LE^* - L_f(M_s - \underline{F_{g\,w}}) \right] - \frac{2\pi}{\tau}(T_s - T_2) \ , \tag{4.39}$$

$$\frac{\partial T_2}{\partial t} = \frac{1}{\tau}(T_s - T_2) + {C_G}^* L_f \underline{F_{2\,w}} \ , \tag{4.40}$$

$$\frac{\partial w_g}{\partial t} = \frac{1}{d_1 \rho_w} \left[{C_1}^* \left(P_g - E_{g\,l} + M_s \right) - \underline{F_{g\,w}} \right] - \frac{{C_2}^*}{\tau}(w_g - {w_{g\,\mathrm{eq}}}^*) \tag{4.41}$$

$$(w_{\min} \leq w_g \leq w_{\mathrm{sat}} - w_{g\,f}) \ , \tag{4.42}$$

$$\frac{\partial w_2}{\partial t} = \frac{1}{d_p \rho_w} \left(P_g - E_{g\,l} - {E_{tr}}^* + M_s - \underline{F_{2\,w}} \right) - C_3 \tau \max(0\,,\ w_2 - {w_{\mathrm{fc}}}^*) \tag{4.43}$$

$$(w_{\min} \leq w_2 \leq w_{\mathrm{sat}} - w_{2\,f}) \ , \tag{4.44}$$

$$\frac{\partial w_{g\,f}}{\partial t} = \frac{1}{d_1 \rho_w} \left(F_{g\,w} - E_{g\,f} \right) \qquad (0 \leq w_{g\,f} \leq w_{\mathrm{sat}} - w_{\min}) \ , \tag{4.45}$$

$$\frac{\partial w_{2\,f}}{\partial t} = \frac{1}{(d_2 - d_1)\,\rho_w} F_{2\,w} \qquad (0 \leq w_{2\,f} \leq w_{\mathrm{sat}} - w_{\min}) \ . \tag{4.46}$$

where $w_{g\,f}$ and $w_{2\,f}$ represent the volumetric soil ice content (m^3 m^{-3}) in the surface and deep-soil reservoirs, respectively. The phase change mass and heat sink (source) terms (F; kg m^{-2} s^{-1}) are expressed as

$$F_{g\,w} = (1 - p_{sng})\ (F_{g\,f} - F_{g\,m}) \ , \tag{4.47}$$

$$F_{2\,w} = (1 - p_{sng})\ (F_{2\,f} - F_{2\,m}) \ , \tag{4.48}$$

where the m and f subscripts represent melting and freezing, respectively. The freezing and melting phase change terms are formulated using simple relationships based on the potential energy available for phase change. They are expressed for the surface soil layer as

$$F_{g\,f} = (1/\tau_i)\ \min\left[K_s\, \epsilon_{s\,f} \max(0,\, T_0 - T_s)/C_I\, L_f,\ \rho_w\, d_1\ (w_g - w_{\min}) \right] \ , \tag{4.49}$$

$$F_{g\,m} = (1/\tau_i)\ \min\left[K_s\, \epsilon_{s\,m} \max(0,\, T_s - T_0)/C_I\, L_f,\ \rho_w\, d_1\, w_{g\,f} \right] \ , \tag{4.50}$$

and for the deep soil layer as

$$F_{2\,f} = (\delta_{2\,f}/\tau_i)\ \min\left[\epsilon_{2\,f} \max(0,\, T_0 - T_2)/C_I\, L_f,\ \rho_w\ (d_2 - d_1)\,(w_2 - w_{\min}) \right] \ , \tag{4.51}$$

$$F_{2\,m} = (1/\tau_i)\ \min\left[\epsilon_{2\,m} \max(0,\, T_2 - T_0)/C_I\, L_f,\ \rho_w\ (d_2 - d_1)\ w_{2\,f} \right] \ . \tag{4.52}$$

The characteristic time scale for freezing is represented by τ_i (s). The phase change efficiency coefficients, ϵ, introduce a dependence on the water mass available for phase changes which are expressed as the ratio of the liquid volumetric water content to the total soil porosity for freezing, and the ratio of ice content to the porosity for melting. The ice thermal inertia coefficient is defined as $C_I = 2(\pi/\lambda_i\, C_i \rho_i \tau)^{1/2}$ (J m^{-2} K^{-1}). The insulating effect of vegetation is modeled using a coefficient defined as

$$K_s = \left(1 - \frac{veg}{K_2} \right) \left(1 - \frac{LAI}{K_3} \right) \ , \tag{4.53}$$

where the dimensionless coefficients have the values $K_2 = 5.0$ and $K_3 = 30.0$ (Giard and Bazile (2000)). The most direct effect of vegetation cover is to slow the rate of phase changes for more dense vegetation cover as energy not used for phase change is assumed to cool/warm the vegetative portion of the lumped soil-vegetation layer.
The deep-soil phase change (freezing) term is multiplied by a factor ($\delta_{2\,f}$) which essentially limits ice production during prolonged cold periods. It is defined as 0 if $z_f \geq z_{f\,\max}$ where

$$z_{f\,\max} = 4/\left(C_G{}^* c_g\right) \tag{4.54}$$

and the actual depth of ice in the soil is defined as

$$z_f = d_2 \left(\frac{w_{2\,f}}{w_{2\,f} + w_2}\right) \qquad (0 \leq z_f < d_2) \tag{4.55}$$

Ice is assumed to become part of the solid soil matrix. This is accomplished by defining the modified porosity (eg. Johnsson and Lundin (1991)) as

$$w_{sat}{}^* = w_{sat} - w_{j\,f} \tag{4.56}$$

where j corresponds to the surface (g) or sub-surface (2) soil water reservoirs. This, in turn, is used to modify the force-restore coefficients (see Boone *et al.* , 2000, for more details).
As a final note, more recently an option to this simple method to compute the phase changes has been added based on the Gibbs-free energy approach. It is especially adapted for the DuFfusion (DF) version of ISBA (see Section 4.1.3), but it can also be used with the FR approach. See Section 4.1.3 for more details. But the soil ice modification to the porosity etc. remains as described in this Section for both phase change options.

4.1.3 Diffusive approach

Governing Equations

The governing equations for the heat and mass transfer from the surface down through the soil column for the snow-free case are expressed as (Boone *et al.* 2000; Decharme *et al.* 2011):

$$c_h \frac{\partial T_g}{\partial t} = \frac{\partial G}{\partial z} + \Phi \tag{4.57}$$

$$\frac{\partial w_l}{\partial t} = -\frac{\partial F}{\partial z} - \frac{\Phi}{L_f \rho_w} - \frac{S_l}{\rho_w} \qquad (w_{min} \leq w_l \leq w_{sat} - w_i) \tag{4.58}$$

$$\frac{\partial w_i}{\partial t} = \frac{\Phi}{L_f \rho_w} - \frac{S_i}{\rho_w} \qquad (0 \leq w_i \leq w_{sat} - w_{min}) \tag{4.59}$$

Eq. (4.57) is the vertical component of the heat transfer equation: heat flow is induced along the thermal gradient and due to convection, c_h is the total heat capacity (J m^{-3} K^{-1}): it is represented by a lumped heat capacity in the surface layer, and by the soil heat capacity (c_g) in the sub-surface layers. λ is the thermal conductivity (W m^{-1} K^{-1}), F is the vertical flow rate of water (m s^{-1}), T_g is the composite soil-vegetation temperature (K) at the surface and the soil temperature only for sub-surface layers, Φ (J m^{-3} s^{-1}) is a latent heat source/sink resulting from phase transformation of soil water, and the soil depth, z (m), is increasing downward.
w_l and w_i in Eq.s (4.58) and (4.344) represent the volumetric liquid water and liquid water equivalent ice contents of the soil ($\mathrm{m}^3\,\mathrm{m}^{-3}$), respectively. They are related to the total volumetric water content ($\mathrm{m}^3\,\mathrm{m}^{-3}$) through

$$w = w_l + w_i \ . \tag{4.60}$$

In Eq. (4.58), S_l (evapotranspiration, lateral inflow) and S_i (sublimation) represent external sources/sinks (kg m^{-3} $\mathrm{s}{-}1$), of the liquid and ice liquid equivalent soil water, respectively, L_f is the latent heat of fusion (3.337×10^5 J kg^{-1}), and ρ_w is the density of liquid water (1000 kg m^{-3}). The total soil porosity is w_{sat} (m^3 m^{-3}), and w_{min} is a minimum liquid water threshold (0.001 m^3 m^{-3}).
The phase change terms on the right-hand sides of Eq.s (4.58) and (4.344) represent a mass transfer between the solid and liquid phases of the soil water. The continuity equation for the total soil volumetric water content is obtained by adding Eq.s (4.58) and (4.344) and then substituting Eq. (4.60) into the resulting expression to have

$$\frac{\partial w}{\partial t} \;=\; -\frac{\partial F}{\partial z} \;-\; \frac{1}{\rho_w}\,(S_i \;+\; S_l) \qquad\qquad (w_{min} \;\leq\; w \;\leq\; w_{sat}) \tag{4.61}$$

Surface and soil heat transfer

Heat flow is along the thermal gradient, so that the soil heat flux (W m^{-2}) can be expressed as

$$G = \lambda \frac{\partial T}{\partial z} \tag{4.62}$$

The soil thermal conductivity and heat capacity are expression as functions of soil properties and moisture. The parameterizations are described below.

Calculation of the thermal properties The thermal heat capacity and thermal conductivity are parameterized as functions of the soil moisture and texture by most SVAT schemes. SVAT schemes which participated in PILPS-phase2c predicted, in general, ground heat fluxes poorly, which is most likely related to thermal conductivity parameterization Liang *et al.* (1996). ISBA uses the formulations from McCumber and Pielke (1981 : MP81) together with parameter values from Clapp and Hornberger (1978) to evaluate the heat capacity and thermal conductivity (Noilhan and Planton, 1989), but it is known that thermal conductivity estimates using the MP81 model tend to be too large for wet conditions (nearing saturation) while underestimating thermal conductivity for dry soils. Also, there is no consideration of frozen soils in this formulation. There are several alternatives to using the MP81 model for thermal conductivity, and one such method is that discussed in Peters-Lidard *et al.* (1998). The layer-averaged soil heat capacity can be written as

$$c_{g\,j} \;=\; (1 - w_{sat}) C_{soil} \rho_{soil} \;+\; w_{l\,j} c_w \;+\; w_{i\,j} c_i \tag{4.63}$$

where c_i and c_w are the heat capacities of ice and liquid water, (J K^{-1} m^{-3}). C_{soil} is the specific heat of the soil (J kg^{-1} K^{-1}) and ρ_{soil} represents the soil dry density. The specific heat (C_{soil}) value of 733 J kg^{-1} K^{-1} for soil minerals/quartz from Peters-Lidard *et al.* (1998) is used. where ρ_{soil} represents the unit weight of the solids (2700 kg m^3). The heat capacity of air in the soil is neglected in Eq. (4.63).
For fine soils or coarse frozen soils, the method of Johansen (1975) was shown by Farouki (1986) to be the most accurate relative to other commonly used methods for calculating thermal conductivity. Following Peters-Lidard *et al.* (1998), the thermal conductivity is calculated as the weighted sum of the dry and saturated thermal conductivities from (Johansen, 1975)

$$\lambda \;=\; K_e\,\lambda_{sat} \;+\; (1 - K_e)\,\lambda_{dry} \tag{4.64}$$

where K_e is the non-dimensional Kersten number.
The dry thermal conductivity is defined as

$$\lambda_{dry} \;=\; \frac{0.135\rho_{soil} \;+\; 64.7}{\rho_{solids} \;-\; 0.947\rho_{soil}} \tag{4.65}$$

where λ_{dry} is in W $\mathrm{m}^{-1}\,K^{-1}$. For crushed rock,

$$\lambda_{dry} \;=\; 0.039\,{w_{sat}}^{-2.2} \tag{4.66}$$

The saturated thermal conductivity is written as

$$\lambda_{sat} \;=\; {\lambda_{soil}}^{(1-w_{sat})}\,{\lambda_i}^{(w_{sat}-\chi_u)}\,{\lambda_w}^{\chi_u} \tag{4.67}$$

where χ_u represents the unfrozen volume fraction of the soil. It is defined as

$$\chi_u \;=\; w_{sat}\,(w_l/w) \qquad\qquad (0 \;\leq\; \chi_u \;\leq\; w_{sat}) \tag{4.68}$$

In Eq. (4.67), λ_i represents the thermal conductivity of ice (2.2 W $m^{-1}\,K$), λ_w represents the thermal conductivity of water (0.57 W $m^{-1}\,K$), and the thermal conductivity of solids is written as

$$\lambda_{soil} \;=\; {\lambda_q}^{q}\,{\lambda_o}^{1-q} \tag{4.69}$$

The quartz content ($0 \leq q \leq 1$) is non-dimensional. It is fit as a function of sand (following the method of Noilhan and Lacarrère (1995) using the data from PL98:

$$q \;=\; 0.038 \;+\; 0.0095\,X_{\mathrm{sand}} \tag{4.70}$$

where the fraction of the soil comprised by sand is represented by X_{sand} (%). The relation is shown graphically in Fig. (4.3). The thermal conductivity of quartz is represented as λ_q (7.7 W $m^{-1}\,K$), and the thermal conductivity of other minerals is represented as λ_o (W $m^{-1}\,K$) where

$$\lambda_o \;=\; \begin{cases} 2 & q > 0.2 \\ 3 & q \leq 0.2 \end{cases} \tag{4.71}$$

The Kersten number is written as

$$K_e \;=\; \begin{cases} 0.7\log_{10}\theta \;+\; 1.0 & \theta > 0.05 \text{ (coarse)} \\ \log_{10}\theta \;+\; 1.0 & \theta > 0.10 \text{ (fine)} \end{cases} \tag{4.72}$$

and for frozen soils it is

$$K_e = \theta \tag{4.73}$$

where θ is the degree of saturation (w/w_{sat}) of the soil layer. Because use of Eq. (4.73) can result in a large jump in K_e as a soil begins to freeze, the following expression is used for partially frozen fine soils:

$$K_e \;=\; (w_l/w)\,(\log_{10}\theta \;+\; 1.0) \;+\; (w_i/w)\theta \tag{4.74}$$

The same weighting scheme in Eq. (4.74) can be used for coarse soils as well.

Numerical discretization of the soil heat equation The governing equations for heat transfer within the soil discretized in N_g layers are described using the classical one-dimensional Fourier law and are written as:

$$\Delta z_j c_{g\,j}\frac{\partial T_{g,j}}{\partial t} \;= G_{j-1} \;-\; G_j \;+\; \Delta z_j\,\Phi_j \qquad \forall = 2, N_g \tag{4.75a}$$

$$\Delta z_j c_{g\,j}\frac{\partial T_{g,j}}{\partial t} \;= \frac{\overline{\lambda}_{j-1}}{\Delta\tilde{z}_{j-1}}\,(T_{g,\,j-1} \;-\; T_{g,\,j}) \;-\; \frac{\overline{\lambda}_j}{\Delta\tilde{z}_j}\,(T_{g,\,j} \;-\; T_{g,\,j+1}) \;+\; \Delta z_j\,\Phi_j \tag{4.75b}$$

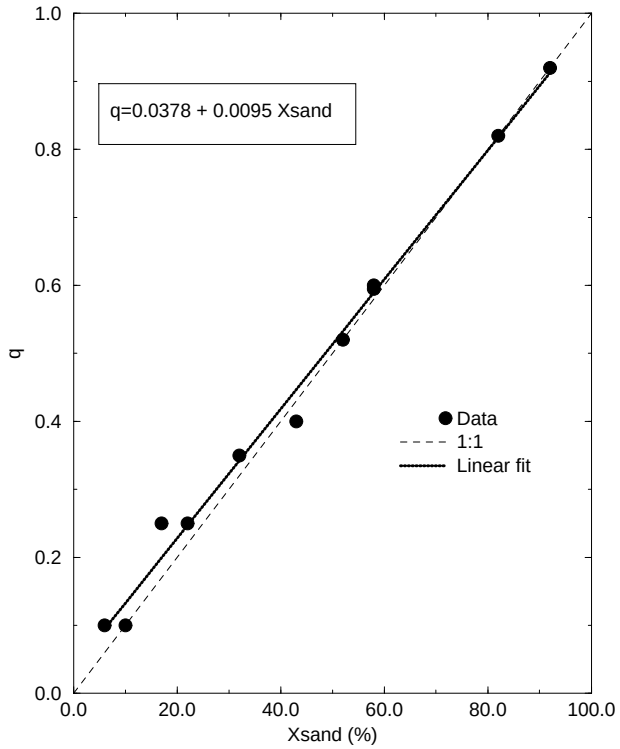

Figure 4.3: The relation between quartz content (q) and sand fraction ($X_{\rm sand}$) of the soil (%). The relationship between quartz and sand content is described by Eq. (4.70). The data are plotted using the values of q from Peters-Lidard *et al.* (1998) and the sand fraction from Cosby *et al.* (1984).

where the heat conduction flux (W m^{-2}) is therefore defined as

$$G_j \;=\; \frac{\overline{\lambda}_j}{\Delta\tilde{z}_j}\left(T_{g,\,j} \;-\; T_{g,\,j+1}\right) \tag{4.76}$$

Δz_j (m) is the thickness of the layer j, $\Delta\tilde{z}_j = \left(\Delta z_j + \Delta z_{j+1}\right)/2$ is the thickness (m) between two consecutive layer mid-points or nodes, C_G is the soil thermal inertia at the surface (J m^{-1} kg^{-2}), $c_{g\,j}$ is the total soil heat capacity(J m^{-3} K^{-1}), and $\overline{\lambda}_j$ (W m^{-1} K^{-1}) is the inverse-weighted arithmetic mean of the soil thermal conductivity at the interface between two consecutive nodes expressed as:

$$\overline{\lambda}_j \;=\; \frac{\Delta z_j + \Delta z_{j+1}}{\left(\Delta z_{j+1}/\lambda_{j+1}\right) \;+\; \left(\Delta z_j/\lambda_j\right)} \;\;. \tag{4.77}$$

In general, the contribution of convective heating to the local soil temperature change is relatively small and can be neglected. Vapor transfer effects have been incorporated and are currently being tested: they are not outlined here. The model grid configuration is shown in Fig. 4.4. The shaded region at the surface represents a vegetation/biomass/litter layer. The prognostic variables ($T_{g,\,j}$, w_l, and w_i) are shown (water store variables will be discussed in subsequent sections).

Boundary conditions Upper boundary condition: To be consistent with the ISBA-FR surface energy budget, the surface temperature evolves according to the heat storage in the soil/vegetation composite and to the thermal gradient between the surface (the same fine superficial layer than for ISBA-FR) and the second

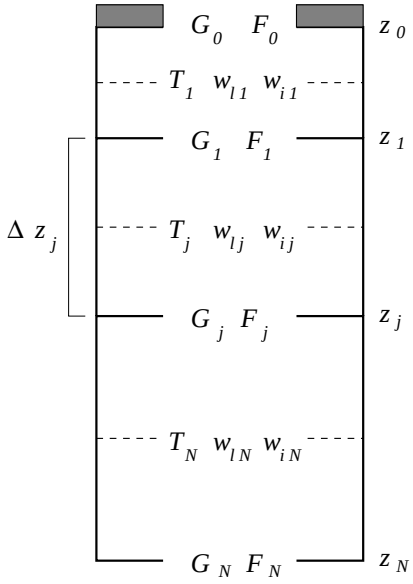

Figure 4.4: The model grid configuration: soil prognostic variables temperature ($T_{g,j}$), liquid volumetric water content ($w_{l\,j}$) and volumetric ice content ($w_{i\,j}$) are layer mean quantities. The soil heat (G_j) and liquid water fluxes (F_j) are evaluated at each level, z_j. The surface energy budget is evaluated defining $T_s = T_{g,1}$. The shaded region at the surface represents a vegetation/biomass/litter. The soil depth, z, is increasing downward (away from the atmosphere).

layer (Boone *et al.* ,2000). Accordingly, the surface temperature is defined as

$$\frac{1}{C_T}\frac{\partial T_{g,1}}{\partial t} = G_0 + \Delta z_1\,\Phi_1 - \frac{C_G}{C_T}\frac{\overline{\lambda}_1}{\Delta\tilde{z}_1}\,(T_{g,1} - T_{g,2}) \tag{4.78a}$$

$$\frac{\partial T_{g,1}}{\partial t} = C_T\,(R_n - H - LE + \Delta z_1\,\Phi_1) - C_G\,\frac{\overline{\lambda}_1}{\Delta\tilde{z}_1}\,(T_{g,1} - T_{g,2}) \tag{4.78b}$$

where the flux between the atmosphere and the surface is represented by G_0 (W m^{-2}). This definition of the prognostic equation for $T_{g,1}$ is similar to that presented by Bhumralkar (1975) and Blackadar (1979). It is the same as the standard Force-Restore method of Noilhan and Planton (1989) if G_1 is expressed as a restore term. The thermal inertia coefficient for the composite surface layer is expressed as

$$C_T = \frac{1}{(veg/C_V) + [(1 - veg)/C_G]} \tag{4.79}$$

where veg represents the vegetation cover fraction. The thermal inertia for the vegetation (C_V) can be case or species dependent. By default, it is computed as

$$C_V = \frac{1}{C_{V,ref} + c_w W_r} \tag{4.80}$$

where W_r (kg m^{-2}) is the vegetation interception reservoir water storage and $C_{v,ref}$ (J K^{-1} m^{-2}) the reference or baseline vegetation heat capacity (defined by the user or ECOCLIMAP) set by default to 1×10^4 J K^{-1} m^{-2} for low vegetation and 2×10^4 J K^{-1} m^{-2} for forests. The soil thermal inertia (J K^{-1} m^{-2}) is defined as

$$C_G = \frac{1}{c_{g,1}\,\Delta z_1} \tag{4.81}$$

where $c_{g,1}$ is the heat capacity of the first soil layer (J K^{-1} m^{-3}: Eq. 4.63). The uppermost soil thickness, Δz_1, must be chosen to be sufficiently thin in order to be consistent with the daily surface temperature cycle (i.e., 0.01 m by default). In the limit when there is no vegetation (i.e., veg = 0), the thermal inertia coefficient collapses into $1/C_T = \Delta z_1 c_g$ so that Eq. 4.78a takes on exactly the same form as the sub-surface soil temperature equations.

Lower boundary condition: The average temperature for the lowest layer is written using Eq.(4.75a) as

$$\frac{\partial T_N}{\partial t} \;=\; \frac{(G_{N-1} \,-\, G_N)}{c_{g\,N}\,\Delta z_N} \tag{4.82}$$

where the heat flux from below z_N is assumed to be negligible, resulting in a zero-flux lower boundary condition (i.e. $G_N = 0$). Note that in order for this assumption to be valid, z_N must be sufficiently large (deep). The annual temperature wave penetration depth is, in general, on the order of several meters (eg., Figs 4.5 and 4.6), so that z_N must be at least this deep in oder to accurately model the soil temperature profile at time scales of an annual cycle or more. An alternate method to increasing the soil depth is to specify the lower boundary flux using an annual mean soil temperature and an appropriate scaling depth (Lynch-Stieglitz, 1994). This depth can be estimated as the annual wave penetration depth [see Eq. (4.86)]. The only drawback is that the mean annual soil temperature and the annual wave penetration depth must be known *a priori*. The advantages are that less model layers can be used (a lower total model depth) thereby reducing computational expense and memory/storage requirements, and the soil temperature profile is "constrained" to some extent by observational data. Currently in the model, there is an option to apply a prescribed T^* (either as a constant or varying in time) at z_N

$$G_N \;=\; \lambda_N \frac{[T_N \,-\, T^*\,(z = z_N)]}{(z_N + z_{N-1})\,/2} \tag{4.83}$$

But note that $G_N = 0$ is the default. Recently the soil depth has been extended for thermal computations in order to ensure that this approximation is reasonable: see Decharme *et al.* (2016) for details.

Vertical grid The soil model grid levels do not necessarily have constant spacing. The assumption that the vertical temperature gradients are largest near the surface and smaller deeper in the soil indicates that the grid spacing can increase with increasing soil depth. It is of interest to specify the first grid level to be thin enough to resolve the diurnal temperature wave. An estimate of this depth is calculated using conductivity calculated by Eq. (4.64) for thawed soils with the relation for wave penetration depth from Dickinson (1988):

$$z_d \;=\; \left(\frac{\lambda_1\,\tau}{c_{g\,1}\,\pi}\right)^{1/2} \tag{4.84}$$

Since the diurnal wave penetration depth (z_d) is a function of soil moisture and texture, an average or maximum value could also be used to a good approximation: this value might represent the z_d depth for the average soil moisture etc. The diurnal wave penetration depths computed using Eq. (4.84) are shown in Fig. (4.6). The depth z_d is plotted as a function of the normalized volumetric water content defined as

$$w_{norm} = \frac{w - w_{wilt}}{w_{sat} - w_{wilt}} \qquad (0 \leq w_{norm} \leq 1) \tag{4.85}$$

The z_d depth usually ranges from 12-18 cm for most soils across their nominal range of soil moisture: values in the range from 12-15 cm could be used for most general cases. It is of interest to compare the method of Johansen to the method of McCumber and Pielke (1981) which is used by many surface vegetation atmosphere transfer (SVAT) schemes including ISBA (Noilhan and Planton, 1989). The z_d values computed using the method of McCumber and Pielke (1981) together with the soil classification and hydrological parameter values For the force-restore method used by ISBA, this variability in z_d is accounted for as there are no fixed soil depths which effect the diurnal cycle. But when using a fixed grid geometry, as is the case for the diffusion method outlined here, z_d calculated from the method of Johansen is more consistent with a fixed grid geometry. These depths represent the depth to which the diurnal wave is felt: but to represent the diurnal cycle of the soil surface or soil-vegetation composite surface accurately in terms of phase and amplitude, the uppermost layer should be considerably thinner: in ISBA the uppermost thickness is chosen as a compromise between thickness, numerical stability (time step) and processes (both hydrological and thermal): see below for more details.

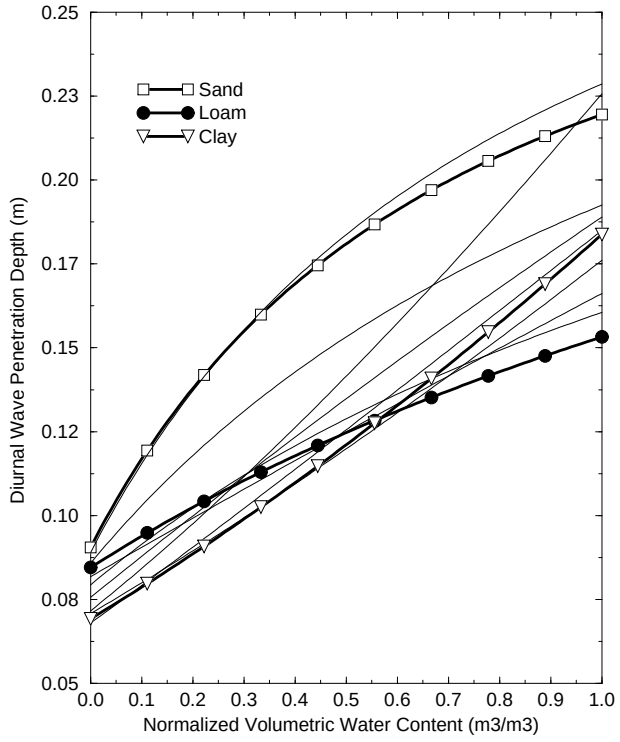

Figure 4.5: The diurnal temperature wave penetration depths (z_d) for the 11 soil classes from Clapp and Hornberger (1978). Depths are plotted as a function of normalized soil water content [Eq. (4.85)]. Thermal conductivity is calculated using the method of McCumber and Pielke (1981) together with soil hydraulic parameter values from Clapp and Hornberger (1978). Soil depths are in m.

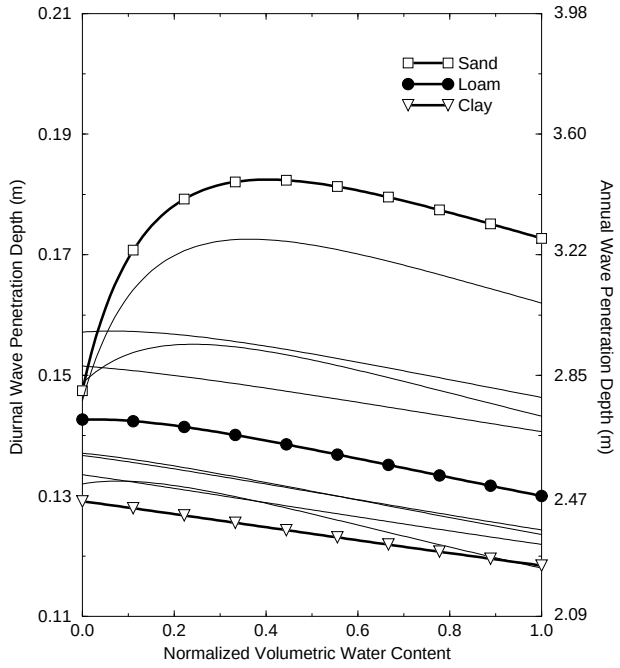

Figure 4.6: The diurnal and annual soil temperature wave penetration depths (z_d) for the 11 soil classes from Clapp and Hornberger (1978). Depths are plotted as a function of normalized soil water content [Eq. (4.85)]. Thermal conductivity is calculated using the method of Johansen (1975) as presented by Peters-Lidard *et al.* (1998). Soil depths are in m: z_d should be used as a guild-line for determining the maximum uppermost soil layer depth, z_1, and the minimum total soil depth, z_N.

The depth of the lower limit of the soil-temperature model domain depends upon the time scale: if annual cycles are to be properly handled, the lower boundary depth z_N can be determined using Eq. (4.84) as

$$z_a = \left(\frac{\lambda \, 365 \, \tau}{c_g \, \pi} \right)^{1/2} \tag{4.86}$$

where z_a denotes the annual wave penetration depth. Note that c_g and λ should be evaluated using an estimate of the total soil column mean water content. The annual wave penetration depths computed using Eq. (4.86) are shown in Fig. (4.6). The depth z_a (labeled on the right side of the figure) is plotted as a function of the normalized volumetric water content. Thus for multi-year simulations, the depths for thermal computations should extend to a depth proportional to the time period considered (thus deeper than those shown in Fig. 4.6).

The heat transfer within the soil is computed using 14 layers up to a depth of 12 m, which corresponds to the lower boundary condition of the soil temperature. Conversely, the hydrological depth varies from 0.2 to 8 m according to the land cover. As shown in Fig. 4.7, if the hydrological lower boundary condition is equal to 1 m for bare soil, the soil moisture is solved within the first eight layers, whereas soil temperatures are computed over all layers. The simulation of freezing and thawing processes is thus facilitated by the consistency between hydrologic and thermal nodes. Because the soil thermal properties require the water and ice content to be known for each layer, the total soil water profile is extrapolated under the hydrological lower boundary condition of the soil to each underlying temperature node, assuming a hydrostatic equilibrium soil moisture profile and the presence of a possible deep water table. The partitioning between liquid water and ice content is then computed using the relationship between the matric potential and the temperature based

on Fuchs *et al.* (1978): see Eq. 4.126. Note that for permafrost regions (shown in the rightmost column of Fig. 4.7), the liquid and solid water prognostic equations extend to the base of the soil in order to more accurately compute the evolution of the permafrost, especially for deeper soil layers.
Finally, the thicknesses of the current 14 layers have been arranged to minimize numerical errors in solving energy and water diffusion equations, especially in the first meter of soil (Decharme *et al.* 2011). Note that the thermal and/or hydrological lower boundary conditions of the soil, as well as the thickness and the number of layers, can be modulated by the user.

Numerical solution of the soil temperature equation Neglecting the phase transformation term, Eq. (4.75a) can be written using an implicit time scheme as

$$T_j^{\,n} \;=\; T_j^{\,n-1} \;+\; \frac{\Delta t}{c_{g\,j}\,\Delta z_j}\left[(1-\varphi)\left({G_{j-1}}^{n-1} \;-\; {G_j}^{n-1}\right) + \varphi\left({G_{j-1}}^{n} \;-\; {G_j}^{n}\right)\right] \tag{4.87}$$

where $\varphi = 1$ (backward difference) is currently used for the soil temperature profile ($\varphi = 1/2$ corresponds to the Crank-Nicolson scheme). Using either scheme, the linear set of diffusion equations can be cast in tridiagonal form and solved with relative ease. Although the Crank-Nicolson scheme is more accurate (second order), the surface energy budget equation is solved in ISBA using the backward difference scheme, so for consistency this scheme is used to evaluate the diffusion term in Eq. (4.75a).

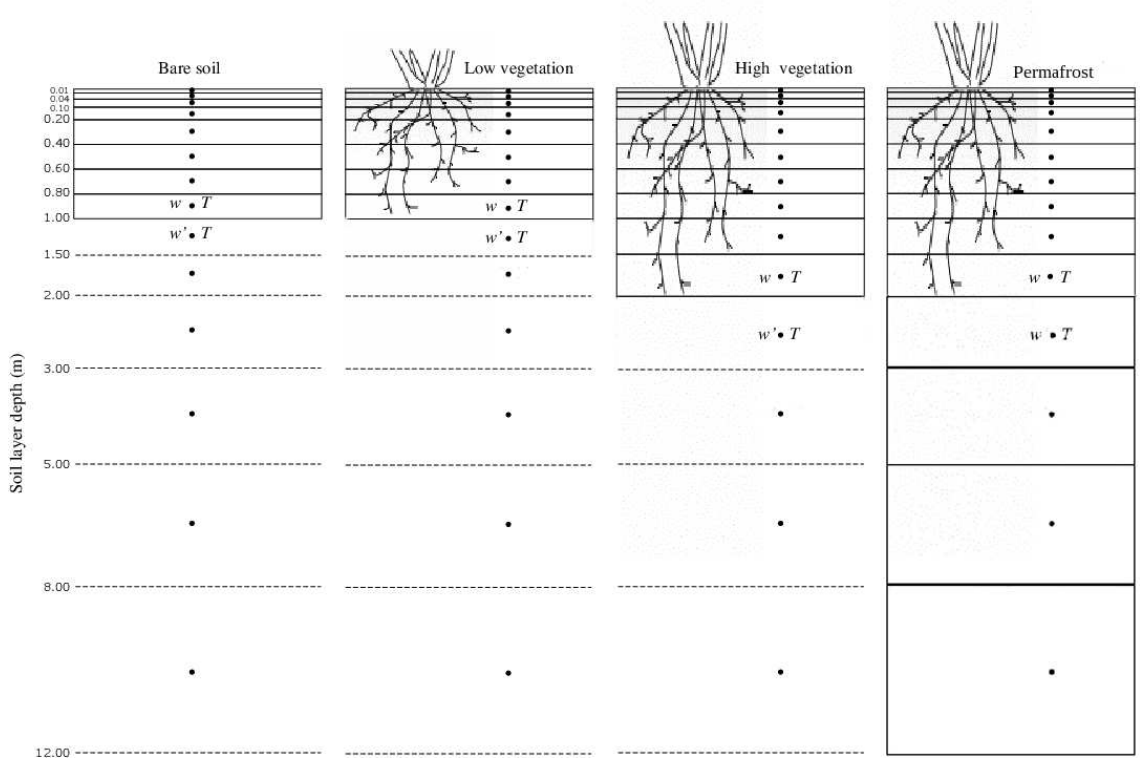

Figure 4.7: The ISBA-DF soil grid configurations. Prognostic variable nodes (for liquid water, w_g, soil ice, w_{gf} and temperature, T_g) are located at the center of each of the layers. There are 14 layers used for thermal computations, and the same default grid thicknesses are used everywhere (note this can be modified by the user). Hydrological grids are enclosed by the solid black lines: thus the soil water prognostic equations do not extend as deeply as the thermal computations except for areas/grid cells with permafrost. See Decharme *et al.* (2013) for more details.

The superscripts $n-1$ and n represent the values at the beginning and end of the time step, Δt, respectively. The solution method is shown in Appendix B. Once the new temperature profile has been determined, phase changes are evaluated and the profile is updated. The phase change method is described in section 4.

Liquid Soil Water

The vertical soil water flux from Eq. (4.58) is derived assuming soil water transfer arises due to pressure gradients and a background drainage, and it is expressed as

$$F \;=\; -k\,\frac{\partial}{\partial z}\,(\psi \,+\, z) \,-\, \frac{D_{\nu\psi}}{\rho_w}\frac{\partial \psi}{\partial z} \tag{4.88}$$

where F is the vertical soil water flux ($\mathrm{m\,s^{-1}}$), k is the hydraulic conductivity ($\mathrm{m\,s^{-1}}$), ψ is the soil matric potential (m), and z is the soil depth (m). The first term on the right hand side of Eq. 4.88 represents Darcy's law for liquid water transfer. The second term represents the water flux due to vapor transfer. The isothermal vapor conductivity $D_{\nu\psi}$ (kg $\mathrm{m^{-2}\ s^{-1}}$) is a function of soil texture, water content and temperature following Braud *et al.* (1993), except for some slight modifications due to the inclusion of soil ice outlined here.

This representation of the fluxes results in the so-called "mixed-form" of the Richard's equation. It permits the use of a heterogenous soil texture profile (by considering the gradient of matric potential which is continuous as opposed to soil water content which is not necessarily continuous when the soil properties vary).

Finally, when soil ice is present, Eq. 4.88 is modified as

$$F \;=\; -k\left(\wp\,\frac{\partial \psi}{\partial z} \,-\, z\right) \,-\, \frac{\wp\, D_{\nu\psi}}{\rho_w}\frac{\partial \psi}{\partial z} \tag{4.89}$$

where the non-dimensional coefficient $\wp$ has been introduced which acts to limit vertical diffusion in the presence of a freezing front (see Eq. 4.96).

Flux parameterization The vertical soil water flux term [Eq. (4.88)] can be expressed in more compact form as:

$$F \;=\; -\eta\,\frac{\partial \psi}{\partial z} \,-\, k \tag{4.90}$$

where η ($\mathrm{m^2\,s^{-1}}$) represents the effective diffusion coefficient. It is expressed as

$$\eta = \wp\left(k \,+\, \frac{D_{\nu\psi}}{\rho_w}\right) \tag{4.91}$$

The first term on the RHS of Eq. 4.90 is the diffusion term and usually is positive (directed upward), the exceptions possibly being during precipitation, snowmelt or perhaps soil thaw events. The second term on the RHS of Eq. (4.90) represents total drainage and is always directed (positive) downward. During strong infiltration events (rainfall, snowmelt etc...) generally k dominates the (downward) water flux. Note that if vapor diffusion is neglected and the soil is not frozen, the vertical flux given by Eq. (4.88) collapses into the standard Darcy flux expression for liquid water movement:

$$F \;=\; -k\,\frac{\partial}{\partial z}\,(\psi \,+\, z) \tag{4.92}$$

Soil Freezing As a soil freezes, ice is assumed to become part of the soil matrix thereby reducing the liquid water holding capacity of the soil. The degree of saturation of the soil by liquid water is expressed as

$$\Theta \;=\; \frac{w - w_i}{w_{sat} - w_i} \;=\; \frac{w_l}{w_{sat\,l}} \qquad (0 \leq \Theta \leq 1) \tag{4.93}$$

where $w_{sat\,l}$ represents the soil liquid water holding capacity. The porosity is decreased in the presence of soil ice as it is assumed ice becomes part of the soil matrix (see Boone *et al.* (2000) for more information). The hydraulic conductivity and soil water potential are related to the liquid volumetric soil water content through the relations (Clapp and Hornberger, 1978):

$$k \;=\; k_{sat}\,\Theta^{2b+3} \tag{4.94}$$

$$\psi = \; \psi_{sat}\,\Theta^{-b} \tag{4.95}$$

where b is an empirical parameter, k_{sat} is the hydraulic conductivity at saturation, ψ_{sat} is the water potential at saturation and w_{sat} is the soil porosity. In recent years, several SVATs (eg. VISA: Yang and Niu, 2003) have adopted the idea that the saturated hydraulic conductivity decreases exponentially with increasing soil depth (Beven and Kirby, 1979). This can be handled by ISBA-DF since Richard's equation is expressed in mixed-form (i.e. a heterogeneous profile of k_{sat} can be specified).
Soil ice has the effect of decreasing the hydraulic conductivity relative to a thawed soil with the same total soil moisture. The ice impedance coefficient is represented by $\wp$. It is calculated following Johnsson and Lundin (1991):

$$\wp \;=\; 10^{-a_\wp\, w_i/w} \tag{4.96}$$

where the coefficient $a_\wp$ is currently assigned a value of 6 proposed by Lundin (1990). This coefficient prevents an overestimation of the upward liquid water flux to the freezing front. Note that the model is rather sensitive to this parameter, and a calibration might be required to obtain optimal agreement with observations. The dependence of $\wp$ on ice content ratio (w_i/w) is shown in Fig. 4.8. Note that the effect of this coefficient is currently under investigation, and that alternate formulations (such as dependence on soil temperature rather than soil ice) will also be explored.

Vapor diffusion The isothermal vapor conductivity can be expressed as

$$D_{\nu\psi} \;=\; D_\nu\,\frac{\partial \rho_\nu}{\partial \psi} \tag{4.97}$$

where ρ_ν represents the water vapor density in the air-filled pore space of the soil, and D_ν represents an effective molecular diffusivity (Milly (1982)). It can be written following Braud *et al.* (1993) as

$$D_\nu \;=\; D_{\nu a}\,\alpha_\nu\,f_{\nu a}\frac{p}{(p - p_\nu)} \tag{4.98}$$

where the tortuosity is $\alpha_\nu = 0.66$, and the atmospheric and soil vapor pressures are represented by p and p_ν, respectively. The function $f_{\nu a}$ is defined as

$$f_{\nu a} = \begin{cases} [w_{sat} - (w_l + w_i)]\,[1 \;+\; (w_l + w_i)\,/\,(w_{sat} - w_k)] & \text{if } (w > w_k) \\ w_{sat} & \text{if } (w \leq w_k) \end{cases}$$

where w_k is a parameter which defines the point corresponding to the loss of continuity of the liquid phase in the soil pores (0.05 $m^3\ m^{-3}$ for the current study). The function $f_{\nu a}$ is related to the available pore space

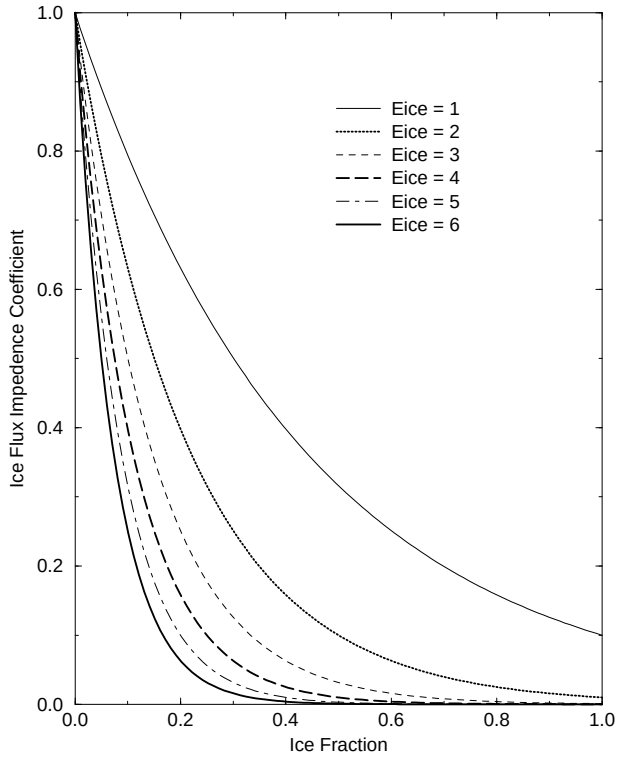

Figure 4.8: The dependence on the water flux impedance factor ($\wp$) on soil ice fraction (w_i/w) for various values of $a_\wp$ (denoted as "Eice" in the figure). This coefficient is multiplied by the vertical soil water flux, and as such can strongly modulate vertical flow of liquid water and subsequent freezing.

for vapor, or volumetric air content ($w_{sat} - w_l - w_i$). The molecular diffusivity coefficient for water vapor is given as

$$D_{\nu a} \;=\; c_\nu \left(\frac{p_0}{p}\right)\left(\frac{T}{T_f}\right)^{n_\nu} \tag{4.99}$$

where $c_\nu = 2.17 \times 10^{-5}$ m^2 s^{-1}, $n_\nu = 1.88$, and $p_0 = 10^6$ Pa. It is assumed that the soil water vapor is in equilibrium with the liquid, and that the air is saturated with respect to the ice present in the soil so that the vapor density can be expressed as

$$\rho_\nu \;=\; \rho_{\nu\,sat}(T)\chi_{sat}\,h_\nu \;+\; (1-\chi_{sat})\,\rho_{\nu\,sat\,i}\min(T,T_f) \tag{4.100}$$

where the humidity is given by

$$h_\nu \;=\; \exp\left(\frac{\psi\, g}{R_\nu\, T}\right) \tag{4.101}$$

The soil ice factor is defined as

$$\chi_{sat} = (w_{sat} - w_i)\,/w_{sat} \tag{4.102}$$

Taking the derivative of ρ_ν with respect to ψ and substituting the resulting expression and Eq. (4.98) into Eq. (4.97) using the ideal gas law for water vapor results in

$$D_{\nu\psi} \;=\; \frac{\alpha_\nu\, p}{(p-p_\nu)}\frac{D_{\nu a}\, f_{\nu a}\, \chi_{sat}\, g\, p_{\nu\,sat}\, h_\nu}{(R_\nu\, T)^2} \tag{4.103}$$

The diffusion coefficient (d_ν) is shown in Fig. (4.9) for four soil textures over the entire range of soil wetness (w_l/w_{sat}) assuming a constant temperature and pressure of 300 K and 101325 Pa, respectively. It is largest,

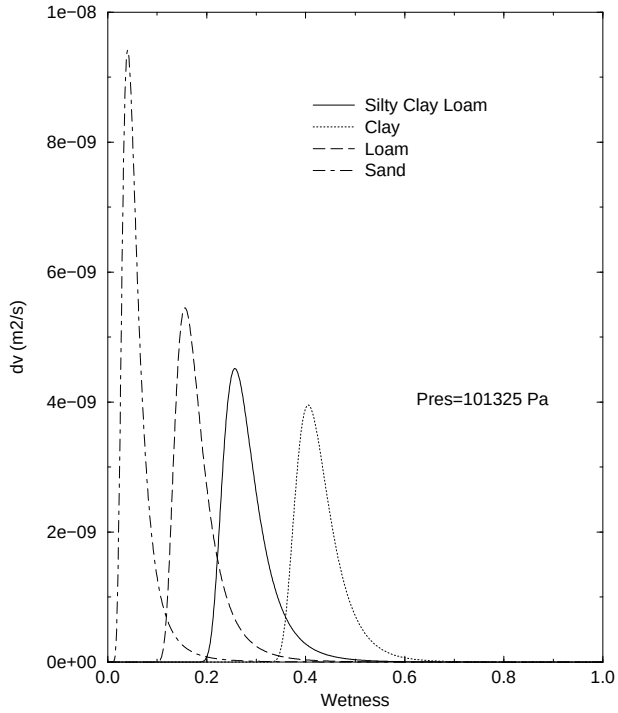

Figure 4.9: Soil vapor diffusion coefficient (d_ν) for four soil textures assuming constant soil temperature and pressure.

in general, for the most coarse textured soils approximately at or below the soil permanent wilting point value. A comparison between the vapor diffusion and the hydraulic conductivity are shown in Fig. (4.10). This shows that vapor diffusion comprises the most significant contribution to the net diffusion process over a soil water range around the wilting point. In the ISBA force-restore method, this vapor phase transfer is parameterized within the coefficient C_1 for dry soil (Braud *et al.* (1993) and Giordani (1996)). As a final note, strictly speaking, vapor diffusion involves latent heating effects which couples the mass and heat eqiuations very tightly over a certain range of temperature and soil moisture. But currently in ISBA, the effect of vapor diffusion is simply modeled by increasing the effective diffusivity of liquid transfer as a first order approach (thus, mass is conserved and energy is unchanged) since historically, the goal was to maintain baresoil evaporation under dry but sufficiently hot surface conditions. Future work could consist in adding the latent heating effect.

Layer averaging Integrating Eq. (4.58) downward into the soil to obtain the prognostic equation for the layer-average volumetric liquid water content for each j layer gives

$$\int_{-z_j}^{-z_{j-1}} \frac{\partial w_l}{\partial t} dz \;=\; -\int_{-z_j}^{-z_{j-1}} \frac{\partial F}{\partial z} dz \;-\; \int_{-z_j}^{-z_{j-1}} \left(S_l - \frac{\Phi}{L_f \rho_w} \right) dz \tag{4.104}$$

where

$$w_{l\,j} \;=\; \frac{1}{\Delta z_j} \int_{-z_j}^{-z_{j-1}} w_l dz \tag{4.105}$$

$w_{l\,j}$ is the layer averaged volumetric liquid water content ($j = 1, ..., N$).
Carrying out the integration in Eq. 4.104 using Eq. 4.105 yields

$$\Delta z_j \frac{w_{l\,j}}{\partial t} \;=\; F\Big|_{-z_j} \;-\; F\Big|_{-z_{j-1}} \;-\; Q_j \;-\; \frac{\Delta z_j\, \Phi_j}{L_f \rho_w} \tag{4.106}$$

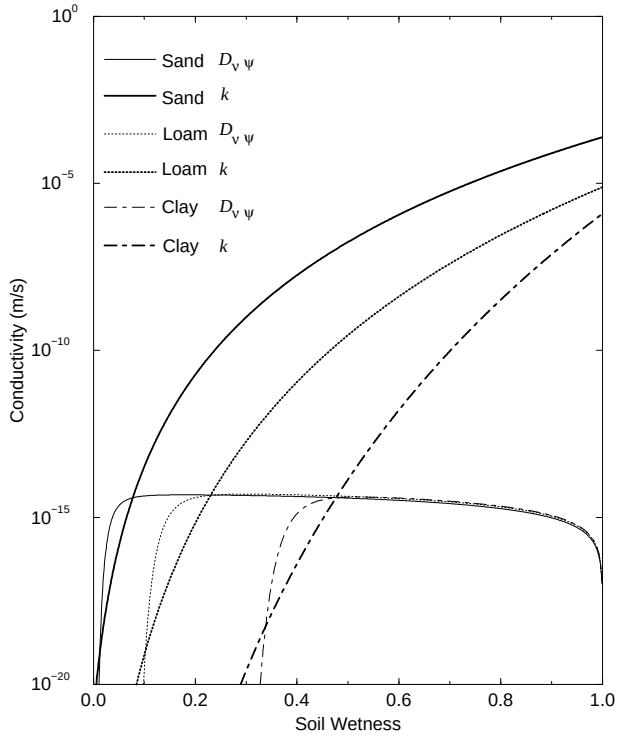

Figure 4.10: The total hydraulic conductivity contributions from liquid water (k) and vapor ($D_{\nu\psi}$) for three soil textures as a function of soil wetness. The soil temperature and surface atmospheric pressure have constant values of 285 K and 10^5 Pa, respectively.

where

$$Q_j \;=\; \Delta z_j \, S_j \tag{4.107}$$

is in kg m^{-2} s-1. The flux across a model level (z_j) is written as

$$F\Big|_{-z_j} \;=\; F_j \;=\; \overline{\eta}_j \left[\frac{\psi_{j+1} - \psi_j}{(\Delta z_j + \Delta z_{j+1})/2} \right] - \overline{k}_j \tag{4.108a}$$

$$\overline{\eta}_j \;=\; \wp_j \left(\overline{k}_j + \frac{\overline{D}_{\nu\psi,j}}{\rho_w} \right) \tag{4.108b}$$

where $\overline{k}_j$ and $\overline{D}_{\nu\psi,j}$ (both in m s^{-1}) represent the geometric means over two consecutive nodes of the soil hydraulic conductivity and isothermal vapor conductivity values, respectively. The inter-facial hydraulic conductivity is defined as

$$\overline{k}_j = \sqrt{k_j\left(\psi_j\right) \times k_{j+1}\left(\psi_{j+1}\right)} \tag{4.109}$$

The choice of an appropriate intra-block approximation for unsaturated hydraulic conductivity has been pointed out as critical in the numerical solution of unsaturated flow by many studies. As discussed in Decharme et al. (2011)/nociteDecharme2011, many studies have demonstrated that the geometric mean generates little weighting error, improves the simulated infiltration front, and is generally applicable in all situations.

A graphic representation of the interpolation method is shown for two contiguous soil layers with different textures (and therefore, different soil hydraulic properties) in Fig. 4.11.

Boundary Conditions

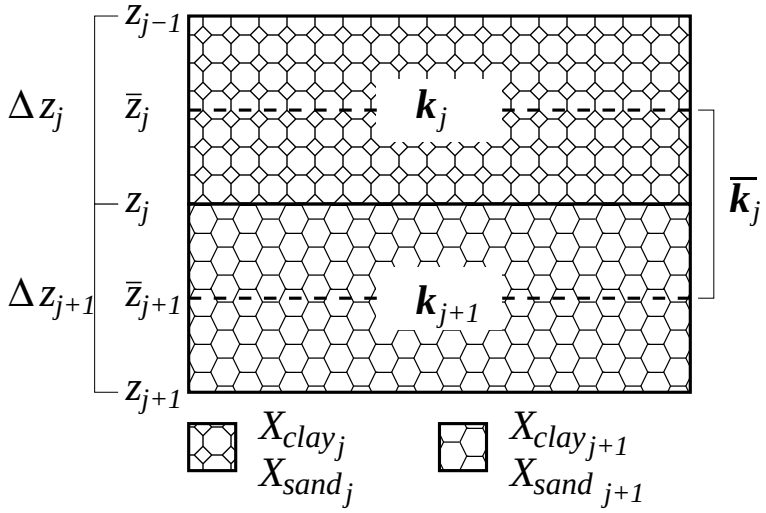

Figure 4.11: The interfacial hydraulic conductivity. $\overline{k}_j$ represents the hydraulic conductivity centered at z_j, and $\tilde{\Delta} z_j = (\Delta z_j + \Delta z_{j+1})/2$.

Lower Boundary The lower boundary condition is modeled as gravitational drainage (vertical diffusion is neglected). The mean water content of the lowest layer is used to evaluate the flux so that from Eq. (4.108a) one can write

$$F_N \;=\; -k_N \tag{4.110}$$

The diffusion term (i.e. capillary rise across the lower model boundary) can be significant, however, when the water table is near z_N. An option exists for utilizing this information using a simple expression consistent with the vertical flux formulation used for the other model layers. In this case, F_N is modified to be

$$F_N \;=\; -\,k_N \left[f_{wtd} \left(\frac{\psi_N - \psi_{sat}}{\Delta z_{wtd}} + 1 \right) \;+\; (1 - f_{wtd}) \right] \tag{4.111}$$

$$\Delta z_{wtd} \;= \min\left(z_N,\, z_{wtd}\right) \;-\; \left(z_N + z_{N-1}\right)/2 \tag{4.112}$$

where f_{wtd} is the gird-cell fraction where capillary rise occurs. It can be 1 at the local scale or depend on topography at larger scales. Indeed, only a fraction of the grid cell corresponding to the flat valleys and alluvial plains should be affected by water capillary rises. This fraction must reflect the subgrid topographical heterogeneity inside each grid cell, which can be significant, for example, when considering the coarse resolution of the climate models. A grid cell with steeper topography would be affected by upward capillary fluxes over a small fraction of the grid cell, unlike those characterized by relatively flatter terrain. See Vergnes et al. (2014) for more details.

Upper Boundary The upper boundary condition represents infiltration. By default, the soil infiltration I is equal to the potential (supply limited) infiltration rate, i.e. $I = R_t$. This case is specially relevant for local scale studies. The soil-water infiltration is put preferentially in the first layer. If this first layer can not contain this amount of water, the remaining is forced into the next layer and so forth (downward).
An Horton runoff option exists that computes the soil infiltration via a Green and Ampt (1911) approach (Decharme et al. 2013). This approach, based on Darcys law, includes the hydrodynamic parameters of the soil and determines the infiltration capacity of soil over the time. It represents the soil infiltration as a

wetting front in which the hydraulic gradient is uniform. In ISBA-DF, the analytical form of the Green-Ampt approach is used to determine the maximum amount of water that infiltrates the soil to a depth close to 0.1 m (the thickness generally used for relatively large time steps). The infiltration capacity, I_c (kg m^{-2} s^{-1}), is therefore parameterized as:

$$I_c = \frac{\rho_w}{z_{nic}} \sum_{i=1}^{nic} \left[\wp_i \, k_{sat,i} \left(\frac{\psi_{sat} - \psi_i}{\Delta z_i} \, + \, 1 \right) \Delta z_i \right] \tag{4.113}$$

where z_{nic} (m) represents the depth of the layer nic that is the nearest 0.1 m, and Δz_i (m) is the thickness of each of the i layers. Finally, the soil-water infiltration in ISBA-DF can be computed by comparing this infiltration capacity with the flux of water reaching the soil:

$$I = \min\left(R_t, \, I_c\right) \tag{4.114}$$

All of the excess water (i.e. defined as $R_t - I$ when it is > 0) is treated as a Horton surface runoff flux whereas the soil infiltration is treated as a moisture source term.

For non-local scale applications, an alternate form of generating surface runoff is needed. In this case, infiltration is computed as:

$$I \;=\; \min(R_t - Q_r, \, I_c) \tag{4.115}$$

It can also be computed via a variable infiltration capacity (VIC: Dumenil and Todoni, 1992) sub-grid surface runoff scheme used in ISBA (Habets *et al.* 1999). In this scheme, Q_r represents sub-grid surface runoff from saturated regions within the computational unit/cell (See Eq.s 4.26-4.28 for the theoretical background). It is computed using a similar form as that for the Force-Restore approach (Eq.s 4.29a-4.30):

$$Q_{r\,\mathrm{crit}} \;=\; \left[1 - \frac{(\overline{w}_r - \overline{w}_{c,min})}{(\overline{w}_{sat} - \overline{w}_{c,min})}\right]^{1/(1+\mathrm{b})} - \frac{R_t \Delta t}{\rho_w z_r} \left[\frac{1}{(1+\mathrm{b})\,(\overline{w}_{sat} - \overline{w}_{c,min})}\right] \tag{4.116a}$$

$$Q_r \;=\; R_t - \frac{\rho_w z_r}{\Delta t} \left\{ (\overline{w}_{sat} - \overline{w}_r) - (\overline{w}_{sat} - \overline{w}_{c,min}) \left[\max\left(0, \, Q_{r\,\mathrm{crit}}\right)\right]^{1+\mathrm{b}} \right\} \tag{4.116b}$$

with the constraints (as in Eq. 4.30, but using a layer averaged $w_{c,min}$):

$$Q_r \;=\; 0 \qquad \text{if} \quad (Q_r < 0) \quad \text{or} \quad (\overline{w}_r \leq \overline{w}_{c,min}) \tag{4.117}$$

Note that currently, $w_{c,min} = w_{wilt}$ by default until further studies can be done. Q_r is evaluated using the average total soil moisture, $\overline{w}_r$, integrated from the surface down to a characteristic depth, z_r. It is defined as

$$\overline{w}_r = \frac{\left(\sum_{j=1}^{N_r} \Delta z_j \, w_j\right) + w_{N_r+1} \max\left(0, \, z_r - z_{N_r}\right)}{\left(\sum_{j=1}^{N_r} \Delta z_j\right) + \max\left(0, \, z_r - z_{N_r}\right)} \qquad (z_r \leq z_N) \tag{4.118}$$

where N_r is the total number of soil layers for which $z_r \geq z_j$ (i.e. the depth is greater than or equal to the lower boundary of the soil layer j). Note that the porosity and wilting point volumetric water contents are also averaged over z_r using the same operator. This depth should be at least several tens of centimeters thick (Liang *et al.* 1996).

It should also be noted that several authors use a form of Darcy's law assuming the soil right at the surface is saturated as the maximum potential infiltration rate (Mahrt and Pan, 1984; Abramopoulos *et al.* 1988). This, however, has a very minimal impact on the infiltration (compared to the above equations) for the time and space scales considered in typical ISBA applications, and the linearization of such a term can pose some numerical problems (the linearized surface flux can actually exceed the amount of water available for infiltration under some rare circumstances).

Solution method The equation for liquid water transfer is solved using:

$$\varrho_j({w_l}_j{}^n - {w_l}_j{}^{n-1}) \;=\; (1-\varphi)\left({F_j}^{n-1} - {F_{j-1}}^{n-1}\right) + \varphi\,({F_j}^n - {F_{j-1}}^n) - {Q_j}^n \tag{4.119}$$

where $\varrho_j = \Delta z_j/\Delta t$, and n indicates the value at the end of the time step, Δt. The Crank-Nicolson time scheme is currently used to integrate the equations in time (i.e., $\varphi = 1/2$). The flux terms can be linearized or an iterative solution method can be used. The linearization method is obviously more attractive for numerical weather prediction applications as it consumes less CPUs, and for this method, an uppermost layer of several cm thickness can safely be used for typical GCM (upper limit for Δt) time steps (Bonan, 1996). Note that updates in mass owing to phase changes (Φ) are evaluated in a subsequent computation (see section 4).

Soil moisture sink term The sink term is composed of soil water losses/gains due to evapotranspiration/condensation and gains due to lateral inflow or so-called soil water excess. The production/reduction of soil ice decreases/increases the liquid soil water content while leaving the total soil water content unchanged.

Evapotranspiration Bare soil evaporation, E_g, is extracted from the uppermost soil layer only. Transpiration, E_{tr}, can be extracted from multiple layers. A normalized root-zone fraction is specified for each soil layer, and is zero for layers below the root zone. Normalized transpiration weights are then calculated based on the specified vertical root zone fraction and the thickness of each model soil layer:

$$\xi_j \;=\; \frac{\Upsilon_j\,\Delta z_j}{\sum_{j=1}^{N}\Upsilon_j\,\Delta z_j} \qquad (0 \le \xi_j \le 1) \tag{4.120}$$

where ξ_j represents the transpiration weight. Note that $\sum_{j=1}^{N}\xi_j = 1$ unless there are no roots, in which case $\xi_j = 0$. Υ_j represents the root fraction:

$$\sum_{j}^{N}\Upsilon_j \;=\; 1\ . \tag{4.121}$$

This parameter is not well known for many regions and transpiration from SVAT models can be highly sensitive to the vertical root zone distribution (Desborough (1997)): this study suggests the use of a uniform distribution. A uniform root zone distribution can be specified by setting Υ_j constant within the root zone soil layer(s), or a simple exponential function dependent on plant cover can be specified (Jackson *et al.* (1996)). In ISBA, the effect of water stress on transpiration is modeled using a normalized soil moisture factor (Noilhan and Planton, 1989; Calvet *et al.* 1998):

$$w_{n\,j} \;=\; \frac{w_{l\,j} - w_{wilt\,j}}{(w_{fc\,j} - w_{wilt\,j})} \qquad (\epsilon \le w_{n\,j} \le 1) \tag{4.122}$$

where w_{wilt} is the wilting point volumetric water content, and ϵ is a small numerical value ($\approx 10^{-3}$). From Eq. (4.122), soil ice in the root zone can hinder plant evaporation even if atmospheric conditions are conducive to transpiration and the total soil water content is above field capacity since freezing produces an effective soil drying (reducing the liquid part).

The factor in Eq. (4.122) is applied to the stomatal conductance so that transpiration can proceed at an unstressed rate relative the soil water for moisture values above field capacity, and is negligible for soils drier than wilting point. The layer-averaged water stress factor, which is applied to the net transpiration, is calculated as Pan and Mahrt (1987)

$$\overline{w}_n \;=\; \sum_{j=1}^{N}\xi_j\,w_{n\,j} \tag{4.123}$$

The above coefficients are simply used to partition the transpiration among the various root-zone soil layers.

Soil moisture excess When the increase over a given time period in observed total soil water content exceeds that of precipitation less evapotranspiration, a laterally induced source (negative sink) is assumed to occur (Calvet *et al.* (1998)). This can be due to lateral inflow of water (most likely) or capillary rise from below the observation depth. Since vertical diffusion across the base of the model is assumed to be negligible, this source is parameterized as lateral inflow. The vertical distribution is assumed to be linear down to the depth of the soil moisture observations:

$$\upsilon_j \;=\; \frac{\delta_{\upsilon\, j}\Delta z_j}{\sum_{j=1}^{N}\delta_{\upsilon\, j}\Delta z_j} \tag{4.124}$$

where υ_j represents the normalized soil water excess coefficient, and $\delta_{\upsilon\, j}$ is a delta function which is either 1 or 0 depending on whether or not excess inflow is occurring in layer j. For applications where soil moisture excess is not available, this source is set to zero.

Liquid water sink The external soil water source/sink term [Eq. (4.107)] is expressed as

$$Q_j \;=\; \xi_j \left(\frac{w_{n\, j}}{\overline{w}_n}\right) E_{tr} \;+\; \delta_{g\, j}\, E_{g\, L} \;-\; \upsilon_j\, Xs \;. \tag{4.125}$$

Xs represents the soil water excess (lateral inflow). $E_{g\, L}$ is the evaporation from the bare soil surface (uppermost layer), and $\delta_{g\, j}$ is a delta function which is unity only the uppermost soil layer ($\delta_{g\, 1} = 1$), and is zero for all the other soil layers. The uppermost layer is prescribed to be thin in order to capture the daily cycle in bare-soil evaporation. The root zone fraction in this layer, Υ_1, is usually set to zero. The transpiration, bare-soil evaporation and water excess terms are in units of $\mathrm{kg\ m^{-2}\,s^{-1}}$.

Soil water phase changes: freeze-thaw

Soil ice [Eq. (4.344)] increases when there is energy available for ice production, while decreases are due to melting and sublimation. In order to avoid a more computationally intensive iterative solution procedure [between Eq.s (4.57)-(4.344)], the soil temperature is first calculated using Eq. (4.87), then the phase change term (Φ_j) is evaluated. The temperature for a given layer at time n will then be adjusted at the end of the time step such that ${T_j}^n \;\rightarrow\; T_f$ if melting or freezing occurs (where T_f is the freezing point temperature).
The method presented in Boone *et al.* (2000) and in Boone (2000) for ISBA-DF has been modified owing to research involving PILPS-2e (Bowling *et al.* (2003)) with ISBA (Habets *et al.* 2002). In original test simulations involving ISBA-DF using the PILPS-2e experimental design and forcing, it was found that nearly all of the near surface water froze, and this caused some unrealistic conditions (although no observations are available to verify this). Boone *et al.* (2000) treated NWP-time-scale events, and soil freezing was not as extensive as in the PILPS-2e domain. Thus, it was decided to adopt an approach which determines a maximum liquid water content as a function of temperature using the Gibbs free energy method. See for example Cox *et al.* (1999), Cherkauer and Lettenmaier (1999) and Koren *et al.* (1999) for examples of this method used in SVATs. Many examples exist in soil-science literature: see Boone (2000) for references. The main difference between this method and the one presented in Boone *et al.* (2000) is that not all of the available liquid water is frozen. The method outlined herein represents a near seamless model change in that it does not augment CPU's significantly, and it requires no additional parameters. It has been documented by Decharme *et al.* (2016).
The relation between the soil water potential and temperature for sub-freezing conditions is from Fuchs *et al.* (1978):

$$\psi^* = \frac{L_f\,(T - T_f)}{g\,T} \tag{4.126}$$

The potential ψ^* can be substituted in the expression for the soil matric potential in order to obtain the maximum unfrozen (liquid) water content at a given soil temperature, T. Currently for ISBA, this is the Brooks and Corey (1966) model as modified by Clapp and Hornberger (1978), so that

$$w_{l\,\max} = w_{\rm sat}\left(\frac{\psi^*}{\psi_{\rm sat}}\right)^{-1/b} \tag{4.127}$$

During phase changes, the total soil water content ($w = w_l + w_i$) for each soil layer is conserved, so that, for example, as a soil freezes, the liquid water content will decrease owing to a corresponding increase in soil ice content (w_i). This concept can be used to establish the maximum temperature at which soil ice is present (again using the Gibbs free energy concept) as

$$T_{\rm max} = \frac{L_f\, T_f}{(L_f - g\,\psi)} \tag{4.128}$$

where the soil liquid water potential is defined as a function of the liquid water content using the relationship from Clapp and Hornberger (1978) [Eq. (4.95)]. The maximum unfrozen fraction ($w_{l\,\max}/w_{\rm sat}$) and $w_{l\,\max}$ as a function of temperature depression are shown in Fig. (4.12). for three soil textures. Note that a larger percentage of liquid water can freeze for more coarse textured soils and that relatively dry soils might have very cold temperatures before any freezing takes place.

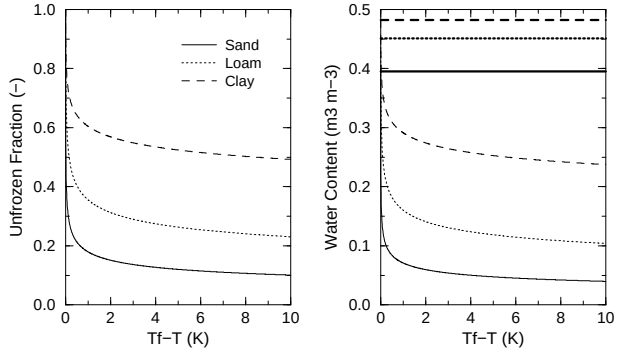

Figure 4.12: The maximum unfrozen fraction ($w_{l\,\max}/w_{\rm sat}$) and $w_{l\,\max}$ as a function of temperature depression for three soil textures. The corresponding porosity values (w_{sat}) are shown in the right panel (thick horizontal lines) as a reference.

The phase change term is parameterized in a manner similar to that presented in Boone (2000), Boone *et al.* (2000) and Giard and Bazile (2000), but with the available thermal energy evaluated using the difference $T_{\rm max} - T$ as opposed to $T_f - T$, and the available liquid water for freezing being defined using $w_l - w_{l\,\max}$ as opposed to $w_l - w_{l\,\min}$. The freezing and melting terms are, respectively:

$$\begin{aligned} \Phi_{f\,j} = &\quad \min\left[K_s\epsilon_f \max\left(0,\, T_{\max\,j} - T_j\right) c_i,\; L_f\rho_w \max\left(0,\, w_{l\,j} - w_{l\,\max\,j}\right)\right]/\tau_i \\ \Phi_{m\,j} = &\quad \min\left[K_s\epsilon_m \max\left(0,\, T_j - T_{\max\,j}\right) c_i,\; L_f\rho_w w_{i\,j}\right]/\tau_i \end{aligned} \tag{4.129}$$

where c_i is the heat capacity of ice (1.883×10^6 J K^{-1} m^{-3}). A parameter which represents the characteristic time scale for phase changes is represented by τ_i (Giard and Bazile, 2000). It can be determined through calibration, possibly (eventually) be related to soil texture. A constant value of 3300 s^{-1} is currently used. The expressions for the phase change efficiencies (ϵ_f and ϵ_m) are parameterized as functions of liquid soil water for freezing and soil ice for melting (similar to the method used by Cogley *et al.* (1990) and Pitman *et*

al. (1991):

$$\epsilon_j = \begin{cases} w_{l\,j}/\left(w_{sat} - w_{i\,j}\right) & \text{if } (T_j \leq T_f) \\ w_{i\,j}/\left(w_{sat} - w_{\min}\right) & \text{if } (T_j > T_f) \end{cases}$$

The principle of using such coefficients is that it is assumed that when the grid box average liquid soil moisture is relatively large, more energy is used for freezing the soil compared to a more dry average soil with the same available energy (for freezing). It is also a rudimentary method for modeling sub-grid freezing effects. The same basic idea holds for soil ice melting.

The surface insulation coefficient, K_s, is modeled following Giard and Bazile (2000) and is written (here in non-dimensional form) as

$$K_s = \left(1 - \frac{veg}{K_2}\right)\left(1 - \frac{LAI}{K_3}\right) \qquad (0 < K_s \leq 1) \tag{4.130}$$

where the values from Giard and Bazile (2000) are used: $K_2 = 5$ and $K_3 = 30$ m^2 m^{-2}. For relatively dense vegetation covers (i.e., large LAI and veg), more energy is used to heat or cool the vegetation while less is used to freeze/thaw the soil water/ice (compared to a surface with less vegetation).

The total phase change is then simply expressed as the difference between the freezing and melting components, although note that one or the other is always zero:

$$\Phi_j = \Phi_{f\,j} - \Phi_{m\,j} \tag{4.131}$$

Using the above model, the phase changes tend to follow the so-called soil specific freezing characteristic curve from Fuchs *et al.* (1978), although there can be considerable scatter about this line owing to $\epsilon < 1$ and $K_s < 1$, and ice can be present at significantly above-freezing layer-average temperatures. In the limit as ϵ and K_s become unity, the scatter is greatly reduced, and the presence of ice at above-freezing temperatures is also greatly reduced.

An example of the application of the above model to a cold climate is shown in Fig. (4.13). The forcing and parameters are from Goose Bay, Canada (Ross Brown, personal communication). The relationship between simulated soil temperature and liquid water content for all 5 soil layers using the model as presented herein is shown in the upper panel, and the relationship for which ϵ and K_s have been set to zero is shown in the lower panel. Each point represents at value at a 30-minute time step for which either $T_j \leq T_f$ or $w_{i\,j} \geq 0.001$ m^3 m^{-3}.

Soil ice and the overall soil water content are decreased due to sublimation. This term is expressed as

$$S_i \;=\; \Delta z_1\, E_{g\,I} \quad , \tag{4.132}$$

where $E_{g\,I}$ represents the liquid water equivalent loss of soil ice from the bare soil (uppermost) model layer (kg m^{-2} s^{-1}).

The temperature and soil water profiles are updated at the end of the time step, Δt, using the calculated phase change term together with:

$$T_j{}^{n\prime} \;=\; T_j{}^{n} + \frac{\Delta t\, \Phi_j}{c_{h\,j}} \tag{4.133}$$

$$w_{L\,j}{}^{n\prime} \;=\; w_{L\,j}{}^{n} - \frac{\Delta t\, \Phi_j}{L_f \rho_w} \tag{4.134}$$

$$w_{I\,j}{}^{n\prime} \;=\; w_{I\,j}{}^{n} + \frac{\Delta t\, \Phi_j}{L_f \rho_w} \tag{4.135}$$

Additional final minor adjustments are made as needed to prevent supersaturation of a layer, etc. The modification of the soil hydrological parameters owing to freezing is described in Section 4.1.2.

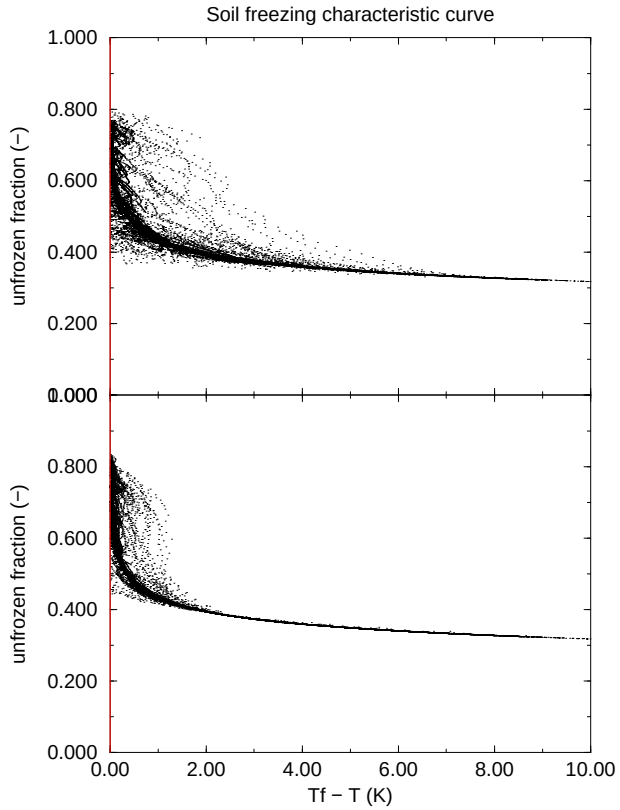

Figure 4.13: The simulated unfrozen liquid water fraction ($w_l / (w_i + w_l)$) as a function of temperature depression ($T_f - T$) for five soil model layers. The forcing are from Goose Bay, Canada. The parameters ϵ and K_s have been set to one in the lower panel.

4.1.4 Soil organic carbon

The physical properties of soil organic carbon (or peat soil) play a significant role for understanding the water and energy budgets of the land surface in northern regions. North-Eurasian soils are very rich in organic carbon because the low soil temperatures in this region inhibit decomposition of dead plant material that accumulates over time, thereby forming peat deposits. Soil organic carbon exhibits very different hydraulic and thermal properties than mineral soil (Boelter 1969; Letts *et al.* 2000). It is characterized by a very high porosity, a weak hydraulic suction, and a sharp vertical hydraulic conductivity profile from high values at the surface to very low values at the subsurface. This generally induces a relatively wet soil with a shallow water table (Letts *et al.* 2000). Its low thermal conductivity and its relatively high heat capacity act as an insulator for soil temperature that prevents the soil from significant warming during the summer (Bonan and Shugart 1989; Lawrence and Slater 2008). Over permafrost regions, the hydraulic and thermal properties of soil organic carbon partly control the soil depth reached by the 0 C isotherm which, in turn, defines the thickness of the active layer during summer (Paquin and Sushama, 2015). However, using the multi-layer version of ISBA over cold regions, winter top soil temperatures tend to be underestimated (Wang *et al.* 2016) while during summer they are generally too warm. It is partly due to the fact that ISBA only accounts for mineral soil properties while many studies pointed out that the specific properties of soil organic carbon are required to simulate realistic soil thermal regime over cold regions (Nicolsky *et al.* 2007; Beringer *et al.* 2001; Lawrence and Slater, 2008; Lawrence *et al.* 2008; Dankers *et al.* 2011).

An optional parameterization of the organic carbon effect on hydraulic and thermal soil properties has been

added by Decharme *et al.* (2016). The parameterization is based on the pedotransfer function of Boelter (1969) and inspired by works of Letts *et al.* (2000) and Lawrence and Slater(2008). The pedotransfer functions of Boelter (1969) link the soil water retention at different pressure levels to the fiber content of a peat soil. Letts et al. (2000) describe the vertical profile of hydraulic properties such as soil matric potential and hydraulic conductivity at saturation for a typical organic soil. The hydraulic properties change sharply from the near surface where peat is weakly decomposed (fibric soil) to the sub-surface with moderately and well decomposed peat (hemic and sapric soils respectively). Lawrence and Slater (2008) proposed a linear combination of such soil organic properties with the standard mineral soil properties.
In ISBA-DF, before averaging soil organic with mineral properties, a typical peat soil profile is computed for the model soil grid using a power function for each hydraulic property, α_{peat}, found in Table 4.1. For each soil layer i, this function is described as:

$$\alpha_{peat}(i) = \alpha_{fibric}\, z(i)^{\beta} \tag{4.136}$$

$$\beta = \frac{\ln\left(\alpha_{sapric}/\alpha_{fibric}\right)}{\ln\left(d_{sapric}/d_{fibric}\right)} \tag{4.137}$$

where z (m) is the depth of the considered soil grid node, α_{fibric} and α_{sapric} are the fibric and sapric parameter values, respectively (Table 4.1). d_{fibric} (m) is the depth arbitrarily set to 0.01 m where the profile

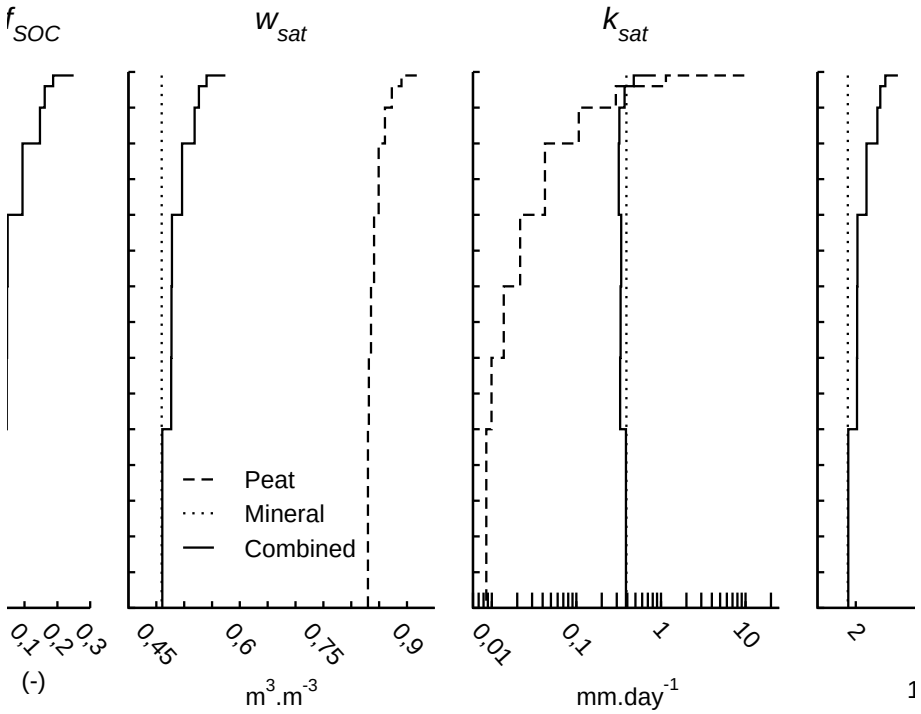

Figure 4.14: Parameterization of the effect of soil organic carbon (SOC) on soil hydraulic and thermal properties. The soil organic carbon density profile, ρ_{soc}, is given by Eq. 4.139 using a top soil organic carbon content of 10 kg m^{-2}, a sub soil content of 15 kg m^{-2}, and via a simple linear interpolation at each soil grid nodes that conserves the total soil carbon mass. The fraction of the soil that is organic, f_{soc}, in each layer is determined assuming a simple relationship between this last soil organic carbon density profile and an idealized peat soil density profile (Eq.4.142). Examples for the soil porosity, w_{sat}, the soil saturated hydraulic conductivity, k_{sat}, and the soil heat capacity, c, are given. Dotted lines represent vertical homogeneous mineral soil properties, dashed lines the idealized peat soil properties, and plain lines the resulting combined soil properties using averaging method summed-up in Table 4.1.

starts to depart from fibric values, and d_{sapric} (m) the depth of 1 m where the soil properties reach the sapric values according to Letts *et al.* (2000).
To determine the organic fraction of soil, the density profile of the soil carbon must be known for the entire soil grid. Using the the Harmonized World Soil Database (HWSD; http://webarchive.iiasa.ac.at/Research/LUC/External-World-soil-database/HTML/), the soil carbon densities in the first 0.3 m, ρ_{top} (kg m^{-3}), and the remaining 0.7 m below, ρ_{sub} (kg m^{-3}), are known:

$$\rho_{top} = \frac{S_{top}}{\Delta d_{top}} \tag{4.138a}$$

$$\rho_{sub} = \frac{S_{sub}}{\Delta d_{sub}} \tag{4.138b}$$

where S_{top} and S_{sub} (kg m^{-2}) are the topsoil and subsoil organic carbon contents respectively, Δd_{top} and Δd_{sub} (m) represent the thicknesses of each observed soil horizon (0.3 and 0.7 m, respectively). We extrapolate the density below 1 m from this observed near-surface profile (Eq. 4.138). The extrapolation assumes that the carbon profile decreases sharply with soil depth according to a power function. The shape of this function is given by the observed profile if the topsoil organic carbon density is superior to the subsoil density. Otherwise, the density of soil carbon below a 1 m depth, ρ_{deep} (kg m^{-3}), is taken equal to the subsoil density:

$$\rho_{deep} = (1-\delta)\,\rho_{sub} + \delta \left(\frac{S_{top}+S_{sub}}{\Delta d_{deep} - \Delta d_{top} - \Delta d_{sub}} \right) \left[\left(\frac{\Delta d_{deep}}{\Delta d_{top} + \Delta d_{sub}} \right)^{\beta} - 1 \right] \tag{4.139}$$

where

$$\delta = \begin{cases} 0 & \forall\, \rho_{top} \leq \rho_{sub} \\ 1 & \forall\, \rho_{top} > \rho_{sub} \end{cases} \tag{4.140}$$

and

$$\beta = \frac{\ln\left[S_{top}/\left(S_{top}+S_{sub}\right)\right]}{\ln\left[\Delta d_{top}/\left(\Delta d_{top}+\Delta d_{sub}\right)\right]} \tag{4.141}$$

Finally, the soil carbon density profile, ρ_{soc} (kg m^{-3}), over the entire soil grid is computed using these three soil horizons and a simple linear interpolation at each grid node that conserves the total soil carbon mass (Fig. 4.14). The fraction of the soil that is organic, f_{soc}, in each layer is determined assuming this simple relationship:

$$f_{soc}(i) = \frac{\rho_{soc}(i)}{\left[1 - w_{sat,peat}(i)\right]\,\rho_{om}} \tag{4.142}$$

where ρ_{om} is the pure organic matter density equal to 1300 kg m^{-3} (Farouki, 1986) and $w_{sat,peat}$ the porosity of the peat soil profile computed using Eq. 4.136 and Table 4.1. As in Lawrence and Slater (2008), this fraction is used to combine the standard mineral soil properties with soil organic properties using weighted arithmetic or geometric averages, depending on the parameter (Table 4.1). An example of this method is shown in Fig. 4.14 for soil porosity, soil saturated hydraulic conductivity and soil heat capacity.

4.1.5 Treatment of the intercepted water

Rainfall and dew intercepted by the foliage feed a reservoir of water content W_r. This amount of water evaporates in the air at a potential rate from the fraction δ of the foliage covered with a film of water, as the remaining part $(1-\delta)$ of the leaves transpires. The fraction of the vegetation covered with water is defined as

$$\delta_v = (1-\omega_{rv}) \left(\frac{W_r}{W_{r,max}} \right)^{2/3} + \frac{\omega_{rv} W_r}{(1+a_{rv}\,LAI)\,W_{r,max} - a_{rv}\,W_r} \tag{4.143}$$

Table 4.1: The peat soil hydraulic and thermal parameter values used in ISBA for fibric and sapric soil. w_{sat} (m^3 m^{-3}) is the porosity, w_{fc} (m^3 m^{-3}) the water content at field capacity specified as matric potential at -0.1 bar for peat soil, w_{wilt} (m^3 m^{-3}) the water content at wilting point (matric potential of -15 bar), b the dimensionless shape parameter of the soil-water retention curve, ψ_{sat} (m) the soil matric potential, k_{sat} (m s^{-1}) the soil hydraulic conductivity at saturation, c (J m^{-3} K^{-1}) the soil heat capacity of organic matter, λ_s (W m^{-1} K^{-1}) the thermal conductivity of soil matrix, and λ_{dry} (W m^{-1} K^{-1}) the dry soil thermal conductivity. For pedotransfer functions of Boelter (1969), the fiber content in fibric soil is assumed to be equal to 76.8 against 21.8 in sapric soil in order to reach soil porosity values close to those of Letts *et al.* (2000). The method for averaging mineral soil properties with peat soil values using the fraction of soil that is organic is also given for each parameter.

α_{peat}	Fibric soil	Sapric soil	Source	Mineral/Peat average
w_{sat}	0.9300	0.8450	Letts et al. (2000) and Boelter (1969)	Arithmetic
w_{fc}	0.3690	0.7190	PTF from Boelter (1969)	Arithmetic
w_{wilt}	0.0730	0.2220	TF from Boelter (1969)	Arithmetic
b	2.7000	12.0000	Letts et al. (2000)	Arithmetic
ψ_{sat}	-0.0103	-0.0101	Letts et al. (2000)	Arithmetic
k_{sat}	2.8×10^{-4}	1.0×10^{-7}	Letts et al. (2000)	Geometric
c	2.5×10^{-6}	2.5×10^{-6}	Farouki (1986)	Arithmetic
λ_s	0.2500	0.2500	Farouki (1986)	Geometric
λ_{dry}	0.0500	0.0500	Farouki (1986)	Geometric

Delire et al. (1997) used the first term on the RHS of Eq. 4.143 for relatively low vegetation (Deardorff, 1978) and the second term for tall vegetation (Manzi and Planton, 1994). A weighting function is used which introduces the vegetation height dependence using the roughness length as a proxy from

$$\omega_{rv} = 2\, z_{0v} \; - \; 1 \qquad\qquad (0 \leq \omega_{rv} \leq 1) \tag{4.144}$$

where the current value for the dimensionless coefficient is $a_{rv} = 2$.
Following Deardorff (1978), we set

$$\frac{\partial W_r}{\partial t} = vegP - (E_v - E_{tr}) - R_r \; ; \; 0 \leq W_r \leq W_{rmax} \tag{4.145}$$

where P is the precipitation rate at the top of the vegetation, E_v is the evaporation from the vegetation including the transpiration E_{tr} and the direct evaporation E_r when positive, and the dew flux when negative (in this case $E_{tr} = 0$), and R_r is the runoff of the interception reservoir. This runoff occurs when W_r exceeds a maximum value W_{rmax} depending upon the density of the canopy, i.e., roughly proportional to $vegLAI$. According to Dickinson (1984), we use the simple equation:

$$W_{rmax} = c_{wrmax} veg\, LAI \tag{4.146}$$

Generally speaking, $c_{wrmax} = 0.2$ kg m^{-2}, although it can be modified slightly for certain vegetation cover.

4.1.6 Spatial variability of precipitation intensities

With this option, the main assumption is that, generally, the rainfall intensity is not distributed homogeneously over an entire grid cell. As a first-order approximation, the sub- grid variability in liquid precipitation, P_i, can be given by an exponential probability density distribution, $f(P_i)$:

$$f(P_i) = \frac{\mu}{P} e^{-\mu \frac{P_i}{P}} \tag{4.147}$$

where P represent the mean rainfall rate over the grid cell and μ a fraction of the grid cell affected by rainfall. μ is calculated using the results of Fan *et al.* (1996), who showed an exponential relationship between the fractional coverage of precipitation and rainfall rate, based on their analyses of over 2 years radar observations and rain gauge measurements over the Arkansas-Red river basin in the southern plains of the United States. This relationship is:

$$\mu = 1 - e^{-\beta P} \tag{4.148}$$

where β is a parameter which depends on grid resolution, dx :

$$\beta = 0.2 + 0.5e^{-0.001dx} \tag{4.149}$$

dx represents represents lengths of square grid cells ranging from 40 km to 500 km. In consequence, the μ parameter is fixed to 1 at high resolution ($\leq 10km$). This Spatial variability of precipitation intensities induces a new expression for the runoff from the interception reservoir, W_r :

$$W_r = P \times e^{\frac{\mu(W_r - W_{rmax})}{P\Delta t}} \tag{4.150}$$

The second consequence is that the Horton runoff, Q_{hort}, is calculated by integrating the difference between the local rainfall and the local maximum infiltration capacity, I_i, as follows:

$$Q_{hort} = \mu \int_{I_i}^{\infty} (P_i - I_i)\, f(P_i) dP_i \tag{4.151}$$

Another assumption is made on the spatial heterogeneity of the local maximum infiltration capacity. Its spatial distribution can also be approximated by an exponential probability density distribution:

$$g(I_i) = \frac{1}{\overline{I}} e^{-\frac{I_i}{\overline{I}}} \tag{4.152}$$

where $\overline{I}$ is the mean maximum infiltration rate over the grid cell. As previously said, $\overline{I}$ is calculated for unfrozen and frozen soil conditions. So Eq.4.151 , without snowmelt, can be noted as :

$$\begin{aligned} Q_{hort} &= \mu(1-\delta_f) \int_0^{\infty} \int_{I_{unf,i}}^{\infty} (P_i - I_{unf,i}) f(P_i) g(I_{unf,i}) dP_i dI_{unf,i} \\ &\quad + \mu\delta_f \int_0^{\infty} \int_{I_{f,i}}^{\infty} (P_i - I_{f,i}) f(P_i) g(I_{f,i}) dP_i dI_{f,i} \end{aligned} \tag{4.153}$$

After some mathematical developments, the Horton runoff in presence of rainfall and snowmelt, S_m, is given following Decharme and Douville (2006):

$$\begin{aligned} Q_{hort} &= (1-\delta_f) \left(\frac{P}{1 + \overline{I_{unf}} \frac{\mu}{P}} + max(0, S_m - \overline{I_{unf}}) \right) \\ &\quad + \delta_f \left(\frac{P}{1 + \overline{I_f} \frac{\mu}{P}} + max(0, S_m - \overline{I_f}) \right) dP_i dI_{f,i} \end{aligned} \tag{4.154}$$

4.1.7 Treatment of the snow

ISBA features several schemes to handle snow on the ground, which are described below. They range from single-layer schemes with a minimal number of prognostic variables and highly simplified treatment of snow thermodynamics, to state-of-the-art multi-layer snowpack schemes (Explicit Snow -ES- and Crocus). Table 4.2 provides an summary of the available snowpack schemes and the corresponding scientific references.

Single-layer	D95	Douville *et al.* (1995a,1995b)
Multi-layer	Explicit-Snow (ES)	Boone (2000); Boone and Etchevers (2001)
Multi-layer	Crocus	Brun *et al.* (1989,1992); Vionnet *et al.* (2012)

Table 4.2: Summary of the snowpack schemes available in ISBA

One-layer snow scheme option

The evolution of the equivalent water content of the snow reservoir is given by

$$\frac{\partial W_s}{\partial t} = P_s - E_s - M_{lt} \tag{4.155}$$

where P_s is the precipitation of snow, and E_s is the sublimation from the snow surface.
The presence of snow covering the ground and vegetation can greatly influence the energy and mass transfers between the land surface and the atmosphere. Notably, a snow layer modifies the radiative balance at the surface by increasing the albedo. To consider this effect, the albedo of snow α_s is treated as a new prognostic variable. Depending if the snow is melting or not, α_s decreases exponentially or linearly with time.
If there is no melting (i.e., $M_{lt} = 0$):

$$\alpha_s(t) = \alpha_s(t - \Delta t) - \tau_a \frac{\Delta t}{\tau} + \frac{P_s \Delta t}{W_{crn}}(\alpha_{smax} - \alpha_{smin}) \qquad (\alpha_{smin} \leq \alpha_s \leq \alpha_{smax}) \tag{4.156}$$

where $\tau_a = 0.008$ is the linear rate of decrease per day, $\alpha_{smin} = 0.50$ and $\alpha_{smax} = 0.85$ are the minimum and maximum values of the snow albedo.
If there is melting (i.e., $M_{lt} > 0$):

$$\begin{aligned} \alpha_s(t) \;=\; & [\alpha_s(t - \Delta t) - \alpha_{smin}] \exp\left[-\tau_f \frac{\Delta t}{\tau}\right] + \alpha_{smin} \\ & + \frac{P_s \Delta t}{W_{crn}}(\alpha_{smax} - \alpha_{smin}) \qquad (\alpha_{smin} \leq \alpha_s \leq \alpha_{smax}) \end{aligned} \tag{4.157}$$

where $\tau_f = 0.24$ is the exponential decrease rate per day. Of course, the snow albedo increases as snowfalls occur, as shown by the second terms of Eqs. 4.156-4.157.
The average albedo of a model grid-area is expressed as

$$\alpha_t = (1 - p_{sn})\alpha + p_{sn}\alpha_s \tag{4.158}$$

Similarly, the average emissivity ϵ_t is also influenced by the snow coverage:

$$\epsilon_t = (1 - p_{sn})\epsilon + p_{sn}\epsilon_s \tag{4.159}$$

where $\epsilon_s = 1.0$ is the emissivity of the snow. Thus, the overall albedo and emissivity of the ground for infrared radiation is enhanced by snow.
Because of the significant variability of thermal properties related with the snow compactness, the snow density, ρ_s, is also considered as a prognostic variable. Based on Verseghy (1991), ρ_s decreases exponentially at a rate of τ_f per day:

$$\rho_s(t) = [\rho_s(t - \Delta t) - \rho_{smax}] \exp\left[-\tau_f \frac{\Delta t}{\tau}\right] + \rho_{smax} + \frac{P_s \Delta t}{W_s}\rho_{smin} \qquad (\rho_{smin} \leq \rho_s \leq \rho_{smax}) \tag{4.160}$$

where $\rho_{smin} = 100$ and $\rho_{smax} = 300$ kg m^{-3} are the minimum and maximum snow densities.

Multi-layer snow scheme options

Two multi-layer snow schemes options are available in ISBA, namely Explicit Snow (ES) and Crocus. Explicit Snow (Boone and Etchevers, 2001; Decharme et al. 2016) is a so-called intermediate complexity scheme which is representative of a class of snow models which use several layers and have simplified physical parameterization schemes (Loth *et al.* 1993; Lynch-Stieglitz, 1994; Sun *et al.* 1999). In contrast, Crocus features a detailed description of processes occurring within the snowpack (Brun *et al.* 1989; 1992; Vionnet *et al.* 2012). Crocus was initially a stand-alone model, and it was recently coupled to ISBA building on the ES model structure. In what follows, the description applies to both ES and Crocus unless otherwise stated.

Compared to the baseline ISBA snow scheme, the explicit multi-layered approach shared by ES and Crocus resolves the large thermal and the density gradients which can exist in the snow cover, distinguishes the surface energy budgets of the snow and non-snow covered portions of the surface, includes the effects of liquid water storage in the snow cover, computes the absorption of incident radiation within the pack, and calculates explicit heat conduction between the snow and the soil. Figure 4.15 provides an overview of the processes handled in the multi-layer snow schemes, coupled to the soil and vegetation components of ISBA.

The multi-layer snowpack schemes Crocus and ES are most consistently used together with ISBA-DF rather than the force-restore soil schemes. In addtion, Crocus handles snow metamorphism, i.e. the physical transformations of snow grains through time, and interactively modifies the vertical discretization of the vertical grid of snow layers to optimize the representation of internal snow processes. In practice, Crocus is generally run with a larger total possible number of snow layers than ES. ES typically uses up to 12 snow layers, while standard Crocus runs use up to 20 or 50 snow layers. The latter configuration is appropriate when the focus is placed on the study of the properties of the snowpack itself (avalanche hazard prediction, snow physical properties, combined use of remote sensing).

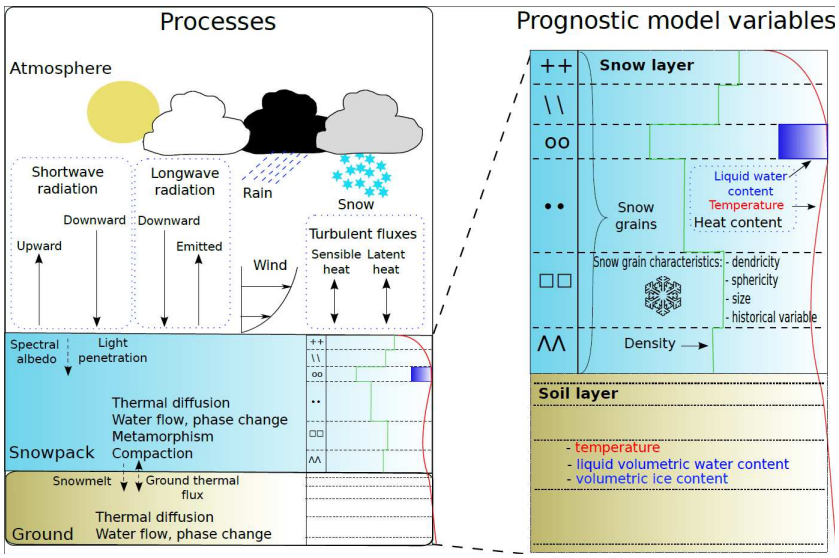

Figure 4.15: Overview of the physical processes and prognostic variables used to characterize the snowpack in the multi-layer snowpack schemes options of ISBA (ES and Crocus). The major differences between the ES and Crocus scheme is that ES does not treat snow metamorphism explicitly, and that the number of snow layers is kept significantly lower than for Crocus (on the order of 3 typically, vs. up to 20 or 50 for Crocus.

The conservation equation for the total snow cover mass is expressed as

$$\frac{\partial W_s}{\partial t} = P_s + p_{sn}\ (P - P_s) - E_s - E_{sl} - Q_n\ \ , \tag{4.161}$$

where E_{sl} represents evaporation of liquid water from the snow surface, and the product $p_{sn}\ (P - P_s)$ represents the portion of the total rainfall that is intercepted by the snow surface while the remaining rainfall is assumed to be intercepted by the snow-free soil and vegetation canopy. The snow-runoff rate, Q_n, is the rate at which liquid water leaves the base of the snow cover.

The snow state variables are the heat content (H_s), the layer thickness (D), and the layer average density (ρ_s). The temperature (T_{sn}) and liquid water content (w_{sl}) are defined using the heat content. The use of the Crocus scheme induces the definition of further variables, which describe the morphological properties of snow grains (d dendricity, s sphericity, g_s grain size, h historical variable and A age of a given snow layer). See Vionnet *et al.* (2012) for details.

The total snow depth, D_s (m) is defined as

$$D_s = \sum_{i=1}^{N_s} D_i \tag{4.162}$$

where a 12-layer configuration is currently used by default (i.e. $N_s = 12$). In ES and Crocus, the thickness of the surface snow layer can be as low as 1 mm although it typically ranges on the order of 0.01 to 0.02 m. The thickness of internal snow layers is on the order of a few cm typically, with a finer mesh towards the air/snow and ground/snow interface. See Vionnet *et al.* (2012) and Decharme *et al.* (2016) for details.

The evolution of snow density in each layer is due to snow compaction resulting from changes in snow viscosity (Brun *et al.* 1989) and wind-induced densification of near surface snow layers (Brun *et al.* 1997). This wind-driven compaction process is assumed to occur when wind velocity exceeds a threshold value that depends on snow surface characteristics. This process is especially important for simulating the evolution of the snow density over polar regions. In ES, additional changes arise from snowfall which generally reduce the snow density and more details can be seen in Decharme *et al.* (2016). In Crocus, snowfall induces the creation of a new snow layer at the surface ; mechanical settling is computed using a Newtonian formalism where the viscosity depends mostly on the snow density and temperature but also on the snow type (see Vionnet *et al.* 2012, for details). When Crocus is used, the slope angle has an impact on the compaction rate, since only the component of the weight perpendicular to the snow layering need be taken into account. In practice, the acceleration of gravity ($g = 9.80665$ m s^2) is then simply multiplied by cos($slope_i$) where $slope_i$ is the slope of the grid point i.

The snow heat content (J m^{-2}) is defined as

$$H_{s\,i} = c_{s\,i}\, D_i\ (T_{sn\,i} - T_0)\ -\ L_f\, \rho_w\, (w_{s\,i} - w_{sl\,i})\ \ , \tag{4.163}$$

where w_s is the total snow layer water equivalent depth (m), w_{sl} is the snow layer liquid water content (m), and c_s is the snow heat capacity (J m^{-3} K^{-1}) (using the same definition as the baseline ISBA snow scheme). The snow heat content is used in order to allow the presence of either cold (dry) snow which has a temperature less than or equal to the freezing point or warm (wet) snow which is characterized by a temperature at the freezing point and contains water in liquid form. The snow temperature and liquid water content can then be defined as

$$T_{sn\,i} \;=\; T_f\ +\ (H_{s\,i} + L_f\, \rho_w\, w_{s\,i})\ /\ (c_{s\,i}\, D_i)\ ; \qquad w_{l\,i} = 0 \tag{4.164}$$

$$w_{sl\,i} \;=\; w_{s\,i}\ +\ (H_{s\,i}/L_f\, \rho_w)\ ; \qquad T_{sn\,i} = T_f \ \text{ and } \ w_{sl\,i} \le w_{sl\,\max i} \tag{4.165}$$

where $w_{sl\,\max i}$ is the maximum liquid water holding capacity of a snow layer, which is based on empirical relations. All water exceeding this flows into the layer below where it can do one or all of the following: add to the liquid water content, refreeze, or continue flowing downward.
Snow heat flow is along the thermal gradient as any snow melt or percolated water within the snow cover is assumed to have zero heat content. The layer-averaged snow temperature equation ($T_{s\,i}$) is expressed as

$$c_{s\,i} D_i \frac{\partial T_{sn\,i}}{\partial t} = G_{s\,i-1} - G_{s\,i} + R_{s\,i-1} - R_{s\,i} - S_{s\,i} \ , \tag{4.166}$$

where S_s represents an energy sink/source term associated with phase changes between the liquid and solid phases of water. Incoming short wave radiation (R_s) transmission within the snowpack decreases exponentially with increasing snow depth. At the surface, it is expressed as

$$R_{s\,0} = R_g \ (1 - \alpha_s) \tag{4.167}$$

where the snow albedo is defined following Brun *et al.* (1992). In ES and Crocus the solar radiation is handled using three separate spectral bands ([0.3-0.8], [0.8-1.5] and [1.5-2.8] μm). First of all, the albedo is computed in each band, as a function of the snow properties in the first snowpack layer for ES and the top 0.03 m of the snowpack for Crocus. In the UV and visible range ([0.3-0.8] μm), snow albedo depends mostly on the amount of light absorbing impurities, but also on its micro-structure. The latter is represented by the optical diameter of snow, d_{opt}, which corresponds to the diameter of a collection of mono-dispersed ice spheres possessing the same hemispherical albedo as the corresponding semi-infinite snow layer. The impact of snow browning due to the deposition of light absorbing impurities is parametrized from the age of the uppermost snow layer. In the near-infrared bands, the spectral albedo depends only on the optical diameter of snow. The optical diameter of snow is currently empirically derived from the snow density and age for ES (Decharme *et al.* 2016) and the microstructure properties of the snow for Crocus (see below, and Vionnet *et al.* 2012). Once the spectral albedo is calculated, in every spectral band the incoming radiation is depleted according to the albedo value, and the remaining part penetrates the snowpack and is gradually absorbed in the snow layers assuming an exponential decay of radiation with depth. The solar flux, Q_s, at a depth z below the snow surface is expressed as follows:

$$Q_s = SW\downarrow \sum_{k=1}^{3} \left\{ \omega_k \, (1 - \alpha_k) \exp \left[- \sum_{j=1}^{i} \left(\beta_{k,j} \, \Delta z_j \right) \right] \right\} \tag{4.168}$$

where $SW\downarrow$ represents the incoming solar radiation, α_k the albedo and $\beta_{k,j}$ the absorption coefficient for the spectral band k and layer j. In the current version, the incoming shortwave radiation Rs is split into three bands using empirical coefficients ω_k equal to 0.71, 0.21 and 0.08 respectively for bands [0.3-0.8], [0.8-1.5] and [1.5-2.8] mm. Future developments will allow for forcing where incoming shortwave radiation is partitioned into several bands. Finally, shortwave radiation excess for thin snow cover (transmitted through the snow) is added to the snow/ground heat flux.
The sub-surface heat (G_s) flux terms are evaluated using simple diffusion. At the surface, this flux is expressed as

$$G_{s\,0} = \epsilon_s \left(R_A - \sigma_{SB} {T_{sn\,1}}^4 \right) \ - \ H \left(T_{sn\,1} \right) \ - \ LE \left(T_{sn\,1} \right) \ - \ c_w \, p_{sn} \left(P - P_s \right) \left(T_f - T_r \right) \ , \tag{4.169}$$

The last term on the right hand side of the above equation represents a latent heat source when rain with a temperature (T_r) greater than T_0 falls on the snow cover, where c_w represents the heat capacity of water (4187 J kg^{-1} K^{-1}). Rainfall is simply assumed to have a temperature which is the larger of the air temperature (T_a) and the freezing point. The latent heat flux from the snow includes the liquid fraction weighted contributions from the evaporation of liquid water and sublimation.

The ISBA surface soil/vegetation layer temperature is then coupled to the snow scheme using

$$\frac{1}{C_T}\frac{\partial T_s}{\partial t} = (1-p_n)\left[R_g\,(1-\alpha)+\epsilon_t\left(R_A-\sigma {T_s}^4\right)-H-LE-\frac{2\pi}{C_T\tau}\,(T_s-T_2)\right] + p_n\ (G_{s\,N}+R_{s\,N}) \tag{4.170}$$

The net surface fluxes to/from the atmosphere are then calculated as the snow-cover fraction weighted sums over the snow and non-snow covered surfaces. When either multi-layer option is used (ES or Crocus), the single-layer snowpack scheme in ISBA is used when the snow cover is relatively thin (arbitrarily defined as 0.05 m depth). When the snow depth exceeds this threshold, the snow mass and heat is transferred to the chosen multi-layer scheme. This prevents numerical difficulties for vanishingly thin snow packs.

Additional features of the Crocus scheme

Evolution of the vertical discretization of the finite-element grid

The dynamical evolution of the number and thicknesses of the numerical snow layers is a key and original feature of Crocus, which aims at simulating the vertical layering of natural snowpacks in the best possible way. The maximum number of numerical layers is an important user-defined set-up option. A minimum of 3 layers is imposed for solving the heat conduction through the snowpack but there is no limitation on the maximum number. As the maximum number of layers increases, the snowpack stratigraphy can be simulated in more detail. According to the research or operational objectives, the user has to find the appropriate balance between the realism and the computational cost of the simulation. An important point to mention is that the snowpack scheme dynamically manages a different vertical grid mesh, in terms of the number and the thickness of snow layers, for each grid point when it is run in parallel mode for a spatially distributed simulation ; this is a common case for snow/atmosphere coupled simulations or for distributed stand-alone simulations.

The adjustment of the snowpack layering is achieved with a set of rules. The procedure is activated at the beginning of each time step according to the following sequence:

- for snowfall over a bare soil, the snowpack is built up from identical layers, in terms of thickness and state variables. Their number depends on the amount of fresh snow and on the maximum number of layers;
- for snowfall over an existing snowpack, it is first attempted to incorporate the freshly fallen snow into the existing top layer, provided its grain characteristics are similar and its thickness is smaller than a fixed limit. The similarity between two adjacent layers is determined from the value of the sum of their differences in terms of d, s and g_s, each weighted with an appropriate coefficient. If the merging is not possible, a new numerical layer is added to the preexisting layers. If the number of layers then reaches its maximum, a search is carried out to identify two adjacent layers to be merged. This is done by minimizing a criterion balancing the similarity between their respective grain characteristics and their thicknesses;
- for no snowfall, a check is carried out to see whether it is convenient to merge too thin snow layers or to split thoses which are thick. This is achieved by comparing the present thickness profile to an idealized profile, which acts as an attractor for the vertical grid. This idealized thickness profile depends on the current snow depth and on the user-defined maximal number of layers (see Figure 4.16 for an example). Merging two layers is only possible for those which are similar enough in terms of grain characteristics. Grid resizing affects only one layer per time step, with a priority given to the

surface and bottom layers, in order to accurately solve the energy exchanges at the surface and at the snow/soil interface;

- for most time steps, no grid resizing is carried out, except that the thickness of each layer decreases according to its compaction rate.

The consistency of the physical prognostic variables is maintained in case of grid resizing. A projection is achieved from the former vertical grid to the new one. Mass, heat content and liquid water content are conserved. When a new numerical snow layer is built from several former layers, its grain characteristics are calculated in order to conserve the averaged weighted optical grain size of the former layers. This insures a strong consistency in the evolution of surface albedo, even when frequent grid resizing occur at the surface in case of frequent snowfalls or surface melting events.

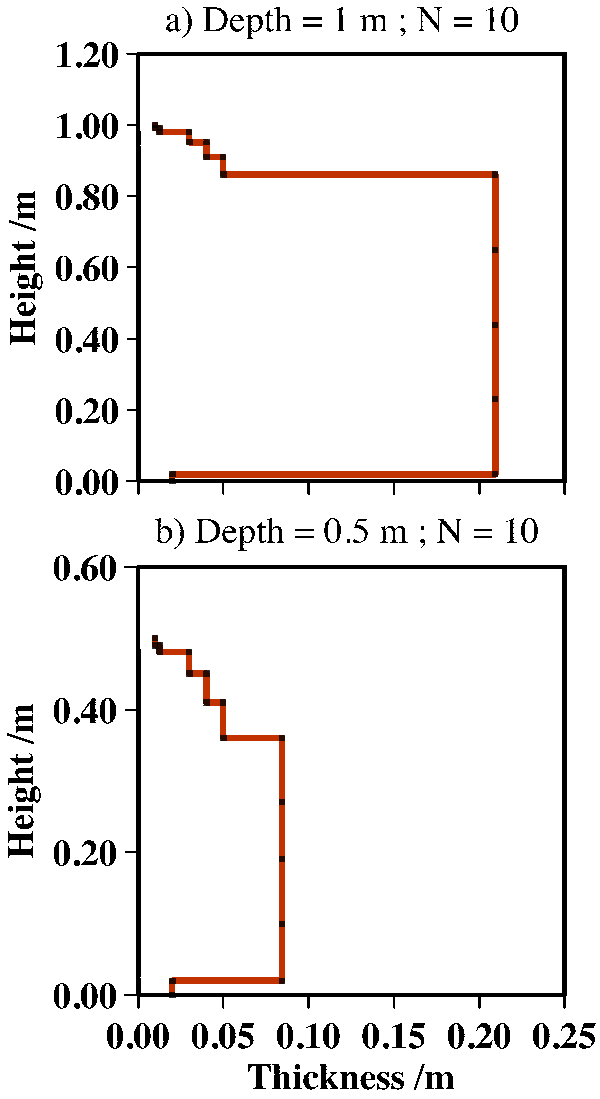

Figure 4.16: Illustration of the optimal vertical grid of Crocus, which depends on total snow depth and on the user-defined maximum number of snow layers.

Snow metamorphism

Snow metamorphism is implemented in the snowpack scheme Crocus through a set of quantitative laws describing the evolution rate of the type and size of the snow grains in each layer (Brun *et al.* 1992). This

is carried out within the subroutine. A distinction is made between dendritic and non-dendritic snow. Snow falls as dendritic snow and remains dendritic until d reaches 0. Snow then reaches the state of rounded crystals, faceted crystals or belongs to an intermediate state. It is is then characterized by its sphericity (s), ranging from 0 to 1, and a grain size, g_s, ranging from 0.3 to 0.4 mm. Such snow is defined as non-dendritic. The metamorphism laws that govern the evolution of snow grain depend on temperature, the temperature gradient, and include wet metamorphism. They are similar to the laws initially described by Brun *et al.* (1992) and are mostly based on empirical fits to experimental data. The metamorphism laws that govern the evolution of snow grain are given in Table 4.3 and 4.4, respectively for dry and wet metamorphism. In the case of temperature gradient metamorphism, fits to experimental data by Marbouty (1980) are used. In this case, the increase of grain size g_s follows:

$$\frac{\delta g_s}{\delta t} = f(T)h(\rho)g(G)\Phi \tag{4.171}$$

where G is the absolute value of the temperature gradient ($|\delta T/\delta z|$) and f, g, h and Φ are dimensionless functions varying from 0 to 1 given by:

$$f = \begin{cases} 0 & \text{if} \quad T - T_{\text{fus}} < -40 \text{ K} \\ 0.011 \times (T - T_{\text{fus}} + 40) & \text{if} \quad -40 \leq T - T_{\text{fus}} < -22 \text{ K} \\ 0.2 + 0.05 \times (T - T_{\text{fus}} + 22) & \text{if} \quad -22 \leq T - T_{\text{fus}} < -6 \text{ K} \\ 1 - 0.05 \times (T - T_{\text{fus}}) & \text{otherwise} \end{cases} \tag{4.172}$$

where T_{fus} is temperature of the melting point for water (K), and h, g and Φ are given below:

$$\Phi = 1.0417.10^{-9} \text{ m s}^{-1} \tag{4.173}$$

$$h = \begin{cases} 1. & \text{if} \quad \rho < 150 \quad \text{kg m}^{-3} \\ 1 - 0.004 \times (\rho - 150) & \text{if} \quad 150 < \quad \rho < 400 \quad \text{kg m}^{-3} \\ 0. & \text{otherwise} \end{cases} \tag{4.174}$$

$$g = \begin{cases} 0. & \text{if} \quad G < 15 \text{ K m}^{-1} \\ 0.01 \times (G - 15) & \text{if} \quad 15 \leq G < 25 \text{ K m}^{-1} \\ 0.1 + 0.037 \times (G - 25) & \text{if} \quad 25 \leq G < 40 \text{ K m}^{-1} \\ 0.65 + 0.02 \times (G - 40) & \text{if} \quad 40 \leq G < 50 \text{ K m}^{-1} \\ 0.85 + 0.0075 \times (G - 50) & \text{if} \quad 50 \leq G < 70 \text{ K m}^{-1} \\ 1. & \text{otherwise} \end{cases} \tag{4.175}$$

In addition to this default metamorphism formulations, three other formulations of metamorphism can be activated. The first one (C13) is similar to the default one but uses the optical diameter and the sphericity as prognostic variables. The second one (T07) is based on the parameterizations from Taillandier *et al.* (2007) and Domine *et al.* (2007) and the last one (F06) is based on the parameterizations from Flanner *et al.* (2006) .For detail of these implementations please refer to Carmagnola *et al.* (2014) .

Snow radiative transfer scheme

In addition to the basic formation of solar energy absorption and snow albedo over three spectral bands described above, a new option is available for solar radiative transfer calculation in the snowpack. The radiative scheme is called TARTES Libois *et al.* (2013) (Two-streAm Radiative TransfEr in Snow model). TARTES is a two-stream radiative transfer scheme based on an analytical formulation of radiative transfer in snow (Kokhanovsky *et al.* (2004)). TARTES computes spectral solar absorption within each layer and diagnoses spectral and broadband albedo. The default spectral resolution is 20 nm. The scheme uses spectral solar irradiance calculated from input broabdand data using a parameterization derived from SBDART

Table 4.3: Metamorphism laws under dry conditions. G is the vertical temperature gradient ($|\delta T/\delta z|$), T the temperature (K) and t is time expressed in days. f, g, h and Φ are empirical functions to predict depth-hoar growth-rate from Marbouty (1980).

	Non-dendritic snow	Dendritic snow
$G \leq 5$ K.m^{-1}	$\frac{\delta s}{\delta t} = 10^9 e^{-6000/T}$ $\frac{\delta g_s}{\delta t} = 0$	$\frac{\delta d}{\delta t} = -2.10^8 e^{-6000/T}$ $\frac{\delta s}{\delta t} = 10^9 e^{-6000/T}$
$5 < G \leq 15$ K.m^{-1}	$\frac{\delta s}{\delta t} = -2.10^8 e^{-6000/T} G^{0.4}$ $\frac{\delta g_s}{\delta t} = 0$	$\frac{\delta d}{\delta t} = -2.10^8 e^{-6000/T} G^{0.4}$
$G > 15$ K.m^{-1}	if $s >$0: $\frac{\delta s}{\delta t} = -2.10^8 e^{-6000/T} G^{0.4}$ and $\frac{\delta g_s}{\delta t} = 0$ if $s =$0: $\frac{\delta s}{\delta t} = 0$ and $\frac{\delta g_s}{\delta t} = f(T)h(\rho)g(G)\Phi$	$\frac{\delta s}{\delta t} = -2.10^8 e^{-6000/T} G^{0.4}$

Table 4.4: Metamorphism laws in the presence of liquid water. θ is the mass liquid water content and t is time expressed in days. v refers to the equivalent volume of snow grain and v'_0 and v'_1 are empirical constants taken from Brun (1989).

	Non-dendritic snow	Dendritic snow
$0 \leq s < 1$	$\frac{\delta g_s}{\delta t} = 0$ $\frac{\delta s}{\delta t} = \frac{1}{16}\theta^3$	$\frac{\delta d}{\delta t} = -\frac{1}{16}\theta^3$
$s = 1$	$\frac{\delta s}{\delta t} = 0$ $\frac{\delta v}{\delta t} = v'_0 + v'_1\theta^3$	$\frac{\delta s}{\delta t} = \frac{1}{16}\theta^3$

with $\theta = 100\frac{W_{\rm liq}}{\rho D}$

(Ricchiazzi *et al.* (1998)) at Col de Porte site. The scientific documentation of TARTES is available at http://lgge.osug.fr/ picard/tartes/.
TARTES simulates the effect of light absorbing impurities as an equivalent black-carbon content. To this respect, three options can be activated :

- "TA1": no impurity
- "TA2": snow impurity content constant to 100 ng g^{-1}
- "TAR" : impurity content = 2*snow age ng g^{-1}

Effects of wind

! As a 1D model, the continental surface scheme ISBA within SURFEX is NOT designed to handle explicitly wind-induced snow redistribution. Indeed, grid points are treated independently from each other. Nevertheless, the Crocus snowpack scheme includes parameterizations that represent some effects of wind drift on the snowpack.

The compaction and the metamorphism of the surface layers during wind drift events are taken into account in a simplified way, as described initially by Brun *et al.* (1997). A mobility index, $M_{\rm O}$, describes the potential for snow erosion for a given snow layer and depends on the microstructural properties of snow (d, s and g_s):

$$M_{\rm O} = \begin{cases} 0.34\,(0.75d - 0.5s + 0.5) + 0.66F(\rho) & \text{dendritic case} \\ 0.34\,(-0.583g_s - 0.833s + 0.833) + 0.66F(\rho) & \text{non-dendritic case} \end{cases} \quad (4.176)$$

Table 4.5: Evolution rates of snow grain properties and density in layer i caused by snow drifiting. t is time expressed in hours and τ represents the time characteristic for snow grains change under wind transport given by Eq. 4.178.

Parameters	Non-dendritic snow	Dendritic snow
Grain properties	$\frac{\delta s}{\delta t} = \frac{1-s}{\tau}$ $\frac{\delta g_s}{\delta t} = \frac{5.10^{-4}}{\tau}$	$\frac{\delta d}{\delta t} = \frac{d}{2\tau}$ $\frac{\delta s}{\delta t} = \frac{1-s}{\tau}$
Snow density	$\frac{\delta \rho}{\delta t} = \frac{\rho_{\max}-\rho}{\tau}$ with $\rho_{\max} = 350$ kg m^{-3}	

where $F(\rho) = [1.25 - 0.0042\,(\max(\rho_{min}, \rho) - \rho_{min})]$ and $\rho_{min} = 50$ kg m^{-3}. The expression for $M_{\rm O}$ in Eq. 4.176 combines the parameterization of Guyomarc'h and Merindol (1998) (first term) developed for alpine snow with a term depending on snow density ($F(\rho)$). The purpose is to extend the use of $M_{\rm O}$ to polar snow which has a density generally larger than 330 kg m^{-3} (upper limit for application of Guyomarc'h and Merindol, 1998). Fresh snow (high values of d, low value of ρ) presents high values of mobility index which tend to decrease with time due to sintering (increase of s) and compaction (increase of ρ). Guyomarc'h and Merindol (1998) combined the mobility index with wind speed, U, to compute a so-called "driftability" index, S_I:

$$S_I = -2.868 \exp(-0.085U) + 1 + M_{\rm O} \tag{4.177}$$

Positive values of S_I indicate that snow drifting can occur while $S_I = 0$ gives the value of the threshold wind speed for snow transport. During a drift event, blown snow particles in saltation break upon collision with the snow surface and tend towards rounded grains (Clifton *et al.* (2006)). For a given snow layer i, a time characteristic for snow grain change under wind transport is computed:

$$\tau_i = \frac{\tau}{\Gamma_{i\ \rm drift}} \quad \text{where } \Gamma_{i\ \rm drift} = \max[0, S_{Ii} \exp(-z_i/0.1)] \tag{4.178}$$

where τ is empirically set to 48 hours. The pseudo-depth in the snow pack, z_i (in m, positive downwards), takes into account previous hardening of snow layers j situated above the current layer i:

$$z_i = \sum_j [D_j \times (3.25 - S_{Ij})] \tag{4.179}$$

Therefore, through the variable $\Gamma_{\rm drift}$, compaction and rounding rates in a snow layer depends on the grain driftability and are propagated to the layers below with an exponential decay until it reaches a non-transportable layer ($S_I \leq 0$). Compaction and rounding rates are detailed in Table 4.5.

As an option and in case of snow drifting, Crocus computes the associated rate of sublimation according to a parameterization developed by Gordon *et al.* (2006). This parameterization allows the estimation of the sublimation rate in a column of blowing or drifting snow, combining existing parameterizations from Schmidt *et al.* (1982), Bintanja *et al.* (1998) and Déry *et al.* (2001). The total sublimation rate of blowing snow Q_s depends on the near-surface meteorological conditions according to:

$$Q_s = A(\frac{T_0}{T_a})^\gamma U_t \rho_a q_{si} (1 - Rh_i)(\frac{U}{U_t})^B \tag{4.180}$$

where T_a is the air temperature (K), T_0 a constant with a value of 273.16 K, U the wind speed, U_t the threshold wind speed for snow transport, ρ_a the air density and Rh_i the relative humidity with respect to ice. q_{si} denotes the saturation specific humidity (kg/kg) at temperature T_a. γ, A and B are dimensionless parameters with values 4.0, 0.0018 and 3.6, respectively. U_t is the threshold wind speed for wind transportation,

obtained by setting S_I = 0. in equation (4.177):

$$U_t = -\frac{\log\left((M_{\rm O} + 1.)/2.868\right)}{0.085} \tag{4.181}$$

Using this option, Crocus subtracts the corresponding mass from the snowpack surface at each model timestep.

4.1.8 The surface fluxes

Only one energy balance is considered for the whole system ground-vegetation-snow (when the 3-layer snow scheme option is not in use). As a result, heat and mass transfers between the surface and the atmosphere are related to the mean values T_s and w_g.
The net radiation at the surface is the sum of the absorbed fractions of the incoming solar radiation R_G and of the atmospheric infrared radiation R_A, reduced by the emitted infrared radiation:

$$R_n = R_G(1-\alpha_t) + \epsilon_t \left(R_A - \sigma_{SB} {T_s}^4\right) \tag{4.182}$$

where σ_{SB} is the Stefan-Boltzmann constant.
The turbulent fluxes are calculated by means of the classical aerodynamic formulas. For the sensible heat flux:

$$H = \rho_a c_p C_H V_a (T_s - T_a) \tag{4.183}$$

where c_p is the specific heat; ρ_a, V_a, and T_a are, respectively, the air density, the wind speed, and the temperature at the lowest atmospheric level; and C_H, as discussed below, is the drag coefficient depending upon the thermal stability of the atmosphere. The explicit snow scheme sensible heat flux is calculated using the same formulation (but with T_{sn}). The water vapor flux E is the sum of the evaporation of liquid water from the soil surface (i.e., $E_{g\,l}$), from the vegetation (i.e., E_v), and sublimation from the snow and soil ice (i.e, E_s and $E_{g\,f}$):

$$\begin{aligned}
LE &= LE_{g\,l} + LE_v + L_i\,(E_s + E_{g\,f}) && (4.184)\\
E_{g\,l} &= (1-veg)(1-p_{sng})\,(1-\delta_i)\;\rho_a C_H V_a\,(h_u q_{sat}(T_s) - q_a) && (4.185)\\
E_v &= veg(1-p_{snv})\rho_a C_H V_a h_v\,(q_{sat}(T_s) - q_a) && (4.186)\\
E_s &= p_{sn}\rho_a C_H V_a\,(q_{sat}(T_s) - q_a) && (4.187)\\
E_{g\,f} &= (1-veg)\,(1-p_{sng})\;\delta_i\,\rho_a C_H V_a\,(h_{ui}\,q_{\rm sat}\,(T_s)\;-\;q_a) && (4.188)
\end{aligned}$$

where L and L_i are the specific heat of evaporation and sublimation, $q_{sat}(T_s)$ is the saturated specific humidity at the temperature T_s, and q_a is the atmospheric specific humidity at the lowest atmospheric level. The snow fractions p_{sn} and p_{snv} are defined by Eq.s 4.5 and 4.1, respectively. The water vapor flux E from the explicit snow surface is expressed as

$$\begin{aligned}
LE\,(T_{sn\,1}) &= LE_{sl} + L_i E_s && (4.189)\\
E_{sl} &= \delta_{sn}\,\rho_a C_{Hs} V_a\,(q_{sat}\,(T_{sn\,1}) - q_a) && (4.190)\\
E_s &= (1-\delta_{sn})\;\rho_a C_{Hs} V_a\,(q_{sat}\,(T_{sn\,1}) - q_a) && (4.191)\\
\delta_{sn} &= w_{sl\,1}/w_{sl\,\max 1}\,; \qquad 0 \le \delta_{sn} \le 1 && (4.192)
\end{aligned}$$

where evaporation of liquid water is zero when $T_{sn\,1} < T_0$. The transfer coefficient (C_{Hs}) is calculated over the snow covered surface using the same formulation as C_H.

The surface ice fraction is is used to partition the bare soil latent heat flux between evaporation and sublimation, and it is defined as

$$\delta_i = w_{g\,f} / \left(w_{g\,f} + w_g \right) \; ; \qquad 0 \leq \delta_i < 1 \; . \tag{4.193}$$

The relative humidity h_u at the ground surface is related to the superficial soil moisture w_g following

$$h_u \; = \; \begin{cases} \frac{1}{2} \left[1 - \cos \left(\frac{w_g}{{w_{fc}}^*} \pi \right) \right] & w_g < {w_{fc}}^* \\ 1 & w_g \geq {w_{fc}}^* \end{cases} \tag{4.194}$$

where the field capacity with respect to the liquid water is defined using the modified soil porosity so that ${w_{fc}}^* = w_{fc}\, w^*_{sat} / w_{sat}$. The humidity for the ice covered portion of the grid box is calculated in a similar fashion as

$$h_{ui} \; = \; \begin{cases} \frac{1}{2} \left[1 - cos \left(\frac{w_{g\,f}}{{w_{fc}}^{**}} \pi \right) \right] & w_{g\,f} < {w_{fc}}^{**} \\ 1 & w_{g\,f} \geq {w_{fc}}^{**} \end{cases} \tag{4.195}$$

where ${w_{fc}}^{**} = w_{fc}(w_{sat} - w_g)/w_{sat}$. In case of dew flux when $q_{sat}(T_s) < q_a$, h_u is also set to 1 (see Mahfouf and Noilhan (1991) for details). When the flux E_v is positive, the Halstead coefficient h_v takes into account the direct evaporation E_r from the fraction δ of the foliage covered by intercepted water, as well as the transpiration E_{tr} of the remaining part of the leaves:

$$h_v = (1 - \delta) R_a / (R_a + R_s) + \delta \tag{4.196}$$

$$E_r = veg(1 - p_{snv}) \frac{\delta}{R_a} \left[q_{sat}(T_s) - q_a \right] \tag{4.197}$$

$$E_{tr} = veg(1 - p_{snv}) \frac{1 - \delta}{R_a + R_s} \left[q_{sat}(T_s) - q_a \right] \tag{4.198}$$

When E_v is negative, the dew flux is supposed to occur at the potential rate, and h_v is taken equal to 1. The aerodynamic resistance is $R_a = (C_H V_a)^{-1}$. The surface resistance, R_s, depends upon both atmospheric factors and available water in the soil; it is given by:

$$R_s = \frac{R_{smin}}{F_1 F_2 F_3 F_4 LAI} \tag{4.199}$$

with the limiting factors F_1, F_2, F_3, and F_4:

$$F_1 \; = \; \frac{f + R_{smin}/R_{smax}}{1 + f} \tag{4.200}$$

$$F_2 \; = \; \frac{w_2 - w_{wilt}}{w_{fc} - w_{wilt}} \quad and \; 0 \leq F_2 \leq 1 \tag{4.201}$$

$$F_3 \; = \; 1 - \gamma \left(q_{sat}(T_s) - q_a \right) \tag{4.202}$$

$$F_4 \; = \; 1 - 1.6 \times 10^{-3} (T_a - 298.15)^2 \tag{4.203}$$

where the dimensionless term f represents the incoming photosynthetically active radiation on the foliage, normalized by a species-dependent threshold value:

$$f = 0.55 \frac{R_G}{R_{Gl}} \frac{2}{LAI} \tag{4.204}$$

Moreover, γ is a species-dependent parameter (see Jacquemin and Noilhan (1990)) and R_{smax} is arbitrarily set to $5000 \; sm^{-1}$.

The surface fluxes of heat, moisture, and momentum can be expressed as

$$(\overline{w'\theta'})_s = \frac{H}{\rho_a c_p T_a/\theta_a} \quad (4.205)$$

$$(\overline{w'r'_v})_s = \frac{E}{\rho_a(1-q_a)} \quad (4.206)$$

$$|\overline{w'V'}|_s = C_D|V_a|^2 = u_*^2 \quad (4.207)$$

where r_v is the water vapor mixing ratio, w is the vertical motion, θ_a is the potential temperature at the lowest atmospheric level. The primes and overbars denote perturbation and average quantities.
For the drag coefficients C_H and C_D, the formulation of Louis (1979) was modified in order to consider different roughness length values for heat z_0 and momentum z_{0h} (Mascart *et al.* (1995)):

$$C_D = C_{DN}F_m \quad (4.208)$$

$$C_H = C_{DN}F_h \quad (4.209)$$

with

$$C_{DN} = \frac{k^2}{[\ln(z/z_0)]^2} \quad (4.210)$$

where k is the Von Karmann constant. Also

$$F_m = 1 - \frac{10Ri}{1+C_m\sqrt{|Ri|}} \quad if\ Ri \le 0 \quad (4.211)$$

$$F_m = \frac{1}{1+\frac{10Ri}{\sqrt{1+5Ri}}} \quad if\ Ri > 0 \quad (4.212)$$

and

$$F_h = \left[1 - \frac{15Ri}{1+C_h\sqrt{|Ri|}}\right] \times \left[\frac{ln(z/z_0)}{ln(z/z_{0h})}\right] \quad if\ Ri \le 0 \quad (4.213)$$

$$F_h = \frac{1}{1+15Ri\sqrt{1+5Ri}} \times \left[\frac{ln(z/z_0)}{ln(z/z_{0h})}\right] \quad if\ Ri > 0 \quad (4.214)$$

where Ri is the gradient Richardson number. The coefficients C_m and C_h of the unstable case are given by

$$C_m = 10{C_m}^* C_{DN}(z/z_0)^{p_m} \quad (4.215)$$

$$C_h = 15{C_h}^* C_{DN}(z/z_{0h})^{p_h} \times \left[\frac{ln(z/z_0)}{ln(z/z_{0h})}\right] \quad (4.216)$$

where C_m^*, C_h^*, p_m, and p_h are functions of the ratio $\mu = ln(z_0/z_{0h})$ only:

$$C_h^* = 3.2165 + 4.3431 \times \mu + 0.5360 \times \mu^2 - 0.0781 \times \mu^3 \quad (4.217)$$

$$C_m^* = 6.8741 + 2.6933 \times \mu - 0.3601 \times \mu^2 + 0.0154 \times \mu^3 \quad (4.218)$$

$$p_h = 0.5802 - 0.1571 \times \mu + 0.0327 \times \mu^2 - 0.0026 \times \mu^3 \quad (4.219)$$

$$p_m = 0.5233 - 0.0815 \times \mu + 0.0135 \times \mu^2 - 0.0010 \times \mu^3 \quad (4.220)$$

4.1.9 ISBA-Multi-Energy-Budget (MEB) Explicit Vegetation

ISBA includes an option to represent forests (using the corresponding patches) using the Multi-Energy-Budget (ISBA-MEB) explicit vegetation scheme (Boone et al., 2017; Napoly et al., 2017) . MEB is based on the classic two-source model for snow-free conditions which considers explicit energy budgets (for computing fluxes and effective surface temperatures) for the soil and the vegetation, and it has been extended to a three-source model in order to include an explicit representation of snowpack processes and their interactions with the ground and the vegetation. The vegetation canopy is represented using the so-called big-leaf method which lumps the entire vegetation canopy into a single effective leaf for computing energy budgets and the associated fluxes of heat, moisture and momentum. One of the first examples of a two-source model designed for atmospheric model studies is Deardorff (1978), and further refinements to the vegetation canopy processes were added in the years that followed leading to fairly sophisticated schemes which are similar to those used today (e.g. Sellers et al., 1986) . The two-source big-leaf approach (e.g. Braud et al., 1995) has been used extensively within coupled regional and global scale land-atmosphere models (Xue et al., 1991; Sellers et al., 1996; Dickinson et al., 1998; Lawrence et al., 2011; Saluelsson et al., 2011) . Some key features of MEB compared to the default ISBA treatment of forests are:

- seperate ground (surface) and vegetation canopy energy budgets. This is in contrast to the single composite soil-vegetation energy budget in ISBA. This permits the estimation of a more realistic surface radiative temperature, and surface flux partitioning.
- a snow fraction which can gradually bury the vegetation vertically thereby transitioning the turbulence and radiative coupling from the snow to the canopy air space to that between the snow and the atmosphere. Note that this differs from the notion of the vegetation snow cover fraction, p_{nv}, of the ISBA composite scheme.
- the detailed solar radiation transfer scheme which is a multi-layer model that considers two spectral bands, direct and diffuse flux components and the concept of sunlit and shaded leaves Carrer et al. (2013). It is used when ISBA-Ags is active: for MEB it is always used.
- a detailed treatment of canopy snow interception and unloading processes and a coupling with the ISBA physically-based multi-layer snow scheme.
- an explicit forest litter layer model (which also acts as the below-canopy surface energy budget when litter covers the soil)
- seperate ground surface and vegetation surface properties (roughness lengths, albedo, emissivity...). Note that the composite surface notion of veg is dropped in MEB.

All of the energy budgets are numerically implicitly coupled with each other and with the atmosphere using the coupling method adapted from Best et al. (2004) which was first proposed by Polcher et al. (1998) .
Currently, forests make up 8 patches for the 19-class option, and three for the 12-class option. ISBA-MEB (referred to hereafter simply as MEB) option can be activated for any number of the forest patches. By default, MEB is coupled to the multi-layer soil (DF) (Boone et al., 2000; Decharme et al., 2011) , and snow (ES) schemes (Boone et al., 2001; Decharme et al., 2016) . MEB can also be coupled to the simple 3-layer soil Force-Restore (3-L) option (Boone et al., 1999) in order to be compatible with certain applications which have historically used 3-L, but by default, it is coupled with DF since the objective is to move towards a less conceptual (more explicit process-based) LSM.

A schematic diagram for a maximum illustrating the various resistance pathways for the turbulent fluxes for the three fully (implicitly) coupled surface energy budgets is shown in Fig. 4.17. The water budget prognostic variables are also indicated. There are six aerodynamic resistance, R_a (m s^{-1}), pathways which are indicated in red and defined as being between; i) the non-snow buried vegetation canopy and the canopy air, $R_{a\,vg-c}$, ii) the non-snow buried ground surface (soil or litter) and the canopy air, $R_{a\,g-c}$, iii) the snow surface and the canopy air, $R_{a\,n-c}$, iv) the ground-based snow-covered part of the canopy and the canopy air, $R_{a\,vn-c}$, v) the canopy air with the overlying atmosphere, $R_{a\,c-a}$), and vi) the ground-based snow surface (directly) with the overlying atmosphere, $R_{a\,n-a}$. Previous papers describing ISBA (Noilhan and Planton, 1989; Noilhan and Mahfouf, 1996) expressed heat fluxes using a dimensionless heat and mass exchange coefficient, C_H: however for the new MEB option, it is more convenient to express the different fluxes using resistances (s m^{-1}) which are related to the exchange coefficient as $R_a = 1/\left(V_a\, C_H\right)$.

The surface energy budgets are formulated in terms of prognostic equations for the temperature evolution of the bulk vegetation canopy, T_v, the snow-free ground surface (soil or litter), T_g, and the ground-based snowpack, T_n (K). The prognostic hydrological variables are: the liquid soil volumetric water content, w_g (m^3 m^{-3}), liquid water equivalent volumetric ice content, W_{gf} (m^3 m^{-3}), snow water equivalent (SWE),

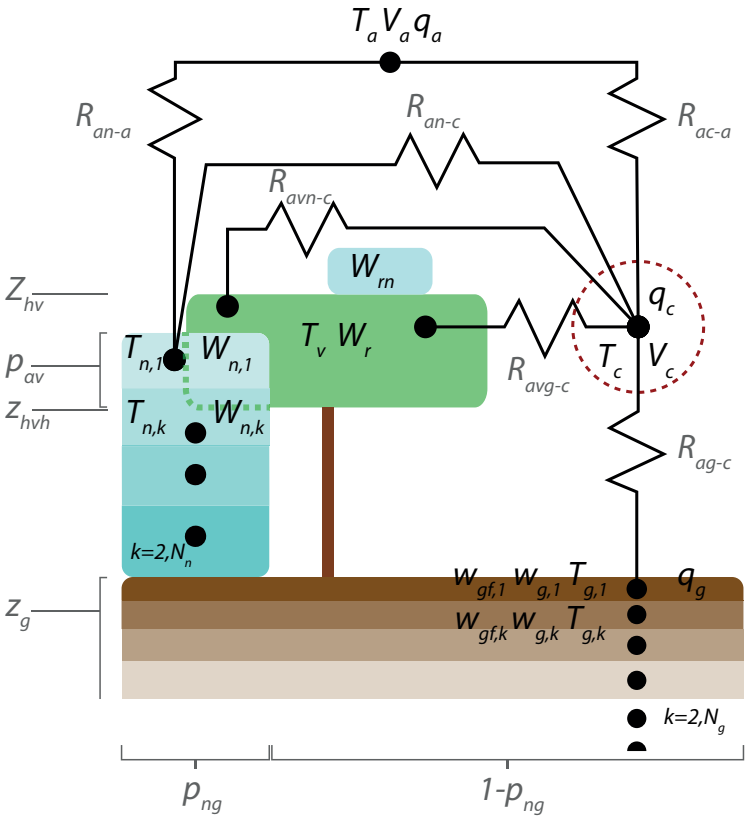

Figure 4.17: A schematic representation of the turbulent aerodynamic resistance, R_a, pathways for ISBA-MEB. The prognostic temperature, liquid water, and liquid water equivalent variables are shown. The canopy air diagnostic variables are enclosed by the red-dashed circle. The ground-based snow pack is indicated using turquoise, the vegetation canopy is shaded green, and ground layers are colored brown. Atmospheric variables (lowest atmospheric model or observed reference level) are indicated using the a subscript. The ground snow fraction, p_{ng} (note, this corresponds to p_{sng} in the text), and canopy-snow-cover fraction, $p_{n\alpha}$, are indicated.

W_n, vegetation canopy intercepted liquid water, W_r, and intercepted snow, W_{rn} (kg m^{-2}). The diagnosed variables which are determined implicitly during the simultaneous solution of the energy budgets are; the surface specific humidity at saturation for each of the three energy budgets, q (kg kg^{-1}), and the canopy air specific humidity, q_c, temperature, T_c and wind speed, V_c (m s^{-1}). The surface snow cover fraction area is represented by p_{sng} as in the (baresoil part of the) composite version of ISBA, while the fraction of the canopy buried by the ground-based snowpack is defined as $p_{\alpha n}$ The snowpack has N_n layers, while the number of soil layers is defined as N_g where k is the vertical index (increasing from 1 at the surface downward). The ground and snowpack uppermost layer temperatures correspond to those used for the surface energy budget (i.e. $k = 1$).

Snow Fractions

The fractional ground coverage by the snowpack, p_{sng}, is defined from Eq. 4.3. The suggested value for the critical snow water equivalent (at which coverage is unity) for MEB is currently $W_{crn} = 1$ (kg m^{-2}). Note that this is considerably lower than the previous value of 10 kg m^{-2} used in ISBA (Douville et al., 1995) , but this value has been shown to improve the ground soil temperatures using an explicit snow scheme within ISBA Brun et al. (2013).
Note that for MEB, the ISBA snow fraction over vegetation, p_{snv} (Eq. 4.1), is not used since it is more consistent with a composite surface. The fraction of the vegetation canopy which is buried by ground-based snow which is deamed to be more consistent with a forest canopy structure is defined as

$$p_{n\alpha} = \frac{(D_n - z_{hv,b})}{(z_{hv} - z_{hv,b})} \qquad (0 \leq p_{n\alpha} \leq 1) \tag{4.221}$$

where D_n is the total ground-based snowpack depth (m), and z_{hvb} represents the base of the vegetation canopy (m) (see Fig. 4.18) which is currently defined as

$$z_{hvb} = a_{hv}\ (z_{hv} - z_{hv,min}) \qquad (z_{hvb} \geq 0) \tag{4.222}$$

where $a_{hv} = 0.2$ and the effective canopy base height is set to $z_{hv,min} = 2$ (m) for forests. The foliage distribution should be reconsidered in further development since literature suggests (e.g. Massman, 1982), that the foliage is not symmetrically distributed in the crown but skewed upward.

Energy Budget

The coupled energy budget equations for a three-source model can be expressed for a single bulk canopy, a ground-based snowpack and a underlying ground surface as

$$\mathcal{C}_v \frac{\partial T_v}{\partial t} = R_{n\,v} - H_v - LE_v + L_f\,\Phi_v \tag{4.223}$$

$$\mathcal{C}_{g,1} \frac{\partial T_{g,1}}{\partial t} = (1 - p_{sng})\,(R_{n\,g} - H_g - LE_g) + p_{sng}\,(G_{gn} + \tau_{n,N_n} SW_{n\,n}) - G_{g,1} + L_f\,\Phi_{g,1} \tag{4.224}$$

$$\mathcal{C}_{n,1} \frac{\partial T_{n,1}}{\partial t} = R_{n\,n} - H_n - LE_n - \tau_{n,1} SW_{n\,n} + \xi_{n,1} - G_{n,1} + L_f\,\Phi_{n,1} \tag{4.225}$$

where $T_{g,1}$ is the uppermost ground (surface soil or litter layer) temperature, $T_{n,1}$ is the surface snow temperature, and T_v is the bulk-canopy temperature (K). Note that the subscript 1 indicates the uppermost layer or the base of the layer (for fluxes) for the soil and snowpack. The ground-based snow fraction is defined as p_{sng}. Note that the terms of Eq. 4.224 are multiplied by p_{sng} to make them patch-relative (or grid-box relative in the case of single-patch mode) since the snow can potentially cover only part of the patch. Within

the snow module itself, the notion of p_{sng} is not used (the computations are snow-relative). But note that when simultaneously solving the coupled equations Eq.s 4.223-4.225, Eq. 4.225 must be multiplied by p_{sng} since snow only covers a fraction of the area to make the snow patch-relative: further details are given in Section 4.1.13.

The phase change terms (freezing less melting: expressed in kg m^{-2} s^{-1}) terms for the snow water equivalent intercepted by the vegetation canopy, the uppermost ground layer, and the uppermost snowpack layer are represented by Φ_v, $\Phi_{g,1}$ and $\Phi_{n,1}$, respectively. L_f represents the latent heat of fusion (J kg^{-1}). The computation of $\Phi_{g,1}$ uses the Gibbs free-energy method (also note that $\Phi_{g,1} = \Phi_{f,1} - \Phi_{m,1}$: see Section 4.1.3), $\Phi_{n,1}$ is based on available liquid for freezing or cold content for freezing (see Section 4.1.7) and Φ_v is described herein (see Eq. 4.339). Note that all of the phase change terms are computed as adjustments to the surface temperatures (after the fluxes have been computed), therefore only the energy storage terms (and not the fluxes) are modified directly by phase changes for each model time step. The last term on the RHS of Eq. 4.225, $\xi_{n,1}$, represents the effective heating or cooling of a snowpack layer caused by exchanges in enthalpy between the surface and sub-surface model layers when the vertical grid is reset (the snow model grid layer thicknesses vary in time).

The surface ground, snow, and vegetation effective heat capacities, $\mathcal{C}_{g,1}$, $\mathcal{C}_v$ and $\mathcal{C}_{n,1}$ (J m^{-2} K^{-1}) are defined, respectively, as

$$\mathcal{C}_{g,1} = \Delta z_{g,1}\, c_{g,1} \tag{4.226}$$

$$\mathcal{C}_v = C_{vb} + C_i\, W_{r,n} + C_w\, W_r \tag{4.227}$$

$$\mathcal{C}_{n,1} = D_{n,1}\, c_{n,1} \tag{4.228}$$

where C_i and C_w are the specific heat capacities for solid (2.106×10^3 J kg^{-1} K^{-1}) and liquid water (4.218×10^3 J kg^{-1} K^{-1}), respectively. The uppermost ground layer thickness is $\Delta z_{g,1}$ (m), and the corresponding heat capacity of this layer is defined as $c_{g\,1}$ (J m^{-3} K^{-1}). There are two options for modeling the thermal properties of the uppermost ground layer. First, they ($c_{g\,1}$ and $\lambda_{g\,1}$) can be defined using the default ISBA configuration for a soil layer with parameters based on soil texture properties which can also incorporate the thermal effects of soil organics (Decharme et al., 2016): see Section 4.3.3. The second option, which is the default when using MEB, is to model the uppermost ground layer as forest litter. This

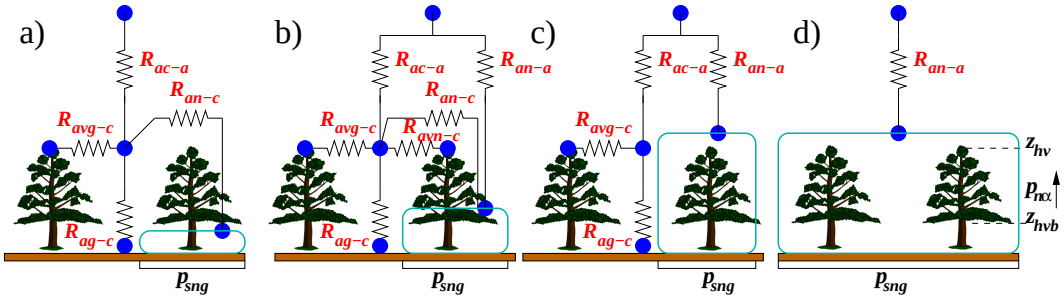

Figure 4.18: A schematic sketch illustrating the role of $p_{n\alpha}$, the fraction of the vegetation canopy which is buried by ground-based snow. In panel a), the snow is well below the canopy base, z_{hvb}, resulting in $p_{n\alpha} = 0$ and the snow has no direct energy exchange with the atmosphere. In panel b), the canopy is partly buried by snow ($0 < p_{n\alpha} < 1$) and the snow has energy exchanges with both the canopy air and the atmosphere. In panel c), the canopy is fully buried by snow ($p_{n\alpha} = 1$) and the snow has energy exchange only with the atmosphere while the soil and canopy only exchange with the canopy air space ($p_{sng} < 1$). Finally, in panel d), both $p_{sng} = 1$ and $p_{n\alpha} = 1$, so that the only exchanges are between the snow and the atmosphere.

means using values of c, λ and Δz which correspond to litter to compute $\mathcal{C}$ in Eq. 4.226 (Napoly et al., 2017): see Section 4.1.9 for details.
The canopy is characterized by low heat capacity which means that its temperature responds fast to changes in fluxes. Thus, to realistically simulate diurnal variations in 2-meter temperature this effect must be accounted for. Sellers et al. (1986) defined the value as being the heat capacity of 0.2 kg m^{-2} of water per unit leaf area index (LAI: m^2 m^{-2}). This results in values on the order of 1×10^4 J m^{-2} K^{-1} for forest canopies in general. For local scale simulations, C_{vb} can be defined based on observational data. In spatially distributed simulations (or when observational data is insufficient), $C_{vb} = 0.2/C_{V,ref}$ where the vegetation thermal inertia, $C_{V,ref}$ is defined as a function of vegetation class by the SURFEX default physiographic database ECOCLIMAP (Faroux *et al.* , 2013). Note that C_V has been determined for the composite soil-vegetation scheme, so the factor 0.2 is used to reduce this value to be more representative of vegetation and on the order of the value discussed by Sellers et al. (1986). Numerical tests have shown that using this value, the canopy heat storage is on the order of 10 W m^{-2} at mid-day for a typical mid-latitude summer day for a forest. The minimum vegetation heat capacity value is limited at 1×10^4 (J m^{-2} K^{-1}) in order to model, in a rather simple fashion, the thermal inertia of stems, branches, trunks, etc. The contributions from intercepted snow and rain are incorporated, where $W_{r,n}$ and W_r (kg m^{-2}) represent the equivalent liquid water content of intercepted canopy snow and liquid water, respectively. The uppermost snow layer thickness is $D_{n,1}$ (m), and the corresponding heat capacity is represented by $c_{n,1}$ (see Section 4.1.7 for details on the explicit snow scheme variables). The numerical solution of the surface energy budget, sub-surface soil and snow temperatures, and the implicit numerical coupling with the atmosphere is described in Appendix 4.1.13.

Turbulent fluxes

In this section, the turbulent heat and water vapor fluxes in Eq.s 4.223-4.225 are described.
The MEB sensible heat fluxes are defined as

$$H_v = \rho_a \frac{(\mathcal{T}_v - \mathcal{T}_c)}{R_{a\,v-c}} \tag{4.229}$$

$$H_g = \rho_a \frac{(\mathcal{T}_g - \mathcal{T}_c)}{R_{a\,g-c}} \tag{4.230}$$

$$H_n = \rho_a \left[(1 - p_{n\alpha}) \frac{(\mathcal{T}_n - \mathcal{T}_c)}{R_{a\,n-c}} + p_{n\alpha} \frac{(\mathcal{T}_n - \mathcal{T}_a)}{R_{a\,n-a}} \right] \tag{4.231}$$

$$H_c = \rho_a \frac{(\mathcal{T}_c - \mathcal{T}_a)}{R_{a\,c-a}} \tag{4.232}$$

$$H = \rho_a \left[(1 - p_{n\alpha}\, p_{sng}) \frac{(\mathcal{T}_c - \mathcal{T}_a)}{R_{a\,c-a}} + p_{n\alpha}\, p_{sng} \frac{(\mathcal{T}_n - \mathcal{T}_a)}{R_{a\,n-a}} \right] \tag{4.233}$$

where ρ_a represents the lowest atmospheric layer average air density (kg m^{-3}). The fluxes between the canopy air space and the vegetation, H_v, the snow-free ground, H_g, and the ground-based snowpack, H_n, appear in the surface energy budget equations (Eq.s4.223-4.225). The sensible heat flux from the ground-based snowpack (Eq. 4.231) is partitioned by the fraction of the vegetation which is buried by the ground-based snowpack, $p_{n\alpha}$, between an exchange between the canopy air space, and the overlying atmosphere (Eq. 4.221). The heat flux between the overlaying atmosphere and the canopy air space is represented by H_c, and it is equivalent to the sum of the fluxes between the different energy budgets and the canopy air space. The total flux exchange between the overlying atmosphere and the surface (as seen by the atmosphere) is defined by H. It is comprised of two components: the heat exchange between the overlying atmosphere and the canopy air space and the part of the ground-based snowpack which is burying the vegetation. The

ground-based snowpack heat flux, H_n (Eq. 4.231), can be split into a part which modulates the heat exchange with the canopy air space, H_{n-c} and the other part which controls the exchanges directly with the overlying atmosphere, H_{n-a}, defined as

$$H_{n-c} = \rho_a \frac{(\mathcal{T}_n - \mathcal{T}_c)}{R_{a\,n-c}} \tag{4.234}$$

$$H_{n-a} = \rho_a \frac{(\mathcal{T}_n - \mathcal{T}_a)}{R_{a\,n-a}} \tag{4.235}$$

$\mathcal{T}_c$ is diagnosed by imposing conservation of the heat fluxes between the surface and the canopy air (As described in Appendix 4.1.13). Using the definition in Eq. 4.235, the total sensible heat flux exchange with the atmosphere (Eq. 4.233) can also be written in more compact form as

$$H = \rho_a \left[(1 - p_{sng}\, p_{n\alpha})\; H_c \;+\; p_{sng}\, p_{n\alpha}\, H_{n-a} \right] \tag{4.236}$$

Finally, the final fluxes for the given patch are aggregated using p_{sng} and $p_{n\alpha}$.

The total canopy aerodynamic resistance is comprised of snow-buried, $R_{a\,vn-c}$, and non-snow buried, $R_{a\,vg-c}$, resistances from

$$R_{a\,v-c} = \left[\frac{(1 - p_{n\alpha})\; p_{sng}}{R_{a\,vn-c}} \;+\; \frac{(1 - p_{sng})}{R_{a\,vg-c}} \right]^{-1} \tag{4.237}$$

The separation of the resistances is done to mainly account for differences in the roughness length between the buried and non-covered parts of the vegetation canopy, so the primary effect of snow cover is to increase the resistance relative to a snow-free surface assuming the same temperature gradient owing to a lower surface roughness, thus $R_{a\,vn-c} \geq R_{a\,vg-c}$. The formulation also provides a continuous transition to the case of vanishing canopy turbulent fluxes as the canopy becomes entirely buried (as $p_{n\alpha} \to 1$). In this case, the energy budget equations collapse into a simple coupling between the snow surface and the overlying atmosphere, and the ground energy budget is simply consists in heat conduction between the ground surface and the snowpack base. The formulations of the resistances between the different surfaces and the canopy airspace and the overlying atmosphere are described in detail in Sect. 4.1.9. The canopy air temperature, which is needed by different physics routines, is diagnosed by combining Eq. s4.229-4.233 and solving for $\mathcal{T}_c$ and using Eq. 4.238 to determine T_c (see Eq. 4.401).

The thermodynamic variable ($\mathcal{T}$: J kg^{-1}) is linearly related to temperature as

$$\mathcal{T}_x = \mathcal{B}_x \;+\; \mathcal{A}_x\, T_x \tag{4.238}$$

where x corresponds to one of the three surface temperatures, canopy air temperature, T_c, or the overlying atmospheric temperature, T_a. The definitions of $\mathcal{A}_x$ and $\mathcal{B}_x$ depend on the atmospheric variable in the turbulent diffusion scheme and are usually defined to cast $\mathcal{T}$ in the form of dry static energy, or potential temperature and are determined by the atmospheric model in coupled mode. If potential temperature is used as the thermodynamic variable in the coupled model diffusion scheme, then the thermodynamic variable coefficients are defined as

$$\mathcal{B}_x = 0 \qquad (x = v, g, n, c, a) \tag{4.239}$$

$$\mathcal{A}_x = C_p/\Pi_s \qquad (x = v, g, n, c) \tag{4.240}$$

$$\mathcal{A}_a = C_p/\Pi_a \tag{4.241}$$

where Π is the non-dimensional Exner function and C_p is the heat capacity of dry air (J kg^{-1} K^{-1}). If the atmospheric variable being diffused is dry static energy then

$$\mathcal{B}_x = 0 \qquad (x = v, g, n, c) \tag{4.242}$$

$$\mathcal{B}_a = g\, z_a \tag{4.243}$$

$$\mathcal{A}_x = C_p \qquad (x = v, g, n, c, a) \tag{4.244}$$

where z_a is the height (m) of the simulated or observed overlying atmospheric temperature, T_a and g is the gravitational constant. The choice of the atmospheric thermodynamic variable is transparent to ISBA-MEB (it is made within the surface-atmosphere coupler). The default (in offline mode and in in-line mode with certain atmospheric models) is using Eq.s 4.239-4.241. Note that the method can be extended to use the actual air heat capacity (including water vapor) if a linearization of the heat capacity is used.
The MEB water vapor fluxes are expressed as

$$E_v = \rho_a\, h_{sv}\, \frac{(q_{sat\,v} - q_c)}{R_{a\,v-c}} \tag{4.245}$$

$$E_g = \rho_a\, \frac{(q_g - q_c)}{R_{a\,g-c}} \tag{4.246}$$

$$E_n = \rho_a\, h_{sn} \left[(1 - p_{n\alpha})\, \frac{(q_{sati\,n} - q_c)}{R_{a\,n-c}} + p_{n\alpha}\, \frac{(q_{sati\,n} - q_a)}{R_{a\,n-a}} \right] \tag{4.247}$$

$$E_c = \rho_a\, \frac{(q_c - q_a)}{R_{a\,c-a}} \tag{4.248}$$

$$E = \rho_a \left[(1 - p_{n\alpha}\, p_{sng})\, \frac{(q_c - q_a)}{R_{a\,c-a}} + p_{n\alpha}\, p_{sng}\, h_{sn}\, \frac{(q_{sati\,n} - q_a)}{R_{a\,n-a}} \right] \tag{4.249}$$

where, in an analogous fashion to the sensible heat flux, the vapor flux between the canopy air space and the vegetation canopy, E_v, the snow-free ground, E_g, and the ground-based snowpack, E_n, correspond to the fluxes in the surface energy budgets (Eq.s 4.223-4.225). The vapor flux between the canopy air and the overlying atmosphere is represented by E_c, and the total vapor flux exchanged with the overlying atmosphere is defined as E. The specific humidity (kg kg^{-1}) of the overlying atmosphere is represented by q_a, while q_{sat} and q_{sati} represent the specific humidity at saturation over liquid water and ice, respectively. For the surface specific humidities at saturation, the convention $q_{sat\,x} = q_{sat}\,(T_x)$ is used. The canopy air specific humidity, q_c, is diagnosed assuming that E_c is balanced by the vapor fluxes between the canopy air and each of the three surfaces considered (the methodology for diagnosing the canopy air thermal properties is described in Appendix 4.1.13, Section 4.1.13). The effective ground specific humidity is defined as

$$q_g = h_{sg}\, q_{sat\,g} + (1 + h_a)\, q_c \tag{4.250}$$

where the so-called humidity factors are defined as

$$h_{sg} = \delta_g\, h_{ug}\, (1 - \delta_i) \left(\frac{L_v}{L} \right) + \delta_{gf}\, h_{ugf}\, \delta_i \left(\frac{L_s}{L} \right) \tag{4.251}$$

$$h_a = \delta_g\, (1 - \delta_i) \left(\frac{L_v}{L} \right) + \delta_{gf}\, \delta_i \left(\frac{L_s}{L} \right) \tag{4.252}$$

The fraction of the surface layer which is frozen, δ_i, is simply defined as the ratio of the liquid water equivalent ice content to the total water content (Eq. 4.193).
The latent heats of sublimation and vaporization are defined as L_s and L_v (J kg^{-1}), respectively. The average latent heat, L, is essentially a normalization factor which ranges between L_s and L_v as a function

of snow cover and surface soil ice. It could be determined in a number of ways. This coefficient ensures conservation of mass between the different surfaces and the atmosphere. One possible method is to diagnose it by inverting the equation for LE_c (multiplying Eq. 4.403 by L thereby eliminating it from the RHS of this equation, and then solving for L), but the resulting equation is difficult to apply since the terms can be either positive or negative, and division by a small number is possible. Here, a more smooth (in time) function is proposed which accounts for each of the surfaces weighted by it's respective fraction:

$$L = \frac{a_{Ls}\, L_s \,+\, a_{Lv}\, L_v}{a_{Ls} \,+\, a_{Lv}} \tag{4.253}$$

where

$$a_{Lv} = \left[\sigma_{f\,LW}\ (1 - p_{nv}) \,+\, (1 - p_{sng})\,(1 - \delta_i)\right](1 - p_{sng} p_{n\alpha}) \tag{4.254a}$$

$$a_{Ls} = \left[\sigma_{f\,LW}\, p_{nv} \,+\, (1 - p_{sng})\ \delta_i \,+\, p_{sng}\right](1 - p_{sng} p_{n\alpha}) \,+\, p_{sng} p_{n\alpha} \tag{4.254b}$$

In the limit as the snow totally buries the canopy vegetation, $L \rightarrow L_s$. In contrast, for snow and surface ice free conditions, $L = L_v$. $\sigma_{f\,LW}$ is a normalized non-dimensional coefficient related to vegetation density (see Eq. 4.298).

The soil coefficient δ_g in Eq.s 4.251-4.252 is defined as

$$\delta_g = \left(\frac{R_{a\,g-c}}{R_{a\,g-c} \,+\, R_g}\right) \delta_{gcor} \tag{4.255}$$

where the soil resistance, R_g, is defined by Eq. 4.323. Note that the composite version of ISBA did not include an explicit soil resistance term, so this also represents a new addition to the model. This term was found to further improve results for baresoil evaporation within MEB, and it's inclusion is consistent with other similar multi-source models (e.g. Xue et al., 1991). The delta function, δ_{gcor}, is a numerical correction term which is required owing to the linearization of $q_{sat\,g}$ and is unity unless both $h_{ug}\, q_{sat\,g} < q_c$ and $q_{sat\,g} > q_c$, in which case it is set to zero. The surface ground humidity factor is defined using the standard ISBA formulation from Noilhan and Planton (1989). Note that it would be more accurate to use q_{sati} in place of q_{sat} for the sublimation of the canopy-intercepted snow and the soil ice in Eq.s 4.245-4.246, respectively, but this complicates the linearization and this has been neglected for now. The snow factor is defined as $h_{sn} = L_s/L$. This factor can be modified so that E_n includes both sublimation and evaporation (Boone and Etchevers, 2000), but the impact of including a liquid water flux has been found to be negligible thus for simplicity, only sublimation is accounted for currently.

The leading coefficient for the canopy evapotranspiration is defined as

$$h_{sv} = (1 - p_{nv})\, h_{svg}\ (L_v/L) \,+\, p_{nv}\, h_{svn}\ (L_s/L) \tag{4.256}$$

where p_{nv} is defined by Eq. 4.335). When part of the vegetation canopy is buried (i.e. $p_{n\alpha} > 0$), a different roughness and LAI are felt by the canopy air space so that a new resistance is computed over the $p_{n\alpha}$ covered part of the canopy as is done for sensible heat flux. This is accounted for by defining

$$h_{svg} = p_{sng}\,(1 - p_{n\alpha})\ \left(\frac{R_{a\,v-c}}{R_{a\,vn-c}}\right) h_{vn} \,+\, (1 - p_{sng})\left(\frac{R_{a\,v-c}}{R_{a\,vg-c}}\right) h_{vg} \tag{4.257a}$$

$$h_{svn} = p_{sng}\,(1 - p_{n\alpha})\ \left(\frac{R_{a\,v-c}}{R_{a\,vn-c}}\right) \,+\, (1 - p_{sng})\left(\frac{R_{a\,v-c}}{R_{a\,vg-c}}\right) \tag{4.257b}$$

The so-called Halstead coefficients in Eq. 4.257a are defined as

$$h_{vg} = \left(\frac{R_{a\,vg-c}}{R_{a\,vg-c} + R_s}\right)(1 - \delta) + \delta \tag{4.258a}$$

$$h_{vn} = \left(\frac{R_{a\,vn-c}}{R_{a\,vn-c} + R_{sn}}\right)(1 - \delta) + \delta \ , \tag{4.258b}$$

The stomatal resistance, R_s, can be computed using either the so-called Jarvis method or the more physically based ISBA-Ag-s method (the current default is AST: see Section 4.2.1). The stomatal resistance for the partially snow-buried portion defined as

$$R_{sn} = R_s / \left[1 - \min\left(p_{n\alpha},\ 1 - R_s/R_{s,max}\right)\right] \qquad (R_{sn} \leq R_{s,max}) \tag{4.259}$$

so that the effect of coverage by the snowpack is to increase the canopy resistance. Note that when the canopy is not partially or fully buried by ground based snowpack ($p_{n\alpha} = 0$) and does not contain any intercepted snow ($p_{nv} = 0$), the leading coefficient for the canopy evapotranspiration simplifies to the same form as the Halstead coefficient from the composite version of ISBA (h_v: Eq. 4.196) as

$$h_{sv} = \left(\frac{R_{a\,vg-c}}{R_{a\,vg-c} + R_s}\right)(1-\delta) + \delta \qquad (p_{n\alpha} = 0 \text{ and } p_{nv} = 0) \tag{4.260}$$

The fraction of the vegetation covered by water is δ and is described in Sect. 4.1.9.
The evapotranspiration from the vegetation canopy, E_v, is comprised of three components:

$$E_v = E_{tr} + E_r + E_{rn} \tag{4.261}$$

where the transpiration, evaporation from the canopy liquid water interception store and sublimation from the canopy snow interception store are represented by E_{tr}, E_r, and E_{rn}, respectively. Using the definitions in Eq.s 4.256-4.258b, the components of E_v can be expressed as 1

$$E_{tr} = \rho_a \left(\frac{L_v}{L}\right)(q_{sat\,v} - q_c)\left[\frac{p_{sng}\,(1-p_{n\alpha})}{R_{a\,vn-c} + R_{sn}} + \frac{1-p_{sng}}{R_{a\,vg-c} + R_s}\right](1-p_{nv})\,(1-\delta) \tag{4.262}$$

$$E_r = \rho_a \left(\frac{L_v}{L}\right)(q_{sat\,v} - q_c)\left[\frac{p_{sng}\,(1-p_{n\alpha})}{R_{a\,vn-c}} + \frac{1-p_{sng}}{R_{a\,vg-c}}\right](1-p_{nv})\,\delta \tag{4.263}$$

$$E_{rn} = \rho_a \left(\frac{L_s}{L}\right)(q_{sat\,v} - q_c)\left[\frac{p_{sng}\,(1-p_{n\alpha})}{R_{a\,vn-c}} + \frac{1-p_{sng}}{R_{a\,vg-c}}\right]p_{nv} \tag{4.264}$$

The complex resistances (bracketed terms in Eq.s 4.262-4.264) arise owing to the inclusion of the effects of burying the snow canopy by the ground based snowpack. If the ground-based snowpack is not sufficiently deep to bury any of the canopy ($p_{n\alpha} = 0$), then the bracketed term in Eq. 4.262 simplifies to $1/\left(R_{a\,vg-c} + R_s\right)$ (note that $R_{a\,vg-c} = R_{a\,v-c}$ when $p_{n\alpha} = 0$ from Eq. 4.237), and likewise the bracketed terms in Eq.s 4.263-4.264 simplify to $1/R_{a\,vg-c}$. Finally, the partitioning between the vapor fluxes from intercepted snow and the snow-free canopy reservoir and transpiration is done using p_{nv}.
Using the definitions of q_g from Eq. 4.250 together with those for the humidity factors, h_{sg} and h_a (Eq.s 4.251 and 4.252, respectively) and the soil coefficient, δ_g (Eq. 4.255), the bare soil evaporation, E_g, components can be expressed as

$$E_{gl} = \rho_a \left(\frac{L_v}{L}\right)(h_{ug}\,q_{sat\,g} - q_c)\left(\frac{\delta_{gcor}}{R_{a\,g} + R_g}\right)(1-\delta_i) \tag{4.265}$$

$$E_{gf} = \rho_a \left(\frac{L_s}{L}\right)(h_{ugf}\,q_{sat\,g} - q_c)\left(\frac{\delta_{gfcor}}{R_{a\,g} + R_{gf}}\right)\delta_i \tag{4.266}$$

where $E_g = E_{gl} + E_{gf}$. The delta function, δ_{gfcor}, is a numerical correction term which is required owing to the linearization of $q_{sat\,g}$ and is unity unless both $h_{ugf}\,q_{sat\,g} < q_c$ and $q_{sat\,g} > q_c$, in which case it is set to zero. Note that the ground resistances, R_g and R_{gf}, are set to zero if the forest litter option is active (the default for forests).

The ground-based snowpack sublimation, E_n (Eq. 4.247), can be partitioned into a vapor exchange with the canopy air space, E_{n-c} and the overlying atmosphere, E_{n-a}, as

$$E_{n-c} = \rho_a \left(\frac{L_s}{L}\right) \left(\frac{q_{sat\,i\,n} - q_c}{R_{a\,n-c}}\right) \tag{4.267}$$

$$E_{n-a} = \rho_a \left(\frac{L_s}{L}\right) \left(\frac{q_{sat\,i\,n} - q_a}{R_{a\,n-a}}\right) \tag{4.268}$$

The corresponding latent heat fluxes can be determined by simply multiplying Eq. 4.262-4.266 by L. Finally, using the definition in Eq. 4.268, the total vapor exchange with the atmosphere (Eq. 4.249) can also be written in more compact form as

$$E = \rho_a \left[(1 - p_{sng}\, p_{n\alpha})\; E_c \;+\; p_{sng}\, p_{n\alpha}\, E_{n-a}\right] \tag{4.269}$$

Radiative fluxes

The R_n terms in Eq.s 4.223-4.225 represent the surface net radiation terms (longwave and shortwave components):

$$R_{n\,x} = SW_{net,x} \;+\; LW_{net,x} \tag{4.270}$$

where $x = n, g$ or v. The total net radiation of the surface is

$$R_n = R_{n\,n} \;+\; R_{n\,g} \;+\; R_{n\,v} \;=\; SW\downarrow - SW\uparrow + LW\downarrow - LW\uparrow \tag{4.271}$$

where the total down-welling solar (shortwave) and atmospheric (longwave) radiative fluxes (W m^{-2}) at the top of the canopy or snow surface (in the case snow is burying the vegetation) are represented by $SW\downarrow$ and $LW\downarrow$, respectively. The total upwelling (towards the atmosphere) shortwave and longwave radiative fluxes, $SW\uparrow$ and $LW\uparrow$, respectively, are simply defined as the downward components less the total surface net radiative fluxes (summed over the three surfaces). The effective total surface albedo and surface radiative temperature (and emissivity) can then be diagnosed for coupling with the host atmospheric model. The τ_n is defined as the solar radiation transmission at the base of a snowpack layer, so that $\tau_{n,1} SW_{n\,n}$ term in Eq. 4.225 corresponds the amount of shortwave radiation which is not absorbed in the uppermost snowpack layer. For sufficiently thin snowpack, solar energy penetrating the snow to the underlying ground surface is expressed as $\tau_{n,N_n} SW_{n\,n}$, where N_n represents the number of modeled snowpack layers (for a deep snowpack, this term becomes negligible).
The total land surface shortwave energy budget can be shown to satisfy

$$SW\downarrow = SW_{net\,g} + SW_{net\,v} + SW_{net\,n} + SW\uparrow \tag{4.272}$$

where $SW_{net\,g}$, $SW_{net\,v}$, $SW_{net\,n}$ represent the net shortwave terms for the ground, vegetation canopy and the ground-based snowpack. The effective surface albedo (which may be required by the atmospheric radiation scheme or for comparison with satellite-based data etc.) is diagnosed as

$$\overline{\alpha}_s = SW\uparrow / SW\downarrow \tag{4.273}$$

The distinction between the visible (VIS) and near-infrared (NIR) radiation components is important in terms of interactions with the vegetation canopy. The shortwave radiation scheme in ISBA-MEB is described by Carrer et al. (2013) (hereafter refered to as CEA13 in this section): it is the radiative scheme used for ISBA-Ags applications for photosynthesis. Note that when using MEB, it is also used for energy budget computations for increased consistency.

The CEA13 scheme requires the vegetation and surface albedos for 2 spectral bands (visible, VIS, and near-infrared, NIR) The VIS wavelengths range from approximately 0.3 to 0.7 $\times 10^{-6}$ m, and NIR wavelengths range from approximately 0.7 to 1.4 $\times 10^{-6}$ m. The vegetation albedos, $\alpha_{v,VIS}$, $\alpha_{v,NIR}$, and the baresoil albedos, $\alpha_{g,VIS}$, $\alpha_{g,NIR}$, are provided by ECOCLIMAP or prescribed within the namelist file. For MEB, the snow free surface is either baresoil or litter, which is assumed for now, to have the same albedo as the soil. MEB is, by default, coupled to the ISBA-ES snow scheme which includes 3 spectral bands for the snow albedo (VIS, NIR and UV): the corresponding albedo values for each band are diagnosed from the prognostic snow age variable as discussed in Decharme *et al.* (2016). Since CEA13 and therefore MEB currently only considers 2 spectral bands for the soil and vegetation, the snow albedo components for the VIS and NIR bands are used within MEB: this can be changed in the future as MEB is more or less transparent to this (it would mean updating the CEA13 scheme). The snow VIS band albedo is used as-is, while the snow NIR albedo is simply computed as

$$\alpha_{n,NIR} = \frac{(\alpha_n - \omega_{VIS}\,\alpha_{n,VIS})}{\omega_{NIR}} \tag{4.274}$$

where α_n is the all-wavelength snow albedo, and the usual spectral weights $\omega_{VIS} = 0.48$ and $\omega_{NIR} = 0.52$ are used. The snow albedos are time-varying and are diagnosed at each time step based on a snow age variable as discussed in Decharme *et al.* (2016). The effective surface albedo required by CEA13 is represented by the aggregatating the snow and baresoil albedo contributions weighted by the ground snow cover fraction, p_{sng}. The effective surface albedo, $\overline{\alpha}_{gn}$, components are then defined as

$$\overline{\alpha}_{gn,VIS} = p_{sng}\,\alpha_{n,VIS} + (1 - p_{sng})\,\alpha_{g,VIS} \tag{4.275}$$

$$\overline{\alpha}_{gn,NIR} = p_{sng}\,\alpha_{n,NIR} + (1 - p_{sng})\,\alpha_{g,NIR} \tag{4.276}$$

CEA13 computes the absortion of the shortwave radiation, SW_{net}, for the vegetation and soil as

$$SW_{net,v} = \omega_{VIS} SW_{net,v,VIS} + \omega_{NIR} SW_{net,v,NIR} \tag{4.277}$$

$$SW_{net,g} = \omega_{VIS} SW_{net,g,VIS} + \omega_{NIR} SW_{net,g,NIR} \tag{4.278}$$

The multi-level transmission computations for direct and diffuse radiation are made, and the sum of the absorbed radiaton is $SW_{net\,v}$. The details of these computations are given by Carrer et al. (2013).
The effective all-wavelength surface (below-canopy) albedo is defined as

$$\overline{\alpha}_{gn} = \omega_{VIS}\,\overline{\alpha}_{gn,VIS} + \omega_{NIR}\,\overline{\alpha}_{gn,NIR} \tag{4.279}$$

which upon substitution of Eq.s 4.275-4.276. can also be expressed as

$$\overline{\alpha}_{gn} = p_{sng}\,\alpha_n + (1 - p_{sng})\,\alpha_g \tag{4.280}$$

where the all-wavelength albedo for the snow, α_n, and the ground, α_g, are computed using the same spectral weighting. Note that the flooded fraction of the gridbox uses a ground-flooded zone composite energy budget, so to consider water surfaces the effective snow-free ground would need to be modified to include the surface water albedo: this will be done in future versions of SURFEX.
The net solar radiation at the surface assumes one reflection from the vegetation back to the ground or snow surface and is defined as

$$SW_{net\,n} = p_{sng}\;SW\downarrow\, T_r\,[1 - \alpha_n + \overline{\alpha}_{gn}\,\overline{\alpha}_v\,(1 - T_r)]\,(1 - \tau_{n,N_n}) \tag{4.281}$$

$$SW_{net\,g} = (1 - p_{sng})\;SW\downarrow\, T_r\,[1 - \alpha_g + \overline{\alpha}_{gn}\,\overline{\alpha}_v\,(1 - T_r)] + p_{sng}\;SW\downarrow\, T_r\,[1 - \alpha_n + \overline{\alpha}_{gn}\,\overline{\alpha}_v\,(1 - T_r)]\,\tau_{n,N_n} \tag{4.282}$$

where T_r (dimensionless: bound between 0 and 1) represents the fraction of the incoming radiation transmitted through the canopy from the multi-level vegetation radiative transfer scheme. It depends strongly on the vegetation density via the pontentially snow-buried LAI_n (see Eq. 4.299). At this point we define the energy absorbed at the snow surface (see the surface energy budget equations: Eq.s 4.224-4.225) as

$$SW_{n\,n} = SW \downarrow T_r \left[1 - \alpha_n + \overline{\alpha}_{gn}\, \overline{\alpha}_v \left(1 - T_r\right)\right] \tag{4.283}$$

Note that the total surface net shortwave energy is obtained by summing Eq.s 4.281 and 4.282 resulting in simply

$$SW_{net\,s} \;=\; SW_{net\,n} + SW_{net\,g} \;=\; SW \downarrow T_r \left\{1 - \overline{\alpha}_{gn} \left[1 - \alpha_v \left(1 - T_r\right)\right]\right\} \tag{4.284}$$

If we assume that none of the shortwave radiation arriving at the snow surface is transmitted to the ground (for sufficinetly deep snowpack, which is often the case), Eq.s 4.281-4.282 simply to

$$SW_{net\,n} \;=\; p_{sng}\; SW \downarrow T_r \left[1 - \alpha_n + \overline{\alpha}_{gn}\, \overline{\alpha}_v \left(1 - T_r\right)\right] \;=\; p_{sng}\, SW_{n\,n} \tag{4.285}$$

$$SW_{net\,g} \;=\; \left(1 - p_{sng}\right)\; SW \downarrow T_r \left[1 - \alpha_g + \overline{\alpha}_{gn}\, \overline{\alpha}_v \left(1 - T_r\right)\right] \tag{4.286}$$

Note that for snow-free conditions, $SW_{net\,n} = 0$, $\overline{\alpha}_{gn} = \alpha_g$, and $\overline{\alpha}_v = \alpha_v$, and so that

$$SW_{net\,g} \;=\; SW \downarrow T_r \left\{1 - \alpha_g \left[1 - \alpha_v \left(1 - T_r\right)\right]\right\} \tag{4.287}$$

so in this case, as $LAI \rightarrow 0$, $T_r \rightarrow 1$ so that $SW_{net\,g} \rightarrow SW \downarrow (1 - \alpha_g)$ thus the net radiation collapses in the limit of vanishing vegetation to that of a baresoil patch. If the surface is totally snow covered and the vegetation is totally buried by snow, then $\overline{\alpha}_{gn} = \alpha_n$, and the ground net shortwave energy is simply $SW_{net\,g} = \tau_{n,N_n} SW \downarrow (1 - \alpha_n)$ and the surface net shortwave energy is $SW_{net} = SW_{net\,n} = SW \downarrow (1 - \alpha_n)\left(1 - \tau_{n,1}\right)$. Note that the total effective albedo (when averaged over daylight hours) is bounded by the maximum and minimum of the prescribed soil and vegetation and prognostic snow all-wavelength albedos.

The effective canopy albedo, $\overline{\alpha}_v$, represents the combined canopy vegetation, α_v, and intercepted snow albedos. Currently, however, we assume that $\overline{\alpha}_v = \alpha_v$ which is based on recommendations by (Pomeroy et al., 1996). They showed that multiple reflections and scattering of light from patches of intercepted snow together with a high probability of reflected light reaching the underside of an overlying branch implied that trees actually act like light traps. Thus, they concluded that intercepted snow had no significant influence on the short-wave albedo or the net radiative exchange of Boreal conifer canopies.

In addition to baseline albedo values required by the radiative transfer model for each spectral band, the model requires the direct and diffusive downwelling solar components. The diffuse fraction can be provided by observations (offline mode) or a host atmospheric model. For the case when no diffuse information is provided to the surface model, the diffuse fraction is computed using the method proposed by Erbs et al. (1982).

The longwave radiation scheme is based on a representation of the vegetation canopy as a plane-parallel surface. The total land surface longwave energy budget can be shown to satisfy

$$LW \downarrow = LW_{net\,g} + LW_{net\,v} + LW_{net\,n} + LW \uparrow \tag{4.288}$$

where $LW_{net\,g}$, $LW_{net\,v}$, $LW_{net\,n}$ represent the net longwave terms for the ground, vegetation canopy and the ground-based snowpack.

The model considers one reflection with three reflecting surfaces (ground, ground-based snowpack and the vegetation canopy: a schematic is shown in Fig. 4.19. The net longwave radiation for the under-story,

snowpack and vegetation canopy are therefore defined, respectively, as

$$LW_{net\,g} = C_g + F_g + J_g + J_n - D_g - G_g - I_g \tag{4.289a}$$

$$LW_{net\,n} = C_n + F_n + K_n + K_g - D_n - G_n - I_n \tag{4.289b}$$

$$\begin{aligned} LW_{net\,v} = & A_g + D_g + G_g + I_g + A_n + D_n + G_n + I_n \\ & - B_g - C_g - E_g - H_g - 2F_g - J_g - L_g - K_g \\ & - B_n - C_n - E_n - H_n - 2F_n - J_n - L_n - K_n \end{aligned} \tag{4.289c}$$

where the upwelling longwave radiation is computed from

$$LW\uparrow = LW\downarrow - LW_{net\,g} - LW_{net\,n} - LW_{net\,v} \tag{4.290}$$

The effective surface radiative temperature (which may be required by the atmospheric radiation scheme or for comparison with satellite-based data etc.) is diagnosed as

$$T_{rad} = \left[\frac{LW\uparrow - LW\downarrow (1 - \overline{\epsilon}_s)}{\overline{\epsilon}_s\, \sigma} \right]^{1/4} \tag{4.291}$$

where σ is the Stefan-Boltzmann constant, and $\overline{\epsilon}_s$ represents the effective surface emissivity. In Eq. 4.291, there are two knowns (LW fluxes) and two unknowns (T_{rad} and $\overline{\epsilon}_s$). Here we opt to pre-define $\overline{\epsilon}_s$ in a manner which is consistent with the various surface contributions as

$$\overline{\epsilon}_s = p_{sng}\, \overline{\epsilon}_{sn} + (1 - p_{sng})\, \overline{\epsilon}_{sg} \tag{4.292}$$

The canopy-absorption weighted effective snow and ground emissivities are defined, respecitvely, as

$$\overline{\epsilon}_{sn} = \overline{\sigma}_{n\,LW}\, \epsilon_v + (1 - \overline{\sigma}_{n\,LW})\, \epsilon_n \tag{4.293}$$

$$\overline{\epsilon}_{sg} = \overline{\sigma}_{g\,LW}\, \epsilon_v + (1 - \overline{\sigma}_{g\,LW})\, \epsilon_g \tag{4.294}$$

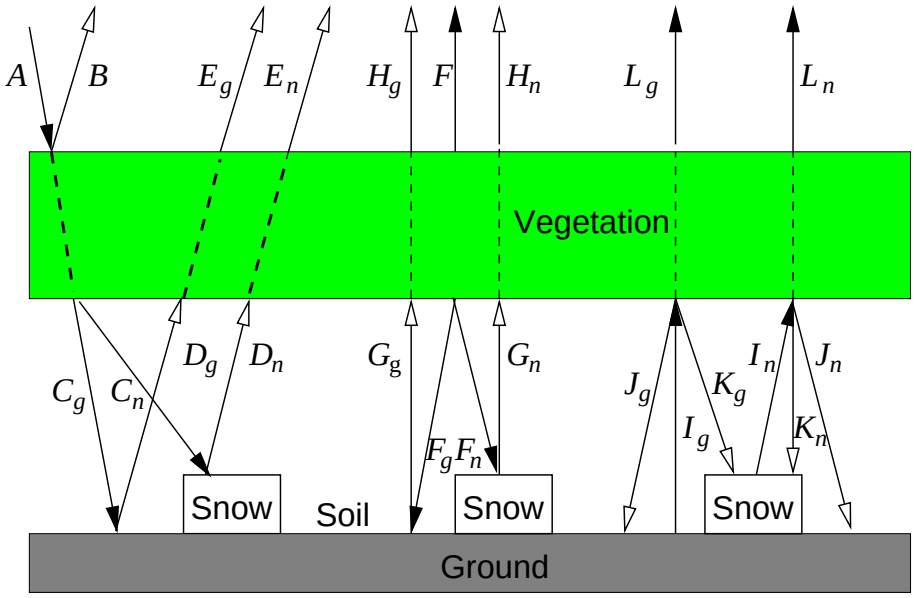

Figure 4.19: Simple schematic for longwave radiation transfer for one reflection and up to three emitting surfaces (in addition to the down-welling atmospheric flux). Hollow arrows indicate fluxes after one reflection.

where ϵ_v, ϵ_g and ϵ_n represent the emissivities of the vegetation, snow-free ground and the ground-based snowpack, respectively. The ground and vegetation emissivities are given by ECOCLIMAP for spatially distributed simulations, or they can be prescribed for local scale studies. The snow emissivity is currently defined as $\epsilon_n = 0.99$. The effect of longwave absorption through the non-snow buried part of the vegetation canopy is included as

$$\overline{\sigma}_{n\,LW} = [1 - p_{sng} - p_{n\alpha}\,(1 - p_{sng})]\,\sigma_{LW} + [p_{sng} + p_{n\alpha}\,(1 - p_{sng})]\,\sigma_{f\,LW} \tag{4.295}$$

$$\overline{\sigma}_{g\,LW} = [1 - p_{sng}\,(1 - p_{n\alpha})]\,\sigma_{LW} + p_{sng}\,(1 - p_{n\alpha})\,\sigma_{f\,LW} \tag{4.296}$$

where the canopy absorption is defined as

$$\sigma_{LW} = 1 - \exp\left(-\tau_{LW}\,LAI\right) = 1 - \chi_v \tag{4.297}$$

and τ_{LW} represents a longwave radiation transmission factor which can be species (or land classification) dependent, and χ_v is defined as a vegetation view factor. The absorption over the under-story snow-covered fraction of the grid box is modeled quite simply from Eq. 4.297 as

$$\sigma_{f\,LW} = 1 - \exp\left[-\tau_{LW}\,LAI_n\right] \tag{4.298}$$

so that transmission is unity (no absorption or reflection by the canopy: $\overline{\sigma}_{LW} = \sigma_{f\,LW} = 0$) when $p_{n\alpha} = 1$ (i.e. when the canopy has been buried by snow). LAI_n is used to represent the LAI which has been reduced owing to burial by the snowpack and is simply defined as:

$$LAI_n = LAI\,(1 - p_{n\,\alpha}) \tag{4.299}$$

From Eq.s 4.292-4.296, it can be seen that when there is no snowpack (i.e. $p_{sng} = 0$ and $p_{n\alpha} = 0$), then the effective surface emissivity is simply an absorption-weighted soil-vegetation value defined as $\overline{\epsilon}_s = \sigma_{LW}\,\epsilon_v + (1 - \sigma_{LW})\,\epsilon_g$.

The complete expression for the vegetation canopy net longwave radiation with an infinite number of reflections can be expressed as a series expansion (e.g. Braud, 2000) as a function of the temperatures of the emitting surfaces (T_v, $T_{g,1}$, $T_{n,1}$), their respective emissivities (ϵ_v, ϵ_g and ϵ_n) and the canopy longwave absorption function, σ_{LW} (Eq. 4.297). The MEB expressions are derived by explicitly expanding the series and assuming one reflection from each emitting source, which is a good approximation since emissivities are generally close to unity (fluxes from a single reflection are proportional to $1 - \epsilon_x$ where x represents g, v or n, and ϵ is close to unity for most natural surfaces).

Snow is considered to be intercepted by the vegetation canopy and to accumulate on the ground below. The canopy-intercepted snow is treated using a composite approach, so that the canopy temperature, T_v, represents the effective temperature of the canopy-intercepted snow composite. The canopy emissivity is therefore simply defined as

$$\overline{\epsilon}_v = (1 - p_{nv})\,\epsilon_v + p_{nv}\,\epsilon_n \tag{4.300}$$

In order to facilitate the use of a distinct multi-layer snow process scheme, we split the fluxes between those

interacting with the snowpack and the snow-free ground. The expressions for the snow-free surface are

$$A_g = LW\downarrow\ (1 - p_{sng}) \tag{4.301a}$$
$$B_g = A_g\, \sigma_{LW}\ (1 - \overline{\epsilon}_v) \tag{4.301b}$$
$$C_g = A_g\ (1 - \sigma_{LW}) \tag{4.301c}$$
$$D_g = C_g\ (1 - \epsilon_g) \tag{4.301d}$$
$$E_g = D_g \left(1 - \sigma'_{LW}\right) \tag{4.301e}$$
$$F_g = \sigma'_{LW}\, \sigma\, \overline{\epsilon}_v\, T_v^4\ (1 - p_{sng}) \tag{4.301f}$$
$$G_g = F_g\ (1 - \epsilon_g) \tag{4.301g}$$
$$H_g = G_g\ \left(1 - \sigma'_{LW}\right) \tag{4.301h}$$
$$I_g = \sigma\, \epsilon_g\, T_g^4\ (1 - p_{sng}) \tag{4.301i}$$
$$J_g = I_g\, \sigma'_{LW}\ (1 - \overline{\epsilon}_v)\ \left(1 - p'_{sng}\right) \tag{4.301j}$$
$$K_g = I_g\, \sigma'_{LW}\ (1 - \overline{\epsilon}_v)\ p'_{sng} \tag{4.301k}$$
$$L_g = I_g\ \left(1 - \sigma'_{LW}\right) \tag{4.301l}$$
$$p'_{sng} = p_{sng}\,(1 - p_{n\alpha}) \tag{4.301m}$$

and the equations for the snow-covered under-story fraction are

$$A_n = LW\downarrow\ p_{sng} \tag{4.302a}$$
$$B_n = A_n\, \sigma_{f\,LW}\ (1 - \epsilon_v) \tag{4.302b}$$
$$C_n = A_n\ (1 - \sigma_{f\,LW}) \tag{4.302c}$$
$$D_n = C_n\ (1 - \epsilon_n) \tag{4.302d}$$
$$E_n = D_n \left(1 - \sigma'_{LW}\right) \tag{4.302e}$$
$$F_n = \overline{\sigma}_{f\,LW}\, \sigma\, \epsilon_v\, T_v^4\, p_{sng} \tag{4.302f}$$
$$G_n = F_n\ (1 - \epsilon_n) \tag{4.302g}$$
$$H_n = G_n\ \left(1 - \sigma'_{LW}\right) \tag{4.302h}$$
$$I_n = \sigma\, \epsilon_n\, T_n^4\, p_{sng} \tag{4.302i}$$
$$J_n = I_n\, \sigma'_{LW}\ (1 - \epsilon_v)\ \left(1 - p''_{sng}\right) \tag{4.302j}$$
$$K_n = I_n\, \sigma'_{LW}\ (1 - \epsilon_v)\ p''_{sng} \tag{4.302k}$$
$$L_n = I_n\ \left(1 - \sigma'_{LW}\right) \tag{4.302l}$$
$$p''_{sng} = p_{sng}\ +\ p_{n\alpha}\,(1 - p_{sng}) \tag{4.302m}$$

where the different terms are again indicated in Fig. 4.19. In MEB, the ground-based snowpack depth can increase to the point that it buries the canopy, thus for both the snow-covered and snow free under-story fractions a modified snow fraction is defined as

$$\sigma'_{LW} = \left(1 - p'_{sng}\right) \sigma_{LW}\ +\ p'_{sng}\, \sigma_{f\,LW} \tag{4.303}$$

The factor, $\sigma_{f\,LW}$, over the understory snow-covered fraction of the grid box is modeled quite simply from Eq. 4.298. The inclusion of the snow-buried canopy fraction in Eq.s 4.301m and 4.302m causes all of the vegetation transmission and below canopy fluxes to vanish as p_{sng} and $p_{n\alpha} \rightarrow 0$ so that the only longwave radiative exchanges occur between the atmosphere and the snowpack in this limit.

Heat Conduction fluxes

The heat conduction fluxes in Eq.s 4.224-4.225 are modeled using Fourier's Law ($G = \lambda \partial T/\partial z$) and have been defined in previous sections (since MEB uses either the multilayer diffusive or 2 to 3 layer Force-Restore hydrology/soil configurations, coupled to the explicit multilayer snow scheme ES). The main potential difference between ISBA and ISBA-MEB is that the heat capacity and thermal conductivity for the ground depend either on the thermal properties of the soil (possibly including organic content) or on the thermal properties of the forest litter in the uppermost layer (Napoly et al., 2017): this parameterization is described in more detail in Section 4.1.9.

Aerodynamic Resistances

The resistances between the surface and the overlying atmosphere, $R_{a\,n-a}$ and $R_{a\,c-a}$, are based on the values of C_H computed from Eq. 4.209 between the overyling atmosphere and the snow surface, and between the overyling atmosphere and the canopy air space, respectively, where $C_{Hx} = (V_a R_{a\,x-a})^{-1}$.
The aerodynamic resistance between the vegetation canopy and the surrounding airspace can be defined as

$$R_{a\,vg-c} = (g_{av} + g^*_{av})^{-1} \tag{4.304}$$

The parameterization of the bulk canopy aerodynamic conductance, g_{av}, between the canopy and the canopy air is based on Choudhury and Monteith (1988). It is defined as

$$g_{av} = \frac{2\,LAI\,a_{av}}{\phi'_v} \left(\frac{u_{hv}}{lw}\right)^{1/2} [1 - \exp(-\phi'_v/2)]. \tag{4.305}$$

where u_{hv} represents the wind speed at the top of the canopy (m s^{-1}), LAI is the leaf area index (m^2 m^{-2}), and the remaining parameters are defined in Table **??**. The conductance accounting for the free convection correction from Sellers et al. (1986) is expressed as

$$g^*_{av} = \left[\frac{LAI}{890}\left(\frac{T_v - T_c}{lw}\right)^{1/4}\right] \qquad (T_v \geq T_c) \tag{4.306}$$

Note that this correction is only used for unstable conditions. The effect of snow burying the vegetation impacts the aerodynamic resistance of the canopy is simply modeled by modifying the LAI to obtain LAI_n using Eq. 4.299. The LAI_n is used in Eq. 4.304 to compute $R_{a\,vn-c}$, and this resistance is limited to 5000 s m^{-1} as $LAI_n \to 0$.
The resistance between the ground and the canopy air space is defined as

$$R_{ag-c} = R_{ag\,n}/\psi_H \tag{4.307}$$

where $R_{ag\,n}$ is the default resistance value for neutral conditions. The stability correction term, ψ_H, depends on the canopy structural parameters, wind speed and temperature gradient between the surface and the canopy air. The aerodynamic resistance is also based on Choudhury and Monteith (1988). It is assumed that the eddy diffusivity, K (m^2 s^{-1}), in the vegetation layer follows an exponential profile:

$$K(z) = K(z_{hv}) \exp\left[\phi_v \left(1 - \frac{z}{z_{hv}}\right)\right] \tag{4.308}$$

where z_{hv} represents the canopy height. Integrating the reciprocal of the diffusivity defined in Eq. 4.308 from z_{0g} to $d + z_{0v}$ yields

$$R_{ag\,n} = \frac{z_{hv}}{\phi_v\,K(z_{hv})}\left\{\exp\left[\phi_v\left(1 - \frac{z_{0g}}{z_{hv}}\right)\right] - \exp\left[\phi_v\left(1 - \frac{d + z_{0v}}{z_{hv}}\right)\right]\right\} \tag{4.309}$$

The diffusivity at the canopy top is defined as

$$K\left(z_{hv}\right) = k\, u_{*hv}\ \left(z_{hv} - d\right) \tag{4.310}$$

The von Karman constant, k, has a value of 0.4. The displacement height is defined as (Choudhury and Monteith, 1988)

$$d = 1.1\, z_{hv} \ln\left[1 + \left(c_d\, LAI_f\right)^{1/4}\right] \tag{4.311}$$

where the leaf drag coefficient, c_d, is defined from Sellers et al. (1996):

$$c_d = 1.328\ \left[\frac{2}{{R_e}^{1/2}}\right] + 0.45\left[\frac{1}{\pi}(1 - \chi_L)\right]^{1.6} \tag{4.312}$$

χ_L represents the Ross-Goudriaan leaf angle distribution function, which has been estimated according to Monteith (1975) (see Table 4.6), and R_e is the Reynolds number defined as

$$R_e = \frac{u_l\, lw}{\upsilon}. \tag{4.313}$$

The friction velocity at the top of the vegetation canopy is defined as

$$u_{*hv} = \frac{k\, u_{hv}}{\ln\left[\left(z_{hv} - d\right)/z_{0v}\right]} \tag{4.314}$$

where the wind speed at the top of the canopy is

$$u_{hv} = f_{hv}\, V_a \tag{4.315}$$

and V_a represents the wind speed at the reference height, z_a, above the canopy. The canopy height is defined based on vegetation class and climate within ECOCLIMAP as a primary parameter. It can also be defined using an external dataset, such as from a satellite-derived product (as a function of space and time). The vegetation roughness length for momentum is then computed as a secondary parameter as a function of the vegetation canopy height. The factor f_{hv} (≤ 1) is a stability dependent adjustment factor taken from the RCA LSM (Samuelsson et al., 2006; Samuelsson et al., 2011). They are defined as

$$f_{hv} = \begin{cases} \left(C_{v,N}\ +\ C_{v,S}\right)\sqrt{C_D}\,/k & \text{if } R_i > 0 \\ \left(C_{v,N}\ +\ C_{v,U}\right)\sqrt{C_D}\,/k & \text{if } R_i \leq 0 \end{cases}$$

where the Richardson number, R_i, is defined in Eq. 4.321. The coefficients are defined as

$$C_{v,N} = \ln\left\{1\ +\ \phi_z\left[\exp\left(\frac{k}{\sqrt{C_{DN}}}\right) - 1\right]\right\} \tag{4.316}$$

$$C_{v,S} = -\,\phi_z\left(\frac{k}{\sqrt{C_{DN}}} - \frac{k}{\sqrt{C_D}}\right) \tag{4.317}$$

$$C_{v,U} = -\ln\left\{1\ +\ \phi_z\left[\exp\left(\frac{k}{\sqrt{C_{DN}}} - \frac{k}{\sqrt{C_D}}\right) - 1\right]\right\} \tag{4.318}$$

where the drag coefficient, C_D, and the drag coefficient for neutral conditions, C_{DN}, are computed between the canopy air space and the free atmosphere above using the standard ISBA surface layer transfer functions (Eq. 4.208 and Eq. 4.210, respectively).

The dimensionless height scaling factor is defined as

$$\phi_z = \frac{\left(z_{hv} - d\right)}{z_r} \qquad \left(\phi_z \leq 1\right) \tag{4.319}$$

The reference height is defined as $z_r = z_a - d$ for simulations where the reference height is sufficiently above the top of the vegetation canopy. This is usually the case for local scale studies using observation data. When MEB is coupled to an atmospheric model, however, the lowest model level can be below the canopy height, so for coupled model simulations $z_r = \max(z_a,\, z_{hv} - d + z_{min})$ where $z_{min} = 2$ (m). Finally, the stability correction factor from Eq. 4.307 is defined as

$$\psi_H = (1 - a_{hv}\, R_i)^{1/2} \qquad (R_i \leq 0) \tag{4.320a}$$

$$= \frac{1}{1 + b\, R_i (1 + c\, R_i)^{1/2}} \left[1 + \left(\frac{R_i}{R_{i,crit}}\right)(f_{z0} - 1)\right] \qquad (R_i > 0 \text{ and } R_i \leq R_{i,crit}) \tag{4.320b}$$

$$= \frac{f_{z0}}{1 + b\, R_i (1 + c\, R_i)^{1/2}} \qquad (R_i > R_{i,crit}) \tag{4.320c}$$

where the Richardson number is defined as

$$R_i = \frac{-g\, z_{hv}\, (T_s - T_c)}{T_s\, {u_{hv}}^2} \tag{4.321}$$

Note that strictly speaking, the temperature factor in the denominator should be defined as $(T_s + T_c)/2$, but this has only a minor impact for our purposes. The so-called critical Richardson number, $R_{i,crit}$, is set to 0.2. This parameter has been defined assuming that some turbulent exchange is likely always present (even if intermittent), but it is recognized that eventually a more robust approach should be developed for very stable surface layers. The expression for unstable conditions (Eq. 4.320a) is from Sellers et al. (1996) where the structural parameter is defined as $a_{hv} = 9$.

It is generally accepted that there is a need to improve the parameterization of the exchange coefficient for extremely stable conditions typically encountered over snow (e.g.s Niu and Yang, 2004; Andreadis et al., 2009) . Since the goal here is not to develop a new parameterization, we simply modify the expression for stable conditions by using the standard function from ISBA. The standard ISBA stability correction for stable conditions is given by Eq. 4.320c where $b = 15$ and $c = 5$. The factor which takes into account differing roughness lengths for heat and momentum is defined as

$$f_{z0} = \frac{\ln(z_{hv}/z_{0g})}{\ln(z_{hv}/z_{0gh})} \tag{4.322}$$

where z_{0gh} is the ground roughness length for scalars. The weighting function (i.e. ratio of R_i to $R_{i,crit}$) in Eq. 4.320b is used in order to avoid a discontinuity at $R_i = 0$ (the roughness length factor effect vanishes at $R_i = 0$) in Eq. 4.320c. An example of Eq. 4.320c is shown in Fig. 4.20 using the z_{0g} from Table **??**, and for z_{0gh}/z_{0g} of 0.1 and 1.0. Finally, the resistance between the ground-based snowpack, $R_{a\,n-c}$, and the canopy air use the same expressions as for the aerodynamic resistance between the ground and the canopy air outlined herein, but with the surface properties of the snowpack (namely the roughness length and snow surface temperature).

Ground resistance

The soil resistance term is defined based on Sellers et al. (1992) as

$$R_g = \exp\left[a_{Rg} - b_{Rg}\, (\overline{w}_g/\overline{w}_{sat})\right] \quad . \tag{4.323}$$

The coefficients are $a_{Rg} = 8.206$ and $b_{Rg} = 4.255$, and the vertically averaged volumetric water content and saturated volumetric water content are given by $\overline{w}_g$ and $\overline{w}_{sat}$, respectively. The averaging is done from one to several upper layers. Indeed, the inclusion of an explicit ground surface energy budget makes it

more conceptually straightforward to include a ground resistance compared to the original composite soil-vegetation surface. The ground resistance is often used as a surrogate for an additional resistance arising due to a forest litter layer, therefore the soil resistance is set to zero when the litter layer option is activated. Finally, the coefficients a_{Rg} and b_{Rg} were determined from a case study for a specific location, and could possibly be location dependent. But currently these values are used, in part, since the litter formulation is the default configuration for MEB for forests as it generally gives better surface fluxes (Napoly et al., 2017).

Water Budget

The governing equations for (water) mass for the bulk canopy, and surface snow and ground layers are written as

$$\frac{\partial W_r}{\partial t} = P_{rv} + \max(0, -E_{tr}) - E_r - D_{rv} - \Phi_v \tag{4.324}$$

$$\frac{\partial W_{r\,n}}{\partial t} = I_n - U_n - E_{rn} + \Phi_v \tag{4.325}$$

$$p_{sng}\frac{\partial W_{n,1}}{\partial t} = P_s - I_n + U_n + p_{sng}\left(P_r - P_{rv} + D_{rv} - F_{nl,1} - E_n + \Phi_{n,1} + \xi_{nl,1}\right) \tag{4.326}$$

$$\rho_w \Delta z_{g,1}\frac{\partial w_{g,1}}{\partial t} = \left(P_r - P_{rv} + D_{rv} - E_g\right)(1 - p_{sng}) + p_{sng} F_{nl,N_n} - R_0 - F_{g,1} - \Phi_{g,1} \tag{4.327}$$

$$\rho_w \Delta z_{g,1}\frac{\partial w_{gf,1}}{\partial t} = \Phi_{g,1} - E_{gf}\,(1 - p_{sng}) \tag{4.328}$$

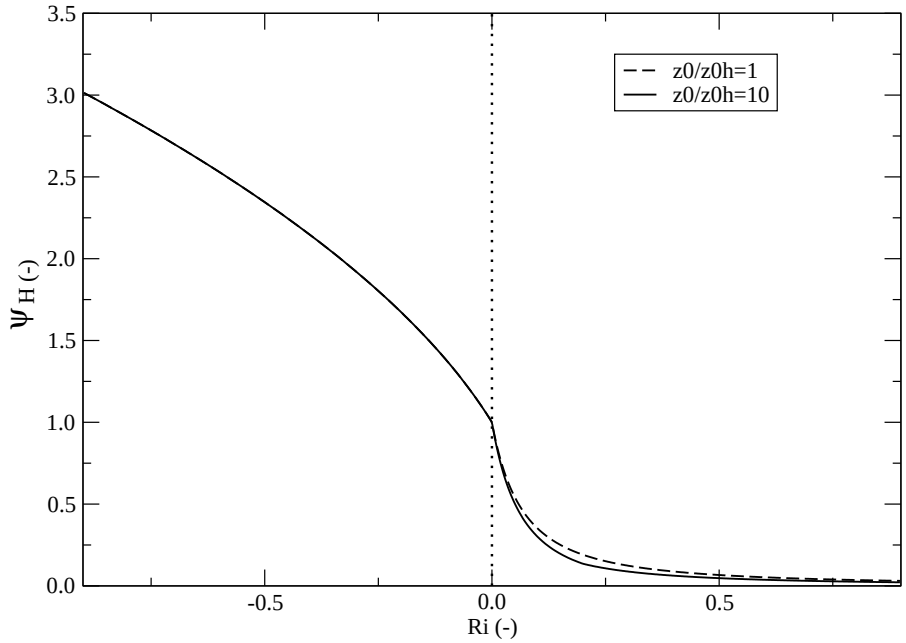

Figure 4.20: Stability correction term is shown using the Sellers formulation for $R_i \leq 0$ while the function for stable conditions adapted from ISBA ($R_i > 0$) for two ratios of z_{0g}/z_{0gh}. The ground surface roughness length is defined in Table 4.6.

Table 4.6: Surface vegetation canopy turbulence parameters which are constant.

Symbol	Definition	Unit	Value	Reference	Comment
a_{av}	canopy conductance scale factor	m s$^{-1/2}$	0.01	Choudhury and Monteith (1988)	Eq. 26
ϕ'_v	attenuation coeff. for wind	-	3	Choudhury and Monteith (1988)	p 386
lw	leaf width	m	0.02		
ϕ_v	attenuation coeff. for mom.	-	2	Choudhury and Monteith (1988)	p 386
z_{0g}	roughness of soil surface	m	0.007		
χ_L	Ross-Goudriaan leaf angle dist.	-	0.12	Monteith (1975)	p 26
u_l	Typical local wind speed	m s^{-1}	1	Sellers et al. (1996)	Eq. B7
υ	Kinematic viscos. of air	m^2 s^{-1}	0.15×10^{-4}		

where W_r and $W_{r\,n}$ represent the vegetation canopy water stores: intercepted water, and the intercepted snow and frozen water (all in kg m^{-2}), respectively. $W_{n,1}$ represents the snow liquid water equivalent (SWE) for the uppermost snow layer of the multi-layer scheme. The soil liquid water and equivalent frozen water equivalent volumetric water content are defined as w_g and w_{gf}, respectively (m^3 m^{-3}).

The interception reservoir, W_r, is modeled as single layer bucket, with losses represented by evaporation, E_r, and canopy drip, D_{rv}, of liquid water which exceeds a maximum holding capacity (see Sect. 4.1.9 for details). Sources include condensation (negative E_r and E_{tr}) and P_{rv} which represents the intercepted precipitation. The positive part of E_{tr} is extracted from the sub-surface soil layers as a function of soil moisture and a prescribed vertical root zone distribution. This equation is the same as that used in ISBA, except for the addition of the phase change term, Φ_v (kg m^{-2} s^{-1}). This term has been introduced owing to the introduction of an explicit canopy snow interception reservoir, $W_{r\,n}$: the canopy snow and liquid water reservoirs can exchange mass via this term which is modeled as melt less freezing. The remaining rainfall ($P_r - P_{rv}$) is partitioned between the snow-free and snow-covered ground surface, where P_r represents the total grid-cell rainfall rate. The canopy snow interception is more complex, and represents certain baseline processes such as snow interception, I_n, and unloading, U_n: see Sect. 4.1.9 for details.

The soil water and snow liquid water vertical fluxes at the base of the surface ground and snow are represented, respectively, by $F_{g,1}$ using Darcy's Law and by $F_{nl,1}$ using a tipping-bucket scheme (kg m^{-2} s^{-1}). The liquid water flux at the base of the snowpack, F_{nl,N_n}, is directed downward into the soil and consists in the liquid water in excess of the lowest model liquid water holding capacity. A description of the explicit snow and soil schemes are given in Sections 4.1.7 and 4.1.3, respectively. R_0 is the so-called surface runoff. It accounts for sub-grid heterogeneity of precipitation, soil moisture and for when potential infiltration exceeds a maximum rate: see Sections 4.1.6 and 4.1.2. The soil liquid water equivalent ice content can have some losses owing to sublimation in the uppermost soil layer, E_{gf}, but it mainly evolves owing to phase changes from soil water freeze-thaw, Φ_g. The remaining symbols in Eq.s 4.324-4.325 are defined and described in Sections 4.1.9 and 4.1.9.

Snow Interception within the canopy

The intercepted snow mass budget is described by Eq. 4.325, while the energy budget is included as a part of the bulk canopy prognostic equation (Eq. 4.223). The positive mass contributions acting to increase intercepted snow on canopy are snowfall interception, I_n, water on canopy that freezes, $\Phi_v < 0$, and sublimation of water vapor to ice, $E_{rn} < 0$. Unloading, U_n, sublimation, $E_{rn} > 0$, and snow melt, $\Phi_v > 0$, are the sinks. All of the terms are in kg m^{-2} s^{-1}. It is assumed that intercepted rain and snow can co-exist on the canopy. The intercepted snow is assumed to have the same temperature as the canopy, T_v, thus there

is no advective heat exchange with the atmosphere which simplifies the equations. For simplicity, when intercepted water on the canopy freezes, it is assumed to become part of the intercepted snow.
The parameterization of interception efficiency is based upon Hedstrom and Pomeroy (1998). It determines how much snow is intercepted during the time step and is defined as

$$I_{n,v,0} = (W^*_{r\,n} - W_{r\,n})\,[1 - \exp(-k_{n,v}\,P_s\,\Delta t)] \tag{4.329}$$

where ${W_{r\,n}}^*$ is the maximum snow load allowed, P_s the frozen precipitation rate and $k_{n,v}$ a proportionality factor. $k_{n,v}$ is a function of ${W_{r\,n}}^*$ and the maximum plan area of the snow-leaf contact area per unit area of ground, $C_{n,vp}$:

$$k_{n,v} = \frac{C_{n,vp}}{{W_{r\,n}}^*} \tag{4.330}$$

For a closed canopy, $C_{n,vp}$ would be equal to one, but for a partly open canopy it is described by the relationship:

$$C_{n,vp} = \frac{C_{n,vc}}{1 - C_{n,vc}\,u_{hv}\,z_{hv}/(w_n\,J_n)} \tag{4.331}$$

where $C_{n,vc}$ is the canopy coverage per unit area of ground which can be expressed as $1 - \chi_v$ where χ_v is the sky-view factor (see Eq. 4.297), and u_{hv} represents the mean horizontal wind speed at the canopy top (Eq. 4.315) which corresponds to the height z_{hv} (m). The characteristic vertical snow-flake velocity, w_n, is set to 0.8 m s^{-1} (Isymov, 1971). J_n is set to 10^3 m which is assumed to represent the typical size of the mean forested down wind distance.
For calm conditions and completely vertically falling snowflakes, $C_{n,vp} = C_{n,vc}$. For any existing wind, snow could be intercepted by the surrounding trees so that high wind speed increases interception efficiency. Generally for open Boreal conifer canopies, $C_{n,vc} < C_{n,vp} < 1$. Under normal wind speed conditions (i.e. wind speeds larger than 1 m s^{-1}), $C_{n,vc}$ (and $C_{n,vp}$) values are usually close to unity.
The maximum allowed canopy snow load, ${W_{r\,n}}^*$, is a function of the maximum snow load per unit branch area, $S_{n,v}$ (kg m^{-2}), and the leaf area index:

$${W_{r\,n}}^* = S_{n,v}\,LAI \tag{4.332}$$

where $S_{n,v}$ is defined as

$$S_{n,v} = \overline{S_{n,v}}\left(0.27 + \frac{46}{\rho_{n,v}}\right) \tag{4.333}$$

$\overline{S_{n,v}} = 6.3$ kg m^{-2} Based on measurements, Schmidt and Gluns (1991) estimated average values of $6.6\overline{S_{n,v}} = 6.3$ kg m^{-2} for pine and 5.9 kg m^{-2} for spruce trees. Because the average value for this parameter only varies by about 10% across these two fairly common tree species, and ECOCLIMAP does not currently make a clear distinction between these two forest classes, we currently use 6.3 as the default value for all forest classes. $\rho_{n,v}$ is the canopy snow density (kg m^{-3}) defined by the relationship:

$$\rho_{n,v} = 67.92 + 51.25\exp[(T_c - T_f)/2.59] \qquad (T_c \le T_{c\,max}) \tag{4.334}$$

where T_c is the canopy air temperature and $T_{c\,max}$ is the temperature corresponding to the maximum snow density. Assuming a maximum snow density of 750 kg m^{-3} and solving Eq. 4.334 for canopy temperature yields $T_{c\,max} = 279.854$ K. This gives values of $S_{n,v}$ in the range 4-6 kg m^{-2}.
The water vapor flux between the intercepted canopy snow and the canopy air, E_{rn} (Eq. 4.264), includes the evaporative efficiency, p_{nv}. This effect was first described by Nakai et al. (1999). In the ISBA-MEB

parameterization, the formulation is slightly modified so that it approaches zero when there is no intercepted snow load:

$$p_{nv} = \frac{0.89\, {S_{nv}}^{0.3}}{1 + \exp\left[-4.7(S_{nv} - 0.45)\right]} \tag{4.335}$$

where S_{nv} is the ratio of snow-covered area on the canopy to the total canopy area:

$$S_{nv} = \frac{W_{r\,n}}{{W_{r\,n}}^*} \qquad (0 \leq S_{nv} \leq 1) \tag{4.336}$$

A numerical test is performed to determine if the canopy snow becomes less than zero within one time-step due to sublimation. If this is true, then the required mass is removed from the underlying snowpack so that the intercepted snow becomes exactly zero during the time-step to ensure a high degree of mass conservation. Note that this adjustment is generally negligible.

The intercepted snow unloading, due to processes such as wind and branch bending, has to be estimated. Hedstrom and Pomeroy (1998) suggest an experimentally verified exponential decay in load over time, t, which is used in the parameterization;

$$U_{n,v} = I_{n,v,0} \exp(-U_{nL} t) = I_{n,v,0}\, c_{nL} \tag{4.337}$$

where U_{nL} is an unloading rate coefficient (s^{-1}) and c_{nL} the dimensionless unloading coefficient. Hedstrom and Pomeroy (1998) found that $c_{nL} = 0.678$ was a good approximation which, with a time step of 15 minutes, gives $U_{nL} = -4.498 \cdot 10^{-6}$ s^{-1}. A tuned value for the RCA-LSM from the Snow Model Intercomparison Project phase 2 (SnowMIP2) experiments Rutter et al. (2009) is $U_{nL} = -3.4254 \times 10^{-6}$ s^{-1} which has been adopted for MEB for now. All unloaded snow is assumed to fall to the ground where it is added to the snow storage on forest ground. Further, corrections to compensate for changes in the original LSM due to this new parameterization have been made for heat capacity, latent heat of vaporisation, evapotranspiration, snow storages and fluxes of latent heat.

Finally, canopy snow will partly melt if the temperature rises above the melting point and become intercepted water, where the intercepted (liquid and frozen) water phase change is simply proportional to the temperature:

$$\Phi_v = \frac{C_i\, W_{r\,n}}{L_f\, \tau_\Phi}\, (T_f - T_v) = \frac{C_i\, S_{nv}\, W^*_{r\,n}}{L_f\, \tau_\Phi}\, (T_f - T_v) \tag{4.338}$$

where $\Phi_v < 0$ signifies melting. T_f represents the melting point temperature (273.15 K) and the characteristic phase change timescale is τ_Φ (s). If it is assumed that the available heating during the time step for phase change is proportional to canopy biomass via the LAI then Eq. 4.338 can be written (for both melt and refreezing) as

$$\Phi_v = S_{nv}\, k_{\Phi v}\, (T_f - T_v) \tag{4.339}$$

Note that if energy is available for melting, the phase change rate is limited by the amount of intercepted snow, and likewise freezing is limited by the amount of intercepted liquid water. The melting of intercepted snow within the canopy can be quite complex, thus currently the simple approach in Eq. 4.339 adopted herein. The phase change coefficient was tuned to a value of $k_{\Phi v} = 5.56 \times 10^{-6}$ kg m^{-2} s^{-1} K^{-1} for the SNOWMIP2 experiments with the RCA-LSM. Currently, this value is the default for ISBA-MEB.

Rain Interception within the canopy

The rain intercepted by the vegetation is available for potential evaporation which means that it has a strong influence on the fluxes of heat and consequently also on the surface temperature. The rate of change of

intercepted water on vegetation canopy is described by Eq. 4.324. The rate that water is intercepted by the over-story (which is not buried by the ground-based snow) is defined as

$$P_{rv} = P_r \left(1 - \chi_v\right) \left(1 - p_{ng} p_{\alpha n}\right) \tag{4.340}$$

where χ_v is a view factor indicating how much of the precipitation that should fall directly to the ground (see Eq. 4.297). The fractional coverage of water within the reservoir is given by Eq. 4.143. The over-story canopy drip rate, D_{rv}, is defined simply as the value of water in the reservoir which exceeds the maximum holding capacity

$$D_{rv} = \max\left(0,\, W_{rv} - W_{rv,max}\right) / \Delta t \tag{4.341}$$

where the maximum liquid water holding capacity is defined from Eq. 4.146. Note that Eq. 4.324 is first evaluated with $D_{rv} = 0$, and then the canopy drip is computed as a residual. Thus, the final water amount is corrected by removing the canopy drip or through-fall. This water can then become a liquid water source for the soil and the ground-based snowpack.

Halstead Coefficient

In the case of wet vegetation, the total plant evapotranspiration is partitioned between the evaporation of intercepted water, and transpiration via stomata by the so-called Halstead coefficient. In MEB, two such coefficients are used for the non-snow buried and buried parts of the vegetation canopy, h_{vg} and h_{vn} (Eq.s 4.258a and 4.258b, respectively). In MEB, the general form of the Halstead coefficient, as defined in Noilhan and Planton (1989) by Eq. 4.196, is modified by introducing the factor k_v to take into account the fact that saturated vegetation can transpire, i.e. when $\delta_v = 1$ (Bringfelt et al., 2001). Thus for MEB, we define $\delta = k_v\, \delta_v$. The intercepted water forms full spheres just touching the vegetation surface when $k_v = 0$ which allows full transpiration from the whole leaf surface. In contrast, $k_v = 1$ would represent a situation where a water film covers the vegetation completely and no transpiration is allowed. To adhere to the interception model as described above, where the intercepted water exists as droplets, we set the value of k_v to 0.25. Note that in the case of condensation, i.e. $E < 0$, $h_v = 1$.
Without a limitation of h_{vg} and h_{vn}, the evaporative demand could exceed the available intercepted water during a time step, especially for the canopy vegetation which experiences a relatively low aerodynamic resistance. To avoid such a situation, a maximum value of the Halstead coefficient is imposed by calculating a maximum value of the δ_v. See Appendix 4.1.13 for details.

Forest Litter

The ground surface in forest regions is generally covered by a litter layer consisting of dead leaves and or needles, branches, fruit, and other organic material. Some LSMs have introduced parameterizations for litter (e.g.s Gonzalez-Sosa et al., 1999; Ogée and Brunet, 2002; Wilson et al., 2012) , but the approach can be very different from one to another depending on their complexity. The main goal of this parameterization within MEB is to account for the generally-accepted first-order energetic and hydrological effects of litter; this layer is generally accepted to have a strong insulating effect owing to its particular thermal properties (leading to a relatively low thermal diffusivity), it causes a significant reduction of ground evaporation (capillary rise into this layer is negligible), and it constitutes an interception reservoir for liquid water which can also lose water by evaporation (Napoly et al., 2017).
Forest litter is represented using a single model layer which generally ranges in thickness from 0.01 to 0.10 m, and in the absence of ancillary data, the default value is 0.03 m. When this option is active, an additional layer is added to the soil for the thermal and energy budget computations with litter-specific

thermal properties. This means that the numerical solution method is identical to that in Appendix 4.1.13, except that litter thermal properties used used for the litter in place of the uppermost soil properties, and the soil grid is shoft down by 1 level (but keeping the same number of soil layers). In terms of hydrology, an additional reservoir is added which uses a relatively simple bucket-type scheme with a litter-specific maximum water storage capacity. The model physics and governing equations are reviewed herein.

Prognostic equations For the litter scheme, two new prognostic equations are added. Currently, it can only be used with the DF soil scheme option (as the energy budget is solved as part of the soil tri-diagnoal matrix). The energy budget for the snow-free litter layer can be expressed as:

$$\mathcal{C}_l \frac{\partial T_l}{\partial t} = (R_{nl} - H_l - LE_l)(1 - p_{sng}) + p_{sng}(G_{gn} + \tau_{n,N_n} SW_{n,n}) - G_l + L_f \Phi_l \tag{4.342}$$

where T_l is the litter temperature (K), Δz_l (m) is the thickness of the litter layer, and $\mathcal{C}_l$ (J K^{-1} m^{-2}) is the effective heat capacity of the litter. $R_{n,l}$, H_l, LE_l, G_l represent the net radiation, sensible heat flux, latent heat flux and ground conduction flux from the litter layer, respectively. Note that when litter is present, $R_{n,l}$, H_l, LE_l correspond to the ground surface fluxes in Sections 4.1.9-4.1.9, and an additional soil layer is added.

The liquid water content of the litter layer evolves following:

$$\frac{\partial W_l}{\partial t} = (P_r - P_{rv} + D_{rv} - E_l)(1 - p_{sng}) + p_{sng} F_{nl,Nn} - D_l - \Phi_l \qquad (0 < W_l < W_{l,max}) \tag{4.343}$$

where E_l represents the litter evaporation rate, D_l is the drainage rate from the litter to the soil (all in kg m^{-2} s^{-1}). Thus when litter is present, D_l represents the potential infiltration rate for the soil (before surface runoff is removed and the actual infiltration into the soil is computed). The remaining flux terms are defined in Section 4.1.9. The maximum liquid water content in the litter reservoir is defined as $W_{l,max} = w_{l,max} \Delta z_l \rho_w$ (kg m^{-2}). The default value for the maximum holding capacity of the litter layer, $w_{l,max}$, is 0.12 m^3 m^{-3} (Putuhena and Cordery, 1996). The liquid water equivalent of ice contained in the litter layer is governed by:

$$\frac{\partial W_{lf}}{\partial t} = \Phi_l - E_{lf} \tag{4.344}$$

where E_{lf} represents the sublimation of ice contained within the litter layer.

Phase Change The phase change rate, Φ_l (kg m^{-2} s^{-1}), is defined as:

$$\Phi_l = \frac{1}{\tau_i} \left\{ \delta_f \min \left[\frac{\rho_i C_i \Delta z_l (T_l - T_f)}{L_f}, W_{lf} \right] + (1 - \delta_f) \min \left[\frac{\rho_i C_i \Delta z_l (T_f - T_l)}{L_f}, W_l \right] \right\} \tag{4.345}$$

where L_f represents the latent heat of fusion (J kg^{-1}), ρ_i is the density of ice (here defined as 920 kg m^{-3}), the freezing point temperature is $T_f = 273.15$ K, and C_i is the specific heat capacity of ice (2.106×10^3 J K^{-1} kg^{-1}). The delta function $\delta_f = 1$ if energy is available for melting (i.e. $T_l - T_f > 0$), otherwise it is $\delta_f = 0$. τ_i is a parameter which represents the characteristic time scale for phase changes: currently the same value for soil is used for litter (see Section 4.1.2) The updated temperature is first computed from Eq. 4.342 with $\Phi_l = 0$, then the phase change is computed as an adjustment to T_l, W_l and W_{lf} as is done for the soil.

Energy Fluxes It is assumed that litter below the canopy is spatially homogeneous so that it intercepts all of the incoming radiation. Thus, the net radiation R_{nl} for the litter layer is the same that for the first soil layer in MEB:

$$R_{n,g} = SW_{net\,g} + LW_{net\,g} \tag{4.346}$$

Note that currently, the soil emissivity and albedo values are used for the litter for spatially distributed simulations pending the development of global datasets of these parameters for litter or the development of an appropriate model to estimate them. For local scale simulations, the values can be defined based on observations.

The below-canopy sensible heat flux, H_l (W m^{-2}), is computed the same way that for the top soil layer in the ISBA model as:

$$H_l = \rho_a \frac{(\mathcal{T}_l - \mathcal{T}_c)}{R_{ag-c}} \tag{4.347}$$

where the aerodynamic resistance between the ground and the canopy air space, R_{ag-c}, is defined in Eq. 4.307. $\mathcal{T}_l$ and $\mathcal{T}_c$ (J kg^{-1}) are thermodynamic variables which are linearly related to temperature and it is analogous in form to Eq. 4.230. The latent heat flux is partitioned between evaporation and sublimation in the litter layer:

$$LE_l = (1 - p_{lf})\ LE_l\ +\ p_{lf}\, LE_{lf} \tag{4.348}$$

where p_{lf} is the fraction of frozen water in the litter layer and

$$LE_l = L_v\, \rho_a\, \frac{[h_{ul}\, q_{sat}\,(T_l)\ -\ q_c]}{R_{ag-c}} \tag{4.349a}$$

$$LE_{lf} = L_s\, \rho_a\, \frac{[h_{ulf}\, q_{sat}\,(T_l)\ -\ q_c]}{R_{ag-c}} \tag{4.349b}$$

where the specific humidity of the canopy air space is represented by q_c. The specific humidity at saturation over liquid water is represented by q_{sat} (kg kg^{-1}). Note, it would be more accurate to use the specific humidity at saturation over ice in Eq. 4.349b, but this complicates the linearization and this effect is neglected for now (Boone et al., 2017). The surface humidity factors for liquid and frozen water are represented by h_{ul} and h_{ulf}, respectively. They are computed as the relative humidity in an analogous fashion as for the soil following Noihan and Planton (1989):

$$h_{ul} = \frac{1}{2}\left[1 - \cos\left(\pi\, \frac{W_l}{W_{l,max}}\right)\right] \tag{4.350}$$

Note that h_{ulf} is computed by replacing W_l and $W_{l,max}$ by the values for the liquid water equivalent ice content. The maximum liquid holding capacity is modified for ice following Boone et al. (2000).

Finally, the ground conduction flux (W m^{-2}) between the litter layer and the underlying soil is computed as:

$$G_l = \frac{T_l\ -\ T_{g,1}}{(\Delta z_l/\lambda_l)\ +\ (\Delta z_{g,1}/\lambda_{g,1})} \tag{4.351}$$

where λ_l and $\lambda_{g,1}$ are the litter and first soil layer thermal conductivities respectively and $\Delta z_{g,1}$ is the thickness of the first soil layer.

Water interception and fluxes The water intercepted by the litter layer corresponds to the sum of the rain passing through the canopy, snow runoff (saturation excess from sufficiently large melt or rainfall), and the drip from the canopy. Note that for simplicity, a gravitational drainage type formulation is not used for litter, but rather a tipping bucket following Ogée and Brunet (2002) as:

$$D_l = \max\,(0, W_l - W_{l,max}) \tag{4.352}$$

Thermal properties The litter thermal conductivity, λ_l (W m^{-1} K^{-1}), is computed according to De Vries (1963) as:

$$\lambda_l = 0.1 + 0.03 \left(\frac{W_l}{\rho_w \, \Delta z_l} \right) \tag{4.353}$$

The effective heat capacity of the litter, $\mathcal{C}_l$ (J m^{-2} K^{-1}), is computed using

$$\mathcal{C}_l = \Delta z_l \, \rho_{ld} \, C_{ld} \; + \; W_l \, C_w \; + \; W_{lf} \, C_i \tag{4.354}$$

where the specific heat capacity of liquid water is $C_w = 4.218 \times 10^3$ (J K^{-1} kg^{-1}). The dry density of the litter is defined as ρ_{ld}. Ogée and Brunet (2002) used a value of dry litter density of 45 kg m^{-3} for a pine forest. Meekins and McCarthy (2001) measured a litter density of 46 kg m^{-3} in a deciduous forest and Kostel-Hughes et al. (1998) estimated values varying between 27 to 38 kg m^{-3} for oak forests. Currently ECOCLIMAP doesn't distinguish between different types of deciduous trees, thus by default, ρ_{ld} is assigned a value of 45 kg m^{-3}. As a proxy for the specific heat of litter, we use the specific heat capacity of organic material from Farouki (1986) which is $C_{ld} = 1.926 \times 10^3$ J kg^{-1} K^{-1}. Currently, constant values for ρ_{ld} and C_{ld} are used for spatially distributed applications or on the local scale, unless observational data are available.

Energy and Mass conservation

The soil and snowpack prognostic temperature equations can be written in flux form for $k = 1, N_g$ soil layers and $k = 1, N_n$ snow layers as

$$\mathcal{C}_{g,k} \frac{\partial T_{g,k}}{\partial t} = G_{g,k-1} \; - \; G_{g,k} \; + \; L_f \, \Phi_{g,k} \tag{4.355}$$

$$\mathcal{C}_{n,k} \frac{\partial T_{n,k}}{\partial t} = G_{n,k-1} \; - \; G_{n,k} \; + \; L_f \, \Phi_{n,k} \; + \; \xi_{n,k-1} \; - \; \xi_{n,k} \; + \; SW_{net,n} \, (\tau_{n,k-1} - \tau_{n,k}) \tag{4.356}$$

The total energy balance of the vegetation canopy-soil-snowpack system is conserved at each time step, Δt, and can be obtained by summing the discrete time forms of Eq. 4.223, Eq. 4.355, and Eq. 4.356 for all soil, snow and the single bulk vegetation layers yielding

$$\begin{aligned} &\mathcal{C}_v \Delta T_v \; + \; \textstyle\sum_{k=1}^{N_g} \mathcal{C}_{g,k} \, \Delta T_{g,k} \; + \; p_{sng} \textstyle\sum_{k=1}^{N_n} \mathcal{C}_{n,k} \, \Delta T_{n,k} \; = \\ &\quad \Delta t \Big[\, (1 - p_{sng}) \, G_{g,0} \; + \; p_{sng} \, (G_{n,0} \; + \; \tau_{n,Nn} SW_{net,n} \; + \; G_{n,0}) \; + \; R_{n\,v} - H_{v-c} - LE_{v-c} + \\ &\quad L_f \left(\Phi_v \; + \; \textstyle\sum_{k=1}^{N_g} \Phi_{g,k} \; + \; p_{sng} \textstyle\sum_{k=1}^{N_n} \Phi_{n,k} \right) \Big] \end{aligned} \tag{4.357}$$

where $\Delta T_x = T_x(t + \Delta t) - T_x(t)$. Note that Eq. 4.356 has been multiplied by p_{sng} to make it patch-relative. The surface boundary conditions for Eq. 4.223 and Eq. 4.225 are, respectively,

$$G_{g,0} = (1 - p_n) \, (R_{n\,g} - H_g - LE_g) \; + \; p_n \, (G_{gn} + \tau_{n,N_n} SW_{n\,n}) \tag{4.358}$$

$$G_{n,0} = R_{n\,n} - H_n - LE_n - H_n - LE_{n-N} \tag{4.359}$$

$$\tau_{n,0} = 1 \tag{4.360}$$

$$\xi_{n,0} = 0 \tag{4.361}$$

Eq. 4.360 signifies that the net shortwave radiation at the surface enters the snowpack, and Eq. 4.361 represents the fact that energy changes owing to the time evolving snow grid can only arise in the surface layer owing to exchanges with the sub-surface layer. Snowfall is assumed to have the same temperature

as the snowpack, thus a corresponding cooling/heating term does not appear in Eq. 4.359, although the corresponding mass increase must appear in the snow water budget equation (see Sect. 4.1.9).
The lower boundary conditions for Eq. 4.355 and Eq. 4.356 are, respectively,

$$G_{g,N_g} = 0 \tag{4.362}$$

$$\xi_{n,N_n} = 0 \tag{4.363}$$

The appearance of the same discrete form for Φ in both the energy and mass budget equations ensures enthalpy conservation. Owing to Eq.s 4.361 and 4.363, the total effective heating of the snowpack owing to grid adjustments is

$$\int_0^{D_{Nn}} \xi_n \, dD_n \;=\; 0 \tag{4.364}$$

where D_{Nn} represents the total snow depth. Thus this term only represents a contribution from contiguous snow layers, not from a source external to the snowpack. The energy storage of the snow-soil-vegetation system is balanced by the net surface radiative and turbulent fluxes and internal phase changes (solid and liquid phases of water substance).
The soil and snowpack prognostic mass equations can be written in flux form for $k = 2, N_{g\,w}$ soil layers and $k = 1, N_n$ snow layers as

$$p_{ng}\,\frac{\partial W_{n,k}}{\partial t} = p_{ng}\,\left(F_{nl,k-1} - F_{nl,k} - \Phi_{n,k} + \xi_{nl,k} - \xi_{nl,k-1}\right) \qquad (k = 2, N_n) \tag{4.365}$$

$$\rho_w\,\Delta z_{g,1}\frac{\partial w_{g,k}}{\partial t} = F_{g,k-1} - F_{g,k} - \Phi_{g,k} - \mathcal{F}_{2,k}\max\left(0,\, E_{tr}\right) \qquad (k = 2, N_{g\,w}) \tag{4.366}$$

$$\rho_w\,\Delta z_{g,1}\frac{\partial w_{gf,k}}{\partial t} = \Phi_{g,k} \qquad (k = 2, N_{g\,w}) \tag{4.367}$$

The total grid-box water budget at each time step is obtained by summing the budget equations for the surface layers (Eq.s 4.324-4.328) together with those for the sub-surface layers (Eq.s 4.365-4.367) to have

$$\begin{aligned} \Delta W_r \,+\, \Delta W_{r\,n} \,+\, p_{ng}\textstyle\sum_{k=1}^{N_n}\Delta W_{n,\,k} \,+\, \rho_w\textstyle\sum_{k=1}^{N_g w}\Delta z_{g,\,k}\left(w_{g\,k} + w_{gf\,k}\right) \;=\; \\ \Delta t\Big[P_r \,+\, P_s \,-\, R_0 \,-\, F_{g,\,N_{gw}} \,-\, (1-p_{ng})\,E_g \,-\, E_v \,-\, p_{ng}\,E_n \\ -\,\Phi_v \,-\, \textstyle\sum_{k=1}^{N_g}\Phi_{g,k} \,-\, p_{ng}\,\textstyle\sum_{k=1}^{N_n}\Phi_{n,k}\Big] \end{aligned} \tag{4.368}$$

where R_0 can simply be a diagnostic or coupled with a river routing scheme. The soil water lower boundary condition, $F_{g,N_{gw}}$ represents the so-called base-flow or drainage leaving the lowest hydrological layer which can then be transfered as input to a river routing scheme (see references above) or to a ground water scheme. In such instances, it can be negative if an option to permit a ground water inflow is activated. The soil liquid water and equivalent frozen water equivalent volumetric water content extend down to layer $N_{g\,w}$, where $N_{g\,w} \leq N_g$. Note that the vertical soil water transfer or evolution is not computed below $z_g\,(k = N_{gw})$, whereas heat transfer can be. In order to compute the thermal properties for deep soil temperature (thermal conductivity and heat capacity for example), soil moisture estimates are needed: values from the soil are extrapolated downward assuming hydrostatic equilibrium
Note that Eq. 4.365 is snow-relative, therefore this equation must be multiplied by the ground-based snow fraction, p_{ng}, to be grid box relative for coupling with the soil and vegetation water storage terms. The lower boundary condition for liquid water flow, F_{nl,N_n}, is defined as the liquid water exceeding the lowest maximum snow layer liquid water holding capacity. ξ_{nl} represents the internal mass changes of a snowpack layer when the vertical grid is reset. When integrated over the entire snowpack depth, this term vanishes (analogous to Eq. 4.364 for the snowpack temperature equation). The coupling of MEB with the interactive flooding scheme will be the subject of future work.

4.1.10 Summary of Useful Parameters

The parameters have been chosen in order to characterize the main physical processes, while attempting to reduce the number of independent variables. They can be divided into two categories: primary parameters needing to be specified by spatial distribution, and secondary parameters which values can be associated with those of the primary parameters.

In the present state of the method, the primary parameters describe the nature of the land surface and its vegetation coverage by means of only four numerical indices: the percentage of sand and clay in the soil, the dominant vegetation type, and the land-sea mask.

The secondary parameters associated with the soil type are evaluated from the sand and clay composition of the soil, according to the continuous formulation discussed in Giordani (1993) and Noilhan and Lacarrère (1995) (see Appendix). These parameters are:

- the saturated volumetric moisture content w_{sat};
- the wilting point volumetric water content w_{wilt};
- the field capacity volumetric water content w_{fc};
- the slope b of the retention curve;
- the soil thermal coefficient at saturation C_{Gsat};
- the value of C_1 at saturation (i.e., C_{1sat});
- the reference value of C_2 for $w_2 = 0.5 w_{sat}$ (i.e., C_{2ref});
- the drainage coefficient C_3 ;
- the diffusion coefficients $C_{4\,ref}$ and C_{4b} ;
- and the coefficients a, p for the w_{geq} formulation.

On the other hand, the parameters associated with the vegetation can either be derived from the dominant vegetation type, or be specified from existing classification or observations. They are

- the fraction of vegetation veg;
- the depth of the soil column d_2 (or the root zone depth);
- the depth of the soil column d_3 (if third soil layer option in use);
- the minimum surface resistance R_{smin};
- the leaf area index LAI;
- the heat capacity C_v of the vegetation;
- the R_{Gl} and γ coefficients found in the formulation of the surface resistance R_s;
- and the roughness length for momentum z_0 and for heat z_{0h}.

Other necessary parameters are

- the albedo α
- the emissivity ϵ.
- and characteristic time scale for phase changes (currently constant) τ_i.

4.1.11 Appendix A: Continuous formulation of the soil secondary parameters

Following Giordani (1993), Noilhan and Lacarrère (1995), the sand and clay composition (i.e., $SAND$ and $CLAY$) are expressed in percentage.

The saturated volumetric water content (m^3m^{-3}):

$$w_{sat} = (-1.08SAND + 494.305) \times 10^{-3} \tag{4.369}$$

The wilting point volumetric water content (m^3m^{-3}):

$$w_{wilt} = 37.1342 \times 10^{-3}(CLAY)^{0.5} \tag{4.370}$$

The field capacity volumetric water content (m^3m^{-3}):

$$w_{fc} = 89.0467 \times 10^{-3}(CLAY)^{0.3496} \tag{4.371}$$

The slope of the retention curve:

$$b = 0.137CLAY + 3.501 \tag{4.372}$$

The soil thermal coefficient at saturation (Km^2J^{-1}):

$$C_{Gsat} = -1.557 \times 10^{-2}SAND - 1.441 \times 10^{-2}CLAY + 4.7021 \tag{4.373}$$

The value of C_1 at saturation:

$$C_{1sat} = (5.58CLAY + 84.88) \times 10^{-2} \tag{4.374}$$

The value of C_2 for $w_2 = 0.5w_{sat}$:

$$C_{2ref} = 13.815CLAY^{-0.954} \tag{4.375}$$

The coefficient C_3:

$$C_3 = 5.327CLAY^{-1.043} \tag{4.376}$$

The coefficient C_{4b}:

$$C_{4b} = 5.14 + 0.115\,CLAY \tag{4.377}$$

The coefficient $C_{4\,ref}$:

$$C_{4\,ref} = \frac{2(d_3 - d_2)}{(d_2\,{d_3}^2)}\log_{10}{}^{-1}\left[\beta_0 + \sum_{j=1}^{3}\left(\beta_j\,SAND^j + \alpha_j\,CLAY^j\right)\right] \tag{4.378}$$

where the β_j $(j = 0, 3)$ coefficients are 4.42×10^{-0}, 4.88×10^{-3}, 5.93×10^{-4} and -6.09×10^{-6}. The α_j $(j = 1, 3)$ coefficients are defined as -2.57×10^{-1}, 8.86×10^{-3} and -8.13×10^{-5}.
The coefficients for the w_{geq} formulation:

$$a = 732.42 \times 10^{-3}CLAY^{-0.539} \tag{4.379}$$

$$p = 0.134CLAY + 3.4 \tag{4.380}$$

4.1.12 Appendix B: Gaussian formulation for the C_1 coefficient

Following Giordani (1993) and Braud *et al.* (1993), for dry soils (i.e., $w_g < W_{wilt}$), the C_1 coefficient in Eq. (13) is approximated by the Gaussian distribution:

$$C_1(w) = C_{1max} \exp\left[-\frac{(w_g - w_{max})^2}{2\sigma^2}\right] \tag{4.381}$$

In this expression,

$$C_{1max} = (1.19 w_{wilt} - 5.09) \times 10^{-2} T_s + (-1.464 w_{wilt} + 17.86) \tag{4.382}$$

$$w_{max} = \eta w_{wilt} \tag{4.383}$$

with

$$\eta = (-1.815 \times 10^{-2} T_s + 6.41) w_{wilt} + (6.5 \times 10^{-3} T_s - 1.4) \tag{4.384}$$

and

$$\sigma^2 = -\frac{W_{max}^2}{2ln\left(\frac{0.01}{C_{1max}}\right)} \tag{4.385}$$

4.1.13 Appendix C: ISBA-MEB Numerical Solution

.

The numerical solution of the full set of coupled thermodynamic prognostic equations (ISBA-MEB surface energy budget, ISBA sub-surface soil and snow, and atmospheric profile) is presented herein. The coupling is numerically implicit and heat and mass (and enthalpy) conservative (flux form equations are used).

Discretization of surface energy budgets

The surface energy budget equations (Eq.s 4.223-4.225) are integrated in time using the implicit backward difference scheme. They can be written in discretized form as

$$\begin{aligned}
\mathcal{C}_v \frac{(T_v^+ - T_v)}{\Delta t} =& \frac{\partial LW_{net\,v}}{\partial T_v}\left(T_v^+ - T_v\right) + \frac{\partial LW_{net\,v}}{\partial T_{g,1}}\left(T_{g,1}^+ - T_{g,1}\right) \\
&+ \frac{\partial LW_{net\,v}}{\partial T_{n,1}}\left(T_{n,1}^+ - T_{n,1}\right) + SW_{net\,v} + LW_{net\,v} \\
&+ \varphi_v\left(\mathcal{A}_v\,T_v^+ - \mathcal{A}_c\,T_c^+\right) \\
&+ h_{sv}\,\varphi_v\,L\left[q_{sat\,v} + \frac{\partial q_{sat\,v}}{\partial T_v}\left(T_v^+ - T_v\right) - q_c^+\right]
\end{aligned} \tag{4.386}$$

$$\begin{aligned}
\mathcal{C}_{g,1} \frac{\left(T_{g,1}^+ - T_{g,1}\right)}{\Delta t} =& \Bigg[\frac{\partial LW_{net\,g}}{\partial T_v}\left(T_v^+ - T_v\right) + \frac{\partial LW_{net\,g}}{\partial T_{g,1}}\left(T_{g,1}^+ - T_{g,1}\right) \\
&+ \frac{\partial LW_{net\,g}}{\partial T_{n,1}}\left(T_{n,1}^+ - T_{n,1}\right) + SW_{net\,g} + LW_{net\,g} \\
&+ \varphi_g\left(\mathcal{A}_g\,T_g^+ - \mathcal{A}_c\,T_c^+\right) \\
&+ \varphi_g\,L\left\{h_{sg}\left[q_{sat\,g} + \frac{\partial q_{sat\,g}}{\partial T_g}\left(T_g^+ - T_g\right)\right] - h_a\,q_c^+\right\} \\
&\Bigg](1 - p_{sng}) + p_{sng}\,\Lambda_{g,n}\left(T_{n,N_n}^* - T_{g,1}^+\right) - \Lambda_{g,1}\left(T_{g,1}^+ - T_{g,2}^+\right)
\end{aligned} \tag{4.387}$$

$$\begin{aligned}
p_{sng}\,\mathcal{C}_{n,1} \frac{\left(T_{n,1}^+ - T_{n,1}\right)}{\Delta t} =& \Bigg\{\frac{\partial LW_{net\,n}}{\partial T_v}\left(T_v^+ - T_v\right) + \frac{\partial LW_{net\,n}}{\partial T_{g,1}}\left(T_{g,1}^+ - T_{g,1}\right) \\
&+ \frac{\partial LW_{net\,n}}{\partial T_{n,1}}\left(T_{n,1}^+ - T_{n,1}\right) + SW_{net\,n} + LW_{net\,n} \\
&+ (1 - p_{n\alpha})\,\varphi_{n-c}\left(\mathcal{A}_n\,T_n^+ - \mathcal{A}_c\,T_c^+\right) \\
&+ p_{n\alpha}\,\varphi_{n-a}\left(\mathcal{B}_n - \mathcal{B}_a + \mathcal{A}_n\,T_n^+ - \mathcal{A}_a\,T_a^+\right) \\
&+ (1 - p_{n\alpha})\,\varphi_{n-c}\,L_s\left[q_{sati\,n} + \frac{\partial q_{sati\,n}}{\partial T_n}\left(T_n^+ - T_c^+\right) - q_c^+\right] \\
&+ p_{n\alpha}\,\varphi_{n-a}\,L_s\left[q_{sati\,n} + \frac{\partial q_{sati\,n}}{\partial T_n}\left(T_n^+ - T_a^+\right) - q_a^+\right] \\
&- \Lambda_{g,1}\left(T_{n,1}^+ - T_{n,2}^+\right)\Bigg\}\,p_{sng}
\end{aligned} \tag{4.388}$$

where Eq. 4.225 has been multiplied by p_{sng} to make it patch-relative for the combined solution of the three budget equations. The $q^+_{sat\,x}$ terms have been linearized with respect to T_x as

$$q^+_{sat\,x} = q_{sat\,x} + \frac{\partial q_{sat\,x}}{\partial T_x}\left(T^+_x - T_x\right) \tag{4.389}$$

where again, $x = n, 1, g, 1$ or v. The longwave radiation terms are also linearized and the derivatives are given by Eq. 4.413. The superscript $+$ corresponds to the values of variables at time $t + \Delta t$, while the absence of a superscript indicates variables evaluated at time t. Note that we have defined $\varphi_x = \rho_a / R_{a\,x}$ (kg m^{-2} s^{-1}) for simplicity. The thermodynamic variable, $\mathcal{T}_x$, in the sensible heat flux terms have been expressed as a function of T_x using Eq. 4.238. Several of the $\mathcal{B}_x$ terms have canceled out in the sensible heat flux terms in Eq.s 4.386-4.388 since they are defined such that $\mathcal{B}_c = \mathcal{B}_v = \mathcal{B}_g = \mathcal{B}_n$. Note that compared to Eq.s 4.223-4.225, the phase change terms (Φ_x) do not appear in Eq.s 4.386-4.388. This is because they are evaluated as an adjustment after the energy budget and the fluxes have been computed.

In Eq. 4.387, T^*_{n,N_n} represents a test temperature for the lowest snowpack layer. It is first computed using an implicit calculation of the combined snow-soil layers to get a first estimate of the snow-ground heat conduction inter-facial flux when simultaneously solving the surface energy budgets. The final snow temperature in this layer, T^+_{n,N_n}, is computed afterwards within the snow scheme: any difference between the resulting conduction flux and the test-flux in Eq. 4.387 is added to the soil as a correction at the end of the time step in order to conserve energy. In practice, this correction is generally small, especially since the snow fraction goes to unity very rapidly (i.e. for a fairly thin snowpack since MEB only uses p_{sng} at the surface, and not p_{snv}). Thus, in this general case, the difference between the test flux and the final flux arise only owing to updates to snow properties within the snow scheme during the time step. Since T^*_{n,N_n} is computed using an implicit solution method for the entire soil-snow continuum, it is also quite numerically stable. The use of a test flux permits a modular coupling between the snow scheme and the soil-vegetation parts of ISBA-MEB.

In order to solve Eq.s 4.386-4.388 for the three unknown surface energy budget temperatures, T^+_v, $T^+_{g,1}$, and $T^+_{n,1}$, equations for the six additional unknowns, T^+_a, T^+_c, q^+_a, q^+_c, $T^+_{g,2}$ and $T^+_{n,2}$, must be defined. They can be expressed as linear equations in terms of T^+_v, $T^+_{g,1}$, and $T^+_{n,1}$, and their derivations are presented in the remaining sections of this Appendix.

Atmospheric temperature and specific humidity

The first step in solving the surface energy budget is to eliminate the lowest atmospheric energy and water vapor variables from the snow surface energy budget equation. They will also be used to diagnose the final flux exchanges between the canopy air space and overlying atmosphere.

The atmospheric turbulence scheme is generally expressed as a second order diffusion equation in the vertical (which is assumed herein) and it is discretized using the backward difference time scheme. Assuming a fixed for zero (the general case) upper boundary condition at the top of the atmosphere, the diffusion equations for the generic variable ϕ can be cast as a linear function of the variable in the layer below following Polcher et al. (1998) as

$$\phi^+_k = B_{\phi,k} + A_{\phi,k}\,\phi^+_{k+1} \qquad (k = 1, N_a - 1) \tag{4.390}$$

where N_a represents the number of atmospheric model layers, $k = 1$ represents the uppermost layer with k increasing with decreasing height above the surface, and the superscript $+$ indicates the value of ϕ at time $t + \Delta t$ (at the end of the time step). The coefficients $A_{\phi,k}$ and $B_{\phi,k}$ are computed in a downward sweep within the turbulence scheme. As shown by Best el al. (2004), the equation for the lowest atmospheric model layer can be expressed using a flux lower boundary condition as

$$\phi^+_{N_a} = B_{\phi,N_a} + A_{\phi,N_a}\,F^+_{\phi,N_a+1} \qquad (k = N_a) \tag{4.391}$$

where F^+_{ϕ,N_a+1} is the implicit surface flux from one or multiple surface energy budgets. For explicit land-atmosphere coupling or offline land-only applications, the coupling coefficients can be set to $A_{\phi,N_a} = 0$ and $B_{\phi,N_a} = \phi_{N_a}$ in the driving code.
From Eq. 4.391, the thermodynamic variable of the lowest atmospheric model variable at time $t + \Delta t$ is defined as

$$\mathcal{T}^+_{N_a} = B_{\mathcal{T},N_a} \; + \; A_{\mathcal{T},N_a} \, H^+ \tag{4.392}$$

Note that using Eq. 4.238, we can rewrite Eq. 4.392 in terms of air temperature as

$$T_a{}^+ = B_{T_a} \; + \; A_{T_a} \, H^+ \tag{4.393}$$

where $B_{T_a} = \left(B_{\mathcal{T},N_a} - \mathcal{B}_a\right)/\mathcal{A}_a$, $A_{T_a} = A_{\mathcal{T},N_a}/\mathcal{A}_a$, and T_a is shorthand for $T(k = N_a)$. Substitution of Eq. 4.233 for H in Eq. 4.393 and solving for T^+_a yields

$$T^+_a = \mathscr{B}_{T_a} \; + \; \mathscr{A}_{T_a} \, T^+_c \; + \; \mathscr{C}_{T_a} \, T^+_n \tag{4.394}$$

where

$$C = \mathcal{A}_a \Big\{ 1 + A_{T_a} \left[\varphi_{c-a} \left(1 - p_{sng} \, p_{\alpha n} \right) + p_{sng} \, p_{\alpha n} \, \varphi_{n-a} \right] \Big\} \tag{4.395a}$$

$$\mathscr{A}_{T_a} = A_{T_a} \, \varphi_{c-a} \, \mathcal{A}_c \left(1 - p_{sng} \, p_{\alpha n} \right) / C \tag{4.395b}$$

$$\mathscr{B}_{T_a} = \Big\{ B_{T_a} \; - \; \mathcal{B}_a \; + \; A_{T_a} \Big[\left(1 - p_{sng} \, p_{\alpha n} \right) \varphi_{c-a} \; \left(\mathcal{B}_c - \mathcal{B}_a \right) + p_{sng} \, p_{\alpha n} \, \varphi_{n-a} \left(\mathcal{B}_c - \mathcal{B}_a \right) \Big] \Big\} / C \tag{4.395c}$$

$$\mathscr{C}_{T_a} = A_{T_a} \, p_{sng} \, p_{\alpha n} \, \varphi_{n-a} \, \mathcal{A}_c / C \tag{4.395d}$$

$$\tag{4.395e}$$

In analogous fashion to determining the air temperature, the specific humidity of the lowest atmospheric model variable at time $t + \Delta t$ is defined from Eq. 4.391 as

$$q^+_a = B_{q,a} \; + \; A_{q,a} \, E^+ \tag{4.396}$$

where again the subscript q, a represents the values of the coefficients A and B for the lowest atmospheric model layer ($k = N_a$). Substitution of Eq. 4.249 for E in Eq. 4.396 and solving for T^+_a yields

$$q^+_a = \mathscr{B}_{q,a} \; + \; \mathscr{A}_{q,a} \, q^+_c \; + \; \mathscr{C}_{q,a} \, q^+_{sati\,n} \tag{4.397}$$

where the coefficients are defined as

$$C = 1 + A_{q,a} \left[\left(1 \; - \; p_{sng} \, p_{\alpha n} \right) \varphi_{c-a} \; + \; \varphi_{n-a} \, h_{sn} \, p_{\alpha n} \, p_{sng} \right] \tag{4.398a}$$

$$\mathscr{A}_{q,a} = A_{q,a} \, \varphi_{c-a} \left(1 \; - \; p_{sng} \, p_{\alpha n} \right) / C \tag{4.398b}$$

$$\mathscr{B}_{q,a} = B_{q,a} / C \tag{4.398c}$$

$$\mathscr{C}_{q,a} = A_{q,a} \, \varphi_{n-a} \, h_{sn} \, p_{\alpha n} \, p_{sng} / C \tag{4.398d}$$

Canopy air temperature and specific humidity

In order to close the energy budgets, T^+_c and q^+_c must be determined.
Assuming conservation of the heat flux between the different surfaces and the canopy air space, we have

$$\left(1 - p_{sng} p_{n\alpha} \right) \; H^+_c \; = \; p_{sng} \; \left(1 - p_{n\alpha} \right) \; H^+_{n-c} \; + \; \left(1 - p_{sng} \right) \; H^+_g \; + \; H^+_v \tag{4.399}$$

which can be expanded as

$$\begin{aligned}\varphi_{c-a}\left(1-p_{sng}\,p_{\alpha n}\right)\times\\ \left(\mathcal{B}_c+\mathcal{A}_c\,T_c^+-\mathcal{B}_a-\mathcal{A}_a\,T_a^+\right)=&\mathcal{A}_c\Big[\varphi_g\left(T_g^+-T_c^+\right)\left(1-p_{sng}\right)+\varphi_v\left(T_v^+-T_c^+\right)\\ &\varphi_{n-c}\left(T_n^+-T_c^+\right)p_{sng}\left(1-p_{\alpha n}\right)\Big]\end{aligned}\tag{4.400}$$

Note that the above conservation equation does not include the part of the snow sensible heat flux which is in direct contact with the atmosphere (H_{n-a}) since it was already accounted for in the expression for T_a^+ via Eq. 4.393. Eliminating T_a^+ using Eq. 4.394 and solving for T_c^+ yields

$$T_c^+=a_{Tc}+b_{Tc}\,T_v^+ + c_{Tc}\,T_g^+ + d_{Tc}\,T_n^+\tag{4.401}$$

with the coefficients

$$\begin{aligned}C=&\varphi_{c-a}\left(1-p_{sng}\,p_{\alpha n}\right)\left(\mathcal{A}_c-\mathcal{A}_a\,\mathscr{A}_{T\,a}\right)+\\ &\mathcal{A}_c\left[\varphi_v+\varphi_g\left(1-p_{sng}\right)+\varphi_{n-c}\,p_{sng}\left(1-p_{\alpha n}\right)\right]\end{aligned}\tag{4.402a}$$

$$a_{Tc}=\Big[\varphi_{c-a}\left(1-p_{sng}\,p_{\alpha n}\right)\left(\mathcal{B}_a-\mathcal{B}_c+\mathcal{A}_a\,\mathscr{B}_{T\,a}\right)\Big]/C\tag{4.402b}$$

$$b_{Tc}=\mathcal{A}_c\,\varphi_v/C\tag{4.402c}$$

$$c_{Tc}=\mathcal{A}_c\,\varphi_g\left(1-p_{sng}\right)/C\tag{4.402d}$$

$$d_{Tc}=\left[\mathcal{A}_c\,\varphi_{n-c}\,p_{sng}\left(1-p_{\alpha n}\right)+\mathcal{A}_a\,\mathscr{C}_{T\,a}\,\varphi_{c-a}\left(1-p_{sng}\,p_{\alpha n}\right)\right]/C\tag{4.402e}$$

In an analogous fashion for canopy air temperature determination, assuming conservation of the vapor flux between the different surfaces and the canopy air space,

$$\left(1-p_{sng}p_{n\alpha}\right)E_c^+ = p_{sng}\left(1-p_{n\alpha}\right)E_{n-c}^+ + \left(1-p_{sng}\right)E_g^+ + E_v^+\tag{4.403}$$

which can be expanded using the definitions of the evaporative fluxes, E_x, from Eq.s 4.245-4.403 together with the definitions of q_g from Eq. 4.250 and q_a^+ from Eq. 4.397 as

$$\begin{aligned}\varphi_{c-a}\left(1-p_{sng}\,p_{\alpha n}\right)\times\\ \left[q_c^+\left(1-\mathscr{A}_{q,a}\right)-\mathscr{B}_{q,a}-\mathscr{C}_{q,a}\,q_{sati\,n}^+\right]=&\Big[\varphi_g\left(h_{sg}\,q_{sat\,g}^+-h_a\,q_c^+\right)\left(1-p_{sng}\right)+\varphi_v\,h_{sv}\left(q_{sat\,v}^+-q_c^+\right)\\ &\varphi_{n-c}\,h_{sn}\left(q_{sati\,n}^+-q_c^+\right)p_{sng}\left(1-p_{\alpha n}\right)\Big]\end{aligned}\tag{4.404}$$

Owing to the linearization of the $q_{sat\,x}$ terms about T_x, Eq. 4.404 can be solved for q_c^+ as a function of the surface energy budget temperatures as

$$q_c^+=a_{qc}+b_{qc}\,T_v^+ + c_{qc}\,T_g^+ + d_{qc}\,T_n^+\tag{4.405}$$

where the coefficients are defined as

$$\begin{aligned} C =& \varphi_{c-a}\,(1\,-\,p_{sng}\,p_{n\alpha})\,(1-\mathscr{A}_{q,a})\,+\,\varphi_g\,h_N\,(1-p_{sng}) \\ &+\,\varphi_v\,h_{sv}\,+\,\varphi_{n-c}\,h_{sn}\,p_{sng}\,(1-p_{n\alpha}) \end{aligned} \tag{4.406a}$$

$$\begin{aligned} a_{qc} =& \Big\{ (1\,-\,p_{sng}\,p_{n\alpha})\,\varphi_{c-a}\,\mathscr{B}_{q,a} + \varphi_v\,h_{sv}\left(q_{sat\,v}\,-\,\frac{\partial q_{sat\,v}}{\partial T_v}\,T_v\right) \\ &+\,\varphi_g\,h_{sg}\left(q_{sat\,g}\,-\,\frac{\partial q_{sat\,g}}{\partial T_g}\,T_g\right)\,(1-p_{sng}) \\ &+\,\varphi_{n-c}\,h_{sn}\left(q_{sati\;n}\,-\,\frac{\partial q_{sati\;n}}{\partial T_n}\,T_n\right)\,p_{sng}\,(1-p_{n\alpha})\Big\}/C \end{aligned} \tag{4.406b}$$

$$b_{qc} = h_{sv}\,\varphi_v\,\frac{\partial q_{sat\,v}}{\partial T_v}/C \tag{4.406c}$$

$$c_{qc} = h_{sg}\,\varphi_g\,\frac{\partial q_{sat\,g}}{\partial T_g}\,(1-p_{sng})\,/C \tag{4.406d}$$

$$d_{qc} = h_{sn}\,\varphi_{n-c}\,\frac{\partial q_{sati\;n}}{\partial T_n}\,p_{sng}\,(1-p_{n\alpha})\,/C \tag{4.406e}$$

Sub-surface temperatures

The sub-surface conduction heat fluxes can be expressed in compact form as

$$G^+_{x,k} = \Lambda_{x,k}\left(T^+_{x,k} - T^+_{x,k+1}\right) \tag{4.407}$$

where $\Lambda_{x,k}$ represents the ratio of the inter-facial thermal conductivity to the thickness between the mid-points of contiguous layers (k and $k+1$). Using the methodology described in Appendix **??** for the atmospheric diffusion scheme, the soil and snow heat diffusion equation (both using the form of Eq. 4.355) can be defined in an analogous fashion as

$$T^+_{g,k} = B_{g,k}\,+\,A_{g,k}\,T^+_{g,k-1} \qquad\qquad (k = 2, N_g) \tag{4.408}$$

where the coefficients $B_{g,k}$ and $A_{g,k}$ are determined during the upward sweep (first step of the tridiagonal solution) from the base of the soil to the sub-surface soil and snow layers as described by Richtmeyer and Morton (1967). The resulting coefficients for the soil are defined as

$$C = (\mathcal{C}_{g\,k}/\Delta t)\,+\,\Lambda_{g\,k-1}\,+\,\Lambda_{g\,k}\,(1-A_{g\,k+1}) \tag{4.409a}$$

$$B_{g\,i} = [(\mathcal{C}_{g\,k}/\Delta t)\;Tg\,k\,+\,\Lambda_{g\,k}\,B_{g\,k+1}]\,/C \qquad (2 \le k \le N_g - 1) \tag{4.409b}$$

$$A_{g\,k} = \Lambda_{g\,k-1}/C \tag{4.409c}$$

The same form holds for the snow layers. The upward sweep is performed before the evaluation of the energy budget, thus Eq. 4.408 is used to eliminate $T^+_{g,2}$ and $T^+_{n,2}$ from Eq.s 4.387 and 4.388, respectively. To do this, the sub-surface implicit fluxes in Eq.s 4.224 and 4.225 can be expressed, respectively, as

$$G^+_{g,1} = \Lambda_{g,1}\left[T^+_{g,1}\,(1\,-\,A_{g,2})\,+\,B_{g,2}\right] \tag{4.410a}$$

$$G^+_{n,1} = \Lambda_{n,1}\left[T^+_{n,1}\,(1\,-\,A_{n,2})\,+\,B_{n,2}\right] \tag{4.410b}$$

Net Longwave radiation flux derrivatives

The first order derivatives of the net longwave radiation terms are needed in order to solve the system of linearized surface energy budget equations (Eq.s 4.386-4.388). The Taylor series expansion (neglecting

higher order terms) is expressed as

$$LW^{+}_{net\,i} = LW_{net\,i} + \sum_{j=1}^{N_{seb}} \frac{\partial L_{net\,i}}{\partial T_j} \left(T_j^{+} - T_j \right) \qquad (i = 1, N_{seb}) \tag{4.411}$$

where N_{seb} represents the number of surface energy budgets, and i and j represent the indexes for each energy budget. The superscript $+$ represents the variable at time $t + \Delta t$, while by default, no superscript represents the value at time t. Eq. 4.411 therefore results in a $N_{seb}\,x\,N_{seb}$ Jacobian matrix (3x3 for MEB). The matrix coefficients are expressed as

$$\frac{\partial LW_{net\,v}}{\partial T_v} = \frac{\partial G_g}{\partial T_v} - \frac{\partial H_g}{\partial T_v} - 2\frac{\partial F_g}{\partial T_v} + \frac{\partial G_n}{\partial T_v} - \frac{\partial H_n}{\partial T_v} - 2\frac{\partial F_n}{\partial T_v} \tag{4.412a}$$

$$\frac{\partial LW_{net\,v}}{\partial T_g} = \frac{\partial I_g}{\partial T_g} - \frac{\partial J_g}{\partial T_g} - \frac{\partial K_g}{\partial T_g} - \frac{\partial L_g}{\partial T_g} \tag{4.412b}$$

$$\frac{\partial LW_{net\,v}}{\partial T_n} = \frac{\partial I_n}{\partial T_n} - \frac{\partial J_n}{\partial T_n} - \frac{\partial K_n}{\partial T_n} - \frac{\partial L_n}{\partial T_n} \tag{4.412c}$$

$$\frac{\partial LW_{net\,g}}{\partial T_v} = \frac{\partial F_g}{\partial T_v} - \frac{\partial G_g}{\partial T_v} \tag{4.412d}$$

$$\frac{\partial LW_{net\,g}}{\partial T_g} = \frac{\partial J_g}{\partial T_g} - \frac{\partial I_g}{\partial T_g} \tag{4.412e}$$

$$\frac{\partial LW_{net\,g}}{\partial T_n} = \frac{\partial J_n}{\partial T_n} \tag{4.412f}$$

$$\frac{\partial LW_{net\,n}}{\partial T_v} = \frac{\partial F_n}{\partial T_v} - \frac{\partial G_n}{\partial T_v} \tag{4.412g}$$

$$\frac{\partial LW_{net\,n}}{\partial T_g} = \frac{\partial K_g}{\partial T_g} \tag{4.412h}$$

$$\frac{\partial LW_{net\,n}}{\partial T_n} = \frac{\partial J_n}{\partial T_n} - \frac{\partial I_n}{\partial T_n} \tag{4.412i}$$

Using Eq. 4.289 to evaluate the derivatives we have

$$\frac{\partial LW_{net\,v}}{\partial T_v} = \frac{4}{T_v} \left(G_g - H_g - 2F_g + G_n - H_n - 2F_n \right) \tag{4.413a}$$

$$\frac{\partial LW_{net\,v}}{\partial T_g} = \frac{4}{T_g} \left(I_g - J_g - K_g - L_g \right) \tag{4.413b}$$

$$\frac{\partial LW_{net\,v}}{\partial T_n} = \frac{4}{T_n} \left(I_n - J_n - K_n - L_n \right) \tag{4.413c}$$

$$\frac{\partial LW_{net\,g}}{\partial T_v} = \frac{4}{T_v} \left(F_g - G_g \right) \tag{4.413d}$$

$$\frac{\partial LW_{net\,g}}{\partial T_g} = \frac{4}{T_g} \left(J_g - I_g \right) \tag{4.413e}$$

$$\frac{\partial LW_{net\,g}}{\partial T_n} = \frac{4}{T_n} J_n \tag{4.413f}$$

$$\frac{\partial LW_{net\,n}}{\partial T_v} = \frac{4}{T_v} \left(F_n - G_n \right) \tag{4.413g}$$

$$\frac{\partial LW_{net\,n}}{\partial T_g} = \frac{4}{T_g} K_g \tag{4.413h}$$

$$\frac{\partial LW_{net\,n}}{\partial T_n} = \frac{4}{T_n} \left(K_n - I_n \right) \, f_{LWn} \tag{4.413i}$$

so that from a coding perspective, the computation of the derivatives is trivial (using already computed quantities). Note that Eq. 4.413i has been corrected relative to Boone et al. (2017) in that the first term on the RHS should be K_n, not J_n. But note that in fact, this correction has almost no impact on the results since this term is nearly two orders of magnitude smaller than the largest term of the net longwave snow term. Also, note that the factor f_{LWn} has been added to this derivative term. It is defined as

$$f_{LWn} \;=\; \min\{1,\, \max\left[0,\, T_{grad\,max} - (T_n - T_v)\right]/T_{grad\,dif}\} \qquad (T_n > T_v) \qquad (4.414)$$

The need for this factor is quite rare: for very thin snow combined with extremely cold conditions, very weak $LW\downarrow$ forcing and strong temperature differences between a relatively warm snow surface and the overlying atmosphere, the derrivative $\partial LW_{net\,n}/\partial T_n$ can pose problems (i.e. the assumption of a linear change in $LW_{net\,n}$ relative to T_n over the given time step is a poor approximation). Note that under these conditions, T_v should be close to T_c, thus we used T_v as a proxy to compute the aforementioned temperature gradient. Thus in these rare instances, this derivative is forced to vanish over some small temperature difference range: $T_{grad\,dif}$, when it exceeds the gradient $T_{grad\,max} - T_{grad\,dif}$. Also note that this (when this zerm is zero) has no impact on numerical stability since the longwave linerization has no effect on this and has no impact on results in the general sense (since it is temporary and the assumed gradieints are so large that they are rarely, if ever during a run, encountered). For example, default values are $T_{grad\,max} = 60$ K and $T_{grad\,dif} = 10$ K, thus it should be evoked rarely, if ever. Indeed, the linearization is needed simply to ensure better phasing of T_{rad} for large model time steps.

Halstead coefficient maximum

A maximum Halstead coefficient is imposed by estimating which value of δ_v that is needed to just evaporate any existing intercepted water, W_{rv}, given the conditions at the beginning of the time step. Assuming that phase changes are small, and neglecting canopy drip and any condensation from transpiration, the time-differenced prognostic equation for intercepted water on canopy vegetation (Eq. 4.324) can be approximated as:

$$\frac{{W_{rv}}^+ - W_{rv}}{\Delta t} = (1-\chi_v)(1-p_{sng}p_{\alpha n})P_r - E_r \qquad (4.415)$$

Assuming that all existing water evaporates in one time step (i.e. $W_{rv}^+ = 0$), and substituting the full expression for E_r (Eq. 4.263) into Eq. 4.415, the maximum value of δ_v can be determined as

$$\delta_{v,max} = \frac{\left[(1-\chi_v)\,(1-p_{sng}p_{\alpha n})\,P_r \;+\; (W_{rv}/\Delta t)\right](L/L_v)}{\rho_a\,(1-p_{nv})\,k_v\Big\{\left[p_{sng}\,(1-p_{\alpha n})\,/R_{avn-c}\right] \;+\; \left[(1-p_{sng})\,/R_{avg-c}\right]\Big\}\,(q_{sat\,v} \;-\; q_c)} \qquad (4.416)$$

Eq. 4.416 is an approximation since all of the variables on the RHS use conditions from the start of the time step, however, this method has proven to greatly reduce the risk for occasional numerical artifacts (jumps) and the associated need for mass corrections (if net losses in mass exceed the updated test value for interception storage).

Surface stresses

Using the same surface-atmosphere coupling methodology as for temperature and specific humidity, the u-wind component in the lowest atmospheric model layer can be expressed as

$$u_a^+ = B_{u\,a} \;+\; A_{u\,a}\,\tau_x^+ \qquad (4.417)$$

The surface u component momentum exchange with the atmosphere is expressed as

$$\tau_x^+ = -u_a^+ \left[(1 - p_{sng}\, p_{n\alpha})\, \varphi_{Dc-a} \;+\; p_n\, p_{n\alpha} \varphi_{Dn-a} \right] \tag{4.418}$$

where it includes stresses from the snow-buried and non-snow buried portions of the surface consistent with the fluxes of heat and water vapor. For simplicity, we have defined

$$\varphi_{Dx} = \rho_a\, V_a\, C_{Dx} \tag{4.419}$$

and C_D is the surface drag coefficient (Eq. 4.208). Eliminating τ_x^+ from Eq. 4.418 using Eq. 4.419 gives

$$u_a^+ = \frac{B_{u\,a}}{1 \;+\; A_{u\,a}\, \varphi_{Dc}} \tag{4.420}$$

where for convenience we have defined the average drag coefficient as

$$\varphi_{Dc} = (1 - p_{sng}\, p_{n\alpha})\, \varphi_{Dc-a} \;+\; p_{sng}\, p_{n\alpha} \varphi_{Dn-a} \tag{4.421}$$

The net u-momentum flux from the surface to the canopy air space is expressed as

$$\tau_x^+ = -\frac{B_{u\,a}\, \varphi_{Dc}}{(1 \;+\; A_{u\,a}\, \varphi_{Dc})} \tag{4.422}$$

Finally, the vector momentum flux in the atmosphere can be computed from the scalar friction velocity:

$$u^* = \left(\frac{\varphi_{Dc}\, V_a^+}{\rho_a} \right)^{1/2} \tag{4.423}$$

where V_a^+ is the updated wind speed (computed from u_a^+ and v_a^+). Note that v_a^+ and τ_y^+ are computed in the same manner, but using $B_{v\,a}$ from the atmosphere (note that $A_{v\,a} = A_{u\,a}$).

Summary: Final solution of the implicitly coupled equations

The fully implicit solution of the surface and atmospheric variables proceeds for each model time step as follows:

1. Within the atmospheric model, perform the downward sweep of the tri-diagonal matrix within the turbulent diffusion scheme of the atmospheric model to obtain the $A_{\phi,k}$ and $B_{\phi,k}$ coefficients for each diffused variable ($\phi = \mathcal{T}$, q, u, and v) for each layer of the atmosphere ($k = 1, N_a$). Update $\mathcal{A}_a$ and $\mathcal{B}_a$, then pass these values along with the aforementioned coupling coefficients at the lowest atmospheric model layer (i.e. $A_{T,a}$, $B_{T,a}$, $A_{q,a}$, $B_{q,a}$, $A_{u,a}$, $B_{u,a}$, and $B_{v,a}$) to the land surface model. These coefficients are then used to eliminate T_a^+ and q_a^+ from the implicit surface energy budget equations (Eq.s 4.386-4.388).

2. Within the land surface model, perform the upward sweep of the tri-diagonal matrix within the soil and snow layers to determine the $A_{n,k}$, $B_{n,k}$, $A_{g,k}$, and $B_{g,k}$, coefficients for the soil and snow layers (from soil layer N_g to layer 2, and again from soil layer N_g to layer 2 of the snow scheme). Note that coefficients for layer 1 of the snow and soil schemes are not needed since they correspond to the linearized surface energy budgets (next step).

3. Within the land surface model, the expressions for T_a^+ (Eq. 4.394), q_a^+ (Eq. 4.397), T_c^+ (Eq. 4.401), q_c^+ (Eq. 4.405), $T_{g,2}^+$ (Eq. 4.410a)and $T_{n,2}^+$ (Eq. 4.410b) can now be substituted into the energy budget equations (Eq.s 4.386-4.388) which can then be readily solved for T_v^+, $T_{g,1}^+$, and $T_{n,1}^+$.

4. Within the land surface model, perform back-substitution (using $T^+_{g,1}$ as the upper boundary condition) to obtain $T^+_{g,k}$ for soil layers $k = 2, N_g$ using Eq. 4.408.

5. Within the land surface model, call the explicit snow-process scheme to update the snow scheme temperature, $T^+_{n,k}$, and the snow mass variables for snow layers $k = 2, N_n$. The implicit snow surface fluxes, $R^+_{n,n}$, H^+_n and E^+_n, are used as the upper boundary condition along with the implicit soil temperature, $T^+_{g,1}$, to compute the updated lower snowpack boundary condition (i.e. the snow-soil inter-facial flux, G_{gn}).

6. Within the land surface model, compute V^+_a (See Section 4.1.13). Diagnose T^+_a, T_c+, q^+_a and q^+_c (again, using the equations mentioned in Step 3) in order to compute the updated (implicit) fluxes. The updated evapotranspiration (Eq.s 4.262-4.266) and snow melt water mass fluxes are used within the hydrology schemes to update the different water storage variables for the soil and vegetation canopy (Eq.s 4.324-4.328).

7. Within the atmospheric model, perform back-substitution (using H^+, E^+, τ^+_x and τ^+_y as the lower boundary conditions: Eq. 4.391) to obtain updated profiles (or turbulent tendencies, depending on the setup of the atmospheric model) of $\mathcal{T}_k$, q_k, u_k and v_k for atmospheric layers $k = 1, N_a$. Finally, the updated upwelling shortwave, $SW\uparrow$, and implicit longwave flux, $LW\uparrow^+$ (or equivalently, the effective emissivity and implicit longwave radiative temperature, T^+_{rad}) are returned to the atmospheric model as lower boundary conditions for the respective radiative schemes.

Alternately, in offline mode, $A_{\phi,a} = 0$ and $B_{\phi,a} = \phi_a$ in the driving routine in Step 1, and the solution procedure ends at Step 6. Finally, if multiple patches and/or tiles are being used within the grid call of interest, the corresponding fractional-area weighted fluxes are passed to the atmospheric model in Step 7.

4.2 ISBA-A-gs surface scheme

Not up-to-date, new version to be released by June 2018

4.2.1 The Model

Introduction

Météo-France is developing SURFEX (SURFace EXternalisée) to be used in operational NWP models, and offline for applications in hydrology and vegetation monitoring (Martin *et al.* (2007)). SURFEX serves the merging of a number of land and ocean surface models. Over land, SURFEX includes ISBA-A-gs, a CO_2 responsive land surface model able to simulate the diurnal cycle of carbon and water vapour fluxes (Calvet *et al.* (1998), Calvet *et al.* (2004), Gibelin *et al.* (2006), Calvet *et al.* (2008)). This latter model accounts for different feedbacks in response to changes in [CO_2], photosynthesis enhancement and transpiration reduction (fertilization and anti-transpirant effects, respectively). Daily values of Leaf Area Index (LAI) and biomass can be produced by ISBA-A-gs.
ISBA-A-gs uses a CO_2 responsive parameterization of photosynthesis based on the model of Goudriaan *et al.* (1985) modified by Jacobs (1994) and Jacobs *et al.* (1996). This parameterization is less detailed than that commonly used in most land surface models (Farquar *et al.* (1980)) for C_3 plants and Collatz *et al.* (1992) for C_4 plants), but it has the same formulation for C_4 plants as for C_3 plants differing only by the input parameters. The model also includes an original representation of the soil moisture stress. Two different types of drought responses are distinguished for both herbaceous vegetation (Calvet (2000)) and forests (Calvet *et al.* 2004), depending on the evolution of the water use efficiency (WUE) under moderate stress: WUE increases in the early soil water stress stages in the case of the drought-avoiding response, whereas WUE decreases or remains stable in the case of the drought-tolerant response.
ISBA-A-gs calculates interactively the leaf biomass and the LAI (defined as the leaf area per unit ground area), using a simple growth model (Calvet *et al.* 1998). The leaf biomass is supplied with the carbon assimilated by photosynthesis, and decreased by a turnover and a respiration terms. LAI is inferred from the leaf biomass multiplied by the Specific Leaf Area ratio, which depends on the leaf nitrogen concentration (Calvet and Soussana (2001), Gibelin *et al.* 2006). Gibelin *et al.* (2006) showed that ISBA-A-gs simulates realistic LAI at the global scale under various environmental conditions. The physics of ISBA-A-gs has been implemented in SURFEX by CNRM. Meanwhile, the physics of ISBA-A-gs has been implemented in the ECMWF land surface scheme TESSEL (Van den Hurk *et al.* (2000)) by KNMI. The A-gs extension of TESSEL is called CTESSEL (Voogt *et al.* (2006), Lafont *et al.* (2006).

Background information

Vegetation patches SURFEX contains the ISBA-A-gs photosynthesis model, for which particular vegetation types need to be distinguished. In each grid box several vegetation types are present, with their own water and energy budget, and their own roughness length. ISBA-A-gs has a reduced number of parameters but is able to represent contrasting vegetation types. The model includes 7 vegetation types: 3 of them are high vegetation types: deciduous broadleaf forest, coniferous forest and evergreen broadleaf forest. The other 4 are low-vegetation types: C_3 grass, C_4 grass, C_3 crops and C_4 crops. The C_3 and C_4 carbon fixation mechanisms correspond to contrasting photosynthetic biochemical pathways. C_3 plants represent the vast majority of the Earths plant biomass. C_4 plants consist mainly of tropical grasses and some of them are cultivated (maize, sorghum, millet, sugar cane).

Table 4.7: Options of ISBA-A-gs

Option	Drought response	Leaf Area Index and leaf biomass	Above-ground biomass (non-woody)
AGS	Calvet *et al.* (1998)	Not calculated (prescribed value is used)	Not calculated
LAI	Calvet *et al.* (1998)	Calculated (from photosynthesis)	Not calculated
AST	Avoiding or Tolerant Calvet (2000), Calvet *et al.* (2004)	Not calculated (prescribed value is used)	Not calculated
LST	Avoiding or Tolerant Calvet (2000), Calvet *et al.* (2004)	Calculated (from photosynthesis)	Not calculated
NIT	Avoiding or Tolerant Calvet (2000), Calvet *et al.* (2004)	Calculated (from photosynthesis)	Calculated (nitrogen dilution)

The canopy resistance in ISBA-A-gs is calculated in the routine COTWORES (or COTWORESTRESS for the most recent version able to differentiate drought-avoiding from drought-tolerant biomes). The photosynthesis model is called from COTWORES (or COTWORESTRESS).

(!) The parameters of ISBA-A-gs cannot be aggregated/averaged. Spatial heterogeneity within a grid cell has to be represented by running the model several times (as many times as the number of patches found within the grid cell).

Options of ISBA-A-gs Five options of ISBA-A-gs (Table 4.7) can be activated by using the NAM_ISBA namelist

(!) The use of the most recent drought response formulation (present in options AST, LST, NIT) is recommended as it is based on meta-analyses of leaf-level observations and was validated successfully at the field and at the global scale (see Rivalland *et al.* (2006), Gibelin *et al.* (2006, 2008) and Calvet *et al.* 2008).
This option is used in CTESSEL (Voogt *et al.* (2006).

Photosynthesis Model (no water stress)

The canopy resistance is calculated from the photosynthesis, which is the net CO_2 assimilation (A_n) of the canopy. An is calculated as a function of different environmental factors based on the approach by Goudriaan *et al.* (1985).
First, CO_2 assimilation limited by the air CO_2 concentration is determined via a saturation equation:

$$A_m = A_{m,max} \left[1 - \exp\left\{-g_m^*(C_i - \Gamma)/A_{m,max}\right\}\right] \tag{4.424}$$

where $A_{m,max}$ is the maximum net CO_2 assimilation, g_m^* is the mesophyll conductance (with no soil water stress), C_i is the CO_2 concentration in the leaf and Γ is the CO_2 concentration at which assimilation com-

pensates respiration, called CO_2 compensation concentration. $A_{m,max}$ depends on temperature via a Q_{10} function:

$$A_{m,max}(T_s) = \frac{A_{m,max}(25) \times Q_{10}^{(T_s-25)/10}}{[1+\exp\{0.3(T_1-T_s)\}]\,[1+\exp\{0.3(T_s-T_2)\}]} \tag{4.425}$$

where $A_{m,max}(25)$ is $A_{m,max}$ at 25°C, Q_{10} is fixed at 2.0, T_s is the skin temperature in °C and T_1 and T_2 are reference temperature values (see Table 4.8). g_m in unstressed soil moisture conditions, g_m^*, depends on temperature via the same Q_{10} function as $A_{m,max}$. The dependence on temperature of Γ is described by:

$$\Gamma(T_s) = \Gamma(25) \times Q_{10}^{(T_s-25)/10} \tag{4.426}$$

where Q_{10} is fixed at 1.5.

Table 4.8: Values of model parameters at 25°C and of parameters in the temperature response functions (T in °C)

Mechanism	Parameter (X)	X(@25)	Q_{10}	T_1 [°]	T_2 [°]
C_3	ϵ_0 $[mg\ J^{-1}]$	0.017	-	-	-
	f_0^*	0.85	-	-	-
	Γ $[ppm]$	45	1.5	-	-
	g_m^* $[mm\ s^{-1}]$	7.0	2.0	5	36[1]
	$A_{m,max}$ $[mg\ m^{-2}\ s^{-1}]$	2.2	2.0	8	38
C_4	ϵ_0 $[mg\ J^{-1}]$	0.014	-	-	-
	f_0^*	0.50	-	-	-
	Γ $[ppm]$	2.8	1.5	-	-
	g_m^* $[mm\ s^{-1}]$	17.5	2.0	13	36
	$A_{m,max}$ $[mg\ m^{-2}\ s^{-1}]$	1.7	2.0	13	38

As can be seen from Table 4.8, some parameters depend only on the photosynthesis mechanism (C_3/C_4). Others, like g_m^*, depend on the vegetation type (Table 4.11). The internal CO_2 concentration C_i, is directly derived from the CO_2 concentration in the air C_s. It is controlled by the air humidity via:

$$C_i = fC_s + (1-f)\Gamma \tag{4.427}$$

and

$$f = f_0^* \left(1 - \frac{D_s}{D_{max}^*}\right) + f_{min} \left(\frac{D_s}{D_{max}^*}\right) \tag{4.428}$$

where D_{max}^* is the maximum specific humidity deficit of the air tolerated by the vegetation (with no soil water stress) and D_s is the actual deficit. If the deficit exceeds D_{max}^*, the plant closes its stomata. f_0^* is the value of f if there is no saturation deficit (with no soil water stress). Both the unstressed D_{max}^* and unstressed f_0^* are parameters that are vegetation type specific (Table 4.11). Depending on vegetation type and stress strategy, soil moisture stress influences these values (see Section 4.2.1). f_{min} is given by:

$$f_{min} = \frac{g_c}{g_c + g_m^*} \tag{4.429}$$

where g_c is the cuticular conductance, its value depending on vegetation type (Table 4.11). The CO_2 assimilation limited by CO_2 concentration is further limited by radiation by:

$$A_n = (A_m + R_d) \left\{ 1 - \exp\left[- \left(\frac{\epsilon\, I_a}{A_m + R_d} \right) \right] \right\} - R_d \tag{4.430}$$

where I_a is the photosynthetically active radiation (PAR), ϵ is the initial quantum use efficiency and R_d is the dark respiration. ϵ is given by:

$$\epsilon = \epsilon_0 \left(\frac{C_i - \Gamma}{C_i + 2\Gamma} \right) \tag{4.431}$$

[1] see section 4.2.3

where ϵ_0 is the maximum quantum use efficiency (Table 4.8). R_d is parameterized simply as:

$$R_d = A_m/9 \tag{4.432}$$

The stomatal conductance to CO_2, g_{sc}, is estimated using a flux-gradient relationship, modified to account for the effect of a specific humidity deficit on stomatal aperture. The first guess g^*_{sc} is given by:

$$g^*_{sc} = \frac{A_n - A_{min}\left[\frac{D_s}{D^*_{max}}\left(\frac{A_n+R_d}{A_m+R_d}\right)\right] + R_d\left[1 - \left(\frac{A_n+R_d}{A_m+R_d}\right)\right]}{C_s - C_i} \tag{4.433}$$

where A_{min} represents the residual photosynthesis rate (at full light intensity) associated with cuticular transfers when the stomata are closed because of a high specific humidity deficit. It is parameterized as:

$$A_{min} = g^*_m(C_{min} - \Gamma) \tag{4.434}$$

where C_{min} is the value of C_i at maximum specific humidity deficit ($D_s = D^*_{max}$):

$$C_{min} = \frac{g_c C_s + g^*_m \Gamma}{g_c + g^*_m} \tag{4.435}$$

Taking into account the ratio of diffusivity of water vapour and CO_2 (=1.6), the first guess of the stomatal conductance to water vapour is:

$$g_s^{first} = 1.6 g_{sc}^{first} \tag{4.436}$$

The diffusion of CO_2 interacts with that of water vapour. The first guess of the stomatal conductance to CO_2, must be corrected for this interaction by:

$$g_{sc} = g_{sc}^{first} + E\frac{M_a}{\rho_a M_v}\frac{C_s + C_i}{2(C_s - C_i)} \tag{4.437}$$

where M_a and M_v are molecular masses of air and water vapour respectively, ρ_a is the air density and E is leaf transpiration based on the first guess of the stomatal conductance to water vapour:

$$E = \rho_a g_s^{first} D_s \tag{4.438}$$

In order to refine the estimation of the stomatal conductances to CO_2 and water vapour, a single iteration over Eqs. 4.436, 4.438 and 4.437 is applied. Finally, the stomatal conductance to water vapour is given by:

$$g_s = 1.6 g_{sc} + g_c \tag{4.439}$$

Soil moisture stress parameterization

Initial version In the initial version of ISBA-A-gs (Calvet *et al.* 1998), the effect of soil moisture stress was applied to the mesophyll conductance, by multiplying g^*_m by the normalized soil moisture. This quantity is referred to by the function f_2:

$$f_2 = \frac{\bar{w} - w_{wilt}}{w_{fc} - w_{wilt}} \tag{4.440}$$

In this version D^*_{max} was fixed at 45 $g\ kg^{-1}$. The value of f_0 for C_3 plants was 0.85 and for C_4 plants 0.5. The routine corresponding to the initial version is called COTWORES.

Table 4.9: Differences between figure 4.21 and the model

	f_{2c}	D_{maxX}	D_{maxN}
Figure	0.5	403	55
Model	0.3	300	30

Improved representation of plant response to drought The initial parameterization is replaced by a more complex one, based on a meta-analysis of several herbaceous and woody vegetation types (Calvet, 2000; Calvet *et al.* 2004). The meta-analysis shows relationships between g_m and D_{max} for low vegetation and between g_m and f_0 for high vegetation. Furthermore, it seems that plants react in two different ways to soil moisture stress. There are plants that try to avoid stress, by reducing the evaporation via stomatal regulation, and/or growing during well-watered conditions. This stress strategy is typified as drought-avoiding (or defensive). Others apply another strategy in order to resist stress, by a more efficient root water-uptake or a more rapid growing cycle. This stress strategy is typified as drought-tolerant (or offensive). Among species within the 7 vegetation classes of ISBA-A-gs both strategies may occur. Therefore, it is not easy to generalize the strategy for each class. It seems most likely that coniferous forests and C_3 crops have a drought-avoiding strategy, whereas an drought-tolerant strategy is assigned to the other classes. In both stress strategies, 2 regimes are distinguished. One with moderate stress, in which the normalized soil moisture f_2 exceeds the critical value f_{2c}. The other with severe stress, where f_2 is less than f_{2c}. The critical value is fixed at 0.3 for global modelling. For local modelling this value may be adapted to available data.

Low vegetation Calvet (2000) discusses the soil moisture stress response by low vegetation types. In unstressed conditions, the following relationship holds for low vegetation types:

$$C_3\ plants: \ \ln(g_m^*) = 2.381 - 0.6103 \ln(D_{max}^*) \tag{4.441}$$

$$C_4\ plants: \ \ln(g_m^*) = 5.323 - 0.8923 \ln(D_{max}^*) \tag{4.442}$$

with g_m^* in mms^{-1} and D_{max}^* in gkg^{-1}.
The negative correlation between g_m and D_{max} indicates that plants that are sensitive to the air humidity (low D_{max} value), compensate the early closing of the stomata by a high mesophyll conductance. On the other hand, plants that are less sensitive to the air humidity have a lower mesophyll conductance. Figure 4.21 shows the stress response for low vegetation types schematically. The symbol θ is equal to f_2. The figure represents an example of a C_3 plant with specific parameter values. Table 4.9 presents differences between the example in the figure and the model values.
The starting point is the unstressed condition (θ=100%). First we follow the drought-avoiding strategy. When stress sets in, D_{max} decreases while g_m increases until the critical soil moisture is reached. This is described by:

$$D_{max} = D_{max}^N + (D_{max}^* - D_{max}^N)\frac{f_2 - f_{2c}}{1 - f_{2c}} \tag{4.443}$$

This strategy leads to less evaporation, but keeps up the CO_2 assimilation, thereby increasing the water use efficiency. Under moderate stress Eq. 4.441 is still valid. Via this equation, the maximum value of g_m, g_m^X,

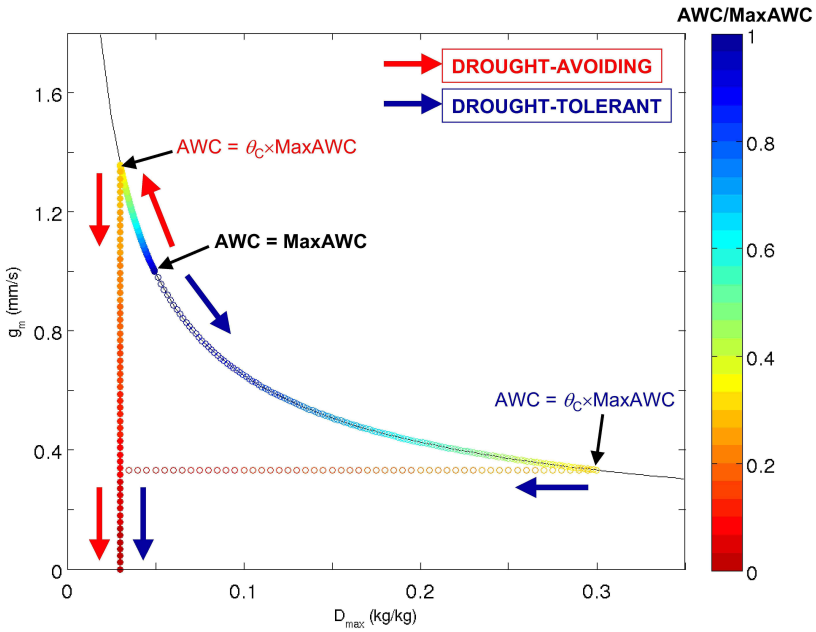

Figure 4.21: Responses of C3 herbaceous plants to soil moisture stress as represented in the ISBA-A-gs model, through the relationship between the mesophyll conductance at 25 °C, gm, and the maximum leaf-to-air saturation deficit, $Dmax$ (adapted from Calvet (2000): drought-avoiding and drought-tolerant (red and blue arrows, respectively). The soil moisture stress is represented by the ratio of the Available soil Water Content (AWC) to the maximum AWC ($MaxAWC$). For moderate soil water stress (i.e. $AWC > \theta_C \times MaxAWC$), the deviation of D_{max} from its unstressed value towards its minimum (0.03 kg kg^{-1}) or maximum (0.30 kg kg^{-1}) value (drought-avoiding and drought-tolerant, respectively), is proportional to AWC, scaled between $MaxAWC$ and $\theta_C \times MaxAWC$. The value of gm is driven by D_{max} through a logarithmic equation (solid line): $ln(gm) = 2.3810.6103 \times ln(Dmax)$, with gm and D_{max} in units of mm s^1 and g kg^1, respectively. For more pronounced soil water stress (i.e. $AWC < \theta_C \times MaxAWC$), either gm or D_{max} (drought-avoiding and drought-tolerant, respectively), decrease from its value at $AWC = \theta_C \times MaxAWC$ to its minimum value, proportional to $AWC/(\theta_C \times MaxAWC)$. As an example, the values $\theta_C = 0.3$ and unstressed $gm = 1\ mm.s^{-1}$ are used (Calvet *et al.* 2012).

follows from the value of D_{maxN}. If the stress goes below the critical value (severe stress), D_{max} does not change anymore, but g_m drops with ongoing severity of stress:

$$g_m = g_m^X \frac{f_2}{f_{2c}} \tag{4.444}$$

Now we follow the drought-tolerant strategy. When stress sets in, D_{max} increases while g_m decreases until the critical soil moisture is reached. This is described by:

$$D_{max} = D_{max}^X + (D_{max}^* - D_{max}^X)\frac{f_2 - f_{2c}}{1 - f_{2c}} \tag{4.445}$$

This strategy leads to more evaporation, thereby possibly decreasing the water use efficiency. If the stress goes below the critical value (severe stress), g_m does not change anymore, but D_{max} drops with ongoing severity of stress:

$$D_{max} = D^X_{max}\frac{f_2}{f_{2c}} \tag{4.446}$$

For low vegetation types in the new parameterization, D^*_{max} follows from g^*_m via Eq. 4.441. f^*_0 for C_3 plants is fixed at 0.95 and for C_4 plants at 0.6. The routine corresponding to the new version is called COTWORESTRESS.

High vegetation Calvet *et al.* (2004) discuss the soil moisture stress response by high vegetation types. In unstressed conditions, the following relationship holds for low vegetation types:

$$\ln(g^*_m) = 4.7 - 7f^*_0 \tag{4.447}$$

with g^*_m in $mm\ s^{-1}$. The product $g_m f_0$ controls A_m, since C_i is influenced by f_0. Therefore the negative correlation between the two parameters makes that CO_2 assimilation flux does not drop too much. Figure 4.22 shows the stress response for high vegetation types schematically. The starting point is the unstressed condition (θ=100%). First we follow the drought-avoiding strategy. When stress sets in, f_0 decreases while g_m keeps its unstressed value until the critical soil moisture is reached. This is described by:

$$f_0 = f^*_0 + (f^*_0 - f^N_0)\frac{1 - f_2}{1 - f_{2c}} \tag{4.448}$$

where f^N_0 is the value of f_0 given by the relationship between g_m and f_0 under severe stress conditions, with $g_m = g^*_m$:

$$\ln(g^*_m) = 2.8 - 7f_0 \tag{4.449}$$

This strategy leads to an increase of the water use efficiency. If the stress goes below the critical value (severe stress), f_0 increases and g_m decreases via:

$$g_m = g^*_m\frac{f_2}{f_{2c}} \tag{4.450}$$

Now we follow the drought-tolerant strategy. When stress sets in, f_0 keeps its unstressed value while g_m decreases until the critical soil moisture is reached. This is described by:

$$g_m = g^*_m - (g^*_m - g^N_m)\frac{1 - f_2}{1 - f_{2c}} \tag{4.451}$$

where g^N_m is the value of g_m given by Eq. 4.449 with $f_0 = f^*_0$. This strategy leads to a decrease of the water use efficiency. If the stress goes below the critical value (severe stress), f_0 increases and g_m decreases via:

$$g_m = g^N_m\frac{f_2}{f_{2c}} \tag{4.452}$$

For high vegetation types in the new parameterization, f^*_0 follows from g^*_m via Eq. 4.447. For D^*_{max} a relationship with g^*_m was developed based on results from Calvet *et al.* (2004):

$$D^*_{max} = -37.97\ln(g^*_m) + 150.4 \tag{4.453}$$

This equation was used in Table 4.11 to determine D^*_{max} in the case of forests.

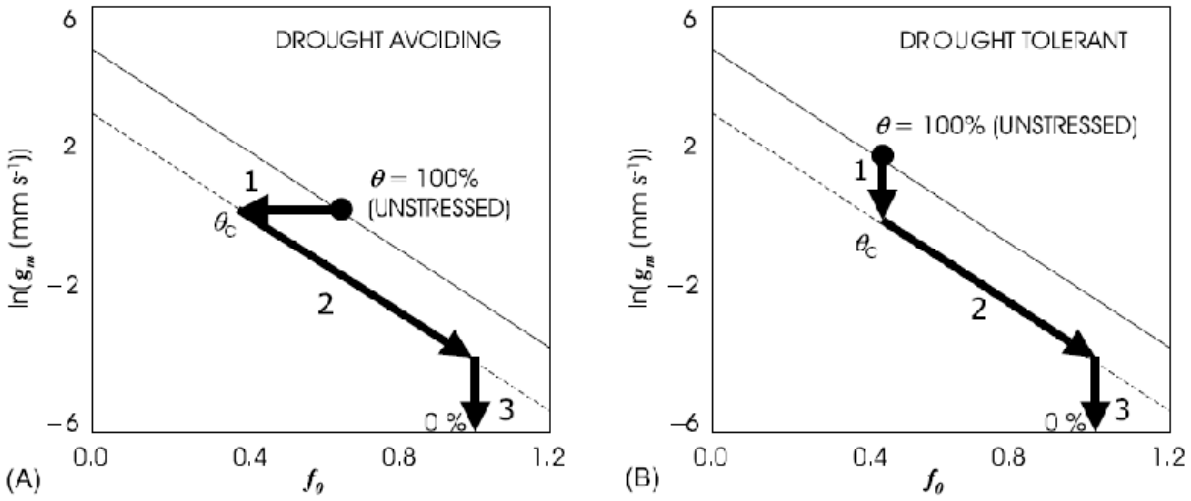

Figure 4.22: Stress responses for high vegetation. Reproduced from Calvet *et al.* (2004)

From leaf to canopy

The photosynthesis model calculates the net CO_2 assimilation at the leaf scale. For the upscaling to the canopy, integration over the canopy is needed. It is assumed that variables T_s, D_s and C_s do not vary within the canopy together with the model parameters. In SURFEX, wet leaves from the interception of rain or leaves covered by snow do not assimilate CO_2. The tile-specific skin temperature T_s is calculated by solving the surface energy balance for each tile. In COTWORES (and COTWORESTRESS), D_s at canopy level is calculated from D_s at the reference atmospheric level from a simple flux-gradient relationship by using the aerodynamic resistance ra and the water vapour flux of the previous time step. For C_s, this is done too, with the net CO_2 flux. The incoming shortwave radiation is attenuated in the canopy. At the top of the canopy, the incoming PAR is assumed to be 48% of the incoming shortwave radiation. The PAR extinction is described by Roujean (1996). The PAR at height z in the canopy is given by:

$$I_a(z) = [1 - K(z)] \times I_a(h) \tag{4.454}$$

where h is the height of the top of the canopy and K is the extinction coefficient given by:

$$K(z) = f(\theta_s) \times K_{df}(z) + [1 - f(\theta_s)] \times K_{dr}(z) \tag{4.455}$$

Where $K_{df}(z)$ and $K_{dr}(z)$ are the extinction coefficients of diffuse and direct light, respectively:

$$K_{df}(z) = 1 - \exp(-0.8bLAI(h - z)/h) \tag{4.456}$$

$$K_{dr}(z) = 1 - \exp\left(-\frac{G}{\cos\theta_s} bLAI(h - z)/h\right) \tag{4.457}$$

where θ_s is the solar zenith angle and G is a parameter that describes the distribution of leaves (a spherical angular distribution is assumed: G=0.5). f is the ratio of diffuse to total downward shortwave radiation at the top of the canopy given by:

$$f(\theta_s) = \frac{0.25}{0.25 + \cos\theta_s} \tag{4.458}$$

b is the foliage scattering coefficient:

$$b = 1 - \frac{1 - \sqrt{1-\omega}}{1 + \sqrt{1-\omega}} \tag{4.459}$$

where ω (=0.2) is the leaf single scattering albedo in the part of the solar spectrum corresponding to the PAR.
Assuming an homogeneous leaf vertical distribution, the integrated canopy net CO_2 assimilation and conductance can be written as:

$$A_{nI} = \frac{LAI}{h} \int_0^h A_n dz \tag{4.460}$$

$$g_{sI} = \frac{1}{r_s} = \frac{LAI}{h} \int_0^h g_s dz \tag{4.461}$$

where r_s is the canopy resistance. The integrations are parameterized with a three-point Gauss quadrature method:

$$A_{nI} = LAI \times \sum_{i=1}^{3} W_i A_n(z_i) \tag{4.462}$$

$$g_{sI} = LAI \times \sum_{i=1}^{3} W_i g_s(z_i) \tag{4.463}$$

where z_i and W_i are the Gauss levels and weights respectively. r_s is used in the calculation of the exchange of water vapour between the vegetation and the atmosphere.

Biomass evolution

The user may define whether the vegetation must be calculated interactively, or must follow from surface climatology fields of LAI. This can be done via a flag (Table 4.7) in the namelist NAM_ISBA (CPHOTO). This section presents the calculations belonging to interactive vegetation.
With a dynamic representation of LAI, the model is able to account for interannual variability, droughts in particular. The interactive LAI is based on biomass evolution due to photosynthetic activity. The biomass module simulates growth and mortality of the vegetation. Throughout SURFEX, the vegetation biomass is expressed in units of kg of dry matter per m^2.

Initial version In the initial version a single biomass reservoir B is considered (Calvet *et al.* 1998). It represents the photosynthetic active biomass, including the leaves and also a proportion of the stem and roots, which provide water for transpiration. Once a day (Δt = 1 day), at midnight, both growth and mortality is calculated:

$$B(t + \Delta t) = B(t) + \Delta B^+ - \Delta B^- \tag{4.464}$$

The growth is based on the accumulated net CO_2 assimilation over the previous day:

$$\Delta B^+ = \frac{M_C}{P_C M_{CO_2}} A_{nI,day} \Delta t \tag{4.465}$$

where P_c is the proportion of carbon in the dry plant biomass, for which a constant value of 0.4 is chosen, and M_C and M_{CO_2} are the molecular weights of carbon and CO_2 (12 and 44 $gmol^{-1}$). $A_{nI,day}$ is the daily accumulated A_{nI} . Mortality can be due to soil moisture stress, diseases and senescence but also to the transportation of organic molecules from the active biomass to stocking and structural organs. It is given by an exponential extinction of B characterized by a time-dependent effective life expectancy:

$$\Delta B^{-} = B\left(1 - \exp\left(-\frac{\Delta t}{\tau}\right)\right) \tag{4.466}$$

and

$$\tau(t) = \tau_M \frac{A_{nfm}(t)}{A_{n,max}} \tag{4.467}$$

where τ_M is the maximum effective life expectancy, depending on vegetation type (Table 4.11), A_{nfm} is the maximum leaf A_n reached on the previous day and $A_{n,max}$ is the optimum leaf A_n obtained when:
$D_s = 0\ g\ kg^{-1}$
$I_a(h) = 500\ W\ m^{-2}$
$T_s = 25$°C for C_3 plants and $T_s = 35$ °C for C_4 plants.

In order to avoid extreme loss of biomass in periods when A_n is low, the following constraint on leaf span time is imposed:

$$\tau \geq \frac{\tau_M}{10} \tag{4.468}$$

The LAI is obtained from the biomass assuming a constant ratio, depending on vegetation type (Table 4.11):

$$\alpha_B = \frac{B}{LAI} \tag{4.469}$$

One other vegetation parameter is needed, in order to enable vegetation to start assimilating CO_2 after a period of unfavourable conditions: a LAI minimum value LAI_{min} (Table 4.11). The routine of biomass loss is called LAILOSS. The routine of biomass growth is called LAIGAIN.

Version with nitrogen dilution

Theory In reality, α_B depends on climate (temperature and CO_2 concentration) and nitrogen fertilisation. In order to account for plant morphology, the nitrogen dilution concept by Lemaire and Gastal (1997) is applied in the new version of biomass evolution. The plant N decline model is a well-established agronomical law relating the plant N in non-limiting N-supply conditions to the accumulated aboveground dry matter. The critical plant N is the value of N maximizing growth, and this value decreases for increasing biomass accumulation following a negative power law. The basis of the model is that the metabolic component of the plant biomass is related to total biomass through an allometric logarithmic law (Calvet and Soussana, 2001). In ISBA-A-gs, the metabolic biomass component is identified as the active biomass, or leaf biomass. The relationship between active biomass B and total, non-woody aboveground biomass B_T is:

$$B_T = \left(\frac{B}{c}\right)^{1/(1-a)} \tag{4.470}$$

where a and c are constant parameters: $c = 0.754$, and a may vary with CO_2 concentration, but for the sake of simplicity a constant value $a = 0.38$ is used (XCA_1x_CO2_NIT). The total aboveground biomass

consists of the active biomass reservoir and the structural aboveground reservoir (B_s), which can be considered as the "living" structural biomass, like the stem. For forests, wood is a dead reservoir and does not contribute to B_s. Within the nitrogen dilution model a relationship between the leaf area ratio LAR and the aboveground nitrogen concentration N_T is applied:

$$LAR = \frac{LAI}{B_T} = eN_T + f \tag{4.471}$$

where e and f are called plasticity parameters and are derived per vegetation type (Table 4.11). Eq. 4.471 can be used as a closure equation to estimate α_B:

$$\alpha_B = \frac{1}{eN_a + f/(cB_T^{-a})} \tag{4.472}$$

where N_a is the nitrogen concentration in the active biomass. It depends on vegetation type and on the nitrogen fertilisation. For further details and derivations see Calvet and Soussana (2001). In this way, α_B has become a model variable depending on B_T . However, for global simulations, it is desirable to keep α_B as a constant parameter in order to let α_B represent rather intrinsic plant characteristics denoting a biological adaptation to average climate and growing conditions (Calvet and Soussana, 2001). For that purpose, Eq. 4.472 can only be solved by iteration. Moreover, LAR and N_T data to derive the plasticity parameters by regression is lacking. However, data is available for leaves in the form of the specific leaf area SLA and the nitrogen content in leaves N_L:

$$SLA = \frac{LAI}{B_L} = eN_L + f \tag{4.473}$$

Both the iteration issue and the availability of data to derive e and f give rise to modify the nitrogen dilution module. Eq. 4.472 is simplified by considering α_B as the ratio of the biomass of green leaves to LAI:

$$\alpha_B = \frac{1}{SLA} = \frac{1}{eN_L + f} \tag{4.474}$$

It must be noted that N_L may decrease for increasing CO_2 concentration (Calvet *et al.* 2008) and section 4.2.3).

Biomass reservoirs The different biomass reservoirs are calculated using a simplified allocation scheme (Calvet and Soussana, 2001). Figure 4.23 presents the allocation scheme schematically. Next to B and B_s, there is a belowground structural biomass reservoir B_{s2}. The active biomass is calculated in the same way as in the initial version (Eq. 40). The B-decline term (Eq. 4.466) is split into a mortality and storage term:

$$\Delta B^- = M_B + S_B \tag{4.475}$$

In the growing phase ($\Delta B^+ \geq \Delta B^-$) the N decline equations can be applied. When the vegetation becomes senescent ($\Delta B^+ < \Delta B^-$), the equations are no longer valid. Therefore a distinction between the two phases is made.

In the growing phase, following the N decline equations, B_T is derived from B using Eq. 4.470 and B_s is the difference between the two terms. The mortality of B_s is assumed to be independent of photosynthesis and is given by:

$$M_{Bs} = B_s \left(1 - \exp\left(-\frac{\Delta t}{\tau_M}\right)\right) \tag{4.476}$$

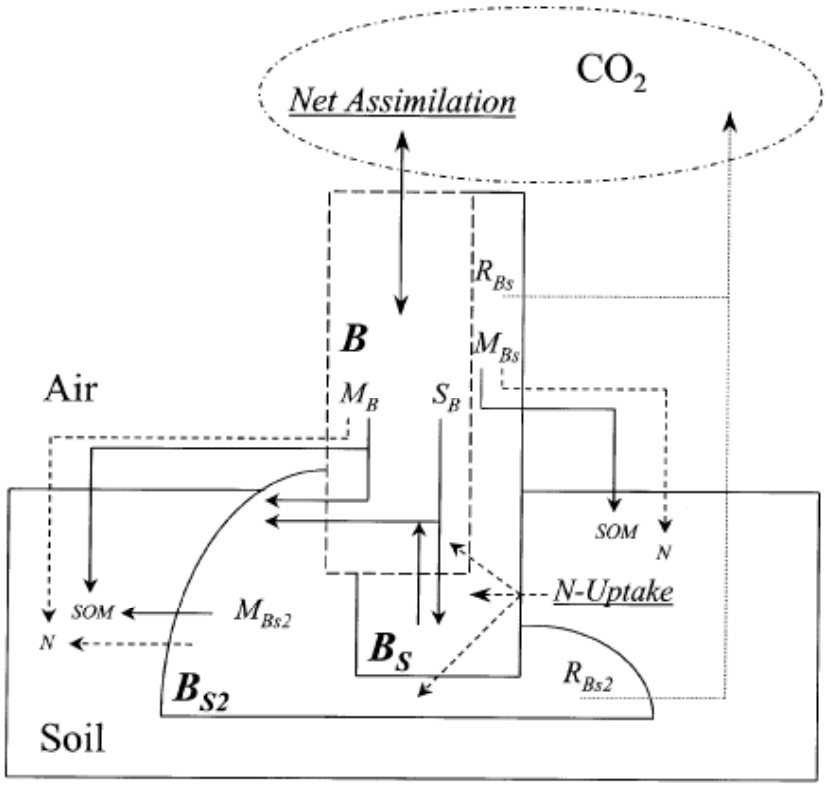

Figure 4.23: Schematic representation of the simple biomass model. Nitrogen (N) and carbon fluxes are represented by dashed and solid lines, respectively. The three biomass (B) compartments are indicated together with storage and mortality terms (S and M, respectively). Heterotrophic respiration (R) is represented by dotted lines. The mortality terms may be used as an input of a model of wood production and SOM. From: Calvet and Soussana (2001)

The structural biomass also looses carbon through respiration. This term is estimated using the common observation that maintenance respiration of non-active biomass is proportional to the biomass value, with a Q_{10} temperature dependence:

$$R_{Bs} = \eta_R B_s Q_{10}^{(T_s-25)/10} \Delta t \tag{4.477}$$

where T_s is the skin temperature in °C, η_R is a respiration rate fixed at $1\% day^{-1}$ and $Q_{10} = 2.0$. Finally, the storage term S_B is calculated as the residual of the structural biomass budget:

$$S_B = \Delta B_s - M_{Bs} - R_{Bs} \tag{4.478}$$

The mortality M_B in Eq. 4.475 is obtained by difference. In situations where S_B exceeds ΔB^- (implying that $M_B < 0$), an alternative formulation of B-decline is employed. It is assumed that there is no loss of active biomass outside the plant system during the considered time step, so $M_B = 0$ and that the difference in total aboveground biomass is the difference between the biomass gain due to daily net assimilation and the mortality and respiration losses of structural biomass:

$$\Delta B_T = \Delta B^+ - M_{Bs} - R_{Bs} \tag{4.479}$$

B_T is derived from this difference and the value at the previous time step. B follows from B_T via Eq. 4.470 and B_s is the difference between the two terms. A new value of the storage term S_B is given by Eq. 4.478. In the senescent phase, B_s evolves independently from B. S_B is set to zero and the mortality and respiration losses are directly applied to B_s:

$$B_s = B_s^{t-1} - M_{Bs} - R_{Bs} \tag{4.480}$$

The belowground structural biomass B_{s2} is not treated by the plant N decline model. The mortality and respiration losses of B_{s2} are calculated using equations similar to Eqs. 4.476 and 4.477:

$$M_{Bs2} = B_{s2}\left(1 - \exp\left(-\frac{\Delta t}{\tau_M}\right)\right) \tag{4.481}$$

$$R_{Bs2} = \eta_R B_{s2} Q_{10}^{(T_{soil}-25)/10} \Delta t \tag{4.482}$$

where T_{soil} is the temperature in °C of the soil layer in the force-restore version of ISBA. Note that both R_{Bs} and R_{Bs2} are calculated every time step and accumulated over one day. B_{s2} is fed by two mechanisms. First, when the storage term S_B is negative (this may happen, e.g., when a cut is prescribed in the model), this quantity is redirected to B_{s2}. Second, when the total aboveground plant biomass B_T is lower than $c^{1/a}$, it is assumed that the mortality term M_B becomes a storage term that increases B_{s2}.
The routine corresponding to the nitro dilution version is called NITRO_DECLINE.

The module can be coupled to a soil organic matter (SOM) model. The SOM is fed by the mortality terms (Calvet and Soussana, 2001). Besides, the model still lacks a wood (dead biomass) reservoir. Those extensions have been developed by Gibelin *et al.* (2008) (ISBA-CC, see Sect. 4.3).

Note: In the model, the biomass loss is calculated before the biomass gain. When NITRO_DECLINE is called and values from the previous day are needed, those are the values of the previous day calculated in NITRO_DECLINE, so before the biomass growth due to photosynthesis (calculated in LAIGAIN) is added to the biomass reservoir. In that case, LAILOSS is not called (in VEGETATION_EVOL).

Respiration

Since the biomass model is not coupled to a soil model, soil respiration needs to be parameterized in another way. In ISBA-A-gs, a simple Q_{10} equation is used to represent the ecosystem respiration, but this method lacks a representation of the effect of soil moisture on the soil respiration. The representation of all the respiration terms (including the heterotrophic respiration and its dependence on soil moisture) was developed by Gibelin *et al.* (2008) in ISBA-CC (see Sect. 4.3).
The CO_2 ecosystem respiration is parameterised by a Q_{10} function, weighted by a soil moisture scaling factor (Albergel *et al.* (2010)):

$$RECO = RE25 \cdot f(w_g) \cdot Q_{10}^{(T_{soil}-25)/10} \tag{4.483}$$

$$f(w_g) = min(1, w_g/w_{fc}) \tag{4.484}$$

where $RE25$ is the reference respiration at 25 °C , T_{soil} is the temperature in °C of the root-zone soil layer (at a depth of about 20cm), w_g is the surface soil moisture, corresponding to the first top cm of the soil, w_{fc} is the soil moisture at field capacity, and Q_{10} is fixed at 2.0.

Table 4.10: Example of harvest estimates ($t\ C\ ha^{-1}\ y^{-1}$)

Vegetation type	Harvest
Deciduous	3.2
Coniferous	2.3
Evergreen	3.2
C_3 grass	2.3
C_4 grass	3.2
C_3 crops	2.3
C_4 crops	3.2

$RE25$ has to be determined per vegetation type in each grid box, assuming equilibrium between multi-annual CO_2 assimilation by photosynthesis (or gross primary production, GPP, i.e. raw carbon uptake by photosynthesis), harvest and ecosystem respiration:

$$GPP_{acc} - Harvest_{acc} = RECO_{acc} = RE25 \left\{ f(w_g) \cdot Q_{10}^{(T_{soil}-25)/10} \right\}_{acc} \tag{4.485}$$

where acc stands for accumulated over the multi-year period. For harvest, examples of yearly harvest estimates per vegetation type are given in Table 4.10. Numbers are based on a 40% carbon content of dry biomass.

Once $RE25$ is calibrated for each vegetation type within each grid box, it may be treated as a surface climatology field, which is input to the model.

CO_2 fluxes

The photosynthesis model is called from COTWORES (or COTWORESTRESS) for all present vegetation tiles (Section 4.2.1).

The net ecosystem CO_2 exchange (NEE) per vegetation type is given by:

$$NEE = GPP - RECO \tag{4.486}$$

Throughout SURFEX, the unit of the kinematic CO_2 flux is $kgCO_2\ kgAir^{-1}\ m\ s^{-1}$ (as opposed to dynamic CO_2 flux units of $kgCO_2\ m^{-2}\ s^{-1}$).

4.2.2 Vegetation parameters

Gibelin *et al.* (2006) have proposed default values for the parameters of the new version of ISBA-A-gs (NIT option). They are listed in Table 4.11 for 7 vegetation types.

Table 4.11: Values of ISBA-A-gs parameters for the ECOCLIMAP vegetation types (g_m^* in $mm\ s^{-1}$, τ_M in days, LAI_{min} in $m^2\ m^{-2}$, D_{max}^* in $g\ kg^{-1}$, f_0^* dimensionless, g_c in $mm\ s^{-1}$, strategy of response to soil moisture stress (drought-tolerant or drought-avoiding), θ_C dimensionless, e in $m^2\ kg^{-1}\ \%^{-1}$, f in $m^2\ kg^{-1}$, and N_l in $\%$

Vegetation type	g_m^*	τ_M	LAI_{min}	D_{max}^*	f_0^*	g_c	Strategy	θ_C	e	f	N_l
Deciduous broadleaf trees	3	230	0.3	109	0.51	0.15	tolerant	0.3	4.83	2.53	2
Evergreen broadleaf trees	2	365	1	124	0.57	0.15	tolerant	0.3	4.83	2.53	2.5
Needle leaf trees	2	365	1	124	0.57	0	avoiding	0.3	4.85	-0.24	2.8
C_3 crops	1	150	0.3	50	0.95	0.25	avoiding	0.3	3.79	9.84	1.3
C_4 crops	9	150	0.3	33	0.6	0.15	tolerant	0.3	7.68	-4.33	1.9
C_3 natural herbaceous	1	150	0.3	50	0.95	0.25	tolerant	0.3	5.56	6.73	1.3
C_4 natural herbaceous	6	150	0.3	52	0.6	0.15	tolerant	0.3	7.68	-4.33	1.3

! In the code, g_m^*, τ_M, LAI_{min}, D_{max}^*, f_0^*, g_c, θ_C, e, f, N_l are named GMES, SEFOLD, LAIMIN, DMAX, FZERO, GC, F2I, CE_NITRO, CF_NITRO, CNA_NITRO, respectively.
GMES and GC are in units of $m\ s^{-1}$, SEFOLD in s, DMAX in $kg\ kg^{-1}$

For herbaceous vegetation: f_0^* is prescribed in MODD_CO2V_PAR, D_{max}^* is derived from the inversion of 4.441.

In the case of trees: f_0^* and D_{max}^* are not prescribed in the code, they are derived from the inversion of Eqs 4.447 and 4.453, respectively.

4.2.3 Discussion

In this section, some issues are discussed that deserve attention for future code development.

Respiration

Ecosystem respiration is a major component of the net CO_2 flux. ISBA-A-gs lacks a soil carbon reservoir and a wood (dead biomass) reservoir. Moreover, roots are not explicitly represented. Those extensions (and the associated respiration fluxes) are present in the ISBA-CC version, which has been coded into SURFEX (see Sect. 4.3). This provides possibilities for respiration calculations for each of the carbon reservoirs, that might replace the present respiration calibration. There is a strong need for direct respiration measurements to validate the parameterization.
With respect to the present Q_{10} calibration of ecosystem respiration, soil moisture effects are not accounted for. This hypothesis is not correct and a simple representation of the surface soil moisture effect on ecosystem respiration has to be introduced in SURFEX. Furthermore, the value of Q_{10} is fixed at 2, because it is generally used in literature about respiration. However, climate conditions may ask for a differentiation in

the Q_{10} value.

Soil moisture stress parameterization

The soil moisture stress parameterization may depend on the way soil hydrology is represented. Since the soil moisture content depends on the soil parameterization, which is different for ISBA-FR and ISBA-DF, this may lead to divergent behaviour. The use of ISBA-A-gs with the ISBA-DF option has still to be tested.

Temperature response of g_m for C_3 plants

Table 4.8 presents for C_3 plants a T_2 of 36 °C for g_m. However, in the beginning of the ISBA-A-gs development, this value was 28 °C (Calvet *et al.* 1998). This was changed during the development of new versions (e.g. Calvet, 2000). This implies that the temperature response of g_m, which is a sensitive parameter for photosynthesis, for C_3 plants approaches the response for C_4 plants, i.e. an optimal temperature for photosynthesis of 32 °C. This is certainly too high for boreal forests and grasslands adapted to cold climates (high latitudes or mountainous areas). The T_2 parameter will have to be adapted as a function of a climatology of air temperature.

Radiative transfer within the vegetation

The radiative transfer equations and the quadrature method described in section 4.2.1 are based on many approximations (Calvet *et al.* 1998). In particular, the representation of (1) scattering of the photosynthetically active radiation (PAR), (2) the interception of the diffuse radiation, within the canopy, may be oversimplified for regions/seasons with a lot of diffuse PAR (clouds, high solar zenith angles), especially for dense canopies.
The radiative transfer influences (1) photosynthesis and the canopy conductance, (2) mortality. Moreover, Calvet *et al.* (2008) have shown that the way light interception within the canopy is modelled may impact the simulated plant response to climate change.

Tropical evergreen forests Simulations with ISBA-A-gs showed that A_n is underestimated in tropical evergreen forest. This may cause an underestimation of net primary production (NPP) and an overestimation of the mortality of leaves. A solution must be found to improve photosynthesis and mortality. Mortality depends on the optimum net CO_2 assimilation (with 500 $W\ m^{-2}$ PAR). For evergreen forests that have a high radiation extinction in the canopy, 500 $W\ m^{-2}$ PAR may not be realistic under optimal conditions. Therefore, mortality might be overestimated. This could be dealt with by either reducing the optimum PAR or by considering a different mortality parameterization. Radiative transfer equations may also be improved for dense canopies in order to account better for diffuse radiation.
For the photosynthesis and canopy resistance, the vegetation parameter values in the photosynthesis model may be reconsidered. Therefore, data sets of tropical evergreen forests are needed to calibrate parameters like g_m and N_a.

Representation of mortality In NITRO_DECLINE, a correction of mortality is introduced for dense canopies. The effective life expectancy of the leaves (governing the exponential decline of B) is increased. Indeed, Eq. 4.467 relates mortality to the factors acting on photosynthesis at the leaf level. The factors accounted for by Eq. 4.467 include self shading since A_{nfm} is the maximum average leaf net assimilation: this quantity depends on LAI, which is employed to compute the extinction of solar radiation (see section 4.2.1). Preliminary tests of the nitrogen dilution option (NIT) showed that at very high values of LAI, the

self shading effect in Eq. 4.467 may trigger exaggerated values of mortality and, finally, underestimated values of biomass. Therefore, Eq. 4.467 was modified such as, for dense canopies, the leaf-level $A_{nfm}/A_{n,max}$ ratio is replaced by a value representative of the canopy:
$LAI\ A_{nfm}/(X\ A_{n,max})$, where X represents the maximum value of the ratio between canopy- and leaf-level optimum net assimilation. The value of X denotes the relative advantage of a well-developed canopy over a single horizontal leaf in terms of net assimilation of CO_2, in optimal conditions. This value was searched for various models parameters such as LAI, and g_m, by performing simulations over one annual cycle at several latitudes. In each configuration, a value of LAI (always higher than 5 $m^2\ m^{-2}$) maximising the ratio between canopy- and leaf-level optimum net assimilation could be found. A logarithmic relationship between the optimal value of X and gm was obtained (X tends to decrease for increasing values of g_m). This relationship depends on latitude because of the influence of maximum solar elevation on X (X is lower at high latitudes). Finally, Eq. 4.467 was rewritten as:

$$\tau(t) = \tau_M \frac{A_{nfm}(t)}{A_{n,max}} Max\left\{1, g_m^{0.321} LAI/LAI_B\right\} \tag{4.487}$$

where g_m is expressed in units of $mm\ s^{-1}$, and LAI_B represents a limit value of LAI depending on latitude (L_a) as:

$$LAI_B = 5.76 - 0.64 \tan\left(Min\left\{\|L_a\|, 73^\circ\right\}\right) \tag{4.488}$$

The LAI_B parameter ranges from 5.6 to 3.6, from equator to latitudes higher than 73°. For values of g_m close to 1 $mm\ s^{-1}$, it represents the maximum LAI value for which the leaf-level net assimilation may be employed to represent mortality. Those equations were derived with the radiative transfer parameterisation described in section 4.2.1 and may be different for another radiative transfer model.

Representation of crops

In ISBA-A-gs, crops are represented like natural vegetation. There is no particular description of the harvested elements like fruits and e.g. grain yield (cereals) is not directly simulated. Nevertheless, Calvet *et al.* (2008) show that the maximum above-ground biomass simulated by the model correlates with the crop yield and that the model is able to simulate realistic time series of LAI values over one annual cycle, and to represent the interannual variability.
Moreover, a simple representation of irrigation was implemented in SURFEX, and the possibility to simulate crops sown at springtime.

Irrigation An irrigation amount of 30mm is added to the precipitation forcing each time the simulated extractable soil moisture content (dimensionless) reaches a predefined threshold. This threshold decreases from 0.70 for the first irrigation, to 0.55 for the second, 0.40 for the third, and 0.25 for the following ones (Calvet *et al.* 2008). The threshold values are declared in MODD_AGRI.

Emergence Whereas the LAI annual cycle of natural vegetation (leaf onset, senescence, regrowth) is driven by climate conditions, crops are sown at dates chosen by the farmers. In ISBA-A-gs, crops sown at wintertime (i.e. emerging at springtime like natural vegetation) like wheat, are simulated in the same way as natural vegetation. The advantage of this is that no ancillary information is needed and that possible regrowths after a drought period are simulated interactively with the climate.
On the other hand, crops developing at summertime cannot be simulated like natural vegetation. An emergence date has to be prescribed and before this date (MODD_AGRI_n), LAI is limited to a minimum value

(e.g. 0.3 $m^2\ m^{-2}$). An harvest date is not prescribed. It is considered that climatic conditions (drought, cold) permit to drive the senescence.
In order to prescribe emergence dates, future developments should couple SURFEX to existing crop calendars, at the global scale.

Representation of nitrogen dilution

The CO_2 fertilization effect tends to increase the vegetation biomass but this effect is limited by nitrogen dilution. In Calvet *et al.* (2008), nitrogen dilution is accounted for by parameterizing the change in leaf nitrogen mass-based concentration N_L in response to [CO_2] rise. The sensitivity of leaf nitrogen concentration versus [CO_2] is accounted for by using the meta-analysis of the literature carried out by Yin 2002 (Yi02). The meta-analysis of Yi02 indicates that, on average, a CO_2-doubling causes a 18% decrease in N_L, but that the N_L response to CO_2 is influenced by a number of factors. A change in [CO_2], from [CO_2] = C_1 to [CO_2] = C_2, produces a change in N_L from N_{L1} to N_{L2} following:

$$\ln\left(\frac{N_{L2}}{N_{L1}}\right) = -a \exp\left[b - \frac{N_{L1}}{N_{Lmax}}\right] \ln\left(\frac{C_2}{C_1}\right) \tag{4.489}$$

with $a = 0.048$ and N_{Lmax}=6.3 %. In the Yi02 study, C_2/C_1 ranges from 0.53 to 3.2. The b parameter may vary significantly from one vegetation type to another. For example, in median radiation and air temperature (T_a) conditions, b = 1.48 for a fertilised crop, b = 2.56 for a deciduous forest, b = 1.81 for a coniferous forest or natural grasslands. The values of b are given by:

$$b = 0.75DF - 0.33FERT + 1.1PPFD + \frac{T_a}{23} \tag{4.490}$$

with $DF = 1$ for deciduous forests (0 for other biomes), and $FERT = 1$ for fertilized ecosystems like crops (0 for other biomes). $PPFD$ is the average photosynthetically active solar radiation reaching the leaf within the vegetation canopy (median value of 0.74 $mmol\ m^2\ s^1$, equivalent to a total solar radiation of 335 $W\ m^2$). In this study, no solar radiation or temperature effect is associated with a change in [CO_2] and the median $PPFD$ and Ta values of Yi02 are used in Eq. 4.490.

Annex 1: Description of the Fortran routine used to calculate the CO_2 flux

SUBROUTINE COTWORESTRESS
This routine is used at the time step of SURFEX (default offline value $\Delta t = 300$ s).
1. The photosynthetically active radiation (PAR) is derived from the incident shortwave radiation. A constant factor of 0.48 is used.

2. Drought-avoiding and drought-tolerant responses to soil moisture stress are simulated for herbaceous and for woody plants (depending on the vegetation type of the considered patch). Namely, the photosynthesis parameters are refreshed to be consistent with the root-zone soil moisture.

3. The CO_2 compensation concentration of photosynthesis (ZGAMMT), the maximum photosynthesis (ZANMAX), and the mesophyll conductance (ZGMEST) are refreshed to be consistent with the leaf temperature (i.e. surface temperature in a single-source configuration).

4. The leaf-to-air saturation deficit within the canopy (depends on leaf temperature and air humidity) is refreshed (ZDSP).

5. The CO_2 concentration within the canopy is refreshed (ZCSP).

6. Ecosystem respiration is refreshed (ZRSOIL).

7. The solar zenith angle is prescribed (PZENITH).

8. Integrated canopy values of photosynthesis (ZTPST), net assimilation (ZTAN), and leaf conductance (ZTGS) are obtained by a 3-point Gauss quadrature method (SIZE(PABC) is equal to 3 ; can be modified).

9. The PAR at each Gauss level is calculated by radiative transfer equations in SUBROUTINE CCETR. In CCETR, the interception of direct and diffuse light is represented. The fraction of diffuse radiation (ZXFD) depends on the solar zenith angle, only.

10. At each Gauss level within the canopy, the photosynthesis model (SUBROUTINE COTWO) is run.

11. The canopy resistance (PRS) is calculated, as well as the net ecosystem exchange of CO_2 (PCO2FLUX).

4.3 The ISBA-CC model

4.3.1 Introduction

The ISBA-CC model is a new version of ISBA developped by Gibelin *et al.* (2008) with the aim of simulating the terrestrial carbon cycle.
ISBA-CC is based on the ISBA-A-gs model (Calvet and Soussana, 2001). The latter simulates the gross photosynthesis rate, the dark leaf respiration, and changes in leaf biomass. Also, ISBA-A-gs simulates the ecosystem respiration using a Q_{10} parameterization based on soil temperature and surface soil moisture (Albergel *et al.* 2010). ISBA-CC and ISBA-A-gs share the same photosynthesis model (Jacobs *et al.* 1996), and the same representation of the photosynthesis response to drought (Calvet (2000), Calvet *et al.* 2004) and of the carbon allocation to the leaf biomass compartment (Calvet and Soussana, 2001). The added value of ISBA-CC is a more detailed representation of (1) the ecosystem respiration, including its autotrophic and heterotrophic components, (2) the biomass compartments, including roots and wood (in the case of trees).
The heterotrophic respiration, produced by the decomposition of the soil organic matter, is represented following the STOMATE carbon model included into the IPSL ORCHIDEE model (Krinner *et al.* (2005)). The litter and the soil organic matter pools are simulated, together with the carbon fluxes from one carbon pool to another, and with the respiration flux to the atmosphere.
The various litter pools are supplied by the fluxes of dead biomass. A specific carbon allocation scheme was implemented in order to represent various biomass components, which were not accounted for by ISBA-A-gs: an explicit representation of roots, and (in the case of trees) of the above-ground and below-ground wood. For all the biomass compartments, turnover and respiration terms are calculated. Also, ISBA-CC simulates the autotrophic respiration, the net primary production (NPP), and the total biomass of the plant.

4.3.2 Allocation scheme

Evolution of the biomass compartments

The ISBA-CC allocation scheme simulates the various carbon reservoirs of the plant. Six biomass pools are considered, in units of $kg\,m^{-2}$, including four above-ground pools and two below-ground pools:

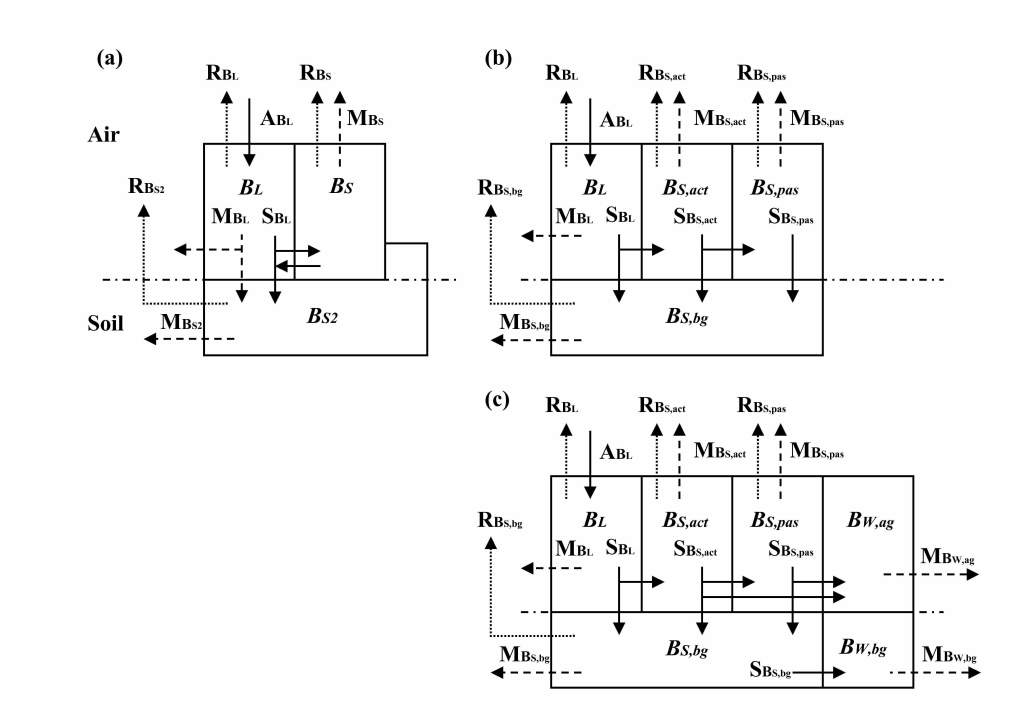

Figure 4.24: Schematic representation of the plant carbon reservoirs and fluxes in (a) ISBA-A-gs (Calvet and Soussana, 2001), and in ISBA-CC for (b) herbaceous (c) and woody vegetation. The various biomass reservoirs are prefixed by B. Input and output fluxes are indicated for each reservoir: allocation and storage (A and S, solid arrows), mortality (M, dashed arrows) and respiration (R, dotted arrows). The autotrophic respiration is the sum of all the biomass respiration terms.

B_L	leaf biomass,
$B_{s,act}$	active structural biomass, linked to B_L through nitrogen dilution,
$B_{s,pas}$	passive structural biomass,
$B_{s,bg}$	below ground structural biomass,
$B_{w,ag}$	above ground woody biomass (for trees),
$B_{w,bg}$	below ground woody biomass (for trees).

This new allocation scheme was based, as much as possible, on the structure of the "NIT" option of ISBA-A-gs, described in (Calvet and Soussana (2001). The B_L and $B_{s,act}$ compartments were not modified and correspond to the B_L and B_s compartments of ISBA-A-gs. Therefore ISBA-CC and ISBA-A-gs simulate the same values of LAI, as LAI is derived from the leaf biomass B_L. $B_{s,pas}$ is a buffer reservoir corresponding to a fraction of the B_{s2} compartment. It is used for the storage of the biomass released by $B_{s,act}$ during the senescence phase. $B_{s,bg}$ represents non-woody roots. $B_{w,ag}$ and $B_{w,bg}$ correspond to above-ground and below-ground wood components, respectively. They are used for woody vegetation types (i.e. broadleaf deciduous and evergreen forests, and coniferous forests).

Figure 4.24 shows the plant carbon reservoirs and fluxes simulated by ISBA-A-gs and by ISBA-CC.

The evolution of all the biomass reservoirs is calculated with a time step Δt of 1 day, following the generic equation 4.491.

$$\Delta B = A_B - D_B - R_B \tag{4.491}$$

A B biomass term is driven by an incoming allocation term A_B, by a respiration carbon loss term R_B, and by a turnover term D_B, expressed in units of $kg\ m^{-2}$. These three terms are detailed below, for all the biomass compartments.

Respiration

The autotrophic respiration results from the oxydation of organic molecules, as part of the plant metabolism. Generally, two autotrophic respiration terms are considered: the growth respiration associated to the production of new plant tissues, and the maintenance respiration, corresponding to the existing biomass.
The respiration terms are calculated at the time step of the model dt and accumulated at the $\Delta t = 1day$ time step.
The B_L respiration term of ISBA-A-gs, R_d, is used in ISBA-CC, also. It is included in the leaf net assimilation term, which is the difference between photosynthesis and dark respiration R_d. R_d corresponds to the sum of the growth respiration and of the maintenance respiration of the leaves.

$$R_{B_L} = \sum_{dt} 10^{-6} \frac{M_C}{P_c\, M_{CO_2}}\, R_{dC}\, dt \tag{4.492}$$

where $\sum dt = \Delta t$, P_c is the fraction of carbon of the dry biomass, assumed to be equal to 40%, M_C and M_{CO_2} are the molecular weights of carbon and CO_2 (12 and $44\, g\, mol^{-1}$, respectively), and R_{dC} is the dark respiration rate integrated from the leaf to the canopy.
The B_s respiration term of ISBA-A-gs, is used in ISBA-CC for $B_{s,act}$.

$$R_{B_{s,act}} = \sum_{dt} B_{s,act}\, \eta_R\, Q_{10}^{(T_s-25)/10}\, dt \tag{4.493}$$

where $Q_{10} = 2$, and $\eta_R = 0.01\ g\ g^{-1}\ j^{-1}$, corresponding to a $B_{s,act}$ biomass loss of $1\ \%$ per day through respiration, at a temperature of 25 °C.
For the other structure biomass pools ($B_{s,pas}$ and $B_{s,bg}$), the linear response to temperature of the maintenance respiration proposed by Ruimy *et al.* (1996) is used:

$$R_{B_{s,pas}} = \sum_{dt} B_{s,pas}\, R_0\, (1 + 0.16\, T_s)\, dt \tag{4.494}$$

$$R_{B_{s,bg}} = \sum_{dt} B_{s,bg}\, R_0\, (1 + 0.16\, T_p)\, dt \tag{4.495}$$

where R_0 is the respiration value at 0 °C, equal to $1.19\ 10^{-4}\ g\ g^{-1}\ j^{-1}$ (as proposed by Ruimy *et al.* (1996) for the sapwood compartment), T_s is leaf temperature and T_p is soil temperature in units of °C. This value can be compared with the scaling factor of $B_{s,act}$ at 0 °C in equation 4.493: $2\ 10^{-3}\ g\ g^{-1}\ j^{-1}$.
$B_{w,ag}$ and $B_{w,bg}$ represent the wood, and no respiration term is associated to these reservoirs.

Decline term

The decline term represents the various processes, other than respiration, able to trigger a biomass decrease. It includes decreases due to mortality and reallocation to other plant elements. It is expressed simply, as an exponential decrease of the biomass. The decline term of the biomass B is expressed by the generic equation:

$$D_B = B\, (1 - e^{-\frac{\Delta t}{\tau}}) \tag{4.496}$$

where τ is a residence time (in days).
The residence time of all the non-woody reservoirs is determined using the τ_M parameter of the ISBA-A-gs model (the maximum leaf span time). For the leaf biomass B_L, the leaf span time τ_{B_L} is calculated daily, based on the photosynthesis efficiency (see Eq. 4.467). The residence time is τ_M for the $B_{s,act}$ and $B_{s,bg}$ biomass compartments, and $\tau_M/4$ for $B_{s,pas}$. For the woody biomass compartments, the span time τ_w is equal to 40 years for broadleaf deciduous forests, 50 years for the coniferous forests, and 30 years for the broadleaf evergreen forests. For the sake of comparison, in the ORCHIDEE model (Krinner *et al.* 2005), the residence time of the wood compartment depends on the climatic zones: 80 years for boreal forests, 40 years for temperate forests, and 30 years for the tropical forests.

$$
\begin{aligned}
D_{B_L} &= B_L \left(1 - e^{-\frac{\Delta t}{\tau_{B_L}}}\right) \\
D_{B_{s,act}} &= B_{s,act} \left(1 - e^{-\frac{\Delta t}{\tau_M}}\right) \\
D_{B_{s,pas}} &= B_{s,pas} \left(1 - e^{-\frac{4\,\Delta t}{\tau_M}}\right) \\
D_{B_{s,bg}} &= B_{s,bg} \left(1 - e^{-\frac{\Delta t}{\tau_M}}\right) \\
D_{B_{w,ag}} &= \begin{cases} 0 & \text{for herbaceous species,} \\ B_{w,ag} \left(1 - e^{-\frac{\Delta t}{\tau_w}}\right) & \text{for woody species.} \end{cases} \\
D_{B_{w,bg}} &= \begin{cases} 0 & \text{for herbaceous species,} \\ B_{w,bg} \left(1 - e^{-\frac{\Delta t}{\tau_w}}\right) & \text{for woody species.} \end{cases}
\end{aligned}
\tag{4.497}
$$

Then, the decline term is broken down into storage and mortality terms, dedicated to the carbon allocation to other biomass reservoirs, and to the litter, respectively.

$$D_B = M_B + S_B \tag{4.498}$$

Allocation

Allocation of carbon to B_L, A_{B_L}, is the same as in the "NIT" option of ISBA-A-gs (Calvet and Soussana, 2001). The leaf biomass is directly supplied by gross assimilation (photosynthesis). The latter includes the net carbon assimilation (A_{nC}), and the dark respiration (R_{dC}) combining the leaf growth respiration and the leaf maintenance respiration. A_{nC} may present negative values, for example at nighttime.

$$A_{B_L} = \sum_{dt} 10^{-6} \frac{M_C}{P_c\, M_{CO_2}} (A_{nC} + R_{dC})\, dt \tag{4.499}$$

where P_c is the carbon fraction of the dry biomass, equal to 40%, M_C and M_{CO_2} are the molecular weights of carbon and CO_2 (12 and 44 $g\ mol^{-1}$, respectively), and A_{nC} and R_{dC} are the net assimilation rate of carbon and the dark respiration, integrated at the canopy level.
The other reservoirs are supplied through biomass translocation. A storage term S_B is derived from the decline term D_B, depending on the reservoir and on the plant type. The following reservoirs can be used to allocate carbon to other reservoirs: B_L, $B_{s,act}$ and $B_{s,pas}$ for herbaceous plants; B_L, $B_{s,act}$, $B_{s,pas}$ and $B_{s,bg}$ for woody plants, as shown in figure 4.24). For the other reservoirs, the decline is entirely converted into mortality: $B_{s,bg}$ for herbaceous vegetation types ; $B_{w,ag}$ and $B_{w,bg}$ for woody vegetation types. Also,

allocation and mortality depend on the phase of plant growth: the growing phase corresponds to an increase of the leaf biomass, i.e. to the net gain of carbon resulting from net assimilation values higher than the decline term B_L; the senescence phase corresponds to a decrease of the leaf biomass. During the growing phase, all the decline D_B terms are converted to storage S_B, whereas during the senescence phase, only a fraction of the decline terms is reallocated, and the other fraction becomes a mortality term M_B supplying the litter.

During the growing phase, the storage terms are calculated as:

$$\begin{aligned} S_{B_L} &= D_{B_L} \\ S_{B_{s,act}} &= D_{B_{s,act}} \\ S_{B_{s,pas}} &= D_{B_{s,pas}} \\ S_{B_{s,bg}} &= \begin{cases} 0 & \text{for herbaceous species,} \\ D_{B_{s,bg}} & \text{for woody species} \end{cases} \\ S_{B_{w,ag}} &= 0 \\ S_{B_{w,bg}} &= 0 \end{aligned} \tag{4.500}$$

During the senescence phase,

$$\begin{aligned} S_{B_L} &= \begin{cases} 0 & \text{si } A_{B_L} - R_{B_L} \leq 0 \\ f_{A,B_L}\,(A_{B_L} - R_{B_L}) & \text{si } 0 < f_{A,B_L}\,(A_{B_L} - R_{B_L}) \leq f_{D,B_L}\,D_{B_L} \\ f_{D,B_L}\,D_{B_L} & \text{si } f_{A,B_L}\,(A_{B_L} - R_{B_L}) > f_{D,B_L}\,D_{B_L} \end{cases} \\ S_{B_{s,act}} &= f_{D,B_{s,act}}\,D_{B_{s,act}} \\ S_{B_{s,pas}} &= f_{D,B_{s,pas}}\,D_{B_{s,pas}} \\ S_{B_{s,bg}} &= \begin{cases} 0 & \text{for herbaceous species,} \\ f_{D,B_{s,bg}}\,D_{B_{s,bg}} & \text{for woody species;} \end{cases} \\ S_{B_{w,ag}} &= 0 \\ S_{B_{w,bg}} &= 0 \end{aligned} \tag{4.501}$$

where $f_{D,B}$ is the biomass B decline fraction reallocated towards other compartments during the senescence. f_{D,B_L}, $f_{D,B_{s,act}}$, $f_{D,B_{s,pas}}$ and $f_{D,B_{s,bg}}$ are equal to 0.5. A number of tests showed that this value permits realistic simulations of the biomass allocation to the various compartments. The senescence B_L storage rate, used to supply the $B_{s,bg}$ compartment (see below), cannot be higher than a fraction of the net carbon supply provided by photosynthesis $(A_{B_L} - R_{B_L})$, and this fraction f_{A,B_L} is equal to 0.5.

Then, the storage terms are used to supply one or several reservoirs.

The supply of $B_{s,act}$ follows Calvet and Soussana (2001). During the growing phase, $B_{s,act}$ is derived from B_L using the nitrogen dilution law. It must be noted that during the growing phase, while the leaf biomass increases, the model is able to simulate a decrease of $B_{s,act}$. This may happen when the growing phase occurs after a temporary senescence phase or after a cut. $A_{B_{s,act}}$ is the supply term of $B_{s,act}$. This term is calculated a posteriori as the sum of the changes in $B_{s,act}$, of the respiration terms $R_{B_{s,act}}$ and of the decline $D_{B_{s,act}}$. $A_{B_{s,act}}$ corresponds to the decline of B_L. During the senescence, $B_{s,act}$ is not supplied any longer.

$$A_{B_{s,act}} = \begin{cases} \Delta B_{s,act} + D_{B_{s,act}} + R_{B_{s,act}} & \text{during the growing phase,} \\ 0 & \text{during the senescence phase.} \end{cases} \tag{4.502}$$

When $B_{s,act}$ decreases while the leaf biomass increases, $B_{s,pas}$ is supplied by the carbon lost by the $B_{s,act}$ reservoir. The $B_{s,pas}$ buffer reservoir avoids the irreversible loss of $B_{s,act}$ biomass through mortality. During the senescence, $B_{s,pas}$ is not supplied any longer.

$$A_{B_{s,pas}} = \begin{cases} 0 & \text{during the growing phase with } A_{B_{s,act}} \geq 0, \\ -A_{B_{s,act}} & \text{during the growing phase with } A_{B_{s,act}} < 0, \\ 0 & \text{during the senescence phase.} \end{cases} \quad (4.503)$$

During the growing phase, $B_{s,bg}$ is supplied by the storage reservoirs: B_L, $B_{s,act}$ et $B_{s,pas}$. During the senescence phase, $B_{s,bg}$ is supplied by the leaf biomass storage reservoir, only.

$$A_{B_{s,bg}} = f_{S,B_L,B_{s,bg}}\, S_{B_L} + f_{S,B_{s,act},B_{s,bg}}\, S_{B_{s,act}} + f_{S,B_{s,pas},B_{s,bg}}\, S_{B_{s,pas}} \quad (4.504)$$

During the growing phase, $f_{S,B_L,B_{s,bg}}$ is the remaining S_{B_L} fraction after the carbon allocation to $B_{s,act}$, following the nitrogen dilution law (equation 4.502). This quantity is updated at the daily time step. During the senescence phase, $f_{S,B_L,B_{s,bg}} = 1$. $f_{S,B_{s,act},B_{s,bg}}$ and $f_{S,B_{s,pas},B_{s,bg}}$ are constant. During the growing phase, they are equal to 1 for herbaceous vegetation types and 0.3 for woody vegetation types, only, as the other fraction is allocated to the wood compartments (equations 4.505 and 4.506). During the senescence phase, they are equal to 0.
For woody vegetation types, the wood compartments are supplied by the storage of $B_{s,act}$ and $B_{s,pas}$ for $B_{w,ag}$, and by the storage of $B_{s,bg}$ for $B_{w,bg}$.

$$A_{B_{w,ag}} = (1 - f_{S,B_{s,act},B_{s,bg}})\, S_{B_{s,act}} + (1 - f_{S,B_{s,pas},B_{s,bg}})\, S_{B_{s,pas}} \quad (4.505)$$

$$A_{B_{w,bg}} = S_{B_{s,bg}} \quad (4.506)$$

Mortality

The mortality of a biomass compartment results from high decline term values, higher than the storage term (if any). The mortality is used to supply the above- and below-ground litter compartments of the soil organic matter scheme. This definition of the mortality differs slightly from the definition used by Calvet and Soussana (2001), who allow the use of a fraction or the B_L mortality to supply the below-ground reservoir B_{s2}. In the ISBA-CC model, this contribution supplies the storage term.

$$M_B = D_B - S_B \quad (4.507)$$

4.3.3 Coupling with the soil organic matter scheme

In order to simulate the terrestrial carbon cycle in a more realistic way, the simple ecosystem respiration equation used in ISBA-A-gs (Albergel *et al.* 2010) is replaced by the soil organic matter scheme used in ORCHIDEE (Krinner *et al.* 2005).

Overview

The soil respiration scheme used in ISBA-CC is derived from the STOMATE (Saclay Toulouse Orsay Model for the Analysis of Terrestrial Ecosystems) carbon model included in the ORCHIDEE (ORganizing Carbon and Hydrology in Dynamic EcosystEms) (Krinner *et al.* 2005) land surface model. The latter is an adaptation of one of the first versions of the CENTURY (Parton *et al.* (1987, 1988) model.

CENTURY simulates the carbon flux and storage and their interactions with the water cycle and nutrient (nitrogen N, sulfur S, and phosphorus P) cycles, in the soil-plant system. It includes a plant growth module, together with a representation of the soil organic matter. Initially, CENTURY was designed for the simulation of the crops and grasslands of the US Great Plains (Parton *et al.* 1987; 1988).
The current version of CENTURY differs from the older version used in STOMATE, but the main attributes are the same (www.nrel.colostate.edu/projects/century/, last access January 2012). Also, CENTURY was improved and validated for other vegetation types and other biomes (Parton *et al.* (1993), Peng *et al.* (1998)), and has become a reference model in the international scientific community.
The model simulates several carbon pools of the soil, corresponding to different organic matter categories, residence time, and location, together with the carbon fluxes from one pool to another.

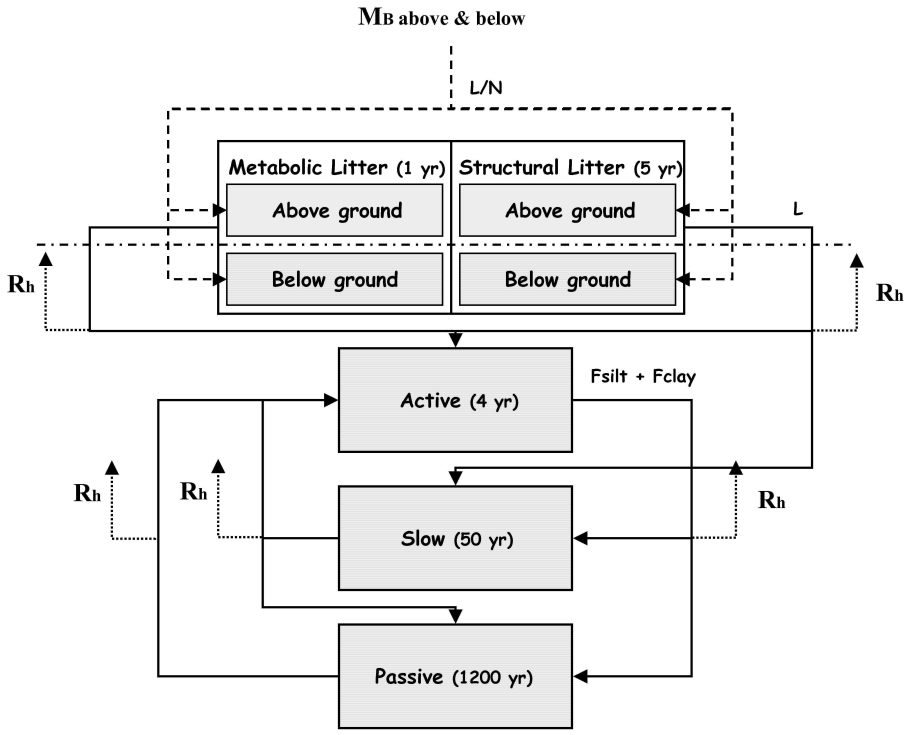

Figure 4.25: Schematic representation of the heterotrophic respiration parameterization of ISBA-CC, adapted from Parton *et al.* (1987). The soil carbon pools are indicated together with input mortality terms (dashed lines), fluxes of carbon exchanged between the pools (solid lines), and fluxes of mineralized carbon (dotted lines). The heterotrophic respiration is the sum of all the fluxes of mineralized carbon. The various carbon pools are reported in Table 4.13.

Four litter categories are simulated: two surface litter compartments, supplied by the mortality fluxes of the above-ground biomass, and two soil litter compartments, supplied by the mortality fluxes of the below-ground biomass. For both above- and below-ground litter, two carbon reservoirs displaying contrasting residence times are considered. The structural litter is made of the lignin and cellulose of the dead vegetation residues, with a residence time of 2 to 5 years. The metabolic litter is made of more labile organic components, with a residence time of 0.1 to 1 year (Parton *et al.* 1988).

Also, three soil organic matter pools are simulated. They are supplied by the organic matter flux produced by the litter compartments (figure 4.25). The active pool represents the soil microorganisms, together with the decomposition products with a short residence time (2 to 4 years). The slow pool represents the soil organic molecules/components characterized by a residence time ranging from 20 to 50 years. The passive pool represents the soil organic molecules/components characterized by a residence time ranging from 800 to 1200 years (Parton *et al.* 1988). These simulated carbon pools do not represent distinct physical entities but, rather, various chemical status of the soil organic matter. At a given soil depth, the soil may contain several types of organic matter, at various decomposition stages. Decomposition is controlled by climatic conditions (soil moisture and soil temperature), by the physical properties of the soil (e.g. texture), and by the chemical composition of the substrate (i.e. the carbon, nitrogen, lignin content of the residues). While CENTURY simulates the nutrient (nitrogen N, sulfur S, and phosphorus P) cycles, and their interactions with the carbon cycle (Parton *et al.* 1987; 1988), this capability was not implemented so far in either STOMATE or ISBA-CC.

Supply of litter compartments

The ISBA-CC allocation scheme, described in Sect. 4.3.2, provides a flux of dead vegetation residues from the various plant elements. These residues supply the litter compartments according to which plant element is considered.
The residues of the above-(below-)ground biomass supply the above-(below-)ground litter compartments.
Also, the structural/metabolic litter compartments are supplied according to the lignin to nitrogen ratio of the residues. The fraction allocated to the metabolic litter F_M is:

$$F_M = 0.85 - 0.018 \frac{L}{N} \tag{4.508}$$

The other fraction F_S is allocated to the structural litter:

$$F_S = 1 - F_M \tag{4.509}$$

Therefore, high L/N values tend to produce more structural litter.
In CENTURY, the lignin content of the biomass depends on the accumulated yearly precipitation, and the nitrogen concentration of the biomass is calculated by the model. In STOMATE, the L/N values are constant and result from the values of L/C and C/N. Table 4.12 shows the L/C, C/N, and L/N values used by ISBA-CC (see Sect. 4.3.2), derived from those used by STOMATE. It must be noted that the C/N could be derived, also, from the P_c/N_L ratio.

Biomass Compartment	L/C	C/N	L/N
B_L	0.22	40	8.8
$B_{s,act}$	0.35	40	14
$B_{s,pas}$	0.35	40	14
$B_{s,bg}$	0.35	40	14
$B_{w,ag}$	0.35	40	14
$B_{w,bg}$	0.35	40	14

Table 4.12: Lignin to carbon, carbon to nitrogen, and lignin to nitrogen ratio for all the biomass compartments of the ISBA-CC model.

Decomposition of the soil organic matter

Changes in soil organic matter pools are represented as:

$$\frac{dC_i}{dt} = K_i^a \, M_d \, T_d \, C_i \tag{4.510}$$

where C_i is the carbon content (in units of $gC\ m^{-2}$) of the soil organic matter pool i (see Table 4.13), K_i^a is the decomposition rate (in units of yr^{-1}) of the soil organic matter pool i, M_d is the response of the decomposition to soil wetness (dimensionless, ranging between 0 and 1), and T_d is the response of the decomposition to soil temperature (dimensionless, ranging between 0 and 1).

Reservoir	Index
Structural above-ground litter	1
Metabolic above-ground litter	2
Structural below-ground litter	3
Metabolic below-ground litter	4
Active carbon pool	5
Slow carbon pool	6
Passive carbon pool	7

Table 4.13: Indices i of the soil carbon pools.

The decomposition rate K_i^a is derived from the maximum decomposition rate K_i, possibly modulated by physical characteristics:

$$\begin{aligned}
K_1^a &= K_1 \, exp(-3 \, L_{s1}) \\
K_2^a &= K_2 \\
K_3^a &= K_3 \, exp(-3 \, L_{s3}) \\
K_4^a &= K_4 \\
K_5^a &= K_5(1 - 0.75(f_{silt} + f_{clay})) \\
K_6^a &= K_6 \\
K_7^a &= K_7
\end{aligned} \tag{4.511}$$

where L_{si} is the fraction of lignin in the structural litter pools, f_{silt} and f_{clay} are the fractions of silt and clay in the soil. High lignin fraction values tend to slow down the decomposition of the structural litter (small values of K_i^a). Similarly, fine-textured soils (high fractions of either silt or clay) tend to stabilize the organic molecules and a lower decomposition rate of the active carbon pool is simulated. In ISBA-CC, the original CENTURY expression for K_5^a, depending on $(f_{silt} + f_{clay})$, is used, while in STOMATE, the $(f_{silt} + f_{clay})$ term is replaced by f_{clay}.

Table 4.14 presents the equivalent residence time values K_i^{-1} (where K_i is the maximum decomposition rate) used in the initial version of CENTURY (Parton *et al.* 1987) and in STOMATE (Krinner *et al.* 2005), for the various carbon pools of the soil. While in CENTURY the maximum decomposition rate K_i is 20% smaller for the above-ground litter than for the below-ground litter, the same value is used for the two litter compartments in STOMATE. Moreover, the K_i value of the passive carbon pool is smaller in STOMATE than in CENTURY. In ISBA-CC, the STOMATE values are used.

In CENTURY, the dependence of the decomposition on soil moisture is represented by a normalized factor, M_d, driven by the ratio of monthly precipitation to the potential evaporation rate. In STOMATE, the original representation of M_d was replaced by a function depending on soil moisture (Krinner *et al.* 2005). It must

Reservoir	$1/K_i$ CENTURY	$1/K_i$ STOMATE
Structural above-ground litter	0.252	0.245
Metabolic above-ground litter	0.068	0.066
Structural below-ground litter	0.204	0.245
Metabolic below-ground litter	0.055	0.066
Active carbon pool	0.137	0.149
Slow carbon pool	5.05	5.37
Passive carbon pool	147.5	241.

Table 4.14: Values of the equivalent residence time K_i^{-1} $(year)$ used in the initial version of CENTURY (Parton *et al.* 1987) and in STOMATE (Krinner *et al.* 2005).

be noted that while the minimum value of M_d is 0 in (Krinner *et al.* 2005), the value actually used in the ORCHIDEE code is 0.25:

$$M_d = \min(0.25, \max\left[1, -1.1\theta^2 + 2.4\theta - 0.29)\right] \tag{4.512}$$

where θ is a normalized soil moisture value ranging between 0 and 1:

$$\theta = \min\left[0, \max(1, \frac{w - w_{wilt}}{w_{fc} - w_{wilt}})\right] \tag{4.513}$$

where w is either the surface or the root-zone soil moisture (see below), in units of $m^3\ m^{-3}$, w_{wilt} is soil moisture at wilting point (in units of $m^3 m^{-3}$), and w_{fc} is soil moisture at field capacity (in units of $m^3 m^{-3}$). In ISBA-CC, this equation was modified, in order to account for the drop in the decomposition rate for high soil moisture values, ranging between wilting point and saturation values (equation 4.514). Indeed, while water is a limiting factor for microbial growth at moderate soil moisture values, above field capacity, an increase in soil moisture content tends to slow down the exchanges of oxygen in the soil, down to anaerobic conditions at saturation. In the latter situation, less CO_2 is emitted through heterotrophic respiration. Following Probert *et al.* (1998) (the APSIM model), the modified equation allows a linear decrease of M_d, from 1 to 0.5, when soil moisture increases from field capacity to saturation. Moreover, the minimum M_d value (at low soil moisture values) is taken as 0.05. The latter is consistent with the group of models described by Paul (2001).

$$\begin{aligned} &\text{For } \theta \leq w_{fc}, \quad M_d = min(0.05, max(1, -1.1\theta^2 + 2.4\theta - 0.29)) \\ &\text{For } \theta \geq w_{fc}, \quad M_d = max(0.5, 1 - 0.5\,\theta_{sat}) \end{aligned} \tag{4.514}$$

where θ_{sat} is another soil moisture index defined as:

$$\theta_{sat} = \frac{w - w_{fc}}{w_{sat} - w_{fc}} \tag{4.515}$$

where w_{sat} is the saturation soil moisture value.
The M_d values used in STOMATE and ISBA-CC are shown by Fig. 4.26.
Since the soil organic matter model does not represent the profile carbon content of the soil, two soil moisture quantities are used in ISBA-CC: the surface soil moisture (a skin soil moisture corresponding to a thin soil layer of about 1cm) and the root-zone soil moisture. For the litter reservoirs, w, w_{wilt}, w_{fc} and w_{sat}

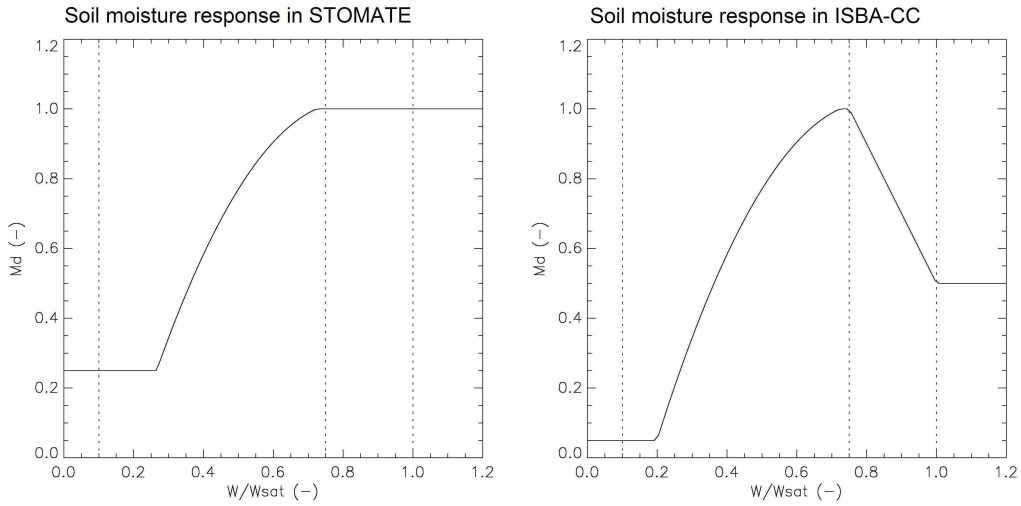

Figure 4.26: Normalized decomposition response function to soil moisture used in (left) STOMATE-ORCHIDEE and (right) ISBA-CC. The three vertical dashed lines indicate (from left to right) w_{wilt}, w_{fc} and w_{sat}.

correspond to the surface soil moisture. For the other reservoirs, w, w_{wilt}, w_{fc} and w_{sat} correspond to the root-zone soil moisture.
In CENTURY, the dependence of the decomposition on temperature is represented by a normalized factor, T_d, driven by the average monthly temperature, according to a bell curve (Parton *et al.* 1987).
In STOMATE, T_d is defined as:

$$T_d = 2^{(\frac{T-30}{10})} \tag{4.516}$$

where T is soil temperature in units of °C. This formulation is used in ISBA-CC, also.
The T_d values used in STOMATE and ISBA-CC are shown by Fig. 4.27.
Since the soil organic matter model does not represent the profile carbon content of the soil, two soil temperature quantities are used in ISBA-CC: the surface temperature T_s and a deep soil temperature T_p. For the litter reservoirs, $T = T_s$. For the other reservoirs, $T = T_p$.

Carbon fluxes

The decomposition of the organic matter contained in the soil carbon reservoir i, dC_i/dt, triggers various carbon fluxes (Fig. 4.25). A fraction of the decomposed organic matter f_{i,CO_2} is mineralized through the respiration process and released as CO_2 to the atmosphere. The other fraction is allocated to the other carbon pools of the soil, based on their resistance to decomposition. The fraction of the decomposition flux from reservoir i to reservoir j is $f_{i,j}$, and:

$$\sum_j f_{i,j} \; + f_{i,CO_2} = 1 \tag{4.517}$$

For the structural litter reservoirs, the decomposition supplies the respiration flux and the stabilisation of carbon into a soil organic matter carbon pool, either active or slow, depending on the lignin content of the

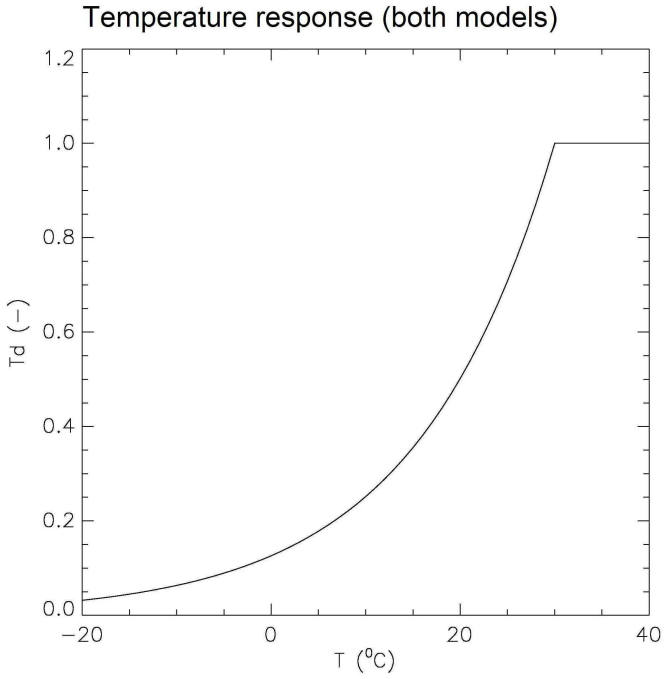

Figure 4.27: Normalized decomposition response function to soil temperature used in both STOMATE-ORCHIDEE and ISBA-CC.

litter and on the nature of the litter (above-ground or below-ground). The lignin tends to reduce both the mineralization and the decomposition of the plant residues.

For the above-ground structural litter, the fractions are defined as:

$$\begin{aligned} f_{1,5} &= 0.55\,(1 - L_1) \\ f_{1,6} &= 0.7\,L_1 \\ f_{1,CO_2} &= 0.45\,(1 - L_1) + 0.3\,L_1 \end{aligned} \tag{4.518}$$

where L_1 is the lignin fraction of the above-ground structural litter reservoir.

For the below-ground structural litter, the fractions are slightly different, in relation to a lower efficiency of the decomposition process to stabilize carbon into the active soil organic matter pool:

$$\begin{aligned} f_{3,5} &= 0.45\,(1 - L_3) \\ f_{3,6} &= 0.7\,L_3 \\ f_{3,CO_2} &= 0.55\,(1 - L_3) + 0.3\,L_3 \end{aligned} \tag{4.519}$$

where L_3 is the lignin fraction of the below-ground structural litter reservoir.

The decomposition of the metabolic litter reservoirs supplies the respiration flux and the stabilization of carbon into the active soil organic matter carbon pool. The fractions are the same for above-ground and below-ground reservoirs:

$$
\begin{aligned}
f_{2,5} &= 0.45 \\
f_{2,CO_2} &= 0.55 \\
\\
f_{4,5} &= 0.45 \\
f_{4,CO_2} &= 0.55
\end{aligned}
\tag{4.520}
$$

The decomposition of the active soil organic matter carbon pool supplies the respiration flux and the slow and passive soil organic matter carbon pools, based on soil texture:

$$
\begin{aligned}
f_{5,6} &= 1 - 0.004 - (0.85 - 0.68\,(f_{silt} + f_{clay})) \\
f_{5,7} &= 0.004 \\
f_{5,CO_2} &= 0.85 - 0.68\,(f_{silt} + f_{clay})
\end{aligned}
\tag{4.521}
$$

The $f_{5,6}$ and f_{5,CO_2} terms are identical to those used in CENTURY. Note that in STOMATE, f_{clay} is used instead of the $(f_{silt} + f_{clay})$ term.
The decomposition of the slow soil organic matter carbon pool supplies the respiration flux and the active and passive soil organic matter carbon pools, based on soil texture:

$$
\begin{aligned}
f_{6,5} &= 0.42 \\
f_{6,7} &= 0.03 \\
f_{6,CO_2} &= 0.55
\end{aligned}
\tag{4.522}
$$

Finally, the decomposition of the passive soil organic matter carbon pool supplies the respiration flux and the active soil organic matter carbon pool.

$$
\begin{aligned}
f_{7,5} &= 0.45 \\
f_{7,CO_2} &= 0.55
\end{aligned}
\tag{4.523}
$$

4.3.4 Description of a simulation with ISBA-CC

Not up-to-date, new version to be released by June 2018
ISBA-CC describes the evolution of several prognostic variables: the plant biomass reservoirs and the soil organic matter reservoirs. Prescribing initial or equilibrium values of these reservoirs is not easy, at both local and global scales. Indeed, accurate observations of these quantities are lacking. More often than not, the various biomass components are not measured separately, or do not correspond to the definition of the modelled compartments. Also, the soil carbon observations are sparse, and generally concern the first top centimeters of the soil, rarely below 30cm, and barely ever below 1m.
In order to avoid drifts in the carbon reservoirs, spin-up simulations must be performed, until equilibrium reservoir values are reached. Whereas the initial CENTURY model was designed to work at a monthly scale, ISBA-CC accounts for the diurnal cycle and is coupled with a land surface model working at the half-hourly time scale or better. As the time scale for reaching equilibrium values is about a few hundred years for wood and several thousand years for the passive soil carbon pool, the spin-up simulations concern very long periods of time. Therefore, the spin-up simulations cannot involve the whole coupled model. Instead, the carbon reservoir spin-up is performed offline, in several steps described below.

1. A first spin-up simulation (a few years) is performed with ISBA-CC in order to initialize the soil moisture reservoirs, together with the biomass reservoirs presenting a relatively high turnover such as leaves and the plant structural biomass. For the woody plant types, the wood allocation terms resulting from this simulation are stored at a daily time step (see Section 4.3.2).

2. An offline program produces the evolution of wood reservoirs, at a daily time step, until equilibrium has been reached, using the allocation and decline terms. The latter depends on the amount of carbon stored in the reservoir (Section 4.3.2), and as such must be recalculated every day.

3. A second ISBA-CC simulation is performed, in order to calculate and store daily surface and deep soil temperature and soil moisture values. Also, the mortality fluxes of the plant biomass reservoirs are obtained.

4. An offline program produces the evolution of the soil carbon reservoirs, at a monthly time step, until equilibrium has been reached, using the mortality fluxes and the soil temperature and soil moisture values, based on the equations listed in Section 4.3.3. The equilibrium is reached after several thousand years. It must be noted that since the use of a monthly time step tends to filter out the variability of the surface soil moisture, the obtained equilibrium values may differ from those that would have been obtained using a daily time step.

5. Finally, a last ISBA-CC simulation permits the spin-up of the litter reservoirs and of the active soil organic matter.

A major shortcoming of this equilibrium method is that on an annual or multi-annual basis, the litter supply and the gross primary production are counterbalanced by the heterotrophic respiration, and by the autotrophic respiration, respectively. Therefore, the average net carbon exchange and net primary production present null values. This method does not permit the determination of long term land carbon sinks and sources. Performing more refined carbon budgets at a global scale is very difficult, as a perfect knowledge of the initial values of the carbon reservoirs and of the land cover/land use history is needed, especially for managed forests and for agricultural lands. However, the seasonal variability of the carbon fluxes can be represented by this method, as well as the impact of extreme events (e.g. droughts). Also, the equilibrium state can be used to initialize impact simulations related to the response of the terrestrial carbon cycle to long term perturbations.
In practise, two SURFEX namelists (NAM_ISBA and NAM_PREP_ISBA_CARBON) have to be modified before performing ISBA-CC runs. In NAM_ISBA, CPHOTO = 'NCB'. In NAM_PREP_ISBA_CARBON, CRESPSL = 'CNT'. The former activates the 6 biomass pools, and the latter activates the soil heterotrophic repiration and the soil organic matter pools. The different steps of spin-up have been coded in a script called spinup_CC.bsh, available on the SURFEX web site. This script automatically perfoms the namelist changes and the simulation repetitions needed for the spin-up. This script can be used as a template and be adapted for specifics needs. Please note that the spin-up procedure is designed for inputs and outputs in ASCII format. In particular, the NetCDF, and FA formats cannot be used.

4.3.5 Conclusion

The ISBA-CC model is a new version of ISBA permitting the detailed simulation of the land-atmosphere carbon exchange. It results from the coupling between ISBA-A-gs (Calvet and Soussana, 2001) and the heterotrophic respiration parameterization used in ORCHIDEE (Krinner *et al.* 2005). This coupling has required a number of developments.
The ISBA-A-gs allocation scheme was upgraded, in order to simulate all the plant biomass compartments, roots and wood in particular (Section 4.3.2). The principles of the initial allocation scheme, proposed by Calvet and Soussana (2001), were extended to the new biomass reservoirs. All the plant respiration terms are now calculated and their sum represents the autotrophic respiration. Also, the mortality of the biomass elements is calculated, and supplies the heterotrophic respiration module. The latter is derived from the

parameterization used in ORCHIDEE (Krinner *et al.* 2005), based on the CENTURY model (Parton *et al.* 1987). It simulates several soil organic matter pools (above-ground and below-ground litter, and the decomposed organic matter), the carbon fluxes between these pools, and the CO_2 flux to the atmosphere generated by the heterotrophic respiration (Section 4.3.3).
A few equations differ from the ORCHIDEE parameterization. The soil texture effect is based on the original CENTURY formulation, i.e. using the silt and clay fraction sum $(f_{silt} + f_{clay})$ instead of the mere clay fraction f_{clay} in ORCHIDEE. Also, the decomposition response to soil moisture is based on the saturation soil moisture value w_{sat}, available in ISBA simulations. This permits the representation of the lower decomposition rates which are observed in anaerobic conditions.
The added value of ISBA-CC is the calculation of the two heterotrophic and autotrophic respiration terms, allowing the simulation of the net primary production (NPP). The latter describes the net carbon flux absorbed by the vegetation. Also, wood compartments are simulated, and even if forest management processes are not represented so far, forest biomass estimates can be used, to some extent, to validate the model simulations.
A complete ISBA-CC simulation has to be made in several steps, including three simulations separated by offline spin-up simulations of (1) the plant biomass reservoirs, and (2) the soil carbon pools.
This method produces equilibrium simulations and does not permit the determination of long term land carbon sinks and sources. However, the seasonal variability of the carbon fluxes can be represented by this method, as well as the impact of extreme events (e.g. droughts) and of climate change.

Bibliography

[1] F. Abramopoulos, C. Rosenzweig, and B. Choudhury. Improved ground hydrology calculations for global climate models (gcms): Soil water movement and evapotranspiration. *J. Clim.*, 1:921–941, 1988.

[2] C. Albergel, J.-C. Calvet, J.-F. Mahfouf, C. Rüdiger, A. L. Barbu, S. Lafont, J.-L. Roujean, J. P. Walker, M. Crapeau, and J.-P. Wigneron. Monitoring of water and carbon fluxes using a land data assimilation system: a case study for southwestern france. *Hydrol. and Earth Syst. Sci.*, 14(6):1109–1124, 2010.

[3] K. M. Andreadis, P. Storck, and D. P. Lettenmaier. Modeling snow accumulation and ablation processes in forested environments. *Water Resour. Res.*, 45(5), 2009. W05429.

[4] Decharme B., E. Martin, and S. Faroux. Reconciling soil thermal and hydrological lower boundary conditions in land surface models. *J. Geophys. Res.*, 118, 2013.

[5] M. J. Best, A. Beljaars, J. Polcher, and P. Viterbo. A proposed structure for coupling tiled surfaces with the planetary boundary layer. *J. Hydrometeorol.*, 5(6):1271–1278, December 2004.

[6] K. J. Beven and M. J. Kirkby. A physically based, variable contributing area model of basin hydrology / un modèle base physique de zone d'appel variable de l'hydrologie du bassin versant. *Hydrol. Sci. Bull.*, 24(1):43–69, March 1979.

[7] Chandrakant M. Bhumralkar. Numerical experiments on the computation of ground surface temperature in an atmospheric general circulation model. *J. Appl. Meteor.*, 14(7):1246–1258, October 1975.

[8] R. Bintanja and M.R. Van den Broeke. The surface energy balance of antarctic snow and blue ice. *J. Appl. Meteor.*, 34(4):902–926, 1995.

[9] A.-K. Blackadar. Modeling the nocturnal boundary layer. In *Third Symp. on Atmospheric Turbulence, Diffusion and Air Quality , Boston, Amer. Meteor. Soc.*, pages 46–49, 1976.

[10] D. H. Boelter. Physical properties of peats as related to degree of decomposition. *Soil Science Society of America Journal*, 33:606–609, 1969.

[11] G. B. Bonan. A land surface model (lsm version 1.0) for ecological, hydrological, and atmospheric studies: technical description and user's guide. Technical report, National Center for Atmospheric Research, Boulder, CO, Tech. Note TN-417+STR, 150 p, 1996.

[12] G. B. Bonan and Shugart H. H. Environmental-factors and ecological processes in boreal forests. *Annu Rev Ecol Syst*, 20:128, 1989.

[13] A. Boone. *Modelisation des processus hydrologiques dans le schema de surface ISBA: Inclusion d'un reservoir hydrologique, du gel et modelisation de la neige*. PhD thesis, University Paul Sabatier, Toulouse, France, 2000.

[14] A. Boone, J. C. Calvet, and J. Noilhan. Inclusion of a third soil layer in a land surface scheme using the force-restore method. *J. Appl. Meteorol.*, 38(11):1611–1630, November 1999.

[15] A. Boone and P. Etchevers. An intercomparison of three snow schemes of varying complexity coupled to the same land surface model: Local-scale evaluation at an alpine site. *J. Hydrometeorol.*, 2(4):374–394, 2001.

[16] A. Boone, V. Masson, T. Meyers, and J. Noilhan. The influence of the inclusion of soil freezing on simulations by a soil-vegetation-atmosphere transfer scheme. *J. Appl. Meteorol.*, 39(9):1544–1569, September 2000.

[17] A. Boone, P. Samuelsson, S. Gollvik, A. Napoly, L. Jarlan, E. Brun, and B. Decharme. The interactions between soil-biosphere-atmosphere (isba) land surface model multi-energy balance (meb) option in surfex - part 1: Model description. *Geosci. Model Dev.*, 30:1–30, 2017.

[18] L.C. Bowling, D.P. Lettenmaier, B. Nijssen, L.P. Graham, D.B. Clark, M. El Maayar, R. Essery, Goers, Y. S., Gusev, F. Habets, B. van den Hurk, J. Jin, D. Kahan, D. Lohmann, X. Ma, S. Mahanama, D. Mocko, O. Nasonova, G. Niu, P. Samuelsson, A.B. Shmakin, K. Takata, D. Verseghy, P. Viterbo, Y. Xia, Y. Xue, and Z.L. Yang. Simulation of high-latitude hydrological processes in the torne kalix basin: Pilps phase 2(e): 1. experiment description and summary intercomparisons. *Global and Planetary Change*, 38:1–30, 2003.

[19] I. Braud. Sispat user's manual. Model Documentation, September 2000 3.0, LTHE, LTHE, BP 53, 38041 Grenoble Cédex 9, France, 2000.

[20] I. Braud, A. C. Dantas-Antonino, M. Vauclin, J.L. Thony, and P. Ruelle. A simple soil plant atmosphere transfer model (sispat), development and field verification. *J. Hydrol.*, 166:213–250, 1995.

[21] I. Braud, J. Noilhan, P. Bessemoulin, P. Mascart, R. Haverkamp, and M. Vauclin. Bare-ground surface heat and water exchanges under dry conditions: Observations and parameterization. *Bound.-Layer Meteorol.*, 66(1):173–200, 1993.

[22] B. Bringfelt, J. Räisänen, S. Gollvik, G. Lindström, L. P. Graham, and A. Ullerstig. The land surface treatment for the Rossby Centre regional atmosphere climate model - version 2. Reports of Meteorology and Climatology 98, SMHI, SE-601 76 Norrköping, Sweden, 2001.

[23] R. H. Brooks and A. T. Corey. Properties of porous media affecting fluid flow. *J. Irrig. Drain. Am. Soc. Civil Eng.*, 17:187–208, 1966.

[24] E. Brun, P. David, M. Sudul, and G. Brunot. A numerical model to simulate snow-cover stratigraphy for operational avalanche forecasting. *J. Glaciol.*, 38:13–22, 1992.

[25] E. Brun, E. Martin, V. Simon, C. Gendre, and C. Coléou. An energy and mass model of snow cover suitable for operational avalanche forecasting. *J. Glaciol.*, 35(121):333–342, 1989.

[26] E. Brun, V. Vionnet, B. Decharme, Y. Peings, R. Valette, A. Boone, F. Karbou, and S. Morin. Simulation of northern eurasian local snow depth, mass and density using a detailed snowpack model and meteorological reanalyses. *J. Hydrometeorol.*, 14:203–219, 2013.

[27] J. C. Calvet, A. L. Gibelin, J. L. Roujean, E. Martin, P. Le Moigne, H. Douville, and J. Noilhan. Past and future scenarios of the effect of carbon dioxide on plant growth and transpiration for three vegetation types of southwestern france. *Atmos. Chem. and Phys.*, 8(2):397–406, 2008.

[28] J.-C. Calvet, S. Lafont, E. Cloppet, F. Souverain, V. Badeau, and C. Le Bas. Use of agricultural statistics to verify the interannual variability in land surface models: a case study over france with isba-a-gs. *Geosci. Model Dev.*, 5(1):37–54, 2012.

[29] J. C. Calvet and J. Noilhan. From near-surface to root-zone soil moisture using year-round data. *J. Hydrometeorol.*, 1(5):393–411, October 2000.

[30] J. C. Calvet, J. Noilhan, and P. Bessemoulin. Retrieving the root-zone soil moisture from surface soil moisture or temperature estimates: A feasibility study based on field measurements. *J. Appl. Meteorol.*, 37(4):371–386, April 1998.

[31] J. C. Calvet, J. Noilhan, J. L. Roujean, P. Bessemoulin, M. Cabelguenne, A. Olioso, and J. P. Wigneron. An interactive vegetation svat model tested against data from six contrasting sites. *Agric. and For. Meteorol.*, 92(2):73–95, July 1998.

[32] J. C. Calvet, V. Rivalland, C. Picon-Cochard, and J. M. Guehl. Modelling forest transpiration and co2 fluxes - response to soil moisture stress. *Agric. and For. Meteorol.*, 124(3-4):143–156, August 2004.

[33] J. C. Calvet and J. F. Soussana. Modelling co2-enrichment effects using an interactive vegetation svat scheme. *Agric. and For. Meteorol.*, 108(2):129–152, June 2001.

[34] C. M. Carmagnola, S. Morin, M. Lafaysse, F. Domine, B. Lesaffre, Y. Lejeune, G. Picard, and L. Arnaud. Implementation and evaluation of prognostic representations of the optical diameter of snow in the surfex/isba-crocus detailed snowpack model. *The Cryosphere*, 8(2):417–437, 2014.

[35] D. Carrer, J.-L. Roujean, S. Lafont, J.-C. Calvet, A. Boone, B. Decharme, C. Delire, and J.-P. Gastellu-Etchegorry. A canopy radiative transfer scheme with explicit fapar for the interactive vegetation model isba-a-gs: Impact on carbon fluxes. *J. Geophys. Res.*, 188:888–903, 2013.

[36] K. A. Cherkauer and D. P. Lettenmaier. Hydrologic effects of frozen soils in the upper mississippi river basin. *J. Geophys. Res.*, 104(D16):19599–19610, 1999.

[37] B. J. Choudhury and J. L. Monteith. A four-layer model for the heat budget of homogeneous land surfaces. *Q. J. Roy. Meteor. Soc.*, 114:373–398, 1988.

[38] R. B. Clapp and G. M. Hornberger. Empirical equations for some soil hydraulic properties. *Water Resour. Res.*, 14(4):601–604, 1978.

[39] A. Clifton, J.D. Ruedi, and M. Lehning. Snow saltation threshold measurements in a drifting-snow wind tunnel. *J. Glaciol.*, 52(179):585–596, 2006.

[40] A. J. Pitman Cogley, J. G. and A. Henderson-Sellers. A land surface for large scale climate models, tech. note 90-1. Technical report, Trent Univ., Peterborough, Ont., 1990.

[41] GJ Collatz, M Ribas-Carbo, and JA Berry. Coupled photosynthesis-stomatal conductance model for leaves of c4 plants. *Funct. Plant Biol.*, 19(5):519–538, January 1992.

[42] B. J. Cosby, G. M. Hornberger, R. B. Clapp, and T. R. Ginn. A statistical exploration of the relationships of soil moisture characteristics to the physical properties of soils. *Water Resour. Res.*, 20:682–690, 1984.

[43] P. M. Cox, R. A. Betts, C. B. Bunton, R. L. H. Essery, P. R. Rowntree, and J. Smith. The impact of new land surface physics on the gcm simulation of climate and climate sensitivity. *Clim. Dyn.*, 15:183–203, 1999.

[44] R. Dankers, Burke E. J., and J. Price. Simulation of permafrost and seasonal thaw depth in the jules land surface scheme. *Cryosphere*, 5:773–790, 2011.

[45] J. Deardorff. Efficient prediction of ground temperature and moisture with inclusion of a layer of vegetation. *J. Geophys. Res.*, 83:1889–1903, 1978.

[46] J. W. Deardorff. A parameterization of ground-surface moisture content for use in atmospheric prediction models. *J. Appl. Meteor.*, 16(11):1182–1185, November 1977.

[47] B. Decharme, A. Boone, C. Delire, and J. Noilhan. Local evaluation of the interaction between soil biosphere atmosphere soil multilayer diffusion scheme using four pedotransfer functions. *J. Geophys. Res.*, 116(D20), October 2011.

[48] B. Decharme, E. Brun, A. Boone, C. Delire, P. Le Moigne, and S. Morin. Impacts of snowpack properties and soil organic carbon content on characteristics and soil temperature profiles simulated by the isba land surface model. *Cryosphere*, 10:853–877, 2016.

[49] B. Decharme and H. Douville. Introduction of a sub-grid hydrology in the isba land surface model. *Clim. Dyn.*, 26(1):65–78, January 2006.

[50] B. Decharme and H. Douville. Global validation of the isba sub-grid hydrology. *Clim. Dyn.*, 29(1):21–37, July 2007.

[51] B. Decharme, H. Douville, A. Boone, F. Habets, and J. Noilhan. Impact of an exponential profile of saturated hydraulic conductivity within the isba lsm: Simulations over the rhone basin. *J. Hydrometeorol.*, 7(1):61–80, February 2006.

[52] C. Delire, J. C. Calvet, J. Noilhan, I. Wright, A. Manzi, and C. Nobre. Physical properties of amazonian soils: A modeling study using the anglo-brazilian amazonian climate observation study data. *J. Geophys. Res.-Atmos.*, 102(D25):30119–30133, December 1997.

[53] S.J. Déry and MK Yau. Large-scale mass balance effects of blowing snow and surface sublimation. *J. Geophys. Res.*, 107(D23):4679, 2002.

[54] C. E. Desborough. The impact of root-weighting on the response of transpiration to moisture stress in a land surface scheme. *Mon. Weather Rev.*, 125:1920–1930, 1997.

[55] R. E. Dickinson, M. Shaikh, R. Bryant, and L. Graumlich. Interactive canopies for a climate model. *J. Clim.*, 11:2823–2836, 1998.

[56] Florent Domine, A-S Taillandier, and William R Simpson. A parameterization of the specific surface area of seasonal snow for field use and for models of snowpack evolution. *Journal of Geophysical Research: Earth Surface*, 112(F2), 2007.

[57] H Douville. Développement et validation locale d'une nouvelle paramétrisation du manteau neigeux. Technical report, Note de travail de GMGEC, N36, Météo-France, 1994.

[58] H. Douville, J. F. Royer, and J. F. Mahfouf. A new snow parameterization for the meteo-france climate model .1. validation in stand-alone experiments. *Clim. Dyn.*, 12(1):21–35, November 1995.

[59] H. Douville, J. F. Royer, and J. F. Mahfouf. A new snow parameterization for the meteo-france climate model .2. validation in a 3-d gcm experiment. *Clim. Dyn.*, 12(1):37–52, November 1995.

[60] H. Dumenil and E. Todoni. A rainfall-runoff scheme for use in the hamburg climate model. *Adv. Theor. Hydrol.*, 9:129–157, 1992.

[61] D. G. Erbs, S. A. Klein, and J. A. Duffie. Estimation of the diffuse radiation fraction for hourly, daily and monthly average global radiation. *Sol. Energy*, 28:293–304, 1982.

[62] Y. Fan, ML. Wood, E.and Baeck, and JA. Smith. The fractional coverage of rainfall over a grid: Analyses of nexrad data over the southern plains. *Water Resour. Res.*, 32:2787–2802, 1996.

[63] O.T. Farouki. *Thermal Properties of Soils*, volume 11. Series on Rock and Soil Mechanics, Trans. Tech., 1986.

[64] Kaptu Tchuent A. T. Roujean J.-L. Masson V. Martin E. Faroux, S. and P. Le Moigne. Ecoclimap-ii/europe : a twofold database of ecosystems and surface parameters at 1 km resolution based on satellite information for use in land surface, meteorological and climate models. *GEOSCIENTIFIC MODEL DEVELOPMENT*, 6(2):563–582.

[65] G. D. Farquhar, S. von Caemmerer, and J. A. Berry. A biochemical model of photosynthetic co2 assimilation in leaves of c3 species. *Planta*, 149:78–90, 1980.

[66] Mark G Flanner and Charles S Zender. Linking snowpack microphysics and albedo evolution. *Journal of Geophysical Research: Atmospheres*, 111(D12), 2006.

[67] M. Fuchs, G. S. Campbell, and R. I. Papendick. An analysis of sensible and latent heat flow in a partially frozen unsaturated soil. *Soil Sci. Soc. Am. J.*, 42:379–385, 1978.

[68] A.C.V. Getirana, A. Boone, and C. Peugeot. Evaluating lsm-based water budgets over a west african basin assisted with a river routing scheme. *J. Hydrometeor.*, 15:2331–2346, 2014.

[69] D. Giard and E. Bazile. Implementation of a new assimilation scheme for soil and surface variables in a global nwp model. *Mon. Weather Rev.*, 128(4):997–1015, April 2000.

[70] A. L. Gibelin, J. C. Calvet, J. L. Roujean, L. Jarlan, and S. O. Los. Ability of the land surface model isba-a-gs to simulate leaf area index at the global scale: Comparison with satellites products. *J. Geophys. Res.-Atmos.*, 111(D18):D18102, September 2006.

[71] A.-L. Gibelin, J.-C. Calvet, and N. Viovy. Modelling energy and co2 fluxes with an interactive vegetation land surface model-evaluation at high and middle latitudes. *Agric. and For. Meteorol.*, 148(10):1611–1628, 2008.

[72] H. Giordani. Expériences de validation unidimensionnelles du schéma de surface np89 aux normes arpège sur trois sites de la campagne efeda 91. Technical report, Note de travail 24 GMME/Météo-France, 1993.

[73] H. Giordani, J. Noilhan, P. Lacarrere, P. Bessemoulin, and P. Mascart. Modelling the surface processes and the atmospheric boundary layer for semi-arid conditions. *Agric. and For. Meteorol.*, 80:263–287, 1996.

[74] E. Gonzalez-Sosa, I. Braud, J.-L. Thony, M. Vauclin, P. Bessemoulin, and J.-C. Calvet. Modelling heat and water exchanges of fallow land covered with plant-residue mulch. *Agr. For. Meteorol.*, 97(3):151–169, 1999.

[75] M Gordon, K. Simon, and P. Taylor. On snow depth predictions with the canadian land surface scheme including a parametrization of blowing snow sublimation. *Atmos.-Ocean, CMOS*, 44:239–255, 2006.

[76] J. Goudriaan, van Laar, H.H., H. van Keulen, and W. Louwerse. *Photosynthesis, CO2 and plant production*, pages 107–122. Plenum Press, New York, Series A, 86, 1985.

[77] G. Guyomarc'h and L. Merindol. Validation of an application for forecasting blowing snow. *Ann. Glaciol.*, 26:138–143, 1998.

[78] F. Habets, P. Etchevers, C. Golaz, E. Leblois, E. Ledoux, E. Martin, J. Noilhan, and C. Ottle. Simulation of the water budget and the river flows of the rhone basin. *J. Geophys. Res.-Atmos.*, 104(D24):31145–31172, December 1999.

[79] F. Habets and G.-M. Saulnier. Subgrid runoff parameterization. *Phys. and Chem. of the Earth, Part B: Hydrol., Ocean. and Atmos.*, 26 (5-6):455–459, 2001.

[80] N. R. Hedstrom and J. W. Pomeroy. Measurements and modelling of snow interception in the boreal forest. *Hydrol. Process.*, 12:1611–1625, 1998.

[81] N. Isymov. An approach to the prediction of snow loads. Technical report, Faulty of Engineering Science, The Univ. of Western Ontario, London, 1971. 442 pp.

[82] R. B. Jackson, J. Canadell, J. R. Ehleringer, H. A. Mooney, O. E. Sala, and E. D. Schulze. A global analysis of root distributions for terrestrial biomes. *Oecologia*, 108(3):389–411, 1996.

[83] C. M. J. Jacobs. *Direct impact of CO2 enrichment on regional transpiration*. PhD thesis, Agricultural University, Wageningen, The Netherlands, 1994.

[84] C.M.J. Jacobs, B.M.M. van den Hurk, and H.A.R. de Bruin. Stomatal behaviour and photosynthetic rate of unstressed grapevines in semi-arid conditions. *Agric. and For. Meteorol.*, 80(24):111–134, July 1996.

[85] B. Jacquemin and J. Noilhan. Validation of a land surface parameterization using the hapex-mobilhy data set. *Bound.-Layer Meteorol.*, 52:93–134, 1990.

[86] O. Johansen. *Thermal conductivity of soils*. PhD thesis, University of Trondheim, Norway, 1975.

[87] H. Johnsson and L.-C. Lundin. Surface runoff and soil water percolation as affected by snow and soil frost. *J. Hydrol.*, 122(14):141–159, January 1991.

[88] Alexander A Kokhanovsky and Eleonora P Zege. Scattering optics of snow. *Applied Optics*, 43(7):1589–1602, 2004.

[89] V. Koren, J. Schaake, K. Mitchell, Q.-Y. Duan, F. Chen, and J. M. Baker. A parameterization of snowpack and frozen ground intended for ncap weather and climate models. *J. Geophys. Res.*, 104:19569–19585, 1999.

[90] F. Kostel-Hughes, T. P. Young, and M. M. Carreiro. Forest leaf litter quantity and seedling occurrence along an urban-rural gradient. *Urban Ecosys.*, 2:263–278, 1998.

[91] G. Krinner, Nicolas Viovy, Nathalie de Noblet-Ducoudré, Jérme Ogée, Jan Polcher, Pierre Friedlingstein, Philippe Ciais, Stephen Sitch, and I. Colin Prentice. A dynamic global vegetation model for studies of the coupled atmosphere-biosphere system. *Glob. Biogeochem. Cycles*, 19(1):1015–, February 2005.

[92] S. Lafont, A. Beljaars, M. Voogt, L. Jarlan, P. Viterbo, B. van den Hurk, and J.-C. Calvet. Comparison of c-tessel co2 fluxes with transcom co2 fluxes. In *Proc. Second Recent Advances in Quantitative Remote Sensing II, Torrent (Valencia), Spain, 474-477*, 2006.

[93] D. Lawrence and A. Slater. Incorporating organic soil into a global climate model. *Clim. Dyn.*, 30:145160, 2008.

[94] D. M. Lawrence, A.G. Slater, V. E. Romanovsky, and D. J. Nicolsky. The sensitivity of a model projection of near-surface permafrost degradation to soil column depth and inclusion of soil organic mater. *J. Geophys. Res.*, 113, 2008.

[95] David Lawrence, Keith W. Oleson, Mark G. Flanner, Peter E. Thorton, Sean C. Swenson, Peter J. Lawrence, Xubin Zeng, Zong-Liang Yang, Samuel Levis, Koichi Skaguchi, Gordan B. Bonan, and Andrew G. Slater. Parameterization improvements and functional and structural advances in version 4 of the community land model. *J. Adv. Model. Earth Syst.*, 3:27p., 2011.

[96] G. Lemaire and F. Gastal. *N uptake and distribution in plant canopies*, pages 3–43. Springer, Berlin, 1997.

[97] M. G. Letts, N. T. Roulet, N. T. Comer, M. R. Skarupa, and D. L. Verseghy. Parametrization of peatland hydraulic properties for the canadian land surface scheme. *Atmos Ocean*, 38:141160, 2000.

[98] E. Wood Liang, Xu and D. Lettenmaier. Surface soil moisture parameterization of the vic-2l model: Evaluation and modification. *Glob. and Planet. Change*, 13:195–206, 1996.

[99] Q Libois, G Picard, JL France, L Arnaud, M Dumont, CM Carmagnola, and MD King. Influence of grain shape on light penetration in snow. *The Cryosphere*, 7(6):1803–1818, 2013.

[100] B. Loth, H.-F. Graf, and J. M. Oberhuber. Snow cover model for global climate simulations. *J. Geophys. Res.*, 98(D6):10451–10464, 1993.

[101] J.-F. Louis. A parametric model of vertical eddy fluxes in the atmosphere. *Bound.-Lay. Meteorol.*, 17:187–202, 1979.

[102] L.-C. Lundin. Hydraulic properties in an operational model of frozen soil. *J. Hydrol.*, 118:289–310, 1990.

[103] M. Lynch-Stieglitz. The development and validation of a simple snow model for the giss gcm. *J. Clim.*, 7(12):1842–1855, December 1994.

[104] J.-F. Mahfouf and J. Noilhan. Comparative study of various formulations of evaporation from bare soil using in situ data. *J. Appl. Meteorol.*, 9:1354–1365, 1991.

[105] J. F. Mahfouf and J. Noilhan. Inclusion of gravitational drainage in a land surface scheme based on the force-restore method. *J. Appl. Meteorol.*, 35(6):987–992, June 1996.

[106] L. Mahrt and H. Pan. A two-layer model of soil hydrology. *Bound.-Layer Meteorol.*, 29:1–20, 1984.

[107] A. O. Manzi and S. Planton. Implementation of the isba parameterization scheme for land surface processes in a gcm-an annual cycle experiment. *J. Hydrol.*, 155:353–387, 1994.

[108] D. Marbouty. An experimental study of temperature-gradient metamorphism. *J. Glaciol.*, 26:303–312, 1980.

[109] E. Martin, P. Le Moigne, and V. Masson. Le code de surface externalisée surfex de météo- france. In *Ateliers de Modélisation de lAtmosphère*, 2007.

[110] P. Mascart, J. Noilhan, and H. Giordani. A modified parameterization of flux-profile relationships in the surface layer using different roughness length values for heat and momentum. *Bound.-Layer Meteorol.*, 72:331–344, 1995.

[111] W. J Massman. Foliage distribution in old-growth coniferous tree canopies. *Canadian Journal of Forest Research*, 12(1):10–17, 1982.

[112] M. C. McCumber and R. A. Pielke. Simulation of the effects of surface fluxes of heat and moisture in a mesoscale numerical model. *J. Geophys. Res.*, 86 (C10):9929–9938, 1981.

[113] J. F. Meekins and B. C. McCarthy. Effect of environmental variation on the invasive success of a nonindigenous forest herb. *Ecol. Appl.*, 11(5):1336–1348, 2001.

[114] P. C. D. Milly. Moisture and heat transport in hysteretic, inhomogeneous porous media: a matric head-based formulation and a numerical model. *Water Resour. Res.*, 18 (3):489–498, 1982.

[115] J. L. Monteith, editor. *Vegetation and the atmosphere*, volume 1. Academic Press, 1975.

[116] Y. Nakai, T. Sakamoto, T. Terajima, K. Kitamura, and T. Shirai. The effect of canopy-snow on the energy balance above a coniferous forest. *Hydrol. Process.*, 13:2371–2382, 1999.

[117] A. Napoly, A. Boone, P. Samuelsson, S. Gollvik, E. Martin, R. Seferian, D. Carrer, B. Decharme, and L. Jarlan. The interactions between soil-biosphere-atmosphere (isba) land surface model multi-energy balance (meb) option in surfex - part 2: Model evaluation for local scale forest sites.

[118] D. J. Nicolsky, V. E. Romanovsky, V. A. Alexeev, and D. M. Lawrence. Improved modeling of permafrost dynamics in alaska with clm3. *Geophys Res Lett*, 34, 2007.

[119] G.-Y. Niu and Z.-L. Yang. Effects of vegetation canopy processes on snow surface energy and mass balances. *J. Geophys. Res.*, 109(D23), 2004. D23111.

[120] J. Noilhan and P. Lacarrère. Gcm grid-scale evaporation from mesoscale modeling. *J. Clim.*, 8(2):206–223, 1995.

[121] J. Noilhan and J. F. Mahfouf. The isba land surface parameterisation scheme. *Glob. and Planet. Change*, 13(1-4):145–159, June 1996.

[122] J. Noilhan and S. Planton. A simple parameterization of land surface processes for meteorological models. *Mon. Weather Rev.*, 117(3):536–549, 1989.

[123] J. Ogée and Y. Brunet. A forest floor model for heat and moisture including a litter layer. *J. Hydrol.*, 255(1):212–233, 2002.

[124] H. Pan and L. Mahrt. Interaction between soil hydrology and boundary layer development. *Bound.-Layer Meteorol.*, 38:185–202, 1987.

[125] J.-P. Paquin and L. Sushama. On the arctic near-surface permafrost and climate sensitivities to soil and snow model formulations in climate models. *Clim. Dyn.*, 44:203228.

[126] W.J. Parton, D.S. Schimel, C.V. Cole, and D.S. Ojima. Analysis of factors controlling soil organic matter levels in great plains grasslands. *Soil Sci. Soc. Am. J.*, 51:1173–1179, 1987.

[127] W.J. Parton, J.M.O. Scurlock, D.S. Ojima, T.G. Gilmanov, R.J. Scholes, D.S. Schimel, T. Kirchner, J.-C. Menaut, T. Seastedt, E. Garcia Moya, A. Kamnalrut, and J.I. Kinyamario. Observations and modeling of biomass and soil organic matter dynamics for the grassland bioma worldwide. *Glob. Biogeochem. Cycles*, 7:785–809, 1993.

[128] W.J. Parton, J.W.B. Stewart, and C.V. Cole. Dynamics of c, n, p and s in grassland soils: a model. *Biogeochem.*, 5:109–131, 1988.

[129] K. Paul. Temperature and moisture effects on decomposition. In M. Kirschbaum and R. Mueller, editors, *Net ecosystem exchange*, pages 95–102. CRC for greenhouse accounting, 18-20 April 2001.

[130] C. Peng, M.J. Apps, D.T. Price, I.A. Nadler, and D.H. Halliwell. Simulating carbon dynamics along the boreal forest transect case study (bftcs) in central canada: 1, model testing. *Glob. Biogeochem. Cycles*, 12:381–392, 1998.

[131] C. D. Peters-Lidard, E. Blackburn, X. Liang, and E. F. Wood. The effect of soil thermal conductivity parameterization on surface energy fluxes and temperatures. *J. Atmos. Sci.*, 55(7):1209–1224, April 1998.

[132] A. J. Pitman, Z.-L. Yang, J. G. Cogley, and A. Henderson-Sellers. Description of bare essentials of surface transfer for the bureau of meteorology research centre agcm. Technical report, BMRC Research Report No. 32, 1991.

[133] J. Polcher, B. McAvaney, P. Viterbo, M. A. Gaertner, A. Hahmann, J. F. Mahfouf, J. Noilhan, T. Phillips, A. Pitman, C. A. Schlosser, J. P. Schulz, B. Timbal, D. Verseghy, and Y. Xue. A proposal for a general interface between land surface schemes and general circulation models. *Glob. and Planet. Change*, 19(1-4):261–276, December 1998.

[134] J. W. Pomeroy and K. Dion. Winter radiation extinction and reflection in a boreal pine canopy: measurements and modelling. *Hydrol. Process.*, 10:1591–1608, 1996.

[135] M.E. Probert, J.P. Dimers, B.A. Keating, R.C. Dalal, and W.M. Strong. Apsim's water and nitrogen modules and simulation of the dynamics of water and nitrogen in fallow systems. *Agric. Syst.*, 56:1–28, 1998.

[136] William M Putuhena and Ian Cordery. Estimation of interception capacity of the forest floor. *J. Hydrol.*, 180(1):283–299, 1996.

[137] Paul Ricchiazzi, Shiren Yang, Catherine Gautier, and David Sowle. Sbdart: A research and teaching software tool for plane-parallel radiative transfer in the earth's atmosphere. *Bulletin of the American Meteorological Society*, 79(10):2101, 1998.

[138] R. Richtmeyer and K. Morton. *Difference method for initial values problems*. Interscience Publishers, second edition, 1967.

[139] V. Rivalland, J.-C. Calvet, P. Berbigier, Y. Brunet, and A. Granier. Transpiration and co2 fluxes of a pine forest: modelling the undergrowth effect. *Ann. Geophys.*, 23:291–304, 2006.

[140] J.-L. Roujean. A tractable physical model of shortwave radiation interception by vegetative canopies. *J. Geophys. Res.*, 101D5:9523–9532, 1996.

[141] A. Ruimy, L. Kergoat, C. Field, and B. Saugier. The use of co2 flux measurements in models of the global terrestrial carbon budget. *Global Change Biology*, 2(3):287–296, 1996.

[142] N. Rutter, R. Essery, J. Pomeroy, N. Altimir, K. Andreadis, I. Baker, A. Barr, P. Bartlett, A. Boone, H. Deng, H. Douville, E. Dutra, K. Elder, C. Ellis, X. Feng, A. Gelfan, A. Goodbody, Y. Gusev, D. Gustafsson, R. Hellstrom, Y. Hirabayashi, T. Hirota, T. Jonas, V. Koren, A. Kuragina, D. Lettenmaier, W.-P. Li, C. Luce, E. Martin, O. Nasonova, J. Pumpanen, R. D. Pyles, P. Samuelsson, M. Sandells, G. Schadler, A. Shmakin, T. G. Smirnova, M. Stahli, R. St ckli, U. Strasser, H. Su, K. Suzuki, K. Takata, K. Tanaka, E. Thompson, T. Vesala, P. Viterbo, A. Wiltshire, K. Xia, Y. Xue, , and T. Yamazaki. Evaluation of forest snow processes models (SnowMIP2). *J. Geophys. Res.*, 114(D6):18, 2009.

[143] P. Samuelsson, S. Gollvik, and A. Ullerstig. The land-surface scheme of the rossby centre regional atmospheric climate model (rca3). Report in Meteorology 122, SMHI, SE-60176 Norrköping, Sweden, 2006.

[144] P. Samuelsson, C. Jones, U. Willén, A. Ullerstig, S. Gollvik, U. Hansson, C. Jansson, E. Kjellström, G. Nikulin, and K. Wyser. The rossby centre regional climate model rca3: Model description and performance. *Tellus A*, 63:1–3, 2011.

[145] R. A. Schmidt and D. R. Gluns. Snowfall interception on branches of three conifer species. *Can. J. For. Res.*, 21:1262–1269, 1991.

[146] R.A. Schmidt. Vertical profiles of wind speed, snow concentration, and humidity in blowing snow. *Bound.-Layer Meteorol.*, 23(2):223–246, 1982.

[147] P. J. Sellers, M. D. Heiser, and F. G. Hall. Relations between surface conductance and spectral vegetation indices at intermediate (100 m^2 to 15 km^2) length scales. *J. Geophys. Res.*, 97:19033–19059, 1992.

[148] P. J. Sellers, Y. Mintz, Y. C. Sud, and A. Dalcher. A simple biosphere model (SiB) for use within general ciculation models. *J. Atmos. Sci.*, 43:505–531, 1986.

[149] P. J. Sellers, D. A. Randall, G. J. Collatz, J. A. Berry, C. B. Field, D. A. Dazlich, C. Zhang, G. D. Collelo, and L. Bounoua. A revised land surface parameterization (SiB2) for atmospheric GCMs. Part I: Model formulation. *J. Climate*, 9:676–705, 1996.

[150] Beven K.J. Silvapalan, M. and E.F. Wood. On hydrologic similarity: 2. a scaled model of storm runoff production. *Water Resour. Res.*, 23:2266–2278, 1987.

[151] S. Sun, J. Jin, and Y. Xue. A simple snow-atmosphere-soil transfer (sast) model. *J. Geophys. Res.*, 104:19587–19579, 1999.

[152] Anne-Sophie Taillandier, Florent Domine, William R Simpson, Matthew Sturm, and Thomas A Douglas. Rate of decrease of the specific surface area of dry snow: Isothermal and temperature gradient conditions. *Journal of Geophysical Research: Earth Surface*, 112(F3), 2007.

[153] B. J. J. M. Van den Hurk, P. Viterbo, A. C. M. Beljaars, and A. K. Betts. Offine validation of the era40 surface scheme, ecmwf techmemo. 295, 42 p. Technical report, ECMWF, Reading, 2000.

[154] J.-P. Vergnes, Decharme B., and Habets F. Introduction of groundwater capillary rises using subgrid spatial variability of topography into the isba land surface model. *J. Geophys. Res.*, 119:11,06511,086, 2014.

[155] D. L. Verseghy. Class: A canadian land surface scheme for gcms. i. soil model. *Int. J. Clim.*, 11(2):111–133, 1991.

[156] V. Vionnet, E. Brun, S. Morin, A. Boone, S. Faroux, P. Le Moigne, E. Martin, and J.-M. Willemet. The detailed snowpack scheme crocus and its implementation in surfex v7.2. *Geoscientific Model Development*, 5(3):773–791, 2012.

[157] M. Voogt, B.J.J.M. van den Hurk, and C. Jacobs. The ecmwf land surface scheme extended with a photosynthesis and lai module tested for a coniferous site, knmi publication: Wr-06-02, 22 pp. Technical report, KNMI, De Bilt, The Netherlands, 2006.

[158] D. A. De Vries. Thermal properties of soils. *Physics of plant environment*, 1963.

[159] W. Wang, A. Rinke, J. C. Moore, D. Ji, X. Cui, S. Peng, D. M. Lawrence, A. D. McGuire, E. J. Burke, X. Chen, B. Decharme, C. Koven, A. MacDougall, K. Saito, W. Zhang, Alkama, R., T. J. Bohn, P. Ciais, C. Delire, I. Gouttevin, T. Hajima, G. Krinner, D. P. Lettenmaier, P. A. Miller, B. Smith, T. Sueyoshi, and A. B. Sherstiukov. Evaluation of airsoil temperature relationships simulated by land surface models during winter across the permafrost region. *Cryosphere*, 10:1721–1737, 2016.

[160] T. B. Wilson, T. P. Meyers, J. Kochendorfer, M. C. Anderson, and M. Heuer. The effect of soil surface litter residue on energy and carbon fluxes in a deciduous forest. *Agr. For. Meteorol.*, 161:134–147, 2012.

[161] E. F. Wood, D. P. Lettenmaier, X. Liang, D. Lohmann, A. Boone, S. Chang, F. Chen, Y. J. Dai, R. E. Dickinson, Q. Y. Duan, M. Ek, Y. M. Gusev, F. Habets, P. Irannejad, R. Koster, K. E. Mitchel, O. N. Nasonova, J. Noilhan, J. Schaake, A. Schlosser, Y. P. Shao, A. B. Shmakin, D. Verseghy, K. Warrach, P. Wetzel, Y. K. Xue, Z. L. Yang, and Q. C. Zeng. The project for intercomparison of land-surface parameterization schemes (pilps) phase 2(c) red-arkansas river basin experiment: 1. experiment description and summary intercomparisons. *Glob. and Planet. Change*, 19(1-4):115–135, December 1998.

[162] Y. Xue, P. J. Sellers, J. L. Kinter, and J. Shukla. A simplified Biosphere Model for Global Climate Studies. *J. Climate*, 4:345–364, 1991.

[163] Z.-L. Yang and G.-Y. Niu. The versatile integrator of surface atmospheric processes (visa): Part 1. model description. *Glob. Planet. Change*, 38:175–189, 2003.

[164] R. J. Zhao. The xinanjiang model applied in china. *J. Hydrol.*, 134:317–381, 1992.

Chapter 5

Surface boundary layer scheme

Contents

5.1 Introduction

Surface atmosphere exchanges, mainly momentum, water and heat surface fluxes, drive the boundary layer evolution, and influence the formation of low level clouds and more generally the synoptic flows and climate system. The modelling of these fluxes is performed by specific surface schemes: Soil-Vegetation-Atmosphere Transfer (SVATs) schemes for vegetation (Chen *et al.* (1997) review the vegetation schemes used in the intercomparison exercice on Cabauw grass site), urban schemes for cities (see a review in Masson (2006)), or schemes dedicated to sea or ice surfaces. The degree of complexity of these schemes is wide. The simplest models are bucket models (e.g. Manabe (1969), Robock *et al.* (1995)), with only one water reservoir in the soil. Next are the so-called big leaf models (Deardorff (1978), Noilhan and Planton (1989) with only one surface energy balance and no canopy. The more detailed schemes have several layers in the soil, several energy budgets (low vegetations, snow and tree canopy) and photosynthesis production to simulate the carbon cycle (see Simon *et al.* (2005)). The same degree of variability exists in the complexity of the physical processes described in urban schemes (see Masson (2006)).
However, the present paper will not discuss on the complexity of the physical and physiological processes of the soil or plants in these schemes. The topic of this paper is to discuss the coupling of surface schemes

to atmospheric models. Independantly of the complexity of the processes, two coupling methods are usually used (fig 5.1):

- single-layer coupled schemes: these surface schemes are forced by only one atmospheric layer (i.e. the lowest atmospheric layer of an atmospheric model, as in fig 5.1b). The surface schemes respond to atmospheric variables at this level (temperature, wind, humidity, incoming radiation, etc...) and they produce averaged upwards turbulent fluxes and radiative quantities (albedo, emissivity, surface temperature). Note that this level is physically supposed to be high enough above the surface to be in the inertial sublayer (or constant flux layer), most schemes using Monin-Obukhov theory to parameterize turbulent fluxes. These exchanges have been normalized in the Assistance for Land-surface Modelling activities (ALMA) norm (see Best *et al.* (2004) and Polcher *et al.* (1998)).
  Because of the simplicity of this type of coupling, these surface schemes can be used off-line (e.g. forced directly by observations), so that they can be used for a wide range of applications (e.g. hydrology). All schemes presented in the offline intercomparison by Chen *et al.* (1997) are single-layer schemes. These schemes can have a separate modelling of the soil and of the canopy, but the coupling with the atmosphere is always done at a forcing level above the canopy. The link between the forcing level and the soil/canopy to compute energy fluxes is usually done using systems of aerodynamical/stomatal resistances (as in Deardorff (1978)), that may depend on many factors, such as plant stress or atmospheric stability.

- multi-layer coupled schemes: these schemes are coupled with several atmospheric levels (fig 5.1c). They interact not by surface fluxes (except for the lowest level), but directly throughout the prognostic variables equations of the atmospheric model at each level. For example, drag forces by the obstacles (trees or buildings) will slow the wind and increase the turbulence, heat (water) fluxes by these obstacles will produce differential heating (moistening) between the levels. Xinmin *et al.* (1999) use such a scheme coupled inline to a planetary boundary layer model to study the influence of the tree density in a forest on the air characteristic within the canopy at day and at night. Recently Simon *et al.* (2005) built a multilayer scheme to describe precisely the water and carbon dioxyde fluxes inside the Amazonian forest. For building canopies, Martilli *et al.* (2002), Coceal and Belcher (2005) and Kondo *et al.* (2005) are example of multi-layer schemes. The drawback of this high resolution description of the atmospheric processes is an intimate coupling of the surface scheme and the atmospheric model. Furthermore, because atmospheric layers are thin near the surface (depth of the order of 1m) to finely describe the air profile in the Surface Boundary Layer (SBL), the time step of the atmospheric model must usually be much smaller in order to insure numerical stability.
  Such schemes are used when one wants to describe very finely the interaction between the atmosphere and the surface features. For example, low vegetation and soil will interact with air temperature near the surface (say 1m), while tree leaves exchange temperature and humidity with higher level air (with other temperature, humidity). This therefore allows a priori a better simulation of the physical and physiological processes. Another interest of these schemes is the direct simulation of air characteristics down to the surface itself, allowing several specific applications (wind stress in forest ridges, air temperature profile between buildings, etc...).

The objective of this paper is to implement into single-layer schemes the fine description of air profiles near the ground of the multi-layer schemes. That way, the single-layer schemes will gain the explicit physical representation of the surface boundary layer thanks to additionnal air layers, and still be coupled to atmospheric models through only one layer.

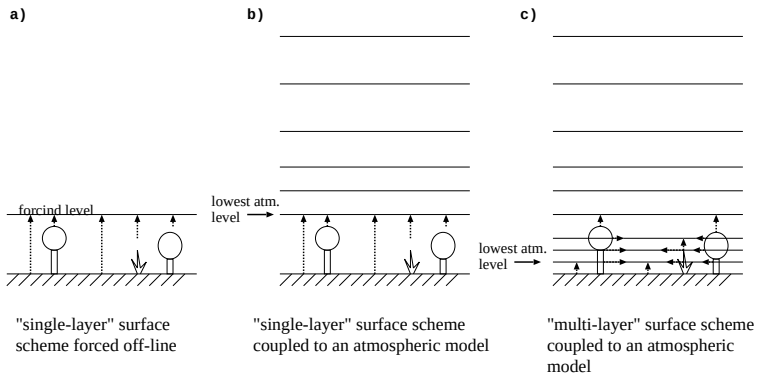

Figure 5.1: Schematic view of surface scheme coupling: a) single-layer surface scheme forced offline. b) single-layer surface scheme forced by an atmospheric model. c) multi-layer scheme forced by an atmospheric model. Dotted arrows show the interactions between surface and coupling/atm. forcing: (a) with the forcing level, (b) the lowest atm level and (c) with all levels intersecting the canopy.

5.2 Theory

5.2.1 Atmospheric equations

The atmosphere can be described by dynamical (3 wind components) and thermodynamical variables (heat content or temperature, water vapor, possibly other water phases quantities). In this study, only the Planetary Boundary Layer was considered, neglecting mean vertical velocity and horizontal turbulent fluxes. The Boussinesq hypothesis is applied for the sake of simplicity. However, the following derivation can be generalized to more complex equation systems. Only the theory is described in the main part of the paper. The numerics for implementation and coupling in models are discussed in the last section.

Using mean horizontal wind components (U, V), potential temperature (θ) and water vapor specific humidity (q), without water phase changes, the equations describing the atmosphere evolution can be written as:

$$\left\{\begin{array}{rcl}
\frac{\partial U}{\partial t} &=& \underbrace{-U\frac{\partial U}{\partial x}-V\frac{\partial U}{\partial y}}_{Adv} \underbrace{-fV}_{Cor} \underbrace{+fV_g}_{Pres.} \underbrace{-\frac{\partial \overline{u'w'}}{\partial z}}_{Turb} \\
\frac{\partial V}{\partial t} &=& \underbrace{-U\frac{\partial V}{\partial x}-V\frac{\partial V}{\partial y}}_{Adv} \underbrace{+fU}_{Cor} \underbrace{-fU_g}_{Pres.} \underbrace{-\frac{\partial \overline{v'w'}}{\partial z}}_{Turb} \\
\frac{\partial \theta}{\partial t} &=& \underbrace{-U\frac{\partial \theta}{\partial x}-V\frac{\partial \theta}{\partial y}}_{Adv} + \underbrace{\dot{Q}}_{Diab.} \underbrace{-\frac{\partial \overline{w'\theta'}}{\partial z}}_{Turb} \\
\frac{\partial q}{\partial t} &=& \underbrace{-U\frac{\partial q}{\partial x}-V\frac{\partial q}{\partial y}}_{Adv} \underbrace{-\frac{\partial \overline{w'q'}}{\partial z}}_{Turb}
\end{array}\right. \tag{5.1}$$

where $U_g = -\frac{1}{f\rho}\frac{\partial p}{\partial x}$ and $V_g = -\frac{1}{f\rho}\frac{\partial p}{\partial y}$ are the geostrophic wind components, $\overline{u'w'}$, $\overline{v'w'}$, $\overline{w'\theta'}$ and $\overline{w'q'}$ are the turbulent fluxes, and $\dot{Q}$ represents the diabatic sources of heat (e.g. radiative tendency).

In addition, a Turbulent Kinetic Energy (TKE, noted $e = \frac{1}{2}(\overline{u'^2} + \overline{v'^2} + \overline{w'^2})$) equation can be used to

describe the turbulence in some atmospheric models:

$$\frac{\partial e}{\partial t} = \underbrace{-U\frac{\partial e}{\partial x} - V\frac{\partial e}{\partial y}}_{Adv} \underbrace{-\overline{u'w'}\frac{\partial U}{\partial z} - \overline{v'w'}\frac{\partial V}{\partial z}}_{Dyn.Prod.} + \underbrace{\frac{g}{\theta}\overline{w'\theta'_v}}_{Therm.Prod.} - \underbrace{\frac{\partial \overline{w'e}}{\partial z}}_{Turb} - \underbrace{\epsilon}_{Diss.} \tag{5.2}$$

where Right Hand Side terms stand for advection of TKE, dynamical production, thermal production, turbulent transport of TKE and dissipation respectively.

5.2.2 Atmospheric equations modified by canopy obstacles

The above equations refer to air parcels that do not interact with any obstacles. Near the surface, when one wants to take into account the influence of obstacles on the flow, these equations must be modified. In atmospheric models, this is done by adding additional terms for each variable, representing the average effect of these obstacles on the air contained in the grid mesh. One should note here that ideally, the volume of the obstacles (trees, buildings) contained into the grid mesh should be removed from the volume of air of the grid mesh. However, this significantly complexifies a lot the atmospheric model, and the approximation to keep the air volume constant even in the presence of obstacles is normally done. This simplification is also chosen here. Then, obstacles impact on the flow is parameterized as:

$$\left\{\begin{array}{rcllll} \frac{\partial U}{\partial t} & = & Adv & +Cor & +Pres. & +Turb(U) & +\mathrm{Drag_u} \\ \frac{\partial V}{\partial t} & = & Adv & +Cor & +Pres. & +Turb(V) & +\mathrm{Drag_v} \\ \frac{\partial \theta}{\partial t} & = & Adv & +Diab. & & +Turb(\theta) & +\frac{\partial \theta}{\partial t}_{canopy} \\ \frac{\partial q}{\partial t} & = & Adv & & & +Turb(q) & +\frac{\partial q}{\partial t}_{canopy} \end{array}\right. \tag{5.3}$$

and

$$\frac{\partial e}{\partial t} = Adv + Dyn.Prod. + Therm.Prod. + Turb + Diss. + \frac{\partial e}{\partial t}_{canopy} \tag{5.4}$$

where,

- $\mathrm{Drag_u}$ and $\mathrm{Drag_v}$ are the drag forces (due to pressure forces against the obstacles) that slow the flow,
- $\frac{\partial \theta}{\partial t}_{canopy}$ is the heating/cooling rate due to the heat release/uptake by the surfaces of the canopy obstacles in the grid mesh,
- $\frac{\partial q}{\partial t}_{canopy}$ is the moistening/drying impact of these obstacles,
- and $\frac{\partial e}{\partial t}_{canopy}$ represents the TKE production due to wake around and behind obstacles as well as the additionnal dissipation due to leaves-induced small-scale turbulence.

The prescription of these terms due to the obstacle impact on the flow are parameterized differently for each multi-level surface scheme, and this is not described in detail here. Parameterizations for dynamical variables are often similar for forest canopies. Wind drag is usually parameterized as the opposite of the square of the wind, as in Shaw and Schumann (1992) or Patton *et al.* (2001): $\mathrm{Drag_u} = -C_d a(z) U \sqrt{U^2+V^2}$ and $\mathrm{Drag_v} = -C_d a(z) V \sqrt{U^2+V^2}$, where C_d is a drag coefficient and $a(z)$ is the leaf area density at height z (this parameter can be derived from Leaf Area Index and vegetation height, assuming a normalized vertical profile of leaves distribution in the canopy). The TKE production/destruction term can be parameterized as the sum of two effects: wake production by the leaves (parameterized as proportionnal to the cubic

power of wind: $\frac{\partial e}{\partial t}_{canopy} \propto C_d(U^2+V^2)^{\frac{3}{2}}$ as in Kanda and Hino (1994)) and the energy loss due to fast dissipation of small scale motions (leaves are of a much smaller scale than the grid mesh). The latter term is often parameterized as proportionnal to the product of wind by TKE ($\frac{\partial e}{\partial t}_{canopy} \propto -C_d e\sqrt{U^2+V^2}$ as in Kanda and Hino (1994), Shen and Leclerc (1997), Patton *et al.* (2003)). Because of the high degree of complexity of the processes involved (and hence of possibles simplifications), parameterizations for temperature and humidity exchanges are much more variables. For example, Sun *et al.* (2006) parameterize heating effects simply as a function of radiation vertical divergence, while more complex vegetation models, as in Park and Hattori (2004), solve leaves temperature and use it to estimate at each atmospheric layer the heat and water vapor exchanges between the forest canopy and the air: $\frac{\partial \theta}{\partial t}_{canopy} \propto a(z)(\theta_l - \theta)$ and $\frac{\partial q}{\partial t}_{canopy} \propto a(z)(q_{sat}(\theta_l) - q)$, where θ_l is the leaves potential temperature and q_{sat} is humidity at saturation (proportionnality coefficients depend on physiological processes of the plant).

For urban canopies, the same drag approach is chosen in general for the effect on wind, and only the wake production term is kept for TKE (because turbulent eddies are large behind buildings, so their dissipation is not as fast as those produced by leaves). Heat exchanges are however more complex and detailled (see Masson (2006) for a review), as radiative trapping and shadows, different building heights, and sometimes even road trees are taken into account in state-of-the-art urban models. An exemple of urban canopy parameterization is given in Hamdi and Masson (2008).

As stated above, these additional terms allow a fine description of the mean variable profiles in the atmospheric model in the SBL (e.g. wind and temperature profile as a function of stability, wind speed in forest canopy, etc...) and of the flow statistics (non constant flux layer inside the canopy for example).

5.2.3 Implementation of the SBL equations into a surface scheme

The objective of this paper is to provide a way to implement such a description of the SBL with a lot of atmospheric layers directly into the surface scheme. Such a scheme could be used offline (figure 5.2a) or coupled to an atmospheric model (figure 5.2b). As seen by comparing with figure 5.2c, the vertical resolution is the same as with a multi-layer model. The problem is that the computation of most of the terms of the equations (advection, pressure forces, diabatic heating) requires the atmospheric model dynamics and physical parameterizations.

The set of equation (5.3) is rewritten by separating the processes as (i) 'large scale forcing' (LS, that are solved by the atmospheric model), (ii) the turbulence and (iii) the canopy effects:

$$\left\{\begin{array}{lcll} \frac{\partial U}{\partial t} & = & LS(U) & +Turb(U) \quad +\mathrm{Drag_u} \\ \frac{\partial V}{\partial t} & = & LS(V) & +Turb(V) \quad +\mathrm{Drag_v} \\ \frac{\partial \theta}{\partial t} & = & LS(\theta) & +Turb(\theta) \quad +\frac{\partial \theta}{\partial t}_{canopy} \\ \frac{\partial q}{\partial t} & = & LS(q) & +Turb(q) \quad +\frac{\partial q}{\partial t}_{canopy} \end{array}\right. \tag{5.5}$$

The TKE equation remains the same:

$$\frac{\partial e}{\partial t} = Adv(e) + Dyn.Prod. + Therm.Prod. + Turb + Diss. + \frac{\partial e}{\partial t}_{canopy} \tag{5.6}$$

To represent the SBL into the single-layer surface scheme, one considers prognostic atmospheric layers, between the surface and the forcing level of the surface scheme (that is the level that is coupled to the

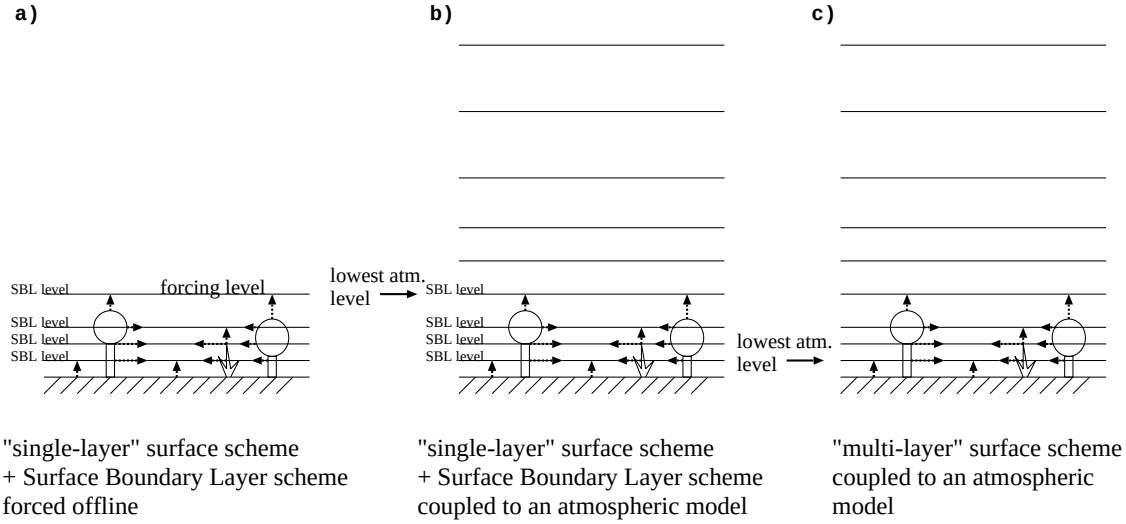

Figure 5.2: Schematic view of the coupling between surface scheme and SBL scheme : a) single-layer surface scheme with SBL scheme forced offline. b) single-layer surface scheme with SBL scheme forced by an atmospheric model. c) multi-layer scheme coupling (as c) in figure 5.1). Dotted arrows show the interactions between surface and SBL scheme (a and b). Upper SBL level is at same height as atmospheric forcing level.

atmosphere). Each of these layers is represented by the wind speed, the potential temperature, the humidity and the Turbulent kinetic energy (all these variables being prognostically computed). They satisfy the set of equations (12.7). In order to solve them, the following assumptions are made:

- The mean wind direction does not vary in the SBL (Rotation due to Coriolis inside the SBL is neglected).
- The advection of TKE is negligible. This assumption is not valid for horizontal scales (and grid meshes) of the order of a few times the canopy height, as equilibrium with forcing condition above is not reached (Belcher *et al.* (2003), Coceal and Belcher (2005)), but it is valid for larger scales.
- The turbulent transport of TKE ($\overline{w'e}$) is negligible near the ground and in the SBL. This assumption is fairly valid, this term being generally important only higher in the BL .
- Above the canopy, the turbulent fluxes are uniform with height (constant flux layer).
- The Large Scale forcing terms ($LS(U), LS(V), LS(\theta), LS(q)$) are supposed to be uniform with height in the SBL. It is assumed, for example, that advection and pressure forces are driven by synoptic flow or by the mesoscale BL flow (e.g. sea breeze). Diabatic effects on temperature are also supposed to be uniform.

Then, the equations can be solved if the turbulent terms in the SBL (see subsection (5.2.5)), the canopy terms (depending on each surface scheme physics), and the (uniform with height) large scale forcing are known or parameterized.

Writing the equations at the forcing level ($z = z_a$), which is supposed to be above the canopy (all canopy terms are set to zero) and therefore in the constant flux layer (the turbulent fluxes are supposed to be uniform,

so that the divergences of turbulent fluxes are small), large scale terms can be estimated from the temporal evolution of the variables at the forcing level:

$$\left\{ \begin{array}{lcl} \frac{\partial U}{\partial t}(z=z_a) & = & LS(U) \\ \frac{\partial V}{\partial t}(z=z_a) & = & LS(V) \\ \frac{\partial \theta}{\partial t}(z=z_a) & = & LS(\theta) \\ \frac{\partial q}{\partial t}(z=z_a) & = & LS(q) \end{array} \right. \tag{5.7}$$

In reality, the constant flux layer hypothesis supposes not a constant turbulent flux but a small variation of the turbulent flux compared to its value. The small decrease/increase of the turbulent flux can lead to tendencies of the mean variables. However, this small variation is generally relatively uniform in the whole boundary layer (e.g. uniform heating of the convective boundary layer). This impact of the fluxes at the scale of the whole BL is included in the LS terms.

5.2.4 Boundary conditions

Finally, one obtains (using only one wind component, as the wind does not veer with height in the SBL):

$$\left\{ \begin{array}{lcllll} \frac{\partial U}{\partial t} & = & \frac{\partial U}{\partial t}(z=z_a) & +Turb(U) & +\mathrm{Drag_u} \\ \frac{\partial \theta}{\partial t} & = & \frac{\partial \theta}{\partial t}(z=z_a) & +Turb(\theta) & +\frac{\partial \theta}{\partial t}_{canopy} \\ \frac{\partial q}{\partial t} & = & \frac{\partial q}{\partial t}(z=z_a) & +Turb(q) & +\frac{\partial q}{\partial t}_{canopy} \end{array} \right. \tag{5.8}$$

And

$$\frac{\partial e}{\partial t} = Dyn.Prod. + Therm.Prod. + Diss. + \frac{\partial e}{\partial t}_{canopy} \tag{5.9}$$

The surface condition for the wind equation is given by the turbulent flux at the surface $\overline{u'w'}(z=0)$. The value at the top of the SBL scheme is given by wind at forcing level: $U = U(z=z_a)$.
The surface condition for the potential temperature equation is given by the turbulent flux at the surface $\overline{w'\theta'}(z=0)$. The value at the top is given by the temperature at forcing level: $\theta = \theta(z=z_a)$.
The surface condition for the humidity equation is given by the turbulent flux at the surface $\overline{w'q'}(z=0)$. The value at the top is given by humidity at forcing level: $q = q(z=z_a)$.

The turbulent fluxes at the surface are computed by the surface scheme, using the atmospheric variables of the lowest level of the SBL (and not at the usual forcing level at z_a). The exact formulation depends on the surface scheme used. For example, a lot of (1 layer) surface schemes use to compute the surface heat (vapor) flux a formulation with exchange coefficients C_h (including a dependancy with stability), surface and air temperatures (humidity) ($\overline{w'\theta'}(z=0) = C_h(\theta_s - \theta_a)$). With the SBL scheme, θ_a is the temperature at first SBL level, and the stability in the lowest layer in near neutral (because of the proximity to the ground -we used 50cm as first layer-).

There is no need of boundary condition for the TKE at the surface or at the forcing level, as no vertical gradient of TKE is used. The only term that needs special computation near the surface is the Dynamical production term, as it uses a vertical gradient of mean wind.

5.2.5 Turbulence scheme

One turbulence scheme is of course needed in the SBL. A TKE turbulence scheme, developed by Cuxart *et al.* (2000), is chosen here. The mixing length is computed as in Redelsperger *et al.* (2001). Mixing and dissipative length scales are not equal, in order to represent accurately the dissipation modification due to the -1 power law of the turbulence in the SBL. Other turbulence schemes may be used.

A summary of the turbulence scheme is given below:

$$\left\{\begin{array}{lcl} \overline{u'w'} & = & -C_u l\sqrt{e}\frac{\partial U}{\partial z} \\ \overline{w'\theta'} & = & -C_\theta l\sqrt{e}\frac{\partial \theta}{\partial z} \\ \overline{w'q'} & = & -C_q l\sqrt{e}\frac{\partial q}{\partial z} \\ \frac{\partial e}{\partial t} & = & \underbrace{-\overline{u'w'}\frac{\partial U}{\partial z}}_{Dyn.Prod.} + \underbrace{\frac{g}{\theta}\overline{w'\theta'_v}}_{Therm.Prod.} - \underbrace{C_\epsilon\frac{e^{\frac{3}{2}}}{l_\epsilon}}_{Diss.} + \frac{\partial e}{\partial t}_{canopy} \end{array}\right. \tag{5.10}$$

with $C_u = 0.126$, $C_\theta = C_q = 0.143$, $C_\epsilon = 0.845$ (from Cheng *et al.* (2002) constants values for pressure correlations terms and using Cuxart *et al.* (2000) derivation). The mixing and dissipative lengths, l and l_ϵ respectively, are equal to (from Redelsperger *et al.* (2001), $\alpha = 2.42$) :

$$\left\{\begin{array}{lcll} l & = & \kappa z/[\sqrt{\alpha}C_u\phi_m^2(z/L_{MO})\phi_e(z/L_{MO})]^{-1} & \\ l_\epsilon & = & l\alpha^2 C_\epsilon/C_u/(1-1.9z/L_{MO}) & \text{if} \quad \mathrm{z/L_{MO} < 0} \\ l_\epsilon & = & l\alpha^2 C_\epsilon/C_u/(1-0.3\sqrt{z/L_{MO}}) & \text{if} \quad \mathrm{z/L_{MO} > 0} \end{array}\right. \tag{5.11}$$

Where L_{MO} is the Monin-Obukhov length, ϕ_u and ϕ_e the Monin-Obukhov stability functions for momentum and TKE.

5.3 conclusion

A formulation allowing to include prognostic atmospheric layers in offline surface schemes is derived from atmospheric equations. The interest of this approach is to use the advanced physical description of the SBL-canopy interactions that was available only in complex coupled multi-layer surface schemes. The coupling only occurs at the bottom level of the atmospheric model that should be coupled above the surface+SBL scheme. Variables that must be exchanged are: incoming radiation and forcing level air characteristics towards the surface scheme, upward radiative and turbulent fluxes from it. The air layers prognostically simulated with the SBL scheme take into account:

- The term that is related to large-scale forcing (e.g. advection). The detail of this term is not known by the SBL scheme. The evolution of the air characteristics at the forcing level is supposed to take into account all these large-scale forcing terms.
- The turbulent exchanges in the SBL (including in the canopy, if any). They will modify vertical profiles in the SBL. For example, the logarithmic profile of wind is directly induced by these turbulent fluxes, and is well reproduced by the SBL scheme.
- The drag and canopy forcing terms. These are computed for each layer, due to the interaction between air and the canopy. These exchanges have to be modeled by the surface scheme to which the SBL scheme is coupled. In the present paper, for forests, it takes into account the dynamical terms: drag and impact on Tke.

The possible applications of a SBL scheme included in surface schemes can be:

- a more physical determination of standard 2m variables and 10m wind. It can be seen as a drastic increase of the vertical resolution of the atmospheric models near the ground, without the drawback of a smaller time step (that would be necessary to resolve the advection on a very fine grid). Furthermore, because the additional air layers are not handled by the atmospheric model, the SBL scheme (associated to a surface single-layer scheme) is easy to couple with Numerial Weather Prediction or research atmospheric models.
- a better description of the turbulent exchanges and the stability in the SBL, including over complex terrain, for low-level flow and dispersion studies near the surface. As future applications, the dispersion processes in presence of canopy (e.g. chemistry vertical diffusion in urban areas) could then be more accurately simulated.
- the inclusion of the detailed physics of the multi-layer schemes (e.g. the interactions of forest or urban canopy with atmospheric layers in the SBL) into single-layer schemes.

5.4 Appendix: Vertical and temporal discretization

5.4.1 Vertical discretization

The vertical grid for the SBL scheme is a staggered grid (figure 5.3). Historical variables (U, θ, q, e) are defined on 'full' levels. The temporal evolution terms due to canopy obstacles ($\mathrm{Drag_u}$, $\frac{\partial\theta}{\partial t}_{canopy}$, $\frac{\partial q}{\partial t}_{canopy}$, $\frac{\partial e}{\partial t}_{canopy}$) are also located on these full levels. The turbulent fluxes computed by the SBL scheme are computed on the 'flux' levels, staggered between the full levels. The height of full levels is exactly at middle height between half levels. Note that the grid can be (and is most of the time) stretched, with a higher resolution near the ground. The ground is the first flux level (to be consistent with the boundary condition provided: the surface turbulent fluxes). The atmospheric forcing level is the upper full level (to be consistent with the upper boundary condition).

5.4.2 Temporal discretization

For any variable X (U, θ, q or e), the evolution equation can be written as:

$$\frac{\partial X}{\partial t} = \frac{\partial X}{\partial t}(z = z_a) - \frac{\partial F(\frac{\partial X}{\partial z})}{\partial z} + For(X) \tag{5.12}$$

where F is the turbulent flux for $X = [U, \theta, q]$, and For contains canopy forcing terms ($\frac{\partial X}{\partial t}_{canopy}$ for $X = [U, \theta, q, e]$) and other RHS forces for $X = [e]$. Note that the turbulent flux terms F depend formally on the vertical derivative of the variable ($\frac{\partial X}{\partial z}$) while canopy forces and RHS TKE forces depend on the variable itself (X).

In order to satisfy the stability of the SBL scheme at large time-steps, an implicit solving is performed. If the coupling at the atmospheric level is explicit, the atmospheric forcing is not modified in the current time-step by the SBL and surface schemes (i.e. $\frac{\partial X}{\partial t}(z = z_a)$ does not change during the SBL solving). Of course, the atmosphere will further evolve in response to the turbulent SBL fluxes (through the atmospheric model turbulence parameterization). In these conditons, the SBL implicit solving writes:

$$\frac{X^+ - X^-}{\Delta t} = \frac{\partial X}{\partial t}^- (z = z_a) - \frac{\partial F}{\partial z}^- - \frac{\partial \frac{\partial F}{\partial z}}{\partial \frac{\partial X}{\partial z}}^- \times \left(\frac{\partial X}{\partial z}^+ - \frac{\partial X}{\partial z}^- \right) + For^- + \frac{\partial For}{\partial X}^- \times (X^+ - X^-) \tag{5.13}$$

Where Δt is the time step, $^-$ subscript stands for previous time-step variable (known), and $^+$ subscript for the future time-step variable (which one seeks to calculate). Such an implicit scheme leads to a linear system linking all variables at each level to those from the levels below and above (due to the vertical gradient at instant $^+$). This system is tridiagonal, and easy to solve numerically.

5.4.3 Implicit coupling with the atmospheric model

It may be necessary in some atmospheric models (essentially due to very long time steps - half an hour- and the turbulence scheme used in the atmospheric model) to couple implicitly the surface (including the SBL scheme here) and the atmosphere. First RHS term in Equation 5.13 is now equal to $[X^+_{(z=z_a)} - X^-_{(z=z_a)}]/\Delta t$. The atmospheric variable at time $^+$ is modified by the surface flux at the forcing level. It is formalized by

Best *et al.* (2004) : $X^+_{(z=z_a)} = A \times F^+_{(z=z_a)} + B$ (where A and B are known). Therefore, Equation 5.13, in case of implicit coupling with the atmosphere, writes:

$$\begin{aligned}\frac{X^+ - X^-}{\Delta t} = & \frac{B - X(z=z_a)^-}{\Delta t} + \frac{A}{\Delta t} \times \left\{ F^-_{(z=z_a)} + \frac{\partial F}{\partial(\frac{\partial X}{\partial z})}^-(z=z_a) \times \left(\frac{\partial X}{\partial z}^+(z=z_a) - \frac{\partial X}{\partial z}^-(z=z_a) \right) \right\} \\ & - \frac{\partial F}{\partial z}^- - \frac{\partial \frac{\partial F}{\partial z}}{\partial \frac{\partial X}{\partial z}}^- \times \left(\frac{\partial X}{\partial z}^+ - \frac{\partial X}{\partial z}^- \right) + For(X)^- + \frac{\partial For}{\partial X}^- \times (X^+ - X^-)\end{aligned} \tag{5.14}$$

This is still a linear system involving variables at future time step at all levels of the SBL scheme, but this system is no longer tridiagonal, because the term $\frac{\partial X}{\partial z}(z=z_a)^+$ (i.e. at upper SBL level) influences directly the variable X^+ at each level. However, such a system is still resolvable, showing the generality of the SBL scheme method proposed here.

Bibliography

[1] S. E. Belcher, N. Jerram, and J. C. R. Hunt. Adjustment of a turbulent boundary layer to a canopy of roughness elements. *J. Fluid Mech.*, 488:369–398, 2003.

[2] M. J. Best, A. Beljaars, J. Polcher, and P. Viterbo. A proposed structure for coupling tiled surfaces with the planetary boundary layer. *J. Hydrometeorol.*, 5(6):1271–1278, December 2004.

[3] T. H. Chen, A. Henderson-Sellers, P. C. D. Milly, A. J. Pitman, A. C. M. Beljaars, J. Polcher, F. Abramopoulos, A. Boone, S. Chang, F. Chen, Y. Dai, C. E. Desborough, R. E. Dickinson, L. Dmenil, M. Ek, J. R. Garratt, N. Gedney, Y. M. Gusev, J. Kim, R. Koster, E. A. Kowalczyk, K. Laval, J. Lean, D. Lettenmaier, X. Liang, J.-F. Mahfouf, H.-T. Mengelkamp, K. Mitchell, O. N. Nasonova, J. Noilhan, A. Robock, C. Rosenzweig, J. Schaake, C. A. Schlosser, J.-P. Schulz, Y. Shao, A. B. Shmakin, D. L. Verseghy, P. Wetzel, E. F. Wood, Y. Xue, Z.-L. Yang, and Q. Zeng. Cabauw experimental results from the project for intercomparison of land-surface parameterization schemes. *J. Clim.*, 10(6):1194–1215, June 1997.

[4] V. Canuto Cheng, Y. and A. Howard. An improved model for the turbulent pbl. *J. Atmos. Sci.*, 59:1550–1565, 2002.

[5] O. Coceal and S. E. Belcher. A canopy model of mean winds through urban areas. *Quart. J. Roy. Meteor. Soc.*, 130:1349–1372, 2005.

[6] P. Bougeault Cuxart, J. and J.-L. Redelsperger. A turbulence scheme allowing for mesoscale and large-eddy simulations. *Q. J. R. Meteorol. Soc.*, 116:1–30, 2000.

[7] J. Deardorff. Efficient prediction of ground temperature and moisture with inclusion of a layer of vegetation. *J. Geophys. Res.*, 83:1889–1903, 1978.

[8] R. Hamdi and V. Masson. Inclusion of a drag approach in the town energy balance (teb) scheme: Offline 1d evaluation in a street canyon. *J. Appl. Meteorol. Climatol.*, 47(10):2627–2644, October 2008.

[9] M. Kanda and M. Hino. Organized structures in developing turbulent flow within and above a plant canopy, using a large eddy simulation. *Bound.-Layer Meteorol.*, 68:237–257, 1994.

[10] Hiroaki Kondo, Yutaka Genchi, Yukihiro Kikegawa, Yukitaka Ohashi, Hiroshi Yoshikado, and Hiroshi Komiyama. Development of a multi-layer urban canopy model for the analysis of energy consumption in a big city: Structure of the urban canopy model and its basic performance. *Bound.-Layer Meteorol.*, 116:395–421, 2005. 10.1007/s10546-005-0905-5.

[11] S. Manabe. Climate and the ocean circulation 1. the atmospheric circulation and the hydrology of the earths surface. *Mon. Weather Rev.*, 97:739–774, 1969.

[12] Alberto Martilli. Numerical study of urban impact on boundary layer structure: Sensitivity to wind speed, urban morphology, and rural soil moisture. *J. Appl. Meteorol.*, 41(12):1247–1266, December 2002.

[13] V. Masson. Urban surface modeling and the meso-scale impact of cities. *Theor. and Appl. Clim.*, 84:35–45, 2006. 10.1007/s00704-005-0142-3.

[14] J. Noilhan and S. Planton. A simple parameterization of land surface processes for meteorological models. *Mon. Weather Rev.*, 117(3):536–549, 1989.

[15] H. Park and S. Hattori. Modeling scalar and heat sources, sinks, and fluxes within a forest canopy during and after rainfall events. *J. Geophys. Res.*, 109:D14 301, 2004.

[16] E. G. Patton, K. J. Davis, M. C. Barth, and P. P. Sullivan. Decaying scalars emitted by a forest canopy - a numerical study. *Bound.-Layer Meteorol.*, 100:91–129, 2001.

[17] E. G. Patton, P. P. Sullivan, and C.-H. Moeng. The influence of a forest canopy on topdown and bottom-up diffusion in the planetary boundary layer. *Q. J. R. Meteorol. Soc.*, 129:1415–1434, 2003.

[18] J. Polcher, B. McAvaney, P. Viterbo, M. A. Gaertner, A. Hahmann, J. F. Mahfouf, J. Noilhan, T. Phillips, A. Pitman, C. A. Schlosser, J. P. Schulz, B. Timbal, D. Verseghy, and Y. Xue. A proposal for a general interface between land surface schemes and general circulation models. *Glob. and Planet. Change*, 19(1-4):261–276, December 1998.

[19] J.-L. Redelsperger, F. Mahe, and P. Carlotti. A simple and general subgrid model suitable both for surface layer and free-stream turbulence. *Bound.-Layer Meteorol.*, 101:375–408, 2001.

[20] A. Robock, K. Y. Vinikov, C. A. Schlosser, N. A. Speranskaya, and Y. Xue. Use of midlatitude soil moisture and meteorological observations to validate soil moisture simulations with biosphere and bucket models. *J. Clim.*, 8:15–35, 1995.

[21] R. Shaw and U. Schumann. Large-eddy simulation of turbulent flow above and within a forest. *Bound.-Layer Meteorol.*, 61:119–131, 1992.

[22] S. Shen and M. Y. Leclerc. Modelling the turbulence structure in the canopy layer. *Agric. and For. Meteorol.*, 87:1–84, 1997.

[23] E. Simon, F. X. Meixner, L. Ganzeveld, and J. Kesselmeier. Coupled carbon-water exchange of the amazon rain forest, i. model description, parameterization and sensitivity analysis. *Biogeosciences*, 2(3):231–253, 2005.

[24] H. Sun, T. L. Clarka, R. B. Stulla, and Black T. A. Two-dimensional simulation of airflow and carbon dioxide transport over a forested mountain part i: Interactions between thermally-forced circulations. *Agric. and For. Meteorol.*, 140:338–351, 2006.

[25] Z. Xinmin, Z. Ming, S. Bingkai, and W. Hanjie. Study on a boundary-layer numerical model with inclusion of heterogeneous multi-layer vegetation. *Adv. in Atmos. Sci.*, 16:431–442, 1999.

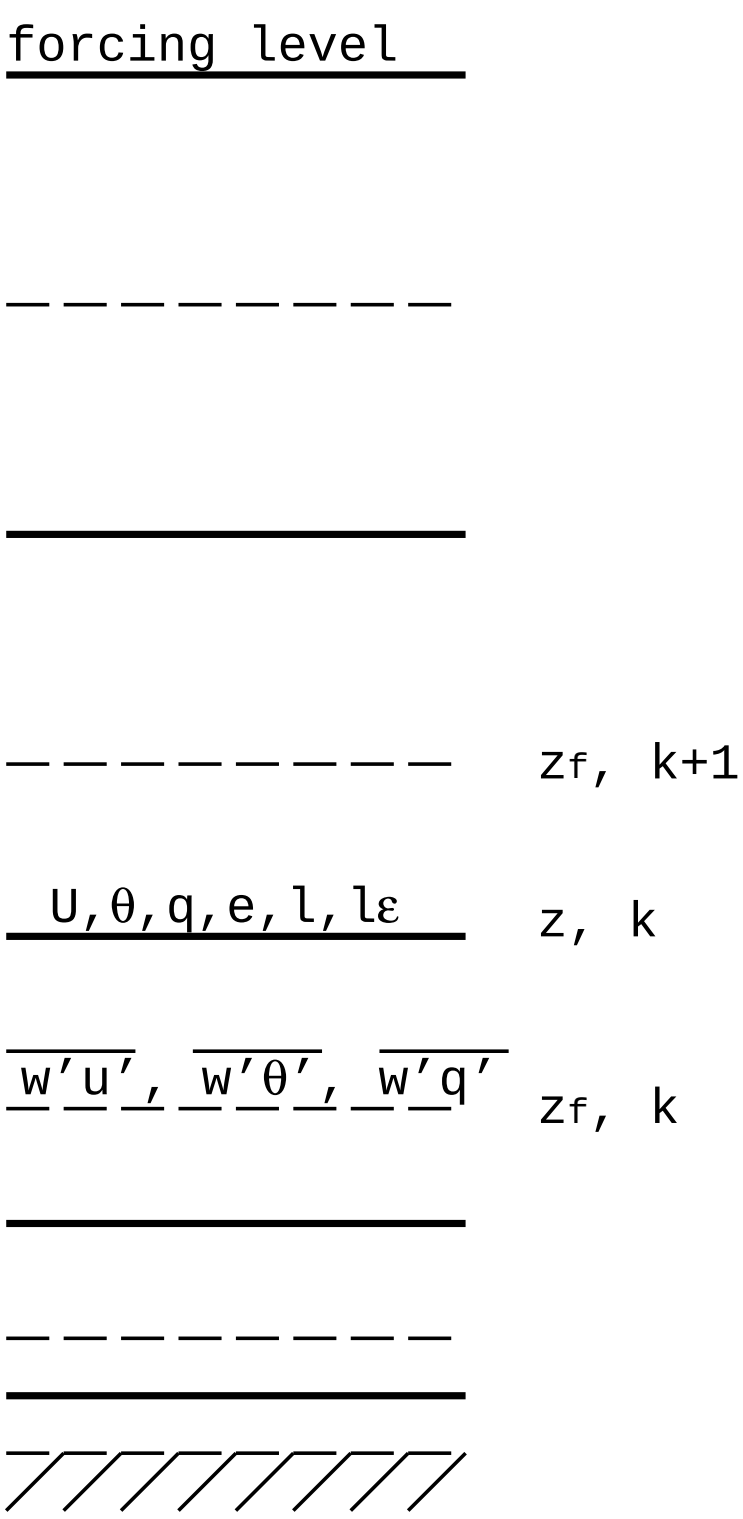

Figure 5.3: Schematic view of the vertical discretization for the SBL scheme. Plain lines are full levels. Dotted lines are flux levels.

Chapter 6

Chemistry and aerosols

Contents

6.1 Dust aerosols

Dust is mobilized from dry desert surfaces when the wind friction speed reaches a threshold wind friction speed of approximately 0.2 m/s. Dust is an important aerosol with annual global emissions ranging from 1000 to 3000 $Tg\ yr^{-1}$ and average global load around 10-30 Tg (Zender *et al.* (2004)).
Dust is mobilized by two related processes called saltation and sandblasting. Saltation is the horizonal movement of soil grains in a turbulent near surface layer. Sandblasting is the release of fine dust when the saltating grains hit the surface. Several papers document these two processes. (Marticorena and Bergametti (1995) and references therein describe the physics of saltations, and Shao *et al.* (1993) describe the physics of sandblasting.

6.1.1 Implementation in the Externalized surface

The dust fluxes are calculated using the Dust Entrainment And Deposition (DEAD) model (Zender *et al.* (2003)). This model is based on Marticorena and Bergametti (1995). The dust fluxes are calculated consistently with the ISBA soil surface scheme. Table 6.1 gives an overview of the main input to the dust production model.

Table 6.1: ISBA variables used by the dust module

PARAMETER	EFFECT ON DUST EMISSION	REFERENCE
wind friction speed	Increase emissions	Marticorena and Bergametti (1995)
Soil moisture	Inhibit emissions	Fecan *et al.* (1999)
Vegetation fraction	Inhibit emissions	Marticorena and Bergametti (1995)
Surface roughness	Inhibit emissions	Laurent *et al.* (2005)
Surface texture	Soil sizes $> 50\mu m$ increase saltation flux	Iversen and White (1982)

6.1.2 Features of the model

Emission process

The production of desert aerosols follows in fact the sandblasting process following the bombing of the aggregates present at the surface by particles in saltation (Figure 6.1). These processes depend on both weather conditions and surface states. Indeed, the kinetic energy of the grains caused by saltation is used in shocks induced by these particles, when they fall to the ground to release and eject fine particles constituting aggregates (Gillette and Goodwin (1974), Gomes *et al.* (1990)). The resistance to wrenching, concerns soil properties like the gravity force and the inter-particle forces. Moreover, emission of aerosols is a threshold phenomenon: it occurs only when the wind friction force exerted on soil grains becomes greater than the forces that maintain them to the ground. When this threshold is exceeded, the soil grains start moving horizontally. The smallest particles can be suspended in the atmosphere and constitute the desert aerosol. The production intensity of fine particles thus depends on the ratio between the transfered kinetic energy flow and the cohesion forces of the particles forming the aggregates.

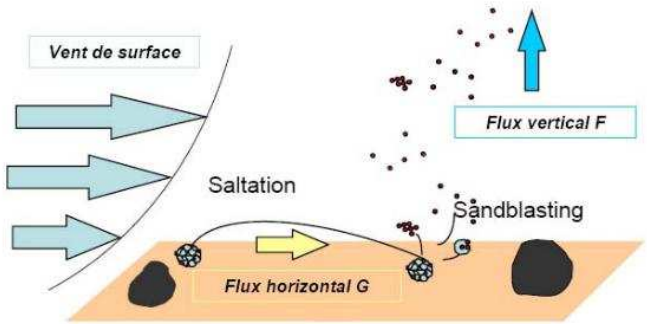

Figure 6.1: illustration of the two main processes involved in the emission of aerosols desert (saltation and sandblasting) when the erosion threshold is exceeded.

Once the particle is injected into the atmosphere, the forces to which it is subjected will control its suspension. It is generally accepted, given the balance of forces, that only particles with a diameter less than about 20 µm can be transported (Nickling (1994)). Those fine particles, named aerosols, constitute the main part of the vertical flow of desert aerosol (F). This vertical flow is defined as the mass of particles crossing per unit of time a unitary surface parallel to the surface.

Parameterization of the friction velocity

Wind is the driving force in the aerosols desert generating process. The ground surface opposes the air flow and slows the air mass at its base. The surface wind is very sensitive to changes in surface characteristics at small scale. These changes may be due, for example, to the presence of vegetation or rocks. In the first few meters of the atmosphere, a surface boundary layer (CLS) develops, in which the horizontal component of the wind speed has a vertical gradient whose intensity depends on the ability of the soil surface to slow the flow (Figure 6.2). For a laminar flow over a horizontal surface, the shear constraint (τ) exerted by the wind on the surface is connected to the vertical gradient of the wind speed (U) by:

$$\tau = \mu \frac{\partial U}{\partial Z} \tag{6.1}$$

Where is the air dynamic viscosity coefficient and Z the height above the ground.

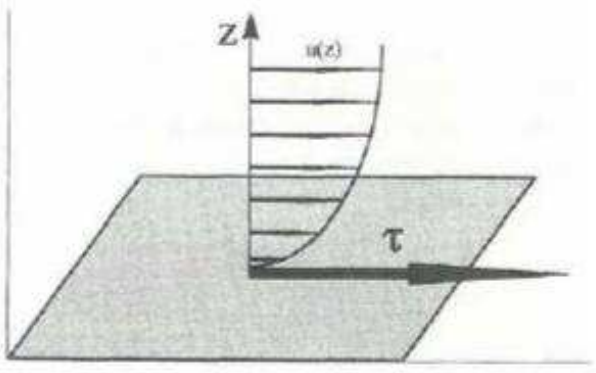

Figure 6.2: Representation of the effect of soil on the airflow and of the shear stress τ exerted by the flow on the ground.

The shear constraint can also be expressed in terms of friction wind speed U_*, which is usually the physical quantity used to quantify friction forces exerted by wind on a surface:

$$\tau = \rho_a U_* \tag{6.2}$$

Where ρ_a is the air density. Under conditions of thermal neutrality, U_* can be determined from the wind speed U at a height z from the ground and the height of aerodynamic roughness (Z_0) using a wind speed logarithmic profile (Priestley (1959):

$$U(Z) = \frac{U_*}{\kappa} \ln(\frac{z}{Z_0}) \tag{6.3}$$

Where $\kappa = 0.4$ is the Von Karman constant.
Physically, Z_0 reflects the length scale of the sink of air momentum induced by the surface roughness. More specifically, Z_0 represents quantitatively the effect of erodible elements (soil grains) or non-erodible ones (rocks or vegetation) on the transfer of wind energy to the surface.

Friction velocity threshold

The resistance of the surface on the motion is represented by the friction velocity threshold U_{*_t}. Indeed, the friction velocity threshold U_{*t} controls both the frequency and the intensity of emissions of aerosols desert, so it is important to parameterize carefully U_{*_t} and give special attention to obtain the quantities it depends on. The erosion threshold is mainly computed from the soil grains diameter D_p, the surface roughness (Rug) and the soil moisture (w). The friction velocity threshold is expressed as:

$$U_{*_t} = U_{*_t}(D_p) \cdot F(Rug) \cdot F(w) \tag{6.4}$$

$U_{*_t}(D_p)$: depends on the friction speed with the diameter of soil grains. $F(Rug)$ and $F(w)$: weighting functions of the influence of roughness and soil moisture. Under idealized conditions, ie for a smooth surface and a loose and dry soil, the friction velocity threshold $U_{*_t}(D_p)$ can be determined using the formulation of Marticorena and Bergametti (1995), which consists in adjusting an empirical expression as a function of the particle diameter. Under standard atmospheric conditions ($\rho_a = 0.00123g \cdot cm^{-3}$, $\rho_p = 2.65g \cdot cm^{-3}$), the friction velocity threshold $U_{*_t}(D_p)$ is given by:

$$U_{*_t}(D_p) = \frac{0.129K}{\left(1.928{Re_{*_t}}^{0.092}\right)^{0.5}} \qquad , 0.03 \leq Re_{*_t} \leq 10 \tag{6.5}$$

$$U_{*_t}(D_p) = 0.129K\left[1 - 0.0858\exp\left(-0.0617\left(Re_{*_t} - 10\right)\right)\right] \, , Re_{*_t} > 10 \tag{6.6}$$

Where $Re_{*_t} = U_{*_t} D_p/\nu$ is the Reynolds number threshold ($\nu = 0.157\ cm^2 s^{-1}$: kinematic viscosity)

and: $K = \left(\frac{\rho_p g D_p}{\rho_a}\right)^{0.5}\left(1 + \frac{0.006}{\rho_p g {D_p}^{2.5}}\right)^{0.5}$

The optimal diameter of the particle is equal to 75 µm.

Influence of soil moisture on friction velocity threshold

The presence of interstitial water between soil grains has the effect of increasing the cohesion of the soil, thus increasing the friction velocity threshold. This increase is integrated in the module DEAD from the parameterization developed by Fecan *et al.* (1999). The proposed equation, expresses the threshlod increase, under wet conditions $U_{*_{tw}}$ compared to that in dry conditions.

$$U_{*_{tw}} = U_{*_t} \qquad for\ w\ <\ w^{'} \tag{6.7}$$

$$U_{*_{tw}} = U_{*_t}\left[1 + 1.21(w - w^{'})^{0.68}\right]^{0.5} \quad for\ w\ >\ w^{'} \tag{6.8}$$

With: w: mass soil moisture (% mass water / mass dry soil). And soil moisture threshold is given by:

$$w^{'} = 0.17(\%clay) + 0.14(\%clay)^2 \tag{6.9}$$

Aerodynamical roughness height

The effects of the internal boundary layer (IBL) on friction velocity threshold, due to the presence of stones, is set in DEAD scheme by Marticorena and Bergametti (1995). The energy distribution is defined in this parameterization as the ratio between the IBL shear friction and the total shear friction of the surface boundary layer (SBL). This ration is given by:

$$f_{eff}(Z_0, Z_{0s}) = 1 - \left[\ln(Z_0/Z_{0s}) / \ln(0.35(10/Z_{0s})^{0.8})\right] \tag{6.10}$$

$Z_{0s} = 33.3 \times 10^{-6}\ m$: roughness length of the smooth surface
$Z_0 = 100.0 \times 10^{-6}\ m$: roughness length of the erodible surface
The friction velocity threshold is expressed as:

$$U_{*_t}(D_p, Z_0, Z_{0s}) = \frac{U_{*_t}(D_p)}{f_{eff}(Z_0, Z_{0s})} \tag{6.11}$$

Surface flux

The horizontal saltation flux (G) is calculated in module DEAD through the White (1979) relationship :

$$G = c \cdot \frac{\rho}{g} {U_*}^3 \left(1 - \frac{U_{*_t}}{U_*}\right)\left(1 + \frac{U_{*_t}}{U_*}\right) \tag{6.12}$$

With $c = 2.61$. The ratio between the vertical flux and the horizontal flux is a function of clay content. For contents between 0 and 20%, this ratio is :

$$\alpha = \frac{F}{G} = 100 \exp\left[(13.4(\%clay) - 6) \times \ln(10)\right] \tag{6.13}$$

In the DEAD module, the fraction of clay is considered constant and is equal to 20%. The final vertical flux is averaged by a pre-determined factor equals to 0.0021 and by the sand fraction.

Mass flux repartition

Upon Alfaro and Gomes (2001) the mass flux is partitioning on the different modes upon the surface friction velocity. More the collision energy is strong more the dust aggregates can be separates into small particles. In surfex, two possibilities are offered. Users can fix the partitioning or the mass flux on the differents modes considered, or compute automatically this partitioning upon the ISBA friction velocity. In this latter case, Alfaro and Gomes (2001) gives the following partitionning:

- u* less than 0.32 $m.s^{-1}$, all particles are emitted in the coarse mode.
- u* at 0.42 $m.s^{-1}$, 63 % of the mass flux is in the bigger coarse mode (D=14.2 μm) , 36 % in the lower coarse mode (D=6.7 μm), and 1 % in the accumulation mode (D=1.5 μ m)
- u* at 0.50 $m.s^{-1}$, 49 % of the mass flux is in the bigger coarse mode (D=14.2 μm) , 43 % in the lower coarse mode (D=6.7 μm), and 8 % in the accumulation mode (D=1.5 μ m)
- u* at 0.66 $m.s^{-1}$, 9 % of the mass flux is in the bigger coarse mode (D=14.2 μm) , 76 % in the lower coarse mode (D=6.7 μm), and 15 % in the accumulation mode (D=1.5 μ m)

Between these friction velocities values, the mass flux partitioning is linearly interpolated.

6.2 Sea Salt emission

Sea salt aerosols are produced as film and jet droplets when bubbles, entrained in the water by breaking waves, disrupt the sea surface (Blanchard, 1983), and at winds speeds exceeding about 9 $m.s^{-1}$, by direct disruption of the wave tops (spume droplets) (Monahan *et al.* (1983)).
Sea Salt emission are parameterized upon the formulation of Vignati *et al.* (2001) (effective source function) or upon a lookup table defined by Schulz *et al.* (2004). Vignati *et al.* (2001) gives a formulation of particles emission upon the wind at 10 meters as:

- $F(R = 0.2\mu m) = 10^{0.09U_{10m}+0.283} particles.cm^{-2}.s^{-1}$
- $F(R = 2\mu m) = 10^{0.0422U_{10m}+0.288} particles.cm^{-2}.s^{-1}$
- $F(R = 12\mu m) = 10^{0.069U_{10m}-3.5} particles.cm^{-2}.s^{-1}$

6.3 Dry deposition of gaseous species

The removal of gases from the atmosphere by turbulent transfer and uptake at the surface is defined as dry deposition. This process enables some chemically reactive gases to be efficiently removed from the atmosphere. Dry deposition is usually parametrized through a deposition velocity v_d, defined by $v_d = -\frac{F_c}{c(z)}$, where F_c is the flux of the considered compound (F_c is assumed constant over the considered range of heights) and $c(z)$ is the concentration at height z (molecules/cm^3). v_d depends on many variables such as wind speed, temperature, radiation, the considered species and the surface conditions. It is commonly described through a resistance analogy often called "Big-Leaf" Model (e.g. Wesely and Hicks (1977)).

$$v_d(z) = \frac{1}{R_a + R_b + R_c}$$

where R_a is the aerodynamic resistance, which is a function of the turbulence in the boundary layer, R_b the quasi-laminar resistance partially controlled by molecular diffusion, and R_c the surface resistance, which combines all the transfer pathways playing a role in the uptake of trace gases by the surface.

Meso-NH surface for dry deposition

As shown fig. 6.3, earth surface is divided into four major parts. On those surfaces calculation of specific parameters are done (friction velocities, surface resistances, ...). The earth splitting is done as follows : town horizontal fraction Masson (2000), inland water and sea surfaces (differents because of their surface temperature) and nature fractions. Nature surface is cut into 9 cover type, which can be reorganized by 'patches' (1 to 9). One 'patch' contains one or several cover types (user choice). These cover types are connected with the Wesely classes of vegetation for the surface resistance data parameters (see table 6.2).

6.3.1 Resistances for dry deposition

Aerodynamic resistance R_a

R_a determines the rate of transport of gases between a given level in the atmosphere and the height of the effective surface sink. It is usually calculated as the bulk aerodynamic resistance to the transfer of momentum : $R_a(z_R) = \frac{1}{\mathbf{C_D V_A}}$, where $\mathbf{C_D}$ is the drag coefficient for momentum (see for example Wesely and Hicks (1977); Sheih *et al.* (1979); Walcek *et al.* (1996)) and $\mathbf{V_A}$ the wind speed (in the following,

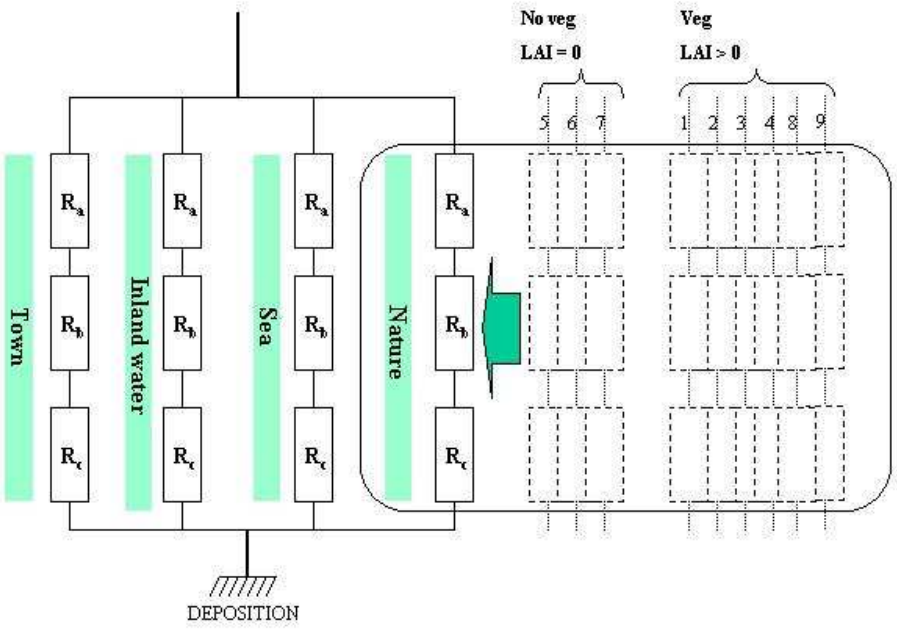

Figure 6.3: *Schematic resistances for dry deposition module in accordance with the surface state. Ra represents the aerodynamic resistance, Rb the quasi-laminar resistance and Rc the surface resistance.*

the parameters which are already used or calculated in the MESO-NH subroutines will be noted in bold characters). The reference height z_R is taken as the lowest atmospheric level in the ISBA scheme.

An alternate way is to use the ISBA calculation of $\mathbf{R_a}$, $\mathbf{R_a(z_R)} = \frac{1}{\mathbf{C_H V_A}}$ which determines the transfer of water vapor. $\mathbf{C_H}$ is then the drag coefficient depending upon the thermal stability of the atmosphere.
Heat drag coefficients are calculated in WATER_FLUX for inland water and sea, in URBAN for artificial land (town) and in ISBA for the other nature cover types or patch. So there is one $\mathbf{R_a}$ different for each different coefficient.
This formulation of $\mathbf{R_a}$ requires an additional term to the quasi-laminar resistance described below.

Quasi-laminar resistance R_b

The component R_b is associated with transfer through the quasi-laminar layer in contact with the surface. R_b quantifies the way in which pollutant or heat transfer differ from momentum transfer in the immediate vicinity of the surface (this is due to the effects of molecular diffusion and the difference of roughness lengths found for momentum and mass transfer). R_b depends on both turbulence characteristics and the molecular diffusion of the considered gas. Transport of a gas through the quasi-laminar layer by molecular diffusion depends on the thickness of the layer, the concentration gradient over the layer and on a diffusion constant, which in turn depends on the radius of the gas molecule and on the temperature. The complexity of vegetation generally limits the accuracy with which the magnitude of this mechanism can be estimated in

Meso-NH nature cover type	Wesely correspondence class
C3 cultures types(low)	(2) Agricultural land
C4 cultures types(hight)	(2) Agricultural land
forest and trees	(4) Deciduous and (5) coniferous forest
grassland	(3) Range land
no vegetation (smooth)	(8) Baren land, mostly desert
no vegetation (rocks)	(11) Rocky open areas with low-growing shrubs
permanent snow and ice	No correspondence
irrigated crops	(9) None forested wetland
irrigated parks gardens or peat bogs	(6) Mixed forest including weet land and (9) none forest wetland

Table 6.2: *Meso-NH vegetative cover type and Wesely connected class for dry deposition calculation*

the field. This resistance can be conveniently written as:

$$R_b = \frac{1}{ku^*} \log(\frac{z_0}{z_c})$$

k is the Von Karman constant and u^* the friction velocity. z_c is the roughness length for the pollutant under investigation (Baldocchi et al. (1987)).
According to Hicks *et al.* (1987), Garrat and Hicks (1973) R_b can be approximated for vegetation and fibrous roughness elements by :

$$R_b = \frac{2}{\mathbf{ku}^*}(\frac{Sc}{Pr})^{2/3}$$

Sc and Pr are the Schmidt and Prandtl numbers respectively. $Pr = 0.72$ and $Sc = \frac{\nu}{D_i}$, with ν the kinematic viscosity of air (0.15 cm^2s^{-1}, 20^o C, p = 1 atm) and D_i the molecular diffusivity of gas i (see table 6.3 for some of these constants). For snow, ice, water and bare soil, R_b can be calculated by (Ganzeveld and Lelieveld (1995)):

$$R_b = \frac{1}{\mathbf{ku}^*}(\frac{Sc}{Pr})^{2/3}$$

This formulation is used for all Meso-NH grid fraction cover with no vegetation (Leaf Area Index = 0), that include artificial land, water and sea.
Definition of friction velocity in MNH is given by : $u^* = \sqrt[4]{< \mathbf{u'w'} >_{\mathbf{xx}}^2 + < \mathbf{v'w'} >_{\mathbf{xx}}^2}$. Where $< u'w' >_{xx}$ and $< v'w' >_{xx}$ represents surface fluxes of horizontal momentum in x and y directions (xx for sea, water, town and nature patch). Molecular diffusivity species/air can be obtain by the knowledge of H_2O/air diffusivity. The coefficient of diffusivity is given by the general formula as:
$D = vl/3 = \frac{0.376kT}{N(MCste)^{0.5}}$
with l mean free path, v mean molecular velocity, k Boltzmann constant, T temperature, N concentration, M molecular mass. So we use for computing molecular diffusivity:

$$D(gaz) = D(H_2O) \left(\frac{M(H_2O)}{M(gaz)} \right)^{0.5}$$

with

$$D(H_2O) = 2.22e-5 + 1.2510^{-7}(T+273) for 193K < T < 0K$$

$$D(H_2O) = 2.22e-5 + 1.4610^{-7}(T+273) for 273K < T < 323K$$

However, these formulations of R_b remain still controversial. Recent results from fields studies indicate that they are not in agreement with experimentally derived results, at least for the transfer of HNO_3 over wheat (Muller *et al.* (1993)). At last, velocity dry deposition is not very sensitive of the choosen definition of R_b (Ganzeveld and Lelieveld (1995)).

Surface Resistance R_c

The surface resistance is the most difficult of the three resistances to describe. R_c values can be obtained from theoretical considerations based for instance on solubility and equilibrium; calculations in combination with simulation of vegetation specific processes, such as accumulation, transfer process through stomata, mesophyll, cuticles, etc ... (Baldocchi *et al.* (1987), Wesely (1989)). The values of R_c are based on measurements of V_d. By determining R_a and R_b from the meteorological measurements, R_c is calculated as the residual resistance. The calculated R_c are then related to surface conditions, time of day, etc ... in order to obtain parametrizations of R_c.

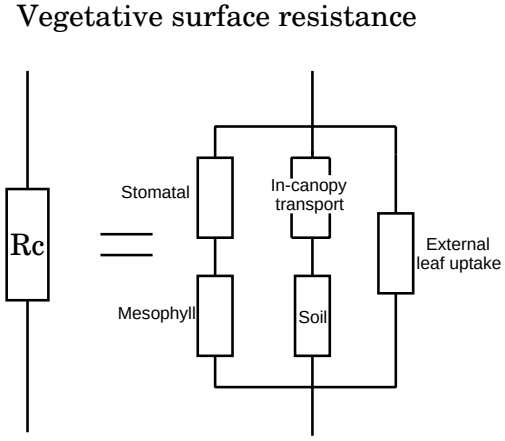

Figure 6.4: *Surface resistance schematic for vegetation.*

R_c is a function of the canopy stomatal resistance R_{stom} and mesophyll resistance R_m, the canopy cuticle or external leaf resistance R_{ext}, the soil resistance R_{soil} and in-canopy resistance R_{inc}, and the resistance to surface waters or moorland pools, R_{wat}, R_{sea} (Erisman and Baldocchi (1994)). In turn, these resistances are affected by leaf area index, stomatal physiology, soil and external leaf surface, pH presence and chemistry of liquid drops and films. In summary, R_c should be calculated as Erisman and Baldocchi (1994) :

- Vegetative surfaces : $R_c = \left(\frac{1}{R_{stom}+R_m} + \frac{1}{R_{inc}+R_{soil}} + \frac{1}{R_{ext}} \right)^{-1}$
- Water surfaces : $R_c = R_{wat}$
- Sea surfaces : $R_c = R_{sea}$
- Bare soil (no vegetation) : $R_c = R_{no}$
- Rock surfaces : $R_c = R_{rock}$
- Snow/ice cover : $R_c = R_{snow}$
- Artificial land : $R_c = R_{town}$

Stomatal and mesophyll resistance R_{stom} and R_m

The stomatal resistance for water vapor is calculated in the ISBA subroutines as

$$\mathbf{R_{stom}} = \frac{\mathbf{R_{smin}}}{\mathbf{F_1 F_2 F_3 F_4 \, LAI}},$$

where $\mathbf{LAI}$ is the leaf area index computed by patch, and F_1, F_2, F_3, F_4 are limiting factors depending on radiation, wetness of soil and temperature. In order to describe the stomatal resistance for another gas, the ISBA $\mathbf{R_{stom}}$ for water vapor should be corrected as followed :

$$R_{stom,x} = \mathbf{R_{stom}} \times \frac{D_{H_2O}}{D_x},$$

D_{H_2O} and D_x are the diffusion coefficients of H_2O and x respectively (Wesely (1989)).

There is not much knowledge on the mesophyll resistance for different gases and the conditions which determine its value. For some gases, such as SO_2 O_3 and NH_3, R_m is experimentally found near zero values (Erisman and Baldocchi (1994)). This is in agreement with the parametrization suggested by Wesely (1989) for the calculation of the mesophyll resistance :

$$R_{mx} = (\frac{H^*}{3000} + 100 f_0)^{-1}$$

In this expression, H^* is the Henry's law constant for the considered gas, f_0 a reactivity factor which determines the rate of reduction of the substance. Two parallel pathways are thus assumed, one for highly reactive gases, the other one for soluble substances. Table 6.3 lists H^* and f_0 for some species (Baer and Nester (1992)).

External leaf uptake R_{ext}

The external leaf uptake can act as an effective sink, especially for soluble gases at wet surfaces. The resistance of the outer surfaces in the upper canopy (leaf cuticular resistance in healthy vegetation) is computed by Wesely (1989), for a dry surface to any gas (x), as :

$$R_{ext.x.dry} = R_{ext}(10^{-5} H^* + f_0)^{-1}$$

In this expression, R_{ext} is given by land category and season in table 6.4, the constants (H^*, f_0) can be found in table 6.3.
The following equation is supposed to give an analytic expression of $\mathbf{R_{ext}}$ in accordance with Wesely table 6.4, and including seasonal variations through the leaf area index $\mathbf{LAI}$:

$$R_{ext} = 6000 - 4000 \tanh(1.6(\mathbf{LAI} - 1.6))$$

These results had been compared with Wesely table in accordance with Méso-NH (ISBA) data of LAI (see fig. 6.3.1).
In case of dew or rain, and according to the same author and Walmsley and Wesely (1996), the equation should be replaced by :

$$R_{ext.x.wet} = [1/(3R_{ext.x.dry}) + (10^{-7} H^* + f_0/R_{extOzone}]^{-1}$$

with

Species	Reactivity factor	Henry's law (M/atm)
Sulfur dioxide	0	$1.6(1 + 2.1\ 10^{-2}/H+)$
Nitric oxide	0	$1.9\ 10^{-3}$
Nitrogen dioxide	0.1	10^{-2}
Nitric acid	0	$5.8\ 10^{6}/H+$
Ozone	1.	$1.5\ 10^{-2}$
Hydrogen peroxide	0	$1.8\ 10^{5}$
Formaldehyde	0	$3.26\ 10^{-4}$
Aldehydes	0	76
Organic acids	0	$1.45\ 10^{-4}$
Organic peroxide	0.25	665
Peroxyacetic acid	0.5	1635
Peroxyacetyl nitrate	0.1	3.6
Other alkanes	0	$1.\ 10^{-3}$
Ethane	0	$1.9\ 10^{-3}$
Ethene	0	$4.9\ 10^{-3}$
Propene	0	$4.7\ 10^{-3}$
Butene and other olefins	0	$1.3\ 10^{-3}$
Toluene	0	0.15
Xylene	0	0.1

Table 6.3: *Reactivity factor and Henry's law constants for different chemical species*

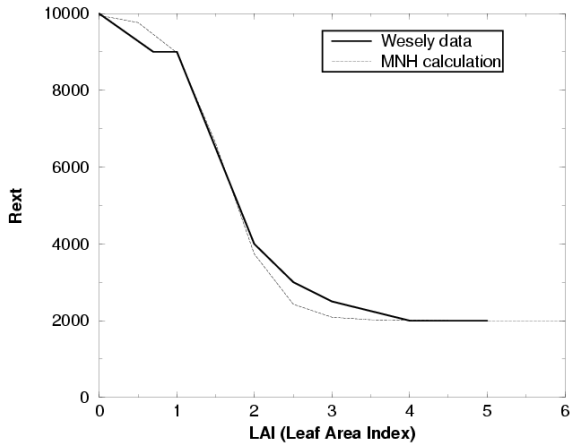

Figure 6.5: $\mathbf{R_{ext}}$ *fonction of* $\mathbf{LAI}$ *(from Wesely table)*

1	2	3	4	5	6	7	8	9	10	11
Midsummer with lush vegetation										
9999	2000	2000	2000	2000	2000	9999	9999	2500	2000	4000
Autumn with unharvested cropland										
9999	9000	9000	9000	4000	8000	9999	9999	9000	9000	9000
Late autumn after frost, no snow										
9999	9999	9000	9000	4000	8000	9999	9999	9000	9000	9000
Winter										
9999	9999	9999	9999	6000	9000	9999	9999	9000	9000	9000
Spring										
9999	4000	4000	4000	2000	3000	9999	9999	4000	4000	8000

Table 6.4: *Input resistances for calculation of external leaf resistance (Wesely,1989) : (1)urban land, (2)agricultural land, (3)range land, (4)deciduous forest, (5)coniferous forest, (6)mixed forest including wetland, (7)water, (8)barren land, mostly desert, (9)nonforested wetland, (10)mixed agricultural and range land, (11)rocky-open areas with low-growing shrubs*

- Rain :

$$R_{extOzone} = (1/(3R_{ext}) + 1/1000)^{-1}$$

- Dew :

$$R_{extOzone} = (1/(3R_{ext}) + 1/3000)^{-1}$$

To apply the same comput for each species we approximate in case of wet soil these formulas by using $R_{extOzone}$ as 3000 s/m .
These formulas should be corrected when surface temperature decreases below -2^{o}C by adding the value $1000\exp(-T-4)$, in order to take into acccount the lesser uptake by surfaces when cold.

In-canopy transport R_{inc}

Deposition to soils under vegetation can be relatively important. Meyers and Baldocchi (1988) found that 20% - 30% of SO_2 was deposited in summer to the soil under a deciduous forest. This transport is due to large-scale intermittent eddies through the vegetation. The corresponding resistance has been parametrized by Erisman and Baldocchi (1994) using data of VanPul and Jacobs (1994) as :

$$R_{inc} = \frac{b\,\mathbf{LAI}\,h}{\mathbf{u}^*}$$

b is an empirical constant estimated at 14 m^{-1}. $\mathbf{LAI} = \mathbf{LAI\_patch}$ is the leaf area index given by patches computed in the GROUND_PARAMn files and $\mathbf{h}$ is the vegetation height which can be calculated as four times the vegetation roughness length (formula of Kondo and Yamazawa (1986), assuming a dense vegetation canopy with similar height).

Soil resitances for surfaces with no vegetation and those under vegetation

Table 6.5 presents a review of soil resistances for SO_2 and O_3 for clay, sand, snow and it is completed with table 6.6, Wesely value for all other vegetation types, town and rock.
For other gases, the resistance can be computed following Wesely (1989) :

$$R_{soilx} = (\frac{H^*}{10^5 R_{soilSO_2}} + \frac{f_0}{R_{soilO_3}})^{-1}$$

According to the same author, this formula should be corrected when surface temperature decreases below -2^{o}C by adding the value :

$$R_{soilx} = R_{soilx} + 1000 \exp(-T - 4)$$

For no vegetation cover soil surface composition (sand, clay) is considered. If it is covered by snow, this formlation will be update by using table 6.5.

$$R_{sandx} = (\frac{H^*}{10^5 R_{sandSO_2}} + \frac{f_0}{R_{sandO_3}})^{-1}$$

$$R_{clayx} = (\frac{H^*}{10^5 R_{claySO_2}} + \frac{f_0}{R_{clayO_3}})^{-1}$$

$$R_{snowx} = (\frac{H^*}{10^5 R_{snowSO_2}} + \frac{f_0}{R_{snowO_3}})^{-1}$$

In this context $R_{no.x}$ for bare ground (no veg.) without snow is the weighted average of R_{sandx} and R_{clayx} as:

$$R_{no.x} = (\frac{\alpha_{sand}}{R_{sandx}} + \frac{\alpha_{clay}}{R_{clayx}})^{-1}$$

with
α_{sand} : percentage of sand in the ground
α_{clay} : percentage of clay in the ground
For all the other type of soil, resistance is calculated with table 6.6 as :

$$\begin{aligned}
R_{rockx} &= (\frac{H^*}{10^5 R_{rockSO_2}} + \frac{f_0}{R_{rockO_3}})^{-1} \\
R_{townx} &= (\frac{H^*}{10^5 R_{townSO_2}} + \frac{f_0}{R_{townO_3}})^{-1} \\
R_{c3x} &= (\frac{H^*}{10^5 R_{c3SO_2}} + \frac{f_0}{R_{c3O_3}})^{-1} \\
R_{c4x} &= (\frac{H^*}{10^5 R_{c4SO_2}} + \frac{f_0}{R_{c4O_3}})^{-1} \\
R_{treex} &= (\frac{H^*}{10^5 R_{treeSO_2}} + \frac{f_0}{R_{treeO_3}})^{-1} \\
R_{grassx} &= (\frac{H^*}{10^5 R_{grassSO_2}} + \frac{f_0}{R_{grassO_3}})^{-1} \\
R_{irrx} &= (\frac{H^*}{10^5 R_{irrSO_2}} + \frac{f_0}{R_{irrO_3}})^{-1} \\
R_{parkx} &= (\frac{H^*}{10^5 R_{parkSO_2}} + \frac{f_0}{R_{parkO_3}})^{-1}
\end{aligned}$$

Type of soil	SO_2	O_3
snow	540 at T <-1^{o}C	2000
	70(2-T) at -1 < T < 1	
sand	1000	200
clay	1000	100

Table 6.5: *Soil resistance*

MNH cover type									
c3	c4	tree	grass	no	rock	snow/ice	irr	park	town
Soil resistance for SO_2									
150	150	500	350	1000	400	no data	0	100	400
Soil resistance for O_3									
150	150	200	200	400	200	no data	1000	700	300

Table 6.6: *Soil resistance for MNH-C decomposition from Wesely table (quasi constant during the year). Values for "snow/ice" and "no" (no veg.) are not used see table 6.5.*

Surfaces resistances for sea and water

For deposition over water surface bodies, the surface resistance can be calculated from the expression recommended by Sehmel (1980) that incorporates wind speed and and air/water partitioning coefficient, rather than from Wesely's tabulated values for water bodies. The surface resistance over water is:

$$R_{waterx} = \frac{2,54.10^{-4}}{H^* \mathbf{T_{water}} \mathbf{u_*}} = Rc_{waterx}$$

$$R_{seax} = \frac{2,54.10^{-4}}{H^* \mathbf{T_{sea}} \mathbf{u_*}} = Rc_{seax}$$

6.3.2 Dry deposition velocity formulation

Artificial land resistance

$$Rglobal^{town} = Ra^{town} + Rb^{town} + Rc^{town}$$

Sea and water resistance

$$Rglobal^{water} = Ra^{water} + Rb^{water} + Rc^{water}$$

$$Rglobal^{sea} = Ra^{sea} + Rb^{sea} + Rc^{sea}$$

Nature final resistance

$$Rglobal^{nature} = \sum_{i=1}^{nvegtype} \left(\frac{\alpha_i}{Ra^{j_{patch}} + Rb^{j_{patch}} + Rc^i} \right)^{-1}$$

with
$i \overset{f}{\longmapsto} f(i) = j_{patch}$ like $i \in [1, nvegtype]$, $f(i) = j_{patch} \in [1, npatch \leq nvegtype]$
and α_i fraction of cover type (9 types)

Dry deposition velocity

Final dry deposition formulation:

$$v_{drydeposition} = \frac{\alpha_{water}}{Rglobal^{water}} + \frac{\alpha_{sea}}{Rglobal^{sea}} + \frac{\alpha_{townmax}}{Rglobal^{town}} + \frac{\alpha_{nature}}{Rglobal^{nature}}$$

where

α_{water} : fraction of water
α_{sea} : fraction of sea
$\alpha_{townmax}$: fraction of town increased
α_{sea} : fraction of nature

Fraction of town has to be increased in order to take account of the non negligible dry deposition on vertical surfaces in artificial area. The increase is done as follows :
$\alpha_{townmax} = \alpha_{town}(1 + 2\frac{H}{L}\,\alpha_{bld})$ with :
α_{town} horizontal fraction of town
H building height
L building caracteristic width
α_{bld} fraction of buildings in artificial areas (only)

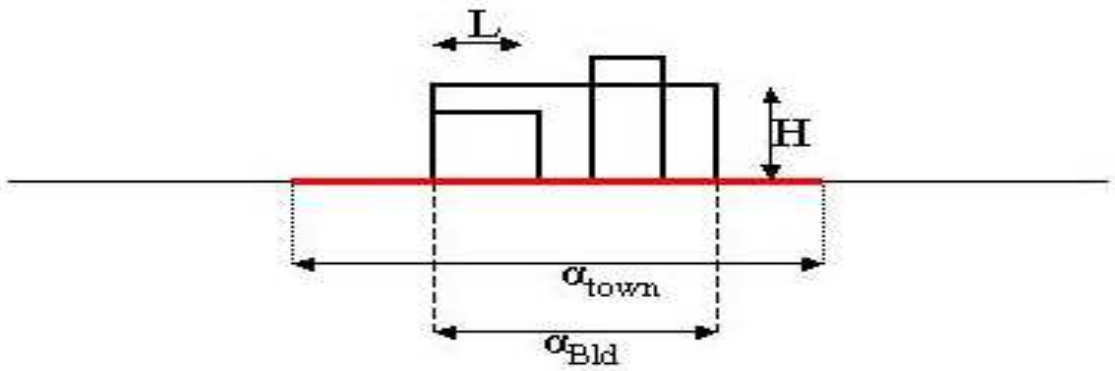

Figure 6.6: *town parameters in MNH (modd_gr_field) to increase fraction of town*

6.4 Dry deposition of aerosols

Brownian diffusivity and sedimentation velocity

Dry deposition and sedimentation of aerosols are driven by the Brownian diffusivity:

$$D_p = \left(\frac{kT}{6\pi\nu\rho_{air}r_p}\right) C_c \tag{6.14}$$

and by the gravitational velocity:

$$V_g = \left(\frac{2g}{9\nu}\left(\frac{\rho_{p,i}}{\rho_{air}}\right) r_p^2\right) C_c \tag{6.15}$$

where k is the Bolzmann constant, T the ambient temperature, ν the air kinematic velocity, ρ_{air} the air density, g the gravitational acceleration, $\rho_{p,i}$ the aerosol density of mode i, and $C_c = 1 + 1.246\frac{\lambda_{air}}{r_p}$ the gliding coefficient. These expressions need to be averaged on the k^{th} moment and mode i as:

$$\hat{X} = \frac{1}{M_{k,i}} \int_{-\infty}^{\infty} X r_p^k n_i (\ln r_p) d(\ln r_p) \tag{6.16}$$

where X represents either D_p or v_g. After integration, we obtain for Brownian diffusivity:

$$\hat{D}_{p_{k,i}} = \tilde{D}_{p_{g,i}} \left[\exp\left(\frac{-2k+1}{2}\ln^2\sigma_{g,i}\right) + 1.246 K n_g \exp\left(\frac{-4k+4}{2}\ln^2\sigma_{g,i}\right)\right] \tag{6.17}$$

with $\tilde{D}_{p_{g,i}} = \left(\frac{kT}{6\pi\nu\rho_{air}R_{g,i}}\right)$
and for gravitational velocity:

$$\hat{Vg}_{p_{k,i}} = \tilde{Vg}_{p_{g,i}} \left[\exp\left(\frac{4k+4}{2}\ln^2\sigma_{g,i}\right) + 1.246 K n_g \exp\left(\frac{2k+4}{2}\ln^2\sigma_{g,i}\right)\right] \tag{6.18}$$

with $\tilde{Vg}_{p_{g,i}} = \left(\frac{2g\rho_{p,i}}{9\nu\rho_{air}} R_{g,i}^2\right)$

Dry deposition

According to Seinfeld and Pandis (1997) and using the resistance concept of Wesely (1989), aerosol dry deposition velocity for the k^{th} moment and mode i is:

$$\hat{v}_{d_{k,i}} = (r_a + \hat{r}_{d_{k,i}} + r_a \hat{r}_{d_{k,i}} \hat{Vg}_{p_{k,i}})^{-1} + \hat{Vg}_{p_{k,i}} \tag{6.19}$$

where surface resistance $\hat{r}_{d_{k,i}}$ is given by

$$\hat{r}_{d_{k,i}} = \left[(\hat{Sc}_{k,i}^{-2/3} + 10^{-3/\hat{St}_{k,i}})\left(1 + 0.24\frac{w_*^2}{u_*^2}\right) u_*\right]^{-1} \tag{6.20}$$

Schmidt and Stokes number are respectively equal to $\hat{Sc}_{k,i} = \nu/\hat{D}_{p_{k,i}}$ and $\hat{St}_{k,i} = (u_*^2/g\nu)\hat{v}_{d_{k,i}}$. One can observe that the friction velocity u_* and the convective velocity w_* depend on meteorological and surface conditions.

6.5 Biogenic VOC fluxes

Biogenic fluxes are parameterize on-line in the surfex code. For a model grid-cell, biogenic fluxes of isoprene and monoterpenes are calculated according to the classical Guenthers approach (Guenther *et al.* (1994, 1995)), using the general formulation :

$$F_x^{cell} = \sum_N \nu_n X.EP_{x,n} X.ECF_{x,n} \tag{6.21}$$

Where Fxcell (in g.m-2.h-1) is the grid-cell averaged biogenic fluxes in which x refers either to isoprene or monoterpenes. ν_n represents the surface fractions occupied by N sub-grid emitting ecosystems (forests,

shrublands, crops, etc). The related emission potential, $EP_{x,n}$, (in $\mu g.m^{-2}.h^{-1}$), accounts for the emission capacity of the underlying nth ecosystem under fixed climatic conditions. According to Guenthers approach, EPiso is standardized to a surface vegetation temperature Ts of 303 K and a photosynthetically active radiation (par) of 1000 $\mu E.m^{-2}.s^{-1}$, whereas EPmono is generally standardized only for Ts =303 K. The temporal evolution of fluxes is given by environmental correction factors ECFx,n calculated from the canopy micro-climates of the N underlying ecosystems. This formulation assumes a simple homogeneous vertical leaf distribution in ecosystem canopies. Over France, emission potential have been pre calculated by GIS treatment of land cover data base (Corine Land Cover), forest composition data for the main tree species (Inventaire forestier national) and species emission factors collected in the literature. The resulting emission potential maps are given at a resolution of 2km and are then interpolated on the MNH grid (during the prepPGD). The environmental correction factor, which accounts for radiation and vegetation temperature variation effects on emissions is calculated using the surface energy budget (calculated by ISBA) and a simple in canopy radiation transfer scheme (similar as ISBA-Ags) for each of the ecosystem (Forest, shrublands, etc) contained in the model grid cells (cf PATCH approach). More details on the method can be found in Solmon *et al.* (2004).

Bibliography

[1] S. Alfaro and L. Gomes. Modeling mineral aerosol production by wind erosion: Emission intensities and aerosol size distributions in source areas. *J. Geophys. Res.*, 106(D16):18075–18084, 2001.

[2] Dennis D. Baldocchi, Bruce B. Hicks, and Pamela Camara. A canopy stomatal resistance model for gaseous deposition to vegetated surfaces. *Atmos. Environ.*, 21(1):91–101, 1987.

[3] J. Erisman and D. Baldocchi. Modelling dry deposition of so2. *Tellus*, 46B:159–171, 1994.

[4] B. Marticorena Fecan, F. and G. Bergametti. Parameterization due to the increase of the aeolian erosion threshold wind friction velocity due to soil moisture for arid and semi-arid areas. *Ann. Geophys.*, 17:149–157, 1999.

[5] L. Ganzeveld and J. Lelieveld. Dry deposition parametrization in a chemistry general circulation model and its influence on the distribution of reactive trace gases. *J. Geophys. Res.*, 100:20999–21012, 1995.

[6] J. Garrat and B. B. Hicks. Momentum, heat and water vapor transfer to and from natural and artificial surfaces. *Quart. J. Roy. Meteor. Soc.*, 99:680–687, 1973.

[7] D. A. Gillette and P. A. Goodwin. Microscale transport of sand-sized soil aggregates eroded by wind. *J. Geophys. Res.*, 79:4080–4084, 1974.

[8] L. Gomes, G. Bergametti, G. Coudé-Gaussen, and P. Rognon. Submicron desert dusts: A sandblasting process. *J. Geophys. Res.*, 95:13927–13935, 1990.

[9] Alex Guenther, C. Nicholas Hewitt, David Erickson, Ray Fall, Chris Geron, Tom Graedel, Peter Harley, Lee Klinger, Manuel Lerdau, W. A. Mckay, Tom Pierce, Bob Scholes, Rainer Steinbrecher, Raja Tallamraju, John Taylor, and Pat Zimmerman. A global model of natural volatile organic compound emissions. *J. Geophys. Res.*, 100(D5):8873–8892, 1995.

[10] Wildermuth M. Guenther, A. Zimmerman P. Natural volatile organic-compound emission rate estimates for u.s. woodland landscapes. *Atmos. Environ.*, 28(6):1197–1210, 1994.

[11] B. Hicks, D. Badolcchi, T. Meyers, R. Hoskers, and D. Matt. A preliminary multiple resistance routine for deriving dry deposition velocities from measured quantities. *Water Air Soil Pollu.*, 36:311–330, 1987.

[12] J. Iversen and B. White. Saltation threshold on earth, mars and venus. *Sedimentol.*, 29:111–119, 1982.

[13] J. Kondo and H. Yamazawa. Measurement of snow surface emissivity. *Bound. Layer. Meteor.*, 34:415–416, 1986.

[14] B. Laurent, B. Marticorena, G. Bergametti, P. Chazette, F. Maignan, and C. Schmechtig. Simulation of the mineral dust emission frequencies from desert areas of china and mongolia using an aerodynamic roughness length map derived from polder/adeos 1 surface products. *J. Geophys. Res.*, 110:D18S04, 2005.

[15] B. Marticorena and G. Bergametti. Modeling the atmospheric dust cycle: 1. design of a soil-derived dust emission scheme. *J. Geophys. Res.*, 100(D8):16415–16430, 1995.

[16] V. Masson. A physically-based scheme for the urban energy budget in atmospheric models. *Bound.-Layer Meteorol.*, 94(3):357–397, March 2000.

[17] E. C. Monahan, C. W. Fairall, K. L. Davidson, and P. J. Boyle. Observed inter-relations between 10 m winds, ocean whitecaps and marine aerosols. *Q. J. R. Meteorol. Soc.*, 109:379–392, 1983.

[18] H. Muller, F. Meixner, G. Kramm, D. Fowler, G. J. Dollard, and M. Possanzini. Determination of hno3 deposition by modified bowen ratio and aerodynamic profile techniques. *Tellus*, 45B:346–367, 1993.

[19] S.A. Nickling, W.G. & Wolfe. The morphology and origin of nabkhas, region of mopti, mali, west africa. *J. Arid Environ.*, 28:13–30, 1974.

[20] C. H. B. Priestley. *Turbulent Transfer in the Lower Atmosphere*. The University of Chicago Press, Chicago, IL, 130 pp., 1959.

[21] M. Schulz, G. de Leeuw, and Y. Balkanski. chapter Sea-salt aerosol source functions and emissions, pages 333–359. Kluwer Academic Publishers, 2004.

[22] J. H. Seinfeld and S. N. Pandis. *Atmospheric Chemistry and Physics: Air Pollution to Climate*. Wiley, 1997.

[23] Y. Shao, M. R. Raupach, and P. A. Findlater. Effect of saltation bombardment on the entrainment of dust by wind. *J. Geophys. Res.*, 98(D7):12719–12726, 1993.

[24] M. Wesely Sheih, C. and B. Hicks. Estimated dry deposition velocities of sulfur over the eastern united states and surrounding regions. *Atmos. Environ.*, 13:1361–1368, 1979.

[25] Fabien Solmon, Claire Sarrat, Dominique Sera, Pierre Tulet, and Robert Rosset. Isoprene and monoterpenes biogenic emissions in france: modeling and impact during a regional pollution episode. *Atmos. Environ.*, 38(23):3853–3865, July 2004.

[26] W. A. J. Van Pul and A. F. G. Jacobs. The conductance of a maize crop and the underlying soil to ozone under various environmental conditions. *Bound.-Layer. Meteorol.*, 63:83–99, 1994.

[27] Elisabetta Vignati, Gerrit de Leeuw, and Ruwim Berkowicz. Modeling coastal aerosol transport and effects of surf-produced aerosols on processes in the marine atmospheric boundary layer. *J. Geophys. Res.*, 106(D17):20225–20238, 2001.

[28] C. Walcek, R. Brost, J. Chang, and M. Wesely. So2, sulfate and hno3 deposition velocities computed using regional landuse and meteorological data. *Atmos. Environ.*, 20:949–964, 1996.

[29] J. Walmsley and M. Wesely. Modification of coded parametrizations of surface resistances to gaseous dry deposition. *Atmos. Environ.*, 30:1181–1188, 1996.

[30] M. Wesely. Parametrizations of surface resistance to gaseous dry deposition in regional scale, numerical models. *Atmos. Environ.*, 23:1293–1304, 1989.

[31] M. L. Wesely and B. B. Hicks. Some factors that affect the deposition rates of sulfur dioxide and similar gases on vegetation. *J. Air. Poll. Control Assoc.*, 27:1110–1116, 1977.

[32] B. R. White. Soil transport by winds on mars. *J. Geophys. Res.*, 84:4643–4651, 1979.

[33] C. S. Zender, R. L. Miller, and I. Tegen. Quantifying mineral dust mass budgets: Terminology, constraints, and current estimates. *Eos Trans. AGU*, 85(48):509–512, 2004.

[34] H. Bian Zender, C. and D. Newman. The mineral dust entrainment and deposition (dead) model: Description and global dust distribution. *J. Geophys. Res.*, 108(D14):4416, 2003.

Part II

LAND COVER: ECOCLIMAP

Chapter 7

Introduction

Ecoclimap is a global database of land surface parameters at 1-km resolution. It is intented to be used to initialize the soil-vegetation-atmosphere transfer schemes (SVATs) in meteorological and climate models. A first version was developed in 2003 (Masson *et al.* (2003)). A second version was developed in 2008 on Europe and is implemented into Surfex. Ecoclimap is designed to satisfy both the Surfex ”tile” approach: each grid box is made of four adjacent surfaces for nature (NAT), urban areas (TWN), sea or ocean (SEA) and lake (WAT), and the Isba ”vegetation types” structure (see tab. 7.1).

ISBA vegetation type (vegtype)	**abbreviation**
bare soil	NO
bare rock	ROCK
permanent snow	SNOW
deciduous broadleaved	TREE
needleleaved	CONI
evergreen broadleaved	EVER
C3 crops	C3
C4 crops	C4
irrigated crops	IRR
temperate grassland	GRAS
tropical grassland	TROG
wetlands, parks and gardens	PARK

Table 7.1: The 12 ISBA vegetation types

It consists first of a global land cover map at 1/120°resolution that is directly read by Surfex. This map proposes a set of classes (or covers) which represent homogeneous ecosystems. Secondly, Surfex interprets these covers in terms of tiles and vegetation types. Land surface parameters (see tab. 7.2 and tab. 7.3 for the list of parameters) depend on tiles, vegetation types and on covers for some of them. A mechanism of aggregation is used to compute the surface parameters for each grid point, according to the horizontal resolution, by combining land covers defined over the 4 tiles and represented by a fraction of the 12 vegetation types (table 7.1) obtained from the 1km resolution land cover map.

In the first version of Ecoclimap, two hundred and fifteen ecosystems were obtained by combining existing

land cover and climate maps, in addition to using Advanced Very High Resolution Radiometer (AVHRR) satellite data. Then, all surface parameters were derived for each of these ecosystems using lookup tables with the annual cycle of the leaf area index (LAI) being constrained by the AVHRR information. The second version uses more recent existing land cover maps. Moreover, ecosystems are now built through an automatic classification process applied on normalized difference vegetation index (NDVI) seven-years time series from SPOT/VEGETATION satellite data, more precise than AVHRR. Existing land cover maps give starting classes which are split in clusters by the classification process. Then, surface parameters are still derived using lookup tables but the annual cycle of the LAI stems from MODIS satellite data. It's possible to run Surfex with LAI values averaged on available years or to choose one particular year.

surface parameter	**abbreviation**	associated tile
leaf area index	LAI	nature (monthly)
height of trees	HT	nature
first soil depth	DG1	nature
root depth	ROOT_DEPTH / DG2	nature
total soil depth	GROUND_DEPTH / DG3	nature
town roughness length	Z0_TOWN	town
albedo of roofs, roads, walls	ALB_ROOF, ALB_ROAD, ALB_WALL	town
emissivity of roofs, roads, walls	EMIS_ROOF, EMIS_ROAD, EMIS_WALL	town
heat capacity of roofs, roads, walls (*3 layers)	HC_ROOF*3, HC_ROAD*3, HC_WALL*3	town
thermal conductivity of roofs, roads, walls (*3 layers)	TC_ROOF*3, TC_ROAD*3, TC_WALL*3	town
width of roofs, roads, walls (*3 layers)	D_ROOF*3, D_ROAD*3, D_WALL*3	town
buildings height	BLD_HEIGHT	town
building shape	WALL_O_HOR	town
building fraction	BLD	town
canyons shape	CAN_HW_RATIO	town
anthropogenic sensible heat fluxes due to traffic, due to factory	 H_TRAFIC, H_INDUSTRY	town
anthropogenic latent heat fluxes due to traffic, due to factory	 LE_TRAFIC, LE_INDUSTRY	town
seeding date	SEED	nature
reaping date	REAP	nature
water supply quantity	WATSUP	nature
flag for irrigation	IRRIG	nature
vegetation fraction	VEG	nature (monthly)
dynamical vegetation roughness length	Z0	nature (monthly)
emissivity	EMIS	nature (monthly)
ratio of z0 for momentum and heat	Z0_O_Z0H	nature

Table 7.2: Surface parameters given by Ecoclimap (1/2)

surface parameter	abbreviation	associated tile
near infrared albedo	ALBNIR_VEG	nature
visible albedo	ALBVIS_VEG	nature
UV albedo	ALBUV_VEG	nature
minimum stomatal resistance	RSMIN	nature
coefficient for the calculation of the surface stomatal resistance	GAMMA	nature
coefficient for maximum water interception storage on capacity on the vegetation	WRMAX_CF	nature
maximum solar radiation usable in photosynthesis	RGL	nature
vegetation thermal intertia coefficient	CV	nature
mesophyll conductance	GMES, GMES_ST	nature (AGS)
ecosystem respiration parameter	RE25	nature (AGS)
cuticular conductance	GC, GC_ST	nature (AGS)
critical normalized soil water content for stress parameterisation	F2I	nature (AGS)
ratio d(biomass)/d(LAI)	BSLAI, BSLAI_ST	nature (AGS)
maximum air saturation deficit tolerated by vegetation	DMAX, DMAX_ST	nature (AGS)
vegetation response type to water stress (true: defensive false: offensive)	STRESS	nature (AGS)
e-folding time for senescence	SEFOLD, SEFOLD_ST	nature (AGS)
minimum LAI	LAIMIN	nature (AGS)
leaf area ratio sensitivity to nitrogen concentration	CE_NITRO	nature (AGS)
lethal minimum value of leaf area ratio	CF_NITRO	nature (AGS)
nitrogen concentration of active biomass	CNA_NITRO	nature (AGS)
root extinction	ROOT_EXTINCTION	nature
ponderation coefficient between root fractions formulations	ROOT_LIN	nature
coefficient for SO2 deposition	SOILRC_SO2	nature
coefficient for O3 deposition	SOILRC_O3	nature
cumulative root fraction	CUM_ROOT_FRAC	nature
biomass/LAI ratio from nitrogen declin theory	BSL_INIT_NITRO	nature

Table 7.3: Surface parameters given by Ecoclimap (2/2)

Chapter 8

Ecoclimap characteristics

8.1 Surface parameters definition

Parameters listed in tab. 7.2 and 7.3 are initialized:

- by cover and vegetation types for LAI, HT, DG (3 layers), SEED, REAP, WATSUP, IRRIG. Indeed, these parameters are not only a feature of a given vegetation type but also of regional considerations;
- by vegetation type for other natural parameters. They are thus viewed as depending on the vegetation type only and not on the location;
- by cover for town parameters: the ”town” tile is not subdivided in types like the ”nature” tile.

Some of the natural parameters receive immediate values whereas others are calculated from some of the former. Tab. 8.1 and tab. 8.2 give modes of obtaining of the natural parameters (lines), by vegetation type (columns). Report to tab. 7.1 to get the meaning of abbreviations of parameters names.
Tab 8.3 delivers values for urban parameters, by type of class. Types of Ecoclimap urban classes come from the Corine Land Cover (CLC) classification that is considered in the two versions of Ecoclimap (see tab. 8.4 for the correspondence).
All these values and formulas date from Ecoclimap-I and come from previous studies. Part of them are mentionned and detailed in Masson *et al.* (2003), other can be found in literature.

8.2 Aggregation method

The aggregation of parameters assumes two aspects:

- the aggregation in ”patchs” of several vegetation types;
- the geographic aggregation linked to the spatial resolution.

Indeed, the Surfex user can choose to work with a number of 1 to 12 patchs of vegetation types. Tab. 8.5 gives the combinations of vegetation types according to the retained number of patches: numbers associated to vegetation types (columns) correspond to patchs to which they are attached, depending on the total number of patches (lines and left column). The Surfex user also chooses his own spatial resolution whose maximum is this of Ecoclimap: 1/120°. When the chosen resolution is coarser, parameters by grid point take aggregated values from the 1-km ones.

The common method for these two kinds of aggregation is nearly linear, apart from the fact that some particular averages are applied to several parameters (see tab. 8.6 for more details) : contributions of every vegetation type to each gridpoint and each patch are weighted and added, next the total value in one point and one patch is brought back to the total number of contributions, that is the total weight, providing the wanted average value of the parameter. As seen in tab. 8.7, weights vary with parameters, depending on the surface on which they make sense.

8.3 Writing of parameters in a latex file

Distribution of classes among tiles and vegetation types, also values of surface parameters are described in a tex file called *class_cover_data.tex*. It can be compiled to get a ps or pdf file that recapitulates all these values in different arrays.

parameter	NO	ROCK	SNOW	TREE	CONI	EVER
LAI	from satellite data by cover and vegetation type					
HT	by cover and vegetation type					
DG1	by cover and vegetation type					
DG2	by cover and vegetation type					
DG3	by cover and vegetation type					
SEED	by cover and vegetation type					
REAP	by cover and vegetation type					
WATSUP	by cover and vegetation type					
IRRIG	by cover and vegetation type					
VEG	0.			0.95	0.95	0.99
GREEN	0.			$MIN(1-e^{-0.5*LAI}, 0.95)$		0.99
Z0	0.1	1.	0.01	HT	HT	HT
EMIS	$VEG*0.97+(1-VEG)*0.94$		1.	$VEG*0.97+(1-VEG)*0.94$		
Z0_O_Z0H	10.					
ALBNIR_VEG	0.3	0.3	0.3	0.25	0.15	0.21
ALBVIS_VEG	0.1	0.1	0.1	0.05	0.05	0.05
ALBUV_VEG	0.06	0.06	0.06	0.525	0.0425	0.038
RSMIN	40.	40.	40.	150.	150.	250.
GAMMA	0.	0.	0.	0.04	0.04	0.04
WRMAXCF	0.2	0.2	0.2	0.1	0.1	0.1
RGL	100.	100.	100.	30.	30.	30.
CV	$2E^{-5}$	$2E^{-5}$	$2E^{-5}$	$1E^{-5}$	$1E^{-5}$	$1E^{-5}$
GMES	0.02	0.02	0.02	0.001	0.001	0.001
GMES_ST	0.003	0.003	0.003	0.003	0.002	0.002
RE25	$3E^{-7}$	$3E^{-7}$	$3E^{-7}$	$3E^{-7}$	$1E^{-7}$	$3E^{-7}$
GC	0.00025	0.00025	0.00025	0.00015	0.	0.00015
GC_ST	0.00015	0.00015	0.00015	0.00015	0.	0.00015
F2I	0.3	0.3	0.3	0.3	0.3	0.3
BSLAI	0.36	0.36	0.36	0.25	0.25	0.25
BSLAI_ST	0.08	0.08	0.08	0.125	0.50	0.25
DMAX	0.1	0.1	0.1	0.1	0.1	0.1
DMAX_ST	0.05	0.05	0.05	0.109	0.124	0.124
STRESS	1.	1.	1.	0.	1.	0.
SEFOLD	90.*XDAY			365.*XDAY		
SEFOLD_ST	150.*XDAY			230*XDAY	365.*XDAY	
LAIMIN	0.3	0.3	0.3	0.3	1.	1.
CE_NITRO	7.68	7.68	7.68	4.83	4.85	4.83
CF_NITRO	-4.33	-4.33	-4.33	2.53	-0.24	2.53
CNA_NITRO	1.3	1.3	1.3	2.	2.8	2.5
ROOT_EXTINCTION	0.961	0.961	0.961	0.966	0.943	0.962
ROOT_LIN	0.05	0.05	0.05	0.05	0.05	0.05
SOILRC_SO2	1000.	400.	100.	500.	500.	200.
SOILRC_O3	400.	200.	3500.	200.	200.	500.
CUM_ROOT_FRAC	$ROOT\_LIN*MIN(\frac{DG}{DG2},1.)+(1-ROOT\_LIN)*\frac{(1-ROOT\_EXT.)^{DG*100.}}{(1-ROOT\_EXT.)^{DG2*100.}}$					
BSL_INIT_NITRO	$1./(CE\_NITRO+CNA\_NITRO+CF\_NITRO)$					

Table 8.1: Lookup tables for Ecoclimap natural parameters, by vegetation type (1/2)

parameter	C3	C4	IRR	GRAS	TROG	PARK
LAI	from satellite data by cover and vegetation type					
HT	by cover and vegetation type					
DG1	by cover and vegetation type					
DG2	by cover and vegetation type					
DG3	by cover and vegetation type					
SEED	by cover and vegetation type					
REAP	by cover and vegetation type					
WATSUP	by cover and vegetation type					
IRRIG	by cover and vegetation type					
VEG	$1 - e^{-0.6*LAI}$			0.95	0.95	0.95
GREEN	$1 - e^{-0.6*LAI}$			$MIN(1 - e^{-0.6*LAI}, 0.95)$		
Z0	$MIN(1., e^{(LAI-3.5)/1.3})$	$MIN(2.5, e^{(LAI-3.5)/1.3})$		$LAI/6$		
EMIS	$VEG * 0.97 + (1 - VEG) * 0.94$					
Z0_O_Z0H	10.					
ALBNIR_VEG	0.3	0.3	0.3	0.3	0.3	0.3
ALBVIS_VEG	0.1	0.1	0.1	0.1	0.1	0.1
ALBUV_VEG	0.06	0.06	0.045	0.08	0.125	0.045
RSMIN	40.	120.	40.	40.	120.	40.
GAMMA	0.	0.	0.	0.	0.	0.
WRMAXCF	0.2	0.2	0.2	0.2	0.2	0.2
RGL	100.	100.	100.	100.	100.	100.
CV	$2E^{-5}$	$2E^{-5}$	$2E^{-5}$	$2E^{-5}$	$2E^{-5}$	$2E^{-5}$
GMES	0.003	0.003	0.003	0.02	0.02	0.02
GMES_ST	0.001	0.009	0.009	0.001	0.006	0.006
RE25	$3E^{-7}$	$2.5E^{-7}$	$3E^{-7}$	$3E^{-7}$	$3E^{-7}$	$3E^{-7}$
GC	0.00025	0.00025	0.00025	0.00025	0.00025	0.00025
GC_ST	0.00025	0.00015	0.00015	0.00025	0.00015	0.00025
F2I	0.3	0.3	0.3	0.3	0.3	0.3
BSLAI	0.06	0.06	0.06	0.36	0.36	0.36
BSLAI_ST	0.06	0.06	0.06	0.08	0.08	0.08
DMAX	0.1	0.1	0.1	0.1	0.1	0.1
DMAX_ST	0.05	0.033	0.033	0.05	0.052	0.05
STRESS	1.	0.	1.	0.	0.	0.
SEFOLD	60.*XDAY			90.*XDAY		
SEFOLD_ST	150.*XDAY					
LAIMIN	0.3	0.3	0.3	0.3	0.3	0.3
CE_NITRO	3.79	7.68	7.68	5.56	7.68	5.56
CF_NITRO	9.84	-4.33	-4.33	6.73	-4.33	6.73
CNA_NITRO	1.3	1.9	1.9	1.3	1.3	1.3
ROOT_EXTINCTION	0.961	0.972	0.961	0.943	0.972	0.943
ROOT_LIN	0.05	0.05	0.05	0.05	0.5	0.5
SOILRC_SO2	150.	150.	0.001	350.	350.	100.
SOILRC_O3	150.	150.	1000.	200.	200.	700.
CUM_ROOT_FRAC	$ROOT\_LIN * MIN(\frac{DG}{DG2}, 1.) + (1 - ROOT\_LIN) * \frac{(1-ROOT\_EXT.)^{DG*100.}}{(1-ROOT\_EXT.)^{DG2*100.}}$					
BSL_INIT_NITRO	$1/(CE\_NITRO + CNA\_NITRO + CF\_NITRO)$					

Table 8.2: Lookup tables for Ecoclimap natural parameters, by vegetation type (2/2)

parameter	**151**	**152**	**155**	**156**	**157**	**158**	**159**	**160**	**161**
ALB_ROOF	0.15								
ALB_ROAD	0.25								
ALB_WALL	0.08								
EMIS_ROOF	0.90								
EMIS_ROAD	0.94								
EMIS_WALL	0.85								
HC_ROOF(1)	$2.11E^6$								
HC_ROOF(2)	$0.28E^6$								
HC_ROOF(3)	$0.29E^6$								
HC_ROAD(1)	$1.94E^6$								
HC_ROAD(2)	$1.28E^6$								
HC_ROAD(3)	$1.28E^6$								
HC_WALL(1)	$1.55E^6$								
HC_WALL(2)	$1.55E^6$								
HC_WALL(3)	$0.29E^6$								
TC_ROOF(1)	1.51								
TC_ROOF(2)	0.08								
TC_ROOF(3)	0.05								
TC_ROAD(1)	0.7454								
TC_ROAD(2)	0.2513								
TC_ROAD(3)	0.2513								
TC_WALL(1)	0.9338								
TC_WALL(2)	0.9338								
TC_WALL(3)	0.05								
D_ROOF(1)	0.05								
D_ROOF(2)	0.4								
D_ROOF(3)	0.1								
D_ROAD(1)	0.05								
D_ROAD(2)	0.1								
D_ROAD(3)	1.								
D_WALL(1)	0.02								
D_WALL(2)	0.125								
D_WALL(3)	0.05								
Z0_TOWN	3.	1.	2.	0.5	2.	0.01	0.1	0.5	1.
BLD_HEIGHT	30.	10.	20.	5.	20.	10.	5.	5.	10.
WALL_O_HOR	1.	0.5	0.5	0.5	1.	0.5	0.5	0.5	1.
BLD	0.5	0.5	0.5	0.1	0.5	0.1	0.1	0.1	0.5
CAN_HW_RATIO	$0.5 * \frac{WALL\_O\_HOR}{1-BLD}$								
H_TRAFIC	20	10.	10.	30.	10.	10.	0.	0.	0.
H_INDUSTRY	10.	5.	20.	0.	20.	0.	0.	0.	0.
LE_TRAFIC	0.	0.	0.	0.	0.	0.	0.	0.	0.
LE_INDUSTRY	0.	0.	0.	0.	0.	0.	0.	0.	0.

Table 8.3: Lookup tables for Ecoclimap urban parameters, by cover

cover name	cover(s) number(s)
dense urban	151
suburban	152,153,154,7
industries and commercial areas	155
road and rail networks	156
port facilities	157
airport	158
mineral extraction and construction sites	159
urban parks	160
sport facilities	161

Table 8.4: Ecoclimap covers numbers for urban classes

patchs	NO	ROCK	SNOW	TREE	CONI	EVER	C3	C4	IRR	GRAS	TROG	PARK
1	1	1	1	1	1	1	1	1	1	1	1	1
2	1	1	1	2	2	2	1	1	1	1	1	1
3	1	1	1	2	2	2	3	3	3	3	3	3
4	1	1	1	2	2	2	3	3	3	4	4	4
5	1	1	1	2	2	2	3	3	4	5	5	4
6	1	1	1	2	2	2	3	3	4	5	5	6
7	1	1	2	3	3	3	4	4	5	6	6	7
8	1	1	2	3	3	3	4	5	6	7	7	8
9	1	1	2	3	4	3	5	6	7	8	8	9
10	1	1	2	3	4	5	6	7	8	9	9	10
11	1	2	3	4	5	6	7	8	9	10	10	11
12	1	2	3	4	5	6	7	8	9	10	11	12

Table 8.5: Combinations of vegetation types according to the retained number of patchs in Surfex

averaging type	name	added element	averaging	affected parameters
ARI	arithmetic	X	Σ/Γ	every but...
INV	inverse	$1./X$	Γ/Σ	RSMIN, CV, HC_ROOF, HC_ROAD, HC_WALL
CDN	inverse of square logarithm	$1./LN(DZ/X)^2$ with DZ height of the first model mass level if available and 20m otherwise	$DZ * e^{-\sqrt{\Gamma/\Sigma}}$	Z0, Z0_TOWN
MAJ	dominant date	no addition: the most frequently occurrent date is selected	none	SEED, REAP

Table 8.6: Averaging types and associated parameters in Ecoclimap. X is a single value of the parameter to average; Σ represents the total of the added weighted elements; Γ represents the total weight of the added weighted elements.

type of weight	name	value	associated parameters
ALL	all	1.	fractions of tiles NAT,TWN,SEA,WAT
NAT	nature	fraction of tile ”nature” (* fraction of added vegtype)	fractions of vegtypes, VEG, Z0, Z0_O_Z0H, EMIS, DG, CUM_ROOT_FRAC, RE25
TRE	tree	fraction of tile ”nature” * (either) fraction of vegtype TREE *(or) fraction of vegtype CONI *(or) fraction of vegtype EVER (non-zero only for trees vegtypes)	HT, DMAX_ST, DMAX
LAI	LAI	fraction of tile ”nature” * fraction of added vegtype * associated LAI value	RSMIN
VEG	fraction of vegetation	fraction of tile ”nature” * fraction of added vegtype * associated VEG value	all remaining natural parameters
TWN	town	fraction of tile ”town”	every town parameter but...
BLD	building	fraction of tile ”town” * fraction of building BLD	ALB_ROOF, EMIS_ROOF, HC_ROOF, TC_ROOF, D_ROOF, ALB_WALL, EMIS_WALL, HC_WALL, TC_WALL, D_WALL, WALL_O_HOR
STR	street	fraction of tile ”town” * (1.-fraction of building BLD)	ALB_ROAD, EMIS_ROAD, HC_ROAD, TC_ROAD, D_ROAD

Table 8.7: Weighting functions and associated parameters in Ecoclimap. Parenthesis indications in the ”value” column refer to what happens in case of calculation defined by patch, ie for all natural parameters but neither for the fractions of tiles and vegetation types nor for the town parameters.

Chapter 9

Ecoclimap-II realization

Ecoclimap-II has been developed on a European field. Its limits are 11W and 62E in longitude and 25N and 75N in latitude.

9.1 The Ecoclimap-II map

9.1.1 The initial map

Existing land cover maps taken into account in this development are:

- Global Land Cover 2000 (GLC2000)[1];
- Corine Land Cover 2000 (CLC2000)[2];

GLC2000 was built from daily SPOT/VEGETATION satellite data for year 2000 (dataset VEGA2000). The spatial resolution is 1/112° (corresponding to $\sim$1.1km) and the projection is latlon. Several regional maps and a global map of 23 classes exist. The latter global map is taken as a basis and classes from available regional maps are added when relevant.
Then, CLC2000 covers only a part of the domain (political Europe) and includes 44 classes. It was realized by photo-interpretation of SPOT and LANDSAT satellite images. The projection is Lambert's azimuthal equivalent and the resolution is 100m. In order to fit Ecoclimap, Corine data are reprojected and brought back to the same resolution. In these conditions, the Corine class number attributed to the pixel at 1-km resolution is this of the most numerous class into the pixel. It's decided to introduce majority classes at more than 70% in the map under construction. It happens that 55% of Corine pixels are kept by this way. So-obtained Corine pixels have priority on GLC information because their contents is better known and supposed to characterize more homogeneous ecosystems.
The resulting map comprises classes from several origins and potentially complementary: their headings and geographic distribution give indications to melt some of them. After a couple of such combinations, a 76-covers map (called **C76** from now on) is finally obtained on the considered area. This map is the reference used for the further classification process. It's thus a mix of GLC2000 and CLC2000.

[1] http://www-gvm.jrc.it/glc2000
[2] http://www.ifen.fr, http://www.eea.eu.int

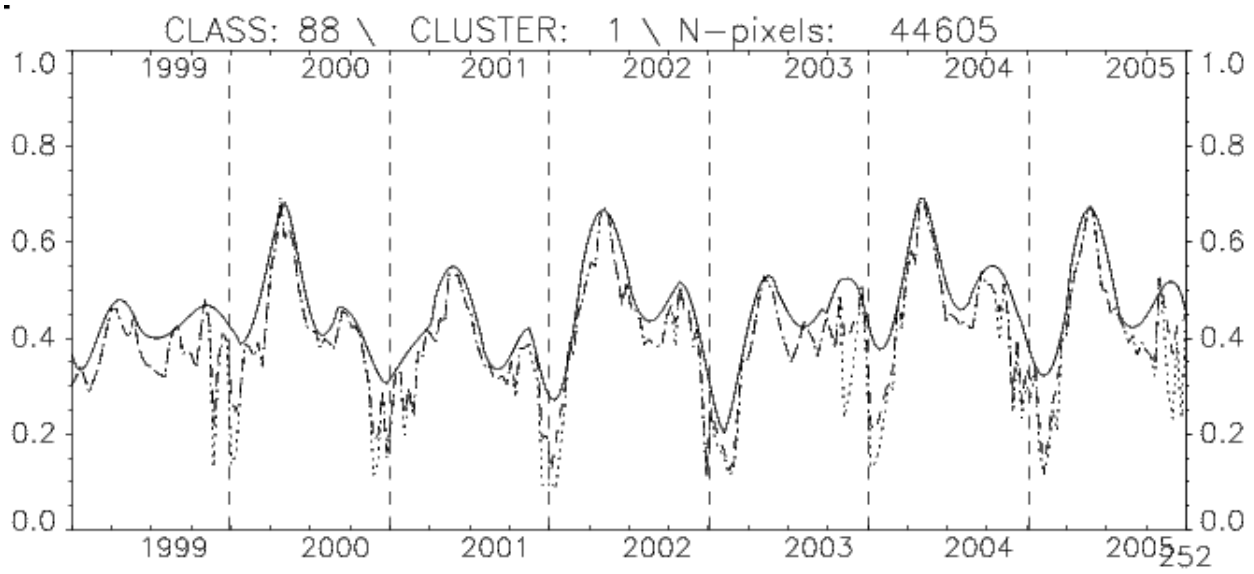

Figure 9.1: Example of NDVI profiles: rough (dotted), masked (dashed), smoothed (solid). (A technical error led to NDVI values overestimated of 0.09 but it has no impact on classification which is relative).

9.1.2 NDVI satellite data

NDVI is deduced from B2 (red) and B3 (near infrared) satellite normalized reflectances (ratios of the reflected over the incoming radiation in each spectral band) according to the formula:

$$NDVI = \frac{B3 - B2}{B3 + B2} \quad (1)$$

This rate usually ranges from 0 to 1. Negative values indicate the presence of snow. Works have shown a correlation between NDVI values and the vegetation photosynthesis activity. The LAI and NDVI annual cycles are supposed to be correlated. In Ecoclimap-I, LAI profiles by cover were obtained from NDVI through the formula:

$$LAI(t) = LAI_{min} + (LAI_{max} - LAI_{min}) * \frac{NDVI(t) - NDVI_{min}}{NDVI_{max} - NDVI_{min}} \quad (2)$$

LAI_{min} and LAI_{max} being set from in-situ measurements or empirically following ISBA simulations. Then, LAI profiles by vegetation types (inside covers) are deduced from these LAI by cover thanks to simple rules, mostly by changing extreme values of the cycle (LAI_{min} and LAI_{max}) depending on the vegetation height in the formula (2), sometimes looking for ”pure” near ”mixte” covers and giving ”pure” LAI to vegetation types in mixte covers. Note that for the NO, ROCK and SNOW vegetation types LAI profiles are equal to zero.

In Ecoclimap-II, NDVI satellite data come from SPOT/VEGETATION[3]. They are decadal, at true 1-km resolution, that is to say that, contrary to AVHRR, one pixel signal is theorically not contaminated by pixels around. Data range from 1999, january to 2005, december.
They are delivered with a mask encoded on 8 bits: 2 bits represent the situations: clear sky, shadow, uncertain, cloud; 1 bit for snow and ice, 1 bit for the land sea mask, and the 4 last bits for the quality of the 4

[3] http://free.vgt.vito.be/, http://www.spot.vegetation.com

satellite radiometric bands. This mask is applied in order to keep clear sky pixels for which the quality of bands B2 (red) and B3 (near infrared) is good. The land/sea/snow distinction is set by to the classification.
The plots of NDVI mean profiles for the covers of the C76 map show that data, even if cleared from aberrant values by the mask, remain noisy. That's why a smoothing is realized at the upper envelope of the rough curve because highest values are supposed better because atmospheric parameters (clouds, water vapor, aerosols) are likely to attenuate the signal reflected to the satellite. Anyway the work on NDVI time series is relative and the exact NDVI values don't matter. The smoothing is based on a 4-degree polynomial. The figure 9.1 shows effects of the mask and smoothing on the mean NDVI signal for a given class. The distance between the rough and the smoothed curves is relative to this mean: the smoothing is done pixel by pixel, filtering out low values entering the mean in the rough case.

9.1.3 The automatic classification process

The classification algorithm is **k-means**. It consists in reading the NDVI profiles of all pixels of one class, then of gathering closest profiles according to the Euclidian distance. Initial center-profiles of clusters are randomly defined and successive iterations are performed: each pixel is linked to the most like-looking center-profile; centers of clusters are recalculated; pixels are linked to the most like-looking center-profile again, and so on. It's thus necessary to fix from the beginning the number of wished clusters by class.
A first map is realized by setting high numbers of clusters by classes, then looking at NDVI profiles and geographic positions of the clusters, and setting new lower numbers of clusters, until a satisfying classification is obtained. This first map comprises 464 classes and is called **C464**.
However, for practical purposes, this method poses several problems:

- When each class of C76 is split into several clusters, the total number of classes increases very fast, rendering reading, interpretation and processing hard;
- it boils down to consider initial classes as frozen and separated each from one another, what can prove false, notably with various initial maps;
- the continuity of analysis is compromised and the quality of NDVI as classification criterion is hard to evaluate. Moreover, numbers of clusters have no option but being arbitrarily posed.

Owing to all these reasons, NDVI is no longer used as a secondary classification criterion: it's admitted that it can rival the initial C76 classes boundaries. Moreover, three quantities are now taken into account during the NDVI classification:

- the Euclidian distance between profiles (still);
- the correlation between profiles, focusing on the shapes of profiles;
- a criterion mixing the two precedents: $\frac{euclidian\ distance}{correlation^2}$, outlining the shapes of profiles without neglecting the distance between them.

The principle is to gather profiles using a threshold for one or the other of the latter criterions. Other conditions come then into the picture:

- the size of classes: for example, the threshold is looser for smaller classes, in order not to encourage the formation of low pixels number classes;
- the NDVI maximum: as NDVI is the expression of vegetation activity, it's not relevant with low-vegetated areas, also low NDVI maximum areas;

- the cover type: water, town and bare soil pixels can't be distinguished through the NDVI, they have to conform the initial nomenclature.

Lastly, comparisons are conducted:

- between profiles of clusters and classes they come from: if the cluster is closer to another class than the one it comes from, it can be linked to the former class;

- families of classes are formed, then splited in a number of clusters equal to the number of classes constituing them, through the automatic classification. Clusters obtained by this totally automatic means are compared to initial classes, in order to verify the robustness of the first method through it consistency with the second one.

At each step, the geographic position, the contents of classes according to the initial nomenclature, NDVI profiles and standard deviations are observed. These operations allow a better approach of the NDVI time series, adapting to the different types of covers and ensuring more mixing and flexibility than if initial boudaries between classes were perfectly respected and if the strict k-means method was applied. At this point, the map under construction comprises 257 classes and is called **C257**.

9.1.4 To the resulting map

Several means are added to complete the new map realization:

- C257 is compared with the map realized by purely respecting the classes boundaries, C464. Every class of each map is splited into 5 clusters through the automatic classification. The distance, the correlation and the standard deviation between each cluster and its mother-class are calculated. Maximum, minimum and median of these quantities are compared for C257 and C464. Results are equivalent whereas the total numbers of classes clearly vary between the two maps.

- C257 is compared to C76. C76 covers are grouped into 14 general types, close to ISBA vegetation types. Then, each C257 class is divided in its contributions to the latter 14 types. Associated NDVI profiles are plotted; geographic distribution of so-obtained clusters is also examined. These operations aim at verifying that mixing of initial classes produce consistent and acceptable results.
  First, given the high resemblance of NDVI profiles of some classes, pixels from a class corresponding to a type (among the 14) that is neither its first nor its second prevailing are moved to a class where the considered type prevails, provided that the resemblance between the two classes is sufficient (on NDVI profiles). The $\frac{distance}{correlation^2}$ criterion is used with a threshold: the moving occurs if the criterion is lower than 1., provided that the correlation is positive and higher than 0.9. This operation allows to considerably reduce the distance between C76 and C257 in terms of nomenclature. It's also verified that geographically gathered parts of land are not contradictory. Results are satisfying. Lastly, on a case by case basis, couple of last reshapings are done. The C257 map becomes at this point **C271** (with 271 classes).

- NDVI profiles are plotted for only part of the pixels of classes. They are plotted for french pixels and on several specialized classes coming from CLC2000: vineyards, orchards, rice fields, olive groves. The goal is to check that those pixels, often melted in larger classes, haven't a very particular behaviour that would have been flooded during the classification. This process leads to add still 2 classes of vineyards. The final resulting map comprises 273 classes and is called **C273**.

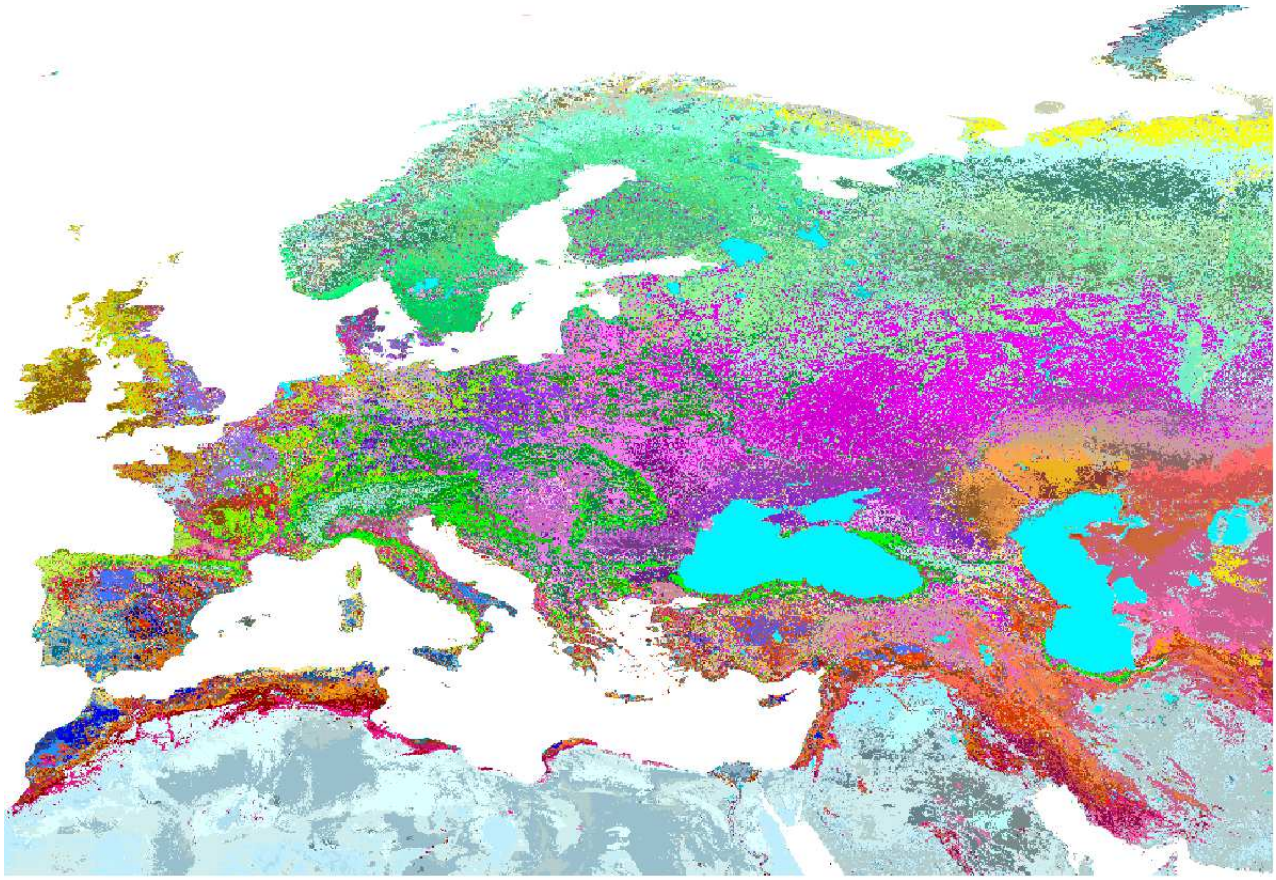

Figure 9.2: Ecoclimap-II C273 map on Europe (one color by class) (latlon projection)

To conclude, the Ecoclimap-II map comprises 273 classes (see fig. 9.2 for an illustration). The classification process combines both an automatic k-means algorithm on NDVI seven-years time series from SPOT/VGT and a more or less leaning constraint provided by an initial map built from existing land cover maps that are CLC2000 and GLC2000. The nomenclature of this map serves to contain the automatic classification and avoid the emergence of incoherent classes.
Note also that the use of seven-years time series data induces that the inter-annual variability is taken into account during the classification process.

9.1.5 Short description of covers

To summarize, it can be said that:

- Distribution of forests over the domain is quite linear and progressive, either on the geographic or on the NDVI profiles sides. The evolution follows a north-east to south-west axis.
- Crops are very regionalized, in areas with well-marked outlines; they doesn't seem to follow a strictly natural logic. Indeed, the human intervention plays a role for these kinds of covers.
- Distribution of shrubs and meadows is intermediate between forests and crops.
- Concerning bare land, snow, inland water and urban areas, resulting classes are very close to those of the initial map C76. Indeed, the NDVI classification doesn't allow to discriminate such types of

covers. However, the analysis of NDVI profiles is efficient to separate pure pixels from mixed ones, and to classify areas functions of the vegetation part of mixed ones. Nevertheless, maintaining such distinctions generates a very important amount of classes. That's why only few of these nuances are really integrated in C273, much with bare land and snow, just a little with inland water, not at all with urban areas. It could be interesting in the future to study the relevance of such distinctions.

Generally, ecosystems are rather homogeneous on large areas in the north continental, and very mixed in the mediterranean perimeter.

For practical purposes, it can be noted that classes are numbered from 301 to 573; sea and oceans present in the European domain take the number 1 from Ecoclimap-I.

9.2 Translation of covers in tiles and vegetation types

The next step is to define every new cover as a linear combination of the 4 tiles (types of surface) and the 12 vegetation types (inside the "nature" tile). The available sources are following:

- (a) Nomenclatures at 1-km resolution from CLC2000, GLC2000 (world, Europe, North Eurasia, Asia, Africa), Ecoclimap-I, C76 (initial map for the classification, see 9.1.1);
- (a)' The nomenclature at 100m resolution from CLC2000;
- (b) Agricultural statistics from Agreste on France, expressed in hectares, available department by department, since 1989. They comprise details about the types of crops;
- (c) a global map about the distribution of C4 vegetation, at 1-degree resolution, provided within the framework of ISLSCP2 and dating from 2003;
- (d) estimates of farm produce by european state, from the FAO;
- (e) data on the maize production by european country in 2003, available on website Maïsadour, in thousands of hectares.

The method is then the following:

- (a) each Ecoclimap-II cover is broken up among classes of considered other maps. Percentages of representation of the second in the first are listed and associated to the titles of the corresponding nomenclatures. The total percentage of the Ecoclimap-II cover in the considered map is indicated (in the case of Corine and GLC regional tiles, only a part of the domain is concerned).
- (b) For AGRESTE, department by department, quantities of forests, meadows, C3 crops, C4 crops, permanent crops and other types of covers are calculated. Values are averaged on the 1999-2006 spell of time. Resulting curves are plotted and overlain with the associated Ecoclimap-II curves, functions of the way of repartition of the covers in the 12 vegetation types.
- (c) The Ecoclimap-II C4 map is resampled at 1-degree resolution in order to compare with the ISLSCP2 map.
- (d) (e) The FAO and Maïsadour estimates haven't been exploited yet.

If the class is included in the CORINE area at more than 50%, the CORINE 100-m information is favoured, instead of 1-km nomenclatures. Amounts of C4, C3, meadows, forests, permanent crops are calibrated thanks to the AGRESTE curves, for well-represented classes on France. The ISLSCP2 map allows to give an idea about the C4 distribution outside France. Note that Agreste provides informations on irrigated surfaces that haven't been exploited yet.

9.3 Initialization of LAI profiles and other parameters

In Ecoclimap, as seen in tab. 8.1 and tab. 8.2, several parameters are initialized at the cover level.

9.3.1 Initialization of heights of trees, ground depths, irrigation and town parameters

First of them, heights of trees are set by using Ecoclimap-I values and the compositions of Ecoclimap-II covers into other nomenclatures (GLC, CLC, Ecoclimap-I). Concerning shrubs classes, a distinction is done between meadows and low-level trees.
Then, the ground depths are set by using exclusively the Ecoclimap-I information, the only available.
These two last parameters would gain by benefiting from other sources of information.
Then, the vegetation type "irrigated crops" is arbitrarily considered as composed of C4 crops only. In Surfex, the modelling of irrigation passes by four parameters (cf tab. 7.2): SEED, REAP, WATSUP and IRRIG. In Ecoclimap-I, by default these variables take constant values that are respectively: 10/05, 01/08, 30 and 1. In Ecoclimap-II, these default values are kept and defined as soon as the "irrigated crops" fraction is not null. It would be worth leaning on these values and precise them according to the classes.
Lastly, town parameters don't change in Ecoclimap-II: Ecoclimap urban classes are the same in the two versions and come directly from the CLC nomenclature.

9.3.2 Initialization of LAI

The LAI (Leaf Area Index) is defined as the ratio of total upper leaf (or needle) surface of vegetation divided by the surface area of the land on which the vegetation grows. The effective LAI seen by the satellite is not the same as the in-situ LAI used by ISBA: the latter is measured on the whole thickness of the vegetation whereas the satellite sees only the top of canopy and deduces the LAI by more or less performing algorithms. It notably often causes saturations for high LAI.

LAI by cover

Two satellite LAI have been examined for Ecoclimap-II: CYCLOPES (SPOT/VEGETATION) and MODIS. Algorithms leading from the satellite bands to the LAI are complex. Land cover maps are included, and the 7 satellite bands (in the case of SPOT) are used. CYCLOPES data range from 2000, January to 2004, December; MODIS data from 2000, March to 2006, December. As for the NDVI (see 9.1.2), a smoothing by pixel at the upper envelop of the LAI profiles is performed. This smoothing is debatable because it makes average LAI values by class very higher than these of rough LAI.
MODIS LAI, CYCLOPES LAI and SPOT/VGT NDVI are plotted by cover so as to be compared. The three products are quite correlated, but MODIS LAI values tend to be higher on forests. Given that MODIS LAI time series are longer and that higher values on forests seem more realistic, MODIS LAI are kept for Ecoclimap-II. Nonetheless, preconceptions relative to the smoothing could lead in the future to review this LAI and its range of values in particular, all the more because tests of smoothing with varying parameters give clearly different results.

Moreover, there is a mask with MODIS data that distinguishes not classed data, built areas, wetlands and marshes, permanent snow, ice and tundra, bare soil or sparse vegetation areas, inland water, missing data. These masked values can be interpolated in the time series, excluded or replaced by zero during the smoothing. It happens that missing data are very numerous at the end of 2000 and 2001, particularly for northern and continental classes. That's why, finally, LAI times series are kept only from 2002, January, in order not to damage average on all years. It appears necessary to replace masked values because of snow, bare soil or water by zero, since LAI are otherwise not realistic (what is seen during the disaggregation coming next). On the contrary, missing and not classed values are interpolated in the limit of 4 successive decades, but those which are not interpolated are ignored during the calculation of means by cover (acceptable insofar as they are not predominant).

Disaggregation of LAI by vegtype inside covers

	fraction of vegetation type									
vegtype	90-100%	80-90%	70-80%	60-70%	50-60%	40-50%	30-40%	20-30%	10-20%	0-10%
CONI	0	6	3	1	3	2	4	4	13	65
TREE	0	2	0	0	1	2	3	6	26	60
EVER	0	0	0	0	0	0	0	0	0	0
GRAS	0	1	4	2	7	10	14	16	17	29
TROG	0	0	0	0	0	0	0	0	0	100
PARK	9	2	0	0	2	0	2	0	3	83
C3	0	1	5	9	9	5	9	5	13	45
C4	0	0	1	1	0	1	0	0	2	95
IRR	0	3	5	3	0	2	3	2	2	81
SNOW	50	0	0	0	0	0	0	0	0	50
NO	3	2	3	4	6	8	6	11	22	35
ROCK	2	0	0	0	0	0	1	5	7	85
total	1	2	3	2	4	4	6	7	15	57

Table 9.1: Percentages of classes (calculated functions of the total numbers of classes by vegetation type) concerned by the fraction (columns) of each of the 12 vegetation types (lines)

nb of vegtypes or tiles n	1	2	3	4	5	6	7	8	9
nb of classes (vegtypes)	13	6	19	44	45	72	44	23	6
nb de classes (tiles)	126	94	53	0	/	/	/	/	/

Table 9.2: Number of classes comprising n vegetation types (second line) or n tiles (third line)

Remains to determine LAI by vegtype inside covers from LAI by cover. Given the complexity of classes in terms of vegetation types composition (see tab. 9.1 and tab. 9.2), an automatic LAI disaggregation technique is welcome. The principle of the applied method is the following:

- LAI 5-years profiles by cover are averaged in order to obtain the annual mean cycles.
- LAI from vegetation types NO, ROCK and SNOW are supposed null and constant.

- In each class, the main vegetation type is put apart. For each of the minority vegetation types, the LAI profile the closest according to the $\frac{distance}{correlation^2}$ criterion is searched, provided that it corresponds to a class where this vegetation type is majority.
- The profile found is taken from the profile of the initial class, weighted by its representation fraction into the class.
- One all minority vegetation types of the classes are thus processed, residual profiles of classes are obtained. Divided by the inverse of the fraction of the majority vegetation type, they are admitted to represent the pure majority profiles, in the classes.
- The whole operation is repeated, replacing initial classes profiles by the previously obtained pure profiles.
- A new set of pure profiles results, for majority vegetation types of classes. Plotting shows that the three profiles, initial (mixte), pure (first extimate), pure (second estimate) differ not much from one another.
- Lastly, 5-years LAI profiles are built by propagating the error between years and the average on the obtained pure profiles.

This method presents two problems:

- The seeking of approached classes only relies on profiles and not on the geographic localisation. Associations of classes coming from totally different climate areas are so expectable.
- The technique of subtracting the secondary profiles to deduce the main profile might produce negative LAI.

The first problem is corrected by introducing two climate maps (Firs on Europe, Koeppe et de Lond on the rest of the world). In the algorithm above, climate proximity is now favoured with the seeking beginning in the most represented climate area, next the second, etc. The second problem is solved by excluding a profile if its subtraction give negative values of LAI. If no suitable profile is found, this which gives the less negative values is linearly transformed in order to keep values just over zero.

This method presents the advantages that it relies only on the LAI profiles of covers, and doesn't create theoritical profiles. It's fast and supple (the longer step is to verify the spatial coherence of the origins of majority and minority profiles) and can be reprocessed in case of modifications of the distribution of classes among the 12 vegetation types. It ensures to diversify vegetation types profiles inside covers and guarantees the exact reconstitution of LAI covers profiles. However, it should be evaluated if the initial approximation between the cover profile and the main vegetation type profile doesn't produce too much bias in the definition of supposed pure profiles. But before, MODIS LAI also need to be validated.

9.4 Study of the discontinuity at the limits of the domain

For practical purposes, if the work area overflows the Ecoclimap-II domain, C273 is completed at its edges by Ecoclimap-I. First, north and major part of west of the domain, there is nearly only sea and ocean (apart from in New-Zemble, but the snow class Ecoclimap-II continues there in the snow class Ecoclimap-I). South and a little west, the boundary is located in the Sahara desert. Except from a possible discontinuity between

bare rock and bare soil, and between very sparse vegetated and desert areas, the impact is so minor. Remains the East to study: from northern Russian tundra to Central Asia deserts, by Russian forests, it's about quite homogeneous areas organized with latitude, what already dulls the discontinuity.
Classes, LAI by class and by vegetation type and vegetation types fractions on both sides are compared. Ecoclimap-II classes generally continue in Ecoclimap-I classes. LAI and fractions are often different, but these discrepancies are rarely enormous.
It's so chosen to begin tests with the straight discontinuity. Then, if the delimitation is too obvious, it will be possible to contemplate a version with a smoothed (but artificial) delimitation.

Chapter 10

Validation elements for Ecoclimap-II

Validation aspects relate to three fields:

- Ecoclimap-II new map has already been quite examined during the processing, through comparisons with other existing land cover maps (GLC, CLC, Ecoclimap-I - see 9.1.3 and 9.1.4). Other tests could be performed, for example a comparison with GlobCover, a global land cover map for the year 2005-2006 using ENVISAT MERIS fine resolution (300m) data, developed by ESA (European Spatial Agency) and distributed by Medias-France.

- Vegetation types fractions have been set in the light of existing land cover map nomenclatures. Other comparisons have been realized with AGRESTE and ISLSCP2 to calibrate values, but also a posteriori with Formosat on a square of 60km at the south-west of Toulouse, France. Formosat describes the land cover, year by year, on this area; the resolution is 20m. This map is produced by the CESBIO[1]. This last comparison gives encouraging results but also reveals the difficulty of different sources to agree: sources are sometimes contradictory, their charasterics and the geographic precision vary and are not necessarily easy to compare. However, the progressive use of more recent sources should allow to still refine this definition. Concerning specialized vegetation types thar are C4 crops, tropical grassland, irrigated crops, a lack of homogeneity inside the covers doesn't allow to get precise fractions. It could be interesting to make a potential new map with covers built by introducing entering informations about such characteristics.

- Difficulties have been met to validate other parameters initialized at the cover level: heights of trees, ground depths, LAI profiles and irrigation parameters. Indeed, complete and reliable sources aren't available. A prospect for the following is thus to find means of validating these quantites. Note again that the organization by covers yields a constraint (especially for irrigation) whose reliance could also be interrogated in the light of such new validating data.

[1] Centre d'Etudes Spatiales de la BIOsphere (spatial study of the biosphere center)

Chapter 11

Conclusion

Ecoclimap-II keeps the same general structure as Ecoclimap-I but several points have changed:

- The new covers relie on a k-means automatic classification process and on recent existing land cover maps (GLC2000, CLC2000);
- The vegetation types fractions and other cover-based parameters are consequently re-initialized, with help from several information sources (AGRESTE, ISLSCP2, land cover maps nomenclatures);
- The LAI profiles by cover come from MODIS satellite data, they are smoothed pixel by pixel;
- The LAI profiles by vegetation type inside covers are built through an original automatic disaggregation process in which only LAI profiles by cover step in;
- LAI profiles are available for the average of 5 years (2002-2006) or for each of these years.

Except from these discrepancies, other surface parameters are still likewise obtained. The geographic and by patch aggregation also remains. Several comparisons with other products have already been done but Ecoclimap-II now needs to be used in order to better qualify improvements and wastes in relation with the first version. Further evolution of the database is considered functions of users returns and of potential newly available validation data.

Bibliography

[1] V. Masson, J.-L. Champeaux, F. Chauvin, C. Meriguet, and R. Lacaze. A global database of land surface parameters at 1-km resolution in meteorological and climate models. *J. Clim.*, 16(9):1261–1282, 2003.

Part III

LAND SURFACE ANALYSIS

Chapter 12

Surface Offline Data Assimilation

Contents

12.1 Introduction

SURFEX Offline Data Assimilation (SODA) is the first implementation of a unified assimilation in SURFEX. The present description is based on the offline version from SURFEX v.8. It is assumed that this version is currently running on your computer, if not, the first step is to install such version before trying to use the SODA scheme. SODA permits the land surface analysis of screen level parameters, soil moisture and vegetation. The screen level analysis relies on a two-dimensional Optimal Interpolation (2D-OI). The soil moisture and/or vegetation analysis rely either on a simplified Extended Kalman Filter or an Ensemble Kalman Filter (EnKF).

12.2 Source code - creation of the binary

SODA is available under the directory $SURFEX_EXPORT/src/ASSIM. Main file is **soda.F90** that performs the various steps of the assimilation : definition of initial perturbed states, reading of fields from SURFEX outputs, writing of fields necessary for the analysis, and finally the surface analysis. The latter being executed by either **assim_nature_isba_oi.F90**, **assim_nature_isba_ekf.F90** or **assim_nature_isba_enkf.F90**.

12.3 Optimal Interpolation soil moisture analysis

Methodology

This soil analysis scheme is based on an local optimum interpolation technique as described in Mahfouf (1991), Giard and Bazile (2000). The analysis increments from the screen-level analysis (2-meter temperature, T_2m and relative humidity, RH_2m) are used to produce increments for the water content given by:

$$\Delta w_s = \alpha_s^T \Delta T_{2m} + \alpha_s^{RH} \Delta RH_{2m} \tag{12.1}$$

and

$$\Delta w_p = \alpha_p^T \Delta T_{2m} + \alpha_p^{RH} \Delta RH_{2m} \tag{12.2}$$

for the superficial volumetric and mean volumetric water content, respectively. The coefficients α_p^T and α_p^{RH} depend on soil texture, increasing as the standard range of variation of soil moisture $\delta w = \delta w_{fc} - \delta w_{wilt}$ (soil water content at field capacity and wilting point, respectively).

12.4 Extended Kalman Filter soil moisture and vegetation analysis

Methodology

The EKF soil moisture analysis used in **SODA** is a point wise data assimilation scheme (Mahfouf *et al.* (2009), Barbu *et al.* (2011, 2014) , Fairbairn *et al.* (2017), Albergel *et al.* (2017)). The analysis update equation of the EKF is:

$$x_a(t_i) = x_f(t_i) + K_i(y_0(t_i) - h_i[x_f]) \tag{12.3}$$

The a, f and o subscripts stand for analysis, forecast and observation, respectively. x is the control vector of dimension N_x, computed at time t_i, that represents the prognostic equations of the LSM M.
y_o is the observation vector of dimension N_y. The Kalman gain matrix K_i is computed at time t_i as:

$$K_i = BH^T(HBH^T + R)^{-1} \tag{12.4}$$

A non-linear observation operator h, enables the extraction of the model counterpart of the observations:

$$y(t_i) = h(x) \tag{12.5}$$

B and R are error covariance matrices characterising the forecast and observations vectors. The cross-correlated terms represent covariances. The operator H (and its transpose H^T) from 12.4 is the Jacobian matrix: the linearized version of the observation operator (defined as N_y rows and N_x columns) that transforms the model states into the observations space. A numerical estimation of each Jacobian element is calculated by finite differences, by perturbing each component x_j of the control vector x by a specific amount δx_j resulting in a column of the matrix H for each integration m:

$$H_{mj} = \frac{\partial y_m}{\partial x_j} \approx \frac{y_m(x + \delta x_j) - y_m}{\delta x_j} \tag{12.6}$$

The background error covariance matrix undergoes an analogous forecast and analysis cycle:

$$B_f(t_i) = M(t_{i-1})B_a(t_{i-1})M^T(t_{i-1}) + Q \tag{12.7}$$

$$B_a(t_i) = (I - K(t_i)H(t_i))B_a(t_i) \tag{12.8}$$

In the forecast step (equation 12.7), the previous analysis, $B_a(t_{i-1})$, is forecast forward in time by the tangent linear of the state forecast model M, and the forecast error covariance matrix Q, is added to account for errors in the model forecast, giving the background error matrix forecast $B_f(t_i)$. The model state analysis decreases the model error, and B is reduced by an analysis step (equation 12.8). The linearization of M is

obtained by the same finite difference method used for H. The control vector evolution from time t_i to time t_{i+1} is then controlled by the following equation:

$$x_f(t_{i+1}) = M_i[x_a(t_i)] \tag{12.9}$$

12.5 Ensemble Kalman Filter soil moisture and vegetation analysis

Although an EnKf analysis is available within SODA (Fairbairn *et al.* (2015)), it is still in consolidation phase.

Bibliography

[1] C. Albergel, S. Munier, D. J. Leroux, H. Dewaele, D. Fairbairn, A. L. Barbu, E. Gelati, W. Dorigo, S. Faroux, C. Meurey, P. Le Moigne, B. Decharme, J.-F. Mahfouf, and J.-C. Calvet. Sequential assimilation of satellite-derived vegetation and soil moisture products using surfex_v8.0: Ldas-monde assessment over the euro-mediterranean area. *Geoscientific Model Development*, 10:3889–3912, 2017.

[2] A. L. Barbu, J.-C. Calvet, J.-F. Mahfouf, C. Albergel, , and S. Lafont. Assimilation of soil wetness index and leaf area index into the isba-a-gs land surface model: grassland case study. *Biogeosciences*, 8:1971–1986, 2011.

[3] A. L. Barbu, J.-C. Calvet, J.-F. Mahfouf, and S. Lafont. Integrating ascat surface soil moisture and geov1 leaf area index into the surfex modelling platform: a land data assimilation application over france. *Hydrol. Earth Syst. Sc.*, 18:173–192, 2014.

[4] D. Fairbairn, A. L. Barbu, J.-F. Mahfouf, J.-C. Calvet, and E. Gelati. Comparing the ensemble and extended kalman filters for in situ soil moisture assimilation with contrasting conditions. *Hydrol. Earth Syst. Sc.*, 19:4811–4830, 2015.

[5] D. Fairbairn, A. L. Barbu, A. Napoly, C. Albergel, J.-F. Mahfouf, and J.-C. Calvet. The effect of satellite-derived surface soil moisture and leaf area index land data assimilation on streamflow simulations over france. *Hydrol. Earth Syst. Sc.*, 21:2015–2033, 2017.

[6] D. Giard and E. Bazile. Implementation of a new assimilation scheme for soil and surface variables in a global nwp model. *Mon. Wea. Rev.*, 128:997–1015, 2000.

[7] J.-F. Mahfouf. Analysis of soil moisture from near surface parameters: A feasibility study. *Journal of Applied Meteorology*, 30:506–526, 1991.

[8] J.-F. Mahfouf, K. Bergaoui, C. Draper, F. Bouyssel, F. Taillefer, and L. Taseva. A comparison of two off-line soil analysis schemes for assimilation of screen level observations. *Journal of Geophysical Research: Atmospheres*, 114(D08), 2009.